Hippo and Sonic Hedgehog signalling pathway modulation of human urothelial tissue homeostasis

Thomas Crighton

PhD

University of York

Department of Biology

November 2020

Abstract

The urinary tract is lined by a barrier-forming, mitotically-quiescent urothelium, which retains the ability to regenerate following injury. Regulation of tissue homeostasis by Hippo and Sonic Hedgehog signalling has previously been implicated in various mammalian epithelia, but limited evidence exists as to their role in adult human urothelial physiology. Focussing on the Hippo pathway, the aims of this thesis were to characterise expression of said pathways in urothelium, determine what role the pathways have in regulating urothelial phenotype, and investigate whether the pathways are implicated in muscle-invasive bladder cancer (MIBC). These aims were assessed using a cell culture paradigm of Normal Human Urothelial (NHU) cells that can be manipulated *in vitro* to represent different differentiated phenotypes, alongside MIBC cell lines and The Cancer Genome Atlas resource.

Transcriptomic analysis of NHU cells identified a significant induction of *VGLL1*, a poorly understood regulator of Hippo signalling, in differentiated cells. Activation of upstream transcription factors PPARγ and GATA3 and/or blockade of active EGFR/RAS/RAF/MEK/ERK signalling were identified as mechanisms which induce VGLL1 expression in NHU cells. Ectopic overexpression of VGLL1 in undifferentiated NHU cells and MIBC cell line T24 resulted in significantly reduced proliferation. Conversely, knockdown of VGLL1 in differentiated NHU cells significantly reduced barrier tightness in an unwounded state, while inhibiting regeneration and increasing cell cycle activation in scratch-wounded cultures. A signalling pathway previously observed to be inhibited by VGLL1 function, YAP/TAZ, was unaffected by VGLL1 manipulation. In MIBC, overexpression of *VGLL1* was observed in a subset of differentiated tumours associated with significantly reduced survival, indicative of dysregulated VGLL1 function.

This study reveals a novel Hippo pathway-independent function of VGLL1, with the protein observed to play an important role in regulating urothelial tissue homeostasis. Consequently, these findings contribute to the current understanding of how dysregulation of tissue homeostasis can facilitate MIBC progression.

Contents

List of figures

List of tables

Acknowledgements

I would first like to thank my supervisors Prof. Jenny Southgate and Dr. Simon Baker for their excellent guidance, encouragement and imparting of wisdom throughout my study. Additional thanks must also go to my thesis advisory panel members Dr. Gareth Evans and Dr. Will Brackenbury, who took the time to evaluate my work and provided a useful sounding board for my ideas throughout my project.

I would like to express my gratitude to all the staff and students of the Jack Birch Unit who ensured that my time of study was an enjoyable one, with special mentions for Dr. Jo Pearson and Dr. Andrew Mason who were an invaluable help to me when getting to grips with the steep learning curves of molecular biology and bioinformatics.

I am extremely grateful for the project funding bestowed by York Against Cancer and hope that I have at least partly repaid their trust in me.

Most of all I would like to thank my parents, step-parents and little brother, as without their endless love and support this would not have been possible.

Author's Declaration

I declare that this thesis is a presentation of original work and I am the sole author. This work has not previously been presented for an award at this, or any other, University. All sources used in this thesis are acknowledged as references.

T. Crighton

November 2020

1. Introduction

1.1 The urinary system

The mammalian urinary tract is a contiguous system consisting of two kidneys, two ureters, a bladder and urethra (Figure 1.1). Urine is produced in the kidneys through the process of glomerular filtration, where excess water and waste product (urea) is filtered from circulating blood. This is subsequently transported from the kidneys to the bladder (via the renal pelvis and ureters) through peristaltic contractions (reviewed by Hickling *et al.,* 2015). The physiological function of the bladder is to store urine at low pressure until the point of voiding (secretion of urine through the urethra; reviewed by Elbadawi, 1996).

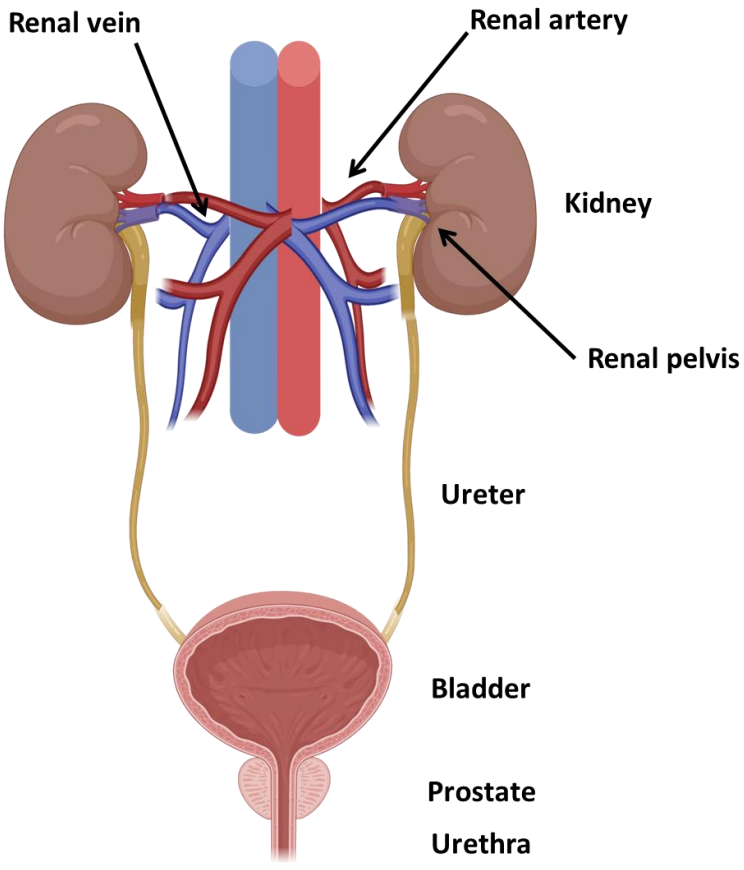

Figure 1.1: Diagram of the male mammalian urinary system

Image adapted from the National Institute of Diabetes and Digestive and Kidney Diseases, 2014.

The regions of the urinary tract ranging from the renal pelvis to the proximal urethra are lined by a unique epithelial tissue known as the urothelium. This is separated from the underlying connective tissue of the lamina propria by a laminin and collagen-based basement membrane. The lamina propria is vascularised and innervated, while also containing stromal cell types such as smooth muscle cells and the extracellular matrix (ECM)-producing fibroblasts (Dixon *et al.*, 1983). The lamina propria is surrounded by smooth muscle bundles which orchestrate the flow of urine through each section of the system (Fig. 1.2). Despite the urothelium of each organ being highly similar to one another morphologically, the bladder and ureters are in fact derived from different embryological derivations, with the bladder arising from the urogenital sinus (endoderm) while the ureters arise from the intermediate mesoderm (Saxén *et al.,* 1987; Baskin *et al.,* 1996).

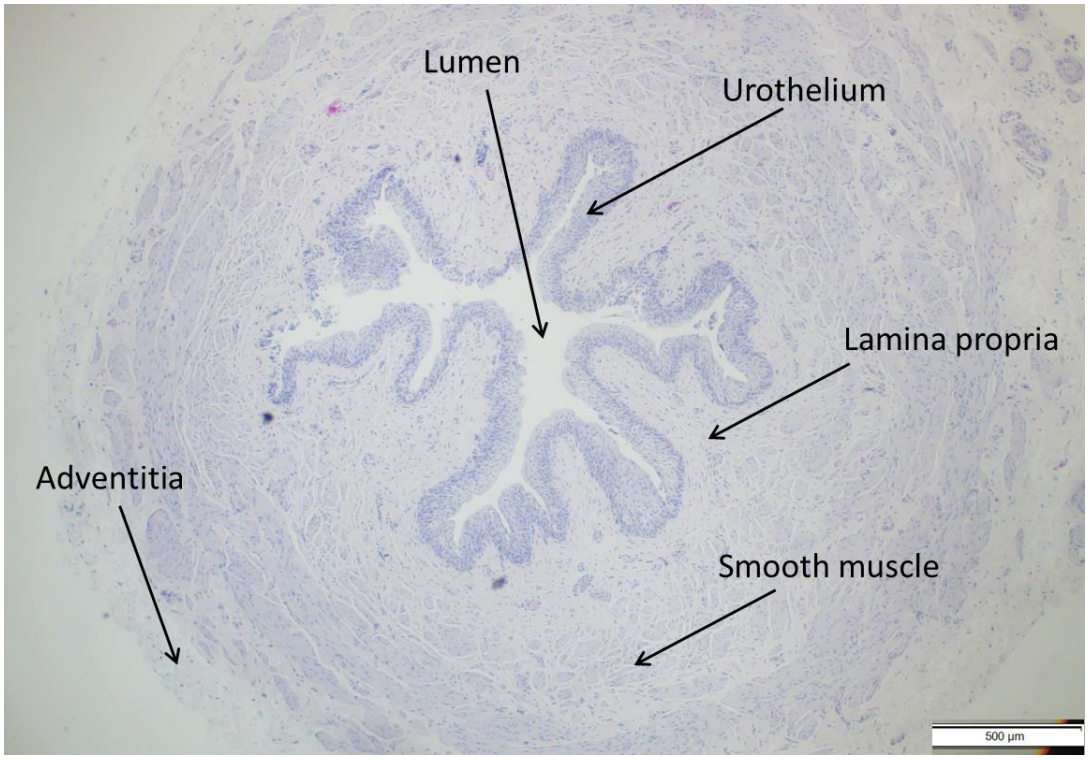

Figure 1.2: Cross section of human ureter

Haematoxylin & eosin stained tissue section of a normal ureter, with the location of the morphologically distinct tissue layers (the fibrous connective adventitia, smooth muscle, lamina propria and urothelium) labelled. Scale bar = 500 µm.

1.2 Urothelium

1.2.1 Urothelial morphology and function

The urothelium is a transitional epithelium, denoting that it is a stratified epithelium which contains characteristics of both simple columnar and stratified squamous epithelia. Human urothelium is typically composed of between 3-6 layers of cells, with a layer of cuboidal basal cells anchored to the basement membrane separated from the lumen-facing superficial cells by a variable amount of intermediate cell layers (Fig. 1.3; Jost *et al.,* 1989). The superficial (or "umbrella") cells are larger than the underlying basal cells and are often bi-nucleate (reviewed by Hicks, 1975). Superficial cells reside in the most highly specialised cell zone of the urothelium and express rigid plaques on their luminal surface known as the asymmetric unit membrane (AUM; Hicks, 1965). Production of AUM and expression of specific tight junction proteins by superficial urothelial cells result in the constitution of the tightest barrier created by any known mammalian epithelium, as measured by transepithelial electrical resistance (TEER; Negrete *et al.,* 1996). The para-cellular and trans-cellular barriers created by tight junction proteins and AUM, respectively, thus grant urothelia the ability to provide a permeability barrier against the reabsorption of urinary-excreted toxins and are therefore vital for maintaining bladder function.

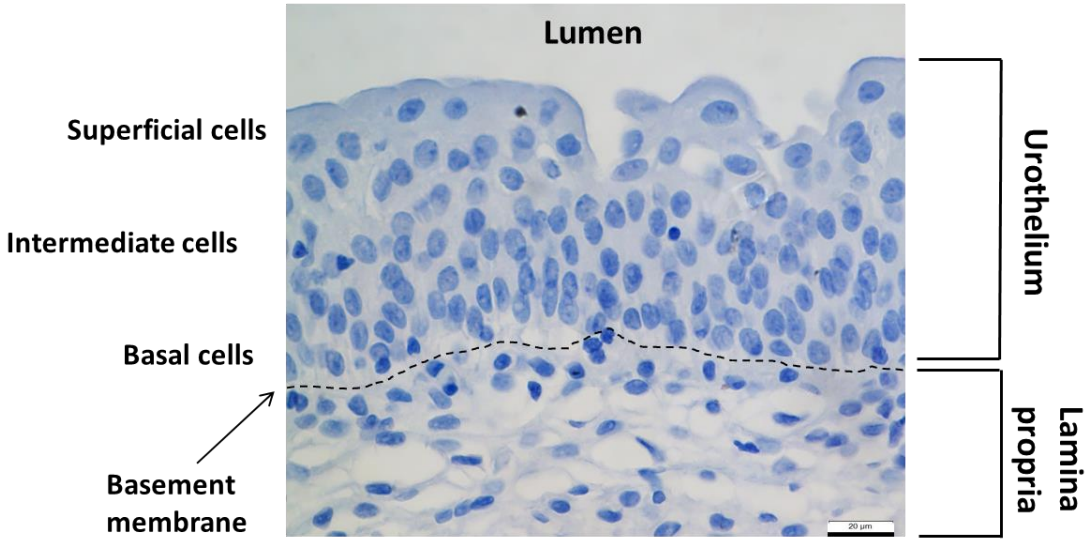

Figure 1.3: Haematoxylin stain of normal human bladder urothelium

Large, AUM-expressing superficial urothelial cells border the bladder lumen, situated above variable layers of intermediate cells and a single layer of basal cells attached to a basement membrane (with approximate localisation highlighted with a black dotted line). Basal cells are separated by the basement membrane from a lamina propria containing stromal cells attached to an ECM. Histology image courtesy of Dr. Jennifer Hinley. Scale bar = 20 µm.

The human urothelium does not contain a resident lymphocyte population (Jost *et al.,* 1989), nor does it regularly participate in mitosis under normal conditions. Initial studies into the mitotic turnover of the urothelium in mice and rats found the tissue to have a mitotic index of <1% (Messier *et al.,* 1960; Walker, 1960). Later molecular studies demonstrated widespread expression of cell cycle-associated Ki67 in the basal and intermediate cells of rat urothelium (Chopra *et al.,* 2008) but a labelling index of S-phase marker BrdU <1% (Dominick *et al.,* 2006), indicative of a non-proliferating tissue. In comparison, a near absence of Ki67 positivity has been observed in multiple studies of human urothelium, thus confirming the human urothelium to be a mitotically quiescent tissue (Varley *et al.,* 2005; Chopra *et al.,* 2008). Despite this characteristic, the adult mammalian urothelium retains a formidable capacity for regenerative proliferation following injury-induced stress. Damage to rodent urothelium by chemical insult was found to result in the

activation of mitosis in all cell layers (Levi *et al.,* 1969) and a rapid recovery of barrier function (Lavelle *et al.,* 2002). This observed switch between a mitotically quiescent (but proliferation capable) and an actively regenerating state forms the primary tenet behind urothelial tissue homeostasis; and as such needs to be tightly regulated in order to avoid a pathological state (Fig. 1.4).

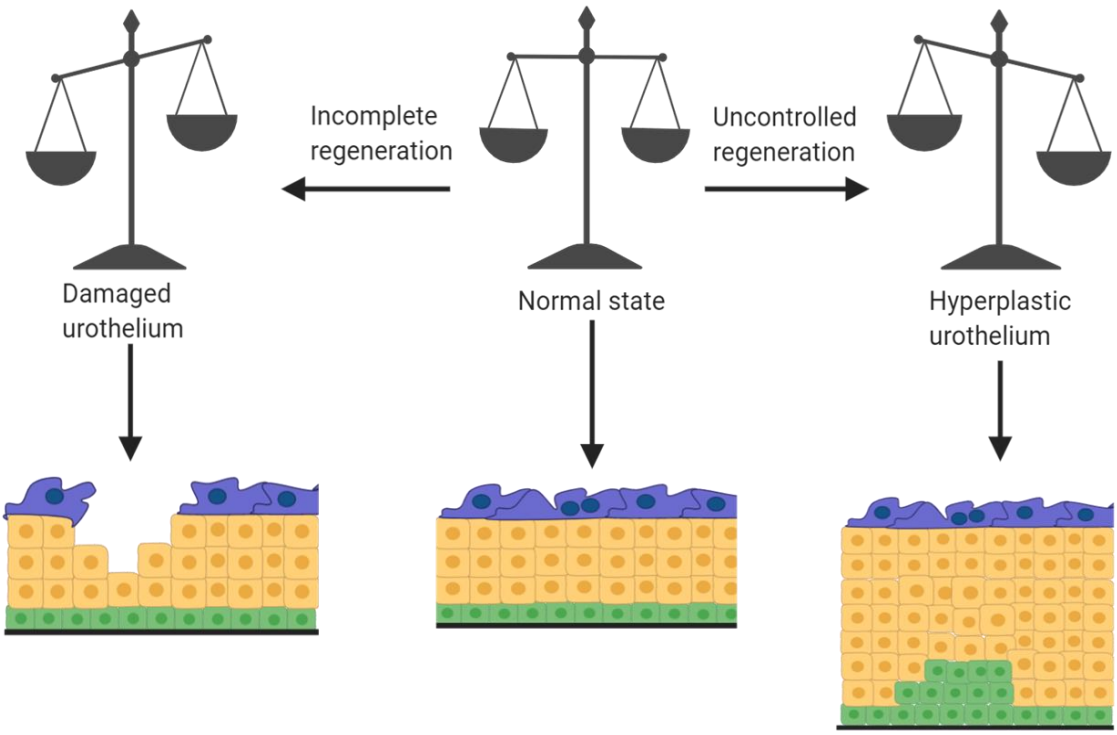

Figure 1.4: The regenerative phenotype of the urothelium

The urothelium is notable for its ability to rapidly proliferate and repair itself following physical, chemical or bacterial injury. An inability to completely repair damaged urothelium compromises barrier function and is indicative of chronic conditions such as interstitial cystitis (Southgate *et al*., 2007). Unrestrained regeneration results in an inactivation of quiescence, urothelial hyperplasia and potentially tumorigenesis. Diagram adapted from review by Balsara *et al*., 2017.

1.2.2 Molecular markers of urothelial cells *in situ*

The cell layers of the urothelium have been shown to express different protein markers which correspond to their state of differentiation within the tissue (reviewed by DeGraff *et al.* 2013). AUM produced at the apical surface of superficial cells is composed of integral membrane proteins known as uroplakins. First discovered in bovine urothelium (Wu *et al.,* 1990), it was subsequently determined uroplakin proteins UPK1a, UPK1b, UPK2 and homologues UPK3a/UPK3b are expressed in humans. Uroplakin proteins are expressed exclusively by superficial cells with the exception of UPK1b which has also been found in some intermediate cell layers (Lobban *et al.,* 1998). Due to their unique status as being expressed only by superficial urothelial cells, expression of UPK1a, UPK2 and UPK3a/b are considered to be markers of a highly differentiated, mature urothelium. The importance of uroplakin expression to urothelial phenotype is supported by gene knockdown studies in mice that demonstrate that loss of *UPK3A* is responsible for a significant elevation in bladder permeability (Hu *et al.,* 2002) while knockdown of *UPK2* resulted in mice with proliferating urothelium (Kong *et al.,* 2004).

Alongside uroplakins, components of intercellular tight junctions are also important in maintaining urothelial barrier integrity. Tight junctions act to limit paracellular movement of water and solutes and are located at the interface of adjacent epithelial cells. The multi-protein complexes are primarily composed of zonular occludens (ZO) and tetra membrane-spanning proteins such as occludin and members of the claudin family. ZO proteins were determined to play a role in stabilising and crosslinking the tight junction proteins to the actin cytoskeleton (Fanning *et al.,* 1998), while claudins are the fibrils which provide the principle physical seal (Furuse *et al.,* 1998). Multiple tight junction proteins have been confirmed histologically to be expressed by human urothelium, including claudin 3, claudin 4, claudin 5, claudin 7, ZO-1 and its alternatively spliced variant ZO-$1^{\alpha+}$ (Varley *et al.,* 2006; Smith *et al.,* 2015).

The urothelium also expresses a number of cytokeratins (CKs), a family of twenty cytoskeletal intermediate filament isotypes which are expressed by most epithelial cell types. Distribution of CK expression in urothelium is dependent on the cell zone

the cell inhabits, with alterations in the level of stratification or differentiation of the tissue resulting in atypical expression patterns (reviewed by Southgate *et al.*, 1999). For example, in normal urothelium CK5 and CK17 are examples of proteins that are localised to basal urothelial cells only, while CK20 is localised exclusively to superficial cells (Schaafsma *et al.,* 1989; Moll *et al.,* 1992). In comparison, CK13 localises to both basal and intermediate cell zones, while CK7, CK8, CK18 and CK19 are expressed abundantly in all layers of the urothelium (Moll *et al.,* 1988). Changes in the normal pattern of CK expression in urothelium is a common diagnostic marker of high-grade malignancy (Moll *et al.,* 1988; Schaafsma *et al.,* 1990).

1.3 Normal Human Urothelial (NHU) cells *in vitro*

1.3.1 NHU cell phenotype

One method for investigating human urothelial cell physiology *in vitro* was achieved by separating urothelial cell sheets from the underlying stroma and growing the isolated cells in culture as non-immortalised, finite cell lines (Southgate *et al.,* 1994). When cultured in low calcium (0.09 mM), serum-free medium environment, Normal Human Urothelial (NHU) cells adopt a sub-basal phenotype that lacks the expression of differentiated urothelial markers such as CK20. Instead, NHU cells express CK14 and CK16, markers of squamous metaplasia not typically found in native urothelium but are upregulated in bladder cancer (Southgate *et al.,* 1994; Harnden *et al.*, 1997). In comparison to urothelium *in situ*, NHU cells are highly proliferative and grow as a dispersed monolayer; with the majority of cells expressing nuclear Ki67 antigen and exhibiting an average doubling time of around 15 hours (Southgate *et al.,* 1994, 2002).

NHU cultures do not require exogenous epidermal growth factor (EGF) to proliferate or survive, but in fact were found to produce their own amphiregulin ligand which powers cell proliferation through an autocrine EGF receptor (EGFR) loop. Autocrine activation of EGFR was found to subsequently instigate cell cycle progression through the activation of downstream RAS/RAF/MEK/ERK signalling via a protein phosphorylation cascade (Varley *et al.,* 2005). The importance of this pathway to NHU cell proliferation was highlighted following treatment of NHU

cultures with EGFR receptor tyrosine kinase (RTK) inhibitor PD153035 or mitogen-activated protein kinase kinase (MEK1/2) inhibitor UO126, which were found to completely curtail cell growth and cause G1 arrest (Varley *et al.,* 2005). NHU cells treated with PD153035 or U0126 were able to reactivate phosphorylated extracellular signal-regulated kinase (ERK1/2) and regain a proliferative phenotype once said inhibitors were removed from the growth medium, demonstrating that urothelial cells retain a degree of plasticity to switch between a quiescent and regenerative state in culture (MacLaine *et al.,* 2008).

1.3.2 NHU cytodifferentiation

1.3.2.1 Induction of cytodifferentiation *in vitro*

When cultured NHU cells were seeded onto de-epithelialised urothelial stroma, the cells regained their stratified, transitional phenotype and inhibited proliferation (Scriven *et al.,* 1997). This discovery indicated that NHU cells retained the capacity to re-differentiate when given the right signalling cues, even if the identity of the paracrine "differentiation-inducing" molecules presumably released by the stroma was unknown. Later studies optimised two distinct methods to induce differentiation in NHU cells in an *in vitro*, stroma-free environment. One method involves pharmacologically inducing differentiation through activation of the nuclear receptor Peroxisome Proliferator-Activated Receptor γ (PPARγ; section 1.3.2.2) with the thiazolidinedione PPARγ agonist troglitazone (TZ) alongside concurrent blockade of autocrine EGFR signalling by PD153035 (Varley *et al.,* 2004a; Varley *et al.,* 2004b). In this "TZ/PD differentiated" state *in vitro,* NHU cultures have been shown to express multiple differentiation-associated targets, including various tight junction proteins and transcript expression of uroplakins *UPK1B* and *UPK2* (Varley *et al.,* 2004a; Varley *et al.,* 2006). However, differentiation via pharmacological means alone was unable to induce stratification of the NHU cultures (Varley *et al.,* 2006).

In contrast, earlier studies had demonstrated that the application of a high calcium medium to NHU cultures resulted in some evidence of stratification but was not sufficient to induce cytodifferentiation or functional barrier formation (Southgate *et*

al., 1994). By growing NHU cells in a physiologically relevant concentration of calcium in addition to the presence of serum, this was found to produce a fully stratified, barrier-forming, "biomimetic" urothelium (Cross *et al.,* 2005). Evidence of the barrier forming potential of the serum-differentiated cells was provided through the measurement of the TEER of the tissue, with readings of >3000 $\Omega.cm^2$ designating a significantly tighter barrier than the accepted >500 $\Omega.cm^2$ threshold for a "tight" epithelial barrier (Fromter *et al.,* 1972; Cross *et al.,* 2005). This differentiation method was similarly demonstrated to reverse the CK14-high/CK13-low NHU phenotype alongside induction of claudin 1, claudin 3, claudin 4, occludin and ZO-1 in a similar localisation to that found *in situ* (Cross *et al.,* 2005; Smith *et al.,* 2015). The similarities in phenotype between differentiated NHU cells and native urothelium have therefore fostered the use of *in vitro* NHU cells as a robust and accurate proxy for predicting human urothelial biology *in situ*.

1.3.2.2 PPARγ

Functional differentiation of the highly specialised superficial cells is predicated on the activation of a complex and specific network of transcription factors that induce the mature phenotype (Varley *et al.,* 2009; Fishwick *et al*., 2017). Initially implicated in the terminal differentiation of adipocyte cells (Rosen *et al.*, 1999), multiple studies have since provided evidence for the role of PPARγ as a 'master regulator' of urothelial cytodifferentiation (Varley *et al.,* 2004a*;* Varley *et al.,* 2006*;* Varley *et al.*, 2009). PPARγ is a member of the PPAR family of nuclear receptors that require ligand binding to activate function (Issemann *et al.,* 1990), although the identity of the natural ligand to PPARγ in native human urothelium is currently undetermined. Studies by Stahlschmidt *et al.* initially proposed the lipid compound 15-deoxy-Δ12,14-prostaglandin J2 (15d-PGJ2) as a potential natural ligand of PPARγ due to its previously defined presence in urine (Hirata *et al.,* 1988). However, analysis of bladders from long term dialysis patients discovered that PPARγ was still expressed in the nuclei of urothelial cells, while addition of 15d-PGJ2 to NHU cells was unable to induce differentiation *in vitro*, suggestive of activation of the nuclear receptor by a PPARγ-specific ligand produced by the urothelium or other surrounding cell types (Stahlschmidt *et al.,* 2005). Upon ligand activation PPARγ heterodimerises to a

different nuclear receptor, Retinoid X Receptor α (RXRα), in the nucleus. The active PPARγ complex can subsequently bind to specific PPAR Response Elements (PPRE) that are located in the promoter region of various genes to induce gene transcription (Kliewer *et al.,* 1992).

Active, phosphorylated ERK1/2 has previously been shown to inhibit PPARγ activity in HEK293T cells by phosphorylating the protein at its serine 82 site (Camp *et al.*, 1997). Active MEK1/2 signalling has also been demonstrated to bind directly to PPARγ in HEK293 cells and inhibit its function independently of ERK1/2 activity through export from the nucleus in HeLa cells (Burgermeister *et al.,* 2007). This evidence suggests that the process of TZ/PD differentiation could work by activating dormant PPARγ in NHU cells while simultaneously blocking the activation of PPARγ inhibitors, thus amplifying the effects of cytodifferentiation in EGFR-blockaded cells. Treatment with the potent PPARγ antagonist T0070907 (T007) or genetic knockdown of PPARγ using small interfering RNA (siRNA) was found to abrogate the differentiation-inducing effect of TZ/PD in NHU cells, thereby confirming the specific role that PPARγ plays in the differentiation process (Varley *et al.,* 2006).

1.3.2.3 Other transcription factors involved in urothelial differentiation

Investigation into the specific timeframe in which certain urothelial differentiation-associated genes were induced determined that expression of the *UPK2* gene took place several days after the onset of TZ/PD treatment in NHU cells. Additionally, no PPRE binding sites where found in or upstream of the promoter site of the *UPK2* gene, suggesting that activation of PPARγ was regulating or inducing the expression of one or multiple intermediary transcription factors that controlled late differentiation (Varley *et al.,* 2004a). Studies in mice supported this hypothesis by identifying grainyhead-like protein 3 (GRHL3) and Kruppel-like transcription factor 5 (KLF5) as two transcription factors which were important for murine urothelial differentiation (Yu *et al.,* 2009; Bell *et al.,* 2011). Primarily noted for its role in epidermal differentiation, GRHL3 was not only found to be vital for barrier formation in mouse urothelium, but it was also found to directly bind to the UPK2 promoter in the RT4 bladder cancer cell line (Yu *et al.,* 2009). Deletion of KLF5 was

found to induce incomplete stratification of the developing murine urothelium upon deletion, with corresponding losses of *Pparg* and *Grhl3* transcript suggestive of the existence of a hierarchy of TFs that are all required in order to induce urothelial differentiation in mice (Bell *et al.,* 2011).

Gene microarray analysis of NHU cells treated with TZ/PD identified Forkhead Box A1 (FOXA1) and Interferon Regulatory Factor-1 (IRF-1) as transcription factors that were induced as early as 12h post treatment and were confirmed to possess high-affinity PPRE sites in their respective promoter regions (Varley *et al.,* 2009). Foxa1 had previously been implicated as an important transcription factor in the development of murine urothelium (Oottamasathien et al., 2007), with knockout of *Foxa1* in female mice found to result in CK14-high squamous metaplasia (Reddy *et al.,* 2015). The role of FOXA1 and IRF-1 in mediating the human urothelial mature differentiation phenotype was confirmed following siRNA knockdown of the respective transcription factors, as this resulted in reduced claudin 3 and CK13 protein in addition to reduced *UPK2* and *UPK3a* transcript expression in TZ/PD differentiated NHU cells (Varley *et al.,* 2009).

Zinc finger transcription factor GATA3 was an example of another gene found to be upregulated after TZ/PD treatment in a similar timeframe to FOXA1 and IRF-1 (Varley *et al.,* 2009). GATA3 can act upstream of FOXA1 (Kouros-Mehr *et al.,* 2006), and due to their roles as “pioneer” transcription factors, both proteins are known to act by binding to areas of heterochromatin to access silenced genes (Cirillo *et al.,* 2002). A study in oestrogen receptor α+ breast cancer demonstrated that the two transcription factors bind to many of the same sites (Jiang *et al.,* 2019), which was consistent with a study that used Formaldehyde-Assisted Isolation of Regulatory Elements coupled with next-generation sequencing (FAIREseq) to identify areas of open chromatin in NHU cells differentiated with TZ/PD for different periods of time. The resulting open chromatin regions identified by FAIRE-seq were found to be enriched by co-occurring FOXA1 and GATA3 transcription factor-binding site motifs in cells differentiated for either 24h or 144h (Fishwick *et al.,* 2017). In comparison, enrichment of PPARγ transcription factor-binding site motifs were found only at the

24h time-point, strengthening the previous observation that PPARγ serves to initiate urothelial differentiation and not to directly control expression of late differentiation-associated genes. As with FOXA1, siRNA knockdown of GATA3 resulted in a loss of CK13 protein and *UPK2* transcript, although expression of FOXA1 was not affected (Fishwick *et al.,* 2017).

Analysis of gene microarray data of a different time course of NHU cells undergoing differentiation via both methods (TZ/PD and serum/Ca^{2+}) separately uncovered that ETS-related transcription factor 3 (ELF3) was the top ranking transcription factor that was significantly induced by both differentiation methods (Böck *et al.,* 2014). A transcription factor previously found to be lost in the urothelium of Klf5-null mice (Bell *et al.,* 2011), ELF3 expression was subsequently confirmed to be PPARγ-mediated in NHU cells, while also negatively affecting *UPK3A* expression and barrier function when knocked down by siRNA (Böck *et al.,* 2014). This added to a body of evidence that suggests that in fact a heterarchy of transcription factors exists to modulate urothelial differentiation; with some defined directionality to the order in which the transcription factors operate (e.g. PPARγ as an instigating factor) but also cooperativity/redundancy between some intermediary factors to drive a differentiated phenotype (Fig. 1.5).

One protein negatively affected by *in vitro* urothelial differentiation in NHU cells is p63, a transcription factor found to directly induce markers of a normal basal urothelial cell phenotype, such as KRT5, in tissues such as skin (Romano *et al.,* 2009). p63 has previously been suspected to mark a population of stem cell-like basal cells in developing mouse urothelium (Pignon *et al.,* 2013), although this observation has yet to be validated in human urothelium, where it is primarily localised to the basal and intermediate cell zones (Fishwick *et al.,* 2017). Analysis of p63 expression in NHU cells determined that the transcription factor was abundant in undifferentiated NHU cultures but reduced following TZ/PD differentiation. Expression of p63 could subsequently be recovered in differentiated cells with GATA3 knockdown (Fishwick *et al.,* 2017). Increased expression of GATA3 and FOXA1 protein in p63 siRNA knockdown NHU cultures further points to an opposing relationship between induction of p63 targets and differentiation-associated

targets upregulated by intermediary transcription factors (Fishwick *et al.,* 2017; Fig. 1.6).

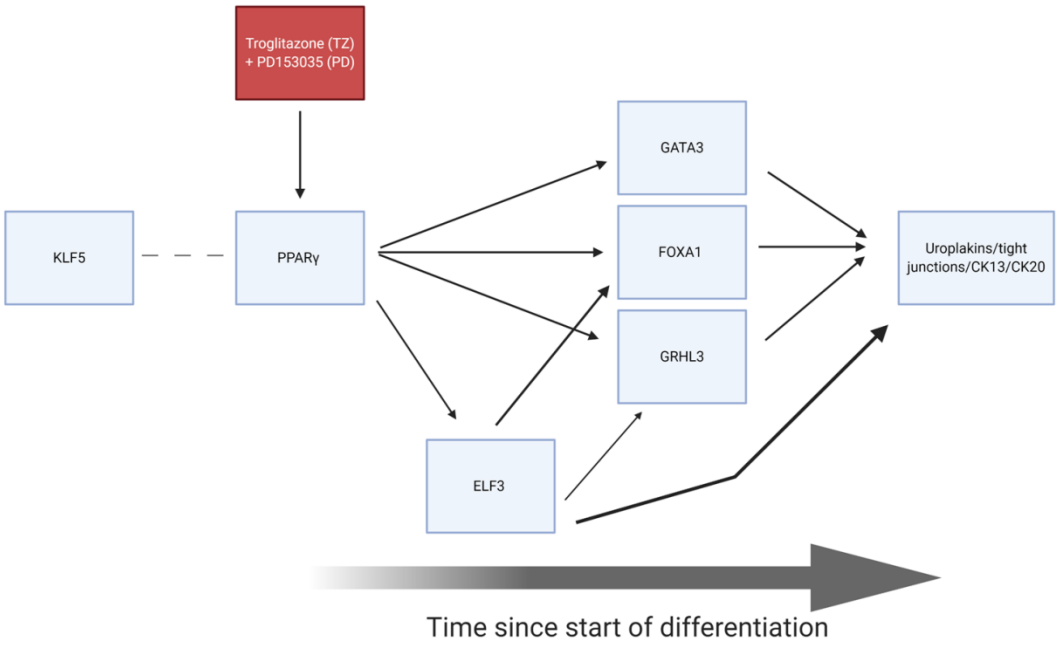

Figure 1.5: Previously proposed transcriptional network of PPARγ-mediated urothelial differentiation

PPARγ is constitutively expressed in urothelial cells (Varley *et al.,* 2004a), with KLF5 expression vital to maintain expression in murine urothelium. Activation of PPARγ by TZ/PD induces the upregulation of intermediary transcription factors through binding of PPARγ to PPRE sites. Knockdown of ELF3 in NHU cells significantly inhibits *GRHL3* and *FOXA1* expression, suggesting that ELF3 lies upstream of these markers (Böck *et al.,* 2014). Multiple days after the initiation of differentiation, a combination of the intermediary transcription factors are able to induce transcription of genes associated with late differentiation, with GATA3 and FOXA1 binding to the same regions of DNA.

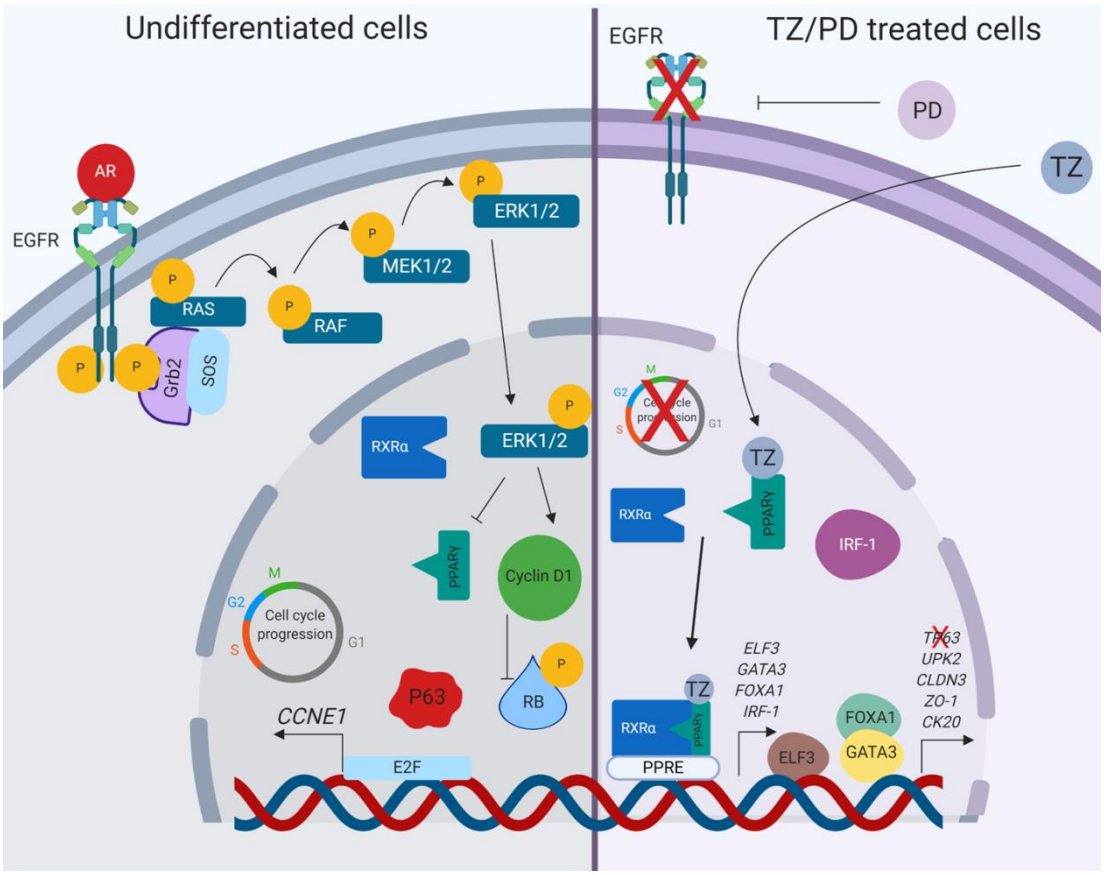

Figure 1.6: Mechanism of NHU cytodifferentiation

In undifferentiated NHU cells, autocrine stimulation of EGFR activates the RAS/RAF/MEK/ERK signalling axis via a protein kinase phosphorylation cascade. Active phosphorylated ERK1/2 (Thr202/Tyr204) has been shown to be able to inactivate PPARγ activation through phosphorylation at Ser82. The RAS/RAF/MEK/ERK pathway is able to contribute to progression through the cell cycle by expression of Cyclin D1 and inactivation of retinoblastoma protein (RB; Weber *et al.,* 1997). Tyrosine kinase inhibitor PD153035 binds to EGFR, blocks RAS/RAF/MEK/ERK activity and inhibits cell cycle progression. TZ binds to inactive nuclear PPARγ, which heterodimerises with RXRα and binds to PPRE sites in the DNA. Intermediary transcription factors such as ELF3, GATA3 and FOXA1 are expressed, which subsequently bind to their motifs in the DNA and induce expression of markers of late differentiation, including uroplakins and components of tight junctions. The basal marker p63 is expressed in NHU cells in an undifferentiated state but inhibited following cytodifferentiation, with expression of the TF appearing to be regulated by the induction of GATA3 (Fishwick *et al.,* 2017). AR= amphiregulin; yellow circles = phosphorylation sites.

1.3.3 NHU cell growth regulation

Despite a clear role for EGFR-mediated ERK1/2 activation in the proliferation of NHU cells (Section 1.3.2.1); other studies have demonstrated that the cells can employ alternative growth regulatory pathways (in both the presence and absence of ERK signalling) to power growth under certain physiological conditions. One example of this is the Phosphoinositide 3-Kinase (PI3K)/protein kinase B (PKB or AKT) pathway, which has been implicated as important in processes such as cell metabolism, growth and survival (Roche *et al.,* 1994; Kauffmann-Zeh *et al.,* 1997). In a similar fashion to PD153035 and U0126, the PI3K inhibitor LY294002 was demonstrated to initially inhibit undifferentiated NHU cell proliferation. However, the drug only succeeded in inhibiting cell growth of sub-confluent cultures transiently, with cultures eventually regaining similar growth rates to control despite repeat administrations of the drug (MacLaine *et al.,* 2008). This delayed response points to a potential reprogramming of mitogenic signalling by NHU cells whereby the cells can switch to other pathways to propagate growth once PI3K/AKT signalling is compromised.

PI3K/AKT signalling has been found to be strongly activated in cells that are in contact (Nelson *et al.*, 2002) and have created cell-cell adherens junctions with one another, which can be achieved by cell confluence or addition of a physiological concentration of calcium to the medium. A primary component of adherens junctions is E-cadherin, a transmembrane glycoprotein that is dependent on calcium to create adhesion between adjacent cells but can also regulate growth signalling through modulation of RTK activity (Shapiro *et al.,* 1995; Takahashi *et al.,* 1996). E-cadherin function is closely associated with β-catenin, a multifunctional protein that stabilises adherens junctions by binding to the cytoplasmic tail of E-cadherin while also acting as a primary signal transducer of the WNT pathway (McCrea *et al.,* 1991; Behrens *et al.,* 1996). Investigation into the interplay between E-cadherin expression, PI3K/AKT and WNT signalling in NHU cells determined that in a high calcium environment, phosphorylated (active) AKT was induced in the nuclei of adhered cells concurrent to the translocation of E-cadherin and β-catenin from the cytoplasm and nucleus, respectively, to a intercellular localisation

(Georgopoulos *et al.,* 2010). Treatment of NHU cells with LY294002 increased nuclear expression of β-catenin (Georgopoulos *et al.,* 2014), while short hairpin RNA (shRNA) knockdown of β-catenin in NHU cells resulted in an induction of E-cadherin and phosphorylated AKT expression (Georgopoulos *et al.,* 2010). β-catenin knockdown cells were highly sensitive to PI3K/AKT inhibition and displayed significantly reduced proliferation compared to control cells treated with LY294002 in both low and high calcium (Georgopoulos *et al.,* 2010), thereby supporting the existence of a mutually exclusive relationship between PI3K/AKT and β-catenin in supporting cell growth in urothelium. While their effect on undifferentiated NHU cell proliferation is well-defined, the role that PI3K/AKT and β-catenin signalling play in the maintenance of differentiated NHU tissue homeostasis (or their effect on expression of urothelial differentiation-associated genes) has yet to be determined.

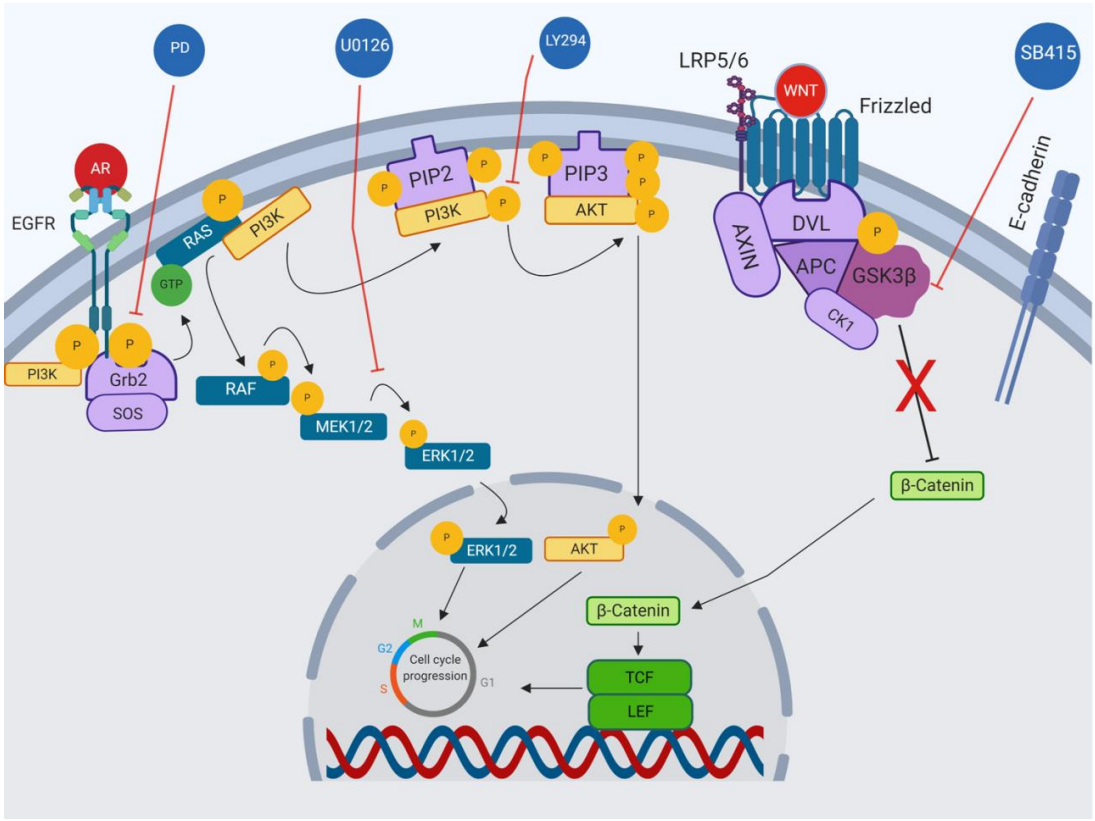

Figure 1.7 Convergence of signal transduction pathways to drive NHU cell proliferation

The primary signal transduction molecules of the RAS/RAF/MEK/ERK, PI3K/AKT and WNT/β-catenin pathways are represented by teal, yellow and green rectangles, respectively. Natural extracellular pathway ligands are represented by red circles while pharmacological small molecule inhibitors of specific components of each pathway are represented by blue circles. For the purposes of the illustration, each pathway is represented in its activated "ON" state. PI3K can be activated through a range of mechanisms, including binding to activated tyrosine kinase residues on a RTK such as EGFR, or activation by RAS (Rodriguez-Viciana *et al.,* 1997). PI3K catalyses the addition of a phosphate group to cell membrane-localised phospholipid component PIP2, generating PIP3. PIP3 has a high affinity for AKT, which translocates to the membrane, undergoes conformational changes and is activated by phosphorylation (Boudewijn *et al.,* 1995). Similarly to ERK1/2, activated AKT can enter the nucleus and affect numerous cellular processes. In the absence of WNT ligands, β-catenin is an integral component of E-cadherin-mediated adherens junctions. The remaining cytosolic β-catenin is targeted by co-ordinated phosphorylation by the destruction complex (APC, AXIN, GSK3β and CK1) which leads to eventual ubiquitination and proteasomal degradation (Aberle *et al.,* 1997). Binding of WNT ligands to the G protein-coupled receptor frizzled results in the transduction of signal to membranous dishevelled (DVL) in the presence of frizzled co-receptor lipoprotein receptor-related protein (LRP) 5/6. AXIN binds to the cytoplasmic tail of LRP5/6 and is inactivated while DVL is phosphorylated and inactivates GSK3β/destruction complex activity (Li *et al.,* 1999). β-catenin is free to translocate to the nucleus, where it can influence gene expression through binding to transcription factors TCF and LEF (Behrens *et al.,* 1996). As demonstrated in previous studies, NHU cells utilise all three pathways, which all exhibit a degree of crosstalk between one another (Varley *et al.,* 2005; Georgopoulos *et al.,* 2010; Georgopoulos *et al.,* 2014).

An added layer of complexity arises following the reprogramming of dominant signal transduction pathways that occurs when urothelial cells become differentiated. Analysis of gene microarray data comparing undifferentiated versus TZ/PD differentiated NHU cultures determined that differentiated NHU cells had significant transcriptional alterations in the canonical TGFβ pathway, a signalling pathway with known roles in tissue repair and migration (Postlethwaite *et al.,* 1987; Montesano *et al.,* 1988). Analysis of TGFβ pathway activation in confluent NHU cultures following scratch wounding revealed that differentiated cells exhibited decelerated migration in the presence of TGFβ receptor I (TGFβRI) inhibitor SB431542, while treatment with exogenous TGFβ1 retarded undifferentiated cell migration (Fleming *et al.,* 2012). Activation of endogenous TGFβ signalling in wounded differentiated NHU cells was manifested through the appearance of nuclear phosphorylated SMAD3 (canonical TGFβ pathway effector) in the cells immediately proximal to the wound edge, with a lack of Ki-67 positive cells indicative of a migratory, rather than proliferative, wound response (Fleming *et al.,* 2012). The results of the preceding study therefore suggested that differentiated urothelial cells utilise alternative signal transduction pathways to undifferentiated cells and by extension, highlights a possible alternative pathway that "differentiated" bladder cancers might exploit to drive cancer development.

1.4 Bladder cancer

1.4.1 Epidemiology

Bladder cancer is the 10th most common cancer in the UK, accounting for 10,187 new cases and 5,407 deaths per year based on the latest statistics (Cancer Research UK, 2019). Approximately 60% of new bladder cancer cases are observed in people aged 75 or over, with a higher incidence observed in men but an average survival rate of 10 years or longer for both genders currently at 50% (Cancer Research UK, 2019). Although the incidence rates of bladder cancer have decreased year-on-year in the Western world, the mortality rate remains relatively stable (Siegel *et al.,* 2019). Prior to approval of anti-PD-L1 immune checkpoint blockade therapy in cases of advanced bladder cancer (Rosenberg *et al.,* 2016), little progress had been made in recent history in producing a treatment for bladder cancer beyond cisplatin-based chemotherapy (Yagoda, 1979), intravesical administration of the Bacillus Calmette-Guérin (BCG) vaccine (Morales *et al.,* 1976) or radical cystectomy (Marshall *et al.,* 1949).

1.4.2 Pathology

Bladder cancer is caused by a variety of environmental factors, most notably smoking and occupational exposure to carcinogenic materials (Jiang *et al.,* 2012; Kogevinas *et al.,* 2003). Urothelial carcinomas make up 90% of all bladder cancers, with squamous cell carcinoma and adenocarcinoma accounting for two rarer forms of the disease (reviewed by Dahm *et al.,* 2003). Cases of urothelial carcinoma, the vast majority of which originate in the bladder, can progress through one of two routes. 80% of total cases are hyperplastic superficial papillary tumours of a non-muscle invasive (NMIBC) nature. NMIBC is rarely life-threatening, but it is one of the most costly cancers to treat on average (Riley *et al.,* 1995) and is highly recurrent, with up to 70% of patients found to experience a recurrence after 5 years (Chamie *et al.,* 2013). 20-30% of recurrent NMIBC tumours are found to progress to a higher stage/grade, with 10% progressing to Muscle-Invasive Bladder Cancers (MIBC). Only 15% of all MIBC patients are assumed to progress from NMIBC however, with the remaining 85% progressing through a non-papillary route where urothelial cells first exhibit carcinoma *in situ* (CIS), a more aggressive, flat superficial

lesion (Schrier *et al.,* 2004). While NMIBC is usually managed by transurethral resection and/or intravesical chemotherapy, MIBC is harder to treat and is associated with a poor survival rate (reviewed by Pang *et al.,* 2019).

As with other epithelial malignancies, urothelial carcinoma is a highly heterogeneous disease at the molecular level. MIBC was calculated to have one of the highest somatic mutational burdens of all human cancers, behind only non-small cell lung cancer and melanoma (Lawrence *et al.,* 2013). Mutational analysis of MIBC in humans found that the most mutated gene was the *TP53* tumour suppressor in 49% of cases (The Cancer Genome Atlas Research Network, 2014), while the most frequently altered genes in NMIBC were the TERT promoter (73%), fibroblast growth factor receptor 3 gene (*FGFR3*; 49%) and the PI3K gene (*PI3KCA*; 26%) (Pietzak *et al.,* 2017).

The genetic diversity displayed by MIBC tumours offers a potential rationale as to why traditional chemotherapeutic treatments have been ineffective in a large percentage of bladder cancer patients. A primary goal of bladder cancer researchers over the past twenty years has therefore been to identify transcriptional differences between MIBC samples. The transcriptional and mutational signatures of tumours could be used to subgroup MIBC (independent of pathologic stage) into clinically relevant subtypes based on expression of specific genes, with the goal of highlighting potential candidate proteins which could be targeted by small molecules in suitable patients.

1.4.3 Molecular subtyping of muscle-invasive bladder cancer

The first study to demonstrate the use of gene microarrays to distinguish between different molecular subtypes of an epithelial malignancy was undertaken by Perou *et al.,* who compared the gene expression patterns from 65 breast tumours and identified the genes with the highest variation in expression. Unsupervised hierarchical clustering was then used to group genes and tumours based on their similarity of expression, thereby creating four clusters of breast tumours with distinct gene expression profiles (Perou *et al.,* 2000). Of these clusters, two were classified as "luminal" and "basal" due to their molecular similarities to the two types of epithelial cell found in normal mammary epithelium: luminal and basal. Similarly to the cells of the urothelium, luminal and basal mammary epithelial cells have distinct expression profiles based on their level of differentiation, with basal cells expressing CK5 and luminal cells expressing CK8/CK18 (Perou *et al.,* 2000).

This study inspired a similar application of gene microarrays to samples of bladder cancer, which was initially used to delineate non-recurring from frequently recurring cases of NMIBC whilst confirming that NMIBC and MIBC have two distinct patterns of expression (Blaveri *et al.,* 2005; Dyrskjøt *et al.,* 2003). Numerous studies since have attempted to create a definitive molecular taxonomy of MIBC based on cohorts of tumours analysed by RNA sequencing (RNAseq), with each approach (and cohort) providing a similar outcome (Sjödahl *et al.,* 2012; Choi *et al.,* 2014a; Damrauer *et al.,* 2014; The Cancer Genome Atlas Research Network, 2014; Robertson *et al.,* 2017; Marzouka *et al.,* 2018; Kamoun *et al.,* 2020).

Whole genome mRNA expression profiling of 73 MIBC samples from the MD Anderson Cancer cohort revealed three distinct molecular subtypes: luminal, basal and 'p53-like'. Interestingly, the luminal and basal subtypes expressed many of the same targets as the corresponding breast cancer subtypes, while there was a significant difference in disease-specific survival between luminal and basal cancers (Choi *et al.,* 2014a). A comprehensive study of analysis of 131 MIBC tumours by The Cancer Genome Atlas (TCGA) determined that their dataset could be split into four clusters by splitting luminal tumours based on *FGFR3* expression (The Cancer Genome Atlas Research Network, 2014). A later TCGA study further discriminated

between subtypes by creating a 'neuronal' classification based on neuroendocrine-like features to give five expression subtypes (Robertson *et al.,* 2017). The most recent consensus taxonomy has expanded MIBC into six distinct groups with identifiable gene expression profiles: Luminal Papillary (LumP), Luminal Non-Specified (LumNS), Luminal Unstable (LumU), Basal/Squamous (Ba/Sq), Neuroendocrine-like (NE-like) and Stroma-rich (Kamoun *et al.,* 2020; Table 1.1). A demonstration of how transcriptional subtyping of MIBC could be clinically beneficial was performed by using unsupervised hierarchical clustering to identify luminal/basal gene markers that could also be labelled in fixed tissue samples using immunohistochemical techniques. Immunohistochemical analysis of protein markers in MIBC samples demonstrated that GATA3 and KRT5/6 (genes identified as being associated to luminal and basal MIBC, respectively) expression could be used to differentiate between luminal and basal subtypes of MIBC with over 90% accuracy (Dadhania *et al.,* 2016).

	LumP	LumNS	LumU	Ba/Sq	NE-like	Stroma-rich
Common copy number alterations of oncogenes/ tumour suppressor genes (% across subtype)	*FGFR3* amp. (10%) *CDKN2A* del. (33%)	*PPARG* amp. (76%)	*PPAR*G amp. (89%) *ERBB2* amp. (33%)	N/A	*RB1* del. (55%)	N/A
Common mutations (% across subtype)	*FGFR3* (40%) *KDM6A* (38%)	*ELF3* (35%)	*TP53* (76%)	*TP53* (61%) *RB1* (25%)	*TP53* (94%) *RB1* (39%)	N/A
Stromal cell infiltration (cell type)	N/A	Fibroblasts	Fibroblasts	Fibroblasts	N/A	Extensive smooth muscle and fibroblast infiltration
Immune cell infiltration (cell type)	N/A	N/A	N/A	CD8 T cells; NK cells	N/A	B cells
Median overall survival (years)	4	1.8	2.9	1.2	1	3.8

Table 1.1: Consensus MIBC subtypes

Summary of core features inherent to each MIBC subtype according to the latest consensus classifications. Table and accompanying data on copy number alterations, mutation rates and evidence of stromal and immune cell infiltration in each tumour subtype was adapted from Kamoun *et al.*, 2020. amp. = amplification; del. = deletion.

1.4.4 Molecular targets in muscle invasive bladder cancer

Overexpression of *EGFR* is one of the hallmarks of basal/squamous tumours, a subset with one of the worst survival rates in MIBC (Kamoun *et al.,* 2020). Basal tumours were found to exhibit a higher proportion of tumours with *EGFR* copy number amplifications compared to non-basal MIBC, while basal/squamous-like cell lines were found to be sensitive to treatment with the EGFR inhibitor Erlotinib, highlighting the marker as a potential drug target in basal/squamous MIBC (Rebouissou *et al.,* 2014). Despite being a feature of normal urothelium, high expression of *TP63* in tumours was associated with an adverse overall survival (Choi *et al.,* 2012) and exhibited an enriched gene signature in *EGFR*-high basal tumours, with six of the top ten most upregulated genes in basal tumours found to be direct targets of p63 isoform ΔNp63α (Choi *et al.,* 2014a). *EGFR* expression was low in luminal MIBC and NMIBC tumours, where instead increased expression of fellow EGFR RTK family members *ERBB2* and *ERBB3* was observed; (Choi *et al.,* 2014a; Dadhania *et al.,* 2016) perhaps indicative of the switch from an EGFR to a ERBB2/ERBB3 expressing phenotype found in NHU cells upon onset of quiescence (Varley *et al.,* 2005). *ERBB2* and *ERBB3* were mutated in 12% and 10% of MIBC cases, respectively, while mutations in *ERBB2* were found in a mutually exclusive pattern with *FGFR3* mutations in NMIBC, with *ERBB2* mutations only associated with higher grade tumours (Pietzak *et al.,* 2017; Robertson *et al.,* 2017).

FGFR3 (encoding Fibroblast Growth Factor Receptor Protein 3) is one of the most frequently mutated genes in bladder cancer, with activating mutations found in 48.6% of NMIBC and 40% of luminal papillary MIBC tumours, primarily located at mutational hotpots S249C and Y373C (Bernard-Pierrot *et al.,* 2006; Tomlinson *et al.,* 2007; Pietzak *et al.,* 2017; Robertson *et al.,* 2017; Kamoun *et al.,* 2020). The most common gene-gene fusion event in MIBC is that of the intrachromosomal translocation of *FGFR3* fused to transforming acidic coiled-coil-containing protein 3 (*TACC3*), leading to constitutive activation of the kinase domain of FGFR3 (Robertson *et al.,* 2017; The Cancer Genome Atlas Research Network, 2014). In its role as a RTK, FGFR3 is expressed by normal urothelium and is speculated to bind to FGF ligands produced by the stroma to modulate differentiation (Tomlinson *et al.,*

2005), although the identity of the specific ligand FGFR3 binds to in this context is currently undetermined. Previous studies have confirmed the ability of NHU cells to express FGFR3 transcript and protein under certain physiological conditions, with the primary isoform of the protein expressed being FGFR3b (Tomlinson *et al.,* 2005; Williams *et al.,* 2013). However, no study has yet elucidated what signalling pathways are required to induce FGFR3 expression in NHU cells, nor have described the effect of its expression on normal human urothelial phenotype.

Initial studies into the characterisation of PPARγ incidence in bladder cancer determined that expression of the nuclear receptor was inhibited in high-grade MIBC samples, suggesting that loss of PPARγ is an important step in MIBC progression (Nakashiro *et al.,* 2001). Independent component analysis of 198 MIBC tumours found that high expression of *PPARG* is associated with the luminal phenotype, with PPARγ-overexpressing tumours displaying an oncogenic addiction which affected viability upon PPARγ inhibition (Biton *et al.,* 2014). This observation is supported by meta-analysis of MIBC cohorts performed by other groups (Choi *et al.*, 2014a; Dadhania *et al.,* 2016; Damrauer *et al.,* 2014; Rebouissou *et al.*, 2014; Robertson *et al.*, 2017). FOXA1 and GATA3 have been speculated to help drive the luminal MIBC phenotype (Warrick *et al.,* 2016), suggesting that PPARγ could control the expression of several genes in luminal tumours via the same mechanisms present in normal, differentiated urothelium. Indeed, siRNA knockdown of PPARγ in the SD48 cell line resulted in a significant deregulation of 198 genes, including 18 genes with known associations to urothelial differentiation (Biton *et al.,* 2014).

While its mutation rate in NMIBC is relatively low, heterodimer partner RXRα was found to experience recurrent gain of function mutations in luminal MIBC tumours that resulted in ligand-independent activation of PPARγ (Halstead *et al.,* 2017; Rochel *et al.,* 2019). Luminal-associated overexpression of PPARγ has also been attributed to gain-of-function mutational hotspots in PPARγ that were found in residues at the PPARγ/RXRα binding interface and was predicted to affect heterodimer formation and increase binding affinity (Rochel *et al.,* 2019).

Downstream targets of PPARγ activation have similarly been implicated in the maintenance of a luminal MIBC phenotype. FOXA1 is mutated in 5% of MIBC, with loss of the TF typically associated with high grade MIBC (DeGraff *et al.,* 2012; The Cancer Genome Atlas Research Network, 2014). GATA3, like FOXA1, is a commonly used marker of luminal MIBC (Dadhania *et al.,* 2016; Robertson *et al.,* 2017). Expression of the protein was decreased in cases of high-grade MIBC when compared to matched non-neoplastic urothelium, where it was expressed in 98% of samples (Miyamoto *et al.,* 2012). Histologically, GATA3 expression in cases of MIBC was correlated to CK20 expression but negatively correlated with Ki67 positivity (Wang *et al.,* 2019). Found in 12% of MIBC cases, *ELF3* is one of the most commonly mutated genes in MIBC (Dadhania *et al.,* 2016). *ELF3* mutations were significantly enriched in the luminal non-specified group, with 35% of tumours harbouring a mutation. Tumours with *ELF3* mutations were commonly found in tumours with altered *PPARG* expression, with 76% of luminal non-specified tumours carrying *PPARG* amplifications or gene fusions (Kamoun *et al.,* 2020). *ELF3* mutational sites in luminal tumours were found to be particularly enriched in the DNA binding ETS domain site, with 20 out of the 22 mutations screened in this domain determined to be luminal tumours (Dadhania *et al.,* 2016).

The preceding observations therefore suggest that the mechanisms of PPARγ-mediated urothelial differentiation are present in a subset of MIBC, yet important transcription factors in this process are often mutated and therefore exhibit aberrant function in comparison to normal urothelium. Loss of the PPARγ-regulated transcriptional machinery is a marker of highly aggressive, *EGFR*-overexpressing basal/squamous MIBC, a disease state which is associated with a low survival rate. A greater understanding of the mechanistic relationship between differentiation-promoting factors and a re-activation of proliferative pathways in normal urothelium may thus aid attempts to produce specific therapeutic treatments for subsets of MIBC based on molecular profiling. A summary of studies that have investigated the phenotype of commonly mutated markers of luminal and basal MIBC in MIBC cell lines *in vitro* is collated in Table 1.2.

Marker	Luminal-like MIBC cell lines	Basal/squamous-like MIBC cell lines	Other MIBC cell lines
EGFR	RT4 and UM-UC-9 cells resistant to Erlotinib treatment (Rebouissou *et al.,* 2014).	Erlotinib significantly reduced 5637 and ScaBer cell growth (Rebouissou *et al.,* 2014).	
p63	Treatment of UM-UC-9 cells with PPARγ agonist rosiglitazone induced expression of PPARγ targets while inhibiting p63 target genes (Choi *et al.,* 2014a).	shRNA knockdown of p63 in UM-UC-14 cells resulted in increased expression of *FOXA1, UPK1A*, *UPK2, ERBB2* and *ERBB3* (Choi *et al.,* 2014a).	
FGFR3	RT4 and RT112 cell lines considered to be 'FGFR3-driven', due to expression of activating oncogenic FGFR3 gene fusion proteins (Williams *et al.* 2013). These FGFR3-dependent cell lines display lower genomic instability and share similarities to the NMIBC phenotype when compared to other MIBC lines (Earl *et al.,* 2015).		
PPARγ	RT4 cells harbour an activating mutation in the PPARG gene, with siRNA depletion of the gene reducing viability in said cells (Rochel *et al.,* 2019).	5637 cells have low, wild-type expression of *PPARG* (Rochel et al., 2019).	
FOXA1	shRNA knockdown of FOXA1 in FOXA1-high RT4 cells resulted in increased proliferation and decreased E-cadherin expression (DeGraff *et al.,* 2012).	5637 cells were *FOXA1*-negative (DeGraff *et al.,* 2012).	FOXA1 overexpression in T24 cells resulted in decreased proliferation and invasiveness (DeGraff *et al.,* 2012).
GATA3		shRNA knockdown of GATA3 in 5637 cells results in significantly increased migration and invasion. GATA3 overexpression in GATA3-negative UM-UC-3 cell line resulted in decreased migration and invasion, attributed to a decrease in N-cadherin and MMP2/MMP9 expression (Li *et al.,* 2014).	
ELF3	High ELF3 expression observed in RT112 cells (Gondkar *et al.,* 2019).	Overexpression of ELF3 reduced N-cadherin expression and cell invasiveness in UM-UC-3 cells (Gondkar *et al.,* 2019).	Overexpression of ELF3 inhibitory lncRNA ELF3-AS1 in T24 cells contributed to increased viability and invasiveness of the cell line (Guo *et al.,* 2019).

Table 1.2: Summary of studies investigating commonly mutated MIBC markers in MIBC cell lines

Studies were separated based on whether the cell line(s) exhibited a luminal-like or basal-like MIBC phenotype. The high-grade MIBC cell line T24 exhibit neither luminal nor basal features, and as such were placed in their own column.

1.5 Thesis aims

Exploiting the reversible phenotypic shifts that NHU cells can undertake between proliferation, differentiation and regeneration has resulted in the discovery of PPARγ as a master regulator of urothelial differentiation, whilst determining that transcription factors downstream of PPARγ such as FOXA1, GATA3 and ELF3 are also important in this process. Context-dependent expression of these transcription factors highlights the sensitive balance of tissue homeostasis in the urothelium, and studying this plasticity in NHU cells has previously been demonstrated to provide insight into the events that accompany urothelial tumorigenesis and progression to an invasive phenotype. Stratification of MIBC into subtypes based on their transcriptomic signature has so far provided a limited clinical benefit to patients through a lack of successful drug treatments based on molecular targets. In order to improve treatment of MIBC, a more focussed elucidation of how various signalling pathways could moderate cancer progression in different subtypes of MIBC is therefore required.

This study highlights two candidate signalling pathways that were hypothesised to modulate urothelial tissue homeostasis and potentially interact with the previously identified signalling machinery that regulate urothelial phenotype: the Hippo and Sonic Hedgehog (SHH) pathways. The role of the SHH pathway in proliferation, regeneration and intercellular paracrine signalling between urothelial and stromal cells in foetal human and adult murine bladder is well established, but its role in adult human urothelium is not understood. Conversely, Hippo pathway signalling has not been studied in mammalian urothelium, but studies in other organ types implicate the pathway in the maintenance of tissue homeostasis. The aim of this thesis was therefore to utilise well-characterised *in vitro* systems (alongside transcriptomic analysis of normal and malignant bladder tissue) to understand how these two pathways affect urothelial physiology through their influence on individual cell phenotype.

The role that Hippo and SHH pathway signalling plays in urothelial phenotype was investigated by meeting the following three key objectives:

- Using a combination of in-house and publically available RNAseq datasets to characterise transcript expression of Hippo and SHH pathway components in normal urothelium (*in situ* and *in vitro* NHU cells) and bladder cancer (MIBC tumours and cell lines; Chapter 3, 4 & 5).

- Investigating what function Hippo pathway signalling plays in the onset of urothelial cytodifferentiation, the maintenance of tissue homeostasis and regulation of urothelial cell propagation in NHU cells (Chapter 3) and bladder cancer cell lines (Chapter 4).

- Determining whether a SHH-mediated paracrine signalling loop between human urothelium and the underlying stroma exists, can be reconstituted *in vitro*, and is subsequently dysregulated in MIBC (Chapter 5).

2. Materials and methods

2.1 General

Practical work for this project was primarily undertaken at the Jack Birch Unit of Molecular Carcinogenesis, Department of Biology, University of York. Selected experiments were performed at the Technology Facility, Department of Biology, University of York or St. James's University Hospital, University of Leeds. Details of suppliers of reagents used in this study can be found in Appendix i.

2.2 H_2O

Recipes of stock buffers are detailed in Appendix ii. All water used in experiments and to make up stock solutions and buffers was purified using an ultrapure water deionisation unit (SUEZ Water). SUEZ-purified water (dH_2O) and buffers used for tissue culture purposes were autoclaved (121 ^{o}C for 20 minutes) prior to use.

To produce water that was nuclease-free (and therefore suitable for molecular biology-based experiments), dH_2O was treated with diethylpyrocarbonate (DEPC) to a final concentration of 0.1%. DEPC-treated dH_2O was subsequently autoclaved (as above) prior to use.

2.3 Ethical approval

NHS Research Ethics Committee and the University of York Biology Ethics Committee approved collection and use of discarded samples of human urothelial tissue. Tissue was sought from patients with no previous history of urological neoplasia, with informed consent obtained for each sample. Prior to isolation of cells, each anonymised sample was given a sequential, unique "Y" number (e.g. Y1947) and the age, gender and operation of the patient were recorded. Each Y number used in this thesis, along with age, gender and operation details can be found in Appendix iii.

2.4 Tissue culture

2.4.1 General

All cell/tissue culture work was performed aseptically in either class II recycling laminar air flow safety cabinets (Medical Air Technology), or an externally ducted cabinet (Envair) when working with retroviruses. Cabinets used for tissue culture work were cleaned with 70% (v/v) ethanol before and after use. Cell cultures were maintained in Heracell™ 240 Incubators (Heraeus®) at a temperature of 37^{o}C in a humidified atmosphere of either 5% CO_2 in air (NHU cells) or 10% CO_2 in air (all other cell types used). Waste medium from cultures was aspirated into Buchner flasks containing 10% (w/v) Virkon® (Fisher Scientific) disinfectant prior to disposal. Fresh medium was applied to cultures every 2-3 days, unless otherwise stated. NHU cells were grown in Cell^{+} culture plasticware (Sarstedt) to promote attachment and growth of primary cells. Other cell types were grown in Primaria® (BD Bioscience) plasticware.

Cell culture centrifugation steps were undertaken in a benchtop centrifuge (Sigma) at 360 x g for 4 minutes unless otherwise stated. To count cells, 10 µl of suspended cells were pipetted onto an Improved Neubauer haemocytometer (VWR) to determine the concentration of cells/mL of medium. An EVOS XL Core (Thermo Fisher) phase-contrast microscope was used to both count cells and take images of cells in culture.

2.4.2 Tissue sample collection

Samples of ureter and bladder were obtained from St. James's University Hospital, Leeds or Pinderfields Hospital, Wakefield. Following surgery, sample biopsies were collected in sterile polystyrene Universal tubes containing sterile transport medium (Appendix ii). Upon arrival at the Jack Birch Unit, samples were stored at 4 ^{o}C for up to 3 days before being processed, as detailed below.

2.4.3 Cell isolation

2.4.3.1 Urothelial cell isolation

The established method of growing primary urothelial cells from patient biopsies was used exactly as previously described (Southgate *et al.,* 1994; Southgate *et al.,* 2002). Tissue samples were dissected to remove excess connective tissue and fat using sterile, autoclaved scissors and forceps. A small representative piece of each sample (~0.5 cm^2) was cut and placed into 10% (v/v) formalin (Appendix ii) for a period of 24-48h to fix the tissue. The tissue was subsequently stored in 70% ethanol in preparation for later histological analysis (Section 2.9.1).

The remaining tissue was cut into sections of approximately 1 cm^2 and placed in Universal tubes containing stripper medium (Appendix ii). Tissue sections were maintained in stripper medium for either 4 hours at 37 ^oC or 16 hours at 4 ^oC before urothelial cells were separated from the underlying stroma through gentle scraping of the sample with forceps. Urothelial cells were collected by centrifugation and resuspended in 2 mL (400 U) of collagenase IV (Appendix ii) at 37 ^oC for 20 minutes to disaggregate the cells. Following collagenase IV treatment, cells were counted, centrifuged, resuspended in Keratinocyte Serum-Free Medium (KSFM; Gibco®; Thermo Fisher) and seeded at a minimum density of 4 x 10^4 cells /cm^2 in $Cell^+$ plasticware.

2.4.3.2 Stromal cell isolation

Upon de-epithelialisation of ureter and bladder samples, pieces of stroma were cut up in transport medium into pieces of around 1 mm^3 in size. The pieces were centrifuged and resuspended in 100 U/mL collagenase IV for 4 hours at 37 ^oC. Stromal pieces were subsequently centrifuged, washed in Dulbecco's Modified Eagle's Medium (DMEM; Gibco®), centrifuged again and transferred to 25 cm^2 Primaria® flasks as explants with minimal (100 µL) DMEM medium containing 10% HyClone™ bovine calf serum (BCS; Fisher Scientific) and 1% L-glutamine (LG; Gibco®). After 2 days the minimal medium was removed and the explants were gently flooded with medium to avoid dislodging explants. Flasks were left in the same medium for 7 days to encourage stromal cell growth from the explants, which

were discarded upon passage of cells. A summary diagram of the steps required to isolate NHU and ureteric-derived stromal cells is provided in Figure 2.1.

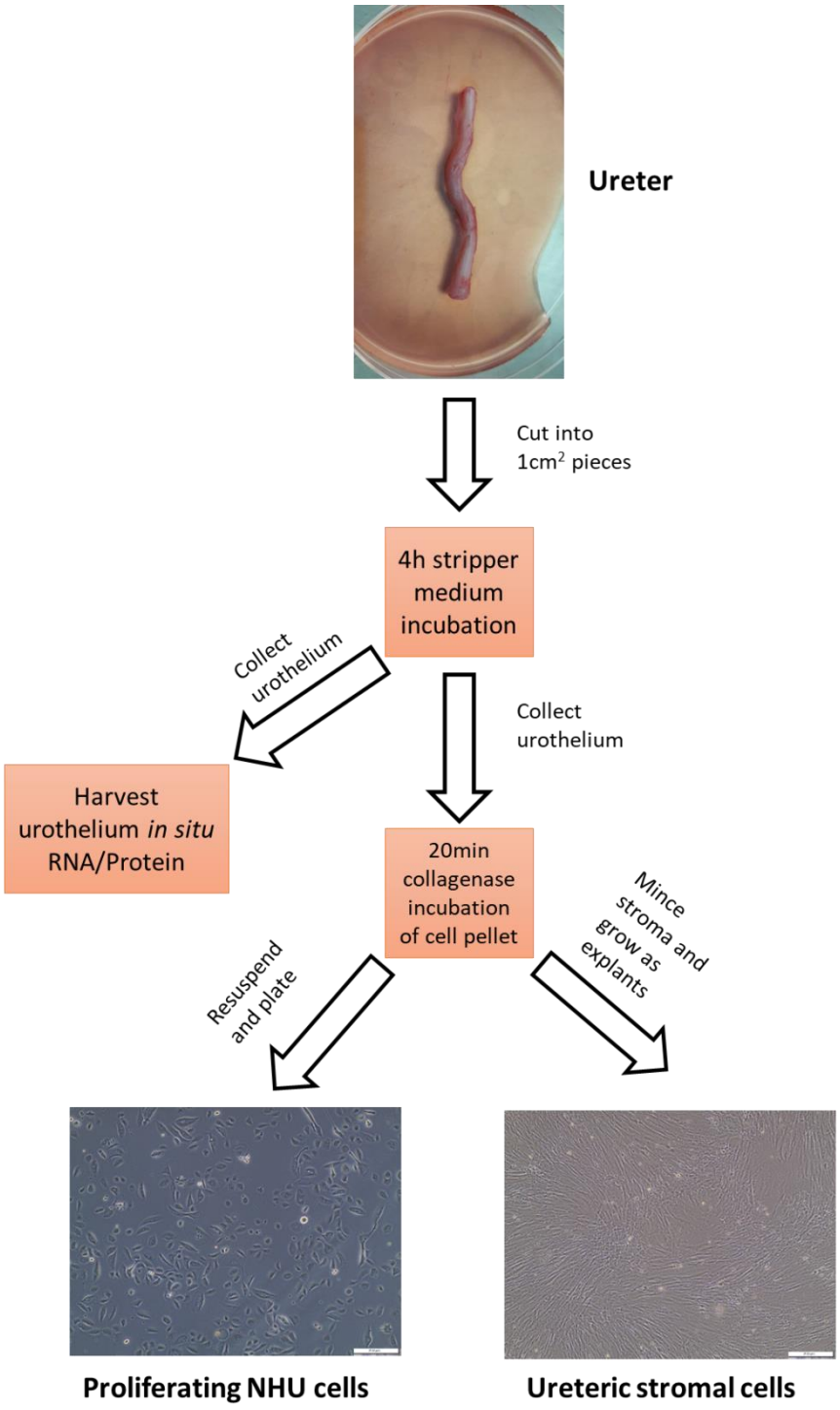

Figure 2.1: Flowchart of urothelial and stromal cell isolation from ureter

Samples in study classified as "Urothelium *in situ*" refer to RNA/protein lysed from normal urothelium that had been stripped from pieces of ureter but were not disaggregated or cultured *in vitro* at any point.

2.4.4 Cell culture

2.4.4.1 Maintenance of NHU cell lines

NHU cells were grown in KSFM supplemented as standard with 5 ng/mL recombinant human EGF and 50 µg/mL bovine pituitary extract (both Gibco®). Additional supplementation with 30 ng/mL cholera toxin (Sigma) was used to create what is referred to as complete KSFM (KSFMc). Upon reaching approximately 90% confluence, NHU cells were passaged through incubation with 0.1% Ethylenediaminetetra-acetic acid disodium salt (EDTA) in Phosphate Buffered Saline (PBS; Appendix ii) at 37 ^{o}C for approximately 5 minutes to promote dissociation of the cells from the Cell^{+} plasticware. Following aspiration of EDTA, cultures were incubated in 0.5- 1 mL Trypsin-Versene (TV; Appendix ii) for 5 minutes, upon which cells would detach from the plasticware after gentle tapping. 100 µL of 20 mg/mL Trypsin Inhibitor (Appendix ii) mixed with 4 mL KSFMc were added to the suspension of detached cells in TV and centrifuged. The resulting pellet was resuspended in KSFMc and split into new plasticware at a ratio of 1:3. All experiments in this study were performed on NHU cells that were of passage number 1-5. Where stated, experiments were replicated using NHU cell lines from multiple independent donors.

2.4.4.2 Maintenance of stromal cell lines

Stromal cells were grown in supplemented DMEM as described in section 2.4.3.2. Stromal cells were passaged as in section 2.4.4.1, except treatment with EDTA lasted for < 1 minute as these cells rapidly dissociated from the plasticware. The addition of Trypsin Inhibitor was also omitted due to the presence of serum in the culture medium. Stromal cells were split into new plasticware at a ratio of 1:3. All experiments in this study were performed on stromal cells that had been passaged fewer than seven times. Where stated, experiments were replicated using stromal cell lines from multiple independent donors.

2.4.4.3 Culture of established cell lines

All established cell lines were originally obtained from the American Type Culture Collection (Middlesex, UK) except for the RetroPack™ PT67 cell line, which was obtained from Takara Bio (formally Clontech; Gothenburg, Sweden). The list of cell lines used in this study, their origin and the growth medium used is detailed in Table 2.1. All cell lines were previously genotyped using a PCR-based short tandem repeat analysis (performed in-house) and were passaged less than 10 times since the genotyping date.

Name	Origin	Medium
HT1376	Bladder cancer	DMEM + RPMI + 5% FBS +1% LG
PT67	Embryonic mouse fibroblast	DMEM + 10% FBS + 1% LG
RT4	Bladder cancer	DMEM + RPMI + 5% FBS + 1% LG
ScaBer	Bladder cancer	DMEM + RPMI + 5% FBS + 1% LG
T24	Bladder cancer	DMEM + RPMI + 5% FBS + 1% LG
UM-UC-9	Bladder cancer	DMEM + RPMI + 10% FBS + 1% LG
3T3-J2	Embryonic mouse fibroblast	DMEM + RPMI + 10% BCS +1% LG
5637	Bladder cancer	RPMI + 5% FBS + 1% LG

Table 2.1: List of established cell lines used in study.

FBS= fetal bovine serum.

2.4.4.4 Pharmacological agonists and antagonists

The list of agonists and antagonists used in this study is detailed in Table 2.2. Compounds were solubilised in sterile tissue culture grade dimethyl sulfoxide (DMSO; Sigma), dH_2O or enterokinase buffer (Appendix ii) and frozen at either -20 ^{o}C or -80 ^{o}C for long term storage in individual aliquots. A 0.1% (v/v) concentration of DMSO was both used as a vehicle control and kept as a constant concentration in treatment arms of every experiment involving the use of DMSO-reconstituted compounds. Compounds used were initially titrated on target cells to determine the optimum concentration of drug to use. The optimum concentrations for use of LY294002, PD153035, SB431542, rSHH, TGFβ, TZ and T0070907 were determined prior to the start of the study. Details of the titrations performed for SAG, PD98059 and U0126 can be found in Section 5.4.3.1 and Appendix viii.

2.4.4.5 ABS/Ca^{2+} differentiation of NHU cells

Functional differentiation of NHU cells was achieved using a previously described protocol (Cross *et al.,* 2005) that results in a functional barrier producing, "biomimetic" urothelium. NHU cells grown to 90% confluence in Cell^{+} plasticware were incubated in KSFMc supplemented with batch selected 5% Adult Bovine Serum (ABS; BioIVT; formally SeraLab) for a period of 3-5 days. 180 µL $CaCl_2$ from a 1 M stock solution was subsequently added /100 mL 5% ABS KSFMc medium to raise the total [Ca^{2+}] concentration from 0.09 mM to 2 mM. Cultures were maintained in this medium (referred to as ABS/Ca^{2+}) for a further 7 days, unless otherwise stated.

Name	Molecular target	Function	Supplier	Vehicle
FR180204 (FR180)	ERK1/2	Antagonist	Tocris	DMSO
GDC-0449	Smoothened (SMO)	Antagonist	Selleck Chemicals	DMSO
LY294002 (LY)	PI3K	Antagonist	Merck Milipore	DMSO
PD153035 (PD)	EGFR	Antagonist	Merck Milipore	DMSO
PD98059	MEK1	Antagonist	Cell Guidance Systems	DMSO
Recombinant Sonic Hedgehog (rSHH)	Patched-1	Agonist	Gift from Dr. Riobo-Del Galdo	EK buffer
Recombinant TGFβ1 (TGFβ)	TGFβRI	Agonist	R&D Systems	4mM HCl + 0.1% BSA
Smoothened Agonist (SAG)	SMO	Agonist	Cayman Chemicals	DMSO
SB431542	TGFβRI	Antagonist	Sigma-Aldrich	DMSO
Troglitazone (TZ)	PPARγ	Agonist	Tocris	DMSO
T0070907 (T007)	PPARγ	Agonist	Tocris	DMSO
U0126	MEK1/2	Antagonist	Merck Milipore	DMSO

Table 2.2: List of agonists/antagonists used in study.

2.4.4.6 Measurement of Transepithelial Electrical Resistance (TEER)

TEER refers to the tightness of barrier produced by ABS/Ca^{2+} differentiated NHU cells grown on 0.4 µm pore Snapwell™ membranes. NHU cells at 90% confluence were harvested with TV and seeded onto Snapwell membranes (surface area of 1.13 cm^2) at a concentration of 5 x10^5 cells/membrane. Upon attachment to the membranes, cultures were treated as described in Section 2.4.4.5. TEER was measured using the cellZscope (nanoAnalytics), an instrument that measures the impedance of barrier-forming cell cultures at user-defined intervals. The units of TEER used were Ω.cm^2, with a TEER barrier measurement of > 500 Ω.cm^2 considered "tight". All elements of the cellZscope instrument (except from the base unit) were autoclaved prior to use to maintain sterility. Six technical replicate membranes were used for each experimental condition. Using sterile forceps, membranes (containing ABS/Ca^{2+} differentiated NHU cells) were placed in stainless steel electrode pots screwed into the base unit of the instrument. Each pot contained 1.6 mL medium while 700 µL medium was added to the apical compartment of each membrane. The electrode-containing lid was lowered vertically onto the base unit and sealed to ensure that each electrode was submerged in the medium contained in each Snapwell in a sterile environment. To measure TEER of the experimental cultures, the instrument was connected to its station contained within a 37 ^oC, 5% CO_2 incubator. The station recorded TEER readings every hour and relayed the readings to a console which converted the data into an .xls document upon completion of the experiment. The cultures were medium changed every 2-3 days, requiring the removal of the instrument from the station and its lid in order to gain access to the membranes. For a summary diagram of the cellZscope assay, see Figure 2.2.

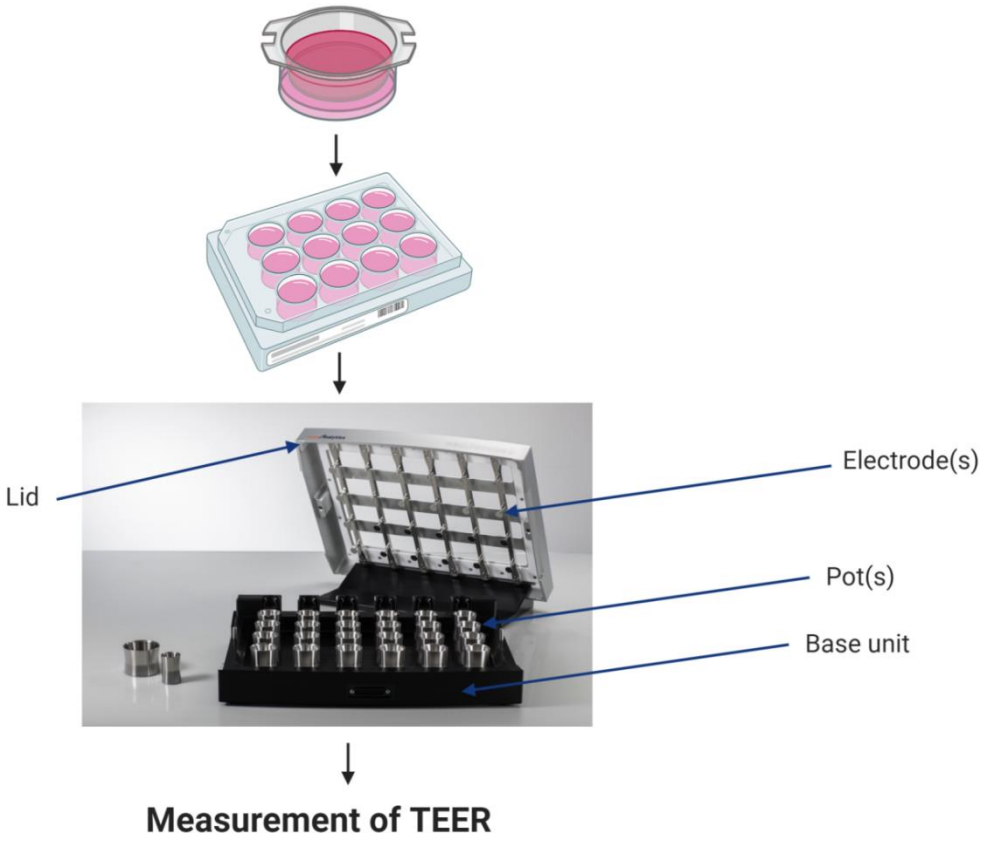

Figure 2.2: Experimental flowchart of measuring urothelial barrier tightness using the cellZscope

Snapwell membranes containing ABS/Ca^{2+} differentiated NHU cells were transferred from tissue culture plasticware to medium-containing pots screwed into the cellZscope. Electrodes in the machine recorded barrier impedance over time and relayed TEER readings to a connected console. Image of the cellZscope console was obtained from the technical manual provided by nanoAnalytics.

2.4.4.7 Scratch wounding of cell cultures grown on membranes

ABS/Ca^{2+} differentiated NHU cells were seeded onto Snapwell membranes and had TEER measurements recorded as described in section 2.4.4.6. Once relative stabilisation of TEER values in cultures was observed, a sterile 200 µL pipette tip was used to create a single, lateral wound per membrane (six technical replicates per condition) and the TEER readings were measured immediately after scratch wounding to confirm that the impedance reading of each membrane had fallen below the threshold of tightness. CellZScope readings were taken every 20 minutes after the scratch to compare the rate of recovery between experimental conditions.

2.4.4.8 Lifting of cell sheets by dispase treatment

Once cultures growing on Snapwell™ membranes had recovered from the scratch wound (as determined by stabilisation of TEER), intact cell sheets were detached from the membranes using 2% (w/v) dispase solution (Sigma-Aldrich) in PBS, warmed to 37 ^{o}C prior to use. Medium was aspirated from the pots before dispase solution was applied to the apical and basal chambers of the pot at the same volume as the previous medium for a period ranging from 20 minutes to 1 hour. After the cell sheets started to lift away from the edges of the membrane, they could be removed by gentle pipetting. To create a single cell suspension, the cell sheets of each condition were combined and pipetted into 5 mL EDTA solution at 37 ^{o}C. Cell sheets were then transferred to 1 mL TV solution for 1 minute before the cells could be disaggregated by vigorous pipetting. The resultant cell populations were subsequently assayed by flow cytometry (Section 2.6).

2.4.4.9 TZ/PD differentiation of NHU cells

A previously described protocol was used to alternatively differentiate NHU cells using pharmacological agents (Varley *et al.,* 2004a). NHU cells at 80% confluence (unless otherwise stated) were grown in KSFMc medium and treated with PPARγ agonist troglitazone (TZ) and EGFR tyrosine kinase inhibitor PD153035 (PD), each at a final concentration of 1 µM for 24 hours. After 24 hours, TZ was removed from the medium and the cells were grown in KSFMc + PD153035 medium for a further period of 48h (72h total) or 120h (144h total). Some experiments, where noted, included parallel cultures of cells pre-treated with PPARγ antagonist T0070907 (T007) for 3h prior to TZ/PD induction to inhibit PPARγ activation. Any cultures pre-treated with T007 were subsequently treated with T007 by itself or with a combination of TZ, PD and T007.

2.4.4.10 *Mycoplasma spp.* testing

To avoid the problems that occur as a result of *Mycoplasma spp.* contamination, primary and established cell lines were routinely checked for extranuclear DNA labelling (an indication of mycoplasma contamination) using a fluorescent DNA labelling method. Cells were seeded onto sterile 12 well glass slides (Hendley Essex) at a density of $1x10^4$ cells/well and left to grow overnight. Slides were washed in

PBS, fixed in a 1:1 mixture of methanol and acetone (both Fisher Scientific) for 30 seconds and left to dry. Cultures were stained with 0.1 µg/mL of fluorescent DNA counterstain Hoechst 33258 (Thermo Fisher) in PBS for 5 minutes while being protected from light by aluminium foil. Cultures were washed in PBS, air dried and mounted in Prolong™ Gold Antifade Reagent (Invitrogen). Slides were subsequently examined for extranuclear Hoechst labelling using an Olympus BX60 microscope with epifluorescence illumination.

2.5 Cell viability assay

The alamarBlue® (Bio-Rad) assay was used to measure proliferation of NHU cell cultures over a period of 9-13 days. Cells were harvested and seeded at a concentration of 2 x 10^4/ mL into ten separate Primaria® 96-well culture plates at a volume of 200 µL/well and left to attach. Six replicate wells were assayed per condition. To determine cell viability, cells were medium changed to 200 µL of 10% alamarBlue in KSFMc at 37 ^{o}C for four hours. Absorbance readings of 570 nm and 600 nm were subsequently measured using a Multiskan Ascent 96-well plate reader (Thermo Scientific). In the absence of viable cells, the active ingredient in alamarBlue reagent (resazurin) is blue. Metabolic activity results in the irreversible reduction of non-toxic, cell-permeable resazurin into resorufin, a compound that produces a bright red fluorescence. In the absence of a cell stress response, the absorbance readings are directly proportional to mitochondrial activity which is used as a proxy for the total number of viable cells per sample. Plates that been incubated with alamarBlue were subsequently discarded, resulting in a separate plate being read each day. The remaining unread plates were medium changed every 2-3 days as standard. The equation used to calculate percentage reduction of alamarBlue reagent per condition using the 570 nm and 600 nm absorbance values is detailed in Figure 2.3.

Percentage alamarBlue reduction =

$$\left[\frac{(34798 \times \text{cell absorbance @570 nm}) - (80586 \times \text{cell absorbance @ 630 nm})}{(155677 \times \text{no cell control absorbance @570 nm}) - (5494 \times \text{no cell control absorbance @ 630 nm})} \right] \text{X } 100$$

Figure 2.3: Equation used to calculate alamarBlue reduction in proliferating samples

34798 = the molar extinction coefficient of oxidised alamarBlue (blue) reagent at 600 nm. 80586 = the molar extinction coefficient of oxidised alamarBlue (blue) reagent at 570 nm. 155677 = the molar extinction coefficient of reduced alamarBlue (red) reagent at 570 nm. 5494 = the molar extinction coefficient of oxidised alamarBlue (red) reagent at 600 nm.

2.6 Cell cycle analysis

To determine what percentage of a cell population was actively in cell cycle, cultures were treated with Bromodeoxyuridine (BrdU; Cambridge Bioscience), a thymidine analogue that is incorporated into the DNA upon replication and therefore serves as a marker of cells in the population that have entered S phase in the assayed timeframe. Cells pulsed with BrdU were subsequently harvested, fixed, labelled and their fluorescent intensity detected by a flow cytometer.

Cells that were cultured for the purpose of cell cycle analysis (other than the cells described in Section 2.4.4.8) were seeded into 75 cm^2 flasks at a concentration of 1 $x10^6$ cells/flask. Upon reaching the desired cell density, cultures were pulsed with 30 µM BrdU for either 1h (MIBC cell lines) or 6h (ABS/Ca^{2+} differentiated NHU cells) in order to capture a suitable population of BrdU+ cells. Following BrdU treatment, cultures were harvested with TV as previously described to obtain a single cell suspension of 1 $x10^6$ cells, washed in PBS and fixed in 70% ethanol kept on ice. Fixed cells were transferred into Falcon™ 15 mL Conical Centrifuge Tubes (Fisher Scientific) and stored at 4 ^oC in 70% ethanol. All subsequent pellet steps were performed by spinning the cells at 2500 x g for 2 minutes. Cells were pelleted and an acid hydrolysis step was performed by resuspending the cells in 2 N HCl with 0.5% Triton X-100 (Sigma) for 30 minutes to denature the DNA and allow access for

the BrdU mAb to bind. Cells were resuspended in 0.1 M sodium tetraborate for 2 minutes, washed in PBS containing 1% (w/v) Bovine Serum Albumin (BSA; Sigma), and resuspended in PBS/1% BSA/0.5% Tween-20. α-BrdU mAb (IIB5, Santa Cruz Biotechnology) was added at a concentration of 1µg antibody/10^6 cells for 1h at ambient temperature. Cells were pelleted and washed before incubation in 50 µL PBS/1% BSA/0.5% Tween 20 containing 5 µg/mL Goat anti-Mouse IgG (H+L) Cross-Adsorbed Secondary Antibody, Alexa Fluor 488 (Invitrogen) for 30 minutes at ambient temperature. Prior to analysis, cells were resuspended in 500 µL PBS containing 20 µg/mL propidium iodide (PI; fluorescent DNA intercalating agent) and 10 µL/mL RNAse A (both Sigma) and incubated at 37 ^{o}C for 30 minutes. A CyAn™ ADP High-speed Analyzer (Beckman Coulter) was used to quantify PI and BrdU fluorescence in samples by flow cytometry. A minimum of 5000 events was counted for each condition. Controls included cells that had incubations with the secondary, but not primary, antibody (Secondary only) and cells that were not incubated with any antibody (PI only). These cells were additionally utilised to set up the correct fluorescence compensation and gated regions during each analysis. The distribution of cells in 2N (G0/G1), S and 4N (G2/M) phases were calculated and analysed in FlowJo (TreeStar) software.

2.7 Gene expression analysis

2.7.1 General

All RNA processing work took place on a designated, DNA amplicon-free bench that had been cleaned with RNaseZap® decontamination solution (Invitrogen). Similarly, all pipettes and gloves used during this process were cleaned in the same manner prior to use. DNAse/RNAse-free pipette tips (Starlab) and DNAse/RNAse-free microfuge tubes (Invitrogen) were also used to inhibit contamination of samples. All steps were performed at ambient temperature unless otherwise stated.

2.7.2 RNA extraction

Cells cultured for the purpose of RNA extraction were grown in 6-well plates. Upon reaching the completion of a time-point or the desired confluence, cultures were washed twice in PBS before addition of 500 µL TRIzol® (Thermo Fisher) reagent per

well of a 6-well plate for 5 minutes to solubilise the cells. Rubber cell scrapers (Sarstedt) were used to collect the sample lysates before the mixtures were transferred to 1.5 mL microfuge tubes and stored at -80 ^{o}C. Samples were thawed on ice and then left at ambient temperature for five minutes before extraction to allow for complete dissociation of nucleoprotein complexes. For each 1 mL of TRIzol used, 0.2 mL neat chloroform was added per sample before the lysates were vortexed for 15 seconds and incubated for a further 3 minutes. Samples were centrifuged at 12000 x g for 15 minutes at 4 ^{o}C to separate the mixture into a pink phenol-chloroform phase, a cloudy interphase and an RNA-containing aqueous phase. The aqueous phases were carefully collected into clean microfuge tubes while the protein and DNA-containing phases were discarded. The collected RNA was precipitated using a 1:1 ratio of isopropanol (Fisher Scientific; formally Honeywell), which was gently mixed with the RNA solution and left for 10 minutes. Samples were spun at 12000 x g for 20 minutes at 4 ^{o}C to collect the precipitated RNA at the bottom of the tubes. Waste supernatant was removed by pouring before the RNA was washed with 1 mL 75% ethanol. After centrifuging the sample at 10000 x g for 5 minutes at 4 ^{o}C, the wash process was repeated to ensure the removal of all salt contaminants. The RNA pellet was allowed to air dry upon pouring off the final 75% ethanol wash before resuspension in 30 µL DEPC-treated dH_2O in a clean microfuge tube.

2.7.3 DNAse treatment of RNA

Removal of residual contaminating DNA from RNA samples was achieved using a DNA-*free*^{TM} DNA removal kit (Thermo Fisher; formally Invitrogen). RNA samples were incubated with 2 U/µL rDNase 1 and a 1:10 dilution of 10x DNase 1 buffer (both Invitrogen) at 37 ^{o}C for 30 minutes. A DNase inactivation reagent slurry was added to the mixture at a 1:10 dilution for 2 minutes at ambient temperature, with vortexing of samples performed every 30 seconds. The DNase inactivation reagent was removed by centrifuging samples at 10500 x g for 90 seconds, with the DNA-free supernatants subsequently transferred to clean microfuge tubes. The concentration and quality of RNA in solution was measured using a NanoDrop^{TM} UV

spectrophotometer (Thermo Fisher). Clean RNA was kept at -80 ^{o}C for long term storage.

2.7.4 Sodium acetate precipitation of RNA

A 260 nm: 230 nm ratio of less than 1.5 indicates contamination of RNA samples with ethanol or salts. In the event that samples contained contaminants, RNA were cleaned with an alcohol and salt precipitation. To a 30 µL solution of RNA, 3.3 µL of 3 M sodium acetate was added alongside 83 µL (2.5 x volume) of 100% ethanol. The mixture was vortexed and stored at -80 ^{o}C for at least 16 hours. The samples were subsequently centrifuged at 12000 x g for 30 minutes at 4 ^{o}C, the supernatant removed and replaced by 500 µL 75% ethanol. The centrifugation and aspiration were repeated before the clean RNA pellets were left to air dry. The pellets were once again resuspended in 30 µL DEPC-treated dH_2O, the concentration quantified using a NanoDrop^{TM} UV spectrophotometer and stored at -80 ^{o}C.

2.7.5 cDNA synthesis

1 µg RNA was used in each complementary DNA (cDNA) synthesis reaction. RNA was mixed with 0.1 µg/µL Oligo$(dT)_{12-18}$ primers (Invitrogen) and DEPC-treated dH_2O up to a total volume of 12 µL. Each RNA sample was used to perform two cDNA synthesis reactions: one containing Superscript II Reverse Transcriptase (Invitrogen) enzyme (RT+) and one with dH_2O replacing reverse transcriptase (RT-). Heating the mixture to 65 ^{o}C for 10 minutes before cooling on ice resulted in the annealing of the primers to the RNA. 7 µL of a master mix containing 4 µL 5X First-Strand buffer, 2 µL 0.1 M dithiothreitol (DTT; both Invitrogen), and 1µL of a 10 mM dNTP mixture (dATP, dTTP, dCTP and dGTP; all Promega) was added to each reaction. 50 U/µL Superscript II Reverse Transcriptase was subsequently added to each RT+, but not RT-, condition. Reaction tubes were incubated at 42 ^{o}C for 50 minutes to induce cDNA synthesis before inactivation of the reverse transcriptase by heating to 70 ^{o}C for 15 minutes. Newly synthesised cDNA was diluted to 100 µL with DEPC-treated dH_2O and stored at -20 ^{o}C.

2.7.6 Primer design

Genome browser Ensembl (https://www.ensembl.org/index.html) was used to search for protein-coding mRNA sequences of genes that were to be amplified by Reverse Transcription Polymerase Chain Reaction (RT-PCR). In instances where genes had multiple protein-coding splice variants, sequences were aligned using Kalign Multiple Sequence Alignment software (https://www.ebi.ac.uk/Tools/msa/kalign/). Primers specific to the aligned sequence were designed using the Primer3 v0.4.0. program (http://bioinfo.ut.ee/primer3-0.4.0/). For quantitative Polymerase Chain Reaction (RT-qPCR) targets, primers were designed using Primer Express™ v3.0.1 (Thermo Fisher) software. Specifications for primers used in this study included a size range of 18-30 base pairs (bp), GC% content between 40-60%, melting temperature (Tm) between 56-65 ^{o}C and an amplicon product size of between 100-450 bp (RT-PCR) or 50-100 bp (RT-qPCR). Target specificity of primers was confirmed using the primer BLAST tool (https://www.ncbi.nlm.nih.gov/tools/primer-blast/). Primer oligonucleotides were ordered from Eurofins Genomics, diluted in DEPC-treated dH_2O to 100mM and stored at -20 ^{o}C. Primer sequences are detailed in Appendix iv.

2.7.7 Primer optimisation

The optimum annealing temperature in which to use primer sets for RT-PCR analysis was determined by gradient PCR using a positive control sample. Genomic DNA was used when primer sets were specific to a DNA sequence located in a single exon, while cDNA expressing the gene was used when the primer product spanned intronic regions. Annealing temperatures of 56-66 ^{o}C were tested to determine the range of temperatures where a single, specific band was formed.

RT-qPCR primer sets were tested for efficiency and specificity prior to use. Positive control DNA (genomic or cDNA expressing the gene) was serially diluted (1:10, 1:100, 1:1000) in triplicate in order to plot a standard curve of cycle threshold (Ct) over $\log_2$ DNA concentration. Primers that generated a single solid peak on the dissociation curve, a standard curve with an R^2 value greater than 0.95 and a gradient of -3.1 (+-5%) were considered to be both specific to the gene of interest

and working at optimum efficiency. The dissociation curves for RT-qPCR primer sets used in this study can be found in Appendix v.

2.7.8 Reverse Transcription Polymerase Chain Reaction (RT-PCR)

Non-quantitative RT-PCR was performed in a T100™ Thermal Cycler (Bio-Rad) using a GoTaq® G2 Flexi kit (Promega). PCR master mixes were formulated containing 1x Green GoTaq® Flexi Buffer, 10 mM dNTP mixture, 25 mM $MgCl_2$, 10 µM forward and reverse primers and 5 U/µL GoTaq® G2 Flexi DNA Polymerase diluted in 30% v/v DEPC-treated dH_2O. For each gene target, 5 µL of cDNA was mixed with 15 µL master mix in individual wells of 8-well PCR tubes (Starlab). Each PCR reaction comprised of the following: an initial DNA denaturing step at 95 ^oC for 2 minutes followed by 25-32 cycles of a 30 second 95 ^oC denaturation, annealing for 30 seconds at 56-65 ^oC (determined through prior optimisation, see section 2.7.7) and an extension step at 72 ^oC for 1 minute/kb of expected PCR product. A final 5 minute extension step at 72 ^oC was completed before the samples were stored at 4 ^oC until ready to be analysed by agarose gel electrophoresis. For each gene target amplified, a genomic DNA positive control and a cDNA-negative, water only control was included. Expression of housekeeping gene *GAPDH* was used as both an internal loading control for RT+ samples and confirmation that RT- samples contained no DNA amplification.

2.7.9 Gel electrophoresis

A 2-3% w/v solution of agarose (Melford Laboratories) in 1x TBE buffer (Appendix ii) was made in order to separate PCR products based on size by electric current. The w/v % of agarose in buffer was determined by the amplicon size of interest. The solution was boiled to solubilise the agarose before addition of DNA intercalating agent SYBR™ Safe DNA Gel Stain (Invitrogen) at a dilution of 1:10,000. Gels were cast by pouring into a tray and allowing to set at ambient temperature. The set gels were submerged in 1x TBE buffer in a gel tank and PCR products electrophoresed next to a HyperLadder™ 100bp (Bioline) or GeneRuler™ 1 kb (Thermo Fisher) DNA ladder, depending on PCR product size. Once the DNA had been adequately separated, the resultant bands were visualised by UV detection using a PXi 4

(Syngene) imaging system and images captured with Genesys image acquisition software v1.5.0.0.

2.7.10 Quantitative Reverse Transcription Polymerase Chain Reaction (RT-qPCR)

RT-qPCR was performed using a Fast SYBR™ Green-based detection method (Thermo Fisher). RT-qPCR master mixes were formulated containing 2x Fast SYBR™ Green Master Mix (a premade mix containing SYBR® Green I Dye, AmpliTaq Gold® Fast DNA Polymerase, dNTPs and optimized buffer components) and 10 µM forward and reverse primers made up to a total volume of 15 µL in DEPC-treated dH_2O. A single PCR reaction used a mixture of 15 µL master mix and 5 µL cDNA product. Each gene target per cDNA sample was loaded in triplicate wells in a MicroAmp® Fast 0.1 mL 96-Well Reaction Plate (Applied Biosystems) and sealed with a plastic adhesive cover. The RT-qPCR reactions were undertaken in a QuantStudio™ 3 Real-Time PCR System and analysed in qPCR Design and Analysis Application software (both Thermo Fisher). Each RT-qPCR reaction comprised of the following: an initial DNA denaturing step at 95 ^{o}C for 20 seconds before 40 cycles of DNA denaturation at 95 ^{o}C for a second followed by elongation for 20 seconds at 60 ^{o}C. For each gene target amplified, a replicate RT- sample was included to confirm absence of non-specific amplification. Expression of housekeeping gene *GAPDH* was included for every RT+ sample as an internal loading control. The resultant data was analysed to determine an average Ct value per triplicate samples, and the difference in Ct value between the gene of interest and *GAPDH* was determined (ΔCt). ΔCt values were normalised to *GAPDH* expression (ΔΔCt) before the fold change in gene expression between experimental and control samples was calculated (2- Δ ΔCt).

2.7.11 RNA Sequencing

RNA extracted from experimental cultures were sequenced using the Illumina platform. RNA extraction and quantitation was performed in the same way as with samples used for PCR (section 2.7.1.1 to 2.7.1.4). RNA samples were diluted to 100 ng/µL in DEPC-treated dH_2O and sent to Oxford Genomics Centre for poly-A RNA-Seq library preparation and Illumina HiSeq 4000 75bp paired-end sequencing.

2.8 Molecular biology

2.8.1 General

Molecular biology techniques were used to a) stably overexpress genes of interest, b) transiently knockdown expression of genes using small interfering RNA (siRNA) and c) induce stable knockdown of gene expression using short hairpin RNA (shRNA) constructs in NHU and MIBC cell lines. Overexpression and knockdown cell lines were generated through either transfection (siRNA) or transduction with replication-disabled retroviral particles.

All microbiological work detailed below was performed in a separate room in accordance with the Good Microbiology Practice guide set out by the University of York Biology Department. Specifically, lab benches were swabbed with 70% (v/v) ethanol before and after handling bacteria, while any waste solution was disinfected with 2% (w/v) Virkon for 24h before disposal.

2.8.2 Generation of overexpressing retroviral vectors

2.8.2.1 PCR amplification of gene of interest

Primers specific to the full length coding sequence of the genes of interest were designed as in section 2.7.6. Specifically, the primers were designed to incorporate sequences matching the forward and reverse strands, while also including restriction enzyme sites and a Kozak sequence (forward strand) to aid in coding sequence translation. NEBcutter v2.0 (http://nc2.neb.com/NEBcutter2/) software was used to determine appropriate restriction sites that allowed for directional ligation of the gene sequence into the multiple cloning sites (MCS) of pGEM®-T Easy and pLXSN vectors. Once designed, primers were purchased from Eurofins Genomics.

To produce cDNA containing the coding sequence required for cloning, suitable RNA was used to synthesise 2 µg of cDNA (see section 2.7.5). The resultant DNA was amplified by PCR using a Phusion® Hot Start Flex kit (New England Biolabs), with the high fidelity DNA polymerase used in order to amplify an error-free product. A PCR master mix was formulated containing 1x Phusion High Fidelity Buffer, 200 µM dNTP mixture, 0.5 µM forward and reverse primers, 0.02 U/µL

Phusion Hot Start Flex II DNA Polymerase and 50 ng cDNA per reaction, diluted to a final volume of 20 µL with DEPC-treated dH_2O. The PCR reaction comprised of the same protocol as detailed earlier (section 2.7.8) with a 60 ^{o}C annealing step for 30 cycles. Ten PCR reactions were performed using the same master mix and cDNA, with one reaction used to verify the production of a single band product of the correct molecular size by agarose gel electrophoresis and the remaining nine pooled together and purified.

2.8.2.2 Purification of PCR product

To separate and concentrate the amplified sequence away from the other components of the PCR reaction, a QIAquick® PCR purification kit (Qiagen) was used. All following centrifuge steps took place at 14,000 x g for 60 seconds. For the volume of PCR reaction left, five times that volume was added of Buffer PB and this mixture was pipetted into a QIAquick column. The mixture was centrifuged to bind the DNA to the column, with the remaining flow-through discarded. Columns were washed in 750 µL Buffer PE and centrifuged twice to discard residual wash buffer. The purified DNA was eluted by adding 50 µL DEPC-treated dH_2O to the centre of the column and centrifuging the solution into a clean microfuge tube. Concentration of the purified product was quantified using a NanoDrop™ UV spectrophotometer. Prior to ligation, the PCR fragment was first A-tailed to allow T-vector cloning into the pGEM-T Easy vector. 6 µL of purified DNA was mixed with 1 µL 25 mM $MgCl_2$, 1 µL *Taq* DNA Polymerase 10X Reaction Buffer, 0.2 mM dATP, 5 U *Taq* DNA Polymerase and DEPC-treated dH_2O to a final volume of 10 µL before the solution was incubated in a 70 ^{o}C heat block for 30 minutes.

2.8.2.3 Ligation of PCR product into plasmid

To determine the amount of amplified DNA required for optimal ligation with the linearised plasmid, the following formula was used:

Insert amount (ng) =

$$\frac{\text{Vector amount (ng) x size of insert (kb)}}{\text{Vector size (kb)}} \text{ x3}$$

Purified DNA was ligated into the subcloning vector system pGEM-T Easy (Figure 2.4) by overnight incubation at 4 ^{o}C using the pGEM®-T Easy Vector System II kit (Promega). The ligation reaction contained the following components: 100 ng of vector DNA, x amount of insert DNA (as determined above), 1 U T4 DNA ligase, and 5 µL 2x Rapid Ligation buffer made up to a 10 µL solution in DEPC-treated dH_2O. A positive control containing Insert DNA (provided with kit) and no template negative control ligation reactions were verified alongside the sequence of interest-containing vectors by transformation.

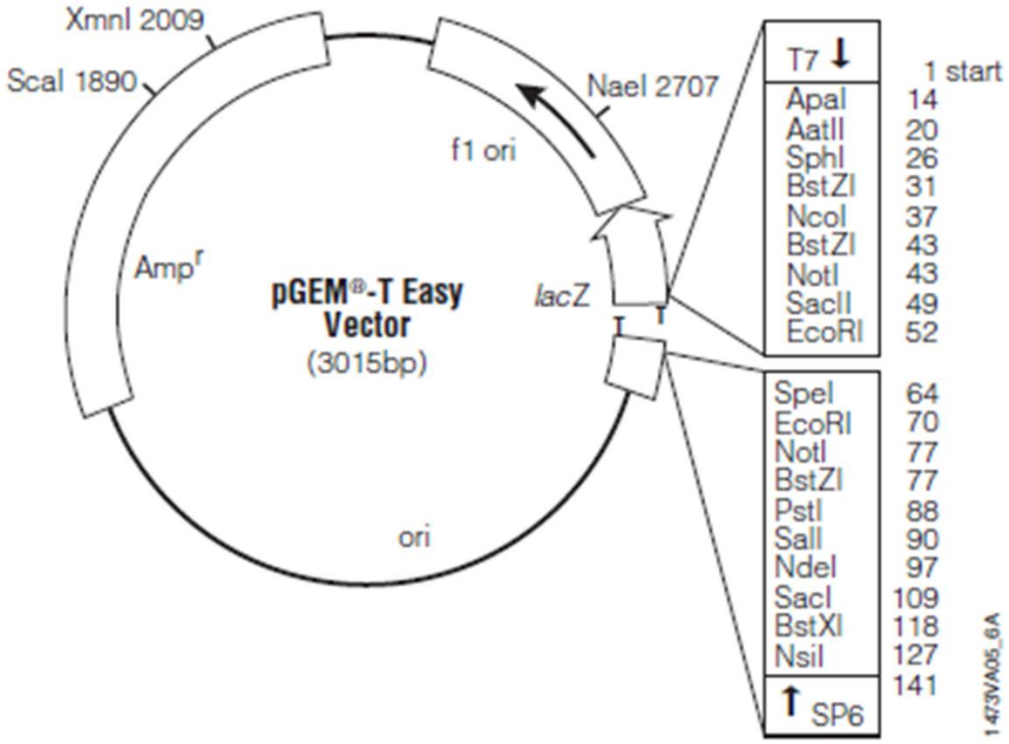

Figure 2.4: Vector map of pGEM-T Easy

pGEM-T Easy vector was purchased from Promega, with the diagram of the plasmid (as seen above) provided in the data sheet. Features of note include an ampicillin resistance (Amp^r) marker, a *lacZ* reporter gene, T7 and SP6 promoter regions and a MCS containing multiple restriction sites.

2.8.2.4 Bacterial transformation

Ligated, circularised plasmid was introduced into XL1-Blue subcloning-grade competent *E. coli* bacteria (Agilent Technologies) by transformation using the manufacturer's recommended protocol. XL1-Blue bacteria were defrosted on ice before 50 µL was pipetted into pre-chilled 15 mL Falcon centrifuge tubes. Between 0.1-50 ng of plasmid (5 µL of ligation reaction mixture) was mixed with the bacteria and swirled gently before incubating on ice for 20 minutes. Controls included bacteria that received no plasmid and bacteria that received 1 µL of the ampicillin-resistant, high copy number pUC18 plasmid. XL1-Blue bacteria underwent heat shock in a pre-warmed water bath at 42 ^{o}C for exactly 45 seconds before the tubes were returned to ice for a further 2 minutes. 900 µL of pre-warmed SOC medium (Invitrogen) was added to each tube and the bacteria was shaken for 30 minutes in a Model G25 Incubator Shaker (New Brunswick Scientific) at 37 ^{o}C to induce growth. To select based on successful uptake of plasmid, the bacterial cultures were pipetted and spread across Petri dishes containing Luria-Bertani (LB)-Agar (Appendix ii) and 100 µg/mL ampicillin (Melford Laboratories). Additionally, 100 µL 2% (w/v in DMSO) X-gal (VWR), 100 µL SOC medium and 100 µL 10 mM IPTG (Formedium) were added to the LB-Agar plates for the purposes of blue/white screening of false positive colonies. Bacteria were incubated on inverted plates at 37 ^{o}C for 16h and subsequently stored at 4 ^{o}C for up to a month.

2.8.2.5 Colony PCR

Validation of successfully ligated and transformed bacteria was performed using colony PCR. A PCR master mix (section 2.7.8) was produced which included primers specific to the T7 (forward) and SP6 (reverse) regions of the plasmid (Appendix iv). White-coloured (recombinant DNA-containing) colonies were picked from the original LB-Agar plate using a yellow pipette tip, transferred onto a new plate and pipetted into PCR mixes in individual wells of 8-well PCR tubes. To induce the growth of bacterial cultures containing the correct plasmid, the yellow tips were ejected into Universal tubes containing 10 mL of ampicillin-treated LB medium (Appendix ii) and incubated in the shaking incubator at 37 ^{o}C overnight. Ten PCR reactions were amplified for 30 cycles with an annealing temperature of 54 ^{o}C.

Products of the PCR reactions were visualised by gel electrophoresis to determine positive clones.

2.8.2.6 Plasmid DNA extraction

Plasmids containing the sequences of interest were extracted from positive bacterial cultures using a QIAprep® Spin Miniprep Kit (Qiagen). 10 mL cultures were first centrifuged at 3000 x g for 10 minutes at 6 ^{o}C before pelleted bacterial cells were resuspended in 250 µL RNAse A-containing resuspension solution (Buffer P1) and transferred to 1.5 mL microfuge tubes at ambient temperatures. An additional 250 µL of SDS-containing Buffer P2 was added and each tube was gently mixed by repeated inversion to lyse the cells. When the solutions reached a viscous consistency, 350 µL neutralisation solution (Buffer N3) was added to each tube and mixed using the same method. Solutions were centrifuged for 10 minutes at 11500 x g to separate plasmids from cellular debris. Plasmid-containing supernatant was applied to QIAprep spin columns and centrifuged for 60 seconds at 11500 x g, resulting in binding of the plasmids to the column. Plasmids were washed once with Buffer PB and once with Buffer PE before elution in 50 µL dH_2O after 60 second centrifugations at 11500 x g. Concentrations of the resultant plasmids were subsequently quantified using a NanoDrop™ UV spectrophotometer.

2.8.2.7 DNA sequencing

To validate the sequence orientation and fidelity in the purified plasmid solutions, 75 ng plasmid was sequenced using a 3730xl DNA Analyzer (Applied Biosystems). The DNA sequencing service was provided by Eurofins Genomics and results analysed in Chromas v2.6.6 software.

2.8.2.8 Restriction digest of subcloned DNA

Restriction digests were used to cut out sequences from the subcloning vector pGEM-T Easy, allowing for subsequent subcloning into the retroviral mammalian expression vector pLXSN (Figure 2.5). 1 µg plasmid was mixed with 5 µL 10x Cut Smart Buffer, 1 µL each of the respective restriction enzymes required to excise the DNA sequence of interest (all from New England Biolabs) and dH_2O to a final volume of 50 µL. This solution was incubated at 37 ^{o}C for 1h 45 minutes before heat

inactivation of the enzymes for 20 minutes at 65 ^{o}C. The pLXSN vector was similarly digested to linearise the plasmid in preparation for ligation with the target sequences.

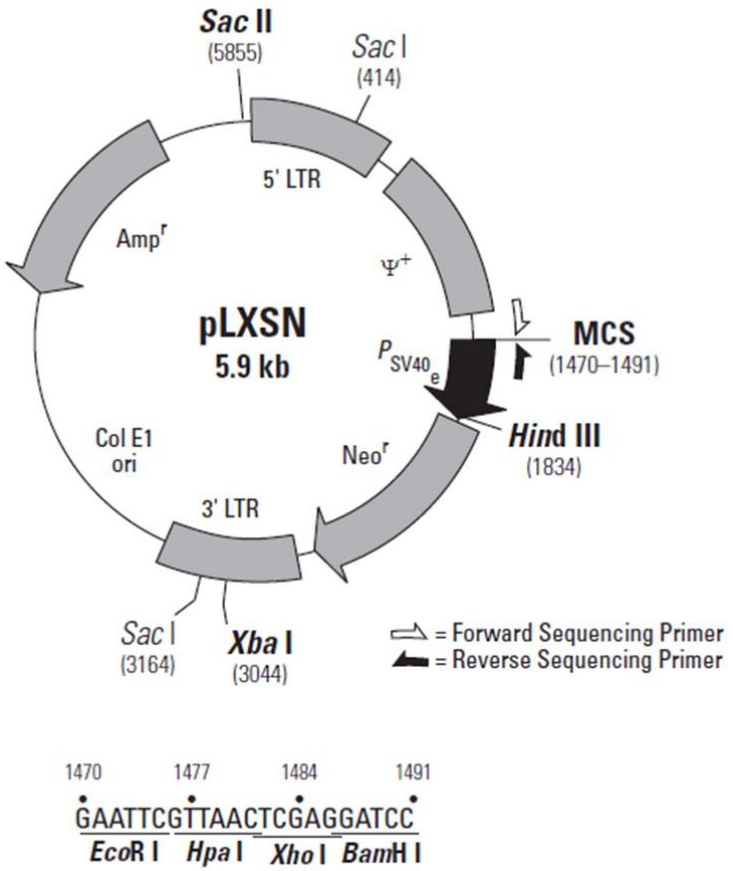

Figure 2.5: Vector map of pLXSN

pLXSN vector was purchased from Clontech, with the diagram of the plasmid (as seen above) provided in the data sheet. Features of note include an Amp^r (for bacterial selection), a neomycin resistance (Neo^r) marker (mammalian cell selection), 5' and 3' long terminal repeats (LTR) for facilitation of gene transfer (and a strong promoter of the inserted transgene), retroviral packaging element ψ+ and a MCS.

2.8.2.9 Gel extraction and purification of plasmid DNA

Prior to gel electrophoresis of products of the restriction digest process (as described in Section 2.7.9), 6x gel loading dye (New England Biolabs) was added to each sample to a final concentration of 1x. Solutions containing linearised pLXSN and the products of the preceding restriction digest were pipetted into a 1% agarose gel and electrophoresed to separate linearised pGEM-T Easy vector

backbone from the target DNA sequence by size. Solutions were pipetted into a well created by a wide gel comb to allow for up to 100 µL of product to be electrophoresed at once. Target DNA was visualised using the minimum possible exposure to UV before it was excised from the gel with a clean scalpel. The gel slices were placed into 1.5 mL microfuge tubes and weighed in preparation for extracting the DNA from the gel using a QIAquick® Gel Extraction Kit (Qiagen). To solubilise the remaining gel, three volumes of solubilisation solution (Buffer QG) was added to every one volume of gel for 10 minutes at 50 ^{o}C (or until complete solubilisation of gel was achieved), before vortexing the tubes to combine the mixture. A 1:1 ratio of isopropanol was added to the sample and mixed before the solution was transferred to a QIAquick spin column and centrifuged at 12000 x g for 1 minute to bind the DNA to the column membrane. 500 µL Buffer QG was added to the bound DNA and centrifuged before the product was washed in Buffer PE and allowed to stand in the column for 5 minutes. Buffer PE was removed by centrifugation and the DNA eluted from the column into a clean microfuge tube in 50 µL dH_2O. Quantification of the concentration of plasmid and insert DNA was calculated using a NanoDrop^{TM} UV spectrophotometer.

2.8.2.10 Dephosphorylation of plasmid

To ensure that the ends of the linearised pLXSN plasmid did not ligate back together during the ligation process, the gel purified pLXSN backbone underwent desphosphorylation of its 5' phosphate group using a FastAP Thermosensitive Alkaline Phosphatase kit (Thermo Scientific). 1 µL FastAP alkaline phosphatase, 2 µL 10x AP reaction buffer and 17 µL linearised pLXSN were mixed and heated at 37 ^{o}C for 10 minutes before the enzyme was inactivated by heating the mixture for 5 minutes at 75 ^{o}C. Purified coding DNA sequences were subsequently ligated into pLXSN, transformed into XL1-Blue cells, chosen by colony PCR, extracted using a Miniprep kit and validated by DNA sequencing as described in sections 2.8.2.3 to 2.8.2.7.

2.8.2.11 Production of bacterial glycerol stocks

Long term storage of plasmid-containing bacteria was achieved by freezing in glycerol (diluted in dH_2O). 750 µL of a 5 mL overnight LB bacterial culture was mixed with 250 µL 80% (w/v) glycerol in a 1.5 mL Cryovial® (Sarstedt) and frozen at -80 ^{o}C. To recover frozen cells, an inoculating loop was used to scrape cells from the frozen Cryovial onto a LB-Agar plate containing ampicillin and left overnight in an inverted position at 37 ^{o}C.

2.8.3 Generation of shRNA constructs

2.8.3.1 Design of shRNA oligonucleotide sequences

The full length coding sequence of interest was input into two shRNA construct designing packages: DSIR (http://biodev.extra.cea.fr/DSIR/DSIR.html) and siRNA Wizard v3.1 (https://www.invivogen.com/sirnawizard/). Three sequences of 19-21 bp size were chosen and input into the shRNA Design Tool (Clontech) which used the target sequences to create 69 bp hairpin sequences, complete with BamHI, EcoRI and MluI restriction digest sites, an RNA Pol III terminator sequence and the hairpin loop sequence TTCAAGAGA. shRNA oligonucleotides were purchased from Eurofins Genomics.

2.8.3.2 Annealing and ligation of shRNA oligonucleotides into pSIREN-RetroQ

Sense and antisense oligonucleotide strands were resuspended separately in dH_2O at a concentration of 100 µM before mixing 1 µL of each oligonucleotide. This mixture was then heated as follows in a T100™ Thermal Cycler to anneal the strands together: heated to 95 ^{o}C for 30 seconds (to disrupt the internal hairpins), heated at 72 ^{o}C for 2 minutes (to anneal the strands), heated at 37 ^{o}C for 2 minutes and heated at 25 ^{o}C for 2 minutes. Double-stranded oligonucleotides were subsequently stored at -20 ^{o}C until use.

Annealed oligonucleotides were ligated into the retroviral expression vector RNAi-Ready pSIREN-RetroQ (Figure 2.6) with a 3h incubation process at ambient temperature. The ligation reaction contained the following components: 2 µL linearised pSIREN vector (25 ng/µL), 1 µL of double-stranded oligonucleotide (diluted to 0.5 µM), 10x T4 DNA Ligase Buffer, 0.5 µL T4 DNA Ligase and 0.5 µL 10 mg/mL BSA (all Promega), diluted to a total volume of 15 µL in dH_2O. A dH_2O only negative control ligation reaction was verified alongside shRNA-containing vectors by transformation.

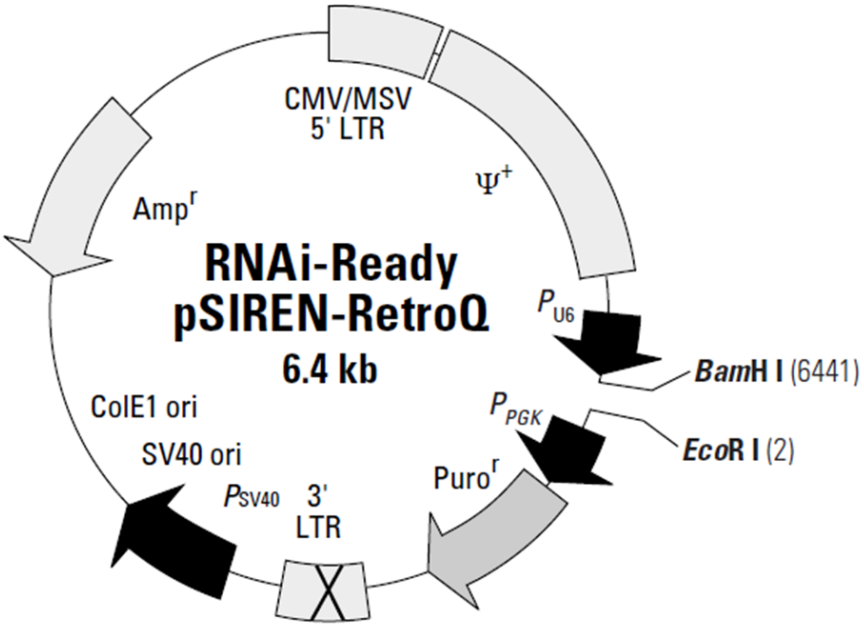

Figure 2.6: Vector map of pSIREN-RetroQ

pSIREN vector was purchased from Clontech, with the diagram of the plasmid (as seen above) provided in the data sheet. The retroviral vector expresses shRNA through its human U6 promoter. Features of note include an Amp^r, a puromycin resistance ($Puro^r$) marker (mammalian cell selection), 5' and 3' LTRs, packaging element ψ+ and BamHI/EcoRI restriction sites flanking the oligonucleotide insertion site.

2.8.3.3 Bacterial transformation and colony PCR

Transformation of XL1-Blue bacteria with ligated pSIREN plasmid was performed as described in section 2.8.2.4. PCR of positive colonies was performed as described in section 2.8.2.5, using primers specific to U6 (forward) and the individual reverse sequence of the gene of interest (reverse) in the three shRNA constructs (Appendix iv). 15 PCR reactions (5 for each construct) were amplified for 30 cycles with an annealing temperature of 60 ^{o}C.

Successful reactions were extracted from bacteria using a Miniprep kit and quantified with a NanoDrop^{TM} UV spectrophotometer, as detailed in Section 2.8.2.6.

2.8.3.4 MluI restriction analysis

Confirmation that the shRNA inserts were correctly inserted into the purified plasmids was achieved by restriction digestion using MluI, an enzyme that does not have a native site in the pSIREN backbone. 500 ng plasmid was mixed with 2 µL 10x restriction enzyme buffer, 1 µL MluI (both New England Biolabs) and dH_2O to a final volume of 20 µL. Samples were heated at 37 ^{o}C for 1h before mixing with 6x gel loading dye and visualising the bands by gel electrophoresis. Reactions that had been cut with MluI were compared to uncut control mixtures that received dH_2O instead of enzyme.

2.8.4 Genetic manipulation of NHU and MIBC cell lines

2.8.4.1 Transfection of retroviral packaging cells

All transfection/transduction work was performed in an externally vented tissue culture cabinet using level 2 containment safety practices. pLXSN and pSIREN plasmids containing target sequences of interest were introduced into the mouse NIH 3T3-derived, 3rd generation retroviral packaging cell line RetroPack™ PT67 (Takara Bio) by transfection. PT67 cells express three genes vital for viral production: *gag*, *pol* and *env*. Transfection of PT67 cells with a retroviral vector that contains the packaging element ψ+ results in the production of infectious but replication-incompetent viral particles.

PT67 cells were maintained in 25 cm^2 flasks until approximately 60% confluence was reached. A transfection mix was made using the Effectene® Transfection Reagent kit (Qiagen) containing the following reagents: 3 µg purified plasmid, 90 µL Buffer EC and 24 µL Enhancer (1 mg/mL). The solution was mixed and then incubated at ambient temperature for 5 minutes before 30 µL Effectene transfection reagent (1 mg/mL) was added and the mixture incubated for 10 minutes. 1 mL of medium was added to the transfection solution and mixed, which was subsequently added to PT67 cells incubated in 4 mL of fresh medium. Additional flasks were used that contained PT67 cells that received a positive control plasmid (pLXSN overexpressing eGFP or pSIREN that produced scrambled shRNA) or negative control (medium only). The pLXSN-eGFP and pSIREN-Scrambled control plasmids were previously generated by former Jack Birch Unit student Dr. Alex Mercado. Cultures were maintained as normal for 16h before a medium change containing no plasmid. 48h after transfection, PT67 cells were passaged into a 75 cm^2 flask and were cultured in medium containing either 500 µg/mL of Neomycin analog G418 (pLXSN expressing cells) or 4 µg/mL Puromycin (pSIREN expressing cells). Cells were cultured and passaged as required until all the cells in the negative control mock transduced flask were killed by antibiotic selection.

2.8.4.2 Transduction of cell lines with retroviral vector

The production of replication-incompetent viral particles by transfected PT67 cells allowed for the collection of virus to infect cell lines of interest by transduction without the risk of retroviral replication.

Virus-producing PT67 cells were cultured in 75 cm^2 flasks until 100% confluency was reached. Cultures were washed once in Dulbecco's PBS (dPBS) to remove antibiotic and medium changed to 10mL (1:1 ratio) DMEM:RPMI containing 5% FBS and 1% LG. Cells were incubated for 16h before the virus-containing medium was harvested and filtered through a 0.45 µm filter (Corning) to exclude PT67 cellular debris. 8 µg/mL Polybrene (Sigma) was added to the medium and mixed to increase the efficiency of gene transfer. The viral medium was subsequently added to actively proliferating NHU or MIBC cells (at approximately 60-70% confluence) in a 75 cm^2 flask and incubated as normal for 6h. After 6h, cells were medium changed back to

their normal medium for 48h. Additional flasks were used that contained cells that received a positive control plasmid (pLXSN overexpressing eGFP or pSIREN that produced scrambled shRNA) or negative control (medium only). 48h post-transduction, cells were passaged into two fresh 75 cm^2 flasks in a 1:2 ratio split. Once attached, these cultures were medium changed into medium containing 100 µg/mL G418 (pLXSN expressing cells) or 1 µg/mL puromycin (pSIREN expressing cells). Cells were cultured and passaged as required until all the cells in the negative control mock transduced flask were killed by antibiotic selection. Cell lines were subsequently maintained in medium containing a reduced concentration of antibiotic (25 µg/mL G418 or 0.25 µg/mL puromycin) until their final use in an assay in order to maintain selection pressure on positive cells.

2.8.4.3 Transfection of NHU cells with siRNA

Commercially available siRNA were used to transiently knockdown expression of genes of interest in NHU cells. Before use, siRNA were solubilised in DEPC-treated dH_2O to a concentration of 10 µM. Optimal cell concentration (and thus transfection efficiency) was achieved by seeding NHU cells at a concentration of 4 x 10^5 cells/well of a 6 well plate and leaving to attach overnight under normal conditions. The transfection mixture was prepared the following day by mixing 1.5 µL Lipofectamine RNAiMAX (Thermo Fisher) with 248.5 µL supplement-free KSFM (as supplements can disrupt the transfection process) while mixing a further 245 µL KSFM with 5 µL siRNA (final concentration of 100 nM). The two solutions were mixed together and incubated at ambient temperature for 20 minutes, resulting in a final transfection mixture volume of 500 µL per well of cells. Cells were washed once in KSFM before adding the 500 µL transfection mixture to cells and incubating under normal conditions for 4h. An additional 500 µL of KSFM was added to each well (total volume 1 mL) after 4h, before preparing the cells to undergo TZ/PD differentiation by adding 1.5 µL 1 mM TZ/PD drug mixture to 500 µL KSFM, three times the working concentration. Three times the amount of KSFM supplements were also added to the 500 µL KSFM (15 ng/mL recombinant human EGF, 150 µg/mL bovine pituitary extract and 90 ng/mL cholera toxin), which was subsequently added to each well and resulted in a 1x concentration of both TZ/PD

and supplements in the final 1.5 mL solution. 24h post TZ/PD treatment, cells were transferred into medium containing PD only, as detailed in section 2.4.4.9. Cells were harvested for RNA and protein 48h after treatment in PD alone (72h total drug treatment) and processed through to gene/protein expression analysis by RT-qPCR and immunoblotting, as detailed in section 2.7.1 and 2.9.3.

2.9 Protein analysis

2.9.1 Immunohistochemistry

2.9.1.1 Paraffin embedding and sectioning

Pieces of normal ureter tissue were fixed in 10% formalin for a period of 24-48h and subsequently stored in Universal tubes containing 70% ethanol at ambient temperature until embedding. The tissues were transferred into labelled System II Hex™ tissue processing cassettes (Cellpath) and submerged in fresh 70% ethanol in a glass jar on an orbital shaker for 10 minutes. Three washes with absolute ethanol and two further washes in isopropanol for 10 minutes on an orbital shaker was required to fully dehydrate the tissue. To facilitate paraffin infiltration and remove the dehydrating agents, tissues underwent four 10 minute washes in xylene (Fisher Scientific). Excess xylene was removed by blotting cassettes with absorbent paper before the cassettes were submerged in a plastic pot containing paraffin wax in a 60 ^{o}C oven for 15 minutes. Cassettes were transferred to fresh wax on three additional occasions, totalling 1h of submersion in wax. Samples were embedded by placing the biopsies in a metal embedding mould filled with wax and allowing to set on a 12 ^{o}C cool plate with the sample orientated as desired. Embedded samples could then be removed from the mould and stored at ambient temperature until use.

Formalin-fixed, paraffin wax-embedded (FFPE) blocks of ureter tissue were cooled to 12 ^{o}C for an hour before use and cut into 5 µm sections using a RM2135 rotary microtome (Leica Biosystems). Cut sections were placed into a 40 ^{o}C water bath before being transferred onto Superfrost® Plus glass microscope slides (Thermo Scientific). Slides were left to air dry and stored at ambient temperature for up to a month until use.

2.9.1.2 Immunolabelling of sections

Slides were heated to 50 ^{o}C on a heat block for 1h before undergoing a series of dewaxing steps: two 10 minute washes followed by two 1 minute washes (all in xylene). The slides subsequently underwent gradual rehydration by first submerging the tissue in absolute ethanol for three minute-long intervals, before a one minute wash in 75% ethanol and a final one minute wash in gently running tap water. To block the endogenous peroxidase activity of red blood cells in a sample, slides were submerged in 3% (v/v) Hydrogen Peroxide diluted in dH_2O for 10 minutes followed by a 10 minute wash in running tap water.

To reverse the effects of formalin fixation on the ability of antibodies to bind to epitopes of interest, different methods of Heat-Induced Epitope Retrieval (HIER) were used on ureter samples. The optimum HIER method for each antibody was determined empirically. The first method involved submerging the slides in 350 mL of 10 mM Citric Acid Buffer pH 6.0 (Appendix ii) in a Pyrex® dish, covering the dish in cling film and heating in the microwave (MW method) at 900 W for 13 minutes (resulting in approximately 10 minutes of boiling buffer) before placing the dish on ice until it had cooled down. The second method involved submerging the slides upright in plastic Coplin jars containing 10mM Citric Acid Buffer pH 6.0 before heating the jars for 10 minutes at 50 kPa in a Fast Slow Pro™ pressure cooker (Sage®; PC method) filled with 2.5 L of water.

After cooling down from HIER, slides were rinsed in a bath of Tris-Buffered Saline (TBS; Appendix ii) plus 0.1% Tween-20 (TBST) and placed in Shandon Sequenza™ slide racks with Shandon Coverplates™ (both Thermo Fisher) to ensure consistent and sustained application of immunolabelling reagents. All immunohistochemistry experiments in this study used the reagents included in the ImmPRESS® Excel Amplified HRP Polymer Staining Kit (Vector Laboratories) to visualise antibody binding. Slide were blocked for non-specific secondary antibody binding with 100 µL 2.5% (v/v) normal horse serum at ambient temperature for 20 minutes before an overnight incubation (16h) at 4 ^{o}C with 100 µL rodent or rabbit-derived primary antibody (concentration empirically determined) diluted in TBST. Each experiment

included negative control (antibody diluent only) and positive control (primary antibody previously confirmed to be urothelial positive in ureter) slides (Figure 2.7).

Slides were washed thrice with TBST to remove excess primary antibody before 15 minute incubation at ambient temperature with 100 µL goat anti-mouse (GaM) IgG or goat anti-rabbit (GaR) IgG amplifier antibody, dependent on the species the primary antibody has been raised in. Slides were washed twice more in TBST to remove unbound secondary antibody before a 30 minute incubation with a third antibody (ImmPRESS Excel Amplified HRP Polymer Reagent anti-goat IgG), thus amplifying the antibody signal. The slides were washed once in TBST and once in distilled water before addition of 3,3'Diaminobenzidine (DAB). Active DAB was produced through the 1:1 mix of ImmPACT® DAB EqV Reagent 1 and ImmPACT DAB EqV Reagent 2, with the mixture applied to the slides for 5 minutes before rinsing the slides with distilled water. When catalysed to its oxidised form DAB forms a brown precipitate, meaning that addition of DAB highlights the localisation of areas of tissue that contain HRP-conjugated antibodies and therefore proteins of interest. Slides were removed from slide racks and counterstained in Mayer's haematoxylin (Sigma-Aldrich) for 3-5 seconds before thoroughly washing in running tap water. Slides underwent gradual dehydration (1x 1 minute wash in 70% ethanol, 3 x 1 minute washes in absolute ethanol, 2x 1 minute washes in xylene) before mounting with DPX (Thermo Fisher) and applying a coverslip. Labelling was then visualised on an Olympus BX60 bright field microscope and images collected using cellSens Standard Micro Imaging Software (Olympus). The list of primary antibodies used in immunohistochemistry experiments in this study are detailed in Table 2.3.

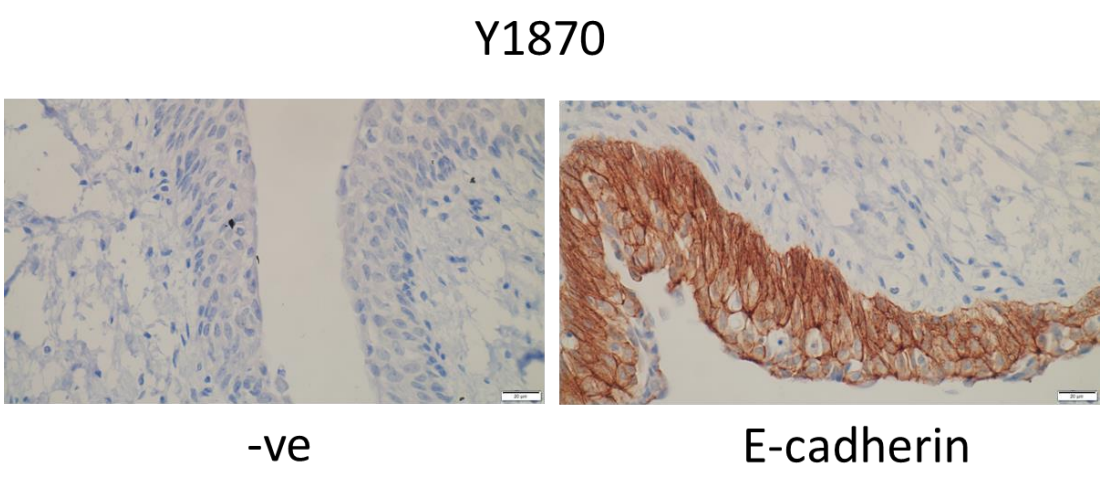

Figure 2.7: Example control immunohistochemistry section images

Images of Y1870 ureter after immunohistochemical (IHC) analysis. For each IHC experiment, a section that received no primary antibody (-ve) and a section that received a positive control antibody derived from the same host species as the test antibody (such as E-cadherin in urothelial cells) was included. Scale bar = 20 μm.

Target	Clone	Host	Clonality	Supplier	Dilution*	HIER method
E-cadherin	HECD-1	Mouse	mAb	Abcam	1:1000	PC
ELF3	HPA003479	Rabbit	pAb	Atlas Antibodies	1:1000	PC
FOXA1	Q-6	Mouse	mAb	Santa Cruz	1:250	PC
GATA3	D13C9	Rabbit	mAb	Cell Signalling	1:800	MW
PPARγ	81B8	Rabbit	mAb	Cell Signalling	1:1000	PC
p63	4A4	Mouse	mAb	Santa Cruz	1:1000	PC
PTCH1	MAB41051	Rat	mAb	R&D Systems	1:100	PC
SHH	5E1	Rat	mAb	Developmental Studies Hybridoma Bank	1:100	PC
VGLL1	HPA042403	Rabbit	pAb	Atlas Antibodies	1:3200	MW

* Concentration of stock antibody vials not disclosed by manufacturers.

Table 2.3: List of antibodies used for immunohistochemistry.

mAb refers to monoclonal antibodies while pAb refers to polyclonal antibodies that were affinity purified prior to purchase.

2.9.2 Indirect immunofluorescence labelling of cells

2.9.2.1 Preparation of fixed adherent cells on slides

Cells were grown on sterilised glass 12-well microscope slides (Hendley-Essex) placed in 4-well quadriPERM® rectangular cell culture dishes (Sarstedt). Typical cell seeding density for cells was as follows: 5 x10^4 cells/mL for undifferentiated NHU and stromal cells, 7 x10^5 cells/mL for NHU cells that were to be ABS/Ca^{2+} differentiated on slides. Each well of the 12-well slide received 50 µL of cells which were allowed to attach for at least 2h at 37 ^oC before the dish was flooded with 5 mL of appropriate medium. Immunofluorescence experiments in this study that feature ABS/Ca^{2+} differentiated NHU cells use cells that were differentiated on the slides, meaning cells were seeded onto the slides in an undifferentiated state and flooded with 5% ABS 2h post-seeding. Cultures were subsequently treated in the manner described in Section 2.4.4.5 until cells had reached 7 days ABS/Ca^{2+} treatment. Scratch wounding of ABS/Ca^{2+} differentiated NHU cells on slides was performed as described in Section 2.4.4.7, with cultures fixed either 30 minutes, 4h or 72h following wounding.

Upon reaching the desired confluence or completion of an experimental treatment, cells were washed twice in PBS before fixation via one of two methods:

i) Methanol:acetone fixation (dehydration of cells using organic solvents). Slides were fixed in a 1:1 ratio of methanol and acetone for 30 seconds in a glass Coplin jar before allowing slides to dry at ambient temperature.

ii) Formalin fixation (crosslinking reagent that preserves cellular structure). Applied 5 mL 10% formalin per slide to the cell culture dish for 10 minutes at ambient temperature before two 5 minute wash steps in PBS. Formalin-fixed slides were subsequently submerged in PBS and kept at 4^oC until use (up to one week following fixation). Formalin-fixed slides required an additional 30 minute incubation in PBS containing 0.5% (w/v) Triton™ X-100 (Sigma-Aldrich) in order to permeabilise the cells and allow intracellular antibody:antigen binding.

2.9.2.2 Immunocytochemistry

Prior to primary antibody application, slides were washed twice for 5 minutes with PBS before the areas around the cells on the slides were dried and an ImmEdge grease pen (Vector Laboratories) was applied to avoid merging of antibodies between wells. Primary antibodies (Table 2.4) were diluted in TBS containing 0.1% BSA and 0.1% sodium azide (NaN_3) and 20-30 µL was added to their respective wells. Each experiment included negative control (antibody diluent only) and positive control (primary antibody previously confirmed to be positive in the cell type assayed) wells (Figure 2.8). Primary antibodies were pre-titrated on a positive control cell type before use with experimental samples to confirm the optimum antibody concentration and fixation method to use. Slides were incubated with primary antibodies overnight (16h) at 4 ^{o}C before removal from the wells by pipetting to prevent cross-contamination of antibody during wash steps. Slides were flushed once with PBS for 5-10 seconds before three 5 minute washes in PBS on the orbital shaker. Slides were fixed in fresh methanol:acetone for 30 seconds and allowed to dry. 20 µL fluorochrome-conjugated secondary antibodies diluted in TBS/0.1% BSA/0.1% NaN_3 (Table 2.5) were applied to wells at ambient temperature for 1h, requiring slides to be protected from light sources by foil to prevent photo-bleaching. Slides were washed twice for 5 minutes with PBS and then incubated with PBS containing 0.1 µg/mL Hoechst 33258, a fluorescent dye that intercalates with double-stranded DNA by binding to its minor groove. Slides were washed once in PBS and once in dH_2O for 5 minutes each before a final drying step, after which the slides were mounted with Prolong™ Gold Antifade Reagent (Thermo Fisher) and covered by glass coverslips. Slides were stored at -20 ^{o}C in the dark until images were captured. Fluorescent labelling was visualised using an Olympus BX60 epifluorescence microscope and digital images collected using cellSens Standard Micro Imaging Software (Olympus).

Target	Clone	Host	Clonality	Supplier	Concentration*	Dilution
p-AKT (Ser473)	#9271	Rabbit	pAb	Cell Signalling	Unknown	1:25
E-cadherin	HECD-1	Mouse	mAb	Abcam	Unknown	1:1000
ELF3	HPA003479	Rabbit	pAb	Atlas Antibodies	Unknown	1:400
p-ERK1/2 (Thr202/Tyr204)	#9101	Rabbit	pAb	Cell Signalling	Unknown	1:200
(Total) ERK1/2	#610123	Mouse	mAb	BD Biosciences	0.25 mg/mL	1:500
GATA3	D13C9	Rabbit	mAb	Cell Signalling	Unknown	1:800
GLI1	OTI4E2	Mouse	mAb	Novus Biologicals	Unknown	1:1600
Ki67	MM1	Mouse	mAb	Leica Biosystems	Unknown	1:400
MCM2	D7G11	Rabbit	mAb	Cell Signalling	Unknown	1:1600
PPARγ	81B8	Rabbit	mAb	Cell Signalling	Unknown	1:100
PTCH1	MAB41051	Rat	mAb	R&D Systems	0.5 mg/mL	1:50
p63	4A4	Mouse	mAb	Santa Cruz	0.2 mg/mL	1:100
p-SMAD3 (Ser423/Ser425)	EP823Y	Rabbit	mAb	Abcam	0.5 mg/mL	1:50
(pan)-TEAD	D3F7L	Rabbit	mAb	Cell Signalling	Unknown	1:800
VGLL1	10124-2-AP	Rabbit	pAb	Proteintech	Unknown	1:1600
VGLL1	HPA042403	Rabbit	pAb	Atlas Antibodies	Unknown	1:1600
(Total) YAP	63.7	Mouse	mAb	Santa Cruz	0.1 mg/mL	1:800

Vimentin	V9	Mouse	mAb	Sigma	Unk.	1:800
ZO-1	1A12	Mouse	mAb	Thermo Fisher	0.5 mg/mL	1:400
ZO-1$^{\alpha+}$	Anti-ZO-1$^{\alpha+}$	Rabbit	pAb	Hycult Biotech	0.1 mg/mL	1:20
ZO-2	#2847	Rabbit	pAb	Cell Signalling	Unknown	1:25
ZO-3	D57G7	Rabbit	mAb	Cell Signalling	Unknown	1:800

Table 2.4: List of primary antibodies used for immunofluorescence.

*Unknown designates that concentration of stock antibody vial was not disclosed by manufacturer.

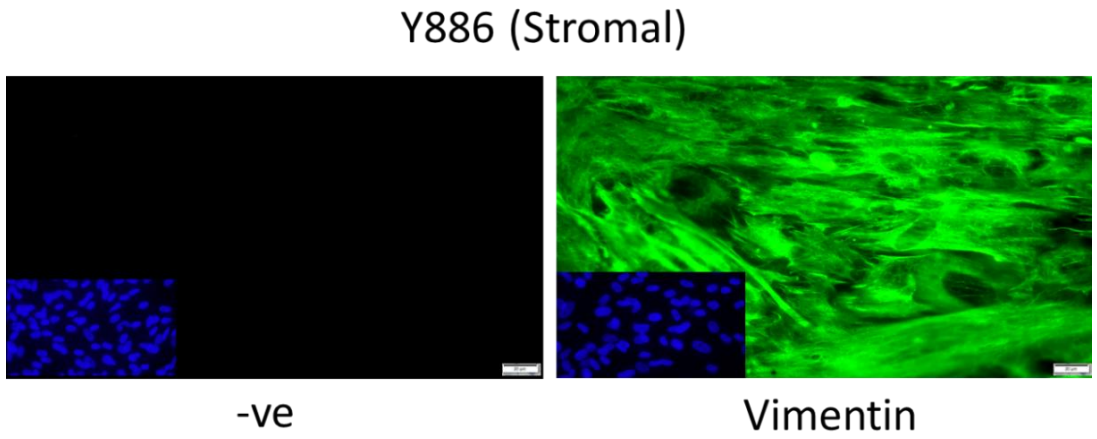

Figure 2.8: Example control immunofluorescence images

Images of Y886 stromal cells grown on glass slides. For each immunofluorescence experiment, a well that received no primary antibody (-ve) and a well that received a positive control antibody (such as vimentin in stromal cells) was included. The smaller image in each left hand corner displays the Hoescht 33258 nuclear staining for each well, indicating intact cell nuclei in each sample. Scale bar = 20 µm.

Target	Conjugate	Host	Class	Supplier	Concentration	Dilution
Anti-mouse (IgG)	Alexa Fluor 488 (green)	Goat	pAb	Invitrogen	2 mg/mL	1:500
Anti-rabbit (IgG)	Alexa Fluor 488 (green)	Goat	pAb	Invitrogen	2 mg/mL	1:500
Anti-mouse (IgG)	Alexa Fluor 555 (red)	Goat	pAb	Invitrogen	2 mg/mL	1:500
Anti-rabbit (IgG)	Alexa Fluor 555 (red)	Goat	pAb	Invitrogen	2 mg/mL	1:1000

Table 2.5: List of secondary immuno-conjugated antibodies used for immunofluorescence.

2.9.3 Western blotting

2.9.3.1 Preparation of protein lysates

Cells cultured for the purpose of protein extraction were grown in either 10 cm dishes (10 mL medium per dish) or 6-well plates (2-3 mL medium per well). Upon reaching the completion of a time-point or the desired cell confluence, 2x Sodium Dodecyl Sulfate (SDS) sample buffer (Appendix ii) solution was premixed with 1 M DTT diluted 1:67 and a Protease Inhibitor Cocktail (both Sigma) diluted 1:100. Cultures were washed twice in cold PBS before 75-150 µL complete SDS sample buffer was added to each well of a 6 well plate to solubilise the cells. While samples were kept on ice, cell scrapers were used to detach and pool the cell lysates in each well before pipetting the solution into chilled 1.5 mL microfuge tubes. Samples were sonicated on ice to disrupt cellular structure using an ultrasonic processor (VWR; formally Jencons Scientific) for two 10 second bursts at 25 W, with 10 seconds of rest in between bursts. Samples were left on ice for 30 minutes before being heated to 95 ^{o}C using a heat block for 5 minutes. Due to the negative effect that SDS can have on the accuracy of downstream quantification of protein content, samples were cooled on ice for a further 10 minutes and centrifuged at 20000 x g for 30 minutes at 4 ^{o}C to separate the lysate from the SDS. Protein lysates were subsequently pipetted into fresh microfuge tubes and stored at -20 ^{o}C until use.

2.9.3.2 Protein quantification

Quantification of protein concentration in lysates for the purposes of normalisation was performed using a Coomassie® Plus Protein Assay Reagent Kit (Thermo Fisher; formally Pierce). Vials containing 2 mg/mL BSA were diluted sequentially in dH_2O to create protein standards of 1000, 750, 500, 250, 125, 25 and 0 (dH_2O only) µg/mL. 10 µL of each standard was added in duplicate to a 96-well plate in addition to 10 µL protein samples (diluted 1:12.5 in dH_2O) in duplicate. Coomassie® Reagent was warmed to ambient temperature before 200 µL was added to each well. The plates were shaken for 30 seconds in a Multiskan Ascent 96-well plate reader before absorbance of standards and samples were measured at 570 nm and 630 nm. The absorbance readings of the BSA standards were used to construct a standard curve which was used to determine the concentration of each test lysate, with duplicate

sample wells giving a final average concentration. Between 10 and 40 µg protein/sample was used in each immunoblot experiment, depending on the predicted expression of proteins of interest in the samples.

2.9.3.3 SDS-Polyacrylamide Gel Electrophoresis (SDS-PAGE)

Protein lysates were prepared for SDS-PAGE by mixing the required concentration of total protein with NuPAGE 4x Lithium Dodecyl Sulfate (LDS) sample buffer (to replace the SDS detergent in the lysis buffer), 10x NuPAGE Sample Reducing Agent and dH_2O to a set volume of between 36 to 46 µL. All NuPAGE reagents, gels and gel tanks were purchased from Invitrogen. Samples were heated to 70 ^{o}C for 10 minutes and briefly centrifuged, resulting in lysate mixes containing denatured, negatively charged proteins. Samples were loaded into two types of pre-cast gel depending on target protein molecular weight: Bolt™ 4-12% Bis-Tris Plus 1.0mm x 10/12 well (proteins < 125kDa) or NuPAGE ™ 3-8% Tris-Acetate 1.0mm x 10 well (proteins >125 kDa). Similarly, three different types of SDS running buffer were used: Tris-Acetate (Tris-Acetate gels), NuPAGE MOPS (Bis-Tris gels focusing on proteins > 50kDa) and NuPAGE MES (Bis-Tris gels for proteins < 50kDa). Gels were placed inside Mini Gel Tanks and submerged in selected running buffer diluted 1:20 in dH_2O before lysate samples were loaded alongside one well containing 5 µL Precision Plus Protein All Blue Standards (Bio-Rad). 200 µL NuPAGE Antioxidant was added to the inner chamber of the gel prior to electrophoresis to ensure that proteins remain in a reduced state throughout the process. SDS-PAGE was performed at 200 V (Bis-Tris gels) or 150 V (Tris-Acetate gels) for between 30 minutes to 1h 15 minutes to allow the negatively-charged, linearised proteins to move through the gel and be separated on the basis of size.

2.9.3.4 Electroblotting

A protein-immobilising polyvinylidene difluoride (PVDF) membrane was cut into an appropriate size and activated by submerging in methanol for 30 seconds, rinsing in dH_2O for 2 minutes and leaving to equilibrate in fresh transfer buffer (Appendix ii). A gel membrane "sandwich" was constructed to fit in a Mini Blot Module (Invitrogen) with the items arranged in the following order: cathode (-) core, sponge pad, filter paper, SDS-PAGE gel, PVDF membrane, filter paper, sponge pad,

anode (+) core. A mini rolling pin was used to ensure that no air bubbles were present between layers of the sandwich. The Mini Blot Module was inserted into the Mini Gel Tank, with the inner chamber filled with ice-cooled transfer buffer and dH_2O added to the outer chamber. Electrotransfer was performed for between 1h and 3h (depending on size of protein targets) at 20 V. Upon completion of protein transfer, membranes were removed from Mini Blot Modules, moved to square plastic dishes and washed in 25 mL TBS. Membranes were reversibly stained with 0.5% (w/v) Ponceau Red staining solution (Appendix ii) for 10 seconds and washed multiple times in dH_2O to visualise the protein content of each lane and to confirm successful transfer.

2.9.3.5 Immunoblotting

In order to prevent nonspecific antibody binding, membranes were blocked with 20 mL of blocking buffer at ambient temperature for 1h on an orbital shaker. Depending on the primary antibody used, blocking buffer consisted of either a) 1:1 mix of TBS with a PBS-based Odyssey Blocking Buffer (Li-Cor) or b) 5% (w/v) A0830,0500 Non-fat Dried Milk Powder (PanReac AppliChem) solubilised in TBS. Primary antibodies (Table 2.6) were diluted in either a 1:1 mix of Odyssey Blocking Buffer and TBST, 5% (w/v) milk powder in TBST or 5% (w/v) BSA in TBST in a volume of 3 mL to 20 mL, depending on the dilution of antibody required. Antibody solution was applied to blots overnight at 4 ^{o}C on an orbital shaker. Membranes underwent four 5 minute wash steps with TBST to remove unbound primary antibody before blots were incubated for 1h at ambient temperature with fluorescent secondary antibodies (Table 2.7) diluted in either a 1:1 ratio of Odyssey Blocking Buffer and TBST or 5% (w/v) milk powder in TBST. Blots were washed four further times for 5 minutes (thrice in TBST, once in TBS) before scanning for fluorescent bands using the Odyssey Infrared Sa Imaging System (Li-Cor). Image Studio v5.2.5 software was used to visualise bands and, where appropriate, determine relative protein expression between samples using densitometry analysis of band intensity. Visualisation of housekeeping protein β-Actin was used for each blot to confirm equal protein loading for each sample. Primary antibodies were titrated on a positive control lysate before use with experimental samples to confirm the

optimum antibody concentration to use. Non-specific binding of secondary antibodies was tested by applying second antibodies to blots that had not received any primary antibody (Fig. 2.9).

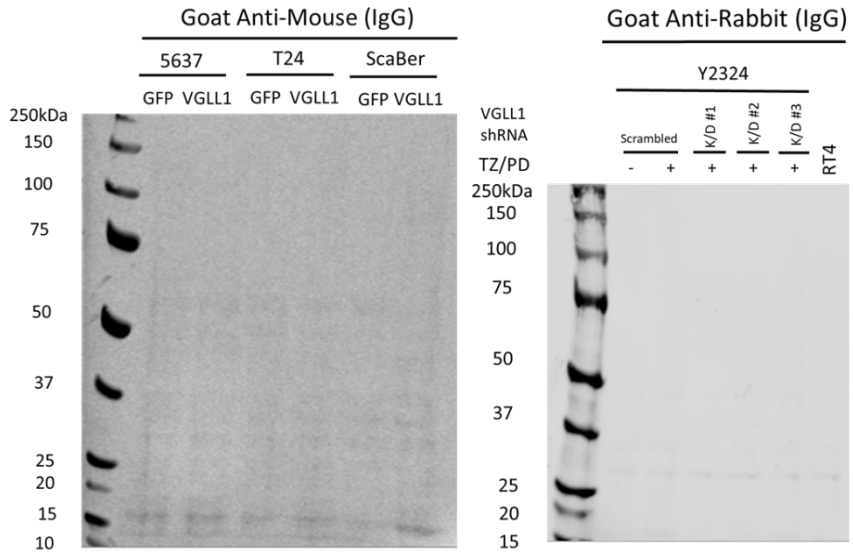

Figure 2.9: Secondary antibody only immunoblotting

Example blots where 0.2 µg/mL Goat Anti-mouse (IgG) Alexa680 and 0.1 µg/mL Goat Anti-rabbit (IgG) DyLight 800 secondary antibody mixes were applied before primary antibody incubation to test for non-specific target binding.

Target	Clone	Host	Class	Supplier	Conc.*	Dilution	Blocking buffer
p-AKT (Ser473)	#9271	Rabbit	pAb	Cell Signalling	Unknown	1:1000	Both
(Total) AKT	#9272	Rabbit	pAb	Cell Signalling	Unknown	1:1000	Odyssey
β-Actin	AC15	Mouse	mAb	Sigma	2 mg/mL	1:250000	Both
Claudin 3	ab52231	Rabbit	pAb	Abcam	1 mg/mL	1:1000	Odyssey
Claudin 4	3E2C1	Mouse	mAb	Thermo Fisher	0.5 mg/mL	1:1000	Odyssey
Cytokeratin 13	1C7	Mouse	mAb	Abnova	Unknown	1:1000	Odyssey
ELF3	EPESER1	Rabbit	mAb	Abcam	Unknown	1:20000	Odyssey
p-ERK1/2 (Thr202/ Tyr204)	#9101	Rabbit	pAb	Cell Signalling	Unknown	1:1000	Both
(Total) ERK1/2	#610123	Mouse	mAb	BD Biosciences	0.25 mg/mL	1:2000	Odyssey
FABP4	D25B3	Rabbit	mAb	Cell Signalling	Unknown	1:1000	Odyssey
FGFR3	B-9	Mouse	mAb	Santa Cruz	0.2 mg/mL	1:1000	Milk
FOXA1	Q-6	Mouse	mAb	Santa Cruz	0.1 mg/mL	1:500	Odyssey
GATA3	D13C9	Rabbit	mAb	Cell Signalling	Unknown	1:1000	Odyssey
GLI1	L42B10	Mouse	mAb	Cell Signalling	Unknown	1:1000	Milk
MCM2	D7G11	Rabbit	mAb	Cell Signalling	Unknown	1:1000	Odyssey
p63	4A4	Mouse	mAb	Santa Cruz	0.2 mg/mL	1:500	Odyssey

PPARγ	D69	Rabbit	pAb	Cell Signalling	Unknown	1:1000	Odyssey
(pan)-TEAD	D3F7L	Rabbit	mAb	Cell Signalling	Unknown	1:1000	Milk
VGLL1	10124-2-AP	Rabbit	pAb	Proteintech	Unknown	1:1000	Both
VGLL1	HPA042403	Rabbit	pAb	Atlas Antibodies	Unknown	1:1000	Both
p-YAP (Ser127)	#4911	Rabbit	pAb	Cell Signalling	Unknown	1:1000	Milk
(Total) YAP	63.7	Mouse	mAb	Santa Cruz	0.1 mg/mL	1:1000	Milk
ZO-3	D57G7	Rabbit	mAb	Cell Signalling	Unknown	1:1000	Odyssey

Table 2.6: List of primary antibodies used for immunoblotting.

*Unknown designates that concentration of stock antibody vial was not disclosed by manufacturer.

Target	Conjugate	Host	Class	Supplier	Conc.	Dilution	Blocking buffer
Anti-mouse (IgG H+L)	Alexa680	Goat	pAb	Thermo Fisher	2 mg/mL	1:10000	Both
Anti-rabbit (IgG H+L)	DyLight 800	Goat	pAb	Rockland	1 mg/mL	1:10000	Both

Table 2.7: List of secondary immuno-conjugated antibodies used for immunoblotting.

2.10 Bioinformatics

2.10.1 General

The RNAseq analysis pipeline described in the following section was performed to analyse the data generated in section 5.4.4. All other RNAseq data was first converted into readable .xlsx files (using a similar pipeline) by Dr. Andrew Mason of the Jack Birch Unit before use in this study.

2.10.2 RNAseq analysis pipeline

2.10.2.1 Preprocessing of sequencing reads

If required, raw paired-end sequencing reads (zipped in .gz files) were trimmed using Trimmomatic v0.36 (Bolger *et al.,* 2014), a program that cuts reads based on user-defined adapter sequences and for low quality using a sliding window quality filtering score. The quality of the resultant reads were confirmed using FastQC v0.11.5 (https://www.bioinformatics.babraham.ac.uk/projects/fastqc/). The shell scripts input to run Trimmomatic and analyse .gz files using FastQC are detailed in Appendix xv.

2.10.2.2 Mapping of reads to reference transcriptome

Preprocessing of paired-end sequences with Trimmomatic resulted in a collection of unpaired reads which were unsuitable for reference-based alignment. Unpaired reads were therefore assigned “pseudo” complementary reads prior to mapping. Reads were mapped to the reference Ensembl human transcriptome (GRCh38-p10) using Kallisto v0.44.0 (Bray *et al.,* 2016). Samples were bootstrapped 100 times in order to ensure the most accurate mapping value for each read. The scripts used to assign pseudo reads to unpaired reads and to map the processed reads to the transcriptome using Kallisto are detailed in Appendix xv.

2.10.2.3 Differential gene expression analysis

Quantification of total read counts per gene was performed in R Studio v3.5.1 using tximport (Soneson *et al.,* 2016), with transcript expression normalised as Transcripts per Million (TPM) then aggregated by gene using the R interface to the Ensembl BioMart (biomaRt v3.9; Durnick *et al.,* 2009). The most differentially

expressed genes between control and treatment conditions were identified using either sleuth v0.30.0 (which accounts for donor-specific variation using the likelihood ratio test; Pimentel *et al.,* 2017), or DESeq2 v1.28.1. The scripts used to run tximport, sleuth and DESeq2 are detailed in Appendix xv.

2.10.3 Other bioinformatics tools

Principle component analysis of variance in expression of genes of interest across RNAseq datasets was performed using the prcomp function of R Studio, with visualisation of the data performed using ggbiplot. The scripts used to run prcomp and ggbiplot are detailed in Appendix xv.

DNA sequences upstream of the promoter of genes of interest were analysed using JASPAR (http://jaspar.genereg.net/) to identify potential transcription factor binding sites.

The open-access cBioPortal for Cancer Genomics resource (Cerami *et al.,* 2012) was used to analyse the mutation and copy number alteration rate of genes of interest in cases of MIBC.

Expression data from RNAseq datasets were visualised as a matrix heat map using Morpheus software (https://software.broadinstitute.org/morpheus/) and grouped through hierarchical clustering. The results of DESeq2 analysis between two subgroups of RNAseq data was visualised using EnhancedVolcano v.1.6.0, which creates a volcano plot from the input data. Enrichment (or suppression) or a previously curated set of genes (the Molecular Signatures Database hallmark gene sets; https://www.gsea-msigdb.org/gsea/msigdb/index.jsp) in a differential expression analysis was analysed using the Gene Set Enrichment Analysis (GSEA) tool fgsea v.1.14.0. The scripts used to run EnhancedVolcano and fgsea are detailed in Appendix xv.

All diagrams included in the thesis were created in BioRender (https://app.biorender.com).

2.11 Statistical Analysis

Data that was represented graphically was created using either Prism 8 (GraphPad) or R studio software. Either the mean or the median value for every condition is displayed on each graph, with error bars on graphs referring to the ± standard deviation from the mean of all replicates. Statistical analysis was performed in Prism 8 using experiments with at least three biological replicates. A Shapiro-Wilk test of normality was performed on each dataset to determine an appropriate use of parametric (or non-parametric) tests. Differences between two sample means was calculated using an unpaired (two-tailed) 't' test, while three or more samples were compared using a one-way analysis of variance (ANOVA) test, with appropriate post-hoc test. The Kaplan-Meier estimator was implemented to determine whether identified subgroups in MIBC had a worse overall survival rate than others. Significance between survival rates was calculated using the Mantel-Cox log-rank test. With the exception of RNAseq differential expression analysis data, a p value ≤0.05 was considered as significant in all experiments. Significance was represented on graphs as: p ≤0.05= *, p ≤0.01= **, p ≤0.001= ***. When analysing differential expression analysis datasets, a false discovery rate-adjusted p value (q value) ≤0.05 was considered as significant.

3. Characterisation of VGLL1 and Hippo pathway signalling in normal human urothelial cells

3.1 Introduction

3.1.1 Hippo signalling pathway

A key question investigated by developmental biologists historically has been to understand the molecular basis for how multicellular organisms can undergo morphogenesis while maintaining a correct size and structure of tissues and organs. Studies in *Drosophila melanogaster* elucidated the importance of several genes, including Warts (*wts*), Salvador (*sav*) and Hippo (*hpo*), as being critically important to maintain tissue size due to an aberrant overgrowth of organs upon their mutation or deletion (Justice *et al.,* 1995; Kango-Singh *et al.,* 2002; Udan *et al.,* 2003). Conversely, deletion of a Wts-interacting protein, Yorkie (Yki), was found to abrogate the tissue overgrowth effect in *wts*, *hpo* and *sav* mutants (Huang *et al.,* 2005). Yki, Wts, Sav and Hpo were later grouped into a signalling pathway known as Hippo, which was found to be highly conserved in mammalian systems (Fig. 3.1). An example of this was demonstrated in mice, whereby the overexpression of the mammalian orthologue of *Yki*, Yes-associated protein (*Yap*), was found to inhibit differentiation and activate aberrant growth in primary mouse keratinocyte cells (Zhang *et al.,* 2011).

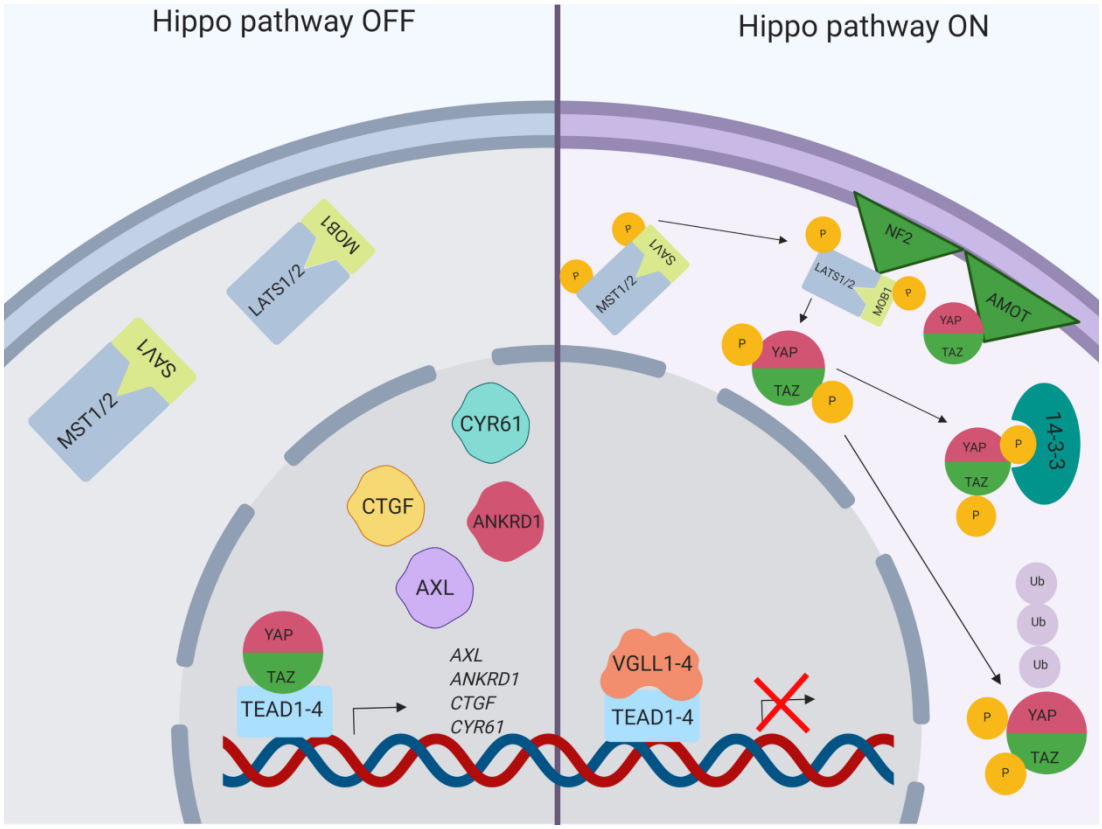

Figure 3.1: Mammalian Hippo pathway signalling

Modulation of active Hippo signalling performs an important function in regulating mammalian cell growth and quiescence. In its "off" state, transcriptional co-activators YAP/TAZ are localised to the nucleus and bind to the transcription factor TEAD family to induce transcription of genes such as *AXL, ANKRD1*, *CTGF* and *CYR61* (Zanconato *et al.,* 2015) in order to activate proliferative or migratory processes. Activation of the Hippo pathway in contact-inhibited cells results in phosphorylation of YAP at its serine 127 (S127) site through sequential kinase activation of cytoplasmic MST1/2 and LATS1/2 (Chan *et al.,* 2005). Phosphorylated YAP is sequestered in the cytoplasm by the regulatory protein 14-3-3, unable to induce transcription of its target genes (Basu *et al.,* 2003). YAP/TAZ can additionally be rendered inactive through retention at the cell membranes by proteins such as angiomotin (AMOT), or processed for poly-ubiquitination and proteasomal degradation after phosphorylation at its serine 381 site (Zhao et al., 2010; Chan *et al.,* 2011). Transcription co-activators of the VGLL family are also able to bind to TEAD proteins, and have been shown to compete with YAP/TAZ to bind to TEAD when both co-activators are present in the same cell. Diagram adapted from a review of Hippo pathway signalling by Yu *et al.* Yellow circles = phosphorylated sites; lilac circles = ubiquitinated sites.

In mammals, YAP has a closely related paralog entitled transcriptional co-activator with PDZ binding motif (TAZ; gene name *WWTR1*). Taz has been previously demonstrated in mice to have the ability to affect phenotype in the same manner as Yap, even when Yap is functionally inactivated through mutation (Nishioka *et al.,* 2009). YAP and TAZ are transcriptional co-activators, meaning that they do not activate transcriptional activity by binding directly to DNA but rather bind to transcription factors as part of a complex to induce transcriptional activity (reviewed by Hansen *et al.,* 2015). YAP/TAZ has been reported to bind to various transcription factors, such as β-catenin and SMAD2/3 (Imajo *et al.,* 2012; Varelas *et al.,* 2008), but have primarily been investigated in relation to members of the family of TEAD transcription factors, of which there are four in humans. Binding of YAP to TEAD1, TEAD3 and TEAD4 was demonstrated to cause the upregulation of expression of genes such as *CTGF* and *ITGB2* in immortalised human breast epithelial cells, resulting in a stimulation of growth (Zhao *et al.,* 2008). Later studies marked both YAP and TAZ as the functional effectors of Hippo pathway regulation, as YAP/TAZ complex with TEAD proteins in the nucleus to induce transcription of various genes involved in processes such as proliferation, migration and tumour cell invasiveness (Stein *et al.,* 2015; Zhao *et al.,* 2019). Beyond the mechanisms of YAP/TAZ regulation highlighted in Figure 3.1, the transcriptional co-activators have additionally been shown to be controlled by a negative feedback loop in immortalised human breast epithelial cells where YAP/TAZ induces transcription of its own regulators such as *NF2* and *LATS2* (Moroishi *et al.,* 2015).

3.1.2 YAP/TAZ function in non-malignant mammalian cells

Due to its regulation by multiple kinases and sequestration events, YAP/TAZ has been found to dynamically shift between intracellular locations in response to stimuli. Similar to the phenotype observed with active β-catenin signalling in NHU cells (Georgopoulos *et al.,* 2014), one stimulus involved in modulating YAP/TAZ localisation appears to be cell density, as human immortalised breast epithelial MCF10A cells grown in sparse cultures exhibited nuclear localisation of YAP that translocated to the cytoplasm upon reaching quiescence (Zhao *et al.,* 2007). Localisation of YAP/TAZ also seems to be affected by scratch wound healing, with

MCF10A cells exhibiting nuclear YAP at the wound edge but cells situated away from the wound expressing cytoplasmic YAP. In this situation, nuclear YAP expression was found to correlate highly with Ki67-positive cells at the wound edge (Zhao *et al.,* 2007), suggesting that activation of YAP may promote re-entry into the cell cycle.

In an *in vivo* context, Yap has been demonstrated to play an important role in tissue regeneration in multiple rodent models. In one particular study, Yap expression was shown to be transiently induced in hepatocytes upon chemical injury of the liver, a highly regenerative organ. When Yap expression was inactivated in conditional knockout mice, hepatocyte cells were found to exhibit significantly reduced proliferation, resulting in defective regeneration of the tissue and the occurrence of abnormal collagen deposition around the wound (Su *et al.,* 2015). A study investigating the response of rat bladder tissue to bladder outlet obstruction described significant upregulation of transcript and protein expression of *Ctgf* and *Cyr61*. This was localised to the smooth muscle and lamina propria regions of the bladder and was positively correlated to areas of collagen deposition (Chaqour et al., 2002). Subsequent analysis of bovine bladder smooth muscle cells determined that *CYR61* was additionally induced *in vitro* following externally applied mechanical strain, with the protein responsible for the induction of mechanotransduction-related genes such as *VEGF* and *ACTA2* (α-smooth muscle actin; Zhou et al., 2005). These results therefore suggest that CTGF and CYR61, which would later be confirmed as YAP/TAZ target genes (Zanconato *et al.,* 2015), may play a role in promoting connective tissue synthesis and inducing fibrosis in multiple rodent tissues following deformation, including the morphologically compliant bladder stroma.

3.1.3 Vestigial-like protein family

The four proteins of the Vestigial-like (VGLL) protein family are the human homologues of Vestigial (Vg), a protein discovered in *Drosophila*. As reported for Yki (YAP orthologue), Vg has no DNA-binding domain of its own and instead binds to Scalloped (Sd; TEAD) to regulate gene expression. This was first determined in developing *Drosophila* embryo, as Vg/Sd binding was demonstrated to be crucial for

the induction of wing formation (Kim *et al.,* 1996). The 25 amino acid binding site motif between Vg and Sd is highly conserved in Vestigial-like mammalian proteins, with VGLL1-4 in this case binding to the mammalian homologues of Sd, TEAD1-4 (Vaudin *et al.,* 1999).

Initial studies of human VGLL1 (originally named TONDU) demonstrated that through retention of the complete Sd/TEAD binding motif, VGLL1 was able to partially restore Vg activity in loss-of-function mutant *Drosophila* (Vaudin *et al.,* 1999). Interestingly, despite the TEAD-interacting domains of mouse Vgll1 and Yap being highly dissimilar to one another at the primary sequence level (Table 3.1), both co-activators adopt a similar conformation when binding to Tead4 through hydrophobic interactions at their ^{41}VxxHF^{45} and ^{65}LxxLF^{69} domains, respectively (Pobbati *et al.,* 2012; Fig. 3.2). Both proteins were found to compete to bind to the C-terminal domain of human TEAD4 and bound the transcription factor with the same affinity, despite the mouse-derived Vgll1 peptide lacking the Ω-loop domain of human YAP (Mesrouze *et al.,* 2014). Competition between VGLL1 and YAP for binding to TEAD4 was investigated in an *in vitro* context in human HEK293 cells, with a proposed switch in dominant binding of TEAD4 from YAP/TAZ to VGLL1 speculated to induce a different collection of genes, suggesting that either the co-activators alter TEAD activity through their specific binding mechanisms or that each protein recruits a unique set of co-factors which alter phenotype (Pobbati *et al.,* 2012).

Protein	**TEAD-interacting interface 1 sequence**	**TEAD-interacting interface 2 sequence**
Vgll1	SVIFT	DINSM**VDEHF**SRAL
Yap	HQIVHV	DSETD**LEALF**NAVMN

Table 3.1: Amino acid sequences of mouse Vgll1/Yap TEAD-interacting regions

The ^{41}VxxHF^{45} and ^{65}LxxLF^{69} regions of Vgll1 and Yap that bind to Tead4 through hydrophobic interactions are highlighted in bold. The TEAD-interacting interface regions were determined by Pobbati *et al.* (Vgll1) and Chen *et al.* (Yap).

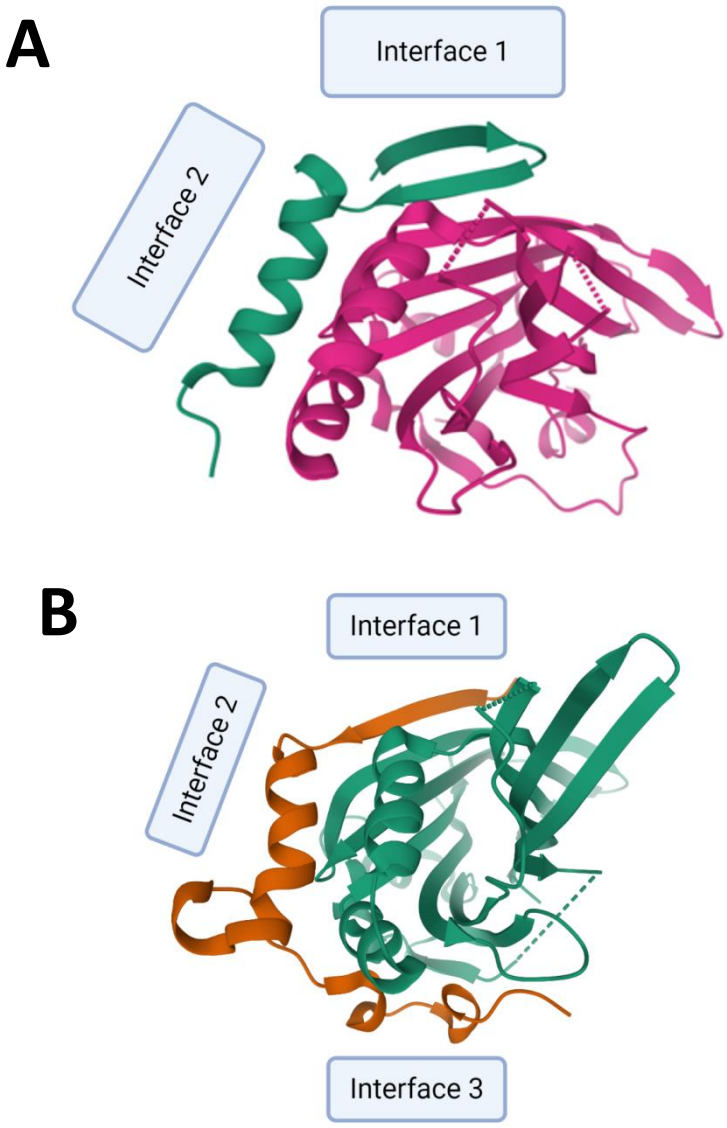

Figure 3.2: Comparison of mouse Vgll1/Tead and Yap/Tead binding

Ribbon cartoon representation of Vgll1 (**A**; cyan shape) and Yap (**B**; gold shape) binding to Tead. Vgll1 binds to Tead4 through hydrophobic interactions at ^{41}VxxHF^{45}, while Yap binds to Tead4 at ^{65}LxxLF^{69}, with both domains residing in the binding interface 2 of each complex. The crystal structures of each protein-protein interaction were determined by Pobbati *et al.* (**A**) and Chen *et al.* (**B**). Graphical representations of the Vgll1/Tead (5Z2Q) and Yap/Tead (3KYS) complexes were obtained from the Protein Data Bank (https://www.rcsb.org/).

3.2 Aims and hypothesis

Control of tissue homeostasis through modulation of the Hippo pathway has been implicated in various mammalian tissues. However, there is currently no published literature that has characterised the Hippo pathway or determined its role in normal human urothelial biology. Furthermore, most studies detailing Hippo signalling in "normal" human cells *in vitro* make use of immortalised cell lines that have largely lost the ability to accurately replicate the homeostatic mechanisms found *in vivo*. Therefore, the overall aims of this chapter were to a) confirm that Hippo pathway signalling was present in urothelial cells, b) understand how activation or inhibition of the pathway is regulated in NHU cells, and c) investigate how the Hippo pathway affects urothelial cellular phenotype in a normal, non-immortalised cell context. It was hypothesised that the differentiated, mitotically-quiescent urothelial cell phenotype is maintained through an activation of Hippo pathway signalling and an inhibition of YAP/TAZ-mediated cell cycle re-entry, potentially through competitive binding of VGLL proteins to TEAD transcription factors. Dysregulation of VGLL protein expression could therefore subsequently lead to an imbalance in urothelial tissue homeostasis and a reactivation of the proliferative, 'wound healing' phenotype.

To investigate this hypothesis, the specific experimental objectives were to:

- Verify the components of Hippo pathway signalling present in urothelial cells and determine whether expression of these components are affected by *in vitro* cell culture or differentiation state (Section 3.4.1).

- Upon validating immunolabelling resources for studying components of the Hippo pathway, to compare expression of Hippo proteins of interest to proteins associated with a differentiated urothelial phenotype in fixed ureter samples by immunohistochemistry, in addition to differentiated and undifferentiated NHU cells by immunoblotting and immunofluorescence (Section 3.4.2).

- After ascertaining transcription factor binding sites upstream of the *VGLL1* gene, to determine what transcription factors control the induction of VGLL1 expression in differentiated NHU cells (Section 3.4.3-5).

- As proliferation of NHU cells is known to use the EGFR/RAS/RAF/MEK/ERK or PI3K/AKT signalling axes depending on context, to investigate whether these pathways are involved in modulating expression of VGLL1 (Section 3.4.6).

- Utilise genetically modified NHU cell lines that overexpress or knockdown VGLL1 (Section 3.4.7) to investigate the role VGLL1 plays in modulating proliferation and ERK, PI3K/AKT and YAP/TAZ signalling (Section 3.4.8); differentiation (Section 3.4.9); and barrier maintenance, wound healing and cell cycle re-entry (Section 3.3.10).

3.3 Experimental approach

3.3.1 Transcriptomic analysis of Hippo pathway genes

Pre-existing data from RNAseq experiments of urothelial cells in different physiological contexts (Fishwick *et al.,* 2017 and unpublished data) were used to compare transcript expression of genes of interest across multiple normal urothelial cell samples. This included gene expression from cells lysed immediately after isolation from ureter (Urothelium *in situ*) in addition to NHU cells grown in serum-free KSFMc medium (Undifferentiated) and NHU cells differentiated using one of two well characterised methods: ABS/Ca^{2+} (Section 2.4.4.5) or TZ/PD (Section 2.4.4.9). Genes of interest included various components of Hippo signalling, the VGLL family of transcriptional co-activators and genes previously cited as being important in regulating urothelial physiology. Upon identification of *VGLL1* as a differentially expressed gene in urothelium, its association to various transcription factor genes in urothelial cells (under different states) was analysed by principal component analysis. The list of 35 transcription factors analysed were taken from a study by Fishwick *et al.* which identified urothelial transcription factors based on matched motif sequences in FAIREseq peaks (indicative of open chromatin regions) in undifferentiated and differentiated NHU cells (Fishwick *et al.,* 2017).

3.3.2 Characterisation of Hippo pathway component protein expression in differentiated urothelium

Antibodies specific to VGLL1, total and phosphorylated (S127) YAP and “pan”-TEAD were validated for use in immunoblotting, immunofluorescence and/or immunohistochemistry-based assays. Additional immunohistochemistry experiments were performed to compare and contrast the localisation and expression of VGLL1 to prominent urothelial transcription factors in two ureter samples.

Immunoblotting and immunofluorescence approaches were used to characterise protein expression of VGLL1, YAP (in an active and phosphorylated state) and TEAD in NHU cells in an undifferentiated state compared to cells differentiated using the TZ/PD and ABS/Ca^{2+} methods. Other targets labelled for in the experiment include a selection of urothelial-associated transcription factors, tight junction proteins

associated with late differentiation and proteins that mark cells as being actively proliferating.

3.3.3 Induction of VGLL1 expression by urothelial transcription factors

As a regulator of urothelial cytodifferentiation, PPARγ has previously been demonstrated to either directly or indirectly induce expression of various differentiation-associated genes in NHU cells (Böck *et al.,* 2014; Varley *et al.,* 2004a; Varley *et al.,* 2006; Varley *et al.,* 2009). To determine whether activation of PPARγ had any involvement in induction of VGLL1 expression, NHU cells were differentiated using TZ/PD but additionally pre-treated with T007 to inhibit PPARγ activity. Five independent cell lines were assayed by RT-qPCR for expression of *VGLL1*, *ELF3* and *FABP4* transcript after 72h of TZ/PD/T007 treatment while VGLL1 protein expression was assayed in three NHU cell lines by immunoblot following the above treatment for periods of 24h, 72h and 144h.

To identify potential candidates of alternative urothelial-associated transcription factors that could drive VGLL1 expression in a differentiated state, the DNA sequence upstream of the *VGLL1* gene was analysed using an online transcription factor binding site tool (JASPAR) to uncover transcription factors predicted to bind in this area.

Following this approach, GATA3 was identified as a potential regulator of VGLL1 expression. To test this hypothesis, commercially available siRNA designed to target regions of the *GATA3* gene sequence (Table 3.2) were used to transiently knockdown GATA3 expression in NHU cells. Three independent NHU cell lines were transfected with control siRNA or one of two GATA3 siRNA before induction of TZ/PD mediated differentiation. RT-qPCR and immunoblot analysis was subsequently performed to determine changes in transcript and protein expression of GATA3, VGLL1 and other proteins of interest.

siRNA information	**Nomenclature in thesis**
Silencer Select Negative Control siRNA	Ctrl siRNA
Silencer Select GATA3 siRNA (S5600)	GATA3 siRNA #1
Silencer Select GATA3 sIRNA (S5601)	GATA3 siRNA #2

Table 3.2: **List of siRNA used in study**

GATA3 siRNA #1 and #2 were predesigned to target the human GATA3 transcript at exons 5 and 6, respectively. The Ctrl siRNA was predesigned to not target any human genes. The above siRNA were purchased from Thermo Fisher.

3.3.4 Effect of active EGFR and downstream signal transduction pathways on VGLL1 expression

To understand whether expression of VGLL1 is modulated through the signalling pathways that power urothelial cell proliferation, the TZ/PD differentiation process was scrutinised through a series of immunoblot assays to determine what components of the treatment process were important for inducing VGLL1 protein. First, VGLL1 expression was analysed in NHU cells treated with PD153035 without concurrent treatment with TZ, with VGLL1 expression compared to that found in TZ/PD differentiated cells. NHU cells were additionally grown to a state of post-confluence and treated with combinations of reagents to understand whether quiescence induced through non-drug means (*i.e.* sustained contact inhibition) affected the phenotype of cells upon treatment. NHU cells were subsequently treated with drugs specific to kinase targets downstream of EGFR to determine whether a downstream pathway of EGFR (namely the RAS/RAF/MEK/ERK signalling axis) is responsible for regulating VGLL1 expression. Finally, the importance of the PI3K/AKT pathway in inducing VGLL1 expression was interrogated in undifferentiated NHU cells grown in high calcium, a state previously demonstrated to induce juxtacrine AKT signalling in contacted cells (Georgopoulos *et al.,* 2010).

Prior to use, each reagent was (or had previously been) titrated on the basis of the minimum concentration required to block active ERK or AKT signalling, thereby eliminating the possibility of erroneous off-target effects. MEK1/2 inhibitor U0126 had been previously utilised in studies at a concentration of 5 µM, but evidence of its efficacy lay in the retardation of growth of proliferating NHU cells (MacLaine *et al.,* 2008) and had not previously been titrated for its specific blockade of MEK signalling. PD98059 (PD98) is an inhibitor of MEK1 (but not MEK2) signalling and was also titrated.

3.3.5 Modulation of NHU cell phenotype using VGLL1 overexpression and knockdown constructs

To understand how the presence or absence of VGLL1 affected NHU cell phenotype, VGLL1 pLXSN overexpression and pSIREN shRNA knockdown constructs were designed and packaged into retroviral vectors for the purposes of transducing NHU cell lines.

Once functional overexpression or knockdown of VGLL1 was confirmed in transfected cultures, cells were studied in multiple assays to determine the effect of VGLL1 expression on different cellular processes. To determine whether VGLL1 was affecting cell proliferation, the comparative differences between cell numbers in control and test cultures was quantified by cell counting at a single time-point or over a time series using the alamarBlue cell viability assay. Changes in signalling molecules known to play a role in NHU cell proliferation, such as *EGFR*, phosphorylated ERK1/2 and PI3K/AKT, in addition to cell cycle markers such as *MKI67* and MCM2, were assayed using RT-PCR and immunoblotting approaches.

Due to previously cited evidence in the literature that suggests a role of VGLL1 (as part of the Hippo pathway) in inhibiting YAP/TAZ-mediated proliferation, this inhibitory relationship was also explored in NHU cells. The ability of VGLL1 to modulate the expression of inactive phosphorylated YAP and the localisation of YAP after scratch wounding was performed using VGLL1 overexpression and knockdown transfected cell lines, respectively.

Expression of differentiation-associated transcription factors and proteins involved in the onset of late differentiation were studied in VGLL1 knockdown transfected cell lines to observe whether manipulation of VGLL1 modulated expression of said proteins.

To ascertain what effect inhibition of VGLL1 has on the strength of the stratified urothelial barrier, the TEER of ABS/Ca^{2+} differentiated VGLL1 knockdown NHU cells was measured in an unwounded state and in the 24h following scratch wounding of cultures, a process that temporarily abolishes barrier integrity. The time taken for cultures to return to a similar TEER reading as recorded pre-scratch was therefore

used to determine whether loss of VGLL1 confers a differential rate of barrier recovery compared to control.

Immunofluorescence analysis of scratch wounded differentiated NHU cells was additionally carried out to uncover whether the expression and localisation of transcription factors, tight junctions and migration-associated signal transducers are modified in VGLL1 knockdown cells after wounding. Cells were fixed in the periods immediately following wounding (30 min or 4h post-scratch) or after the cultures have successfully healed the wound (72h post-scratch) to observe different stages of the wound healing process. Markers that label cells that have entered the S-phase of the cell cycle (BrdU) or any non-G0 phase of the cell cycle (Ki67 and MCM2) were utilised to determine whether VGLL1 knockdown cultures had a differential proportion of cell cycle-active cells upon concluding the wound healing process. Due to a notable modulation of the wound migratory-associated TGFβ pathway in VGLL1 knockdown differentiated NHU cells, the expression of VGLL1 and its association to cell cycle activity was finally studied in untransfected ABS/Ca^{2+} differentiated NHU cells pre-treated with agonists and inhibitors of TGFβ signalling to deduce whether a similar phenotype was observed.

3.4 Results

3.4.1 RNAseq analysis of urothelium *in situ* and NHU cells

3.4.1.1 Expression of differentiation-associated genes in urothelial cells

Transcription factors *PPARG, GATA3*, *FOXA1*, *ELF3* and *TP63* have all previously been implicated in helping to regulate urothelial differentiation (Section 1.3.2). To contextualise Hippo pathway signalling activity in human urothelium, expression of these transcription factors were first analysed by RNAseq. RNAseq analysis confirmed that all of the aforementioned genes were expressed by urothelium *in situ* (Fig. 3.3). *PPARG*, *GATA3, FOXA1* and *ELF3* displayed consistent expression between urothelium *in situ* and differentiated NHU cell samples; with each gene being highly expressed. Culturing NHU cells in an undifferentiated state was found to cause a significant reduction in expression of all four genes when compared to urothelium *in situ* or differentiated NHU cells ($p \leq 0.001$). Despite being expressed by native urothelium and having a similar amount of expression in differentiated NHU cells, expression of *TP63* (p63) was found to be significantly higher when NHU cells were in an undifferentiated state compared to when differentiated ($p \leq 0.001$). Uroplakin gene *UPK2* was used as a marker of late differentiation, with high expression in urothelium *in situ* and differentiated NHU cells but significantly reduced expression in undifferentiated cells ($p \leq 0.001$).

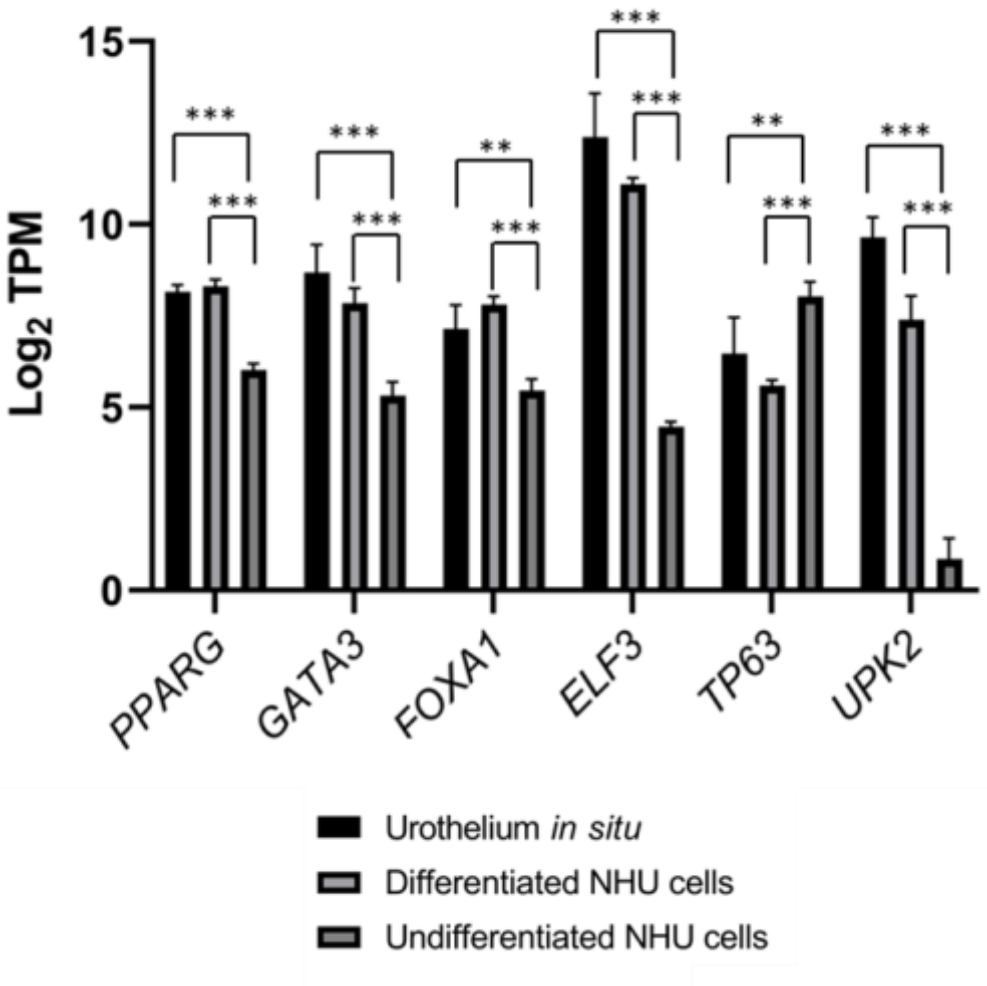

Figure 3.3: Induction of urothelial transcription factor gene expression in differentiated urothelial cells

RNAseq data analysis of *PPARG*, *GATA3*, *FOXA1*, *ELF3*, *TP63* and *UPK2* gene expression in urothelium *in situ* and NHU cells in differentiated and undifferentiated states in three biological replicates. Gene expression was measured in Transcripts per Million mapped reads (TPM), with error bars representing standard deviation of the mean. Due to the high expression of *ELF3* transcript, TPM values were Log_2 transformed to allow for greater visualisation of the data. Significance between groups was determined by two-way ANOVA with Tukey's multiple comparisons post-hoc test. **= $p \leq 0.01$; ***=$p \leq 0.001$. Other significant changes between groups were omitted for clarity and are detailed in Appendix xii.

3.4.1.2 YAP/TAZ, YAP/TAZ target gene and TEAD expression in urothelial cells

YAP1 and *WWTR1* (TAZ) were expressed by urothelial cells *in situ* but expression of previously determined YAP/TAZ target genes *AXL*, *ANKRD1*, *CTGF* and *CYR61* in this condition were either low or absent, suggesting that the conventional YAP/TAZ signal transduction pathway was not active in adult normal human ureteric urothelium (Fig. 3.4). Investigation of the TEAD family determined that *TEAD1* and *TEAD3* were expressed by urothelium *in situ*, but not *TEAD2* or *TEAD4*. Expression of YAP/TAZ target genes *AXL*, *CTGF* and *CYR61* was found to be significantly increased *in vitro,* with *AXL* and *CYR61* expression found to be highest when NHU cells were undifferentiated, whereas expression of *CTGF* retained a consistent expression regardless of the differentiation state of the cells ($p \leq 0.001$). YAP/TAZ target gene *ANKRD1* was not found to be expressed in any urothelial cell state. Confirming what was found in *in situ* samples, *TEAD1* and *TEAD3* appeared to also be the predominant members of the TEAD family in NHU cells due to their expression in both undifferentiated and differentiated states. The following observations therefore point to potential YAP/TAZ-TEAD activity in urothelial cells in a proliferative, undifferentiated state that is reduced when cells are in a quiescent, differentiated state.

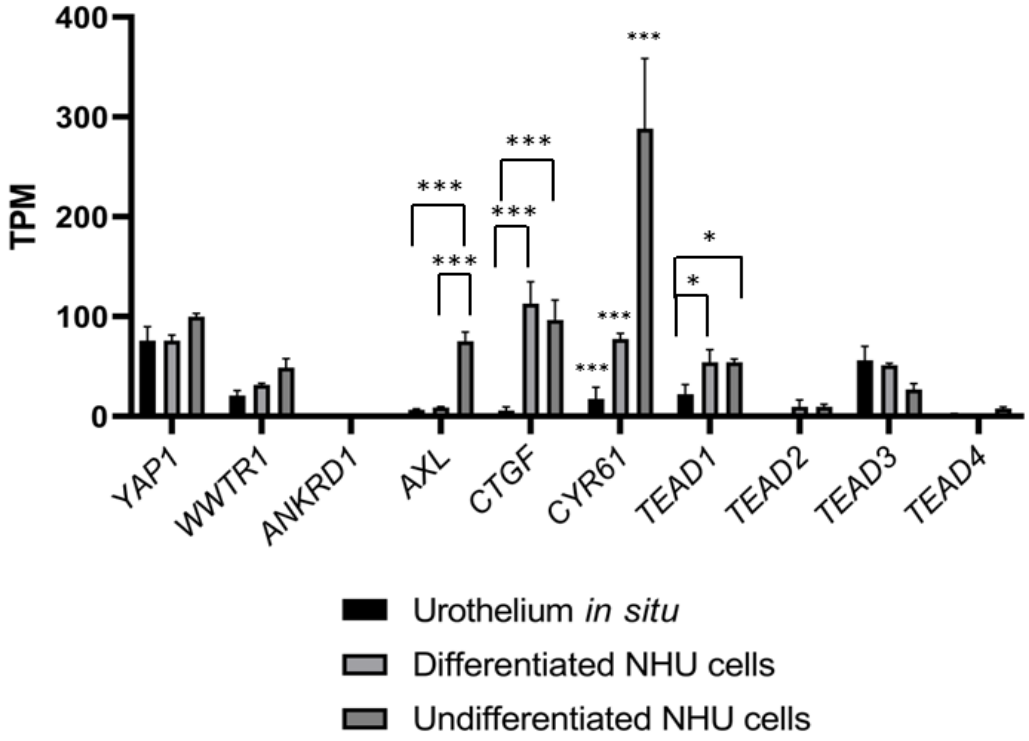

Figure 3.4: YAP/TAZ target genes *AXL, CTGF* and *CYR61* are induced by *in vitro* culture of urothelial cells

RNAseq data analysis of *YAP1*, *WWTR1*, *ANKRD1*, *AXL*, *CCN1*, *CCN2*, *TEAD1*, *TEAD2*, *TEAD3* and *TEAD4* gene expression in urothelium *in situ* and NHU cells in differentiated and undifferentiated states (n=3 independent samples). Significance between groups was determined by two-way ANOVA with Tukey's multiple comparisons post-hoc test. *= p≤0.05; **= p≤0.01; ***=p≤0.001. Other significant changes between groups were omitted for clarity and are detailed in Appendix xii.

3.4.1.3 Pattern of VGLL family expression in urothelial cells

Transcript expression of *VGLL1*, *VGLL3* and *VGLL4* was present in both urothelium *in situ* and in NHU cells in both differentiated and undifferentiated states (Fig. 3.5A). *VGLL1* was the most highly expressed member of the VGLL family, with the highest expression found in ABS/Ca^{2+} differentiated NHU cells and the lowest expression determined to be in undifferentiated NHU cells, with each condition having significant differences in expression when compared with one another ($p \leq 0.001$). No significant difference in *VGLL3* and *VGLL4* expression was observed between urothelial conditions, whereas *VGLL2* was found to be not expressed by any urothelial sample. When comparing expression of genes in a TZ/PD differentiation time-course, it was determined that *VGLL1* was most highly expressed by NHU cells differentiated for 144h ($p \leq 0.001$), while as before *VGLL2* was not found to be expressed and *VGLL3* and *VGLL4* expression was consistent between conditions (Fig. 3.5B).

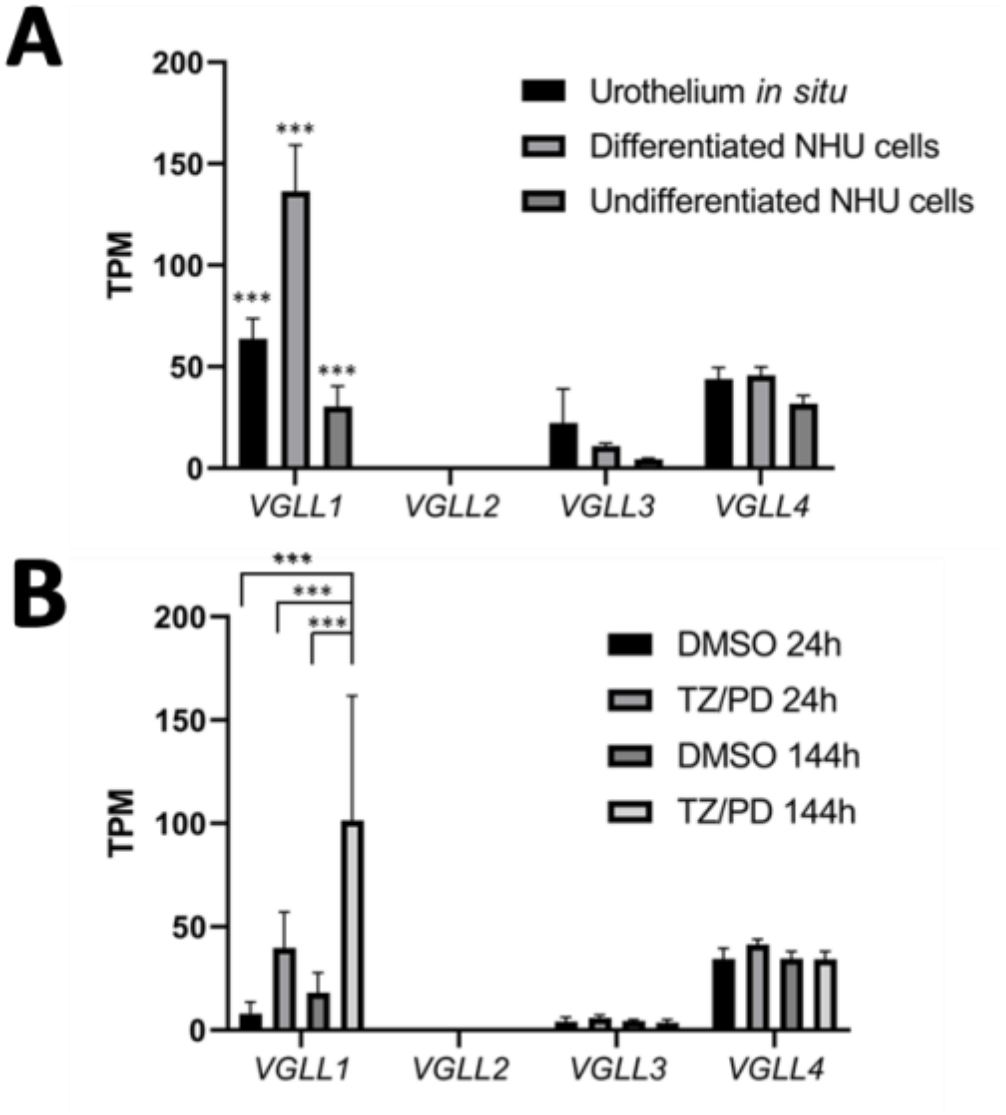

Figure 3.5: *VGLL1* is the most dominantly expressed transcript of the VGLL family in urothelial cells

RNAseq analysis of VGLL family member transcript expression in urothelium *in situ* and *in vitro* cultured NHU cells (n=3 independent samples). Graph (**A**) denotes expression of *VGLL1*, *VGLL2*, *VGLL3*, and *VGLL4* in RNAseq samples from urothelium *in situ*, ABS/Ca^{2+} differentiated NHU cells and accompanying isogeneic NHU cells provided with no differentiation cues. Graph (**B**) displays the expression of the same genes in NHU cells treated with either TZ/PD or DMSO control for periods of 24h or 144h. Significance between groups was determined by two-way ANOVA with Tukey's multiple comparisons post-hoc test. ***=p≤0.001.

Principal component analysis of various urothelial RNAseq samples was subsequently performed with transcript expression of *VGLL1* and a list of predefined urothelial-associated transcription factors (n=35) to determine whether a correlation existed between *VGLL1* and said genes in urothelium. The analysis revealed that the first principal component (PC1) explained 42.9% of the variance in gene expression, while PC2 explained 24.3% and PC3 explained 9.3% (Fig. 3.6). Based on the distribution of the urothelial sample types in the analysis, it appeared that PC1 represented the differences in the differentiation state between samples (with ABS/Ca^{2+} differentiated NHU cells at one side of the X axis and sub-confluent undifferentiated NHU cells on the other) whilst PC2 represented inherent differences in transcription factor expression between *in vitro* and *in situ* urothelium across the Y axis. Expression of *FOXA1*, *RARG*, *POU5F1* (OCT4)*, IRF1, GATA3* and *PPARG* were found to associate strongly with functionally differentiated urothelial samples, while *TP63* and *E2F7* were associated with undifferentiated NHU samples. *VGLL1* expression was also found to associate with the differentiation-associated genes, with expression found to closely align with that of *FOXA1, RARG* and *POU5F1*. Overall, the results of this section suggest that *VGLL1* is the predominantly expressed member of the VGLL family in urothelial biology, and that its function is closely associated with differentiation. Moreover, a concurrent downregulation of YAP/TAZ target genes *AXL* and *CYR61* potentially suggested an inhibition of YAP/TAZ signalling and a functional activation of the Hippo pathway in differentiated urothelium. A visual summary of the transcriptomic changes that occur in the Hippo pathway upon urothelial cytodifferentiation is provided in Fig. 3.7 and Table 3.3.

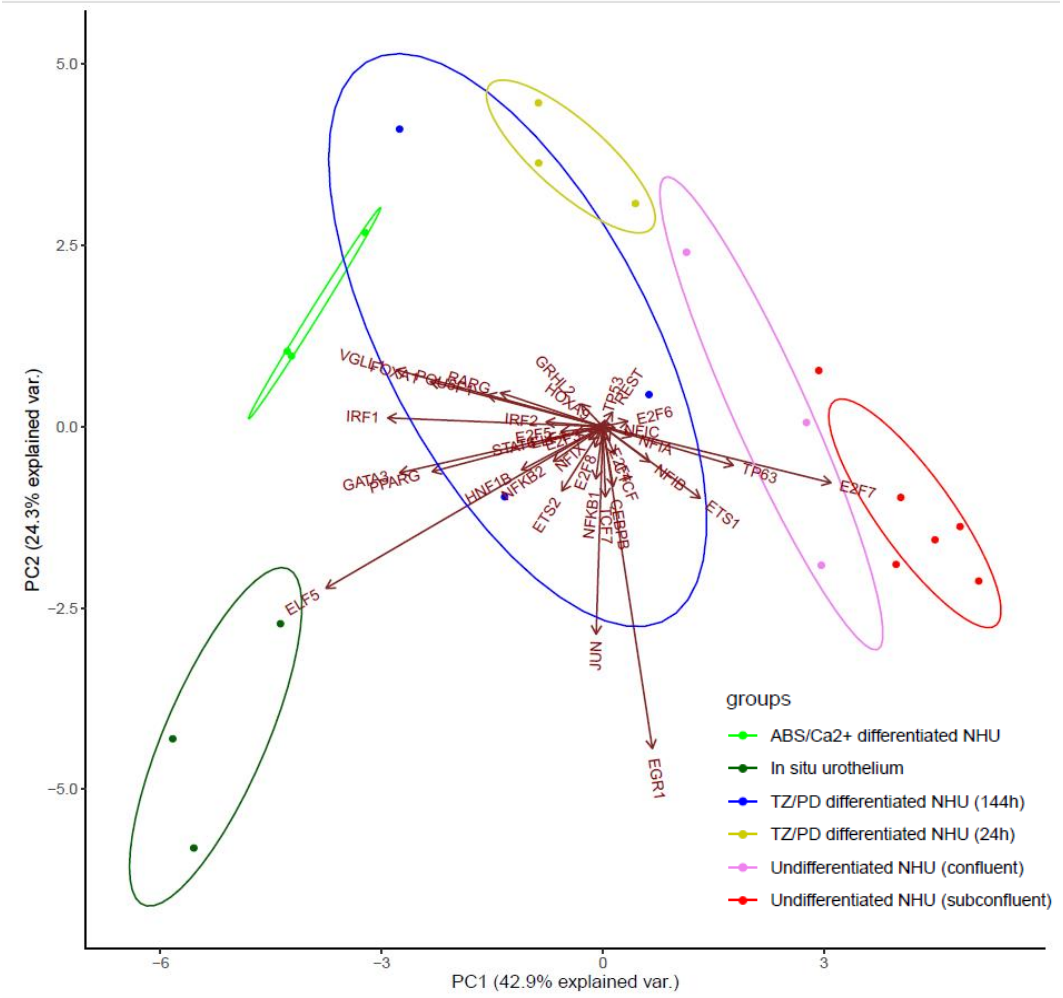

Figure 3.6: *VGLL1* expression in urothelial cells aligns with expression of differentiation-associated transcription factors

Unscaled principal component analysis plot of RNAseq samples lysed under different physiological conditions (n=3 samples of *in situ*, ABS/Ca^{2+} differentiated, TZ/PD differentiated and undifferentiated cells in a confluent state, n=6 samples of subconfluent undifferentiated cells), separated on the basis of expression of *VGLL1* and the cohort of urothelial transcription factor genes identified by Fishwick *et al* (n=35). Each dot represents a different RNAseq sample while each condition type is represented by a different icon colour, with ellipses representing 95% confidence intervals.

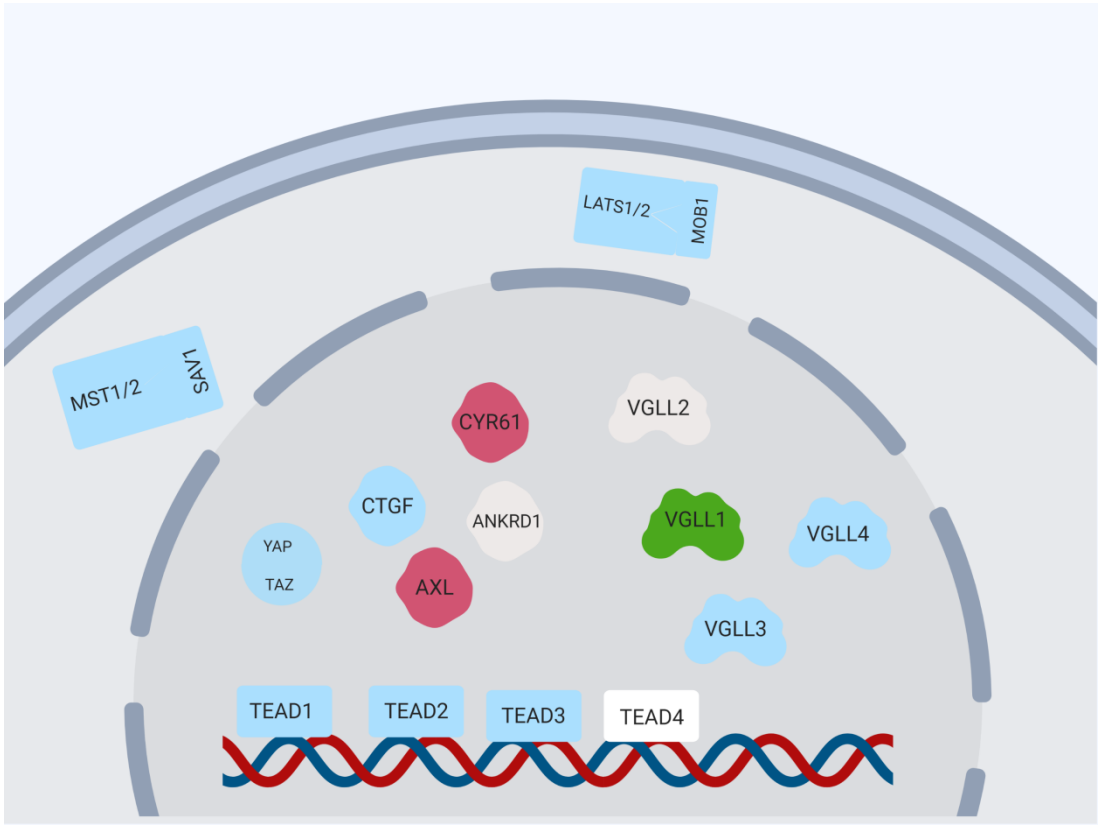

Figure 3.7: Schematic representation of transcriptomic changes in Hippo pathway genes in NHU cells following ABS/Ca^{2+} differentiation

Genes that experienced a $\log_2$ fold change ≤ -2 downregulation in expression after urothelial cytodifferentiation are coloured red while genes with a $\log_2$ fold change ≥ 2 are coloured green. Genes which did not differ between conditions are coloured blue, while *ANKRD1*, *VGLL2* and *TEAD4* are coloured white due to being absent from NHU cells. Differences in fold change for each gene is detailed in Table 3.3.

Gene	Log_2 fold change
VGLL1	2.162
VGLL3	1.283
VGLL4	0.526
YAP1	-0.395
WWTR1	-0.638
AXL	-3.109
CTGF	0.225
CYR61	-1.893
TEAD1	-0.003
TEAD2	-0.003
TEAD3	0.930
STK4 **(MST1)**	-0.034
STK3 **(MST2)**	-0.401
SAV1	-0.196
LATS1	0.044
LATS2	0.101
MOB1A	-0.306

Table 3.3: Log_2 fold change differences in Hippo pathway component transcript expression in ABS/Ca^{2+} differentiated NHU cells compared to undifferentiated NHU cells

Genes with a log_2 fold change ≥ 2 upregulation in ABS/Ca^{2+} differentiated cells are highlighted in green, while genes with a log_2 fold change decrease ≤ -2 are highlighted in red.

3.4.2 Characterisation of Hippo pathway component protein expression in comparison to proteins associated with a differentiated urothelial phenotype

3.4.2.1 Immunohistochemical analysis of VGLL1 and urothelial transcription factors of interest in native urothelium

In order to characterise VGLL1 protein expression in urothelium, validation of two commercially available VGLL1 antibodies was performed on urothelial cells by immunoblotting, immunofluorescence and immunohistochemical approaches (Appendix vi). Subsequent immunohistochemical analysis of two normal FFPE human ureters with the HPA042403 antibody confirmed that VGLL1 was expressed by normal *in situ* urothelium, supporting the evidence found at the transcript level (Fig. 3.8A). VGLL1 expression was observed to be localised solely to the urothelium, with no labelling found in the infiltrating lymphocytes or cells of the lamina propria. VGLL1 expression was found in both the nuclear and cytoplasmic compartments of urothelial cells, with slight differences in the intensity of cytoplasmic expression visualised between ureter samples. In both ureters, a gradient of nuclear VGLL1 expression was found between the lumen-facing superficial cells and underlying intermediate and basal cell layers.

Labelling of various urothelial transcription factors in the same ureter samples was subsequently performed to compare their expression patterns to that of VGLL1. Unlike VGLL1, transcription factors PPARγ (Fig. 3.8B), GATA3 (Fig. 3.8C) and FOXA1 (Fig. 3.8D) were found to have homogeneous, nuclear expression in urothelial cells of all layers. Localisation of VGLL1 expression appeared most similar to ELF3 expression, which was also found to be most highly expressed in superficial cells (Fig 3.8E). As per its previously cited role in helping to develop the basal urothelial phenotype (Section 1.3.2.3), p63 was expressed exclusively in the nuclei of basal and intermediate cell layers of the urothelium (Fig. 3.8F).

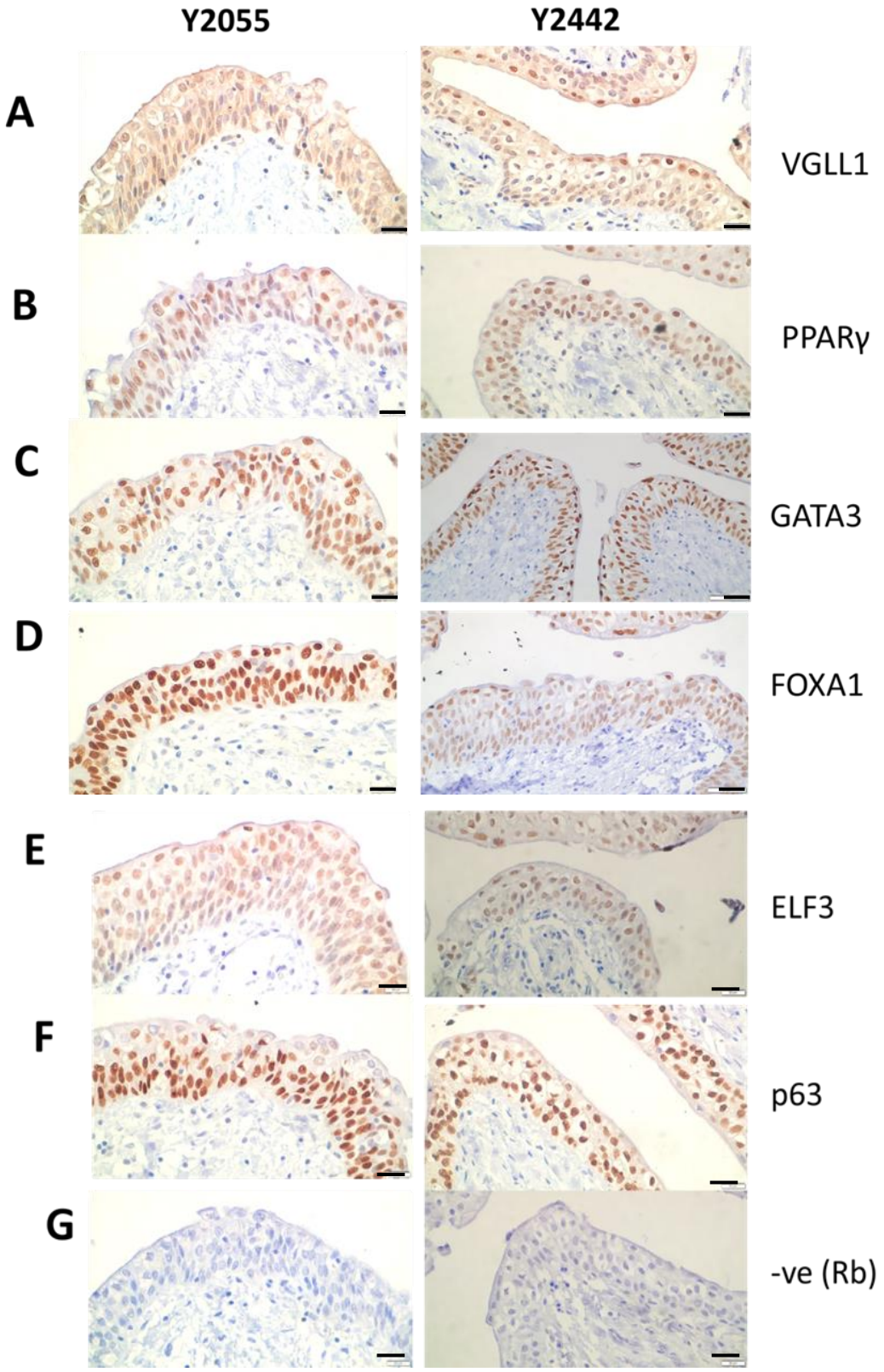
Y2055
Y2442
A
VGLL1
B
PPARγ
C
GATA3
D
FOXA1
E
ELF3
F
p63
G
-ve (Rb)

Figure 3.8: VGLL1 displays both nuclear and cytoplasmic labelling in urothelium *in situ*
Immunohistochemical analysis of VGLL1 (**A**), PPARγ (**B**), GATA3 (**C**), FOXA1 (**D**), ELF3 (**E**) and p63 (**F**) expression in sections of two normal human ureters, Y2055 and Y2442. The phenotype of VGLL1 expression was indicative of four independent samples of ureter, images of which can be found in Appendix vi and xii. Sections that were labelled with no primary antibody **(G)** were used as negative controls. Scale bar= 20 μm.

3.4.2.2 Immunoblotting of differentiation-associated markers and Hippo pathway components following NHU cytodifferentiation

Expression of VGLL1, YAP and TEAD (following validation of antibodies specific to total and phosphorylated forms of YAP and "pan-TEAD", as detailed in Appendix vi) protein in urothelial cells was examined after NHU cells had undergone differentiation by both TZ/PD and ABS/Ca^{2+} methods, with additional analysis of protein lysed from freshly isolated urothelium to compare to expression *in situ* (Fig. 3.9A). NHU cells grew as a monolayer, with the cells closely resembling the "cobblestone-like" morphology of other epithelia upon reaching confluence (Fig. 3.9B-C). Treatment of NHU cells with TZ/PD caused the cells to adopt a more compact morphology, alongside the occasional formation of rosette-like structures across the monolayer (Fig. 3.9D). Cellular stratification could be observed in cells treated with ABS/Ca^{2+} (Fig. 3.9E).

A

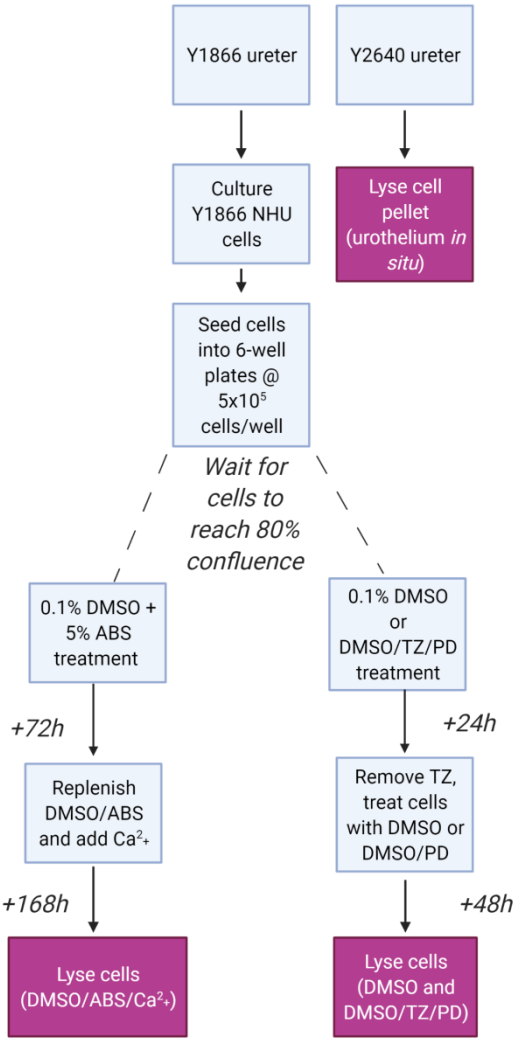
Y1866 ureter
Y2640 ureter
Culture Y1866 NHU cells
Lyse cell pellet (urothelium *in situ*)
Seed cells into 6-well plates @ 5x10^5 cells/well
Wait for cells to reach 80% confluence
0.1% DMSO + 5% ABS treatment
0.1% DMSO or DMSO/TZ/PD treatment
+72h
+24h
Replenish DMSO/ABS and add Ca^{2+}
Remove TZ, treat cells with DMSO or DMSO/PD
+168h
+48h
Lyse cells (DMSO/ABS/Ca^{2+})
Lyse cells (DMSO and DMSO/TZ/PD)

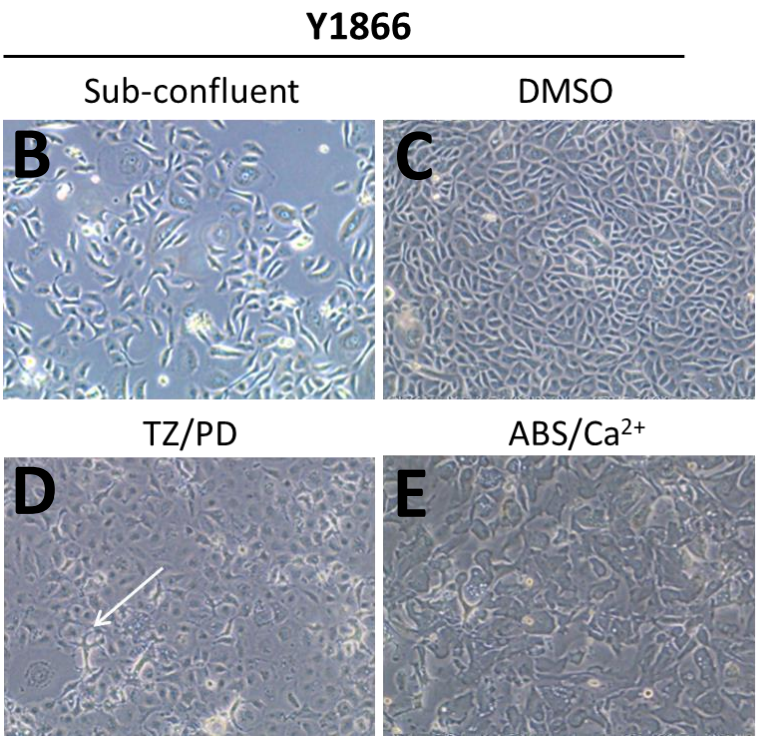
Y1866
Sub-confluent
DMSO
B
C
TZ/PD
ABS/Ca^{2+}
D
E

Figure 3.9: NHU cell morphology in undifferentiated and differentiated states

A) Experimental flowchart of Y1866 NHU cells (n=1) undergoing differentiation via both established *in vitro* methods. Cells were seeded into 6-well plastic plates and allowed to grow to approximately 80% confluence. Wells were split between cells receiving treatment with DMSO/TZ/PD (or vehicle control only) for 72h, or cells pre-treated with ABS (+ DMSO) for 72h. TZ/PD cells were lysed after 72h, while ABS cells were additionally supplemented with Ca^{2+} for an additional period of 7 days (10 days total in ABS). ABS/Ca^{2+} treated cells were media changed every 48h until lysis. A separate ureter sample, Y2640, was lysed immediately upon urothelial cell isolation and was used as a proxy for protein expression in urothelium *in situ*. **B-E)** Phase micrograph images of Y1866 cells in a state of sub-confluence or at confluence at the conclusion of TZ/PD and ABS/Ca^{2+} treatments. The white arrow indicates the appearance of rosette-like formations following TZ/PD treatment.

Immunoblot analysis of PPARγ, PPARγ target genes FOXA1 and ELF3, and markers of tight junction formation, namely claudin 3, claudin 4 and ZO-3, were labelled to confirm induction of urothelial cytodifferentiation. PPARγ, FOXA1, ELF3 and claudin 4 were found to be expressed in Y1356 cells following both differentiation methods (Fig. 3.10A-B), whereas claudin 3 and ZO-3 were found to be exclusively expressed in NHU cells after ABS/Ca^{2+} differentiation (Fig. 3.10B). p63 was found to be highly expressed by undifferentiated and urothelium *in situ*, but expression was reduced in TZ/PD treated cells and abrogated in ABS/Ca^{2+} differentiated cells (Fig. 3.10A).

VGLL1 protein expression was not found in sub-confluent cells, but similarly to transcription factors PPARγ, FOXA1 and ELF3 was found to be expressed following both 72h treatment with TZ/PD and by the 12 day ABS/Ca^{2+} differentiation procedure (Fig. 3.10C). Following densitometry analysis of the mean expression of VGLL1 between conditions, it was determined that there was a significant difference in expression between undifferentiated cells and every other condition (Fig. 3.10D; $p \leq 0.05$). Comparatively, all NHU samples assayed were found to be labelled by the pan-TEAD antibody in at least one location in the specified region of TEAD protein size, which ranges from 47.9 kDa (TEAD1) to 49.2 kDa (TEAD2; Fig. 3.10C). The most intense pan-TEAD band appeared in the ABS/Ca^{2+} differentiated cell sample, with this band found at a lower MW than the weaker bands found in undifferentiated and TZ/PD differentiated cells. This potentially indicated the dominant protein expression of the TEAD family members TEAD1 or TEAD3 in ABS/Ca^{2+} differentiated cells, consistent with the expression pattern found at the transcript level (Section 3.4.1.2). However, due to the close similarities in molecular weight between all four transcription factors labelled by the antibody, any attempt to definitively identify labelling of specific TEAD proteins was unfeasible without genetic manipulation, or further labelling with antibodies specific to individual TEAD proteins. Interestingly, expression of both total and phosphorylated forms of YAP remained consistent between all three cell conditions (Fig. 3.10C), suggesting no difference in the total amount of inactivated YAP in NHU cells upon differentiation.

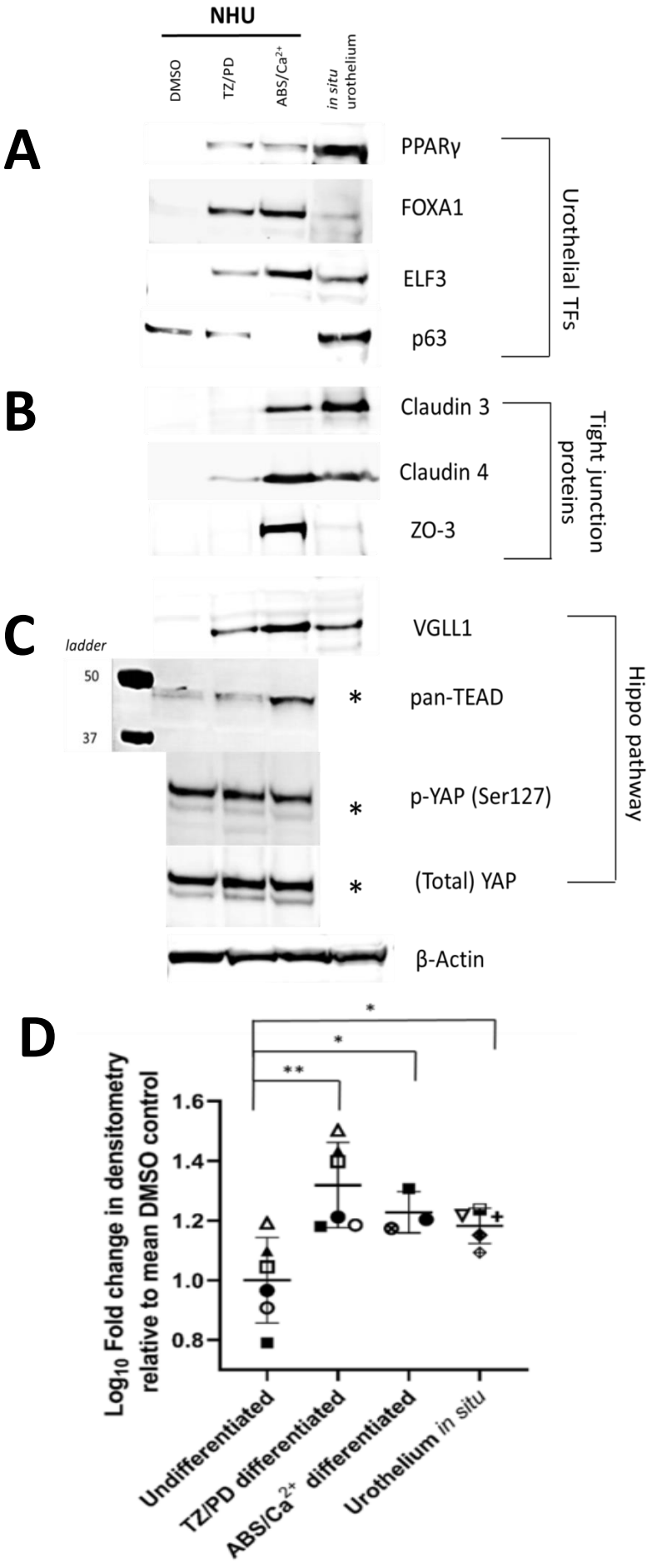
NHU
DMSO
TZ/PD
ABS/Ca2+
in situ urothelium
A
PPARγ
FOXA1
ELF3
p63
Urothelial TFs
B
Claudin 3
Claudin 4
ZO-3
Tight junction proteins
C
ladder
50
37
VGLL1
pan-TEAD
p-YAP (Ser127)
(Total) YAP
β-Actin
Hippo pathway
D
Log10 Fold change in densitometry relative to mean DMSO control
1.6
1.4
1.2
1.0
0.8
Undifferentiated
TZ/PD differentiated
ABS/Ca2+ differentiated
Urothelium in situ

Figure 3.10: VGLL1 protein expression is induced by TZ/PD and ABS/Ca^{2+} differentiation in a similar manner to that of urothelial differentiation-associated transcription factors whilst YAP expression remains consistent

Immunoblotting images of PPARγ, FOXA1, ELF3 and p63 (**A**), claudin 3, claudin 4 and ZO-3 (**B**), VGLL1, pan-TEAD, and YAP (total and phosphorylated forms; **C**) expression in Y1866 NHU cells (n=1) treated with DMSO or TZ/PD for 72h, ABS/Ca^{2+} for 7 days or lysed from freshly isolated Y2640 urothelium (n=1). TEAD expression was labelled for using a pan-TEAD rabbit mAb which recognises endogenous expression of all four TEAD proteins in the 48-50 kDa range (as demonstrated by accompanying image of protein ladder). Expression of housekeeping protein β-Actin was used to confirm equal loading of samples. Lanes marked with an asterisk represent protein samples that could not be assayed due to a lack of remaining lysate. **D)** Quantification of VGLL1 expression by immunoblotting densitometry analysis in biological replicates of each condition assayed (n=6 for DMSO, n=5 for TZ/PD and urothelium *in situ*, n=3 for ABS/Ca^{2+}). The icons of the same shape and shading represent densitometry values from donor-matched urothelial samples. Differences in expression are represented as a Log_{10} fold change in comparison to the mean DMSO expression value. Significance between groups was determined by Welch's ANOVA with a Dunnett's T3 multiple comparisons post-hoc test. *=p≤0.05; **=p≤0.01.

3.4.2.3 Immunofluorescence of differentiation-associated markers, proliferation-associated markers and VGLL1 following NHU cytodifferentiation

VGLL1 was expressed in the nuclei of NHU cells following both differentiation protocols (Fig. 3.11A). Expression of the protein appeared heterogeneous across cultures, with some nuclei labelled more intensely than others. As observed during initial validation of the HPA042043 antibody (Appendix vi), additional cytoplasmic labelling of VGLL1 was found in some cells following TZ/PD treatment, but a greater proportion of cytoplasmic localisation was observed when cells were ABS/Ca^{2+} differentiated. Expression of PPARγ (Fig. 3.11B), ELF3 (Fig. 3.11C) and GATA3 (Fig. 3.11D) were similar found to be induced in the nuclei of cells following both differentiation methods. The pattern of p63 (Fig. 3.11E) expression supported the phenotype determined by immunoblotting, with nuclear p63 expression high in undifferentiated cells but reduced following treatment, with ABS/Ca^{2+} differentiated cells exhibited the lowest expression (Fig. 3.11E). Interestingly, dual labelling of the GATA3 and p63 antibodies together demonstrated a primarily mutually exclusive relationship between the two targets, with the majority of the differentiated NHU cell nuclei that remained p63-positive appeared to be found in cells that had weak GATA3 labelling (Fig. 3.11F).

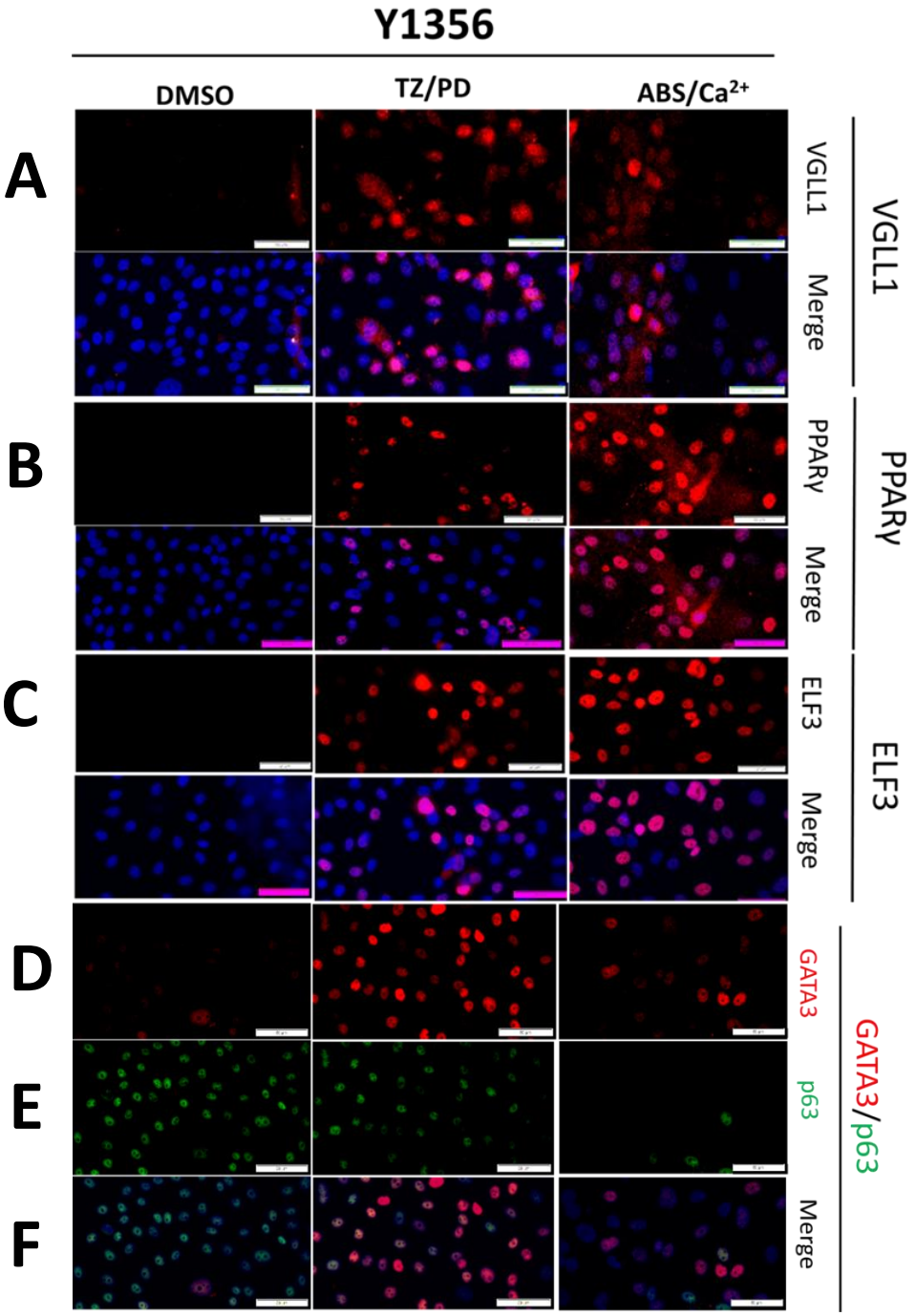

Figure 3.11: Induction of nuclear VGLL1 and differentiation-associated proteins after TZ/PD and ABS/Ca^{2+} treatment

Y1356 cells were seeded onto glass slides and treated in the same manner as cells in section 3.4.2.2. Following formalin fixation and Triton X-100 permeabilisation, cells were labelled with VGLL1 (**A**), PPARγ (**B;** 81B8 antibody) and ELF3 (**C**), or dual labelled with GATA3 (**D**; red fluorescence) and p63 (**E**; green fluorescence) before visualisation. Images were all taken at same exposure and are shown with or without overlaid Hoechst 33258 DNA staining. Scale bar= 50µm.

Expression of tight junction proteins in NHU cells were also investigated to uncover whether ZO-2 and ZO-3 localised to cell membranes under the same conditions found to induce previously observed membranous localisation of ZO-1 (Section 1.3.2.1). All three proteins displayed very low or absent expression in undifferentiated NHU cells, while treatment of cells with TZ/PD induced cytoplasmic expression of ZO-1/ZO-$1^{\alpha+}$ (Fig. 3.12A) and ZO-2 (Fig. 3.12B), but not ZO-3 (Fig. 3.12C). ABS/Ca^{2+} differentiation was found to result in the translocation of all three proteins to the membranous regions of cells, with the observations made in this and the previous section confirming that ZO-3 was a robust marker of stratified differentiation in NHU cells.

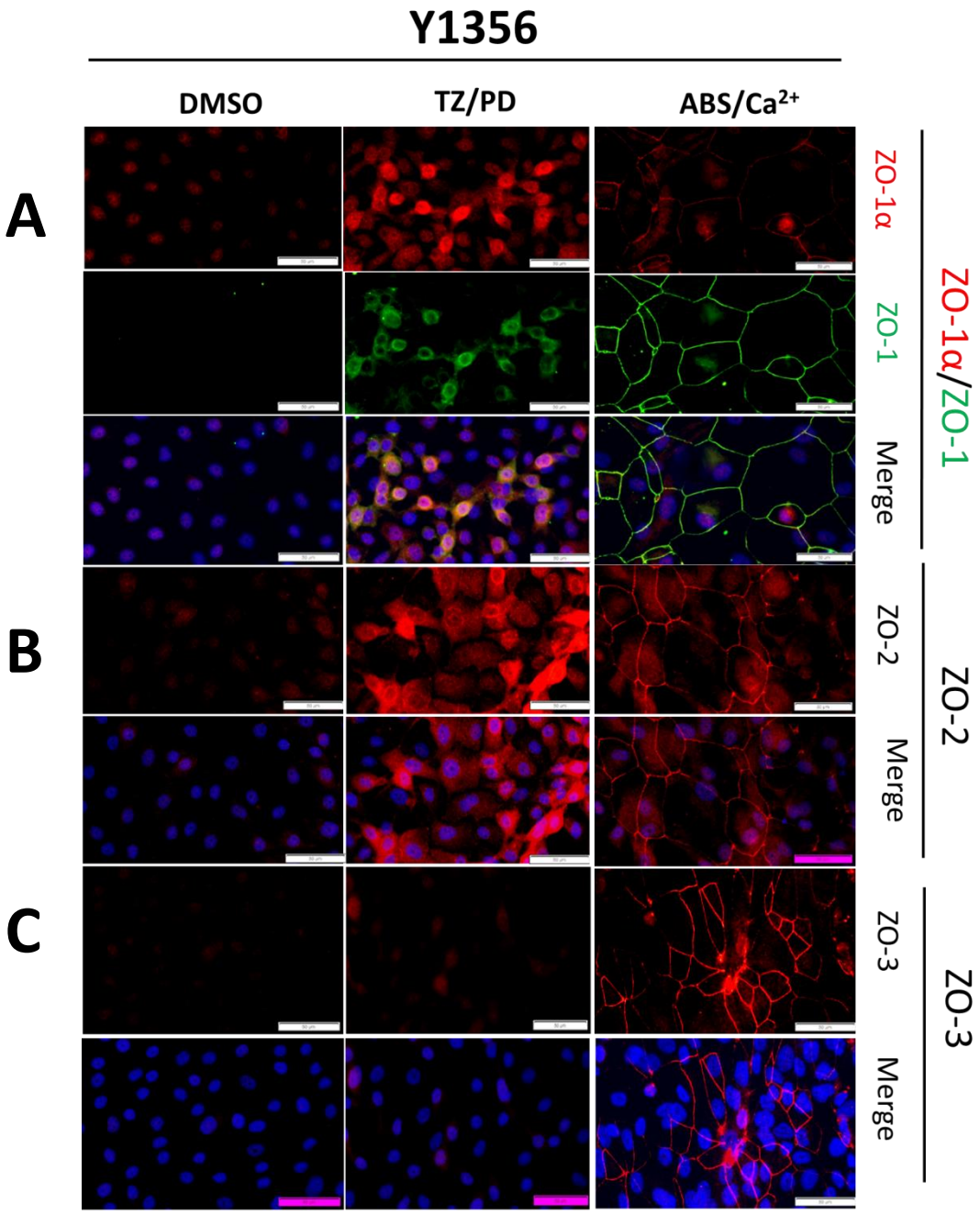

Figure 3.12: Induction of membranous tight junction protein localisation following ABS/Ca^{2+} differentiation

Immunofluorescence analysis of tight junction proteins ZO-1 (dual labelled with the ZO-$1^{\alpha+}$ isoform; **A**), ZO-2 (**B**) and ZO-3 (**C**) expression in Y1356 cells undergoing TZ/PD and ABS/Ca^{2+} differentiation (n=1). Images were all taken at same exposure and are shown with or without overlaid Hoechst 33258 DNA staining. Scale bar= 50µm.

To visualise the effect of blocking proliferation in differentiated NHU cells, cell cycle-associated proteins Ki67 and MCM2 were labelled for in each cell state. Expression of both proteins was high in the actively proliferating undifferentiated cells, but experienced a reduction in expression when cells were TZ/PD treated (Fig. 3.13A). Sub-nuclear localisation of Ki67 between the two cell states suggested that the cells had switched from a predominantly S-phase population (Undifferentiated) to including a greater proportion of cells in G1 phase (TZ/PD Differentiated). Differentiation of the cells by ABS/Ca^{2+} was found to have the greatest effect on the onset of quiescence, as only a small population of cells remained positive for either protein. As expected, expression of active, phosphorylated ERK1/2 was lost from the nuclear and perinuclear regions of NHU cells upon treatment with TZ/PD due to the downstream effects of directly blocking EGFR (Fig. 3.13B).

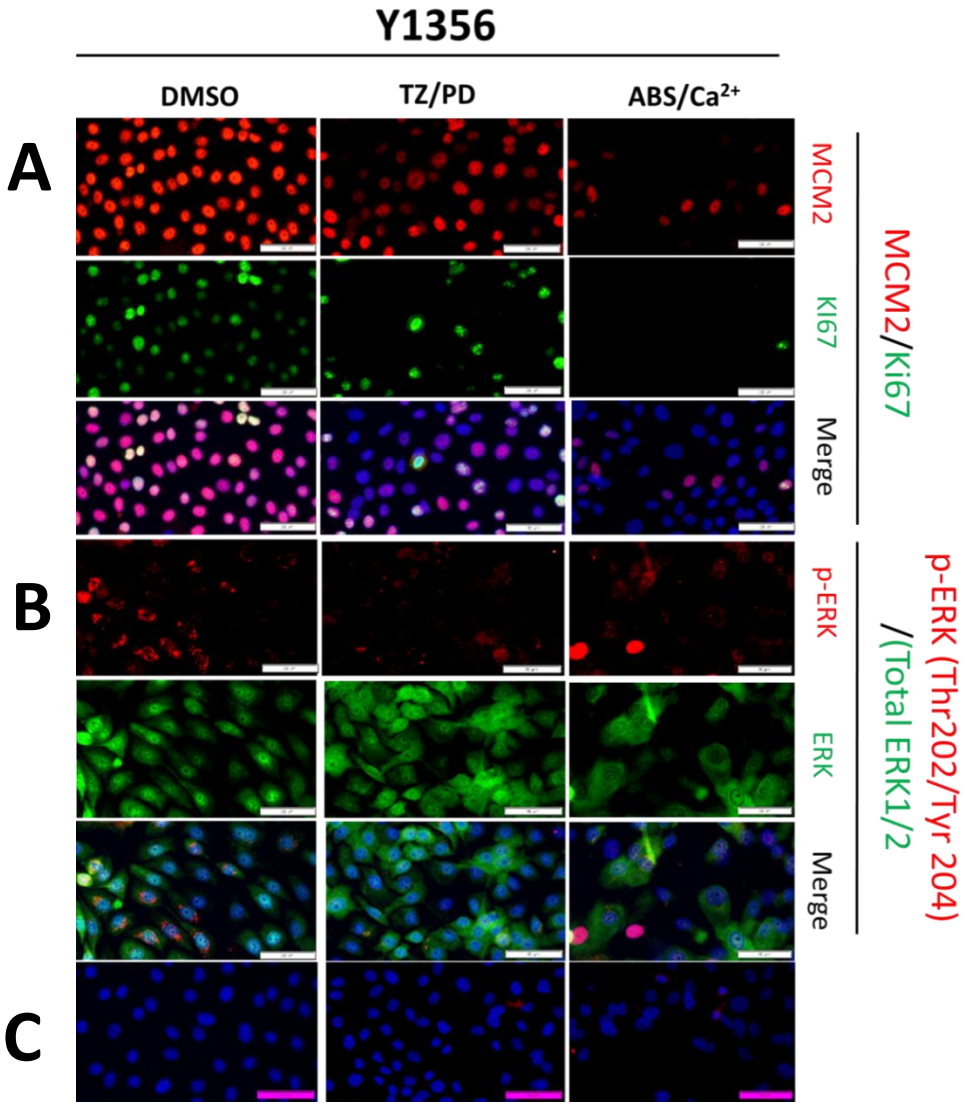

Figure 3.13: Loss of proliferation-associated protein expression after TZ/PD and ABS/Ca^{2+} treatments

Dual labelling of MCM2 (red fluorescence) with Ki67 (green fluorescence; **A**) and p-ERK1/2 (Thr202/Tyr204; red fluorescence) with Total ERK1/2 (green fluorescence; **B**) antibodies in Y1356 cells differentiated using TZ/PD and ABS/Ca^{2+} methods (n=1). Cells receiving no primary antibody (**C**) were used as a negative control for Figures 3.11-13. Images were all taken at same exposure and are shown with or without overlaid Hoechst 33258 DNA staining. Scale bar= 50µm.

3.4.3 Expression of VGLL1 following inhibition of PPARγ-mediated differentiation in NHU cells

3.4.3.1 Transcript expression of *VGLL1* following selective inhibition of PPARγ in TZ/PD differentiated cells

The preceding characterisation experiments had determined that VGLL1 was consistently up-regulated following the PPARγ-mediated TZ/PD differentiation process. A time-course of NHU cells receiving TZ/PD treatment alongside concurrent application of T007 for different periods of time was therefore completed to evaluate VGLL1 expression in PPARγ-inhibited cells (Fig. 3.14A). The cell morphology indicative of TZ/PD differentiation appeared to be maintained when cells were pre-treated with T007 (Fig. 3.14B). As expected, *VGLL1*, *ELF3* and PPARγ target gene *FABP4* transcript were significantly induced after 72h of TZ/PD treatment ($p \leq 0.001$; Fig. 3.14C). While *ELF3* and *FABP4* experienced a significant reduction in expression when concurrently treated with T007 ($p \leq 0.05$), no significant difference was found between TZ/PD and TZ/PD/T007 cultures in regards to *VGLL1* expression. The lack of a significant inhibition of *VGLL1* transcript in the TZ/PD/T007 condition appeared to be attributable to an large variation in expression between samples, as while three cell lines (Y1897, Y1947 and Y2351) were found to have inhibited *VGLL1* to a similar extent as *ELF3*, Y1946 cells experienced no inhibition, while Y1226 cells exhibited a notably higher expression of *VGLL1* compared to its corresponding TZ/PD condition.

A

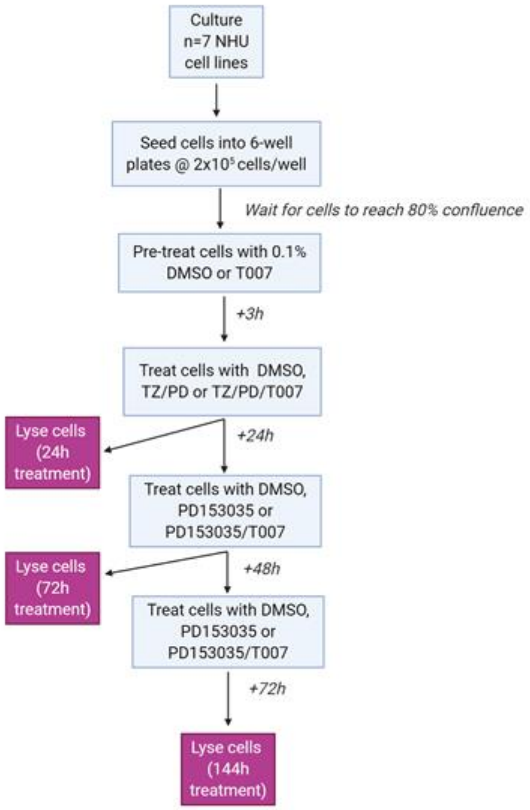
Culture n=7 NHU cell lines
Seed cells into 6-well plates @ 2x10⁵ cells/well
Wait for cells to reach 80% confluence
Pre-treat cells with 0.1% DMSO or T007
+3h
Treat cells with DMSO, TZ/PD or TZ/PD/T007
Lyse cells (24h treatment)
+24h
Treat cells with DMSO, PD153035 or PD153035/T007
Lyse cells (72h treatment)
+48h
Treat cells with DMSO, PD153035 or PD153035/T007
+72h
Lyse cells (144h treatment)

B

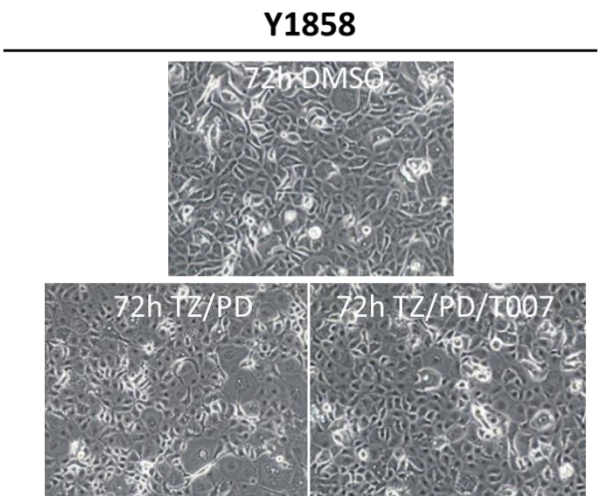
Y1858
72h DMSO
72h TZ/PD
72h TZ/PD/T007

C

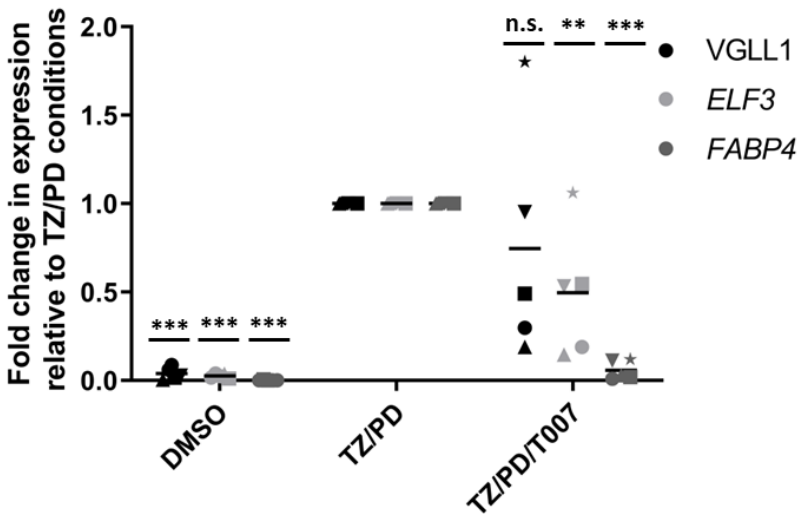
Fold change in expression relative to TZ/PD conditions
2.0
1.5
1.0
0.5
0.0
***
***
***
n.s.
**
***
VGLL1
ELF3
FABP4
DMSO
TZ/PD
TZ/PD/T007

Figure 3.14: PPARγ antagonism significantly inhibits *FABP4* and *ELF3*, but not *VGLL1*, transcript expression following 72h TZ/PD differentiation

A) Experimental flowchart of NHU cells undergoing a time-course of TZ/PD treatment. At the point of reaching 80% confluence, cells were pre-treated with T007 in order to inhibit any latent PPARγ activity in the undifferentiated cells. Cells were subsequently treated with a combination of either TZ/PD or TZ/PD/T007 and lysed after periods of 24h, 72h, and 144h. All conditions were treated with 0.1% DMSO to control for non-specific solvent effects. **B)** Phase micrograph images of Y1858 cells after treatment with the above conditions, with images captured immediately preceding lysis of cells at the 72h time-point. **C)** RT-qPCR analysis of *VGLL1*, *ELF3* and *FABP4* expression in NHU cells treated with vehicle control, TZ/PD or TZ/PD/T007 for a period of 72h. Differences between conditions were displayed as a fold change in transcript expression compared to TZ/PD differentiated cells. Significant downregulation of PPARγ target gene *FABP4* in TZ/PD differentiated NHU cells treated with T007 demonstrated the efficacy of T007 treatment to inhibit PPARγ activity. The experiment was replicated in five independent cell lines, with icons of the same shape representing matched donors and icons of the same shading representing the different genes assayed. Significance between conditions was calculated using a two-way ANOVA with Tukey's post-hoc test. *=p≤0.05; ***=p≤0.001.

3.4.4.2 VGLL1 protein expression following a TZ/PD/T007 treatment time-course in NHU cells

Similar to what was observed at the transcript level, VGLL1 appeared to have decreased expression in TZ/PD differentiated cells pre-treated with T007, although unlike FABP4, expression which was not completely blocked by PPARγ inhibition (Fig. 3.15A). When quantifying the expression of VGLL1 protein across multiple timepoints and biological replicates, it was determined that there a significant reduction of VGLL1 after T007 treatment at the 24h time-point only, with the reduction in expression observed at later timepoints non-significant due to variability between cell lines (Fig. 3.15B). Overall, evidence at the transcript and protein level therefore suggested that activation of PPARγ did play a role in the initial induction of VGLL1 in NHU cells, with this effect seen most acutely in the early stages of TZ/PD differentiation. However, the less pronounced effect of T007 on VGLL1 expression observed at later time-points (and increased variability between cell lines at these points) suggested the existence of other variables which influenced expression of the gene/protein.

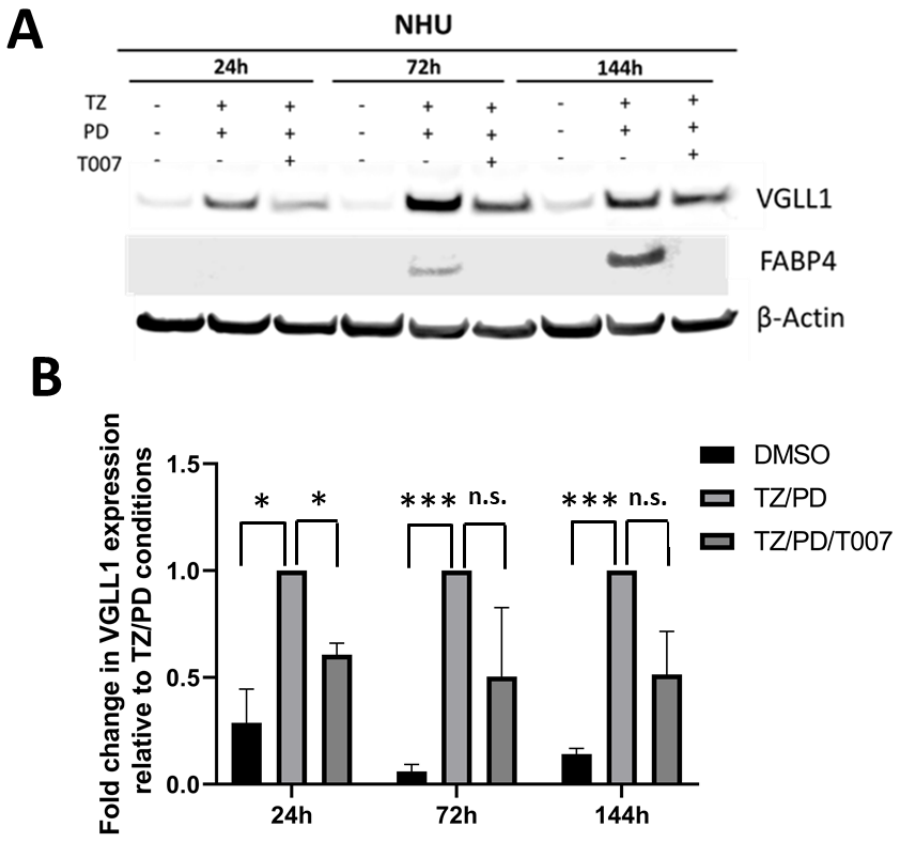

Figure 3.15: Blockade of PPARγ activity has a time-sensitive effect on the induction of VGLL1 protein in actively differentiating NHU cells

Immunoblot analysis of VGLL1 expression in NHU cells treated with a combination of TZ, PD153035 and T007 for periods of 24h, 72h and 144h. All conditions were treated with 0.1% DMSO to control for non-specific solvent effects. Image (**A**) is a representative immunoblot image of VGLL1 and FABP4 expression in TZ/PD/T007 treated cells, with FABP4 expression used to confirm, like at the transcript level, that T007 treatment was successful in blocking PPARγ activation. Expression of β-Actin was used to confirm equal loading of samples. Image (**B**) is immunoblot densitometry analysis of (**A**), with expression of VGLL1 from three independent biological replicates quantified. Differences between conditions was quantified by comparing the fold change in VGLL1 expression after TZ/PD treatment compared to each other condition at each timepoint. Significance between conditions was calculated using a two-way ANOVA with Tukey's post-hoc test. *=p≤0.05; **=p≤0.01. Immunoblot images of replicate experiments can be found in Appendix xii.

3.4.4 Bioinformatics analysis of the *VGLL1* promoter region

To predict the identity of alternative transcription factors that drive VGLL1 expression in NHU cells via bioinformatics, the transcription factor binding site predictor program JASPAR was used to identify potential binding motifs in the DNA sequence up to 6000bp upstream of the *VGLL1* gene. Predicted binding domains for PPARγ were searched for as part of the analysis, but no PPRE sites were discovered in the upstream sequence, or sites for transcription factors ELF3 or IRF-1. However, several potential binding sites were identified for GATA3, FOXA1 and KLF5 at a relative confidence score of at least 0.95 (Table 3.4). The urothelial differentiation-associated transcription factor with the closest potential binding site to the *VGLL1* start codon was GATA3, found less than 30 bp away from the start codon. The consensus sequence of GATA3 binding upstream of *VGLL1* is depicted in Fig. 3.16.

Figure 3.16: Multiple sequence alignment of the GATA3 binding motif in the DNA sequence upstream of the *VGLL1* promoter

Sequence logo was created using the WebLogo application (https://weblogo.berkeley.edu/logo.cgi; Crooks *et al.,* 2004).

Gene name	Relative score	Binding site start (bp)	Binding site end (bp)	Predicted sequence
GATA3	1.0	3848	3855	AGATAAGA
GATA3	0.99	5056	5061	AGATAG
GATA3	**0.99**	**5966**	**5971**	**AGATAG**
GATA3	0.99	1963	1968	AGATAG
GATA3	0.99	2175	2182	AGATAAGG
FOXA1	0.99	4052	4062	TGTTTGCTTTG
KLF5	0.98	2688	2697	GCCCCTCCCA
GATA3	0.98	3533	3538	TGATAG
GATA3	0.97	5148	5155	TGATAAGG
GATA3	0.97	2810	2817	TGATAAGG
GATA3	0.97	1639	1646	TGATAACA
GATA3	0.95	4847	4852	AGATTG
GATA3	0.95	5585	5590	AGATTG
GATA3	0.95	5833	5838	AGATTG
GATA3	0.95	1218	1223	AGATTG
GATA3	0.95	2134	2139	AGATTG
GATA3	0.95	2399	2404	AGATTG
GATA3	0.95	307	314	AGATAATA
KLF5	0.95	3818	3827	TCCACTCCCC
FOXA1	0.95	802	816	TATTTATTTACTTAT
FOXA1	0.95	284	294	TGTTTACTCAA

Table 3.4: List of potential binding sites for urothelial-associated transcription factors in the DNA sequence upstream of *VGLL1*.

The sequence upstream of *VGLL1* (starting from 6000bp upstream of the promoter) was inputted into JASPAR (http://jaspar.genereg.net/) to identify potential binding sites for PPARγ, FOXA1, GATA3, ELF3, IRF-1 and KLF5. Only hits with a relative score of 0.95 (maximum 1) or above were searched for, ensuring that only binding sites with a prediction score of at least 95% accuracy are displayed. The GATA3 binding site closest to the *VGLL1* start codon is highlighted in bold. Information on potential RARγ and OCT4 binding motifs in the DNA region analysed was not available on JASPAR.

3.4.5 Effect of siRNA knockdown of GATA3 on VGLL1 expression

To determine the role of GATA3 transcriptional activity on the induction of VGLL1, NHU cells were transfected with siRNA specific to GATA3 and subsequently TZ/PD differentiated for a period of 72h. RT-qPCR analysis of the resultant conditions confirmed that TZ/PD differentiation in cells transfected with control siRNA induced significant increases in *GATA3* and *VGLL1* when compared to undifferentiated control (Fig. 3.17; $p \leq 0.001$). A significant reduction of *GATA3* expression was found in TZ/PD treated cells after transfection with both GATA3 siRNA constructs ($p \leq 0.001$), confirming the efficacy of said reagents. Expression of *VGLL1* was also revealed to be significantly lower in TZ/PD treated cells transfected with either GATA3 siRNA compared to TZ/PD differentiated cells transfected with control siRNA ($p \leq 0.01$). However unlike *GATA3*, expression of *VGLL1* was not inhibited to the baseline expression found in control undifferentiated cells, with a significant difference in expression also found between undifferentiated control cells and TZ/PD treated cells with GATA3 knockdown ($p \leq 0.001$; Appendix xii).

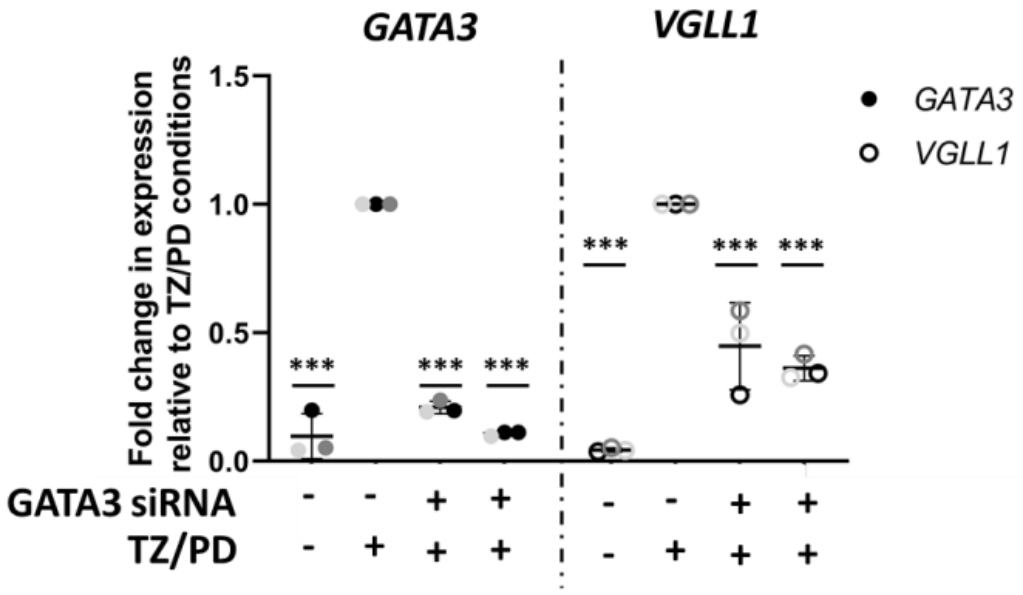

Figure 3.17: siRNA knockdown of GATA3 results in an inhibition of *VGLL1* transcript expression

RT-qPCR analysis of *GATA3* and *VGLL1* expression in undifferentiated NHU cells treated with 0.1% DMSO only and transfected with control siRNA (icons designated -/-), TZ/PD differentiated cells transfected with control siRNA (-/+) and TZ/PD treated cells transfected with GATA3 siRNA #1 (left sided +/+) or #2 (right sided +/+). All conditions were treated with 0.1% DMSO to control for non-specific solvent effects. Differences between conditions were displayed as a fold change in expression compared to TZ/PD differentiated cells transfected with control siRNA. The experiment is representative of three independent cell lines, with icons of the same shading representing matched donors. Significance between conditions was calculated using a two-way ANOVA with Tukey's post-hoc test. **=p≤0.01; ***=p≤0.001. All significant values displayed on the graph represent the significant differences between Ctrl siRNA TZ/PD treated cells against the other conditions. A full list of conditions with significant differences in expression can be found in Appendix xii.

Immunoblotting analysis of samples from two additional cell lines (Y1652 and Y2442) supported the pattern of expression seen at the transcript level, as expression of GATA3 and VGLL1 were reduced when TZ/PD differentiated cells were transfected with GATA3 siRNA (Fig. 3.18A-B). It was additionally observed that the GATA3 siRNA transfected cells experienced an upregulation of p63 protein, consistent with the phenotype found in an earlier study (Section 1.3.2.3). One cell line (Y2303) was found to only experience a modest inhibition of GATA3 from both GATA3 siRNA constructs, which was reflected in a negligible effect on VGLL1 expression (Fig. 3.18C). As a result of this, overall densitometry analysis of the three samples revealed no significant differences in expression of *VGLL1* or *GATA3* in TZ/PD differentiated NHU cells transfected with control siRNA compared to GATA3 siRNA transfected cells (Fig. 3.18D). Analysis of phase-contrast images from each cell line and condition prior to protein lysis revealed that despite seeding all conditions at the same initial cell number, Y2303 cells had reached a noticeably higher final cell density when compared to Y1652 and Y2442 conditions, perhaps accounting for the discrepancy observed in the relative amount of VGLL1 and GATA3 inhibition (Fig. 3.18E). Overall, the preceding results at the transcript and protein level indicated that activation of PPARγ and GATA3 transcriptional processes both played a role in the induction of VGLL1 in NHU cells (Fig. 3.18F), although confounding factors such as cell density and the length of time that cultures were actively differentiating may affect this induction.

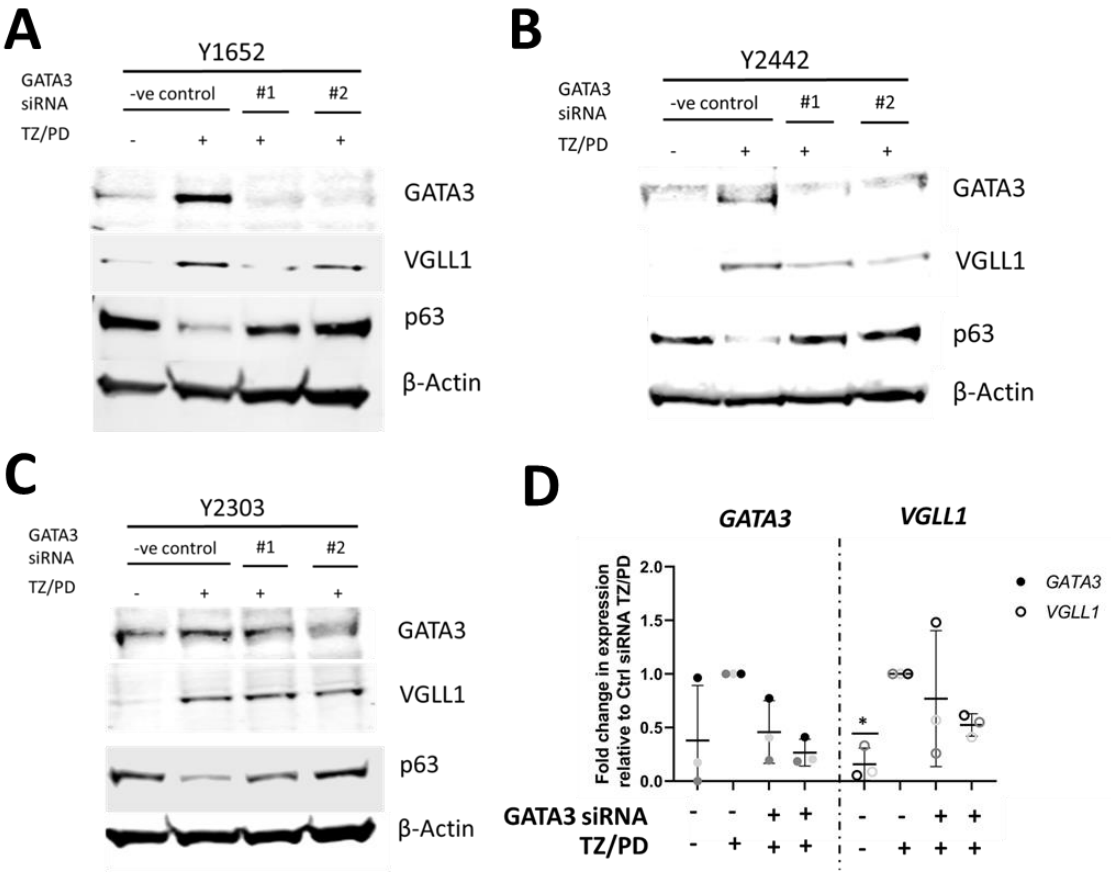
A
Y1652
GATA3 siRNA
-ve control
#1
#2
TZ/PD
- + + +
GATA3
VGLL1
p63
β-Actin
B
Y2442
GATA3 siRNA
-ve control
#1
#2
TZ/PD
- + + +
GATA3
VGLL1
p63
β-Actin
C
Y2303
GATA3 siRNA
-ve control
#1
#2
TZ/PD
- + + +
GATA3
VGLL1
p63
β-Actin
D
GATA3
VGLL1
Fold change in expression relative to Ctrl siRNA TZ/PD
2.0
1.5
1.0
0.5
0.0
*
GATA3
VGLL1
GATA3 siRNA - - + + - - + +
TZ/PD - + + + - + + +
E
DMSO (Ctrl siRNA)
TZ/PD (Ctrl siRNA)
TZ/PD (GATA3 siRNA #1)
TZ/PD (GATA3 siRNA #2)
Y1652
Y2442
Y2303

F

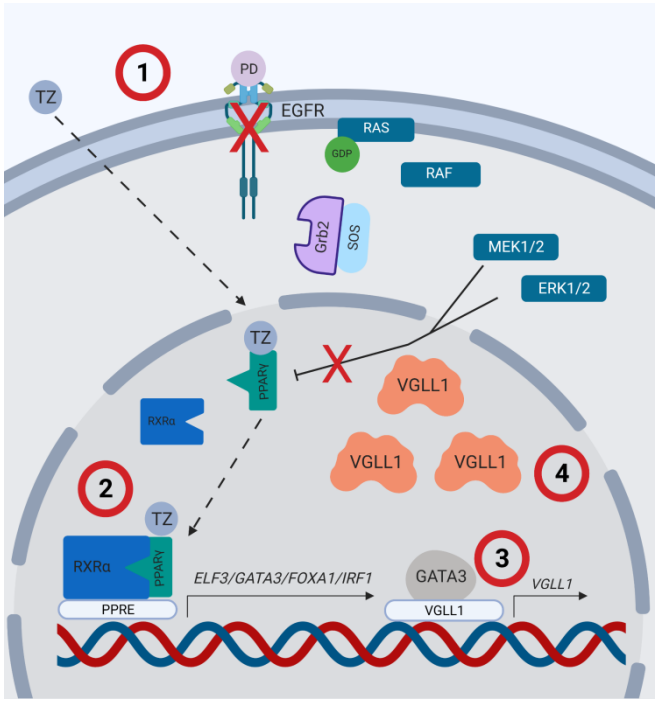

Figure 3.18: Loss of GATA3 results in an inhibition of VGLL1 protein expression in subconfluent NHU cells

Immunoblot analysis of GATA3, VGLL1 and p63 expression in Y1652 (**A**), Y2442 (**B**) and Y2303 (**C**) TZ/PD treated NHU cells after transfection with either control siRNA or two siRNA specific to GATA3. Expression of β-Actin was used to confirm equal loading of samples. **D)** Immunoblot densitometry analysis of (**A-C**), with expression of GATA3 and VGLL1 from three independent biological replicates quantified. Differences between conditions were quantified by comparing the fold change in expression in control siRNA TZ/PD treated cells compared to each other condition. Significance between conditions was calculated using a two-way ANOVA with Tukey's post-hoc test. **E)** Phase micrograph image from each cell line and condition preceding lysis of cells at the 72h time-point. **F)** Interpretation of the molecular events upstream of VGLL1 in differentiated NHU cells, as determined in Fig. 3.14-3.17. **1.** Concurrent treatment of NHU cells with TZ and PD results in binding of TZ to inactive PPARγ and blockade of the active RAS/RAF/MEK/ERK signalling pathway, respectively. **2.** Agonist-activated PPARγ heterodimerises with RXRα and binds to PPRE in DNA, inducing transcription of various PPARγ target genes, including *GATA3*. **3.** GATA3 binds to one or multiple sites upstream of the *VGLL1* promoter, inducing transcription of the gene. **4.** TZ/PD differentiated cells express VGLL1 protein as quickly as 24h post-differentiation. Inhibition of PPARγ activity or siRNA knockdown of GATA3 were both found to inhibit VGLL1 expression, although the effect of either treatment became less pronounced when cells had reached confluency and/or had underwent differentiation for a longer period of time.

3.4.6 Determination of VGLL1 expression after treatment of NHU cells with inhibitors of the EGFR/MEK/ERK and PI3K/AKT pathways

3.4.6.1 Treatment of NHU cells with the standard TZ/PD protocol ± TZ

The results collated in Section 3.4.3-3.4.5 suggested that variables beyond agonist-based activation of upstream transcription factors could potentially influence the induction of VGLL1 in NHU cells. To understand the specific role that PPARγ-independent EGFR blockade had on VGLL1 expression, NHU cells were treated with TZ/PD or PD153035 alone for 72h. It was discovered that PD153035 treatment was sufficient to induce expression of both VGLL1 and ELF3 when compared to control (Fig. 3.19). However, treatment with both TZ and PD153035 appeared to be additive, as expression of both proteins was higher in TZ/PD treated cells when compared to PD153035 treated cells. Expression of PPARγ or FOXA1 was found to be only slightly induced by PD153035 treatment alone, with a full induction of expression only observed in TZ/PD treated cells when compared to control.

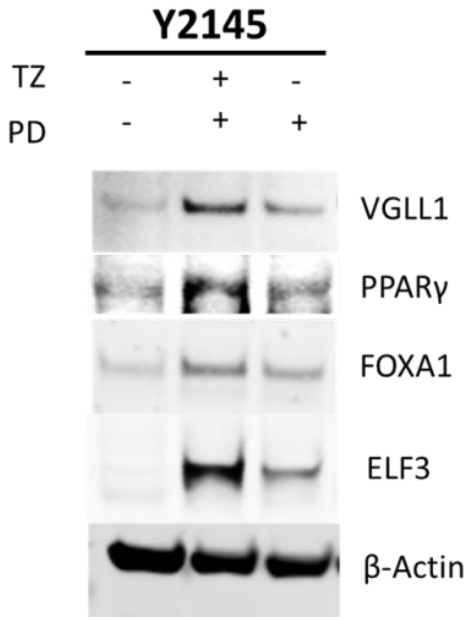

Figure 3.19: Expression of VGLL1 and ELF3 can be induced through EGFR blockade of NHU cells

Immunoblot analysis of Y2145 NHU cells (n=1) treated using the standard TZ/PD protocol as outlined in Section 2.4.4.9, in addition to a condition that consisted of cells receiving 1 μM PD153035 only for 72h to inspect the effects of EGFR blockade alone on expression of proteins of interest. All conditions were treated with 0.1% DMSO to control for non-specific solvent effects. Expression of β-Actin was used to confirm equal loading of samples.

3.4.6.2 Effect of TZ and PD153035 treatment in NHU cells grown to post-confluence

The specific role that inhibition of proliferation in contact-inhibited cells plays on VGLL1 expression was determined by lysing cells in both a sub-confluent state and after they had been allowed to propagate to a state of post-confluence (as defined as cells that had been visually confirmed to reach confluence 6 days prior); at which point they were treated with a combination of TZ, PD153035 and T007 for 72h (Fig. 3.20A). Expression of VGLL1 was found to be induced in DMSO-treated cells that reached a state of post-confluence when compared to DMSO-treated sub-confluent cells (Fig. 3.20B-D). However, significant differences in VGLL1 expression compared to sub-confluent control were only found when confluent cells were additionally treated with PD153035 alone or in combination with TZ or T007 (Fig. 3.20E; $p \leq 0.001$). Activating PPARγ with TZ was found to either have a negligible or reductive effect on VGLL1 expression in confluent NHU cells. In comparison, ELF3 and GATA3 (but not FOXA1) also appeared to be induced by confluency, with expression of the genes further activated when cells were treated with TZ and PD153035 separately (ELF3) or just PD153035 (GATA3; Fig. 3.20B-D). Conversely, expression of p63 (n=2 samples) was inhibited by TZ/PD differentiation in post-confluent NHU cells as observed previously, yet neither the onset of confluence nor the addition of TZ or PD in isolation was sufficient to affect expression of the transcription factor, suggesting an additive effect of TZ and PD is required to inhibit p63.

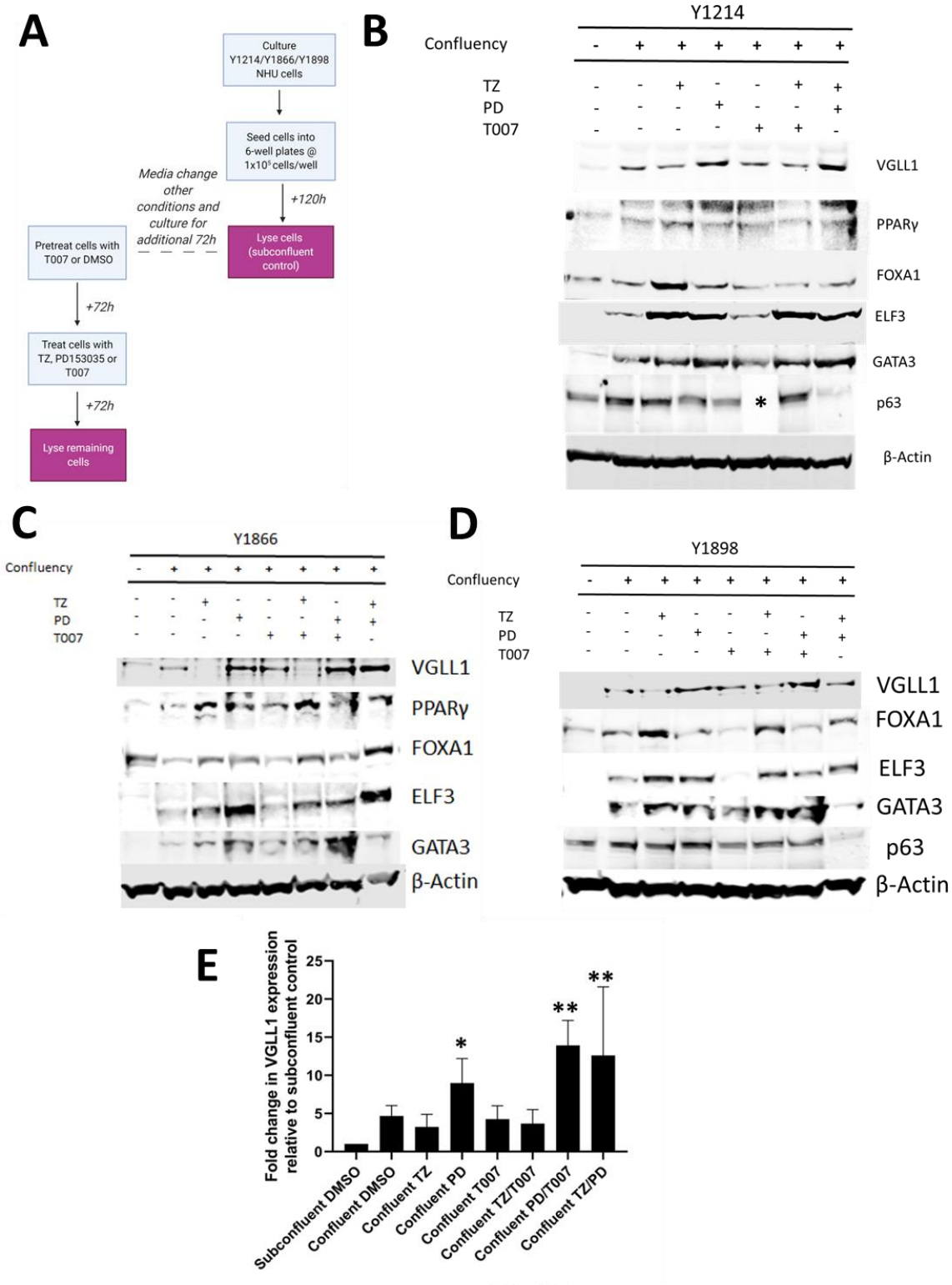
A
Culture Y1214/Y1866/Y1898 NHU cells
Seed cells into 6-well plates @ 1x10⁵ cells/well
+120h
Lyse cells (subconfluent control)
Media change other conditions and culture for additional 72h
Pretreat cells with T007 or DMSO
+72h
Treat cells with TZ, PD153035 or T007
+72h
Lyse remaining cells
B
Y1214
Confluency
TZ
PD
T007
VGLL1
PPARγ
FOXA1
ELF3
GATA3
p63
β-Actin
C
Y1866
Confluency
TZ
PD
T007
VGLL1
PPARγ
FOXA1
ELF3
GATA3
β-Actin
D
Y1898
Confluency
TZ
PD
T007
VGLL1
FOXA1
ELF3
GATA3
p63
β-Actin
E
Fold change in VGLL1 expression relative to subconfluent control
Subconfluent DMSO
Confluent DMSO
Confluent TZ
Confluent PD
Confluent T007
Confluent TZ/T007
Confluent PD/T007
Confluent TZ/PD

Figure 3.20: Onset of EGFR blockade-mediated cell quiescence induces VGLL1 expression

A) Experimental flowchart of NHU cells treated with a combination of reagents upon reaching a state of post-confluence (n=3 independent samples). Cells were lysed at sub-confluence in order to compare any changes in expression of proteins once cells became quiescent. Once cells had reached visual confluence, they were pre-treated with either 0.1% DMSO only or 5 µM T007 for 72h to ensure inhibition of nascent PPARγ activity. Confluent cells were subsequently treated with a combination of TZ, PD153035 or T007 for a further 72h before lysis. All conditions were treated with 0.1% DMSO to control for non-specific solvent effects. **B-D)** Immunoblot analysis of VGLL1, PPARγ, FOXA1, ELF3 GATA3 and p63 (in blots **B**, **D**) expression in the conditions outlined in (**A**) in Y1214 (**B**), Y1866 (**C**) and Y1898 (**D**) cells**.** Lanes marked with an asterisk represent protein samples that could not be assayed due to a lack of remaining lysate. Expression of β-Actin was used to confirm equal loading of samples. **E)** Densitometry analysis of VGLL1 expression in three independent NHU cell lines. Significance between groups was determined by a one-way ANOVA with Tukey's multiple comparisons post-hoc test. *= $p \leq 0.05$; **=$p \leq 0.01$. A full list of conditions with significant differences in VGLL1 expression can be found in Appendix xii.

3.4.6.3 Expression of VGLL1 and PPARγ target genes after treatment of NHU cells with inhibitors against EGFR, MEK1/2 and ERK1/2

To elucidate the identity of the kinases downstream of EGFR that were responsible for VGLL1 expression following blockade of function, NHU cells were treated with various drug inhibitors ± TZ for 72h, with fresh drugs administered daily (Fig. 3.21A). MEK inhibitors U0126 and PD98059 and ERK inhibitor FR180204 (FR180) were titrated on their ability to inhibit active ERK signalling prior to this experiment (Appendix viii). Cells used in this experiment were specifically treated at a low density and had not reached visual confluence at the point of lysis, thereby ensuring that the final cell phenotype was not affected by confluence-mediated effects. Upon completion of 72h treatment, noticeable differences in cell density were observed in cells treated with PD153035 or UO126 (but not PD98059 or FR180) when compared to DMSO control (Fig. 3.21B), suggesting that these reagents were having a greater effect on cell proliferation or survival. Cells treated with TZ alongside each of the inhibitors appeared to have less dense cultures after 72h treatment than when the cells were treated with the inhibitors in isolation.

A

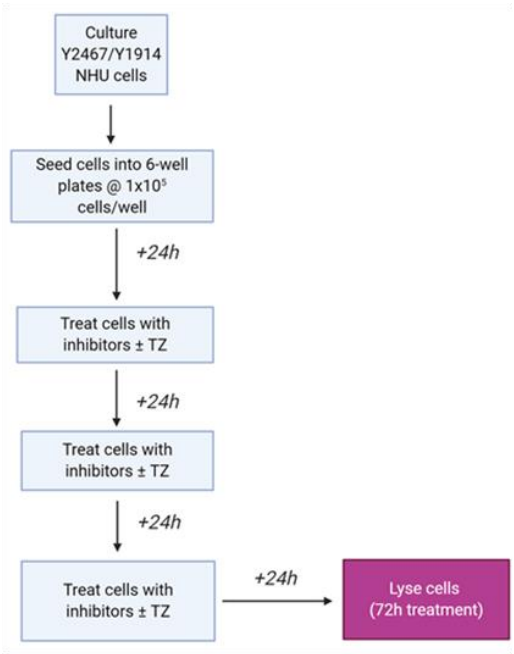
Culture Y2467/Y1914 NHU cells
Seed cells into 6-well plates @ 1x10⁵ cells/well
+24h
Treat cells with inhibitors ± TZ
+24h
Treat cells with inhibitors ± TZ
+24h
Treat cells with inhibitors ± TZ
+24h
Lyse cells (72h treatment)

B

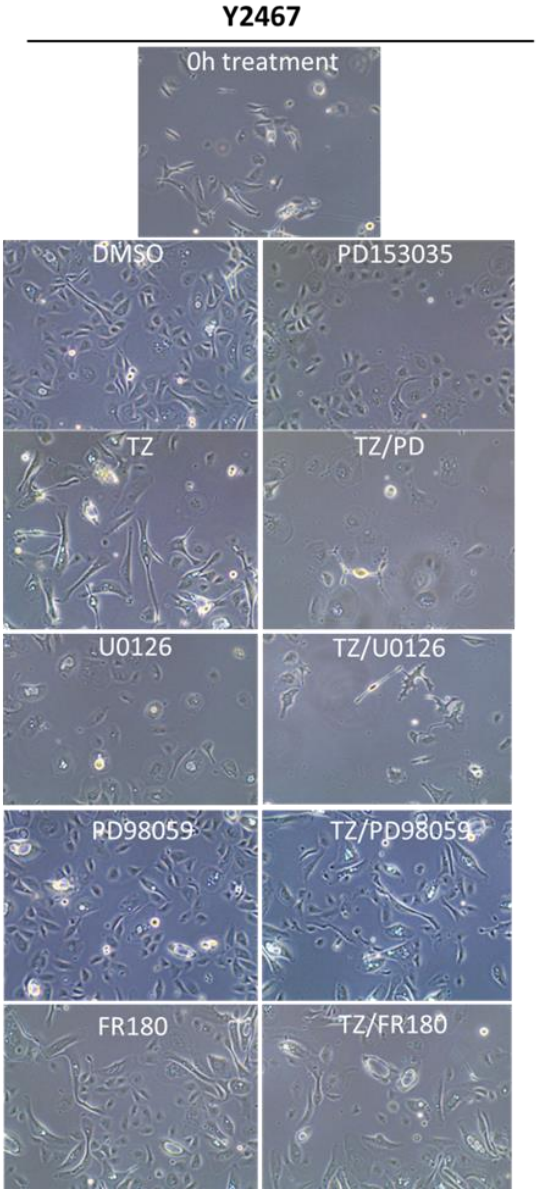
Y2467
0h treatment
DMSO
PD153035
TZ
TZ/PD
U0126
TZ/U0126
PD98059
TZ/PD98059
FR180
TZ/FR180

Figure 3.21: Sub-confluent NHU cell morphology following treatment with inhibitors of EGFR/RAS/RAF/MEK/ERK signalling ± TZ

A) Experimental flowchart of NHU cells undergoing treatment with PD153035, U0126, PD98059 or FR180 in the presence or absence of TZ for 72h (n=2 independent samples). Cells were seeded at a low density to ensure that they would not reach visual confluence before the end of the treatment program. Cells were treated with the different reagents 24h post-seeding, with fresh drug-containing medium replenished every 24h. All conditions were treated with 0.1% DMSO to control for non-specific solvent effects. Cultures were lysed after 72h of treatment. **B)** Phase micrograph images of Y2467 cells before treatment (top image) or after 72h treatment with reagents (all other images) captured immediately preceding lysis. The morphology and cell density of each condition appeared consistent between two independent NHU cell lines.

VGLL1 and ELF3 were induced by TZ/PD and PD alone; mirroring what was observed when cells were grown to post-confluence (Fig. 3.22A-B). FOXA1, but not VGLL1 and ELF3, was additionally induced through activation of PPARγ by TZ alone in Y2467 cells (Fig. 3.22A). VGLL1 was additionally expressed after treatment with U0126, PD98059 or FR180 when applied in isolation, suggesting that inhibition of the entire RAS/RAF/MEK/ERK pathway is required for the induction of VGLL1 in sub-confluent NHU cells (Fig. 3.22A-B). Interestingly, VGLL1 expression was lost in U0126, PD98059 and FR180-treated cells when the cells were treated concurrently with TZ, potentially indicative of a hitherto unknown tyrosine kinase-independent function of EGFR that permits VGLL1 induction when cells are TZ/PD treated. FOXA1 expression displayed a similar pattern of expression to VGLL1 after being treated with the various inhibitors, while ELF3 was expressed after treatment with U0126, but not PD98059 or FR180 (or TZ/UO126, similar to the phenotype observed with VGLL1). Overall, the following results indicate that induction of VGLL1 expression in NHU cells is linked to the inhibition of EGFR signalling via its RAS/RAF/MEK/ERK kinase axis.

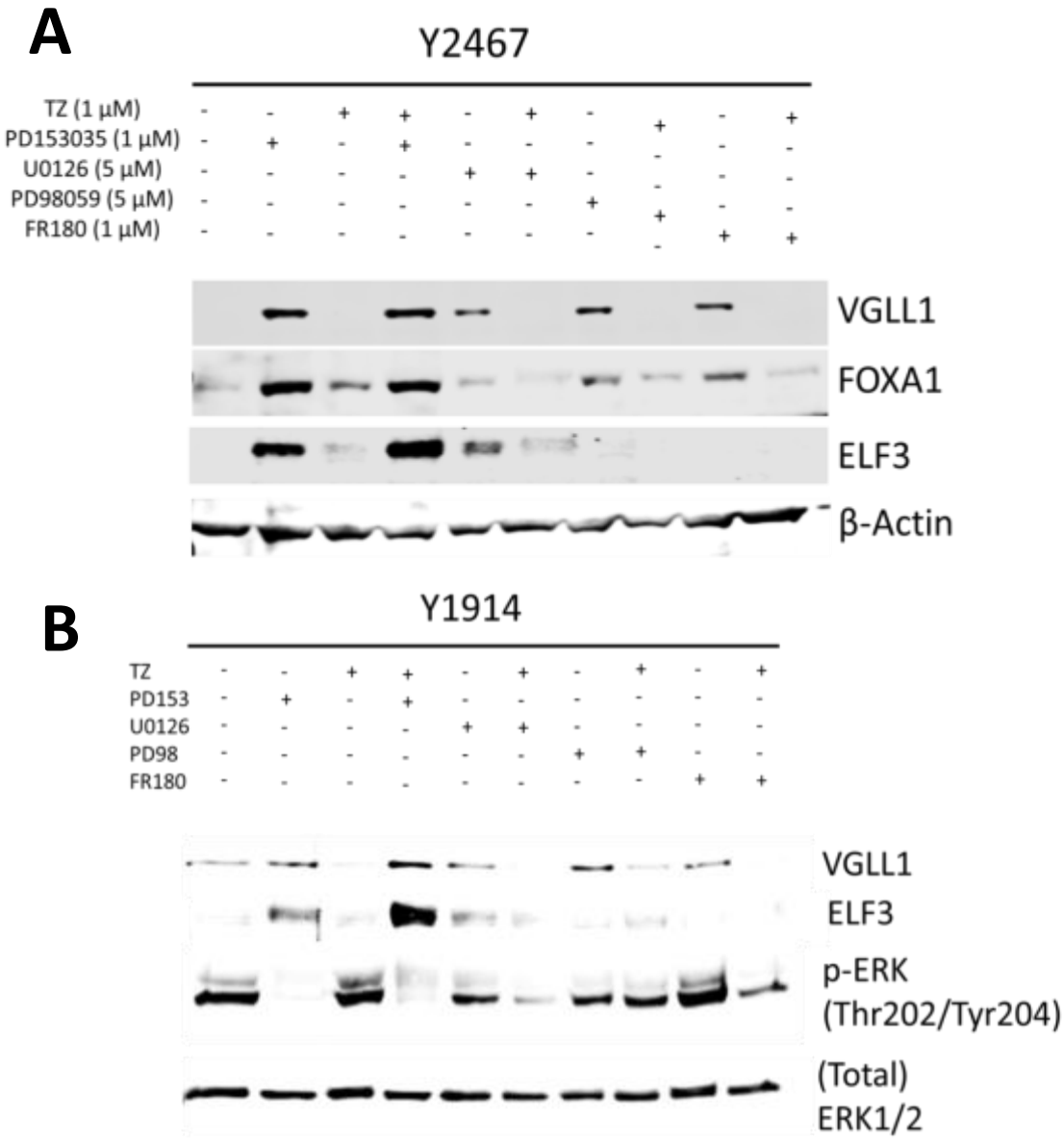

Figure 3.22: Active RAS/RAF/MEK/ERK signalling blocks VGLL1 expression in sub-confluent NHU cells

Immunoblot analysis of the conditions outlined in Figure 3.21 in Y2467 (**A**) and Y1914 (**B**) cells. Treatment of NHU cells with U0126, PD98059 and FR180 were all found to induce VGLL1 expression in addition to PD153035 in sub-confluent cultures. Expression of β-Actin (Y2467) or Total ERK1/2 (Y1914) was used to confirm equal loading of samples.

3.4.6.4 Expression of VGLL1 in high Ca^{2+} medium after treatment with EGFR and PI3K/AKT inhibitors

Following the observations that VGLL1 is expressed both as a result of blockade of EGFR/RAS/RAF/MEK/ERK signalling and in cells that are contact-inhibited, it was hypothesised that induction of the protein may require activation of PI3K/AKT signalling, a pathway previously demonstrated to be important in mediating the proliferation of undifferentiated NHU cells following blockade of downstream EGFR signalling.

Undifferentiated Y1336 cells (n=1) were grown on glass slides in medium containing 2 mM Ca^{2+} in order to induce nuclear p-AKT activity following formation of calcium-mediated cell-cell adherens junctions, with these slides compared to cultures either grown in low calcium or treated with LY294002 or PD153035 (Fig. 3.23A). NHU cells grown in high Ca^{2+} were discovered to exhibit a striking increase in both nuclear and cytoplasmic VGLL1 when compared to cells grown in low calcium (Fig. 3.23B). Y1336 cells grown in high Ca^{2+} were confirmed to have formed cell-cell adherens junctions through visualisation of E-cadherin in DMSO + Ca^{2+} and PD153035 + Ca^{2+} conditions (Fig. 3.23C). Interestingly, the intense intercellular border localisation of E-cadherin was lost in cells that were treated with LY294002 in high Ca^{2+} (Fig. 3.23C), a condition that was demonstrated to have weak nuclear phosphorylated AKT expression (Fig. 3.23D). Conditions that exhibited strong nuclear p-AKT expression (*i.e.* DMSO + Ca^{2+}, PD153035 and PD153035 + Ca^{2+}) were all found to have induced VGLL1 expression, while conditions with low/absent nuclear expression of p-AKT (DMSO, LY294002, LY294002 + Ca^{2+}) correlated with low expression of VGLL1 (Fig. 3.23B,D). The following observations therefore presented preliminary evidence for the potential role of active PI3K/AKT signalling in the induction of VGLL1 in undifferentiated NHU cells, a pathway that is activated through EGFR/RAS/RAF/MEK/ERK blockade and/or addition of a physiologically relevant concentration of Ca^{2+} to the medium (Fig. 3.23E).

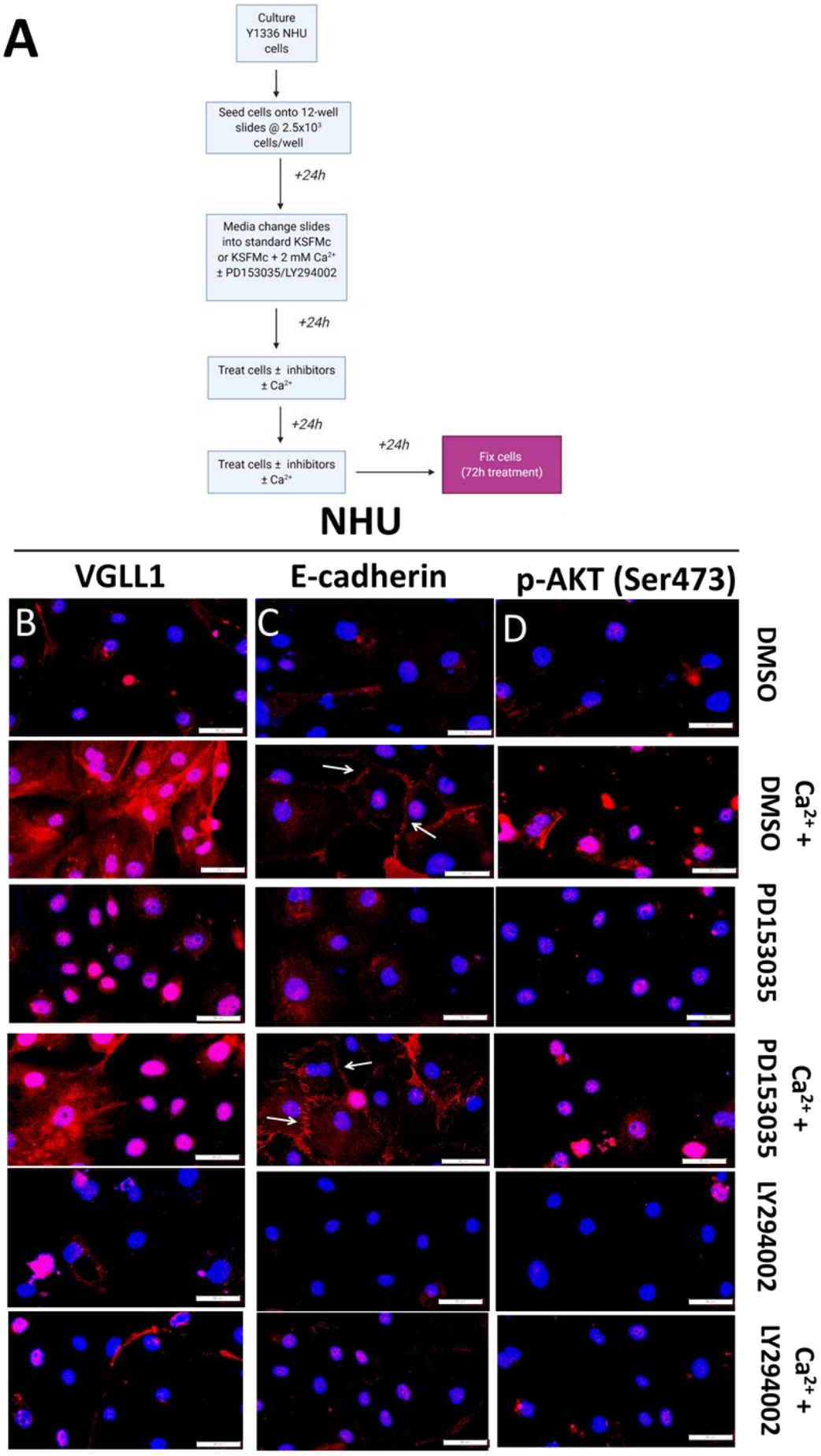
A
Culture Y1336 NHU cells
Seed cells onto 12-well slides @ 2.5x10³ cells/well
+24h
Media change slides into standard KSFMc or KSFMc + 2 mM Ca²⁺ ± PD153035/LY294002
+24h
Treat cells ± inhibitors ± Ca²⁺
+24h
Treat cells ± inhibitors ± Ca²⁺
+24h
Fix cells (72h treatment)
NHU
VGLL1
E-cadherin
p-AKT (Ser473)
B
C
D
DMSO
Ca²⁺ + DMSO
PD153035
Ca²⁺ + PD153035
LY294002
Ca²⁺ + LY294002

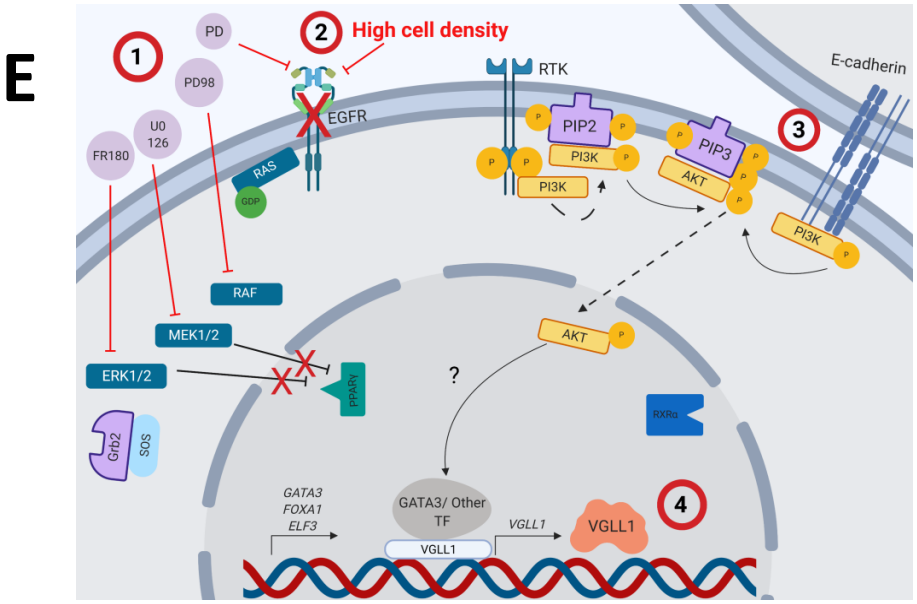

Figure 3.23: Induction of VGLL1 via Ca^{2+}-mediated PI3K/AKT signalling in undifferentiated NHU cells

A) Experimental flowchart of Y1336 cells undergoing treatment with DMSO only, PD153035 or LY294002 in the presence or absence of 2 mM Ca^{2+} for 72h (n=1 cell line). Cells were treated with the different inhibitors and Ca^{2+} 24h post-seeding; with fresh drug/Ca^{2+}-containing medium replenished every 24h. All conditions were treated with 0.1% DMSO to control for non-specific solvent effects. Cultures were fixed after 72h of treatment. **B-D)** Immunofluorescence analysis of VGLL1 (**B**), E-cadherin (**C**) and p-AKT (Ser473; **D**) expression in Y1336 cells treated in the manner described in (**A**). Addition of Ca^{2+} induced the localisation of E-cadherin to the intercellular borders of cells in DMSO or PD153035-treated cultures, as indicated by white arrows. Images were all taken at same exposure and are shown with overlaid Hoechst 33258 DNA staining. Scale bar= 50µm. Labelling of total and phosphorylated forms of ERK (in addition to cells receiving no primary antibody) was additionally performed, images of which can be found in Appendix xii. **E)** Interpretation of the molecular events upstream of VGLL1 in undifferentiated NHU cells, as determined in Fig. 3.18-3.22. Inhibition of the EGFR/RAS/RAF/MEK/ERK pathway in sub-confluent NHU cells (**1**; n=2), culturing of the cells to the point of post-confluence (**2**; n=3) and/or the production of Ca^{2+}-mediated adherens junctions in contacted cells (**3**; n=1) were all observed to induce expression of VGLL1 independent of PPARγ agonism in NHU cells (**4**). This mechanism appeared to be related to activation of PI3K/AKT signalling, as nuclear p-AKT was observed in NHU cells treated with PD153035 and/or Ca^{2+}, thereby suggesting the existence of a hitherto unknown RTK in urothelium that induces PI3K/AKT activity in the absence of EGFR signalling. It was not determined as part of this study whether nuclear AKT affected the expression of VGLL1 through induction of urothelial transcription factors, such as GATA3.

Non-urothelial cell systems have previously demonstrated a change in the localisation of YAP/TAZ in response to physiological cues (Section 3.1.2). To determine whether YAP translocates in response to signal transduction pathway blockade and/or Ca^{2+} administration, dual-labelling of total YAP and pan-TEAD was additionally performed in Y1336 cells. In control cells, it was determined that expression of total YAP was predominantly nuclear, although cytoplasmic expression was occasionally observed in cells that were in close contact with one another (Fig. 3.24). Intense nuclear labelling was still observed in cultures treated with high Ca^{2+}, PD153035 and/or LY294002, yet cells in these conditions were additionally observed to have increased cytoplasmic expression of the protein. In comparison, TEAD proteins labelled with the pan-TEAD antibody exhibited strong nuclear expression in cells in all conditions except when treated with LY294002, which induced increased cytoplasmic labelling (Fig. 3.24). The preceding results therefore suggested that while the total amount of YAP expression remains consistent in NHU cells following differentiation (Section 3.4.2.2), its subcellular localisation is sensitive to factors such as the modulation of proliferation-associated pathways and/or the induction of adherens junctions. However, an inverse correlation between the ratio of nuclear YAP and the induction of VGLL1 was not observed.

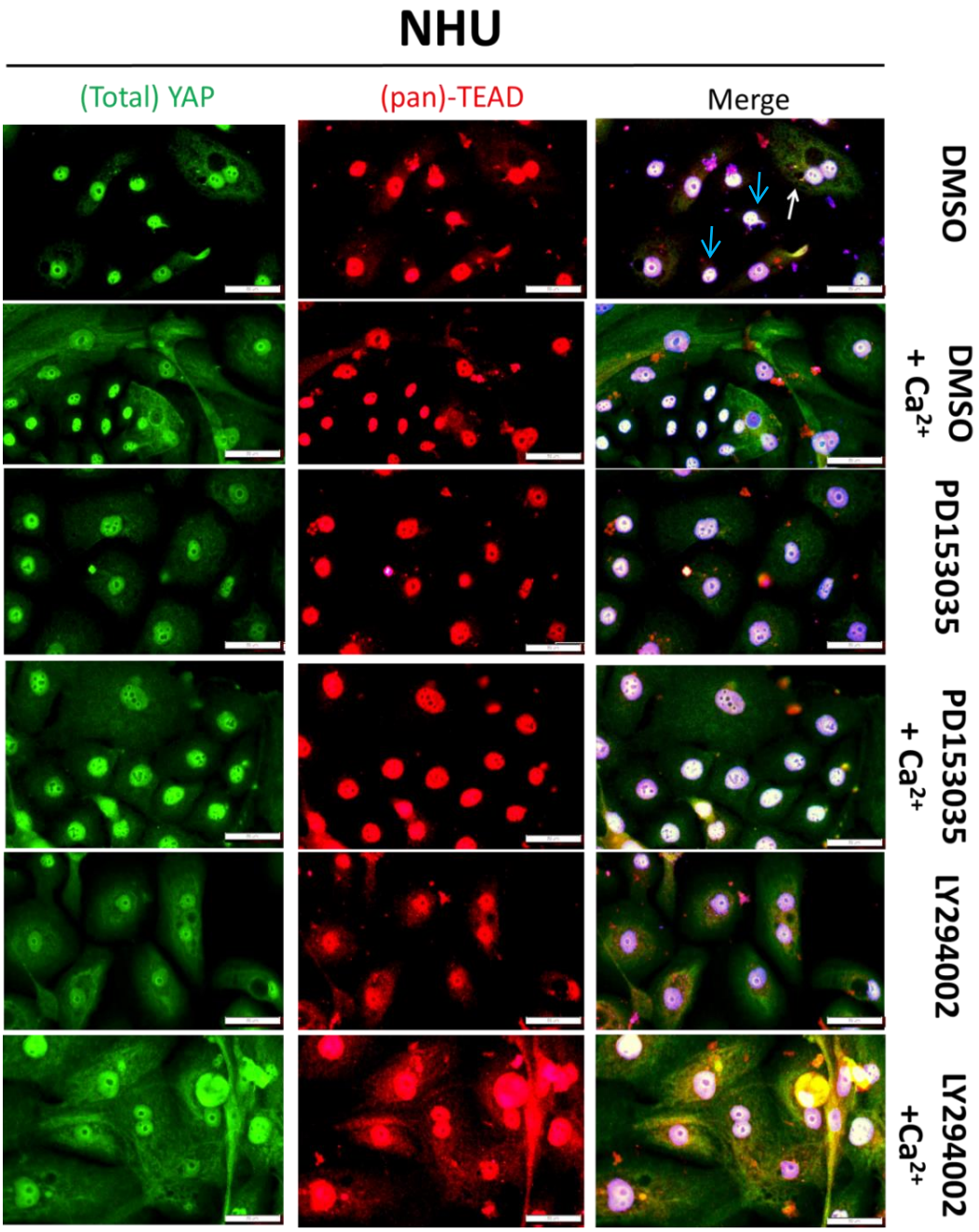

Figure 3.24: Stimuli-dependent translocation of YAP expression in undifferentiated NHU cells

A) Immunofluorescence analysis of total YAP (green fluorescence) and pan-TEAD (red fluorescence) expression in the same cell line and conditions outlined in Figure 3.23. Blue arrows indicate examples of control cells with exclusively nuclear YAP expression, while the white arrow indicates weak cytoplasmic YAP/TAZ expression in cells that were in close contact with one another. Images were all taken at same exposure and are shown with or without overlaid Hoechst 33258 DNA staining. Scale bar= 50µm.

3.4.7 Generation of genetically modified NHU cell lines that overexpress or knockdown VGLL1 expression

3.4.7.1 Generation and verification of stable transfected VGLL1-overexpressing NHU cell lines

To attempt to elucidate the function of VGLL1 in NHU cells, a retroviral vector that overexpresses VGLL1 in human cells was generated as detailed in Appendix ix. Following transduction of PT67 retroviral packaging cell lines with pLXSN-eGFP or pLXSN-VGLL1 and antibiotic selection with 500 µg/mL G418, NHU cell lines were transfected with retroviral particles and maintained in 100 µg/mL G418 until complete cell death in the mock-transfected NHU cultures was observed. Functional overexpression of VGLL1 was confirmed in transfected undifferentiated NHU cells by immunoblotting (Fig. 3.25). Immunoblotting of lysates in Figure 3.25 was performed by Dr. Joanna Pearson of the Jack Birch Unit.

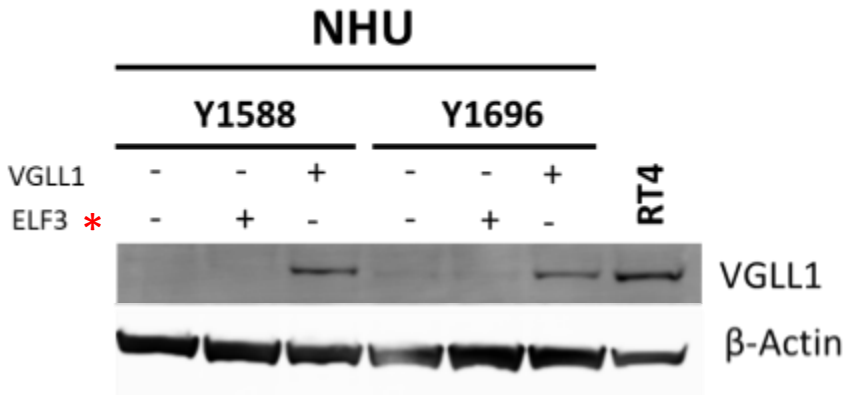

Figure 3.25: Forced expression of VGLL1 protein in undifferentiated NHU cells

NHU cell lines Y1588 and Y1696 were transfected with pLXSN-GFP or pLXSN-VGLL1 and positive cells selected for through maintenance in antibiotic-containing medium. Following selection, transfected NHU cells were lysed and immunoblotting analysis of VGLL1 expression was used to confirm overexpression of said proteins in both cell lines. Bladder cancer cell line RT4 was used as a positive control for VGLL1 expression. Expression of β-Actin was used to confirm equal loading of samples. Samples transfected with a pLXSN-ELF3 overexpression construct (red asterisk) were additionally included in this immunoblot but are not relevant to this study.

3.4.7.2 Generation and verification of stable transfected VGLL1 shRNA knockdown NHU cell lines

VGLL1 shRNA knockdown constructs were generated as detailed in Appendix x. PT67 cells were transduced with pSIREN-Scrambled or pSIREN containing one of three shRNA constructs specific to VGLL1. Following antibiotic selection with 4 μg/mL puromycin, NHU cell lines were transfected with the retroviral particles and maintained in 1 μg/mL puromycin until complete cell death in the mock-transfected NHU cultures was observed (Fig. 3.26A). Successful knockdown of VGLL1 by all three shRNA constructs was confirmed in TZ/PD differentiated transfected NHU cells by immunoblotting (Fig. 3.26B). VGLL1 shRNA #2 was determined to most effectively knockdown VGLL1 expression and was thus selected to be the construct used in subsequent experiments that required VGLL1 knockdown.

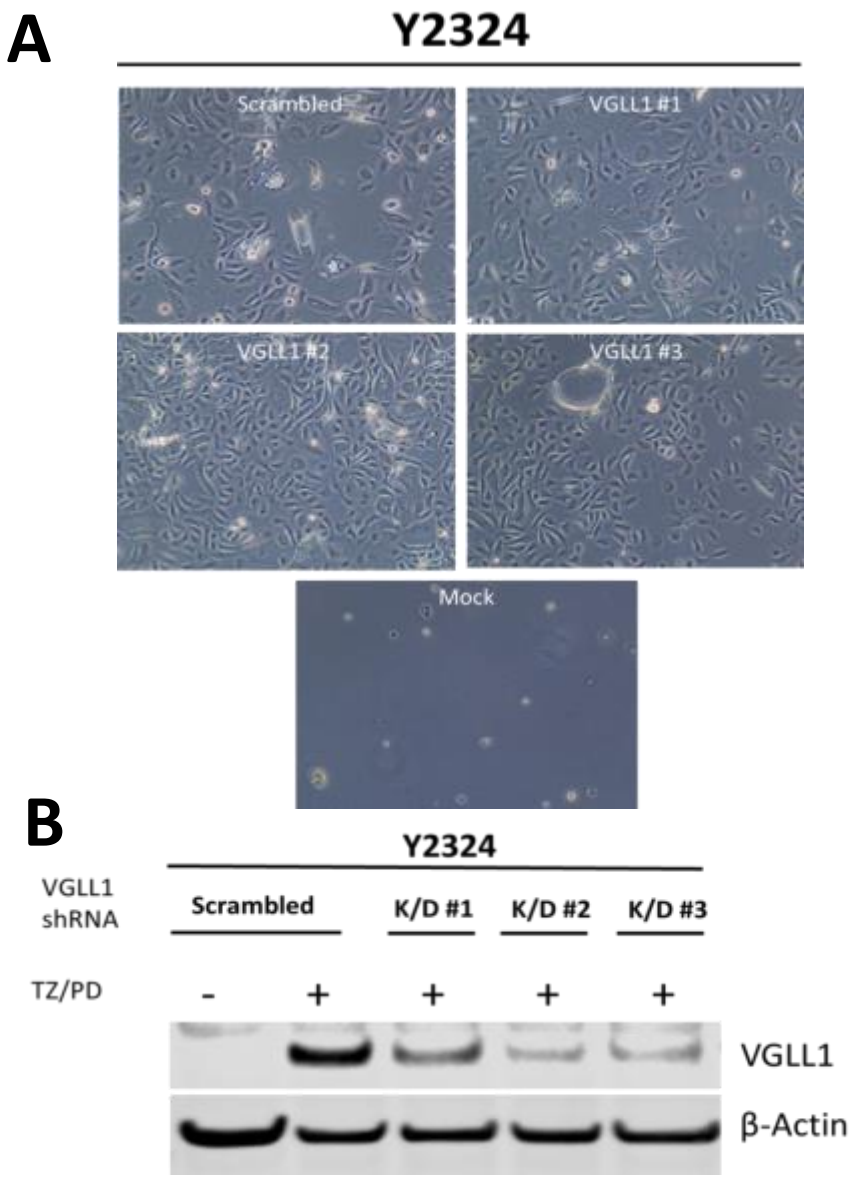

Figure 3.26: Knockdown of VGLL1 expression in differentiated NHU cells transfected with three VGLL1 shRNA constructs

Y2324 cells were transfected with pSIREN-Scrambled, pSIREN-VGLL1 #1, pSIREN-VGLL1 #2 or pSIREN-VGLL1 #3 and positive cells selected for through maintenance in antibiotic-containing medium. Panel (**A**) depicts phase micrograph images of Y2324 cells taken 10 days after transduction (8 days of antibiotic selection). The mock-transduced control demonstrated the efficacy of puromycin administration on untransduced cells. Following selection, transfected cells were grown to 80% confluence and treated using the standard TZ/PD differentiation method for 72h (**B**)**.** Scrambled control cells alternatively received treatment with vehicle control as a negative control for VGLL1 expression. β-Actin was used to confirm equal loading of samples.

3.4.8 Effect of forced expression of VGLL1 on signal transduction pathways and proliferation in NHU cells

3.4.8.1 Evaluation of NHU cell proliferation after VGLL1 overexpression

Following the creation of stable NHU cell lines that overexpressed VGLL1, it was observed that cells overexpressing VGLL1 appeared to be at a consistently lower cell density than the eGFP control transfected cell type (Fig. 3.27A). To address the hypothesis that forced expression of VGLL1 was resulting in a reduction of proliferation, transfected NHU cells were seeded at equal densities and the total cell numbers for each condition were counted 48h post-seeding. Despite each cell line having lower cell counts when overexpressing VGLL1, there was no significant difference between groups at this time point (Fig. 3.27B).

Transfected cell lines were subsequently assayed with alamarBlue to track the proliferation rate of the cells over a period of 9-13 days. This method determined that cell lines overexpressing VGLL1 consistently had a slower proliferation rate when compared to eGFP control (Fig. 3.27C-E), with significant differences in the amount of time required to reach a 30% and 60% reduction of alamarBlue reagent (Fig. 3.27F; $p \leq 0.001$). The observable difference in growth rate appeared to manifest 3-4 days after seeding; a period where the control cells consistently entered an exponential growth phase.

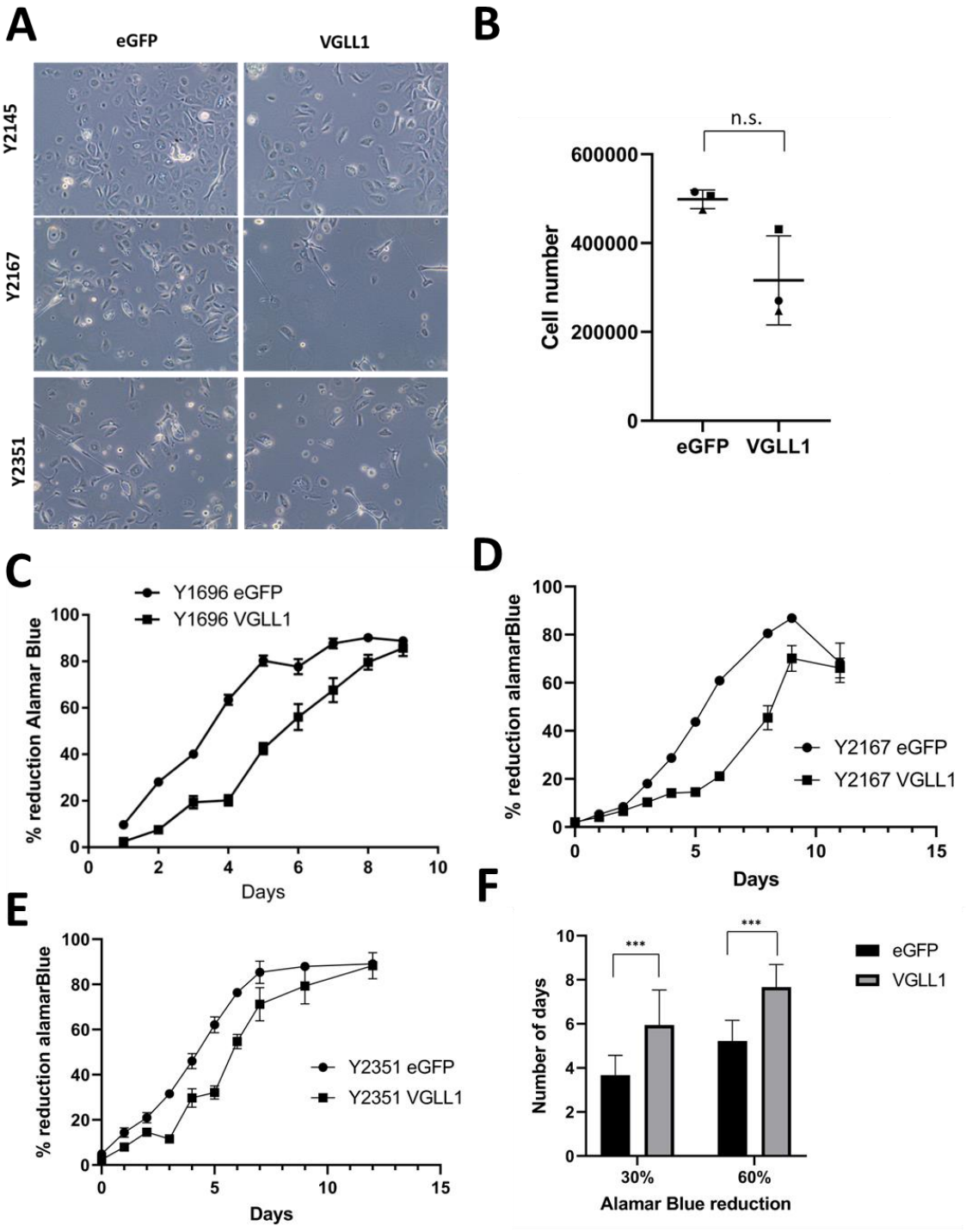
A
eGFP
VGLL1
Y2145
Y2167
Y2351
B
n.s.
Cell number
600000
400000
200000
0
eGFP
VGLL1
C
Y1696 eGFP
Y1696 VGLL1
% reduction Alamar Blue
Days
D
% reduction alamarBlue
Y2167 eGFP
Y2167 VGLL1
Days
E
% reduction alamarBlue
Y2351 eGFP
Y2351 VGLL1
Days
F
Number of days
***
***
eGFP
VGLL1
30%
60%
Alamar Blue reduction

Figure 3.27: Overexpression of VGLL1 retards growth of proliferating NHU cells

A-B) Three independent NHU cell lines overexpressing VGLL1 or eGFP control were seeded at the same density ($5x10^5$ cells/flask) and cultured for 48h to compare the rate of propagation. Figure (**A**) displays phase micrograph images of each cell lines prior to trypsinisation and counting. Image (**B**) depicts the total number of cells counted for each condition. The icons of the same shape represent values from donor-matched NHU samples. **C-E)** The growth rate of Y1696 (**C**), Y2167 (**D**) and Y2351 (**E**) cells transfected with eGFP or VGLL1 overexpressing vectors over 9-13 days, as analysed by alamarBlue assays. Image (**F**) depicts the significant differences in time eGFP and VGLL1 overexpressing cells took to reach 30% and 60% reduction in alamarBlue reagent, a proxy for total cell density. Each data point in figures (**C-E**) represents the mean of six technical replicates $\pm$ SD. The data points in figure (**F**) represent the mean number of days from 18 technical replicates of three independent biological samples (n=6 per cell line). Significance between groups was calculated using a paired two-way T-Test (**B**) or multiple unpaired two-way T-tests with Holm-Sidak's multiple comparisons post-hoc test (**F**). ***=p≤0.001.

3.4.8.2 Effect of VGLL1 overexpression on EGFR expression and ERK1/2 activation

After confirming that high expression of VGLL1 was having a negative effect on the growth rate of NHU cells, the gene expression of *EGFR* and *MKI67* (Ki67) was analysed in sub-confluent VGLL1 overexpressing Y1696 cells to determine whether the EGFR growth signalling pathway (and subsequently activation of the cell cycle) was modulated by VGLL1. Non-quantitative RT-PCR analysis of transfected Y1696 cells (n=1) found that expression of both genes was decreased in VGLL1 overexpressing cells compared to control (Fig. 3.28A).

However, subsequent immunoblotting analysis of two transfected NHU cell lines revealed no difference in phosphorylated ERK1/2 expression between eGFP and VGLL1 overexpressing conditions (Fig. 3.28B-C), suggestive of alternative signalling pathways that were being modulated in VGLL1 overexpressing cells.

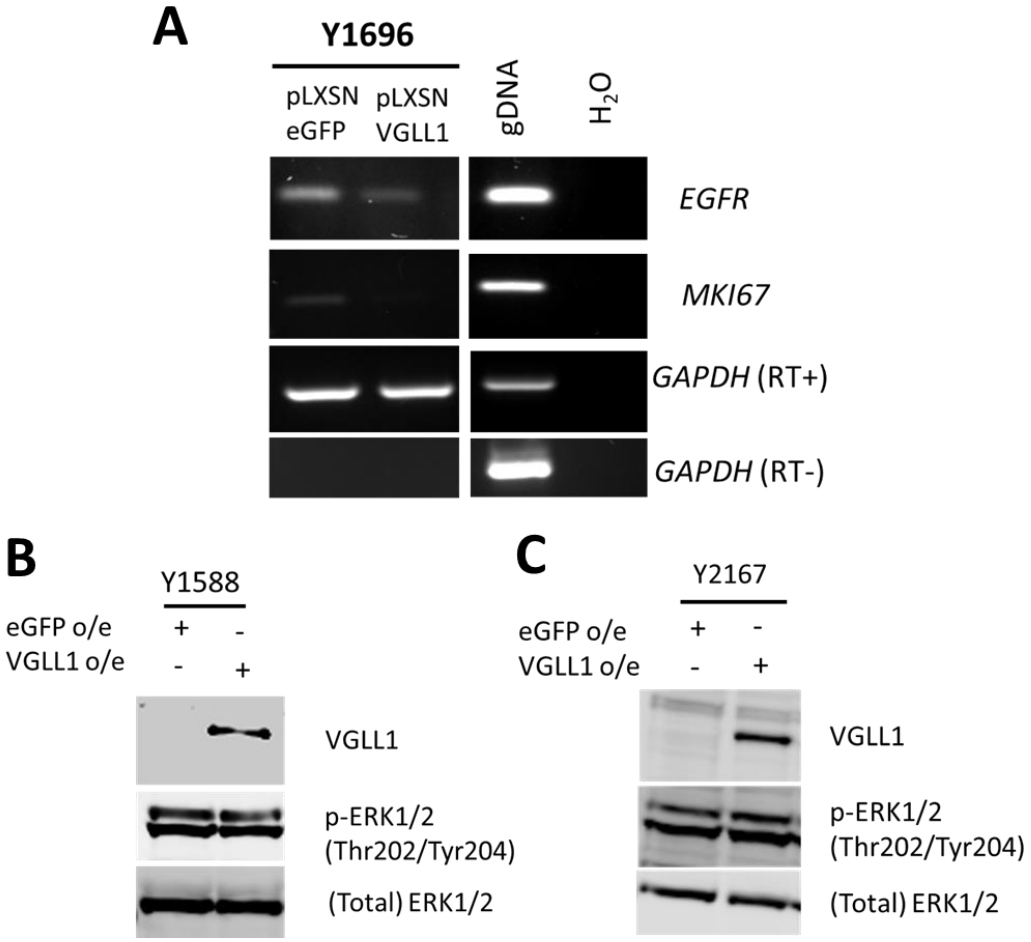

Figure 3.28: Overexpression of VGLL1 inhibits *EGFR* and *MKI67* transcript but has no effect on activation of ERK

A) RT-PCR analysis of *EGFR* and *MKI67* transcript expression in Y1696 cells (n=1) transfected with VGLL1 or eGFP control overexpression constructs. Cells were lysed at sub-confluence in order to ascertain the specific role of VGLL1 in modulating expression of the above genes. Each cDNA synthesis used 1 µg starting template RNA, with cDNA undergoing PCR amplification up to 27 cycles. Housekeeping gene *GAPDH* was used to confirm equal loading between samples (25 cycles). The primers used produced positive gDNA bands of the same size, while a no template (H_2O only) sample was used as a negative control for each primer set. **B-C)** Immunoblotting analysis of VGLL1, p-ERK1/2 and Total ERK1/2 in Y1588 (**B**) and Y2167 (**C**) cells overexpressing VGLL1 or eGFP control (n=2 independent cell lines). Expression of Total ERK1/2 was used to confirm equal loading of samples.

3.4.8.3 Modulation of PI3K/AKT, YAP and cell cycle activity in VGLL1 overexpressing NHU cells

Forced overexpression of VGLL1 in Y1696 cells was performed to uncover whether VGLL1 could affect the activation state of YAP (and thus potential YAP-mediated proliferation) in NHU cells. Due to a prior observation that suggested a modulation of YAP localisation through cell-cell contact (Section 3.4.6), cultures were lysed in both a sub-confluent state and once the cells had reached a post-confluent state to see whether this conferred additional changes in phosphorylated YAP expression. Despite overexpression of VGLL1 (and an induction of VGLL1 expression in eGFP control cells at the point of post-confluence), no change in the expression of p-YAP or total YAP/TAZ was observed (Fig. 3.29A), indicating that VGLL1 was not having an effect on the proportion of inactive YAP.

Examination of phosphorylated AKT in the same cell line revealed a notable inhibition of expression in sub-confluent cells, alongside a concurrent inhibition of cell cycle-associated MCM2 expression in both sub-confluent and post-confluent cells (Fig. 3.29A). This result thereby implicated PI3K/AKT signalling as a possible pathway that is modulated downstream of VGLL1 overexpression, thus potentially accounting for the reduced cell cycle activity (and proliferation rate) observed in these cells (Fig. 3.29B).

A

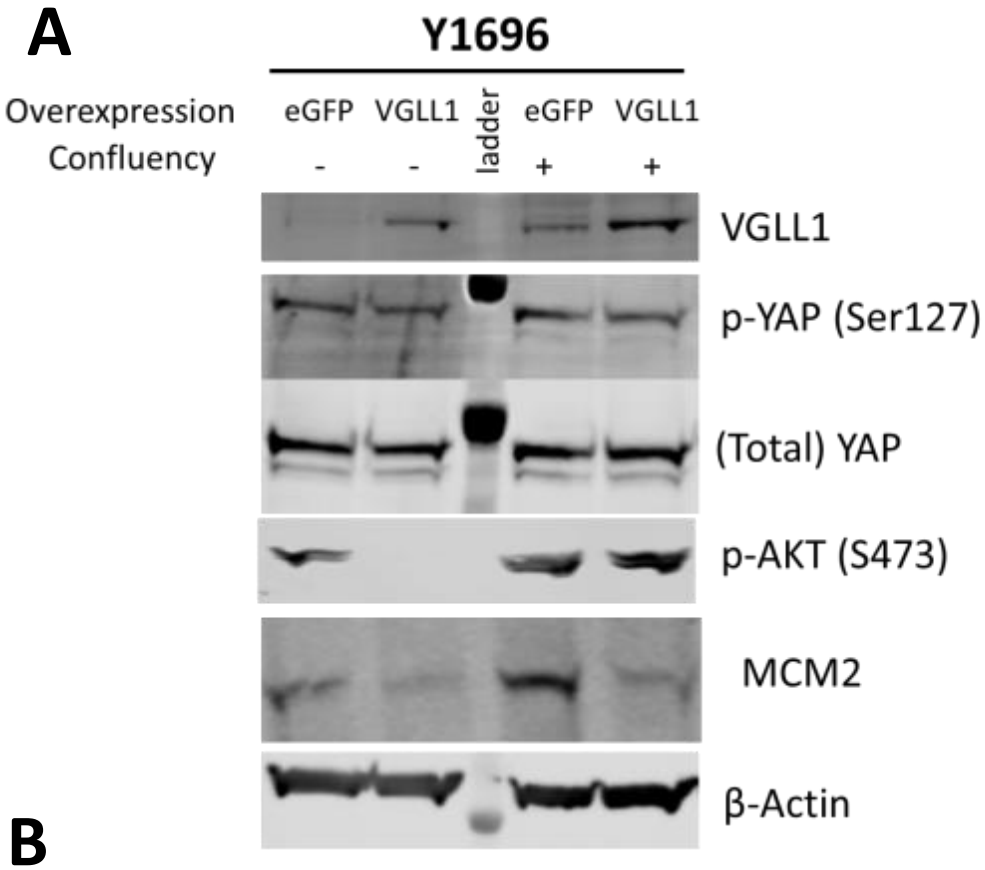
Y1696
Overexpression
Confluency
eGFP
VGLL1
ladder
eGFP
VGLL1
-
-
+
+
VGLL1
p-YAP (Ser127)
(Total) YAP
p-AKT (S473)
MCM2
β-Actin

B

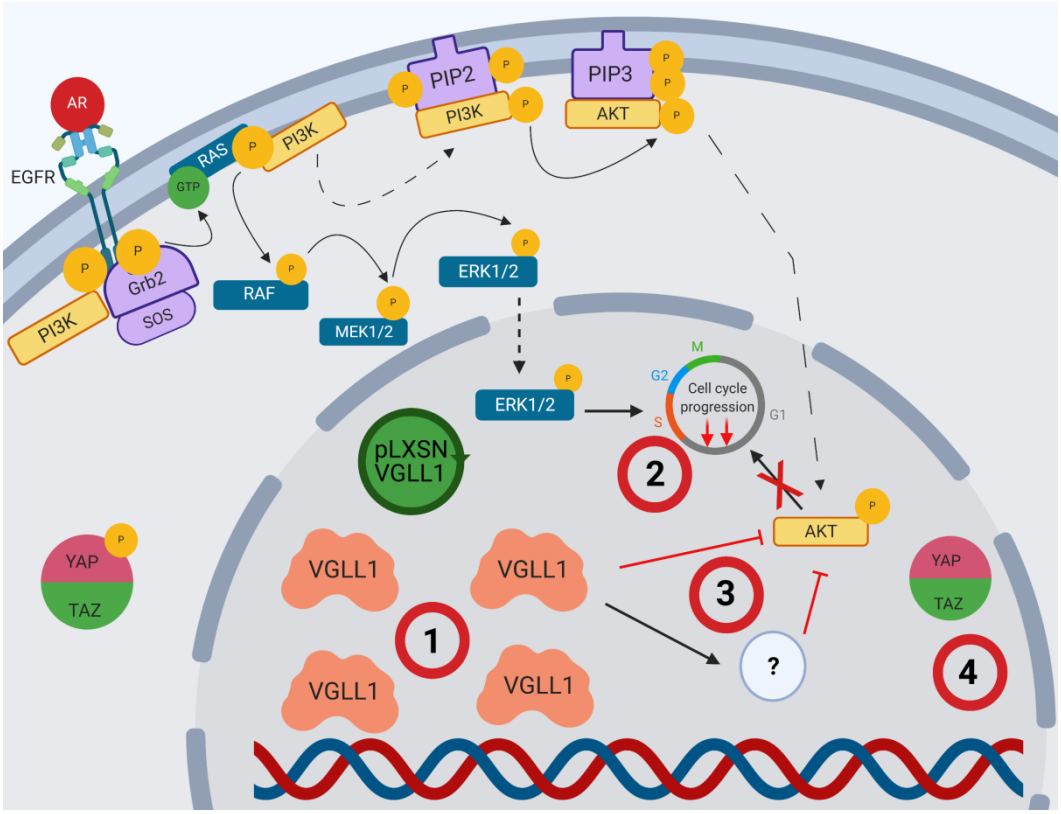
AR
EGFR
RAS
GTP
PI3K
PIP2
PIP3
AKT
Grb2
SOS
RAF
MEK1/2
ERK1/2
ERK1/2
Cell cycle progression
M
G2
S
G1
pLXSN VGLL1
2
AKT
YAP
TAZ
VGLL1
VGLL1
1
VGLL1
VGLL1
3
?
YAP
TAZ
4

Figure 3.29: Overexpression of VGLL1 inhibits p-AKT and MCM2 expression but has no effect on p-YAP expression in sub-confluent or confluent NHU cultures

A) Immunoblot analysis of VGLL1, total and phosphorylated YAP (S127), phosphorylated AKT (S473) and MCM2 expression in Y1696 (n=1) cells following transfection with either control eGFP or VGLL1 overexpressing constructs. Cells were lysed in a sub-confluent state or in a state of post-confluence in order to observe the additional effects of confluency on the expression of the above proteins. Expression of β-Actin was used as a loading control. **B)** Interpretation of the molecular events downstream of VGLL1 overexpression, as determined in Fig. 3.27-3.29. Transfection of undifferentiated NHU cells with pLXSN-VGLL1 resulted in high ectopic expression of VGLL1 protein (**1**). Cells overexpressing VGLL1 exhibited a consistently reduced proliferation rate (**2**; n=3). This altered phenotype did not occur through modulation of active ERK1/2 (n=2), but possibly as a result of inhibiting phosphorylated AKT (**3**; n=1). Whether VGLL1 expression negatively affects proliferation through directly modulating AKT activity, or indirectly through activation of an intermediary factor, such as TEAD, was not determined as part of the overexpression study. VGLL1 overexpression was not found to have an effect on the amount of active or inactive (phosphorylated) YAP expression in undifferentiated cells (**4**; n=1).

3.4.9 Modulation of differentiation and proliferation-associated protein expression by VGLL1

To determine what effect that VGLL1 had on expression of proteins involved in the maintenance of a differentiated urothelial phenotype, NHU cell lines transfected with all three VGLL1 shRNA constructs (Y2324) or with the most inhibitory VGLL1 shRNA #2 (n=3 independent cell lines) were immunoblotted to analyse expression of numerous proteins. It was determined that upon inhibition of VGLL1, expression of PPARγ, FABP4 and transitional cell marker CK13 were reduced compared to control in all three knockdown cell lines (Fig. 3.30A). Expression of tight junction protein claudin 4 was also found to be heavily inhibited in all knockdown cell lines, suggesting that inhibition of VGLL1 could additionally result in a loss of barrier integrity in differentiated cells. As observed in previous experiments using the VGLL1 shRNA constructs, VGLL1 shRNA #1 delivered the weakest relative knockdown of VGLL1, reflected in the expression of GATA3 and ELF3 which exhibited a greater inhibition in cells transfected with VGLL1 shRNA #2. Densitometry analysis of the expression of urothelial transcription factors in three independent cell lines transfected with scrambled shRNA or VGLL1 shRNA #2 determined that knockdown of VGLL1 conferred a significant loss of GATA3, PPARγ and ELF3 expression compared to scrambled TZ/PD differentiated control (Fig. 3.30B; $p \leq 0.01$). A slight decrease in FOXA1 expression was observed by immunoblotting, but no significant change was observed after analysis.

In comparison, analysis of p63 and phosphorylated AKT expression (two proteins observed to be inhibited by TZ/PD differentiation) discovered that both proteins exhibited an increase in expression in VGLL1 shRNA #2 transfected cells. The results gained using knockdown constructs therefore demonstrated that the presence of VGLL1 appeared to play a role in regulating the expression of proteins involved in the urothelial differentiation phenotype, with a loss of the protein associated with an increase in proliferation-associated protein expression.

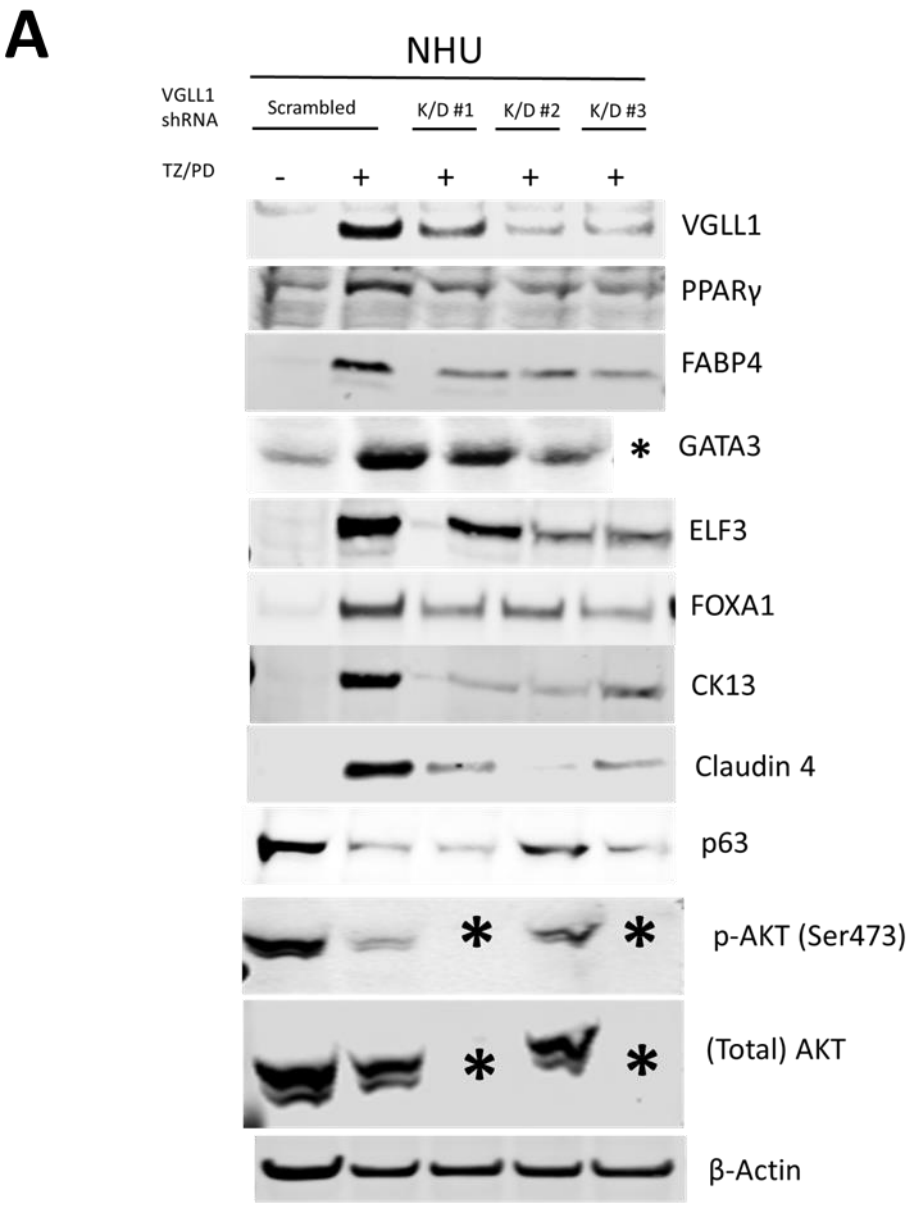
A
NHU
VGLL1 shRNA
Scrambled
K/D #1
K/D #2
K/D #3
TZ/PD
- + + + +
VGLL1
PPARγ
FABP4
GATA3
ELF3
FOXA1
CK13
Claudin 4
p63
p-AKT (Ser473)
(Total) AKT
β-Actin

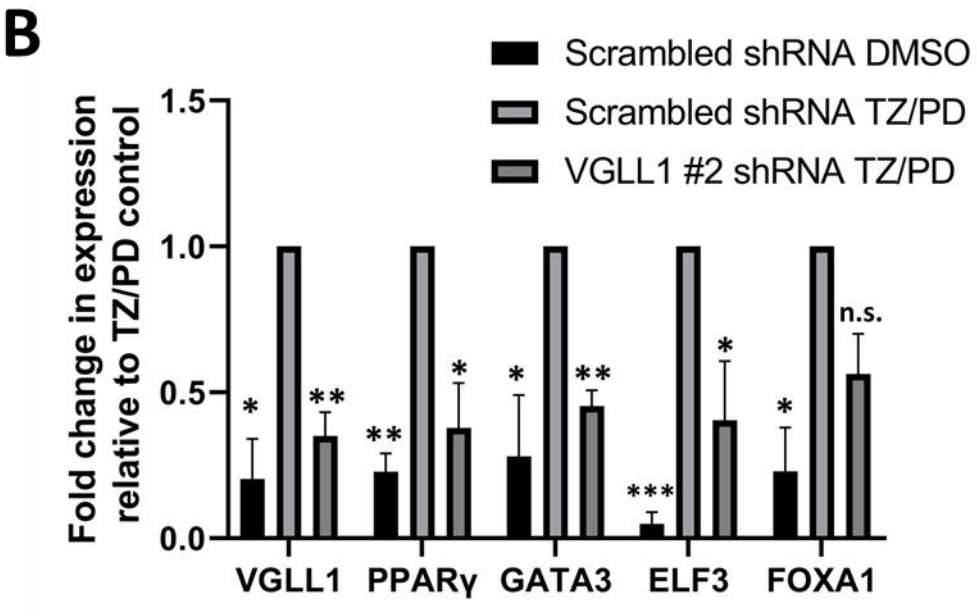
B
Scrambled shRNA DMSO
Scrambled shRNA TZ/PD
VGLL1 #2 shRNA TZ/PD
Fold change in expression relative to TZ/PD control
1.5
1.0
0.5
0.0
n.s.
VGLL1
PPARγ
GATA3
ELF3
FOXA1

Figure 3.30: Knockdown of VGLL1 results in reduced expression of differentiation-associated proteins

A) Immunoblotting analysis of VGLL1, PPARγ, FABP4, GATA3, ELF3, FOXA1, CK13, claudin 4, p63 and total and phosphorylated AKT expression in Y2324 cells transfected with either scrambled shRNA or three shRNA constructs specific to VGLL1 after 72h TZ/PD treatment. All conditions were treated with 0.1% DMSO to control for non-specific solvent effects. The expression pattern of VGLL1, PPARγ, GATA3, ELF3 and FOXA1 in the scrambled or VGLL1 k/d #2 conditions was representative of three independent cell lines (n=1 for FABP4, CK13, Claudin 4, p63, phosphorylated and total AKT). The asterisk represents protein samples that could not be assayed due to a lack of remaining lysate. Expression of β-Actin was used to confirm equal loading of samples. **B)** Quantification of VGLL1, GATA3, PPARγ, FOXA1 and ELF3 expression by immunoblotting densitometry analysis in three biological replicates of scrambled shRNA transfected NHU cells (treated with TZ/PD or vehicle control) and TZ/PD treated VGLL1 shRNA #2 transfected cells. Differences in expression are represented as a fold change in expression in comparison to the mean scrambled TZ/PD expression value. Significance between groups was determined using a two-way ANOVA with Tukey's multiple comparisons post-hoc test. *=p≤0.05; **=p≤0.01. Immunoblot images from the biological replicates can be found in Appendix xii.

3.4.10 Role of VGLL1 in the differentiated NHU wound healing phenotype

3.4.10.1 Analysis of barrier integrity in VGLL1 knockdown differentiated NHU cells

After observing a reduction in expression of proteins known to be important for maintaining barrier function in VGLL1 knockdown differentiated NHU cells, measurement of the strength of the urothelial barrier was performed through electrophysiological analysis of NHU cells transfected with VGLL1 shRNA #2 or scrambled control (Fig. 3.31A). Immunoblotting analysis of lysates from each condition confirmed a reduction of VGLL1 expression in the VGLL1 knockdown ABS/Ca^{2+} differentiated cells (Fig. 3.31B).

Measurement of barrier tightness using the cellZscope found that the strength of the barrier in both cell types increased at an almost identical rate in the 24h following the onset of ABS/Ca^{2+} differentiation (Fig. 3.31C). However upon achieving a stable barrier, it was observed that VGLL1 knockdown cells displayed a consistently weaker barrier in comparison to scrambled cells, even following spikes in tightness due to medium changes ($p \leq 0.001$). Measurement of barrier integrity following scratch wounding of cultures revealed that VGLL1 knockdown cells additionally appeared to recover at a slower rate than scrambled cells and failed to return to the mean barrier tightness of pre-wounded cells after a 24h recovery period (Fig. 3.31D). Analysis of the time taken for each culture to recover to 75% of its pre-wounded barrier tightness confirmed that VGLL1 knockdown cells were significantly slower to recover (Fig. 3.31E; $p \leq 0.05$).

A

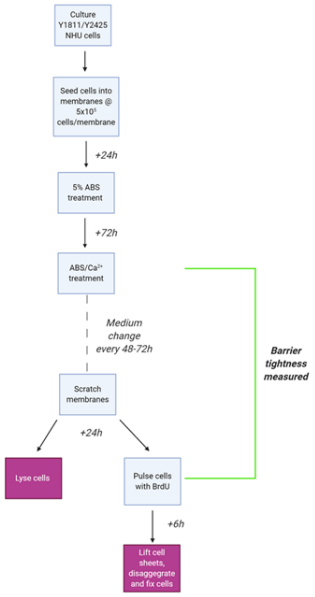
Culture Y1811/Y2425 NHU cells
Seed cells into membranes @ 5x10⁵ cells/membrane
+24h
5% ABS treatment
+72h
ABS/Ca²⁺ treatment
Medium change every 48-72h
Scratch membranes
+24h
Lyse cells
Pulse cells with BrdU
+6h
Lift cell sheets, disaggregate and fix cells
Barrier tightness measured

B

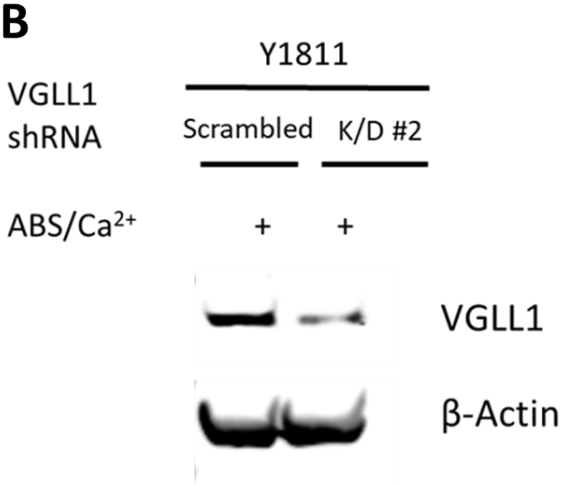
Y1811
VGLL1 shRNA
Scrambled
K/D #2
ABS/Ca2+
+
+
VGLL1
β-Actin

C

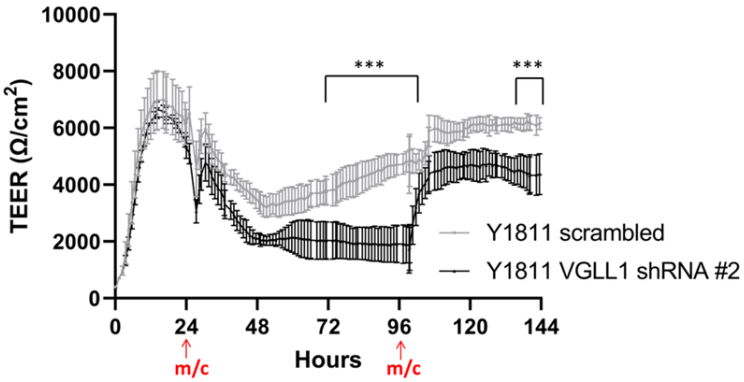
TEER (Ω/cm²)
10000
8000
6000
4000
2000
0
***
***
Y1811 scrambled
Y1811 VGLL1 shRNA #2
0
24
48
72
96
120
144
Hours
m/c
m/c

D

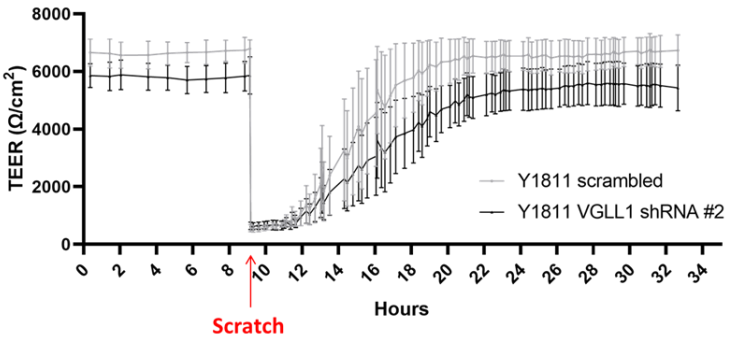
TEER (Ω/cm²)
8000
6000
4000
2000
0
Y1811 scrambled
Y1811 VGLL1 shRNA #2
0
2
4
6
8
10
12
14
16
18
20
22
24
26
28
30
32
34
Hours
Scratch

E

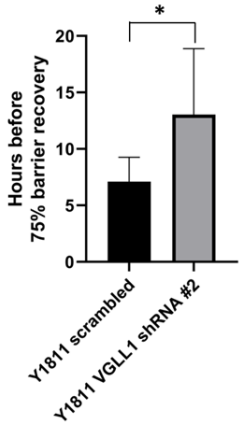
*
Hours before 75% barrier recovery
20
15
10
5
0
Y1811 scrambled
Y1811 VGLL1 shRNA #2

Figure 3.31: VGLL1 knockdown results in decreased barrier tightness and ability to heal after scratch wounding in differentiated NHU cells

A) Experimental flowchart of NHU cells (n=2 cell lines) that underwent ABS/Ca^{2+} differentiation while measuring the tightness of their barriers with the cellZscope. Cells were seeded onto Snapwell membranes and cultured in KSFMc for 24h before a 72h pretreatment with 5% ABS alone. Barrier tightness was measured upon adding Ca^{2+} to the medium of ABS treated cells, with measurements taken every hour for a period of 144h. Y1811 cells (n=1) were additionally scratch wounded after 144h and barrier tightness measurements were recorded every 20 minutes for a period of 24h to analyse the ability of each cell type to recover its barrier. At the conclusion of the 24h recovery stage, membranes were either lysed for use in immunoblot analysis or pulsed with BrdU for 6h and fixed for analysis of S-phase positive cells in each culture. A description of the latter findings can be found in Section 3.4.10.5. **B)** Immunoblot analysis of the conditions outlined in (**A**), demonstrating a reduction in VGLL1 expression when knocked down compared to control. Expression of β-Actin was used to confirm equal loading of samples. **C)** Barrier impedance of ABS/Ca^{2+} differentiated Y1811 cells transfected with scrambled or VGLL1 #2 shRNA. The pattern of barrier tightness is representative of two independent cell lines, with the TEER readings for biological replicate Y2425 found in Appendix xii. **D)** Y1811 cells were scratch wounded and the recovery of barrier integrity was measured over a period of 24h. Six technical replicates of each condition in (**C**+**D**) were measured for barrier impedance, with TEER measured in Ω/cm^2. **E)** The amount of hours each replicate required to recover 75% of the TEER of its last reading prior to scratch wounding was calculated. Significance between groups was determined using a two-way repeated measure ANOVA with Sidak's multiple comparisons post-hoc test (**C**) or an unpaired T test (**E**). *=$p \leq 0.05$; ***=$p \leq 0.001$.

3.4.10.2 Immunofluorescence analysis of urothelial transcription factors in VGLL1 knockdown differentiated NHU cells after scratch wounding

To understand the molecular basis behind a lag in wound recovery in VGLL1 knockdown cells, transfected NHU cell lines were ABS/Ca^{2+} differentiated for 7 days before being scratch wounded and allowed to recover for different periods of time (Fig. 3.32A).

Phase micrograph images of ABS/Ca^{2+} differentiated NHU cells transfected with either construct determined that no observable differences in morphology could be observed between conditions prior to wounding (Fig. 3.32B). Images taken 30min and 4h after scratch wounding revealed that the wounds had yet to heal at either time-point, whereas after 72h cell lines transfected with either shRNA had successfully closed the wound.

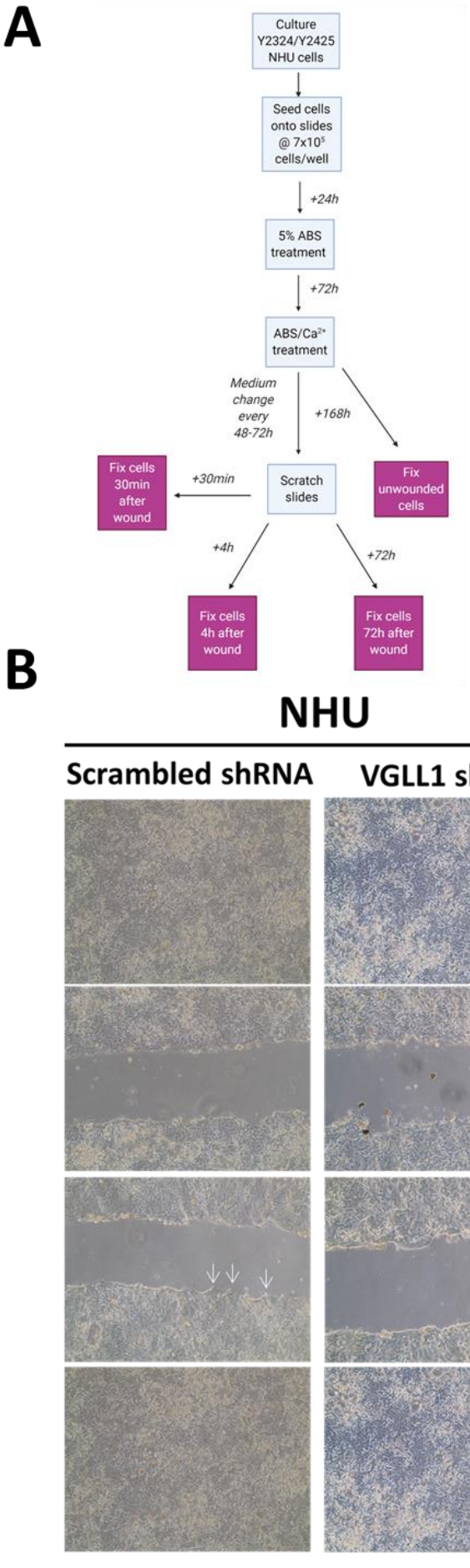
A
Culture Y2324/Y2425 NHU cells
Seed cells onto slides @ 7x10^5 cells/well
+24h
5% ABS treatment
+72h
ABS/Ca2+ treatment
Medium change every 48-72h
+168h
Fix cells 30min after wound
+30min
Scratch slides
Fix unwounded cells
+4h
+72h
Fix cells 4h after wound
Fix cells 72h after wound
B
NHU
Scrambled shRNA
VGLL1 shRNA
Unwounded
30min wound
4h post-wound
72h post-wound

Figure 3.32: Comparison of scrambled and VGLL1 knockdown ABS/Ca^{2+} differentiated NHU cell morphology following scratch wounding

A) Experimental flowchart of NHU cells (n=2 independent cell lines) that were ABS/Ca^{2+} differentiated for 7 days on glass slides before being scratch wounded and allowed to heal for different periods of time before formalin fixation. Cultures that had not received a scratch were fixed concurrently to provide a comparison to the expression pattern of proteins in cells that had undergone scratch wounding. Additional slides fixed at periods of 30min and 72h (in addition to 4h) after wounding were prepared in the case of the Y2425 cell line. Slides fixed at 72h were additionally used to quantify expression of Ki67 and MCM2 positivity in cultures, as described in Section 3.4.10.6. **B)** Phase micrograph images of ABS/Ca^{2+} differentiated VGLL1 knockdown Y2425 cells that were either scratch wounded and fixed 30min, 4h or 72h after wounding or fixed in an unwounded state. Cellular debris from the cells inhabiting the space that was scratched can be visualised in the images taken 30min post-scratch. White arrows in images taken 4h after wounding indicate the appearance of filopodia-like projections at the wound edge of recovering cultures, which appeared to be more prevalent in control cells than VGLL1 knockdown cells.

Analysis of unwounded cultures confirmed a reduction in VGLL1 expression in VGLL1 knockdown cells (Fig. 3.33A). Knockdown of VGLL1 was not found to modulate the frequency or intensity of nuclear p63 expression in unwounded cells, but similar to previous observations when dual-labelling GATA3 and p63, there appeared to be a mutually exclusive relationship between VGLL1 and p63 in regards to the dominant nuclear expression of each protein in a given cell. Expression of both proteins was found at the wound edge of 30min post-scratch cells (Fig. 3.33B), while increased expression of p63 was found 72h post-scratch in VGLL1 knockdown cells (Fig. 3.33C), suggestive of a potential increase in expression of proliferation-associated targets following wound recovery.

PPARγ was found to have reduced nuclear expression in the area directly behind the wound edge and exhibit a cytoplasmic expression pattern at the wound edge of scrambled cells at both time-points (Fig. 3.33E-F). Interestingly, this translocation of PPARγ was not observed in VGLL1 knockdown cells, with nuclear PPARγ found to be consistently retained across the wound edge at either time-point (Fig. 3.33E-F). An initial concern was that this phenomenon was a result of non-specific fluorescence due to the trapping of antibody in the cell debris present at the wound edge immediately following scratch wounding. However, this phenotype was additionally consistently observed across the wound edge in scrambled (but not VGLL1 knockdown) cells 4h after scratching, a period of time in which most of the dead cells were visually confirmed to have been cleared from the wound edge.

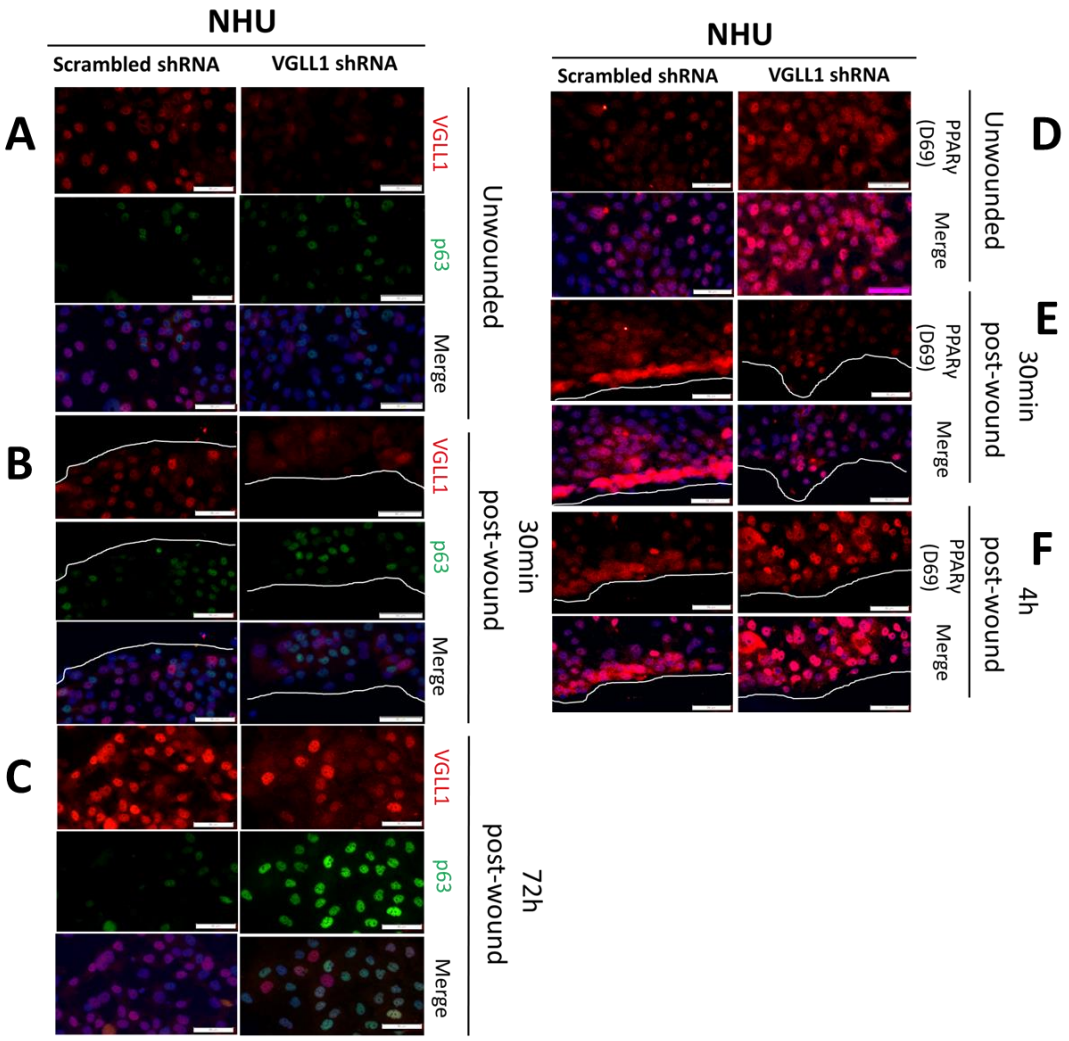

Figure 3.33: VGLL1 knockdown affects the expression and localisation of urothelial transcription factors in scratch wounded NHU cells

A-C) Immunofluorescence analysis of VGLL1 (red fluorescence) and p63 (green fluorescence) expression in ABS/Ca^{2+} differentiated VGLL1 knockdown NHU cultures that had been scratch wounded and fixed after different periods of time. Panels (**A-C**) display images of cells in an unwounded state (**A**) or 30min (**B**) and 72h (**C**) after wounding. **D-F)** Immunofluorescence analysis of PPARγ (D69 antibody) expression in VGLL1 knockdown NHU cultures in an unwounded state (**D**), or 30min (**E**) and 4h (**F**) after scratch wounding. White lines indicate the position of the wound edges. Images were all taken at same exposure and are shown with or without overlaid Hoechst 33258 DNA staining. Scale bar= 50µm. Cells receiving no primary antibody at all time-points were used as negative controls, images of which can be found in Appendix xii.

3.4.10.3 Analysis of tight junction integrity in VGLL1 knockdown differentiated NHU cells after scratch wounding

Following its previous validation as a specific marker of stratified urothelium (Section 3.4.2.3), expression of tight junction protein ZO-3 was analysed in two independent cell lines to understand whether the maintenance of tight junctions is altered in wounded differentiated NHU cells with inhibited VGLL1 expression. Expression of ZO-3 appeared normal in unwounded VGLL1 knockdown cells, with a membranous expression pattern observed which was similar to that found in scrambled control cells (Fig. 3.34A,C). However, observation of the 4h post-scratch cultures revealed a reduction in membranous ZO-3 expression at the wound edge of scrambled Y2324 (Fig. 3.34B) and Y2425 (Fig. 3.34D) cells, indicative of a dissolution of tight junctions. In comparison, VGLL1 knockdown Y2324 cells exhibited a complete retention of ZO-3 at the wound edge (Fig. 3.34B), thereby implicating a failure to dissolve tight junctions at the wound edge as a potential reasoning behind the lag in wound recovery noted in this cell type. While some dissolution of ZO-3 at the wound edge was observed in VGLL1 knockdown Y2425 cells, this cell type exhibited a comparatively stronger expression of the protein than the corresponding scrambled culture (Fig. 3.34D).

ZO-1 expression was additionally analysed in this assay (n=1), but no change in the localisation of this protein was observed in either scrambled or VGLL1 knockdown cells at either time-point assayed (Fig. 3.34E-F), suggesting that ZO-1 is dissolved at a later stage of wound recovery than was examined here.

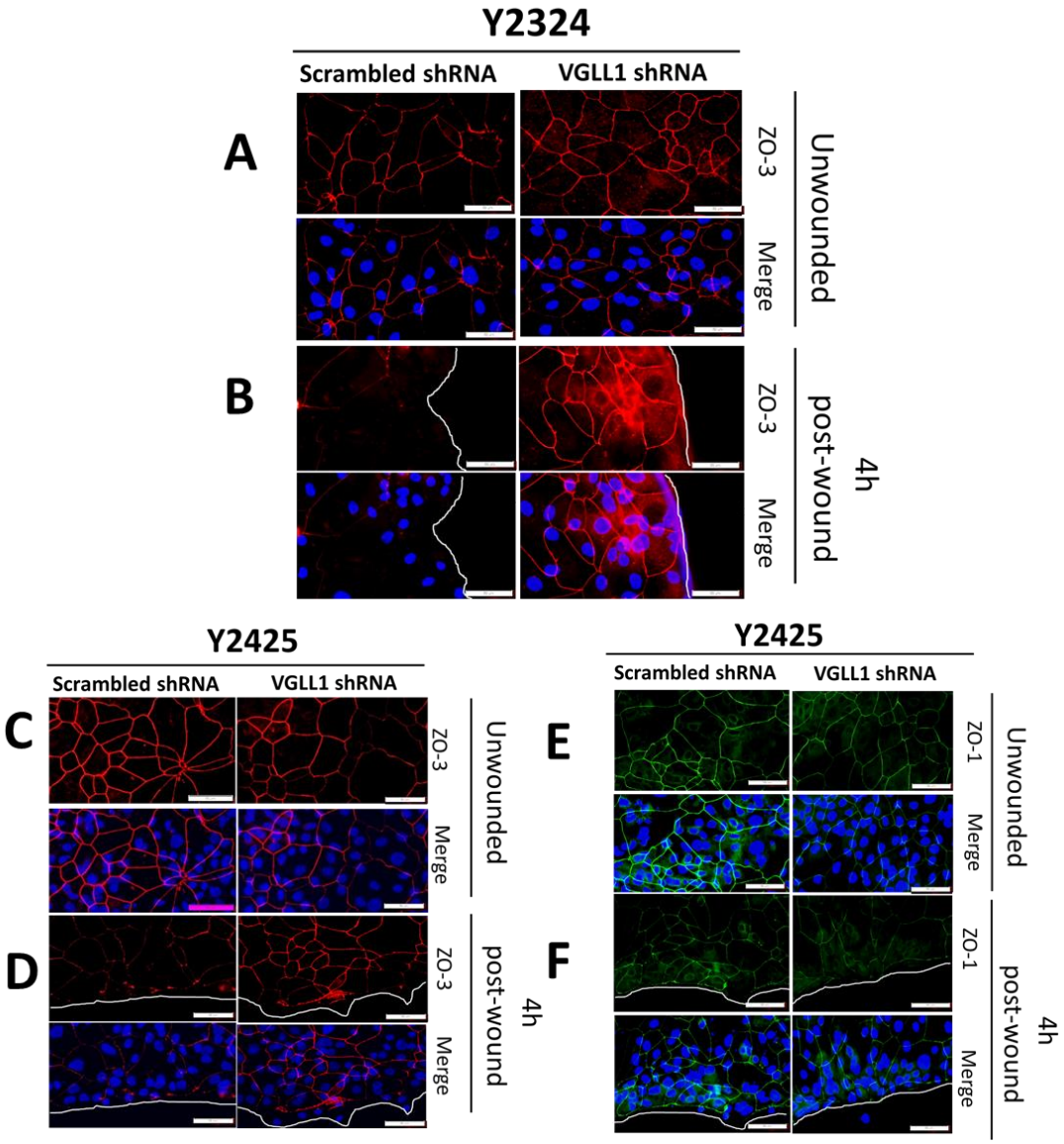

Figure 3.34: VGLL1 knockdown affects the dissolution of ZO-3 but not ZO-1 at the wound edge of scratch wounded NHU cells

A-B) Immunofluorescence analysis of ZO-3 expression in Y2324 differentiated VGLL1 knockdown NHU cultures that had been scratch wounded and fixed after different periods of time. Panels display images of cells captured in an unwounded state (**A**) or 4h (**B**) after wounding. **C-F)** Immunofluorescence analysis of ZO-3 (**C-D**) and ZO-1 (**E-F**) expression in Y2425 differentiated VGLL1 knockdown NHU cultures that had been scratch wounded and fixed after different periods of time. Panels display images of cells captured in an unwounded state (**C, E**) or 4h (**D, F**) after wounding. White lines indicate the position of the wound edges. Images were all taken at same exposure and are shown with or without overlaid Hoechst 33258 DNA staining. Scale bar= 50µm.

3.4.10.4 Immunofluorescence analysis of migration and proliferation-associated proteins in VGLL1 knockdown differentiated NHU cells following scratch wounding

The canonical TGFβ pathway (as controlled through activation of signal mediator SMAD3 by phosphorylation at its Ser423 and Ser425 sites) has previously been shown to play an important role in the wound recovery phenotype of differentiated NHU cells (Section 1.3.3). To determine whether this signalling pathway is impaired in VGLL1 knockdown cells, expression of phosphorylated SMAD3 was analysed in the context of scratch wounding in two independent cell lines. Expression of p-SMAD3 was similar in both transduced cell types in an unwounded state; with punctuate, sub-nuclear labelling found throughout both cultures (Fig. 3.35A). Immediately following wounding, this punctum-like p-SMAD3 signal was lost in the nuclei of cells situated away from the wound (Fig. 3.35B), but was retained in scrambled cells at the wound edge at both time points (Fig. 3.35C-D). In comparison, nuclear p-SMAD3 expression was lost both at and away from the wound edge in VGLL1 knockdown cells at both time points following scratch wounding, indicating an inhibition of the TGFβ-mediated wound recovery phenotype (Fig. 3.35B-D).

Expression of cell cycle marker Ki67 was additionally analysed to understand whether the urothelial wound response was also mediated through activation of proliferation. As expected, expression of Ki67 was very low in both cell types in an unwounded state (indicative of a quiescent cell population); although positive nuclei were observed more frequently in the VGLL1 knockdown culture (Fig. 3.35E). Analysis of cells in the period of 4h post-scratch determined that neither cell type had Ki67 positive cells at the wound edge (Fig. 3.35F), thereby implying that the initial process of wound recovery was that of migration and not proliferation.

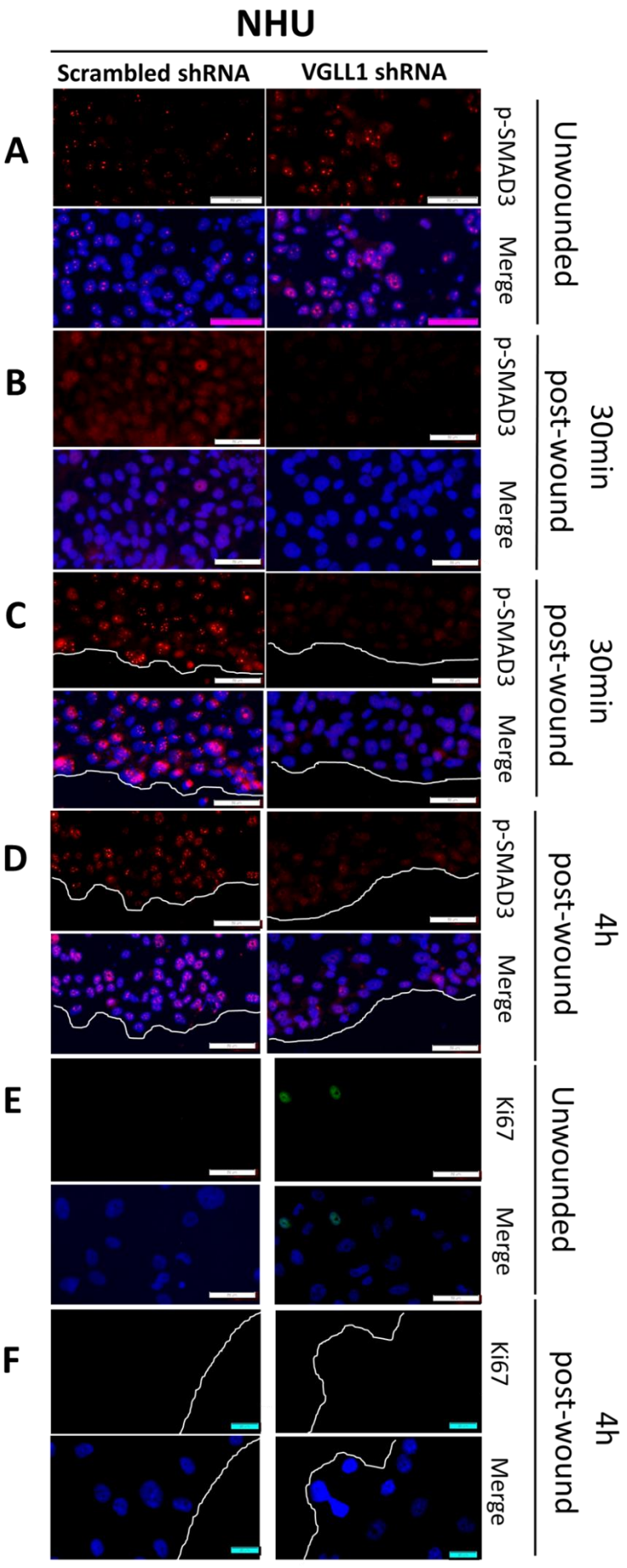
NHU
Scrambled shRNA
VGLL1 shRNA
A
B
C
D
E
F
p-SMAD3
Merge
Ki67
Merge
Unwounded
30min post-wound
30min post-wound
4h post-wound
Unwounded
4h post-wound

Figure 3.35: Phosphorylated SMAD3 expression is lost at the wound edge of mitotically quiescent scratch wounded VGLL1 knockdown NHU cells

A-D) Immunofluorescence analysis of phosphorylated (Ser423/Ser435) SMAD3 expression in ABS/Ca^{2+} differentiated VGLL1 knockdown NHU cultures that had been scratch wounded and fixed after different periods of time. Cultures that had not been scratched were used as unwounded controls (**A**), with cells transfected with either shRNA displaying nuclear expression of p-SMAD3. Panels (**B**-**C**) represent cells that were fixed 30min after wounding, with images captured both away from the wound (**B**) and at the wound edge (**C**). Panel **D** represent images captured 4h post-scratch. **E-F)** Immunofluorescence analysis of Ki67 expression in Y2324 ABS/Ca^{2+} differentiated VGLL1 knockdown NHU cultures (n=1) that had been fixed in an unwounded state (**E**) or 4h after scratch wounding (**F**). The expression pattern of p-SMAD3 is representative of two transfected NHU cell lines. Images from the biological replicate can be found in Appendix xii. White lines indicate the position of the wound edges. Images were all taken at same exposure and are shown with or without overlaid Hoechst 33258 DNA staining. Scale bar= 50µm (**A-D**); 20µm (**E-F**).

YAP/TAZ signalling has previously been cited as an important pathway in the wound healing process (Section 3.1.2). To understand the role that YAP/TAZ signalling plays in the migratory phenotype of wounded ABS/Ca^{2+} differentiated NHU cells (and whether the presence of VGLL1 affects this), expression of YAP was observed in VGLL1 knockdown cells following scratch wounding. Similarly to the phenotype previously observed in PD153035-treated cells (Section 3.4.6.4), YAP expression in ABS/Ca^{2+} differentiated cells appeared to be localised to both nuclear and cytoplasmic compartments of cells in an unwounded state (Fig. 3.36A). Analysis of scratch wounded cultures determined that a mixture of nuclear and cytoplasmic YAP was also found at the wound edge of scrambled and VGLL1 knockdown cells (Fig. 3.36B-C), indicating that a translocation YAP to a more nuclear, active state does not occur as part of the migratory phenotype of wounded NHU cells. Furthermore, loss of VGLL1 appears to have no effect on this process, suggesting that other factors independent of VGLL1 are responsible for the nucleo-cytoplasmic shuttling of YAP.

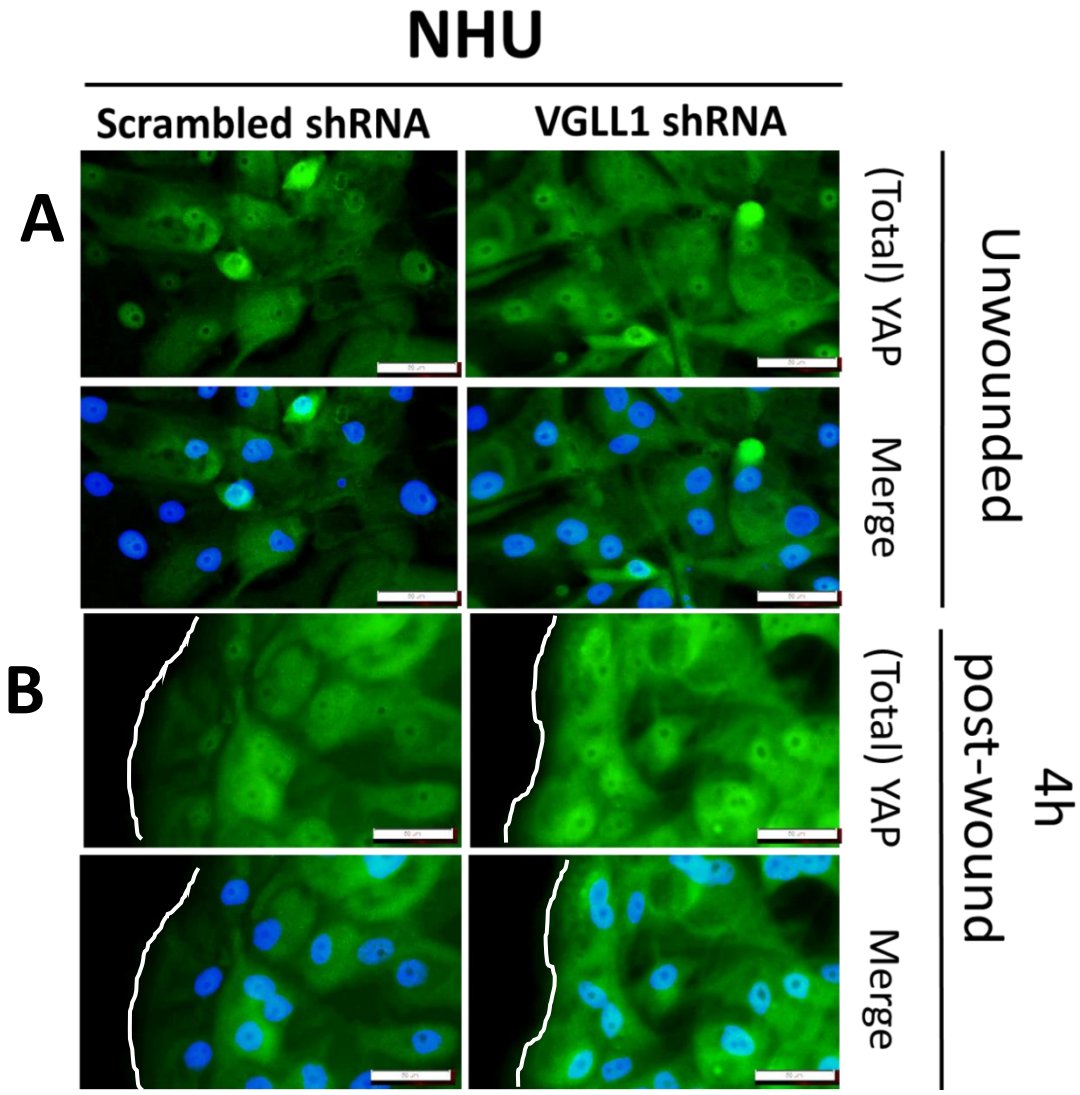

Figure 3.36: Localisation of YAP is not altered following scratch wounding of ABS/Ca^{2+} differentiated NHU cells

Immunofluorescence analysis of total YAP expression in ABS/Ca^{2+} differentiated VGLL1 knockdown NHU cultures fixed in an unwounded state (**A**), or 4h (**B**) after wounding. The expression pattern of the above targets is representative of two independent transfected NHU cell lines. Images from the biological replicate can be found in Appendix xii. White lines indicate the position of the wound edges. Images were all taken at same exposure and are shown with or without overlaid Hoechst 33258 DNA staining. Scale bar= 50µm.

3.4.10.5 Quantification of VGLL1 knockdown differentiated NHU cells in S phase following wound closure

The results of Section 3.4.8 demonstrated that forced expression of VGLL1 negatively affected the proliferative potential of undifferentiated NHU cells, while the observational findings of the preceding section suggested that inhibition of the protein in differentiated (mitotically quiescent) NHU cells may have resulted in an increased proportion of cells that were actively proliferating. To quantify whether knockdown of VGLL1 in differentiated NHU cells led to a further reactivation of cell cycle upon conclusion of wound healing, Y1811 cells were pulsed with BrdU 24h after scratch wounding for 6h (cells fixed 30h post-scratch) to observe if there was a difference in the amount of S-phase positive cells in VGLL1 knockdown cells compared to control. The forward versus side scatter plots of both Y1811 conditions revealed high amounts of debris in each sample, which could have resulted from insufficient disaggregation of tightly bound cells from the original cell sheet, or simply due to the large size of stratified differentiated NHU cells (Fig. 3.37A). Cell populations were gated based on their propidium iodide fluorescence intensities (Fig. 3.37B) and BrdU positive populations quantified (Fig. 3.37C). MIBC cell line 5637 was processed in tandem with the Y1811 samples due to its high S-phase activity, with 41.3% of all events confirmed to exhibit BrdU positivity. In comparison, only 0.82% of events from scrambled differentiated NHU cells were found to be BrdU positive, indicative of a negligible increase in S-phase positivity in the period of 30h post-wounding. Differentiated cells with VGLL1 knockdown were found to have a 2.41 fold increase in the amount of BrdU positive cells (1.98% of all events) compared to scrambled control; suggestive of VGLL1 having an effect on progression into S-phase in NHU cells following wound recovery (Fig. 3.37C, E).

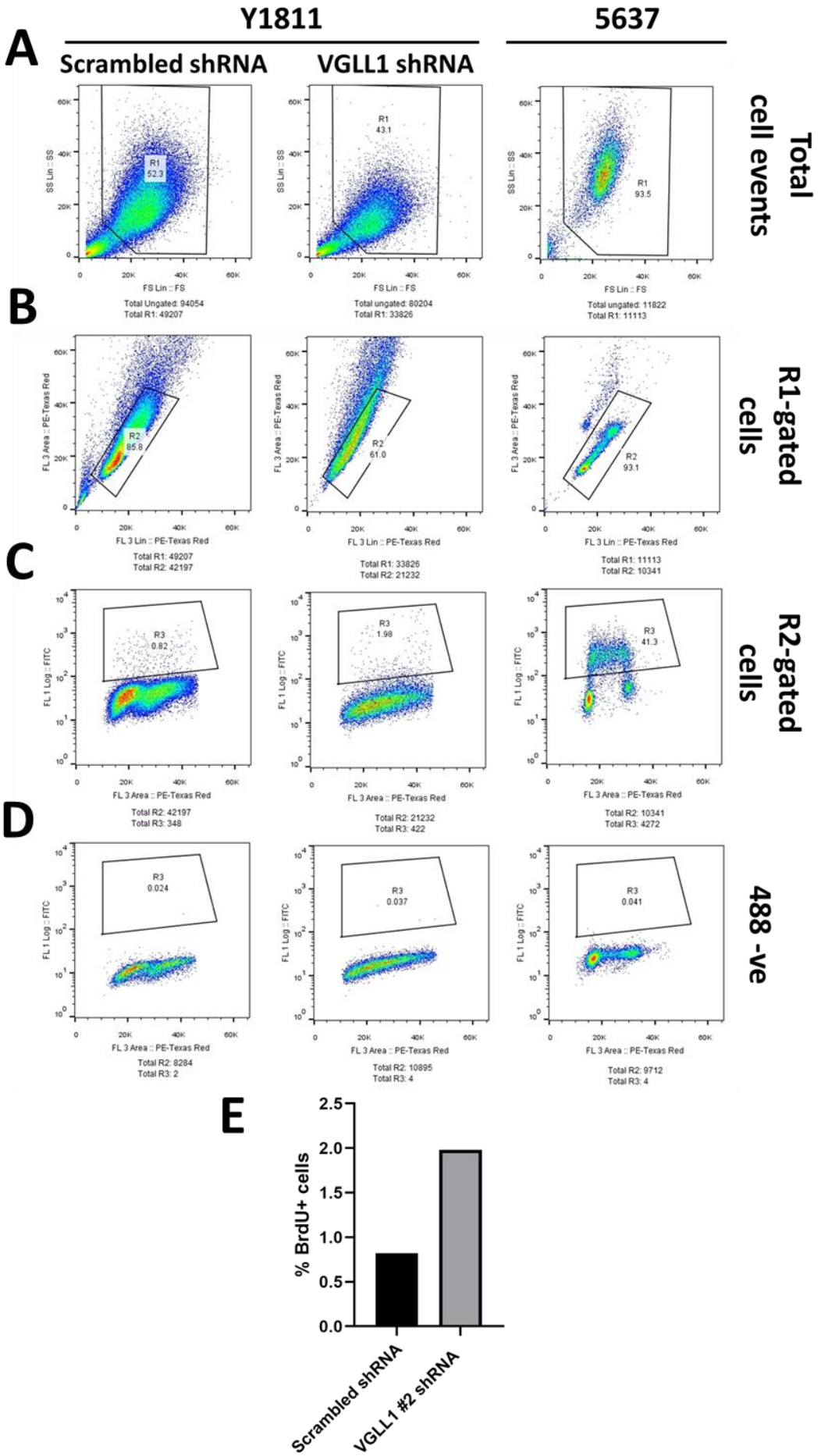
A
Y1811
5637
Scrambled shRNA
VGLL1 shRNA
Total cell events
R1
52.3
R1
43.1
R1
93.5
Total Ungated: 94054
Total R1: 49207
Total ungated: 80204
Total R1: 33826
Total ungated: 11822
Total R1: 11113
B
R1-gated cells
R2
85.8
R2
61.0
R2
93.1
Total R1: 49207
Total R2: 42197
Total R1: 33826
Total R2: 21232
Total R1: 11113
Total R2: 10341
C
R2-gated cells
R3
0.82
R3
1.98
R3
41.3
Total R2: 42197
Total R3: 348
Total R2: 21232
Total R3: 422
Total R2: 10341
Total R3: 4272
D
488 -ve
R3
0.024
R3
0.037
R3
0.041
Total R2: 8284
Total R3: 2
Total R2: 10895
Total R3: 4
Total R2: 9712
Total R3: 4
E
% BrdU+ cells
2.5
2.0
1.5
1.0
0.5
0.0
Scrambled shRNA
VGLL1 #2 shRNA

Figure 3.37: Scratch wounded VGLL1 knockdown cells exhibit a larger S-phase population upon re-activation of proliferation

Y1811 cells (n=1) containing scrambled or VGLL1 #2 shRNA were ABS/Ca^{2+} differentiated and scratch wounded, as described in Section 3.4.10.1. 24h following scratch wounding, cultures were pulsed with BrdU for 6h before disaggregation and fixation with ethanol. Single cells were subsequently labelled with a BrdU-specific primary and GaM 488 secondary antibody and fluorescence detected by flow cytometry. **A)** Forward versus side scatter (FS Lin vs SS Lin, respectively) dot plots of samples, with relevant populations gated (gate R1). **B)** Propidium iodide scatter (PE-Texas Red Lin vs PE-Texas Red Area) plots of R1-gated events, with relevant populations gated (gate R2). **C)** Propidium iodide versus BrdU scatter (PE-Texas Red Area vs FITC Log, respectively) plots of R2-gated events. 5637 cells were initially processed to determine the area of S-phase positive events (gate R3), which was subsequently applied to both Y1811 samples. **D)** Propidium iodide versus BrdU scatter plots of R2-gated events from samples that were antibody labelled but received no BrdU pulse. **E)** Quantification of the R3-gated events (BrdU-positive cells) in Y1811 conditions as a percentage of all events.

3.4.10.6 Quantification of Ki67/MCM2-positive VGLL1 knockdown differentiated NHU cells following wound closure

Previously unpublished work from The Jack Birch Unit suggested that a peak re-activation of cell cycle occurs 72h after scratch wounding differentiated NHU cell cultures, as determined by quantification of Ki67-positive cells over time. To uncover whether VGLL1 knockdown conferred a greater activation of cell cycle-positive cells at the peak activation time, expression of Ki67 and MCM2 were analysed in transduced cultures left to heal for 72h.

As observed previously (Section 3.4.10.4), unwounded Y2425 cells were found to have a small but noticeable increase in cell cycle positivity when VGLL1 was knocked down, with 1.3% of nuclei positive for Ki67 in VGLL1 knockdown cells versus 0.6% positivity in scrambled cells (Fig. 3.38A,C). A four-fold increase in Ki67 positivity was observed in scrambled cells 72h following wounding compared to unwounded control (2.5% positive nuclei), but in comparison VGLL1 knockdown cells experienced a large increase in Ki67 positivity, with 51.6% of cells expressing Ki67 at the same time-point (Fig. 3.38B-C). The pattern of MCM2 positivity mirrored that of Ki67 in each condition and time-point, albeit with a greater percentage of positive cells in each culture (70.4% positivity in VGLL1 knockdown cells 72h following scratching). To confirm that the observed phenotype was not due to differences in cell density between cell types, the number of cell nuclei analysed per image was counted, with no significant differences found between conditions 72h post-scratch (Fig. 3.38D). Analysis of these markers in this context therefore contributed to evidence that suggested that VGLL1 plays a role in modulating the ability of NHU cells to enter the cell cycle (Fig. 3.38E).

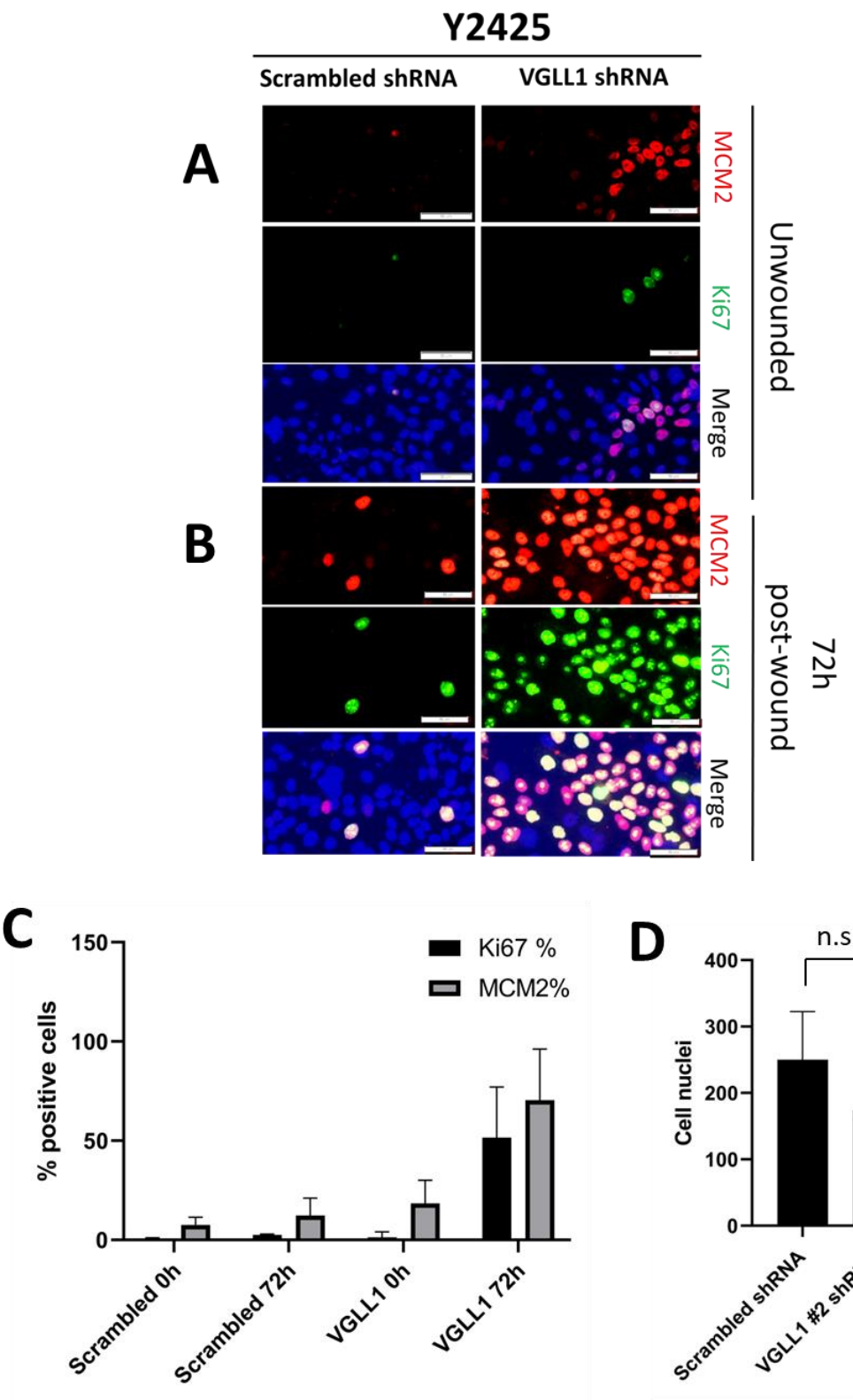
Y2425
Scrambled shRNA
VGLL1 shRNA
A
B
MCM2
Ki67
Merge
Unwounded
72h post-wound
C
% positive cells
150
100
50
0
Ki67 %
MCM2%
Scrambled 0h
Scrambled 72h
VGLL1 0h
VGLL1 72h
D
n.s.
Cell nuclei
400
300
200
100
0
Scrambled shRNA
VGLL1 #2 shRNA

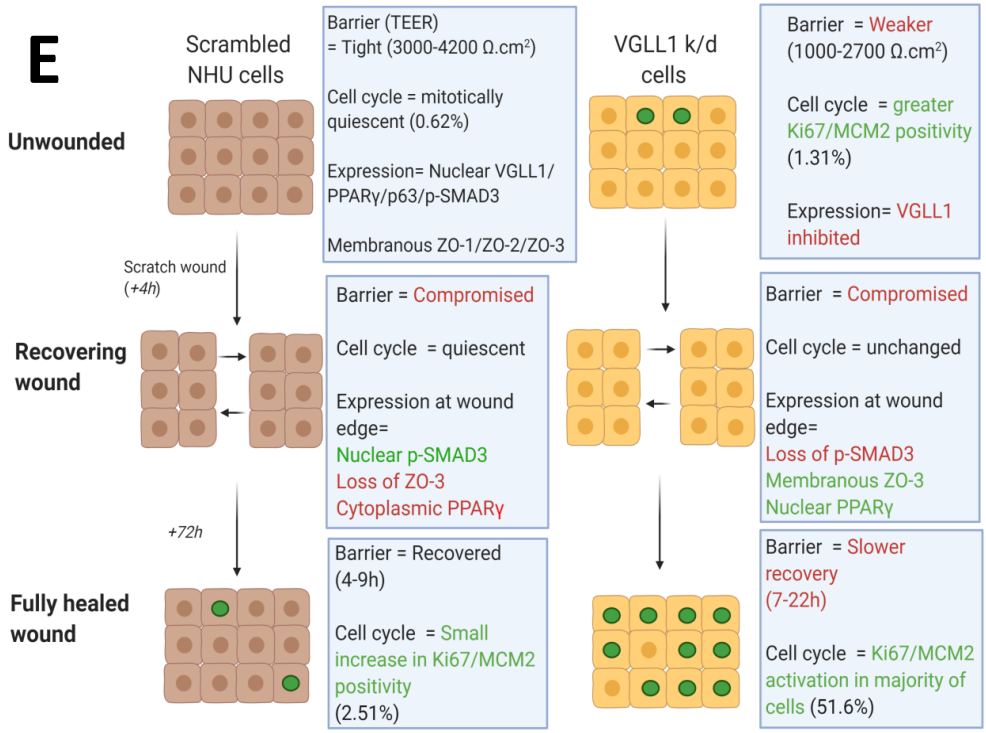

Figure 3.38: Scratch wounded VGLL1 knockdown cells are predisposed to re-enter the cell cycle after wounding

Immunofluorescence analysis of dual-labelled MCM2 (red fluorescence) and Ki67 (green fluorescence) expression in Y2425 ABS/Ca^{2+} differentiated VGLL1 knockdown NHU cultures (n=1 cell line) in an unwounded state (**A**) or 72h following scratch wounding (**B**). **C)** Quantification of Ki67 and MCM2 positive nuclei in figures (**A**-**B**). Six representative images were captured for each condition, with % positive nuclei for each protein marker calculated in ImageJ. **D)** The mean number of cell nuclei for each 72h post-wound condition (n=6 images) was calculated, with significance between groups determined using an unpaired T test. Images were all taken at same exposure and are shown with or without overlaid Hoechst 33258 DNA staining. Scale bar= 50µm. **E)** Summary of the changes in phenotype observed in unwounded, wounded and post-wounded differentiated NHU cells following VGLL1 knockdown, as determined in Fig. 3.30-3.38. Knockdown of VGLL1 resulted in cultures that exhibited a weaker barrier in an unwounded state (n=2 cell lines), yet were slower to recover a tight barrier following wounding (n=1). While actively recovering from wounding, VGLL1 knockdown cells were found to retain nuclear PPARγ and membranous ZO-3 expression, while expressing reduced migratory-associated p-SMAD3 at the wound edge (all n=2). Following completion of the healing process, inhibition of VGLL1 expression resulted in a greater increase of cell cycle activation than was observed in control cultures (n=1 cell line by flow cytometry, n=1 by immunofluorescence). Nuclei labelled green in diagram represent urothelial cells with activated cell cycle signalling.

3.4.10.7 Immunofluorescence analysis of scratch wounded differentiated NHU cells treated with TGFβ signalling agonist and antagonist

The preceding results suggested that VGLL1 plays an important role in regulating both the initial wound healing response (as determined by expression of p-SMAD3 and ZO-3 at the wound edge) and the activation of proliferation following wound closure (as determined by BrdU labelling and Ki67/MCM2 expression) in differentiated NHU cells. To observe whether a similar phenotype arose following VGLL1-independent modulation of the TGFβ signalling pathway, untransfected differentiated NHU cell lines Y1837 and Y2696 were pre-treated with 2 ng/mL rTGFβ1 (henceforth referred to as TGFβ) or 3 μM SB431542 (a specific TGFβRI inhibitor) for 3h before scratch wounding of cultures and examination of proteins of interest 4h and 72h post-wounding.

As before, p-SMAD3 was found to exhibit widespread nuclear expression in unwounded control cells (Fig. 3.39A) but accumulated in the nuclei of cells at the wound edge in DMSO treated cultures 4h post-wound (Fig. 3.39B). Expression of p-SMAD3 confirmed the efficacy of the reagents used, as TGFβ treated cells exhibited intense expression at the wound edge (Fig. 3.39C) while expression was abrogated in SB431542 treated cells (Fig. 3.39D). Interestingly, expression of p-SMAD3 was found to be inhibited in control cells 72h post-wound (Fig. 3.39E) when compared to TGFβ treated cells (Fig. 3.39F) at the same time-point, suggestive of a failure to regain basal activity of p-SMAD3 following activation of the TGFβ-mediated wound response in the absence of an exogenous agonist.

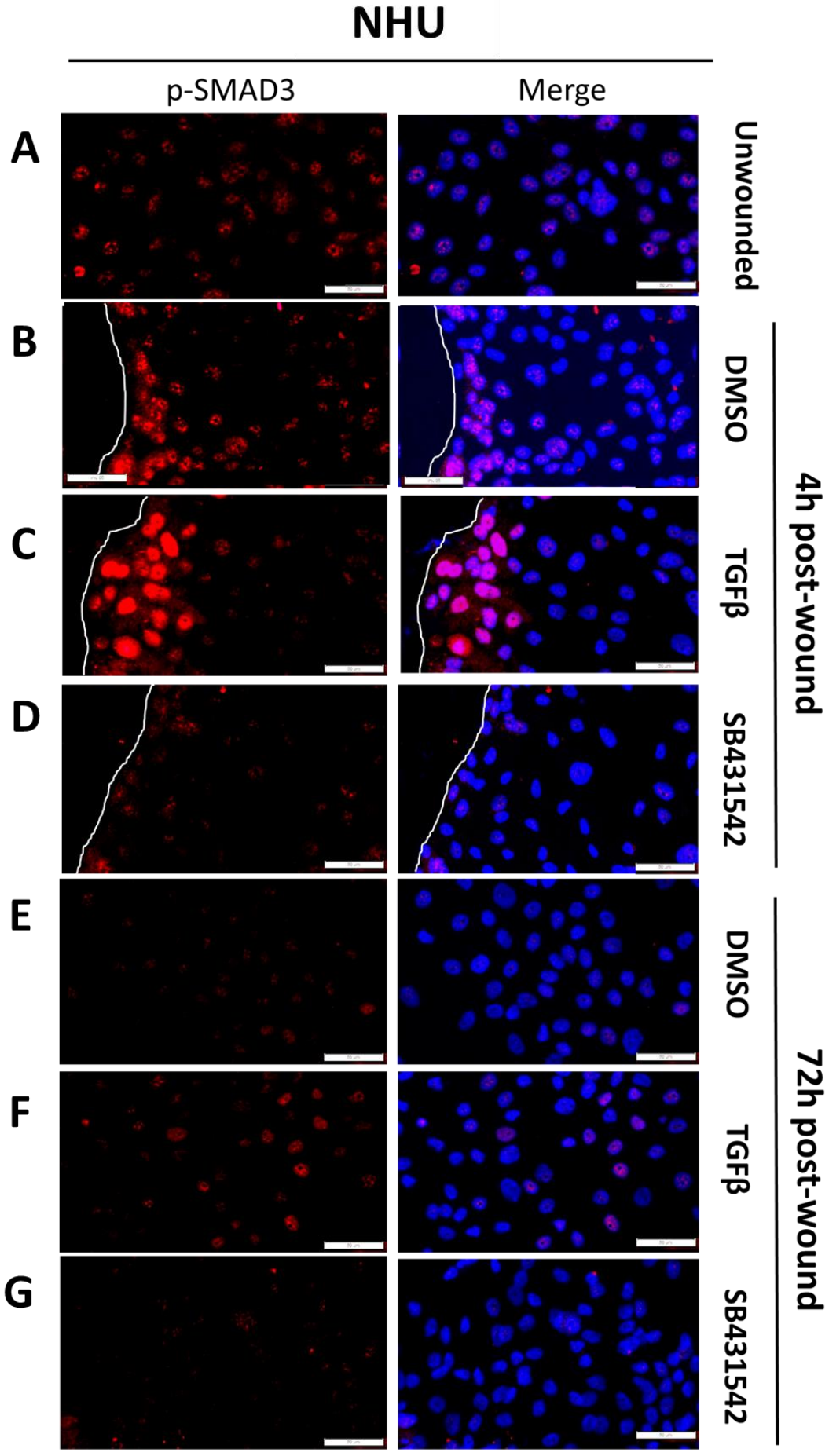
NHU
p-SMAD3
Merge
A
B
C
D
E
F
G
Unwounded
DMSO
TGFβ
SB431542
DMSO
TGFβ
SB431542
4h post-wound
72h post-wound

Figure 3.39: Treatment of differentiated NHU cells with TGFβ induces high nuclear p-SMAD3 activity at the wound edge following scratching

Immunofluorescence analysis of p-SMAD3 (Ser423/Ser435) expression in ABS/Ca^{2+} differentiated NHU cultures that had been scratch wounded and fixed after different periods of time. Panels (**A-D**) display images of cells in an unwounded state (**A**) or 4h post-wounding following 3h pre-treatment with DMSO (**B**), 2 ng/mL TGFβ (**C**) or 3 μM SB431542 (**D**)**.** Panels (**E-G**) display images of cells that had been scratch wounded and fixed after 72h following pre-treatment with DMSO (**E**), TGFβ (**F**) or SB431542 (**G**)**.** All conditions were treated with 0.1% DMSO to control for non-specific solvent effects. The expression pattern of p-SMAD3 is representative of two transfected NHU cell lines. Images from the biological replicate can be found in Appendix xii. White lines indicate the position of the wound edges. Images were all taken at same exposure and are shown with or without overlaid Hoechst 33258 DNA staining. Scale bar= 50μm.

Analysis of ZO-1 and ZO-3 expression in two wounded NHU cultures revealed that TGFβ treatment resulted in an accelerated dissolution of ZO-3 from the wound edge when compared to DMSO or SB431542 treated cells in Y2665 cells (Fig. 3.40B-E), but not Y1837 cells (Fig. 3.40G-I), indicating (as observed previously in Section 3.4.10.3) the inherent variability in the speeds in which different NHU cell lines activate wound recovery mechanisms. In comparison, ZO-1 expression was not found to be modulated at the wound edges of either cell line following any treatment, mirroring the phenotype observed in transfected cell lines.

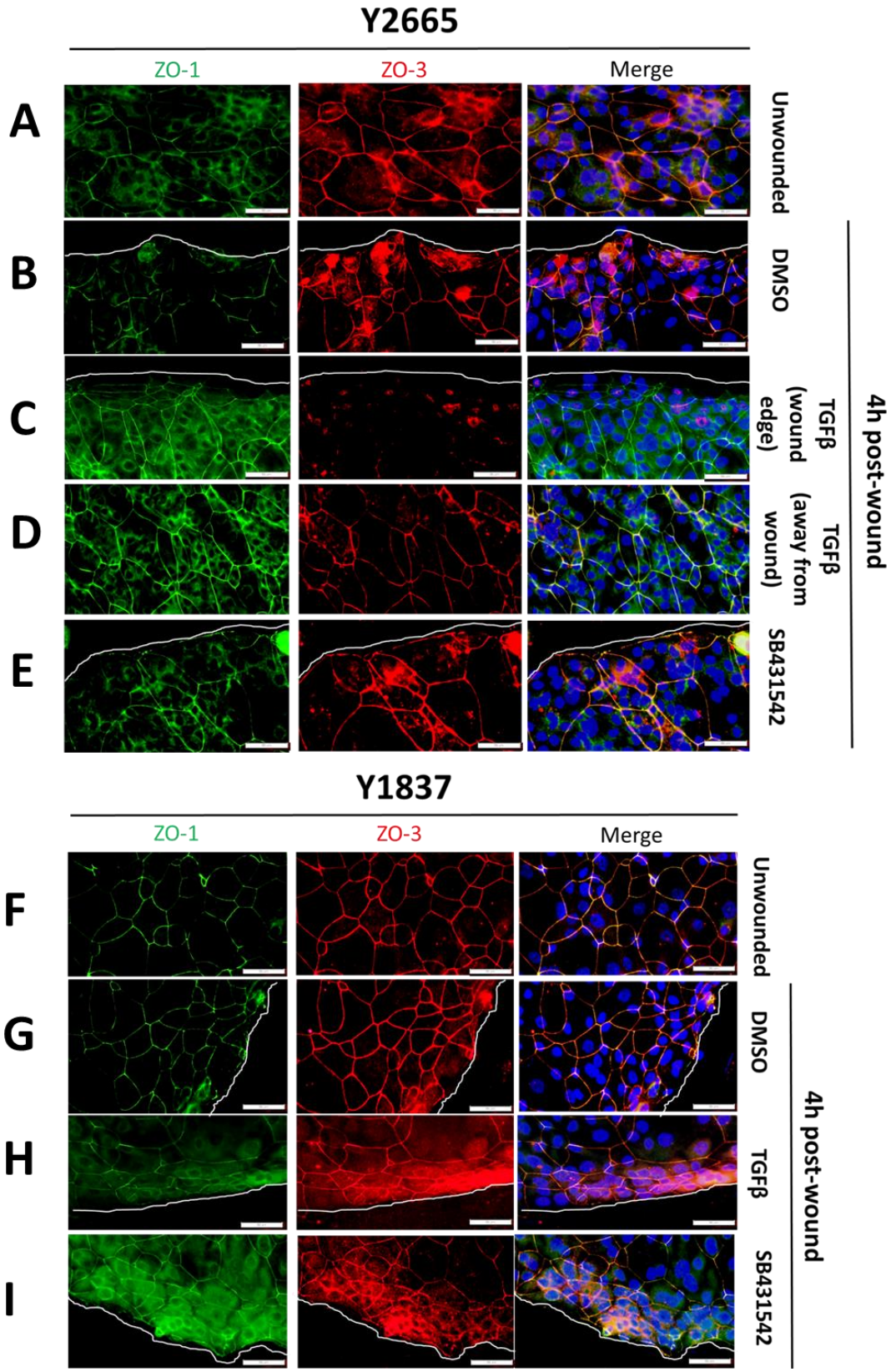
Y2665
ZO-1
ZO-3
Merge
A
B
C
D
E
Unwounded
DMSO
TGFβ (wound edge)
TGFβ (away from wound)
SB431542
4h post-wound
Y1837
ZO-1
ZO-3
Merge
F
G
H
I
Unwounded
DMSO
TGFβ
SB431542
4h post-wound

Figure 3.40: TGFβ treatment can induce dissolution of ZO-3 from the wound edge following scratch wounding

A-E) ZO-1 (green fluorescence) and ZO-3 (red fluorescence) expression in Y2665 differentiated NHU cultures that had been scratch wounded and fixed in an unwounded state (**A**), or after 4h following pre-treatment with DMSO (**B**), TGFβ (**C-D**) or SB431542 (**E**)**.** TGFβ treated cultures exhibited dissolution of ZO-3 at the wound edge (**C**) but retained expression in cells situated away from the wound (**D**). **F-I)** ZO-1 (green fluorescence) and ZO-3 (red fluorescence) expression in Y1837 differentiated NHU cultures that had been scratch wounded and fixed in an unwounded state (**F**), or after 4h following pre-treatment with DMSO (**G**), TGFβ (**H**) or SB431542 (**I**)**.** White lines indicate the position of the wound edges. Images were all taken at same exposure and are shown with or without overlaid Hoechst 33258 DNA staining. Scale bar= 50μm.

Control and TGFβ treated wounded NHU cells were found to exhibit intense cytoplasmic PPARγ at the wound edge (Fig. 3.41B-C) while SB431542 treated cells retained a primarily nuclear localisation of the protein (Fig. 3.41D), mirroring the phenotype observed in scrambled control (cytoplasmic PPARγ) and VGLL1 knockdown (nuclear PPARγ) observed previously.

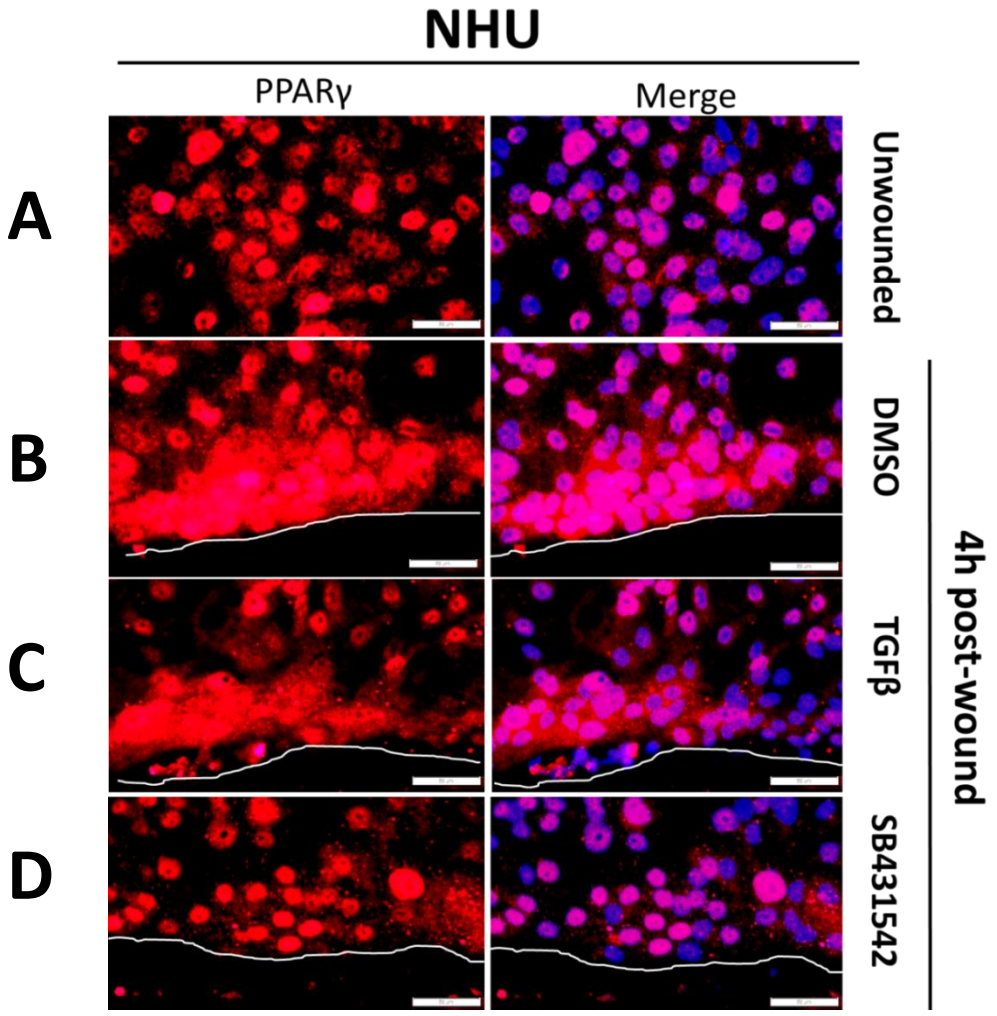

Figure 3.41: Inhibition of TGFβ results in retention of nuclear PPARγ at the wound edge of differentiated NHU cells

PPARγ (81B8 antibody) expression in ABS/Ca^{2+} differentiated NHU cultures that had been scratch wounded and fixed after different periods of time. Panels (**A-D**) display images of cells in an unwounded state (**A**) or 4h post-wounding following pre-treatment with DMSO (**B**), TGFβ (**C**) or SB431542 (**D**)**.** The expression pattern of PPARγ is representative of two transfected NHU cell lines. Images from the biological replicate can be found in Appendix xii. White lines indicate the position of the wound edges. Images were all taken at same exposure and are shown with or without overlaid Hoechst 33258 DNA staining. Scale bar= 50μm.

VGLL1 expression did not exhibit any notable changes in expression or localisation across any treatment in a post-wounded state (Fig. 3.42A-D); suggesting that expression of the protein was not affected by TGFβ pathway activation or inhibition.

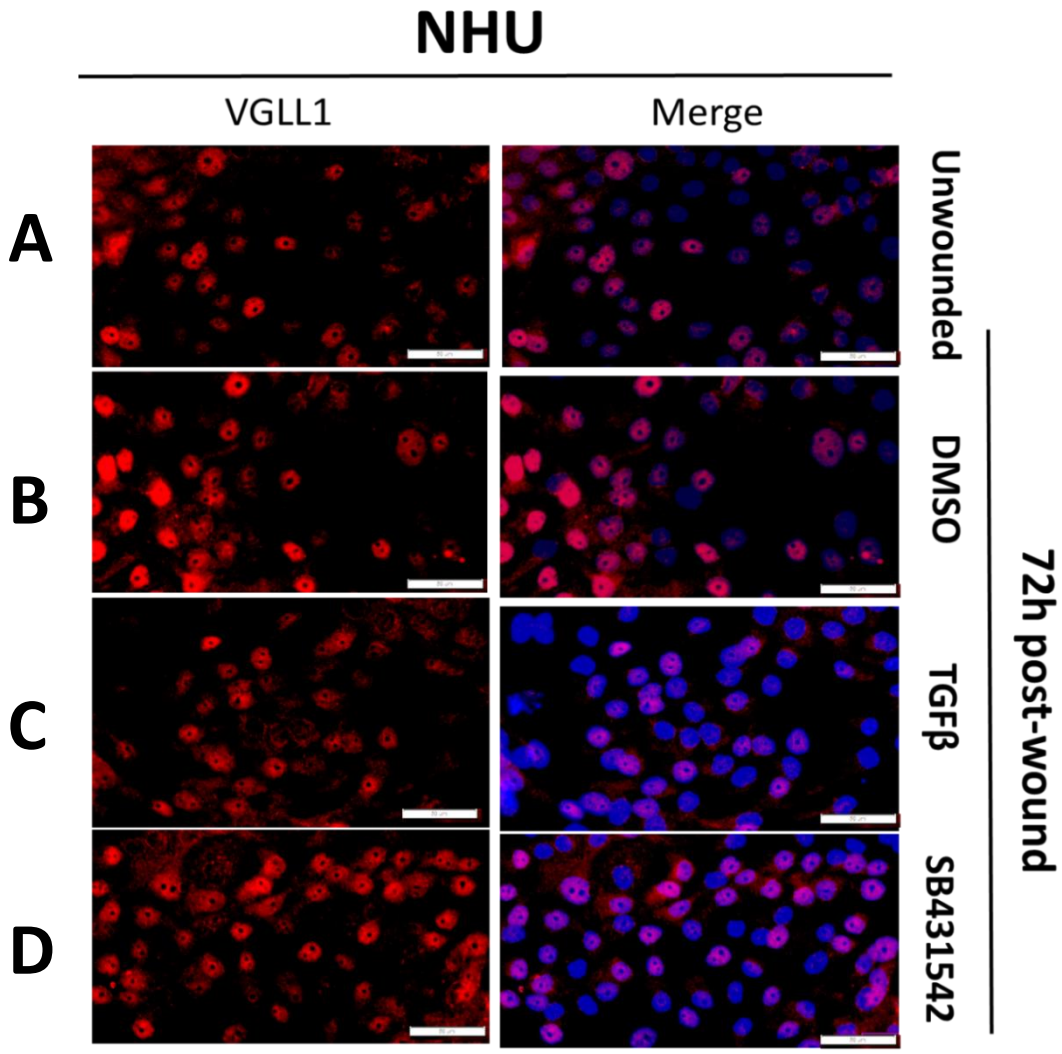

Figure 3.42: VGLL1 expression is not modulated in differentiated NHU cells following TGFβ agonism or antagonism

VGLL1 expression in ABS/Ca^{2+} differentiated NHU cultures that had been scratch wounded and fixed after different periods of time. Panels (**A-D**) display images of cells in an unwounded state (**A**) or 72h post-wounding following pre-treatment with DMSO (**B**), TGFβ (**C**) or SB431542 (**D**)**.** The expression pattern of VGLL1 is representative of two transfected NHU cell lines. Images from the biological replicate can be found in Appendix xii. Images were all taken at same exposure and are shown with or without overlaid Hoechst 33258 DNA staining. Scale bar= 50µm.

Analysis of Ki67 expression in the assayed cell lines revealed an increase in positivity from 2.2% to 5.5% when comparing unwounded control cells (Fig. 3.43A, E) to DMSO treated cells left to recover for 72h (Fig. 3.43B, E). Treatment with TGFβ served to inhibit cell cycle activation following recovery from scratch wounding (1.3% Ki67 index; Fig. 3.43C, E) while cells pre-treated with SB431542 exhibited an increased percentage of Ki67 expression (14.1%; Fig. 3.43D, E). As before, the expression pattern of MCM2 tallied with that of Ki67 but was expressed by a greater percentage of cells in the population (18.5% positivity in 72h DMSO cultures versus 29.4% positivity in SB431542 treated cultures). The preceding observations therefore indicated that inhibition of autocrine TGFβ signalling prior to the scratch wounding of differentiated NHU cells had a similar effect on cell phenotype as inhibition of VGLL1 via shRNA knockdown (Fig. 3.43F) thereby implicating both VGLL1 and TGFβ signalling as important modulators of the urothelial wound recovery response.

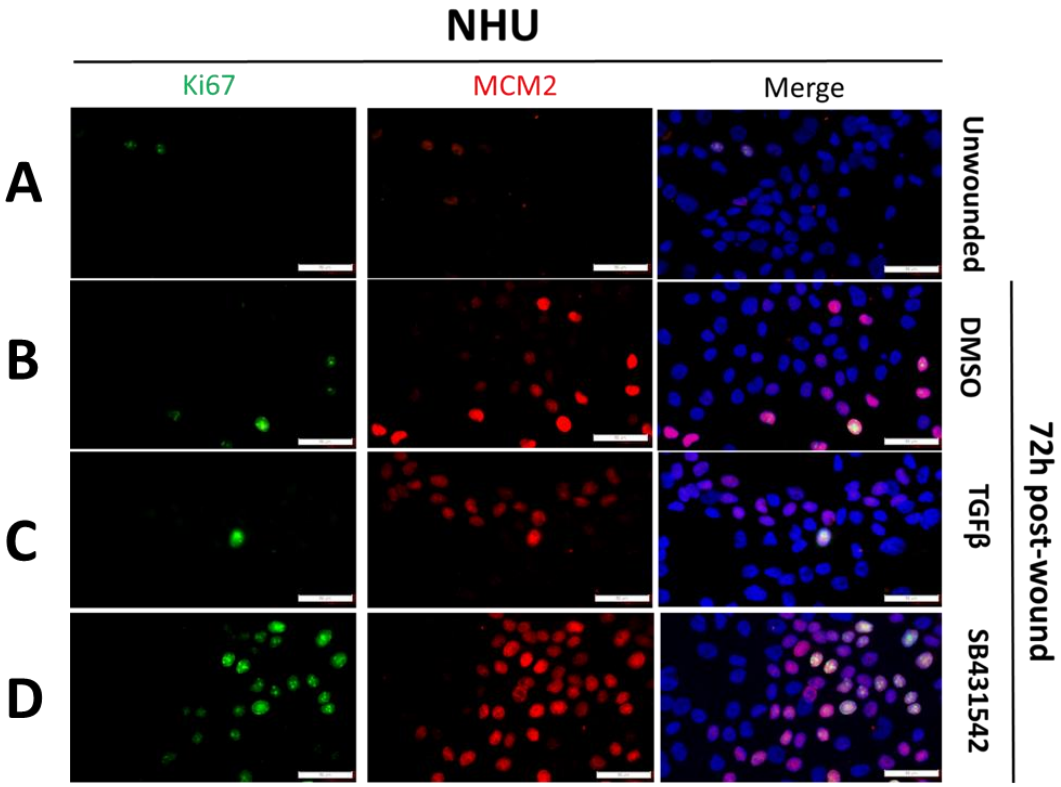
NHU
Ki67
MCM2
Merge
A
B
C
D
Unwounded
DMSO
TGFβ
SB431542
72h post-wound

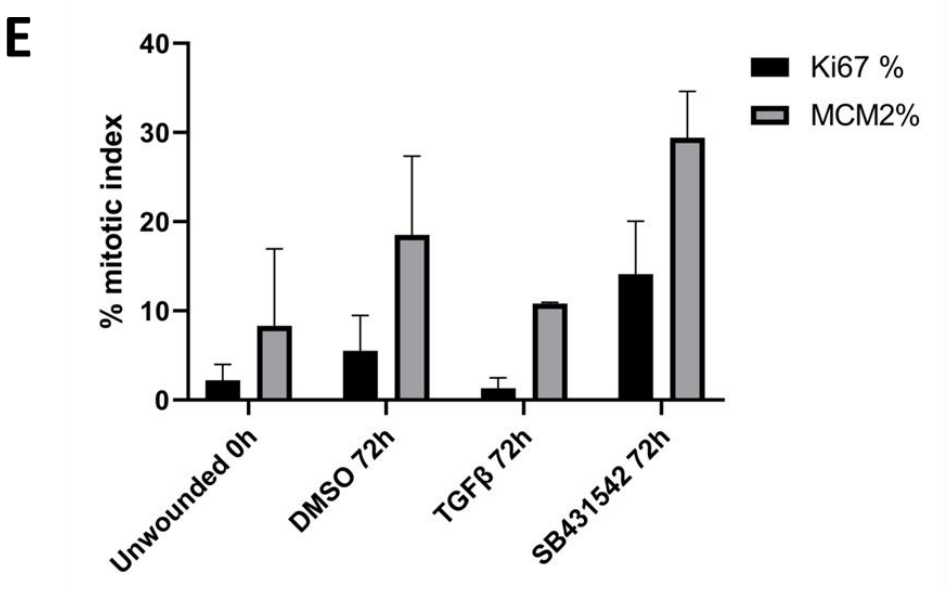
E
% mitotic index
40
30
20
10
0
Ki67 %
MCM2%
Unwounded 0h
DMSO 72h
TGFβ 72h
SB431542 72h

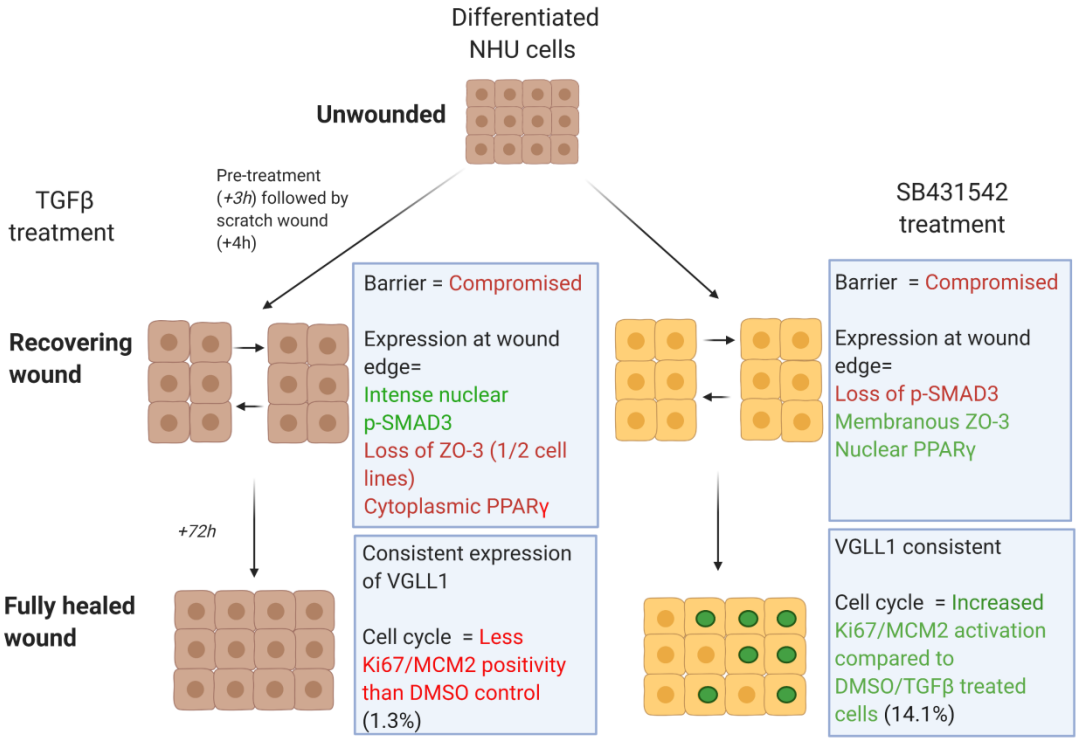

Figure 3.43: TGFβ pathway inhibition results in increased cell cycle activity in wounded differentiated NHU cells in a similar manner to inhibition of VGLL1 expression

A-E) Analysis of dual-labelled Ki67 (green fluorescence) and MCM2 (red fluorescence) expression in ABS/Ca^{2+} differentiated NHU cultures (n=2). Panels (**A-D**) display images of cells in an unwounded state (**A**) or 72h post-wounding following pre-treatment with DMSO (**B**), TGFβ (**C**) or SB431542 (**D**)**.** The expression pattern of the above targets is representative of two transfected NHU cell lines. Images from the biological replicate can be found in Appendix xii. Images were all taken at same exposure and are shown with or without overlaid Hoechst 33258 DNA staining. Scale bar= 50µm. **E)** Quantification of Ki67 and MCM2 positive nuclei in figures (**A**-**D**). Eight representative images were captured for each condition from two independent NHU cell lines (n=16 images for each condition total), with % positive nuclei for each protein marker calculated in ImageJ. **F)** Summary of the changes in phenotype observed in wounded and post-wounded differentiated NHU cells following activation or inhibition of TGFβ signalling with TGFβ or SB431542, respectively. These experiments revealed that TGFβ pathway inhibition resulted in a similar phenotype to wounded cells with VGLL1 knockdown, as evidenced by a retention of nuclear PPARγ and loss of p-SMAD3 at the wound edge of SB431542-treated cultures, followed by a notable increase in cell cycle activity (all n=2). Nuclei labelled green represent urothelial cells with activated cell cycle signalling.

3.5 Discussion

3.5.1 Expression of Hippo pathway genes in urothelium

This chapter provides the first systematic transcriptomic characterisation of Hippo pathway components in urothelium, with RNAseq analysis revealing several gene components (*TEAD1*, *TEAD3, STK4, STK3, LATS1, LATS2, MOB1A, VGLL4*) that were expressed in both *in situ* and *in vitro* urothelium regardless of differentiation state. However, only the predicted transcriptional co-activator *VGLL1* displayed an association with a differentiated urothelial phenotype.

3.5.2 Context-specific induction of VGLL1 expression in urothelial cells

3.5.2.1 Identification of PPARγ and GATA3 as transcription factors involved in VGLL1 induction

The role of transcription factors PPARγ and GATA3 in the induction of VGLL1 in differentiated NHU cells was investigated due to the previous identification of PPARγ and GATA3 as pivotal regulators of normal urothelial cytodifferentiation (Varley *et al.,* 2004a; Varley *et al.,* 2004b; Varley *et al.,* 2006; Varley *et al.,* 2009; Fishwick *et al.,* 2017). The results achieved by inhibiting said transcription factors in differentiating NHU cells by pharmacological or genetic means revealed that the induction of VGLL1 was a complex process that seemingly encompassed the activation of multiple transcription factors, modulation of proliferation-associated signalling pathways and a sensitivity to cell density.

Inhibition of PPARγ in TZ/PD differentiated NHU cells was determined to have a highly variable effect on VGLL1 transcript and protein induction, with T007 treatment resulting in inhibition of VGLL1 protein expression at an earlier time-point (24h) which failed to be uniformly reproduced in cell lines at later stages of differentiation (72h), a time in which inhibition of GATA3 had a comparatively more potent effect on VGLL1 expression in 2/3 cell lines. While a previous study had highlighted a co-localisation between VGLL1 protein and *GATA3* transcript at an early stage of human embryonic placental development (Soncin *et al.,* 2018), this is the first evidence that indicates that GATA3 transcriptional activity is upstream of VGLL1 expression. The accumulative observations made in the preceding

experiments therefore pointed to a model whereby PPARγ plays an important role in the initial differentiation process to dictate *VGLL1* transcription, but that this influence subsequently lessens over the process of differentiation as intermediate transcription factors such as GATA3 become activated, a phenotype consistent with the role of PPARγ as a pioneer urothelial transcription factor (Varley *et al.,* 2009). That NHU cell lines exhibited such differential responses to T007 treatment/GATA3 knockdown did not appear to be as a result of inherent differences between cell line origin (all cell lines used in this chapter were ureter-derived), but instead appeared to be related to subtle differences in cell density and the modulation of signalling pathways that entailed.

Previous studies into the mechanisms that control NHU differentiation following treatment with TZ and PD153035 in isolation or concurrently determined that dual administration of the reagents produced a synergistic effect, therefore concluding that blockade of downstream EGFR signalling was necessary for consistent activation of PPARγ and expression of both immediate downstream targets (*FOXA1, IRF1)* and late differentiation markers, such as *UPK2* and claudins 3, 4 and 5 (Varley *et al.,* 2004a; Varley *et al.,* 2006; Varley *et al.,* 2009). The results collated through interrogation of the TZ/PD differentiation method in this study support the assertion that administration of TZ alone is able to induce expression of some differentiation-associated proteins such as FOXA1, ELF3 and PPARγ itself in post-confluent NHU cells. However, this approach did little to induce expression of other differentiation-associated proteins such as GATA3 and VGLL1, which required inhibition of the EGFR/RAS/RAF/MEK/ERK signalling axis. This is an interesting observation, as the prevailing view of GATA3 is that its expression is solely downstream of PPARγ activation, as demonstrated in a study of PPARγ overexpression in PPARγ/GATA3-null normal human buccal cells (Hustler *et al.,* 2018). That GATA3 and VGLL1 (but not PPARγ) protein are induced in NHU cells following growth to post-confluence challenges this previous view, and suggests potential alternate routes of GATA3 expression.

One possible hypothesis for this observation is that induction of GATA3 in PD153035-treated or post-confluent NHU cells may be as a result of an activation of previously labile (but present) PPARγ through inhibition of its ERK-mediated phosphorylation (Varley *et al.,* 2004a), although this possibility was not explored as part of this study. As the onset of confluence has previously been demonstrated to negatively affect the activation of ERK1/2 in undifferentiated NHU cells (Georgopoulos *et al.,* 2014), it is therefore possible that induction of GATA3 protein requires PI3K/AKT signalling activation, a pathway identified in this study to be active following PD153035 treatment. Treatment of AKT knockdown MCF-7 cells with the oestrogen receptor α ligand estradiol resulted in a differential expression of genes predicted to have binding sites in the *GATA3* promoter compared to control (Bhat-Nakshatri *et al.,* 2016), whilst PI3K/AKT signalling has previously been demonstrated to be required to stabilise GATA3 protein in differentiated T cells (Cook *et al.,* 2010). However, whether this signalling relationship also exists in urothelial cells has yet to be confirmed.

3.5.2.2 Relationship of VGLL1 induction to PI3K/AKT signalling

Preliminary evidence in this chapter demonstrated the potential induction of VGLL1 expression in undifferentiated NHU cells grown in high Ca^{2+}, with expression of the protein lost when cells were concurrently treated with PI3K/AKT inhibitor LY294002. A potential relationship between VGLL1 and PI3K/AKT signalling has previously been observed by Kim *et al.* in specimens of gastric cancer, as tumours with high *VGLL1* expression were found to correlate positively with PI3K genes *PI3KCA* and *PI3KCB*. Treatment with LY294002 or siRNA knockdown of *PI3KCA*/*PI3KCB* in gastric cancer cell line NUGCB3 resulted in an inhibition of VGLL1 expression, which was hypothesised to be as a result of β-catenin signalling as inhibition of AKT signalling led to a loss of active β-catenin and a reduction in β-catenin occupancy on the VGLL1 promoter (Kim *et al.,* 2019a). However, this does not likely appear to be relevant in NHU cells as VGLL1 expression is significantly induced following PD153035 treatment, a phenotype that results in a reduction of active β-catenin in the nucleus. Additionally, treatment of undifferentiated NHU cells with LY294002 serves to increase nuclear β-catenin expression (Georgopoulos

et al., 2014), highlighting how these signalling pathways can crosstalk in a different manner depending on cell type.

3.5.2.3 Other transcription factors potentially involved in VGLL1 expression

siRNA knockdown of GATA3 was insufficient to completely inhibit VGLL1 expression in TZ/PD differentiated cells, implicating the existence of other differentiation-associated transcription factors that work synergistically with GATA3 to regulate VGLL1 expression. Principal component analysis of *VGLL1* expression in urothelium when compared to urothelial transcription factors revealed a close association to *FOXA1*, *RARG* and *POUF51* (OCT4) expression. Sequence analysis performed in this study additionally highlighted multiple FOXA1 binding motifs in the DNA region upstream of the *VGLL1* promoter, although care must be taken to not over-interpret the findings of such predictive tools.

FOXA1 is a known target gene of PPARγ activation in urothelium (Varley *et al.,* 2009) and its differentiation-associated expression appears to be independent of GATA3, as demonstrated following GATA3 siRNA knockdown in TZ/PD differentiated NHU cells (Fishwick *et al.,* 2017). However, a study of mouse embryonic carcinoma cells revealed that the Foxa1 promoter contains a retinoic acid response element and that treatment of these cells with retinoic acid rapidly induced *Foxa1* expression (Jacob *et al.,* 1999), potentially implicating RARγ as an alternate regulator of key genes that drive the urothelial differentiation process.

A close association of *VGLL1* expression to *POU5F1* in urothelium is interesting, as OCT4 protein has previously been determined to not be expressed in NHU cells (Wezel *et al.,* 2013). However, the study by Wezel *et al.* focussed on expression of the pluripotency-associated OCT4A splice variant in undifferentiated NHU cells, meaning that the expression of OCT4 variants (such as OCT4B) in NHU cells and their effect on the differentiated phenotype is currently unknown. The respective roles of FOXA1, RARγ and OCT4 in inducing VGLL1 expression was not explored in this study, but future work that determines their relative importance (if any) in mediating expression of the transcriptional co-activator may help to increase understanding of the complex transcriptional machinery required to induce a fully differentiated urothelial phenotype.

3.5.3 The role of VGLL1 in differentiated urothelial tissue repair

3.5.3.1 Effect of VGLL1 knockdown on differentiated urothelium

Stable knockdown of VGLL1 resulted in reduced expression of a variety of differentiation-associated proteins following the onset of differentiation, including PPARγ, GATA3, ELF3, CK13 and Claudin 4. The effect that this loss of regulation had on the phenotype of ABS/Ca^{2+} differentiated NHU cells manifested as a tissue that exhibited a consistently weaker barrier, yet took longer to regenerate following scratch wounding. To understand how these seemingly contradictory observations were possible, the molecular changes that occurred following different stages of the urothelial wound repair process was interrogated in both VGLL1 knockdown cells and untransfected cells treated with modulators of TGFβ signalling, a pathway previously implicated in mediating a urothelial wound response (Fleming *et al.,* 2012). Affecting NHU physiology through VGLL1 knockdown or inhibition of TGFβ signalling resulted in a convergent phenotype, thereby further implicating autocrine TGFβ-mediated SMAD3 activation as a key signalling event in both the initial wound repair response in addition to highlighting a role in the subsequent return to quiescence of differentiated urothelium. The key observations made following analysis of scratch wounded VGLL1 knockdown and TGFβ/SB431542-treated ABS/Ca^{2+} differentiated NHU cells were summarised previously in Figures 3.37 and 3.42, respectively.

3.5.3.2 TGFβ-mediated dissolution of tight junctions

Dissolution of tight junction proteins has been demonstrated to be a key event in the early stages of urothelial wound repair (Lavelle *et al.,* 2002; Kreft *et al.,* 2005), while activation of TGFβ signalling has previously been implicated as a key modulator of tight junction dissolution in non-urothelial murine and porcine cell models (Ozdamar *et al.,* 2005; Pierucci-Alves *et al.,* 2012). The scratch wound experiments undertaken in this chapter indicate that a TGFβ-mediated mechanism appeared to affect the dissolution of tight junctions in wounded urothelium, as demonstrated by an accelerated loss of ZO-3 at the wound edge of TGFβ pre-treated cells and retention of ZO-3 at the wound edge of VGLL1 knockdown cells when compared to their corresponding control cell lines. Furthermore, cells that

retained ZO-3 at the wound edge (*i.e.* VGLL1 knockdown cells) exhibited a concurrent inhibition of migration-associated p-SMAD3 activity. These observations therefore implicate VGLL1 as an important mediator of the TGFβ/SMAD3-mediated wound healing/migratory phenotype in NHU cells, and that loss of VGLL1 function results in an impaired wound response. In comparison, expression of fellow ZO family member ZO-1 was found to be retained at the leading wound edge of differentiated NHU cells following all time points and cell treatments; this reflected the phenotype previously observed in wounded mice bladders (Kreft *et al.,* 2006).

The expression and localisation of VGLL1 itself did not appear to change in scratch wounded cultures pre-treated with either TGFβ or SB431542, suggesting that the effect on cell phenotype mediated by VGLL1 knockdown was taking place upstream of TGFβ/SMAD3 signalling.

3.5.3.3 Localisation of PPARγ following wounding

An additional observation of wounded differentiated NHU cells was the increased cytoplasmic proportion of PPARγ that was consistently observed at the wound edge of control cells or TGFβ-treated cultures. In comparison, nuclear retention of PPARγ was observed at the wound edge of cultures with inhibited p-SMAD3 expression (*i.e.* VGLL1 knockdown and SB431542-treated cells). Various studies have demonstrated the ability of PPARγ agonism to negatively regulate TGFβ signalling activity (Ghosh *et al.,* 2004; Reka *et al.,* 2010; Liu *et al.,* 2019), with this function speculated to arise in human hypertrophic scar fibroblasts following TZ treatment due to PPARγ-specific induction of miR-145, an inhibitor of SMAD3 expression (Zhu *et al.,* 2015). Conversely, deletion of Pparγ in mouse fibroblasts resulted in constitutive expression of p-Smad3 that was independent of Tgfβ agonism (Ghosh *et al.,* 2008) and was associated with an accelerated rate of wound healing (Sha *et al.,* 2012). The observations made in this study therefore serve to suggest that PPARγ may play a similar role of SMAD3 regulation in urothelium, and that to circumvent inhibition of p-SMAD3 activity and drive the required migratory response in normal wounded differentiated NHU cells, the protein is sequestered from the nuclei of cells in an as-of-yet uncharacterised mechanism.

3.5.3.4 Reactivation of proliferation following wound closure

Following successful closure of the wound and regeneration of a tight barrier, a modest increase in cell cycle activity was observed in control differentiated NHU cells throughout the population, indicative of a re-activation of proliferation that occurs at a later stage of recovery (*i.e.* 24-72h post-wounding) than the initial migratory response (0-10h post-wounding). Pre-treatment of cultures with TGFβ inhibited cell cycle activity to a greater degree than control, whilst VGLL1 knockdown or SB431542 treatment resulted in a striking increase in BrdU, Ki67 and MCM2 labelling, additionally implicating VGLL1 regulation of the TGFβ/p-SMAD3 signalling axis as an important modulator of differentiated cell proliferation. TGFβ has a known role in inducing cell cycle arrest through SMAD3-mediated induction of the cyclin-dependent kinase inhibitor $p15^{INK4b}$ (Hannon *et al.*, 1994; Reynisdóttir *et al.,* 1995; Frost *et al.,* 2001), a process that was speculated to cause the cytostasis observed in undifferentiated NHU cells following treatment with TGFβ (Fleming *et al.,* 2012). Activation of TGFβ signalling has additionally been implicated in an increased expression of fellow cyclin-dependent kinase inhibitor $p27^{Kip1}$ through stabilisation of the protein and inhibition of its proteasomal degradation (Reynisdóttir *et al.,* 1995; Lecanda *et al.,* 2009). The observations recorded in this chapter therefore suggest that this growth arrest function of TGFβ signalling is also relevant in differentiated NHU cells, and creates a compelling argument to observe whether induction of $p15^{INK4b}$ and/or $p27^{Kip1}$ is modified in TGFβ-treated cells compared to VGLL1 knockdown/SB431542-treated cells to confirm this hypothesis.

3.5.4 Chapter conclusions

The collated observations of NHU cells in this chapter have led to the following conclusions, summarised below and in Figure 3.44. Transcriptomic analysis identified VGLL1 as a transcriptional co-activator that is significantly induced following urothelial cytodifferentiation. A blockade of the constitutively active RAS/RAF/MEK/ERK signalling axis in undifferentiated NHU cells and the activity of transcription factors PPARγ and GATA3 were implicated in playing important roles in inducing expression of VGLL1, a process which may additionally require active PI3K/AKT signalling. Forced expression of VGLL1 in undifferentiated NHU cells

negatively affected proliferation, potentially as a consequence of inhibited PI3K/AKT signalling whilst appearing to have no effect on the activation of YAP. This led to the following chapter addressing whether these observations are reiterated in transfected MIBC cell lines with a VGLL1-low background. Examination of wounded differentiated NHU cells revealed a striking relationship between the expression of VGLL1 and the ability of cells to activate TGFβ-mediated p-SMAD3 signalling, a pathway that is demonstrably important for mediating both the initial wound healing response in addition to regulating the ability of differentiated cells to reactivate proliferative processes. Inhibition of VGLL1 in differentiated NHU cells appeared to dysregulate the balance of SMAD3 activation in a post-wounded cell population, thereby resulting in a lack of control over cell cycle re-entry. Predictions as to how this previously unreported role of VGLL1 functions at a mechanistic level are explored through the analysis of transcriptomic data in the following chapter.

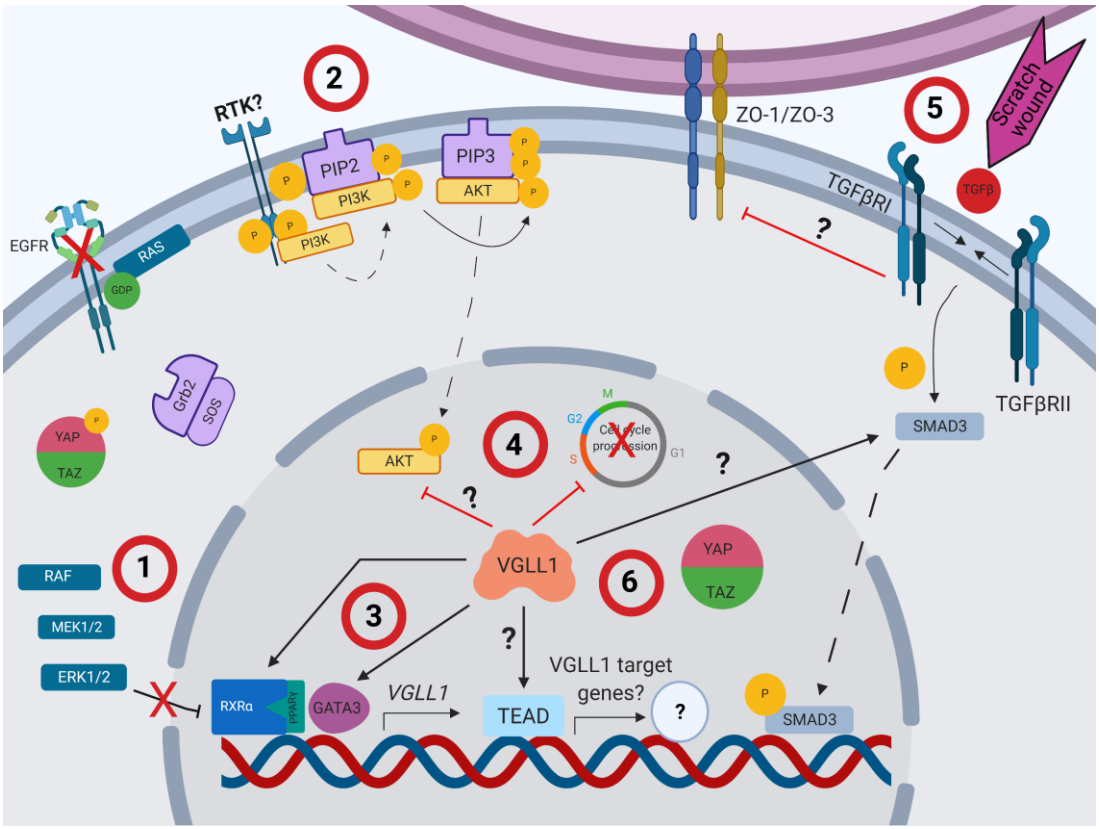

Figure 3.44: The predicted phenotype of VGLL1 in differentiated urothelium

In differentiating urothelium, the RAS/RAF/MEK/ERK signalling pathway is inhibited (**1**) and PI3K/AKT signalling is transiently activated (**2**). Activation of PPARγ and expression of fellow urothelial transcription factor GATA3 are important for inducing *VGLL1* expression, with the subsequent inhibition of PPARγ and GATA3 observed in VGLL1 knockdown cells indicative of a potential positive homeostatic relationship between VGLL1 and the transcription factors in differentiated urothelium (**3**). Forced expression of VGLL1 retarded the proliferation of NHU cells, potentially through inhibition of phosphorylated AKT (**4**). In mitotically quiescent, differentiated urothelium, an absence of VGLL1 was demonstrated to affect both barrier tightness and the normal process of tissue regeneration following scratch wounding (**5**), where the phenotype of nuclear SMAD3 activation and a dissolution of membranous ZO-3 was lost. Comparatively, the presence or absence of VGLL1 was not found to have any effect on the active proportion of YAP in NHU cells (**6**), a finding in opposition to that of previous studies. Outstanding questions on the function of VGLL1 are highlighted on the diagram with question marks, examples of which include whether forced expression of VGLL1 reproducibly inhibits PI3K/AKT signalling, whether the protein binds to TEAD transcription factors to facilitate its function, the identity of VGLL1-specific target genes, how the presence of VGLL1 affects autocrine TGFβ signalling following scratch wounding and in turn, how this process is related to the dissolution of tight junctions.

3.6 Summary of results

- VGLL1 was expressed in *in vivo* human urothelium, with expression localised to both nuclear and cytoplasmic compartments of cells. VGLL1 transcript and protein expression was found to be differentiation-associated in cultured NHU cells, with significant increases in expression when cells were treated using the TZ/PD or ABS/Ca^{2+} methods. This induction of VGLL1 expression coincided with a loss of proliferation and a gain of tight junction protein expression.

- Expression of VGLL1 following TZ/PD differentiation was affected independently by inhibition of PPARγ or GATA3 in certain physiological contexts. Blockade of downstream targets of EGFR signalling (MEK1/2 and ERK1/2) through the use of inhibitors, or the onset of cell contact-inhibition were also implicated in the induction of VGLL1 expression in undifferentiated NHU cells.

- Overexpression of VGLL1 in undifferentiated NHU cells resulted in a reduced rate of proliferation. RAS/RAF/MEK/ERK signalling appeared unaffected by VGLL1 overexpression, implicating the modulation of other proliferation-associated signalling pathways, such as PI3K/AKT.

- shRNA knockdown of VGLL1 caused a reduction in the expression of differentiation-associated proteins. This manifested in a corresponding reduction in the overall barrier strength of cultures, yet cells were found to be slower to repair barrier integrity after scratch wounding. Analysis of this phenomenon determined that scratch wounding of VGLL1 knockdown cells resulted in a retention of nuclear PPARγ and membranous ZO-3 and a loss of p-SMAD3 at the wound edge, thus potentially accounting for the lag in recovery.

- Mitotically quiescent ABS/Ca^{2+} differentiated cultures were observed to have greater population of cells actively in the cell cycle when VGLL1 expression was inhibited in an unwounded state. VGLL1 knockdown differentiated NHU cells exhibited a greater increase in BrdU, Ki67 and MCM2 positivity compared to control following recovery from scratch wounding, implicating VGLL1 as a modulator of cell cycle re-entry.

- Components of YAP/TAZ signalling, including TEAD1, TEAD3 and YAP were expressed in NHU cells. Overexpression of VGLL1 appeared to not induce inactivation of YAP through phosphorylation in undifferentiated cells, while knockdown of VGLL1 had no effect on the proportion of nuclear, active YAP in wounded differentiated cells. Localisation of YAP in NHU cells was however found to be modulated by cell-cell contact and inhibition of EGFR signalling.

4. Effect of VGLL1 expression on bladder cancer cell phenotype

4.1 Hippo pathway dysregulation in cancer

Mutations in regulatory components of the Hippo pathway can affect tissue homeostasis and have a causal role in cancer initiation, as evidenced in numerous forms of human cancer. The most well documented instances of Hippo pathway mutations in cancer have been found in malignant mesothelioma, where inactivating mutations of the neurofibromin 2 (*NF2*) gene are found in around 23% of cases of tumour samples and 50% of cell lines (Murakami *et al.,* 2011; Wang *et al.,* 2018). NF2 is a cytoskeletal protein that binds directly to inhibitory kinases LATS1/2 and helps to regulate activation of YAP/TAZ (Plouffe *et al.,* 2016). Cells with mutated *NF2* therefore exhibit aberrant activation of YAP/TAZ target genes, cell cycle progression and increased migration (Fujii *et al.*, 2012; Mizuno *et al.,* 2012). Human lung cancer specimens were also found to exhibit reduced expression of inhibitory binding protein angiomoitin (AMOT) compared to healthy tissue, with a concurrent increase of nuclear YAP/TAZ suggestive of an additional mechanism by which normal regulation of YAP/TAZ is abrogated (Hsu *et al.,* 2015).

Of the VGLL family, VGLL4 is the best characterised in human disease, with evidence that it acts as a tumour suppressor in oesophageal, liver and colorectal cancer by competing with YAP/TAZ for binding to TEAD proteins (Jiang *et al.,* 2015; Jiao *et al.,* 2017; Zhang *et al.,* 2014). This observation led to the production of a VGLL4 mimicking peptide which was demonstrated to suppress growth in both human gastric cancer cell lines and an *in vivo* mouse model of gastric cancer; a disease characterised by its aberrant YAP signalling (Jiao *et al.,* 2014). No study has yet described a tumour suppressive role for VGLL1 in cases of human cancer; although given the sequence similarity of the Sd/TEAD binding motifs of VGLL1 and VGLL4 it may be predicted to have such a role through competitive inhibition of YAP/TAZ, as previously seen in an *in vitro* model of prostate cancer (Section 3.1.3).

Reports of Hippo pathway dysregulation in urothelial carcinoma have previously been conflicting; with one study suggesting that YAP protein expression (detected immunohistochemically) was decreased in tissue samples of NMIBC and MIBC

compared to control (Latz *et al.,* 2016), whilst another study used RT-qPCR, immunoblotting and immunohistochemistry to demonstrate an increase in *YAP1* transcript and nuclear YAP protein in MIBC samples compared to normal tissue (J. Y. Liu et al., 2013). One explanation for this discrepancy could be due to the choice of YAP antibody used in each study, with the rabbit polyclonal antibody employed by Latz *et al.* later discontinued by Santa Cruz Biotechnology due to concerns over its mono-specificity.

4.2 Aims and hypothesis

The results from Chapter 3 discovered that VGLL1 is differentiation-associated in NHU cells and suggested that the protein plays a role in tissue homeostasis. It is therefore axiomatic that VGLL1 function would be predicted to be somehow dysregulated in cases of MIBC. The overall aims of this chapter were to a) examine VGLL1 function through genetic manipulation of its expression in bladder cancer cell lines and b) characterise *VGLL1* expression in MIBC using publically available datasets.

Based on the previous observations of VGLL1 expression and function in normal urothelium, it was hypothesised that *VGLL1* expression would be associated with luminal MIBC tumours and not with the less-differentiated basal/squamous MIBC tumours. It was additionally hypothesised that *VGLL1* expression would be downregulated in MIBC unless the regulatory feedback pathways that act on VGLL1 are dysregulated.

The specific experimental objectives of this chapter were to:

- Quantify *VGLL1* transcript expression in bladder cancer cell lines (Section 4.4.1) and TCGA MIBC cohort (Section 4.4.6) and compare to its expression in normal urothelium.

- Generate VGLL1-overexpressing MIBC cell lines using cell lines identified in Section 4.4.1 that exhibit low/absent expression of the protein (Section 4.4.2). Investigate the effect that VGLL1 overexpression has on the modulation of proliferation-associated signal transduction pathways (Section 4.4.3-4) and cell cycle progression (Section 4.4.5) in VGLL1-low MIBC.

- Identify subgroups of MIBC tumours with outlier expression of *VGLL1* in order to observe whether said groups exhibit differences in tumour phenotype compared to other TCGA MIBC samples (Section 4.4.6).

4.3 Experimental approach

4.3.1 Transcriptomic analysis of Hippo pathway genes in bladder cancer cell lines

The transcriptomic phenotype of eight bladder cancer cell lines was analysed using a publically-available RNAseq dataset (BioProject Accession #PRJNA382834; MD Anderson Cancer Center) to elucidate whether the cell lines in question stratified into luminal and basal/squamous-like groups based on expression of previously determined luminal and basal/squamous MIBC marker genes (Choi *et al.,* 2014b; Robertson *et al.,* 2017; Marzouka *et al.,* 2018). Expression of *VGLL1* and various components of the Hippo pathway were subsequently quantified to observe whether these genes associated with specific cell line subtypes and determine whether expression was altered in an *in vitro* bladder cancer context in comparison to the expression found in normal urothelium *in situ*. VGLL1 protein expression in bladder cancer cell lines UM-UC-9, HT1376, RT4, ScaBer, T24 and 5637 was observed by immunoblotting in order to validate the phenotype observed at the transcript level.

4.3.2 Modulation of bladder cancer cell line phenotype using a VGLL1 overexpression construct

Following generation and validation of VGLL1-overexpressing 5637, T24 and ScaBer bladder cancer cell lines, the phenotype of the lines was analysed through a variety of different experiments. To further examine and potentially verify that VGLL1 is not acting in opposition to a YAP/TAZ signalling axis, the expression and localisation of the total and phosphorylated forms of YAP in the cell lines was observed by immunoblotting and immunofluorescence. Additionally, expression of previously cited YAP/TAZ downstream target genes *ANKRD1*, *CTGF* and *CYR61 (Zanconato et al.,* 2015) was quantified by qRT-PCR to determine whether VGLL1 overexpression had an effect on markers of YAP/TAZ signalling.

Expression of cell cycle marker Ki67 and key components of the EGFR/RAS/RAF/MEK/ERK and PI3K/AKT signalling pathways were analysed in the three cell lines by RT-PCR, immunoblotting and immunofluorescence. Changes to cell cycle activity following VGLL1 overexpression was additionally assayed by

quantifying the proportion of T24 and 5637 cells in S phase by flow cytometry of BrdU-positive cells.

4.3.3 Investigation of *VGLL1* phenotype in MIBC

Transcript expression of *VGLL1* in bladder cancer was analysed using the RNAseq resource of TCGA cohort of MIBC tumours (n=404; The Cancer Genome Atlas Research Network, 2014). The tumours of the cohort were separated into six molecular subtypes using a transcriptomic-based, computationally-devised consensus classifier (Kamoun *et al.,* 2020) and expression of *VGLL1* was compared to that found in in-house RNAseq samples of normal urothelium *in situ* (n=6). Principal component analysis of *VGLL1* and Hippo pathway components or urothelial-associated transcription factor expression (devised from a list of genes curated by Fishwick *et al.,* 2017) in MIBC was subsequently performed to determine what genes (and in what MIBC molecular subtype) correlated with *VGLL1* expression.

Descriptive statistics was used to identify an outlier group of tumours based on the distribution of *VGLL1* expression across the overall MIBC cohort. The mutation status of *VGLL1* and other genes that exhibited a significantly higher mutation frequency in the tumour subset was examined in an attempt to identify possible gene alterations that would result in dysregulated *VGLL1* expression. Information regarding the somatic mutations and copy number alterations present in TCGA cohort for each gene analysed was obtained from cBioPortal (https://www.cbioportal.org/).

Differential expression analysis was performed by comparing the transcriptome of the identified tumour subset to the remaining MIBC tumours to assess the genes that are affected in tumours that harbour *VGLL1* dysregulation. Gene Set Enrichment Analysis (GSEA) of the differentially expressed genes was performed to confirm whether the significantly upregulated or downregulated genes appeared together in the previously curated Hallmark gene sets (downloaded from the Molecular Signatures Database; https://www.gsea-msigdb.org/gsea/index.jsp).

Expression of all the genes highlighted in the analysis was first confirmed in the MIBC cohort to ensure that the differential expression observed in the subset was biologically relevant. Finally, the mortality rate of the identified tumour subset was assessed to determine whether *VGLL1* dysregulation was associated with an altered patient survival time.

4.4 Results

4.4.1 Transcriptomic analysis of bladder cancer cell lines

4.4.1.1 Molecular subtyping of bladder cancer cell lines

Hierarchical clustering of bladder cancer cell lines HT1197, HT1376, RT112, RT4, ScaBer, T24, UM-UC-9 and 5637 alongside in-house sequenced samples of normal urothelium *in situ* (n=3 independent urothelial samples) was performed based on expression of genes previously found to be associated with either luminal (n=13) or basal (n=6) MIBC. Cell lines RT4 and RT112 exhibited high relative expression of luminal MIBC-associated genes such as *GATA3, ELF3*, *FOXA1* and *FGFR3* and thus clustered most closely to the expression profile of normal urothelium *in situ* (Fig. 4.1), marking these cell lines as being relatively well-differentiated. Conversely, cell lines 5637 and ScaBer had high relative expression of basal/squamous MIBC markers, such as *KRT5, KRT6A* and *EGFR*. UM-UC-9 cells were found to express several components of luminal MIBC biology, including very high expression of PPARγ (TPM = 2261), yet also had relatively low expression of luminal MIBC markers such as *KRT13* and *UPK1A*. As a result, UM-UC-9 cells were more closely aligned with HT1197 and HT1376, cell lines that exhibited traits of both luminal (*GATA3, ERBB3, CDH1*) and basal (*CDH3*, *EGFR*) MIBC. The highly invasive MIBC cell line T24 exhibited low relative expression of both luminal and basal/squamous MIBC markers, thus indicating its identity as an outlier cell line in this comparison.

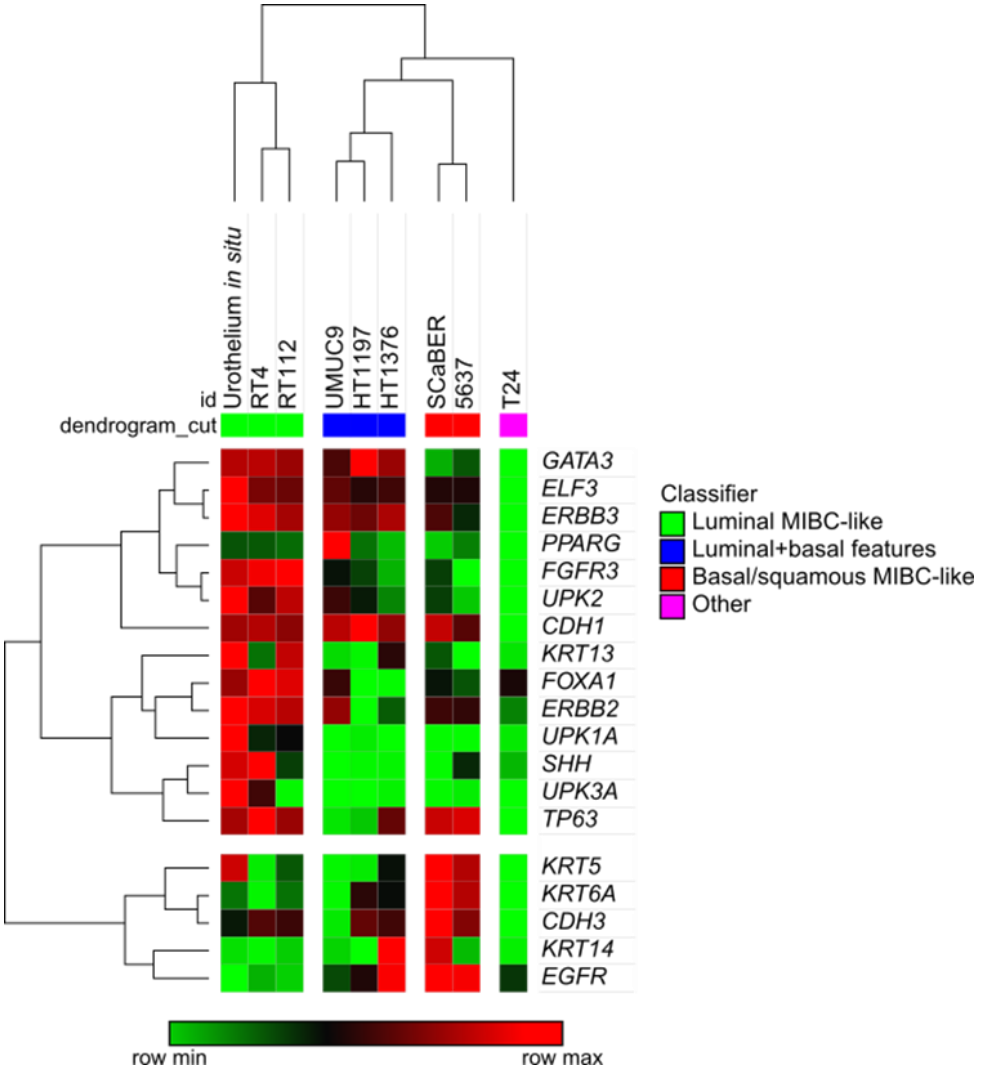

Figure 4.1: Bladder cancer cell lines stratify based on expression of luminal and basal MIBC markers

Unsupervised hierarchical clustering performed on RNAseq Log_2 transformed expression of previously identified markers of luminal and basal/squamous MIBC (n=19 genes) in a cohort of bladder cancer cell lines (n=8) compared to normal urothelium *in situ* (mean TPM of n=3 biological replicates). Samples were clustered using the one minus Spearman rank correlation method with complete linkage. Clustering was performed using Morpheus software (https://software.broadinstitute.org/morpheus/). A summary of some of the previously identified mutations inherent to the eight cell lines is provided in Appendix xiii.

4.4.1.2 Transcript expression of VGLL1 and TEAD transcription factor genes in bladder cancer cell lines

Five of the eight bladder cancer cell lines examined displayed an increased expression of *VGLL1* transcript compared to the mean expression observed in normal urothelium *in situ*, including the luminal-derived RT4, RT112 and UM-UC-9 cell lines, in addition to the HT1197 and HT1376 cell lines that displayed both luminal and basal MIBC characteristics (Fig. 4.2). Conversely, expression of *VGLL1* in basal/squamous-like cell lines 5637 and ScaBer was notably lower in comparison to normal urothelium, while expression in T24 cells was absent. Similarly to normal urothelium, expression of *TEAD1* and *TEAD3* remained the predominantly expressed TEAD genes in RT4, RT112, UM-UC-9, HT1197 and HT1376 cells. However, increased expression of *TEAD2* and *TEAD4* was observed in all (*TEAD4*) or the majority (*TEAD2*) of cell lines when compared to the previously low expression observed in normal urothelium, highlighting a hitherto unknown induction of these genes in MIBC.

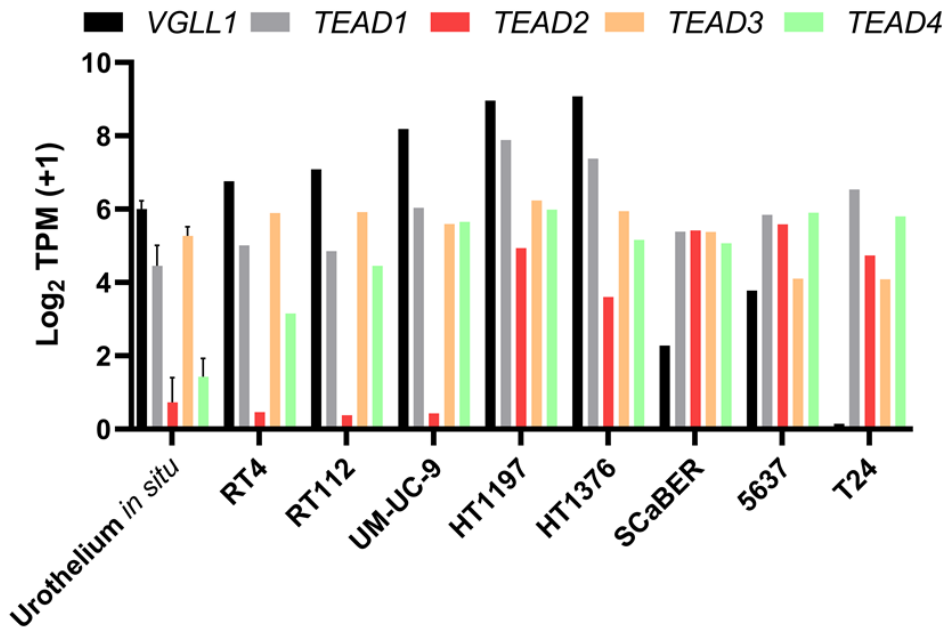

Figure 4.2: *VGLL1* and all four TEAD genes are expressed by bladder cancer cell lines

RNAseq data analysis of *VGLL1*, *TEAD1*, *TEAD2*, *TEAD3* and *TEAD4* gene expression in eight bladder cancer cell lines and normal urothelium *in situ* (n=3 independent samples). Gene expression is measured in Transcripts per Million mapped reads (TPM), with TPM values Log_2 transformed to allow for greater visualisation of the data.

4.4.1.3 Comparison of VGLL1 to YAP/TAZ target gene expression in bladder cancer cell lines

Analysis of various YAP/TAZ target genes in bladder cancer cell lines determined that expression was either consistent (*CYR61*) or decreased (*ANKRD1, AXL, CTGF*) in luminal-derived cell lines RT4, RT112 and UM-UC-9 when compared to normal urothelium *in situ* (Fig. 4.3). In comparison, cell lines with low *VGLL1* expression (ScaBer, 5637, T24) were found to exhibit higher expression of all four genes, including the normally absent *ANKRD1*. This descriptive analysis therefore identified a trend whereby the majority of bladder cancer cell lines that exhibited overexpression of YAP/TAZ target genes in comparison to normal urothelium (*i.e.* basal/squamous-like or other high grade MIBC cell lines) were additionally found to have reduced (or absent) expression of *VGLL1*. However, this pattern was not replicated in HT1197 cells, which exhibited overexpression of both *VGLL1* and all four YAP/TAZ target genes in comparison to normal urothelium.

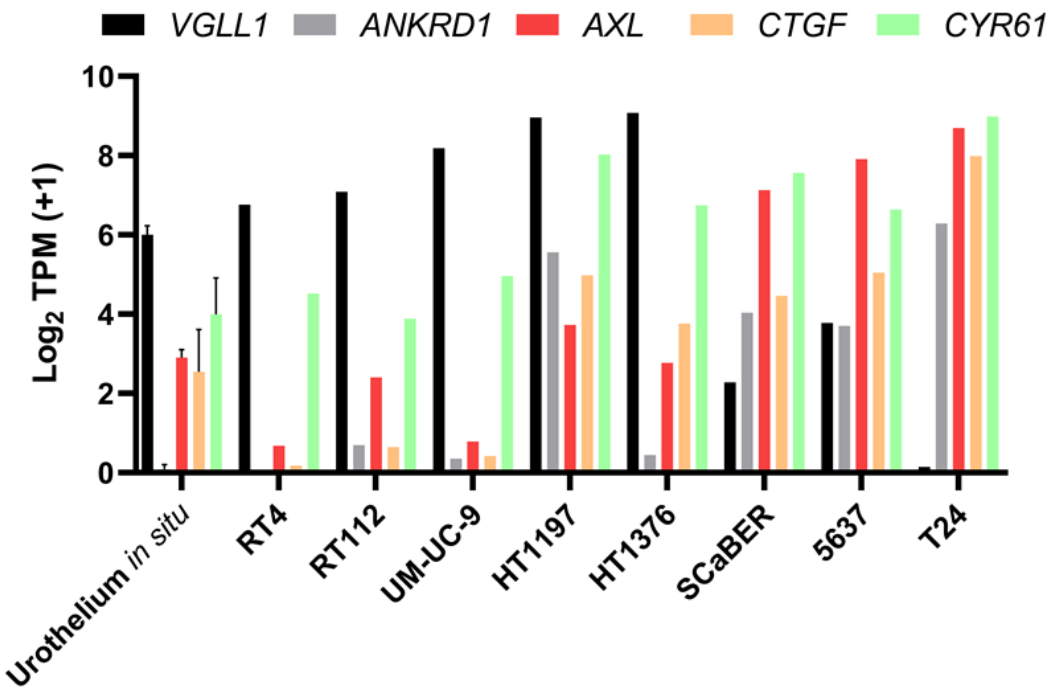

Figure 4.3: Low expression of *VGLL1* corresponds with high expression of YAP/TAZ target genes in basal/squamous-like bladder cancer cell lines

RNAseq data analysis of *VGLL1* expression compared to that of previously cited YAP/TAZ target genes *ANKRD1*, *AXL*, *CTGF* and *CYR61* in eight bladder cancer cell lines and normal urothelium *in situ* (n=3 independent samples). TPM values were Log_2 transformed for clarity.

4.4.2 VGLL1 protein expression in bladder cancer cell lines

Expression of VGLL1 protein in six of the previously assayed bladder cancer cell lines (alongside lysate from normal urothelium *in situ*) was analysed by immunoblotting. The assay confirmed high expression of VGLL1 in UM-UC-9, HT1376 and RT4 cells, alongside a relatively low (ScaBer, 5637) or absent (T24) expression of VGLL1 protein in the high grade MIBC cell lines compared to normal urothelium (Fig. 4.4). Based on the previous overall results, it was therefore concluded that ScaBer, 5637 and T24 cells would make suitable candidates to study the effects of VGLL1 overexpression on bladder cancer cell phenotype.

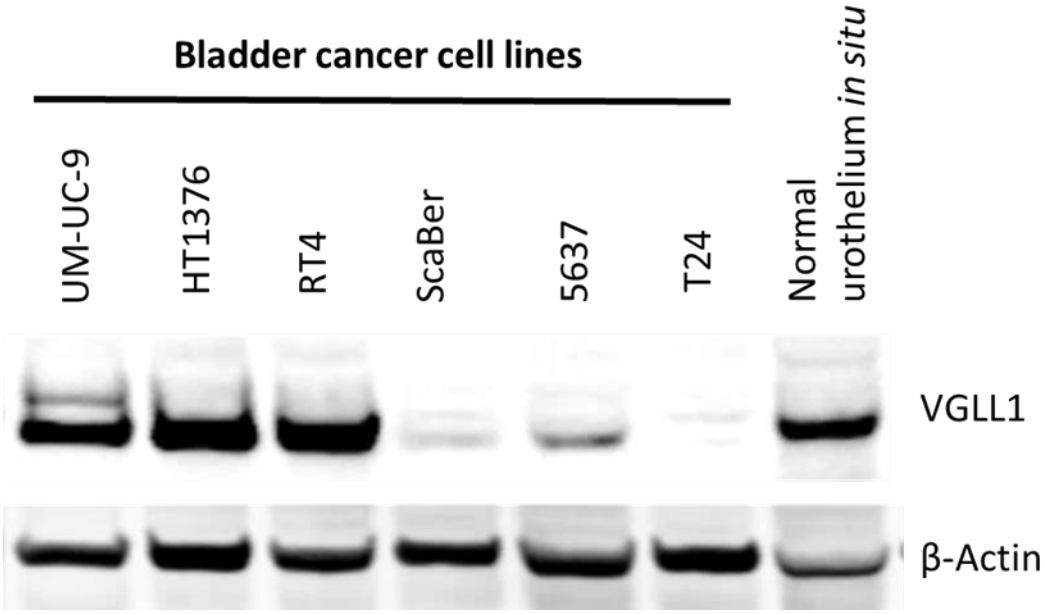

Figure 4.4: VGLL1 protein expression is low in basal/squamous MIBC-like bladder cancer cell lines

Immunoblotting image of VGLL1 expression in six bladder cancer cell lines compared to lysate from freshly isolated (normal) Y2414 urothelium. Expression of β-Actin was used to confirm equal loading of samples.

4.4.3 Generation and verification of stable transfected VGLL1-overexpressing bladder cancer cell lines

Following identification of 5637, T24 and ScaBer as 'VGLL1-low' bladder cancer cell lines, the three lines were transfected with pLXSN-VGLL1 overexpressing retroviral particles (constructs generated as described in Appendix ix) and maintained in 100 µg/mL G418 to select for transfected cells (Fig. 4.5A). Overexpression of *VGLL1* transcript in all three cell lines was confirmed by qRT-PCR, with 5637 and ScaBer exhibiting a 50 and 22 fold change increase in expression, respectively, while T24 cells exhibited a 179,906 fold increase in expression due to the near absence of transcript in the corresponding control cells (Fig. 4.5B). Immunoblotting analysis of the three transfected cell lines subsequently confirmed overexpression of VGLL1 at the protein level (Fig. 4.5C).

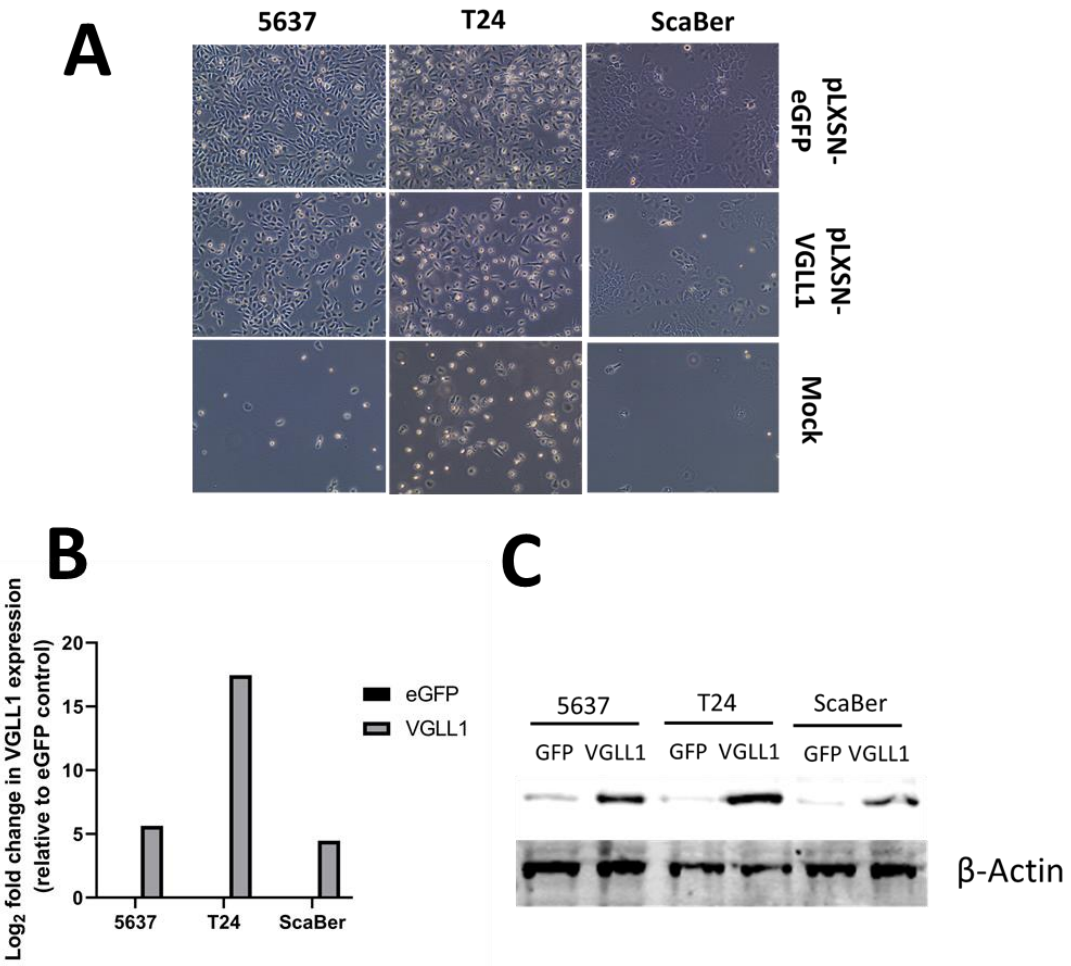

Figure 4.5: Overexpression of VGLL1 in VGLL1-low bladder cancer cell lines transfected with pLXSN-VGLL1 retrovirus

Bladder cancer cell lines 5637, T24 and ScaBer were transfected with pLXSN-GFP or pLXSN-VGLL1 and positive cells selected for through maintenance in antibiotic-containing medium. Panel (**A**) depicts phase micrograph images of the aforementioned cells taken 4 days (T24) or 6 days (5637, ScaBer) following the initiation of antibiotic selection. The mock-transduced controls demonstrated the efficacy of G418 administration on untransduced cells, which remained under antibiotic selection until complete death of the cell line was observed. **B)** Following selection, transfected cell lines were lysed and qRT-PCR analysis of *VGLL1* expression was used to confirm overexpression of the gene in all three lines. Differences between cell lines were displayed as a Log_2 fold change in *VGLL1* expression (normalised against *GAPDH*) compared to each corresponding eGFP control cell line. **C)** Immunoblot analysis of VGLL1 expression in 5637, T24 and ScaBer cells transfected with pLXSN-eGFP or pLXSN-VGLL1. Expression of β-Actin was used to confirm equal loading of samples.

4.4.4 Modulation of YAP/TAZ signalling in VGLL1-overexpressing bladder cancer cell lines

4.4.4.1 Phosphorylated YAP expression in VGLL1-overexpressing bladder cancer cell lines

To determine whether overexpression of VGLL1 influenced the proportion of inactive, phosphorylated YAP in VGLL1-low, YAP/TAZ signalling-high bladder cancer cell lines, transfected 5637 and ScaBer cells were lysed and analysed by immunoblotting. Despite confirmation that both cell lines experienced an induction of VGLL1 protein when transfected with pLXSN-VGLL1, no change in the expression of the total or phosphorylated forms of YAP was observed (Fig. 4.6).

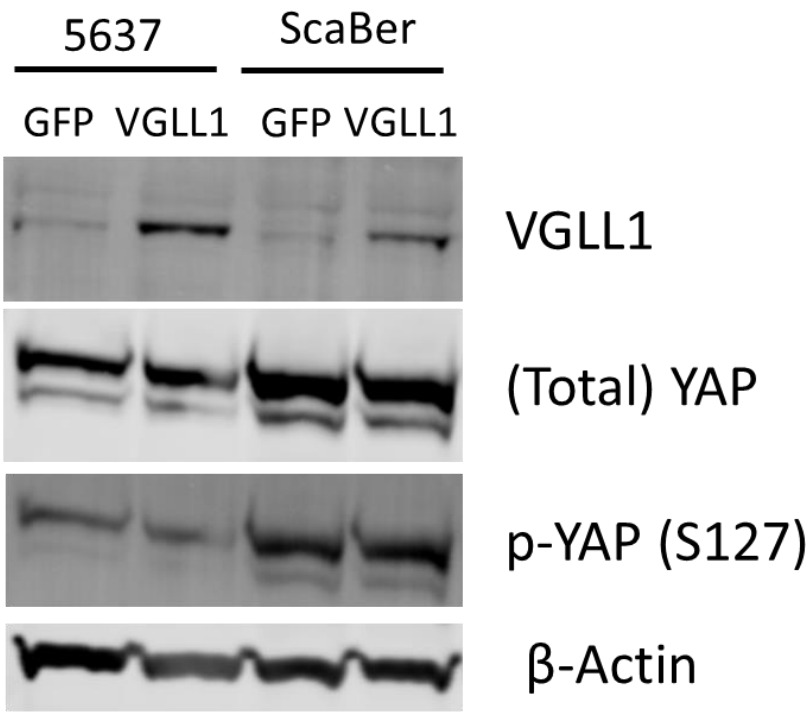

Figure 4.6: Overexpression of VGLL1 had no effect on total or phosphorylated expression of YAP in 5637 and ScaBer cells

Immunoblot analysis of VGLL1, total YAP and phosphorylated YAP (S127) expression in n=2 MIBC cell lines (5637 and ScaBer) overexpressing VGLL1 or eGFP. This experiment was performed prior to the generation and propagation of VGLL1 and eGFP-overexpressing T24 cells, and as such was not included in the immunoblot. Expression of β-Actin was used to confirm equal loading of samples.

4.4.4.2 Localisation of YAP in VGLL1-overexpressing bladder cancer cell lines

The localisation of total YAP has previously been demonstrated to be sensitive to variables such as treatment with PD153035 in NHU cells (Section 3.4.6.4). The sub-cellular localisation of total YAP in 5637, T24 and ScaBer cells was thus compared between pLXSN-eGFP and pLXSN-VGLL1 transfected cells by immunofluorescence. In pLXSN-eGFP control cells, total YAP expression was observed to be solely nuclear in 5637 and T24 cells, while exhibiting nuclear and cytoplasmic expression in ScaBer cells (Fig. 4.7A). No notable changes in the localisation of YAP was observed in any of the three cell lines transfected with pLXSN-VGLL1, although the relative intensity of nuclear (total) YAP did appear reduced in T24 cells in comparison to control.

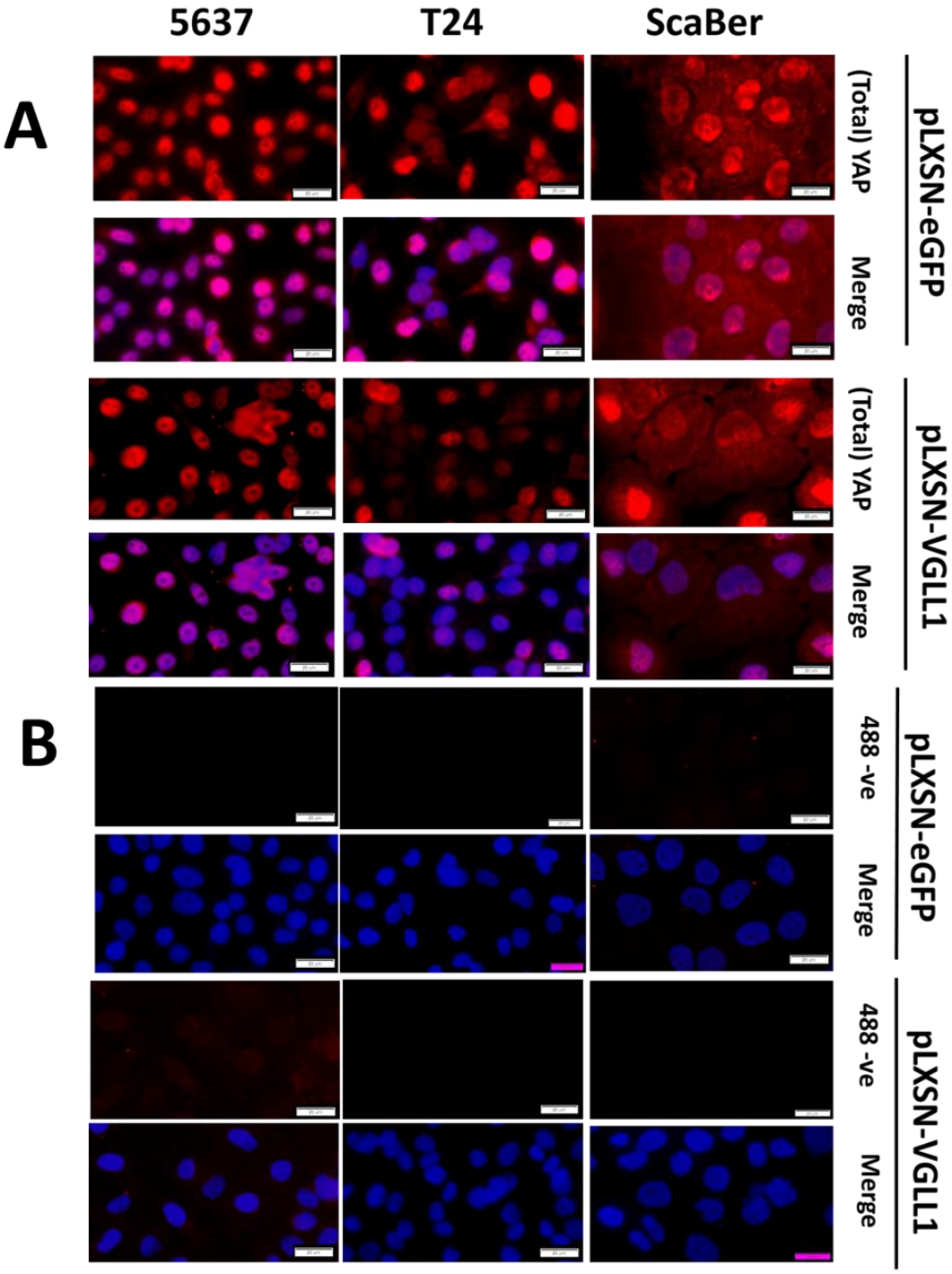

Figure 4.7: Overexpression of VGLL1 had no effect on the subcellular localisation of YAP in VGLL1-low bladder cancer cell lines

MIBC cell lines overexpressing VGLL1 or eGFP (5637, T24 and ScaBer) were seeded onto glass slides, fixed using formalin and Triton X-100 permeabilised. Cells were subsequently labelled with Total YAP antibody (**A**) or received no primary antibody (**B**) before visualisation. Images were all taken at same exposure and are shown with or without overlaid Hoechst 33258 DNA staining. Scale bar= 20µm.

4.4.4.3 YAP/TAZ target gene transcript expression in VGLL1-overexpressing bladder cancer cell lines

Transcript expression of markers of YAP/TAZ signalling was quantified in the transfected cell lines to determine whether expression was affected by VGLL1 overexpression. Of the cell lines and gene targets assayed, only *ANKRD1* (2.31 fold increase in T24 cells only) and *CTGF* (2.54 fold decrease in 5637 cells only) expression was observed to change between control and VGLL1 overexpressing cell lines, with no gene found to be significantly altered between conditions (Fig. 4.8). Overall, the results of this section demonstrate a negligible effect of VGLL1 overexpression on YAP/TAZ signalling in VGLL1-low bladder cancer cell lines, with no change observed in the localisation of YAP in addition to weak, inconsistent modulation of YAP/TAZ target genes.

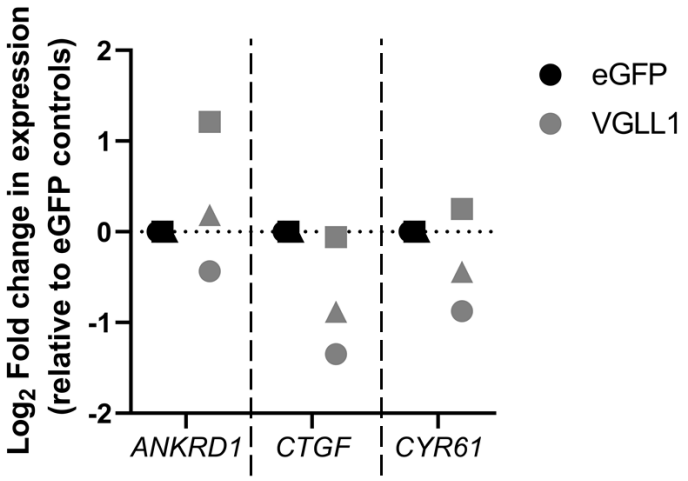

Figure 4.8: Overexpression of VGLL1 had no effect on transcript expression of YAP/TAZ target genes in VGLL1-low bladder cancer cell lines

RT-qPCR analysis of *ANKRD1, CTGF* and *CYR61* expression in n=3 MIBC cell lines (5637, T24 and ScaBer) overexpressing VGLL1 or eGFP control. The primers purchased specific to *AXL* did not produce a singular product during the initial quality control assessment and therefore were not used in the subsequent RT-qPCR analysis. Circle icons represent 5637 samples, square icons represent T24 samples and triangle icons represent ScaBer samples. Differences between conditions were displayed as a Log_2 fold change in expression compared to each corresponding eGFP control, with expression of each target gene normalised against housekeeping gene *GAPDH*. Significance between groups was calculated using a two-way ANOVA with Sidak's post-hoc test.

4.4.5 Modulation of proliferation-associated pathways in VGLL1-overexpressing bladder cancer cell lines

4.4.5.1 *EGFR* and *MKI67* transcript expression in VGLL1-overexpressing cell lines

To ascertain whether overexpression of VGLL1 affected the same signalling pathways in bladder cancer cell lines as to what was previously observed in NHU cells (Section 3.4.8), expression of *EGFR* and *MKI67* in transfected 5637, ScaBer and T24 cells was analysed by non-quantitative RT-PCR. Similar to the phenotype observed in undifferentiated NHU cells, expression of *EGFR* and *MKI67* appeared reduced in T24 cells overexpressing VGLL1 compared to control (Fig. 4.9). In comparison, VGLL1-overexpressing ScaBer cells appeared to have reduced expression of *MKI67*, but not *EGFR*, while expression of both genes appeared to be consistent between 5637 conditions.

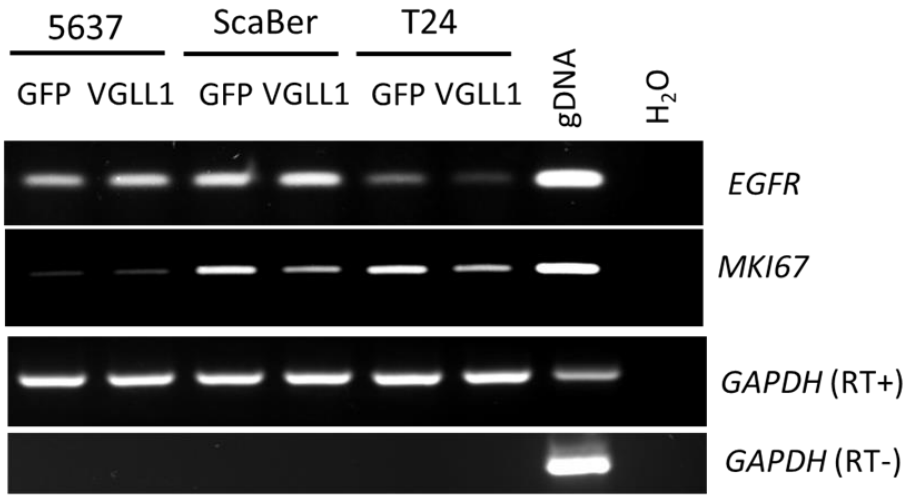

Figure 4.9: Overexpression of VGLL1 resulted in reduced transcript expression of *EGFR* and *MKI67* in T24 cells

RT-PCR analysis of *EGFR* and *MKI67* transcript expression in n=3 MIBC cell lines (5637, ScaBer and T24) transfected with VGLL1 or eGFP control overexpression constructs. Each cDNA synthesis used 1 µg starting template RNA, with cDNA undergoing PCR amplification up to 27 cycles. Housekeeping gene *GAPDH* was used to confirm equal loading between samples (25 cycles). The primers used produced positive gDNA bands of the same size, while a no template (H_2O only) sample was used as a negative control for each primer set.

4.4.5.2 EGFR/ERK and PI3K/AKT signalling in VGLL1-overexpressing cell lines

To elucidate what signalling pathways downstream of EGFR were being affected by VGLL1 overexpression, immunoblotting of transfected bladder cancer cell lines (lysed in a sub-confluent state) was performed. No change in the expression of the total or phosphorylated forms of EGFR was found between 5637 and ScaBer conditions, while expression of neither protein was observed in T24 cells (Fig. 4.10). Expression of total ERBB2 remained unchanged between all conditions, while modulation of p-ERK1/2 appeared to be cell-line dependent, as 5637 cells exhibited a slight increase in p44 expression while T24 cells had slightly decreased p44 when overexpressing VGLL1. Of the three cell lines assayed, only VGLL1-overexpressing T24 cells were found to inhibit phosphorylated AKT expression compared to control, replicating the phenotype observed in proliferating, undifferentiated NHU cells overexpressing VGLL1 (Section 3.4.8.3).

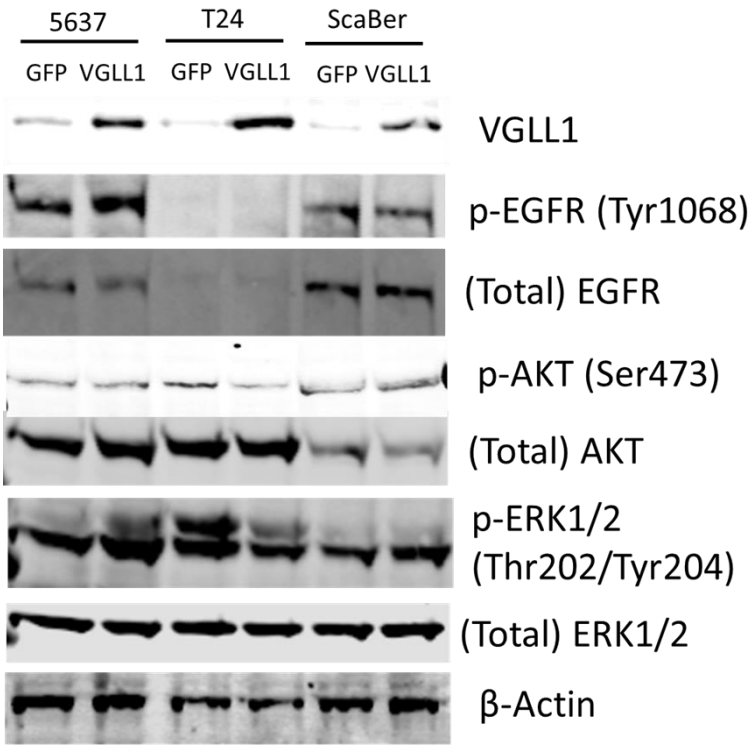

Figure 4.10: Inhibition of p-AKT expression in VGLL1-overexpressing T24 cells

Immunoblotting analysis of n=3 MIBC cell lines (5637, T24 and ScaBer) transfected with either VGLL1 or eGFP overexpressing constructs. Cell lines were compared based on their expression of VGLL1, EGFR (total and phosphorylated forms), total ERBB2, AKT (total and phosphorylated expression) and ERK1/2 (total and phosphorylated forms). Expression of β-Actin was used to confirm equal loading of samples.

4.4.5.3 Ki67 activity in VGLL1-overexpressing cell lines

Expression of the cell cycle marker Ki67 was visualised in the three transfected bladder cancer cell lines by immunofluorescence. Comparison between the respective pLXSN-eGFP and pLXSN-VGLL1 transfected cells revealed little difference in the expression of Ki67 in 5637 (widespread positivity) and ScaBer (scattered positivity) cells (Fig. 4.11). However, overexpression of VGLL1 in T24 cells resulted in a notable reduction in Ki67 expression when compared to the eGFP control, suggestive of a reduction in cell proliferation.

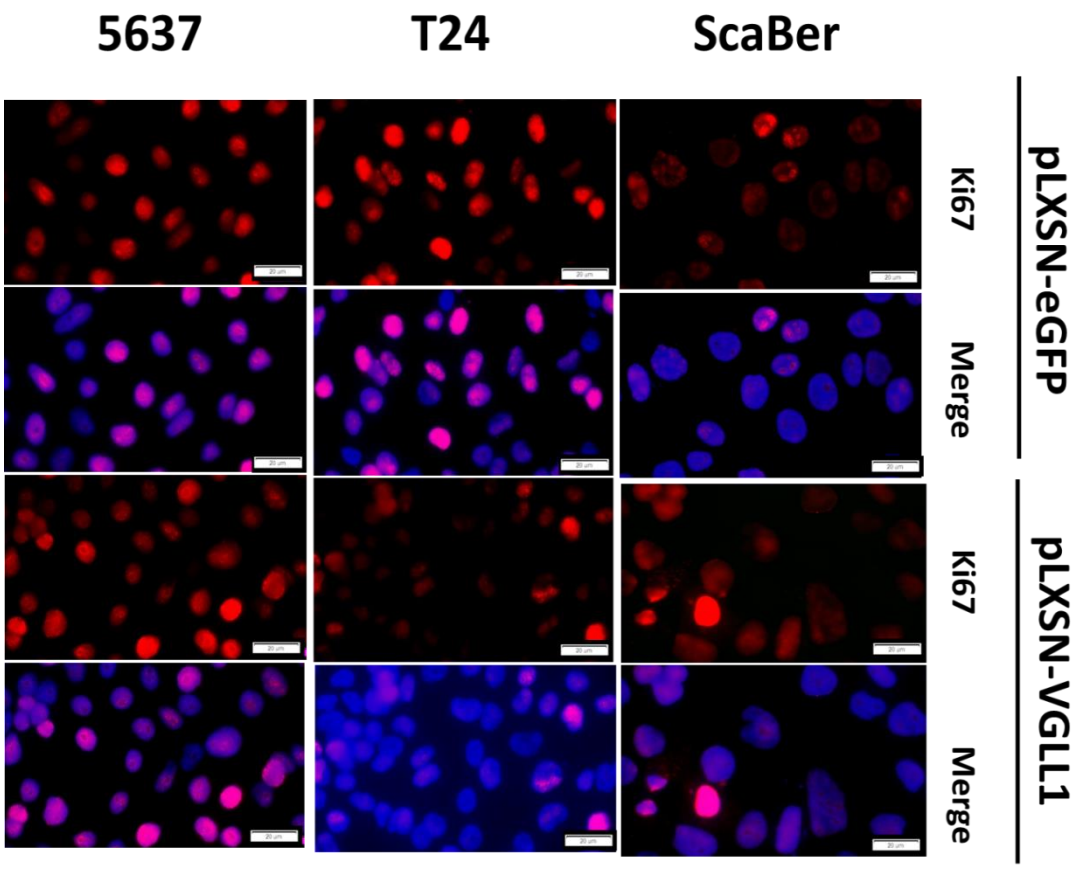

Figure 4.11: Overexpression of VGLL1 reduces Ki67 positivity in T24 cells

The 5637, T24 and ScaBer transfected cell lines used in Figure 4.7 were additionally assayed by immunofluorescence to determine cell cycle activity following VGLL1 overexpression. Cells were labelled with an antibody specific to Ki67 prior to visualisation. Cell lines receiving no primary antibody were used as negative controls, images of which can be found in Figure 4.7B. Images were all taken at same exposure and are shown with or without overlaid Hoechst 33258 DNA staining. Scale bar= 20µm.

4.4.6 Cell cycle analysis of VGLL1-overexpressing bladder cancer cell lines

Following the results of the previous section, transfected T24 cells (n=3 independent experiments) were BrdU pulsed to determine whether the reduced cell cycle activity observed in VGLL1-overexpressing cells was reflected in the proportion of S-phase positive cells in the population. Fixed, BrdU-pulsed cells were processed by flow cytometry and gated to exclude cellular debris and doublet events (Fig. 4.12A-B). Analysis of BrdU fluorescence in the gated events determined that VGLL1-overexpressing T24 cells had a significantly higher proportion of cells in G0/G1 phase and a corresponding significant reduction of cells in S phase when compared to eGFP control (Fig. 4.12C-F; $p \leq 0.05$).

Conversely, processing of transfected 5637 cells (n=2 independent experiments) in the same manner revealed no significant differences in the proportion of G0/G1 or S-phase populations of pLXSN-eGFP and pLXSN-VGLL1 cell lines (Fig. 4.13A-F). Overall, the results of this (and the preceding) section demonstrate that VGLL1 overexpression had a minimal effect on the phenotype of 5637 and ScaBer cells. In comparison, transfected T24 cells shared similarities in phenotype to that observed with VGLL1-overexpressing undifferentiated NHU cells in terms of inhibition of AKT signalling and a reduction in cell cycle activity.

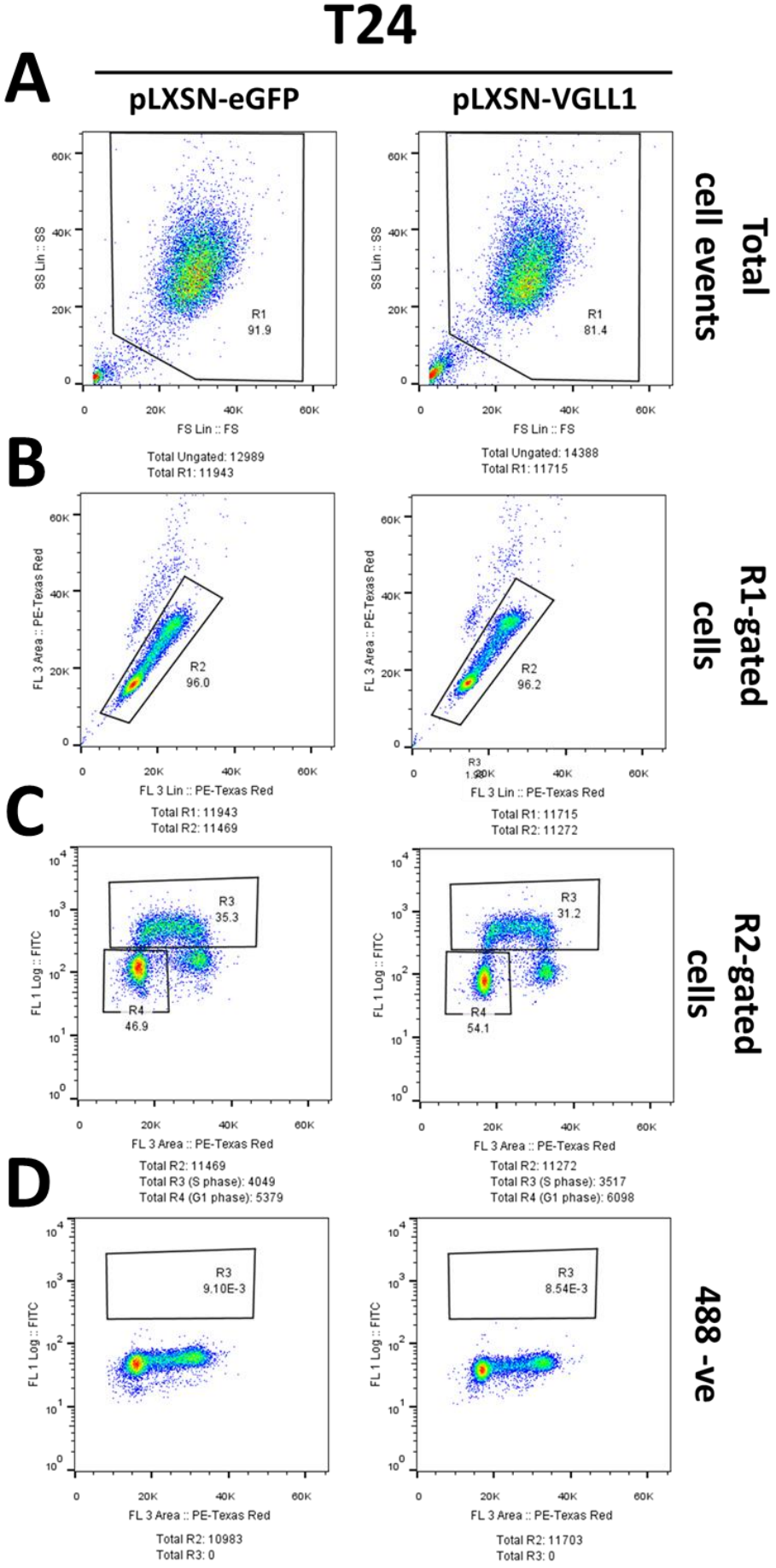
T24
A
pLXSN-eGFP
pLXSN-VGLL1
Total cell events
SS Lin :: SS
FS Lin :: FS
R1
91.9
R1
81.4
Total Ungated: 12989
Total R1: 11943
Total Ungated: 14388
Total R1: 11715
B
R1-gated cells
FL 3 Area :: PE-Texas Red
FL 3 Lin :: PE-Texas Red
R2
96.0
R2
96.2
Total R1: 11943
Total R2: 11469
Total R1: 11715
Total R2: 11272
C
R2-gated cells
FL 1 Log :: FITC
R3
35.3
R4
46.9
R3
31.2
R4
54.1
Total R2: 11469
Total R3 (S phase): 4049
Total R4 (G1 phase): 5379
Total R2: 11272
Total R3 (S phase): 3517
Total R4 (G1 phase): 6098
D
488 -ve
R3
9.10E-3
R3
8.54E-3
Total R2: 10983
Total R3: 0
Total R2: 11703
Total R3: 0

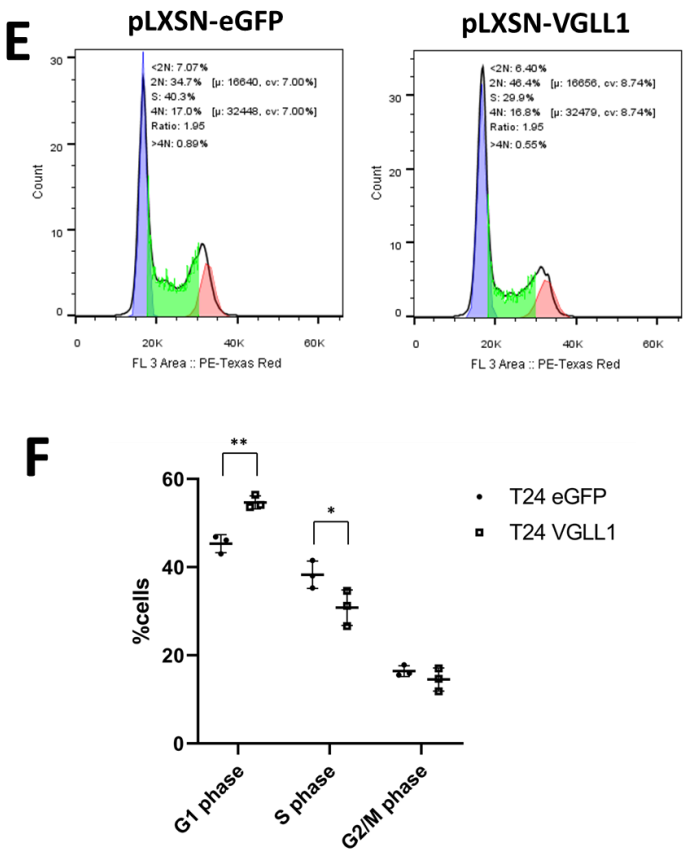

Figure 4.12: VGLL1 overexpression resulted in G0/G1 arrest in T24 cells

T24 cells (n=3) transfected with either eGFP or VGLL1 overexpression constructs were pulsed with BrdU for 1h before trypinisation and fixation with ethanol. Single cells were subsequently labelled with a BrdU-specific primary (and GaM 488 secondary) antibody and fluorescence detected by flow cytometry. **A)** Representative forward versus side scatter (FS Lin vs SS Lin, respectively) dot plots of samples, with relevant populations gated (gate R1). **B)** Propidium iodide scatter (PE-Texas Red Lin vs PE-Texas Red Area) plots of R1-gated events, with relevant populations gated (gate R2). **C)** Propidium iodide versus BrdU scatter (PE-Texas Red Area vs FITC Log, respectively) plots of R2-gated events. This plot was used to determine the percentage of cells in S (R3 gate) and G0/G1 phase (R4 gate) in each sample. **D)** Propidium iodide versus BrdU scatter plots of R2-gated events from samples that were antibody labelled but received no BrdU pulse. **E)** Representative propidium iodide cell cycle profile histograms of each condition. **F)** The percentage of T24 cells in G1, S and G2/M phase (as determined by BrdU fluorescence) were recorded across three separate experiments and quantified. Significance between groups was calculated using a two-way ANOVA with Sidak's post-hoc test. *=p≤0.05; **=p≤0.01. The propidium iodide versus BrdU scatter plots of the two replicate experiments can be found in Appendix xiii.

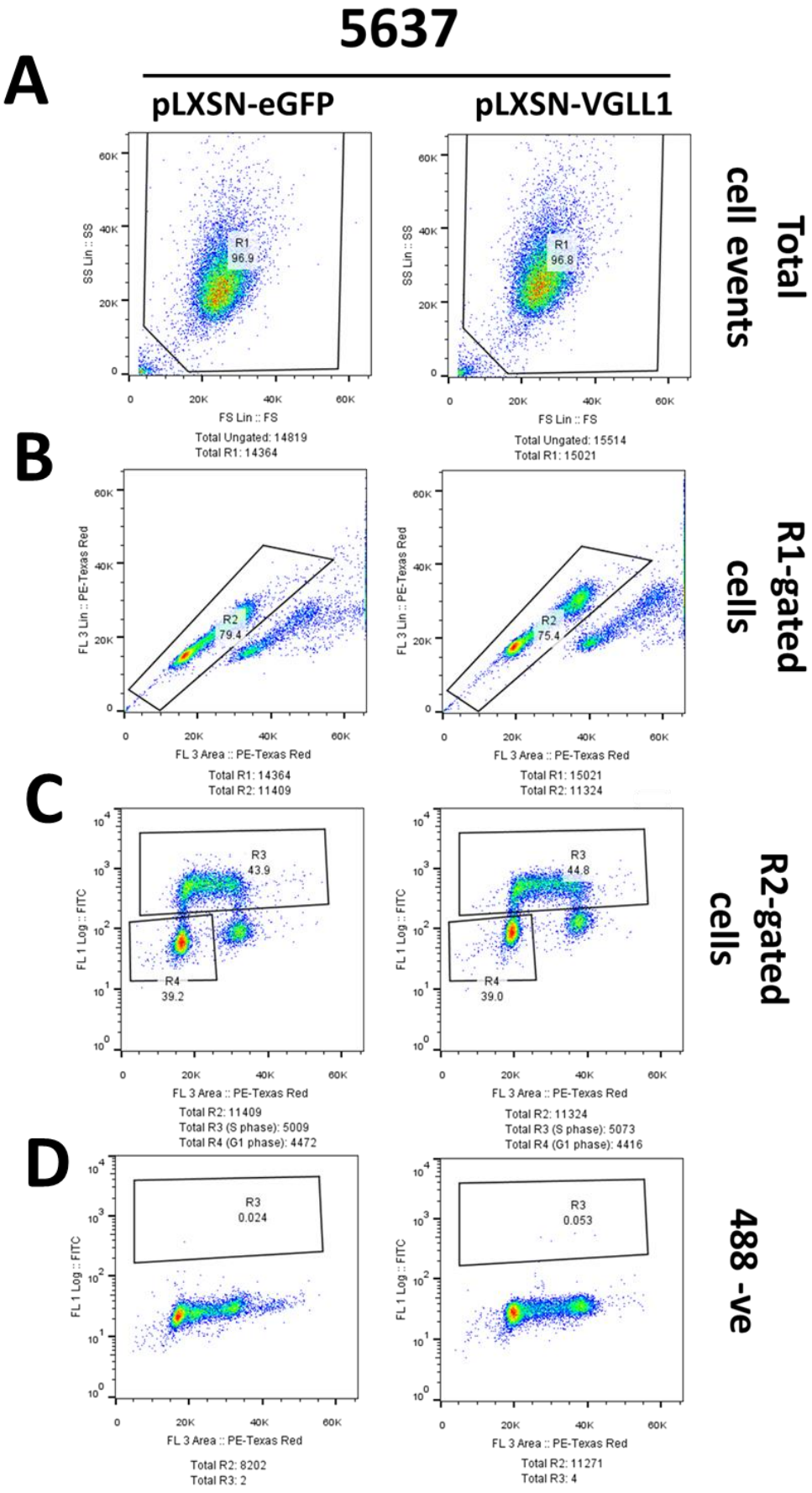
5637
A
pLXSN-eGFP
pLXSN-VGLL1
Total cell events
SS Lin :: SS
FS Lin :: FS
R1
96.9
96.8
Total Ungated: 14819
Total R1: 14364
Total Ungated: 15514
Total R1: 15021
B
R1-gated cells
FL 3 Lin :: PE-Texas Red
FL 3 Area :: PE-Texas Red
R2
79.4
75.4
Total R1: 14364
Total R2: 11409
Total R1: 15021
Total R2: 11324
C
R2-gated cells
FL 1 Log :: FITC
R3
43.9
44.8
R4
39.2
39.0
Total R2: 11409
Total R3 (S phase): 5009
Total R4 (G1 phase): 4472
Total R2: 11324
Total R3 (S phase): 5073
Total R4 (G1 phase): 4416
D
488 -ve
R3
0.024
0.053
Total R2: 8202
Total R3: 2
Total R2: 11271
Total R3: 4

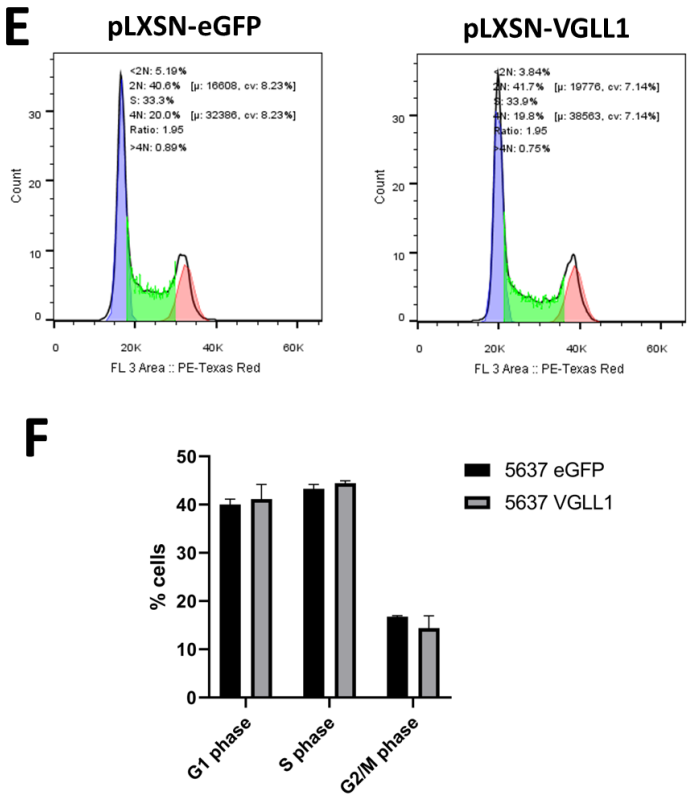

Figure 4.13: VGLL1 overexpression had a negligible effect on the cell cycle profile of 5637 cells

Flow cytometry analysis of 5637 cells (n=2) transfected with either eGFP or VGLL1 overexpression constructs. Cells were pulsed with BrdU for 1h before trypinisation, fixation with ethanol and labelling with BrdU primary and 488 GaM secondary antibodies. **A)** Representative forward versus side scatter (FS Lin vs SS Lin, respectively) dot plots of samples, with relevant populations gated (gate R1). **B)** Propidium iodide scatter (PE-Texas Red Lin vs PE-Texas Red Area) plots of R1-gated events, with relevant populations gated (gate R2). **C)** Propidium iodide versus BrdU scatter (PE-Texas Red Area vs FITC Log, respectively) plots of R2-gated events. This plot was used to determine the percentage of cells in S (R3 gate) and G1 phase (R4 gate) in each sample. **D)** Propidium iodide versus BrdU scatter plots of R2-gated events from samples that were antibody labelled but received no BrdU pulse. **E)** Representative propidium iodide cell cycle profile histograms of each condition. **F)** The percentage of 5637 cells in G0/G1, S and G2/M phase (as determined by BrdU fluorescence) were recorded across two separate experiments and quantified. Significance between conditions was calculated using a two-way ANOVA with Sidak's post-hoc test, with no significant differences found between the percentages of cells found in different phases of the cell cycle. The propidium iodide versus BrdU scatter plots of the replicate experiment can be found in Appendix xiii.

4.4.7 *VGLL1* expression in MIBC

4.4.7.1 Transcriptomic analysis of Hippo pathway components in MIBC subtypes

Expression of *VGLL1* transcript was assessed in TCGA MIBC cohort of tumour samples, with each tumour stratified into one of six consensus molecular subtypes. Compared to expression of in-house sequenced, stroma-free normal urothelium *in situ*, no significant differences in *VGLL1* expression was observed in any of the subtypes apart from luminal unstable, which was found to have significantly higher expression of the gene ($p \leq 0.05$; Fig. 4.14). Despite not exhibiting a significant difference in expression to normal urothelium, basal/squamous tumours were found to have significantly reduced expression of *VGLL1* when compared to each luminal subtype ($p \leq 0.001$). The basal/squamous subtype displayed a wide range of *VGLL1* expression, as it contained three of the ten highest *VGLL1* TPM values in the MIBC cohort yet also included a group of tumours with very low or absent expression of the gene. Five of the six tumours of the neuroendocrine-like subtype were found to have very low/absent *VGLL1* expression, although due to the low sample number this difference in expression was not significant. This analysis therefore suggested that apart from a subset of basal/squamous and neuroendocrine-like tumours, expression of *VGLL1* was primarily retained in cases of MIBC.

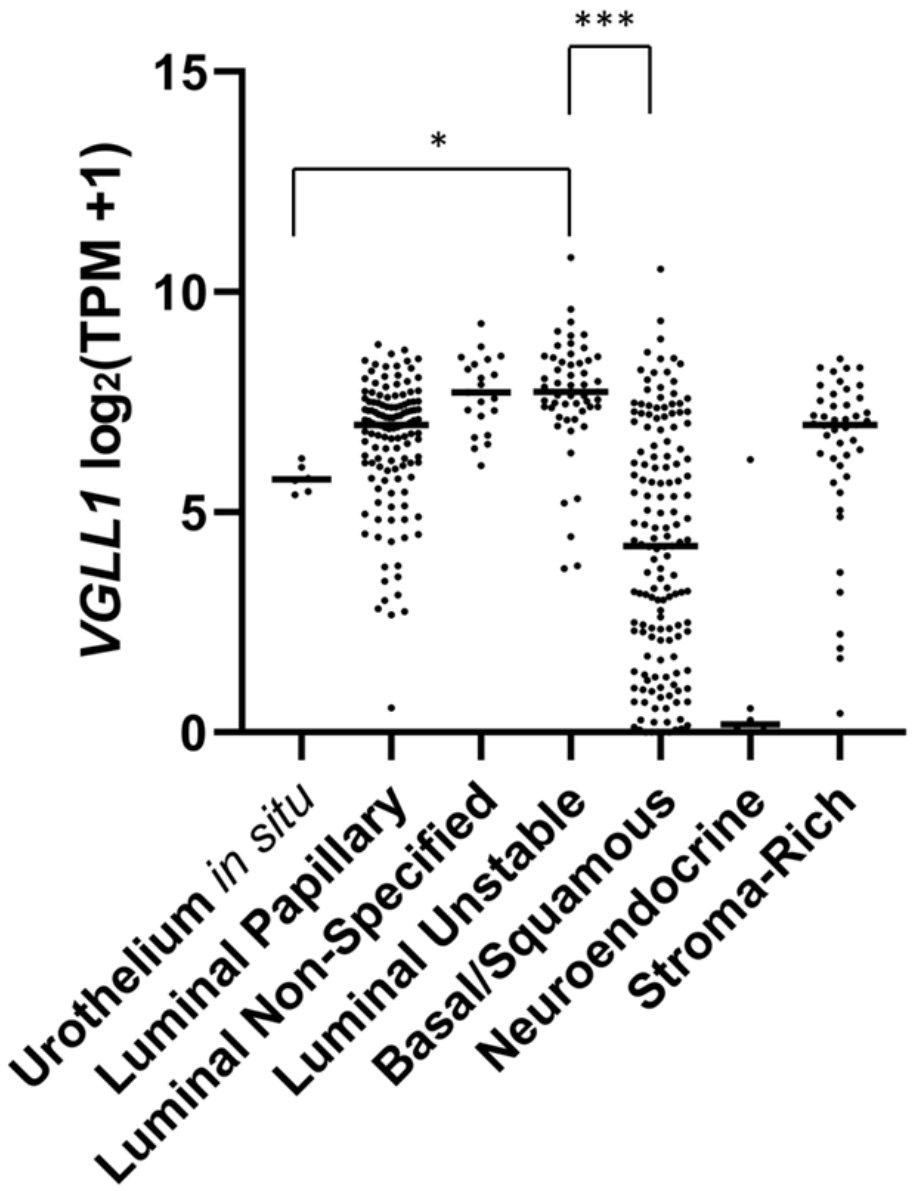

Figure 4.14: *VGLL1* expression is retained in a majority of MIBC tumours

RNAseq gene expression data from TCGA MIBC cohort (n=404) was separated into the consensus molecular subtypes based on previously published (Kamoun *et al.* 2020) gene classification and compared to normal urothelium *in situ* samples processed in-house (n=6). Gene expression is displayed as Log_2 transformed TPM, with the bars representing the median TPM value for each subtype. Significance between groups was determined by a Kruskal-Wallis ANOVA with Dunn's multiple comparisons post-hoc test. *=p≤0.05; ***=p≤0.001. Other significant changes between groups were omitted for clarity and are detailed in Appendix xiii.

The results of Section 4.4.4 suggested that an inhibitory relationship between VGLL1 expression and YAP/TAZ signalling did not exist in MIBC. To examine the possibility that VGLL1 and YAP/TAZ associated with different TEAD transcription factors in urothelium, a principal component analysis of TCGA cohort (separated into molecular subtypes) with transcript expression of *VGLL1* in addition to *YAP1*, *WWTR1*, YAP/TAZ downstream target genes and TEAD genes was performed. The variance in the data was primarily split (PC1; 40.1%) between samples of luminal and basal origin, with *VGLL1* expression associated with tumours of primarily luminal derivation (Fig. 4.15). Conversely, expression of *YAP1* and YAP/TAZ signalling markers *AXL*, *ANKRD1*, *CTGF* and *CYR61* were associated with a mixture of basal/squamous and stroma-rich tumours. Expression of the two TEAD transcription factors also found in normal urothelium, namely *TEAD1* and *TEAD3*, were found to align separately to the two aforementioned tumour groups, with *TEAD3* aligning with *VGLL1* and *TEAD1* correlated with *YAP1* and YAP/TAZ target gene expression. This finding supported the assertion that VGLL1 and YAP possibly bind to different TEAD transcription factors in urothelial cells, which would account for the lack of modulation observed in YAP/TAZ signalling when VGLL1 expression was forced in NHU cells (Section 3.4.8; 3.4.10) or basal/squamous MIBC cell lines.

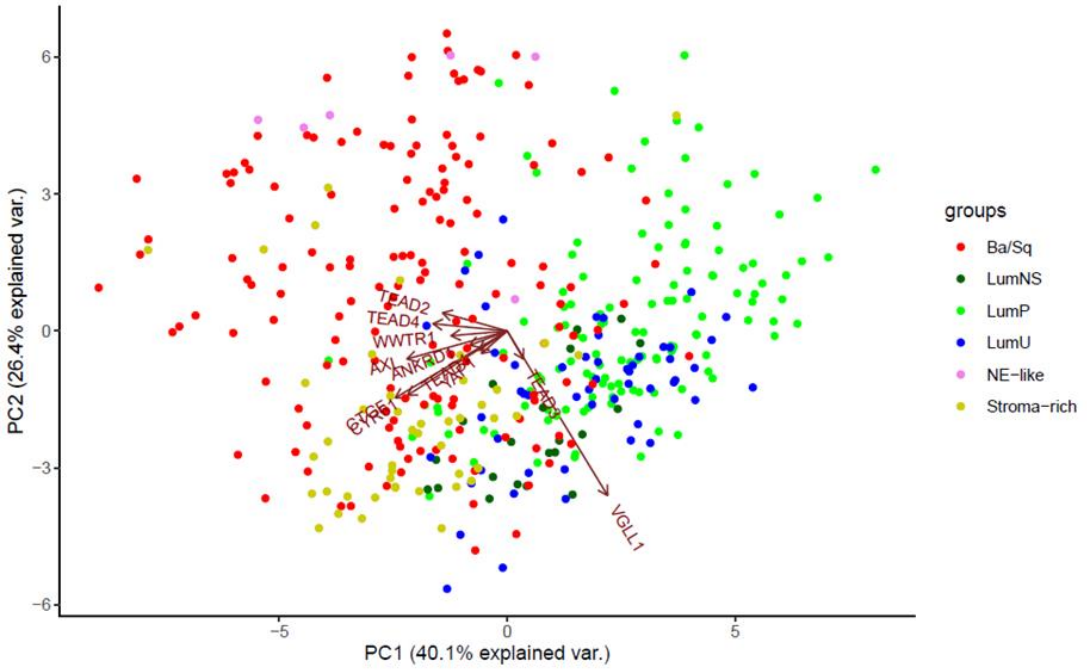

Figure 4.15: *VGLL1* and *YAP1/WWTR1* are associated with different TEAD genes and MIBC molecular subtypes

Unscaled principal component analysis plot of TCGA MIBC samples separated on the basis of expression of *VGLL1*, *YAP1*, *WWTR1,* YAP/TAZ target genes and TEAD genes. Each dot represents a different RNASeq sample while each MIBC consensus molecular subtype is represented by a different icon colour.

To elucidate what genes could potentially be induced through VGLL1-mediated TEAD3 transcriptional activity, analysis of genes in MIBC that were positively correlated to both *VGLL1* and *TEAD3* expression was performed. 247 genes were found to have a Pearson correlation coefficient ≥ +0.35 with either *VGLL1* or *TEAD3*, while 35 of those genes were revealed to be positively correlated to both *VGLL1* and *TEAD3* (Table 4.1). When combining Pearson correlation coefficient scores, the most correlated gene to a combination of *VGLL1* and *TEAD3* (excluding *VGLL1* and *TEAD3*) was *PARD6B*, a gene involved in the regulation of tight junction assembly. Other genes of interest that correlated to both *VGLL1* and *TEAD3* in MIBC included the Ras homolog family member A (RHOA)-interacting factor *PLEKHG6* and the tight junction-localised *CGN* (cingulin). All three genes were confirmed to be expressed by NHU cells, with an induction of expression observed following ABS/Ca^{2+} differentiation for each gene (Fig. 4.16).

Gene	Pearson's *r* (*VGLL1*)	Pearson's *r* (*TEAD3*)	Combined Pearson's *r*
TEAD3	+0.382	+1	1.382
VGLL1	+1	+0.382	1.382
PARD6B	+0.596	+0.465	1.061
PLEKHG6	+0.537	+0.470	1.007
SLC44A2	+0.556	+0.434	0.99
SLC17A5	+0.561	+0.357	0.918
AC108112.1	+0.489	+0.420	0.909
DAG1	+0.536	+0.356	0.892
SPINT1	+0.422	+0.464	0.886
CREB3L2	+0.443	+0.426	0.869
NR2F2	+0.431	+0.438	0.869
SEPT8	+0.484	+0.371	0.855
MSX2	+0.448	+0.405	0.853
CGN	+0.414	+0.434	0.848
SLC37A1	+0.431	+0.406	0.837
GATA2-AS1	+0.406	+0.429	0.835
TMEM214	+0.441	+0.384	0.825
SLC29A3	+0.448	+0.374	0.822
B3GNT3	+0.377	+0.428	0.805
RHOU	+0.436	+0.366	0.802
SLC11A2	+0.431	+0.366	0.797
RBM47	+0.392	+0.396	0.788
TAB3	+0.412	+0.372	0.784
OTUD7B	+0.401	+0.380	0.781
NIPAL1	+0.371	+0.407	0.778
PWWP2B	+0.416	+0.361	0.777
TIGD2	+0.368	+0.405	0.773
TUFT1	+0.390	+0.381	0.771
SOWAHB	+0.383	+0.384	0.767
TTC39A	+0.395	+0.368	0.763
RAB15	+0.396	+0.353	0.749
AC022872.1	+0.388	+0.353	0.741
TMEM62	+0.368	+0.370	0.738
SMAGP	+0.377	+0.356	0.733
AC004982.2	+0.374	+0.356	0.73

Table 4.1: Genes positively correlated to *VGLL1* and *TEAD3* in MIBC

A Pearson correlation coefficient (*r*) was calculated between *VGLL1/TEAD3* and every other gene quantified in TCGA MIBC cohort. Genes that were positively correlated ($r \geq +0.35$) to both *VGLL1* and *TEAD3* were included in the list. *PARD6B* was found to be the gene with the highest combined *r* score in the analysis.

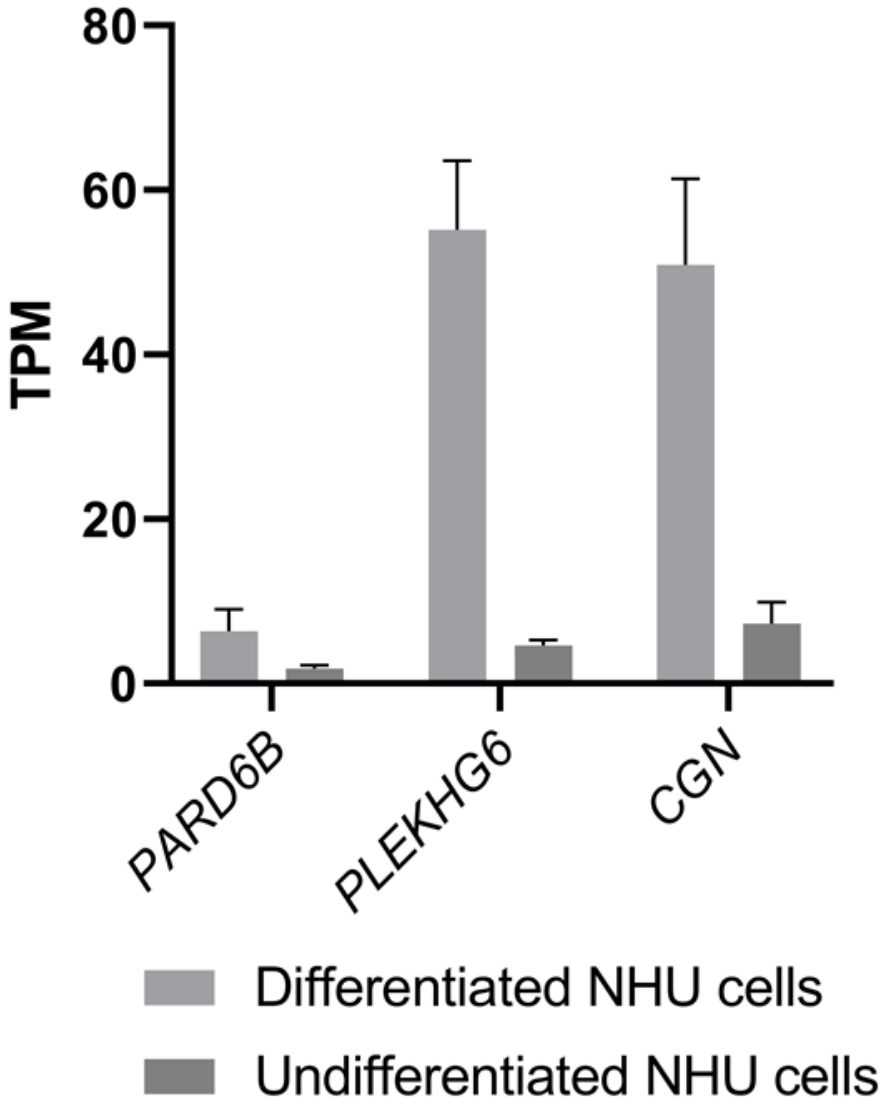

Figure 4.16: Validation of potential VGLL1/TEAD3 target gene expression in NHU cells

RNAseq data analysis of *PARD6B*, *PLEKHG6* and *CGN* transcript expression in NHU cells in undifferentiated and ABS/Ca^{2+} differentiated states (n=3 independent samples).

4.4.7.2 Relationship of *VGLL1* expression to urothelial-associated transcription factors in MIBC

Investigation of VGLL1 expression in normal urothelium previously revealed a close association of *VGLL1* transcript to *FOXA1*, *RARG* and *POUF51* expression in ABS/Ca^{2+} differentiated NHU cells (Section 3.4.1), while GATA3 was additionally implicated as an important upstream transcription factor of VGLL1 in TZ/PD differentiated cells (Section 3.4.5). To analyse what transcription factors most closely correlated to *VGLL1* expression in a MIBC context, a principal component analysis of TCGA cohort was performed, with tumours separated on the basis of expression of *VGLL1* alongside the list of (normal) urothelial-associated transcription factors utilised in Section 3.4.1.3. This analysis revealed that *VGLL1* expression associated with the luminal papillary and luminal unstable subtypes and was highly correlated with *POU5F1* expression, as seen in samples of normal urothelium (Fig. 4.17). In comparison to normal urothelium, expression of *VGLL1* was more closely associated with *GATA3*, *PPARG* and *HNF1B* (genes which had previously associated with both *in situ* and ABS/Ca^{2+} differentiated NHU cells) in luminal MIBC, while expression was less correlated to *FOXA1* and *RARG* expression. Despite being strongly associated with proliferative, undifferentiated NHU cells *in vitro*, *TP63* expression aligned to a mixture of luminal papillary and basal/squamous tumours in MIBC.

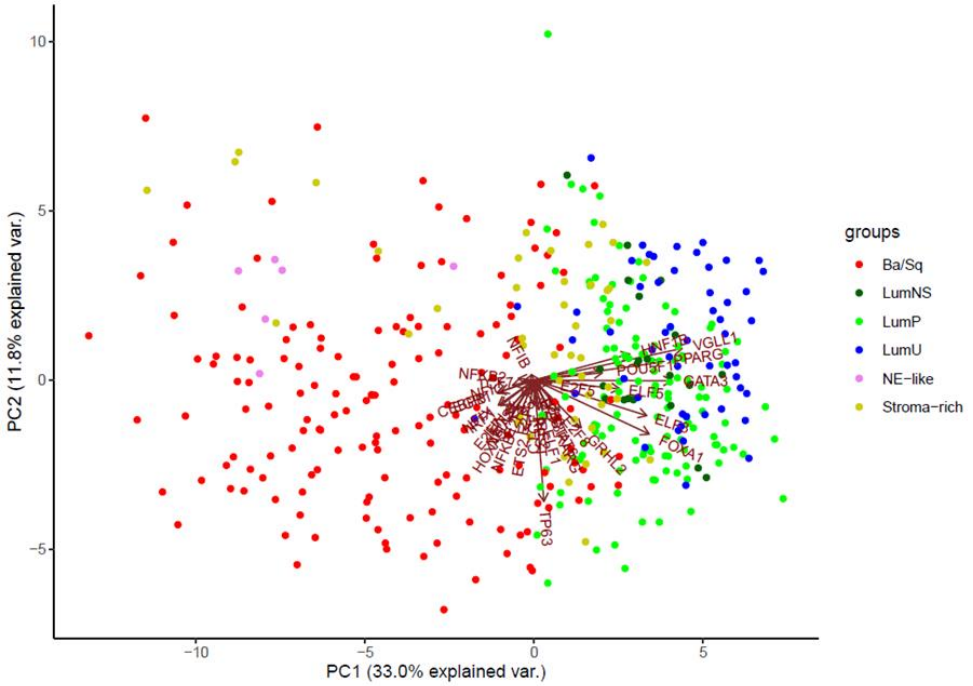

Figure 4.17: *VGLL1* closely correlates with *POU5F1*, *HNF1B, GATA3* and *PPARG* expression in luminal MIBC

Unscaled principal component analysis plot of TCGA MIBC samples separated on the basis of expression of *VGLL1* and the transcription factors previously identified by Fishwick *et al.* to possess unique motifs in FAIREseq peaks in differentiated and undifferentiated NHU cells (n=35 genes). Each dot represents a different RNASeq sample while each MIBC consensus molecular subtype is represented by a different icon colour.

Analysis of the mutational status of *VGLL1* in TCGA MIBC cohort revealed that the gene was not mutated in any MIBC sample and exhibited copy number alterations in only 1.5% of samples (n=4 copy number amplifications and n=2 homo-deletions), suggesting that any aberrant expression of *VGLL1* in MIBC was a result of alterations to factors that induce or interact with VGLL1 (Fig. 4.18). When examining the mutational status of the transcription factors closely associated with *VGLL1* expression in MIBC, *GATA3* was found to exhibit copy number amplification in one of the tumours with amplified *VGLL1* expression, while *PPARG* was amplified in two *VGLL1*-amplified tumours alongside a missense point mutation in a third. In comparison, alteration and mutation rates of *POU5F1* and *HNF1B* in MIBC were low, with neither gene found to be altered in any of the four tumours with *VGLL1* alterations.

Figure 4.18: Genetic alterations of *VGLL1* and urothelial-associated transcription factors in MIBC

Profile of genetic alterations and mutations in *VGLL1*, *GATA3, PPARG, POU5F1* and *HNF1B* genes in TCGA MIBC cohort. For clarity, only a proportion of the tumours in the cohort are displayed, with the remaining tumours expressing wild-type versions of all five genes. Mutation data and graphic were obtained from the cBioPortal for Cancer Genomics (https://www.cbioportal.org/)

4.4.7.3 Mutation status of *VGLL1*-high MIBC

To examine whether MIBC tumours with increased expression of *VGLL1* collectively exhibited similar patterns of mutational load and/or gene expression (regardless of molecular subtype), all tumours of TCGA MIBC cohort were separated on the basis of *VGLL1* transcript expression (Fig. 4.19). Of the 404 tumour samples analysed, 14 were determined to have *VGLL1* TPM values exceeding the 1.5 x interquartile range (IQR) value of 431.8, and thus were considered outliers in the distribution. These tumours were grouped to create the "*VGLL1*-high" subset of MIBC, which consisted primarily of tumours of luminal derivation (eight of which were subtyped as luminal unstable tumours) yet also contained three basal/squamous tumours. Further information on the identity of the samples in the *VGLL1*-high subset can be found in Table 4.2.

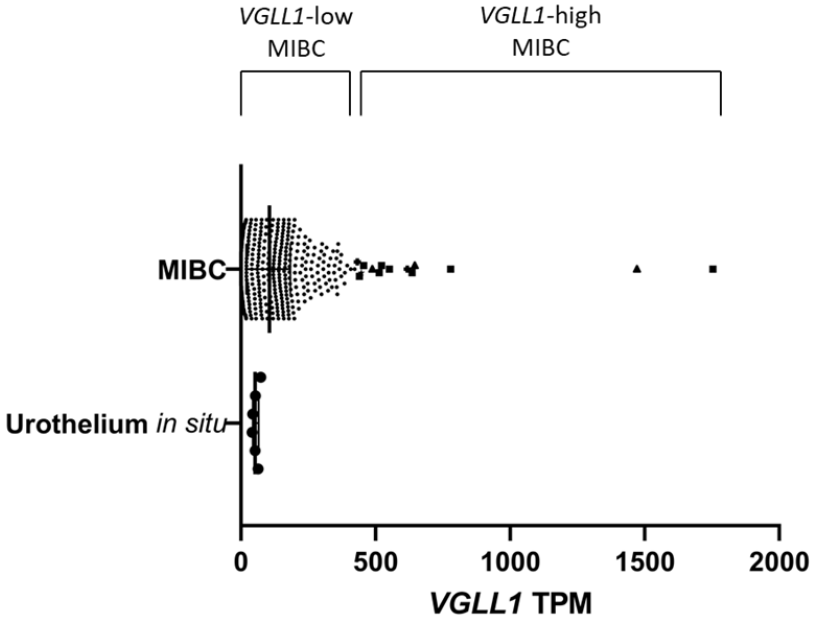

Figure 4.19: Stratification of MIBC into *VGLL1*-high and *VGLL1*-low subsets

Visualisation of unlogged *VGLL1* expression across all TCGA MIBC samples (n=404), with the bars representing the median and interquartile range (IQR) values. Unlogged expression of *VGLL1* in samples of normal urothelium *in situ* (n=6) were included for comparison. In the *VGLL1*-high subset, square icons represent luminal unstable tumours, triangle icons represent basal/squamous tumours, cross icons represent luminal non-specified tumours and a star icon represents a luminal papillary tumour. The 1.5 x IQR rule was applied to confirm that the *VGLL1* TPM values of each tumour in the designated *VGLL1*-high subset were outliers of the overall pattern of distribution (1.5 x IQR TPM value = 431.8).

Sample #	Molecular subtype	*VGLL1* TPM	*VGLL1* copy number amplification	*GATA3* amplification	*PPARG* amplification
A9KW	LumU	1754.0	Yes	No	Yes
A2LD	Ba/Sq	1471.9	Yes	Yes	Yes
A3SR	LumU	779.5	No	Yes	No
A6TH	Ba/Sq	646.5	No	No	No
A6B1	LumU	636.2	No	No	No
A3JV	LumNS	618.7	No	No	Yes
A3VY	LumU	551.4	No	Yes	No
A9KI	LumU	522.6	No	Yes	No
A3QH	LumU	513.7	No	No	No
A9ST	Ba/Sq	488.8	No	No	No
AAMX	LumU	456.4	No	No	No
A3PH	LumP	447.1	No	No	Yes
A40G	LumU	440.4	No	No	No
A3IT	LumNS	432.5	No	No	No

Table 4.2: List of tumours in the *VGLL1*-high subset of MIBC

Tumours of the MIBC cohort (n=404) that were determined to have outlier expression of *VGLL1* were grouped to form the *VGLL1*-high subset (n=14). The two samples with the highest *VGLL1* expression (#A9KW and A2LD) were found to have alterations in *VGLL1* and *PPARG* gene copy number, while the A2LD sample additionally exhibited *GATA3* copy number amplification.

Analysis of the mutations inherent to the *VGLL1*-high subset was performed to determine whether any mutations were overrepresented in this group compared to the entire MIBC cohort. 24 genes were found to be mutated in over 25% (4/14 tumours) of the subset, with commonly mutated tumour suppressor *TP53* and striated muscle gene *TTN* found to be mutated in 9/14 tumours (Table 4.3). However, when applying a binomial test to observe whether the increased mutation frequency of the genes was significantly different to that of the frequency observed across the MIBC cohort, it was determined that mutations in these genes was not enriched in the *VGLL1*-high subset. The most prevalently mutated gene that was found to be significantly enriched in *VGLL1*-high tumours was the SWI/SNF chromatin remodelling complex gene *ARID1A* (AT-rich interactive domain-containing protein 1A; $p \leq 0.01$) which was observed in 8/14 tumours, including the three tumours with the highest *VGLL1* expression (Table 4.4). *ARID1A* was additionally the only gene in the list that was mutated in both HT1376 and HT1197 cell lines, the MIBC cell lines previously determined to have the highest expression of *VGLL1* (Table 4.3; Fig. 4.1). Analysis of *VGLL1* expression across all *ARID1A*-mutated tumours in the MIBC cohort revealed a significant increase in expression when compared to tumours with wild-type *ARID1A* (Fig. 4.20; $p \leq 0.001$), suggesting that dysregulation of this gene may be a causative factor behind instances of high *VGLL1* expression observed in some cases of MIBC.

The mutation status of *NF2* and *AMOT* (components of the Hippo pathway that are frequently mutated in other forms of cancer, as discussed in Section 4.1) in the *VGLL1*-high subset was also examined. This analysis revealed that the VGLL1-high subtype contained no mutations in *NF2* and two mutations in *AMOT* (samples #A6B1 and A3VY), suggesting that mutation of Hippo pathway regulatory components was not a causative factor behind *VGLL1* dysregulation in MIBC.

Gene	Mutation frequency in *VGLL1*-overexpressing subset (n=14)	Mutation frequency in TCGA (n=404)	pval	Mutation(s) in HT1376 cell line	Mutation(s) in HT1197 cell line
TP53	64.3%	48.3%	0.1058	Yes	No
TTN	64.3%	47.5%	0.0983	Yes	No
ARID1A	57.1%	24.8%	**0.0078**	Yes	Yes
FAT3	42.9%	11.0%	**0.0021**	No	No
MUC16	42.9%	28.7%	0.1121	No	Yes
CSMD3	35.7%	13.7%	**0.0257**	No	No
RB1	35.7%	17.6%	0.0592	Yes	No
SYNE1	35.7%	20.3%	0.0896	Yes	No
ABCA13	28.6%	9.1%	**0.0264**	No	Yes
ANKHD1-EIF4EBP3	28.6%	N/A		No	No
ATP10A	28.6%	4.7%	**0.0030**	No	Yes
ATP1A2	28.6%	2.7%	**0.0004**	No	No
ERBB2	28.6%	12.3%	0.0617	No	No
FRY	28.6%	7.6%	**0.0151**	No	No
HERC2	28.6%	7.8%	**0.0164**	No	No
HYDIN	28.6%	6.1%	**0.0074**	No	No
KDM6A	28.6%	26.0%	0.2252	Yes	No
MALAT1	28.6%	11.4%	0.0504	No	No
NES	28.6%	4.7%	**0.0030**	No	No
RYR2	28.6%	19.1%	0.1600	No	No
SLC38A2	28.6%	3.4%	**0.0009**	No	No
SYNE2	28.6%	12.7%	0.0670	No	No
UBR5	28.6%	6.9%	**0.0111**	No	No
USP34	28.6%	9.1%	**0.0264**	No	No

Table 4.3: Overrepresented mutations in the *VGLL1*-high subset of MIBC

Point mutation data for the tumours in the *VGLL1*-high MIBC subset (n=14) and the *VGLL1*-overexpressing HT1376 and HT1197 MIBC cell lines were collated to determine the most common mutations inherent to these tumours. The relative mutation frequencies for each gene across all MIBC samples was used to calculate whether the observed mutation frequency of the genes enriched in the subset was statistically significant, with significant p values highlighted in bold. Mutation data for HT1376 and HT1197 cells were obtained from the Catalogue of Somatic Mutations in Cancer (COSMIC) database (https://cancer.sanger.ac.uk/cosmic), while additional information on the *ARID1A* mutations inherent to these cell lines can be found in Appendix xiii.

	A9KW (LumU)	A2LD (Ba/Sq)	A3SR (LumU)	A6TH (Ba/Sq)	A6B1 (LumU)	A3JV (LumNS)	A3VY (LumU)	A9KI (LumU)	A3QH (LumU)	A9ST (Ba/Sq)	AAMX (LumU)	A3PH (LumP)	A40G (LumU)	A3IT (LumNS)
TP53		X	X				X	X	X	X	X	X	X	
TTN	X	X					X	X	X	X	X	X	X	
ARID1A	X	X	X			X		X				X	X	X
FAT3		X		X					X	X	X		X	
MUC16						X	X		X		X	X		X
CSMD3		X		X	X	X	X							
RB1				X				X		X		X	X	
SYNE1			X				X		X				X	X
ABCA13				X			X	X			X			
ANKHD1-EIF4EBP3				X	X			X						X
ATP10A						X	X			X		X		
ATP1A2							X			X	X			X
ERBB2				X						X	X		X	
FRY								X	X	X				X
HERC2							X			X	X		X	
HYDIN			X							X			X	X
KDM6A		X							X		X	X		
MALAT1					X		X			X				X
NES	X									X		X		X
RYR2		X		X					X					X
SLC38A2			X				X		X	X				
SYNE2							X				X	X		X
UBR5				X			X				X	X		
USP34	X						X	X			X			

Table 4.4: Matrix of overrepresented mutations in the *VGLL1*-high MIBC subset

The 14 tumours of the *VGLL1*-high MIBC subset were arranged in order of *VGLL1* expression, with sample #A9KW displaying the highest *VGLL1* TPM value and #A3IT displaying the lowest *VGLL1* TPM value of the subset. *ARID1A* was found to be mutated in 8/14 tumours of the subset, with 7/8 tumours classified as luminal MIBC.

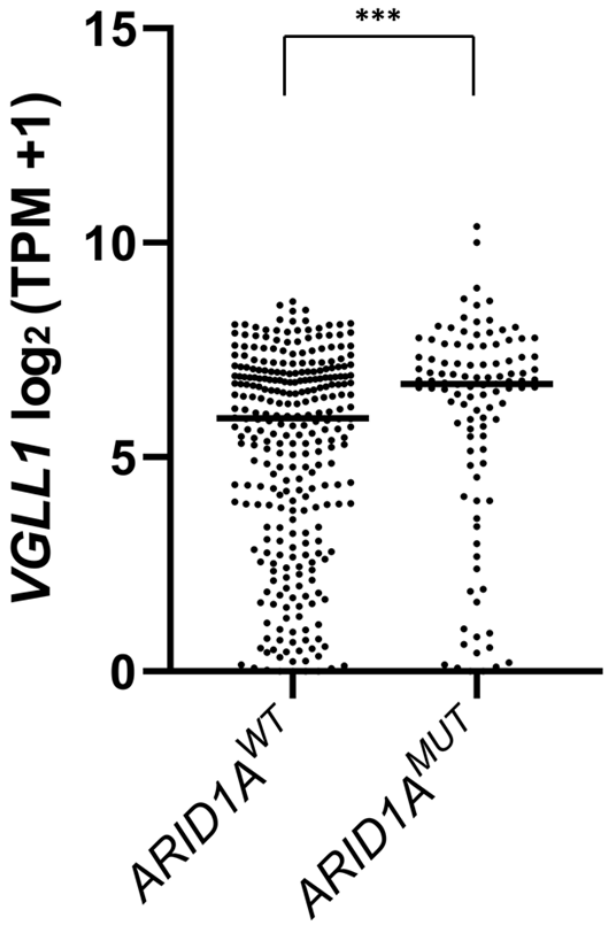

Figure 4.20: Mutations to *ARID1A* result in elevated expression of *VGLL1* in MIBC

MIBC tumours were split based on expression of either the wild-type (n=296) or mutated versions (n=108) of the *ARID1A* gene and examined on the basis of (log_2 transformed) *VGLL1* expression. Significance between groups was determined by a Mann-Whitney test. ***=p≤0.001.

Examination of commonly mutated genes in MIBC revealed six genes that were not mutated in any sample in the *VGLL1*-high subset, with two of these genes (*FGFR3* and *ELF3*) additionally found to be highly expressed in the subset (Table 4.5). However, none of the aforementioned genes were found to be significantly underrepresented in the subset following a binomial test analysis.

Gene	Mutation frequency in *VGLL1*-high subset (n=14)	Mean expression in *VGLL1*-high group (TPM)	Mutation frequency in TCGA (n=404)	pval	Mutation(s) in HT1376 cell line	Mutation(s) in HT1197 cell line
FGFR3	0%	82.3	14.2%	0.1172	No	No
FAT1	0%	3.6	12.5%	0.1542	Yes	No
ELF3	0%	305.2	12.3%	0.1592	No	Yes
RYR1	0%	0.6	12.3%	0.1592	No	No
LRP1B	0%	0.0	11.8%	0.1724	No	No
PCLO	0%	1.3	10.3%	0.2183	No	No

Table 4.5: Underrepresented mutations in *VGLL1*-high MIBC tumours

The most common point mutations in MIBC were collated to determine if any genes were not mutated in the *VGLL1*-high basal/squamous subset (n=14). Only genes found to be mutated in at least 10% of all MIBC samples and in none of the *VGLL1*-high tumour subset were included.

4.4.7.4 Gene expression profile of *VGLL1*-high MIBC

Differential expression analysis of the *VGLL1*-high MIBC subset versus the remaining (*VGLL1*-low) MIBC tumours (n=390) determined that 1047 genes had an absolute fold change ≥ 2 and a q value ≤0.05 (Fig. 4.21A). GSEA analysis of the differentially expressed genes in the comparison highlighted enrichment of cell cycle-associated E2F transcription factor targets, G2/M phase checkpoint markers and genes involved in adipogenesis in the *VGLL1*-high subset (Fig. 4.21B). However, investigation into the genes that comprise the various enriched gene sets revealed that only *CCNE1* (cyclin E1, a member of the HALLMARK_E2F_TARGETS gene list) and *ESPL1* (separase; HALLMARK_G2M_CHECKPOINT) were found to be significantly upregulated (q ≤0.01). Examples of genes found to be significantly upregulated in the *VGLL1*-high subset included E2F1 binding factor *ARID3A* and genes involved in the inhibition of apoptosis (*FAM9C, CAPN6*). Four of the most downregulated genes in the *VGLL1*-high subset were basal/squamous MIBC markers *KRT5*, *KRT6A*, *KRT6B* and *KRT14*, consistent with the primarily luminal MIBC-derived identity of the group. Pathways that were observed to be significantly suppressed in the subset included genes induced by p53 activity (*CASP1, CLCA2*) and genes involved in mediating an inflammatory response (*CD55*, *CD69*, *CXCL10, IL1A*) or apoptosis (*CASP1*, *CD44*, *CD69*, *DPYD*, *FASLG*, *GSTM1*, *IGFBP6*, *IL1A*, *NEFH*, *PRF1*). Signalling components of the WNT (*WNT3A, WNT5A, WNT10A*), TGFβ (*TGFB2*, *TGFBI*) and FGF (*FGF5*, *FGF9*, *FGFBP1*) pathways were additionally observed to have significantly reduced expression in *VGLL1*-high tumours.

The expression of transcription factors *PPARG*, *GATA3, FOXA1*, *ELF3*, *RARG*, *HNF1B* and *POU5F1* was examined to determine whether (the primarily luminal) tumours that exhibited overexpression of *VGLL1* additionally had dysregulated expression of genes involved in urothelial differentiation. While no significant differences in expression for any of the aforementioned genes was observed between groups, expression of PPARγ target gene *FABP4* was found to be significantly downregulated in the *VGLL1*-high subset, possibly indicative of a reduction in active PPARγ signalling in the subset in comparison to *VGLL1*-low tumours.

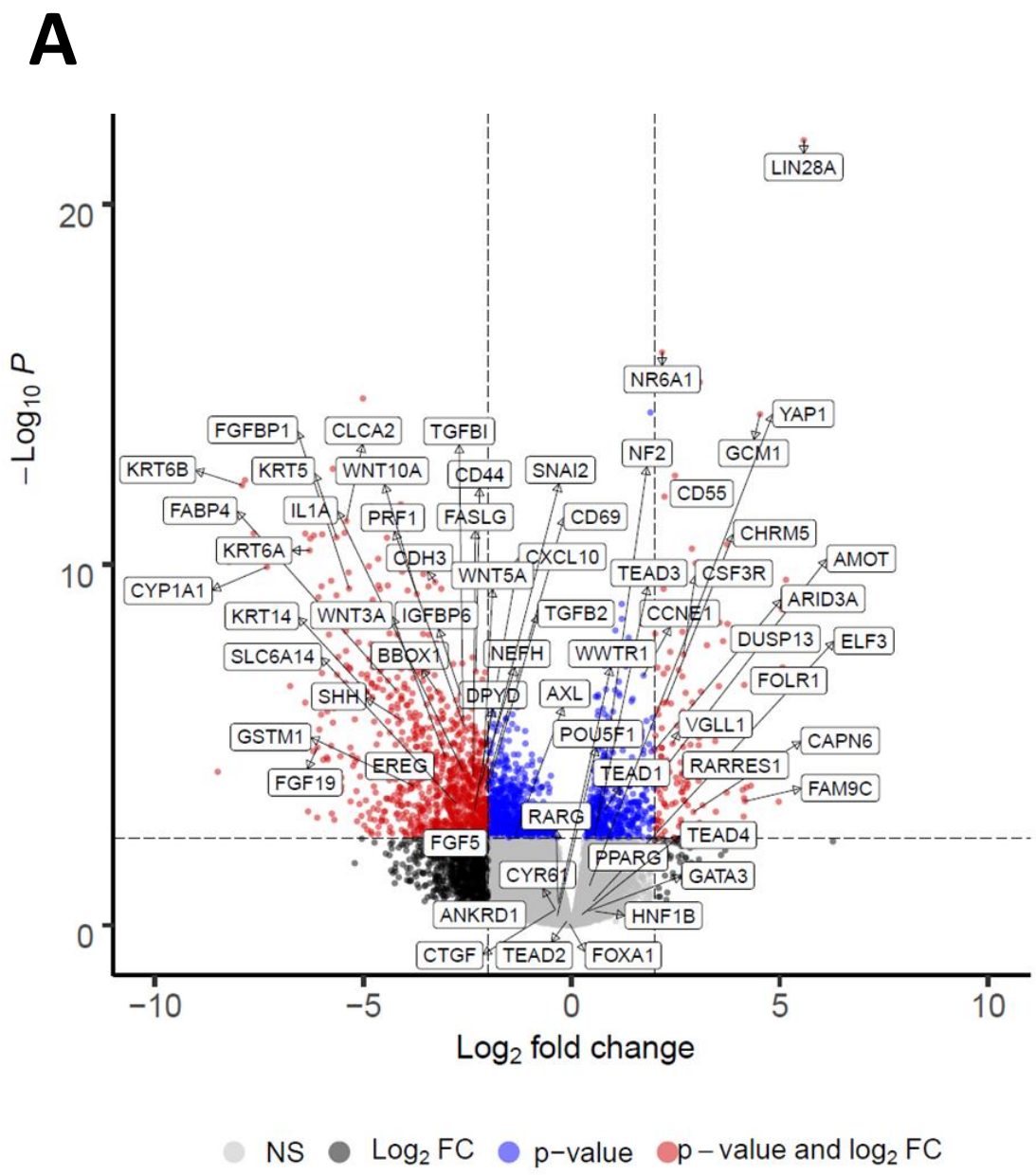

Figure 4.21: *VGLL1*–high MIBC tumours have decreased expression of apoptosis-associated genes and increased expression of cell cycle-associated genes

A) Volcano plot of the most differentially expressed genes in *VGLL1*-high MIBC tumours (n=14) in comparison to *VGLL1*-low tumours (n=390). Genes that pass the criteria of having a q value ≤0.05 and a $\log_2$ fold change in expression ≥ 2 or ≤-2 are represented as red dots. Notable genes that pass the criteria set above are highlighted on the plot. A complete list of genes with a q value ≤0.05 and a $\log_2$ fold change in expression ≥ 2 or ≤-2 can be found in Appendix xiii.

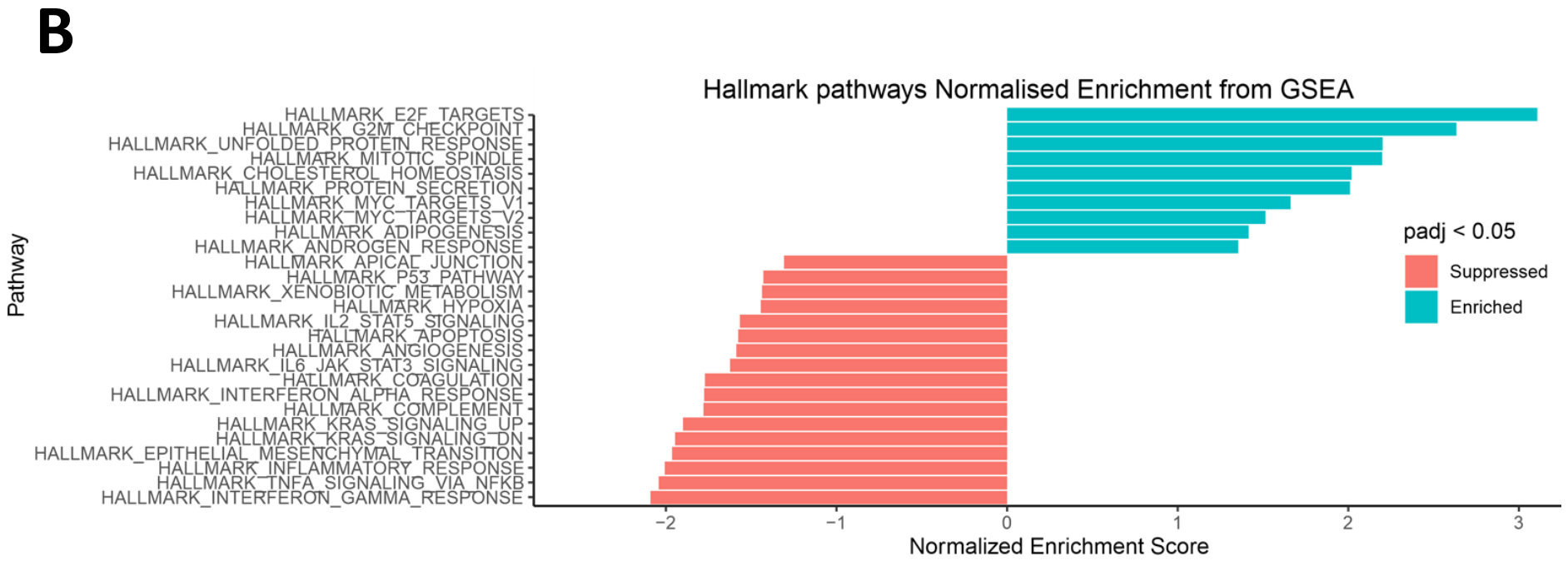

Figure 4.21: *VGLL1*–high MIBC tumours have decreased expression of apoptosis-associated genes and increased expression of cell cycle-associated genes

B) GSEA analysis of signalling pathways that are differentially expressed between *VGLL1*-high and *VGLL1*-low basal/squamous subsets. Each pathway analysed is assigned a normalised enrichment score, with only pathways that have a significant q value ≤0.05 displayed.

To determine whether the altered phenotype of the *VGLL1*-high MIBC tumours affected the survival rate of patients in the group; a Kaplan-Meier survival analysis was performed. Comparison between *VGLL1*-high and *VGLL1*-low MIBC subtypes revealed that 57% of patients exhibiting the *VGLL1*-high phenotype had died within 18 months of diagnosis (compared to 28% of *VGLL1*-low patients), resulting in significantly reduced overall survival ($p \leq 0.01$; Fig. 4.22). The preceding analysis therefore revealed that overexpression of *VGLL1* in cases of MIBC was associated with a suppression of apoptosis, a gain in genes involved in cell cycle progression and an increased mortality rate.

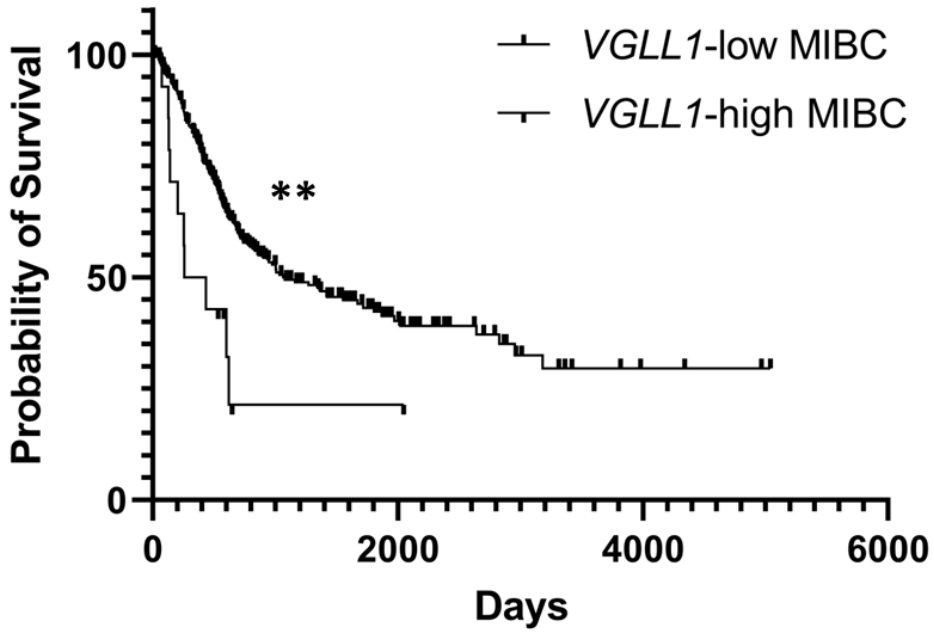

Figure 4.22: *VGLL1*–high MIBC patients have reduced overall survival

Kaplan-Meier survival plot of the groups created by separating MIBC tumours into *VGLL1*-high and *VGLL1*-low subtypes. The Log-Rank (Mantel-Cox) test was used to determine significance between the overall survival of groups. Median survival time of *VGLL1*-high basal/squamous subset (n=14) = 346 days, *VGLL1*-low basal/squamous group (n=390) = 1077 days. **=p<0.01.

4.5 Discussion

4.5.1 VGLL1-mediated effects on cell phenotype following forced expression

Overexpression of VGLL1 resulted in a G0/G1 arrest of T24 cells and a concurrent inhibition of phosphorylated AKT, reflecting the phenotype of undifferentiated NHU cells observed in the previous chapter. Collectively, these observations potentially suggest the existence of a negative feedback loop between VGLL1 and PI3K/AKT signalling, whereby VGLL1 is induced in normal cells following PI3K/AKT activation in adherens junction-forming cells (as observed in preliminary data in the previous chapter) which serves to subsequently inhibit PI3K/AKT signalling in an as-of-yet uncharacterised mechanism following induction of the protein. This hypothesis may serve to explain the phenotype observed in a *Pten*-inactive mouse model of prostate cancer tumorigenesis, whereby forced overexpression of Gata3 was observed to inhibit phosphorylated Akt expression and delay tumour progression (Nguyen *et al.,* 2013). However, it must be noted that the evidence in support of VGLL1 requiring active PI3K/AKT signalling for induction (in NHU cells) while additionally inhibiting the pathway upon high expression of the protein (in NHU and T24 cells) is based off of evidence from single experiments, and would thus need to be replicated in further samples in order to confirm this phenotype.

Another potential caveat that arises when critically evaluating the aforementioned results is due to the use of a retroviral cloning vector that facilitates constitutive expression of VGLL1 in cell types where the gene typically has low/absent expression. While the use of retroviral vectors to induce ectopic expression of a gene is a commonly accepted tool in molecular biology research (reviewed by Prelich, 2012), such an approach inevitably has various limitations that need to be considered. One such limitation is that overexpression likely results in a much stronger expression of the gene/protein than would commonly be found *in situ*, thus making comparisons to biologically relevant states difficult. Rather than fulfilling its wild-type function, overexpressing a protein in this ectopic manner may also instigate an abnormal phenotype, whereby the protein of interest exhibits an unusual localisation or binds to unnatural substrates or binding partners as a result of its aberrantly high expression (reviewed by Prelich, 2012).

The opposing effect that VGLL1 expression had on various processes when comparing the phenotypes of VGLL1 overexpressing (undifferentiated NHU and T24) and VGLL1 knockdown (differentiated NHU) cells does however suggest that forced expression of the gene was capable of producing biologically relevant inferences on VGLL1 function in this context. Examples of such observations include the effect that VGLL1 expression had on cell cycle, where VGLL1 overexpression resulted in G0/G1 arrest and reduced proliferation while VGLL1 knockdown increased Ki67/MCM2 activity, and on p-AKT expression, which was inhibited when VGLL1 was overexpressed but experienced increased expression compared to control when VGLL1 was inhibited. Additionally, the phenotypic changes resulting from VGLL1 overexpression were found to be cell line-specific, as negligible differences to the aforementioned variables were observed in 5637 or ScaBer cells when compared to their respective control cell lines. This observation therefore suggested that the cellular machinery required for normal VGLL1 function (and evidently present in differentiated urothelium) is also expressed to some degree in undifferentiated NHU and T24 cells, whereas phenotypic differences (such as mutations of select genes) resulted in the non-functionality of VGLL1 when ectopically expressed in 5637 or ScaBer cells.

4.5.2 *VGLL1* expression in MIBC

The transcriptomic analysis of MIBC tumours performed in this chapter confirmed an association of *VGLL1* with luminal MIBC, whilst identifying a subgroup of (primarily luminal) tumours that were found to exhibit aberrant overexpression of *VGLL1* despite the gene possessing a low copy number alteration frequency and no mutations in the MIBC cohort. This observation was suggestive of a previously undescribed dysregulation of feedback that controls expression of the gene.

Currently little is known about the role of VGLL1 in human disease, although recently published studies have implicated the protein as a prognostic marker in human gastric (Kim *et al.,* 2019a; Im *et al.,* 2020) and pancreatic (Bradley *et al.,* 2020) cancers. High expression of *VGLL1* has previously been identified in TCGA breast cancer cohort, which revealed an association of the gene with the highly invasive triple-negative subtype. Subsequent analysis of the cohort determined that

FOXA1 and *GATA3* were two of the most negatively regulated genes to *VGLL1* expression, *VGLL1*-high breast tumours had a significantly reduced rate of overall survival and that overexpression of *VGLL1* was not as a result of copy number amplification (Castilla *et al.,* 2014). It would therefore be interesting to compare the mutational backgrounds of *VGLL1*-high triple-negative breast cancer and *VGLL1*-high MIBC to understand whether dysregulation of the gene in both cancer types arises from (and results in) a similar phenotype.

The basal/squamous and neuroendocrine-like MIBC subtypes both contained groups of tumours that exhibited low or undetectable expression of *VGLL1*. These subgroups were not examined further as part of this study, but future analysis that determines the similarities between the gene expression profiles of *VGLL1*-low and *VGLL1*-high MIBC may help to elucidate specific markers of dysregulated VGLL1 function.

4.5.3 Phenotype of *VGLL1*-high MIBC subgroup

4.5.3.1 Enrichment of *ARID1A* mutations in subgroup

Analysis of the *VGLL1*-high MIBC tumours revealed an enrichment of mutations in the *ARID1A* gene, encoding for the SWI/SNF nucleosome remodelling complex subunit ARID1A. The SWI/SNF complex acts to modify the structure of chromatin and allow for transcription factor access to their respective enhancer or promoter regions (Kwon *et al.,* 1994), whilst the specific role of ARID1A has been determined to be to recruit the fellow members of the complex to DNA in open regions of chromatin, as marked by acetylation of histone H3 K27 (H3K27ac; Hurlstone *et al.,* 2002; Wilsker *et al.,* 2004; Alver *et al.,* 2017). Inactivating mutations in the *ARID1A* gene have been demonstrated to result in aberrant transcriptional activity and a reduction in H2K27ac (Mathur *et al.,* 2017), activation of PI3K/AKT signalling (Yang *et al.*, 2019) and a loss of DNA damage repair processes (Watanabe *et al.,* 2014).

ARID1A is one of the most commonly occurring mutations in MIBC (Robertson *et al.,* 2017) and has been associated with high-grade, highly invasive tumours (Li *et al.,* 2016a). Alterations to *ARID1A* have previously been identified to be primarily

inactivating in MIBC (Robertson *et al.,* 2017), a finding that supports the predicted loss-of-function phenotype observed in the *ARID1A*-mutated, *VGLL1*-high tumours. Additionally, these tumours were found to significantly downregulate multiple genes (including *CASP1, CD55, CXCL10, GATM1, IGFBP6, WNT3A* and *WNT10A*) previously identified to be *ARID1A*-dependent through microarray comparison of wild-type and *Arid1a*-null mouse uterine epithelial cells (Kim *et al.,* 2015a), whilst upregulating genes such as *CCNE1* which function in opposition to the predicted role of VGLL1 in modulating cell cycle arrest in normal urothelium. The following observations therefore suggest that the *VGLL1*-high subgroup consists of tumours that exhibit a loss of both ARID1A and VGLL1 normal function.

The tumours of the *VGLL1*-high MIBC subset appear to share phenotypic similarities with the HT1376 and HT1197 MIBC cell lines as they also exhibit high expression of *VGLL1* and mutated *ARID1A,* marking these cell lines as potentially suitable *in vitro* analogues of the "VGLL1-dysregulated" urothelial phenotype. In comparison, analysis of the mutational signature of T24 cells (Appendix xii) revealed that this cell line expresses wild-type *ARID1A*, which may explain why the cell line was similarly amenable to the effects of VGLL1 overexpression observed in undifferentiated NHU cells.

How expression of wild-type ARID1A functions to enable VGLL1-mediated transcriptional activity in normal urothelium is currently undetermined and would require further study. Loss of enhancer/promoter accessibility following *ARID1A* inactivation is one possible rationale behind a loss in VGLL1 functionality, with deletion of ARID1A previously demonstrated to result in a significant depletion of H3K27ac in sites predicted to be bound to by TEAD4 in colorectal cancer cell line HCT116 (Mathur *et al.,* 2017). Alternatively, ARID1A could bind directly to a VGLL1 transcriptional complex at enhancer regions to facilitate gene transcription. A similar mechanism was demonstrated in murine liver, where Arid1a was shown to directly bind to Yap/Tead to regulate hepatocyte wound healing, with Arid1a-mediated chromatin accessibility responsible for a significant enrichment of Hippo, TGFβ and tight junction assembly pathway genes (Li *et al.,* 2019). That *VGLL1*-high tumours exhibit a loss of VGLL1-mediated function yet display high expression of

the gene would suggest that alterations to *ARID1A* may also serve to remove an as-of-yet uncharacterised negative feedback loop on *VGLL1* expression, resulting in a phenotype of overexpression.

4.5.3.2 Effect of *ARID1A* alterations on PI3K/AKT signalling

A potential rationale for the overexpression of *VGLL1* observed in this tumour subtype may arise from the previously examined relationship between ARID1A and PI3K/AKT signalling in human cancer. Inactivating alterations to *ARID1A* are commonly found to co-occur with mutations in the *PI3KCA* and *PTEN* genes in ovarian and endometrial cancer (Liang *et al.,* 2012; De *et al.,* 2019), leading to aberrant activation of PI3K/AKT signalling. While mutations in *PI3KCA* and *PTEN* were not found to be similarly enriched in the *VGLL1*-high MIBC subtype, aberrant PI3K/AKT signalling may still be predicted to occur in these tumours due to the previously observed effects on AKT activation following knockdown of *ARID1A* in nasopharyngeal carcinoma cell lines (Yang *et al.,* 2019), in addition to an increased sensitivity to PI3K/AKT pathway inhibitors in the *PI3KCA*/*PTEN*-WT fibroblast cell line MRC-5 following ARID1A depletion (Samartzis *et al.,* 2014). Unrestrained PI3K/AKT pathway activation may therefore serve to further induce high expression of non-functional VGLL1 in this tumour subtype.

4.5.3.3 Potential treatments against *ARID1A*-mutated tumours

A notable gene that was found to be not mutated in the *VGLL1*-high subset was *FGFR3*, a gene that was similarly found to be induced in NHU cells following PD153035 (but not LY294002) treatment (Appendix vii). A previous study has highlighted that a mutually exclusive relationship exists between alterations to *ARID1A* and *FGFR3* in cases of bladder cancer (Balbás-Martínez *et al.,* 2013), while the identity of FGFR3 as an upstream RTK of PI3K/AKT signalling has previously been described (Salazar *et al.,* 2009; Okada *et al.,* 2019; Yin *et al.,* 2020). The preceding observations therefore potentially implicate the requirement for normal FGFR3 signal transduction (and possible subsequent PI3K/AKT activation) in this tumour type and thus highlight a potential therapeutic option.

Based on the effect that loss of ARID1A function has on human cells, treatment with inhibitors that target either components of the DNA damage response system

such as ATR kinase (Williamson *et al.,* 2016), or histone deacetylases (HDACs; Fukumoto *et al.,* 2018) have been previously hypothesised to display a potential therapeutic benefit to cancers that harbour *ARID1A* mutations. Indeed, a recent study that treated the *ARID1A*-mutated, *VGLL1*-high MIBC cell line HT1197 with pan-HDAC inhibitor panobinostat caused a downregulation of E2F target genes and upregulation of p53 and inflammatory pathway genes, in effect a reversal of the phenotype observed in the *VGLL1*-high MIBC tumour subtype expression profile (Gupta *et al.,* 2019).

4.5.4 Identification of potential VGLL1/TEAD3 target genes in urothelium

Of the four TEAD genes, *VGLL1* expression was confirmed to most closely correlate with *TEAD3* in MIBC. Whilst a functional binding relationship between the transcription factor and co-activator in urothelial cells remains to be validated, this observation (in addition to the transcript and protein expression of the TEAD factors in normal urothelium examined in the previous chapter) suggested that TEAD3 is the predominant TEAD transcription factor that VGLL1 binds to in urothelium. Examination of the genes that both *VGLL1* and *TEAD3* positively correlated with in MIBC provided an insight into what genes could possibly be induced by normal VGLL1/TEAD3 transcriptional activity in urothelium, including *PARD6B*, *PLEKHG6* and *CGN*, all targets which were confirmed to be expressed at the transcript level in differentiated NHU cells.

PARD6B encodes a member of the PAR6 family that are required to regulate epithelial cell polarity through its role as part of the polarity complex, a complex that additionally contains Protein Kinase C ζ (PKCζ) and PAR3 (Joberty *et al.,* 2000). PAR3 localises to tight junctions in the apical regions of cells (Ebnet *et al.,* 2003), while PAR6 binds to PAR3 and acts as a scaffold protein to recruit PKCζ to the complex (Joberty *et al.,* 2000). The role of the polarity complex in tight junction regulation was demonstrated in a study of normal murine mammary epithelium, as Par6 localised with Zo-1 and TgfβrI at apical tight junctions. Stimulation (and heterodimerisation) of the Tgfβ receptor complex resulted in Par6 phosphorylation by TgfβrII and a dissolution of tight junctions, with cells expressing mutated Par6 unable to dissolve tight junctions following TGFβ treatment (Ozdamar *et al.,* 2005).

This TGFβ-dependent dissolution of the tight junctions was demonstrated to result from Par6-mediated proteasomal degradation of Rho GTPase RhoA by the E3 ubiquitin ligase Smurf1 (Ozdamar *et al.,* 2005). Using non-tumorigenic MCF10A cells, PARD6B shRNA knockdown was additionally demonstrated to inhibit PKCζ phosphorylation, promote re-entry into the cell cycle and induce activation of AKT signalling (Marques *et al.,* 2016). Dysregulation of the PKCζ/PARD3/PARD6B complex subsequently leads to loss of cell polarity and has been associated with a more invasive and chemoresistant phenotype in lung adenocarcinoma (Zhou *et al.,* 2017).

RHOA has previously been demonstrated to play a multifaceted role in tight junction regulation, as depending on the induction of specific downstream effector proteins it can either contribute to an increase in epithelial barrier TEER (Hasegawa *et al.,* 1999; Schlegel *et al.,* 2011) or result in dissolution of cell-cell contacts (Zhang *et al.,* 2013). Expression of PLEKHG6 and cingulin (CGN) appear to be important in regulating this activation, as demonstrated through a requirement of PLEKHG6/RHOA binding to induce invasiveness in MDA-MB-231 human breast cancer cells (D. Wu et al., 2009), and an increase in RhoA-mediated cell cycle activity following knockdown of Cgn in Madin-Darby canine kidney cells (Guillemot *et al.,* 2006). The preceding findings therefore implicate *PARD6B, PLEKHG6* and *CGN* as potential target genes of the VGLL1/TEAD3 transcriptional program, with the previously identified function of these genes offering a potential rationale behind some of the changes to cell phenotype observed when VGLL1 expression is genetically modified in NHU cells.

4.5.5 Chapter conclusions

Overall, data presented in this chapter confirmed that forced expression of VGLL1 does little to affect expression of YAP or its downstream targets in MIBC cell lines, consistent with the results observed in NHU cells and indicative of a lack of competitive signalling between the two transcriptional co-activators in urothelial cells. Further discussion on the lack of a relationship observed between VGLL1 and YAP/TAZ signalling can be found in Chapter 6. Overexpression of VGLL1 was however found to inhibit PI3K/AKT signalling and contribute to cell cycle arrest in

T24 cells in a similar manner to that observed in undifferentiated NHU cells. The aforementioned alterations to cell phenotype were not replicated in the basal/squamous MIBC cell lines 5637 and ScaBer, suggesting that their respective mutational backgrounds predisposes these cells to be unresponsive to normal VGLL1 function. Examination of the phenotype of *VGLL1* expression in the context of MIBC revealed a subgroup that exhibits overexpression of the gene, an enriched *ARID1A* mutational signature and a poor survival rate. This observation, alongside analysis of potential genes expressed through VGLL1/TEAD3 activity, has provided potentially fascinating insights into how VGLL1 functions to regulate tissue homeostasis, all of which would be worth further study.

4.6 Summary of results

- VGLL1 transcript and protein expression was retained in luminal-derived bladder cancer cell lines but reduced or lost in basal/squamous-like bladder cancer cell lines, with low expression of *VGLL1* appearing to correlate with high expression of YAP/TAZ target genes. However, overexpression of VGLL1 in 5637, T24 and ScaBer MIBC cell lines had a negligible effect on YAP phosphorylation state, YAP localisation or expression of YAP/TAZ downstream target genes, supporting the observations made in NHU cells that VGLL1 does not directly affect YAP/TAZ signalling in urothelial cells.

- VGLL1 overexpression in T24 (but not 5637 or ScaBer) cells inhibited AKT signalling and reduced the proportion of cells actively proliferating, similar to the phenotype found in VGLL1-overexpressing undifferentiated NHU cells.

- MIBC tumours primarily retained *VGLL1* expression in comparison to normal urothelium. While the *VGLL1* gene itself was not mutated in MIBC, analysis of an outlier *VGLL1*-high subgroup revealed significant enrichment of mutations in the chromatin remodelling gene *ARID1A*. Tumours with aberrant expression of *VGLL1* upregulated genes involved in cell cycle progression and suppressed expression of pro-apoptotic genes, suggestive of a loss of normal VGLL1 function in these tumours.

5: Investigation of canonical and non-canonical Sonic Hedgehog pathway activity in urothelial and stromal cells

5.1 Introduction

Interactions between epithelia and the underlying fibroblasts, smooth muscle cells and other cells of mesenchymal origin that make up the stroma are known to play a pivotal role in the regulation of mammalian tissues (Howlett *et al.,* 1986). As previously stated (Section 1.1), the urothelium is supported by a layer of fibroblast-containing connective tissue that makes up the lamina propria (Hodges *et al.,* 1977). Cells of the lamina propria help to mediate processes such as development, tissue repair and differentiation of urothelium (Jerman *et al.,* 2020), while also being implicated in contributing to a neoplastic phenotype (reviewed by Southgate *et al.,* 1999).

5.1.1 Urothelial stromal cell phenotype

Immunohistochemical analysis of adult human ureters determined that expression of cytoskeletal-related proteins such as α-smooth muscle (SM) actin, smoothelin, caldesmon and desmin were localised primarily to smooth muscle bundles, with low, scattered expression of said proteins in the lamina propria and blood vessels (Baker *et al.,* 2008; Kimuli *et al.,* 2004) . By contrast, SM myosin and vimentin were expressed primarily in the lamina propria and less so by smooth muscle bundles, with all layers of the stroma negative for Ki67 (Baker *et al.,* 2008). Similarly to NHU cells, non-immortalised normal (ureter-derived) human stromal (NuHS) cells can be grown in culture, but unlike urothelial cells do not experience contact inhibition upon reaching confluence. These cells were unable to proliferate in a serum-free environment, yet expressed Ki67 and cyclin D1 while exhibiting an initial exponential growth rate when grown in the presence of serum, suggestive of a phenotypic shift away from mitotic quiescence in serum-supplemented culture (Baker *et al.,* 2008). When grown *in vitro*, NuHS cells retained expression of stromal protein markers such as α-SM actin and vimentin (Baker *et al.,* 2008; Kimuli *et al.,* 2004). However, delineation of the identity of stromal cell types primarily retained

in vitro was considered unfeasible due to the lack of markers specific to one cell type, alongside a significant reduction in expression of markers such as SM myosin and smoothelin when grown in culture (Baker *et al.,* 2008).

5.1.2 Stromal/urothelial interactions

Initial attempts to expand adult epithelial cell cultures and reproduce their normal morphology *ex vivo* determined that cell types, such as epidermal keratinocytes, were unable to propagate *in vitro* without the presence of an accompanying fibroblast population (Rheinwald *et al.*, 1975). Soon after, rodent urothelium was found to survive transiently in culture when grown from dissected bladder explants (Elliott *et al.,* 1975), but exhibited poor viability following a period of over two weeks when grown on standard (plastic) Petri dishes (Chlapowski *et al.,* 1979). Full differentiation of murine urothelium *in vitro* was only achieved by combining urothelial cells with mouse embryonic 3T3 fibroblast cells and a collagen matrix, whereas cells grown on a collagen substrate or alongside irradiated 3T3 cells only were both found to display a degree of histological abnormality. This suggested that both the cellular and non-cellular components of the stroma were required to induce a urothelial phenotype close to that found *in situ*, while also highlighting that the permissive signals produced by the stromal element could be produced by a non-isologous stromal cell type (originating from embryonic mouse compared to adult rat; Howlett *et al.,* 1986). Culturing of urothelial cells with a three dimensional stromal support remained the prevailing approach in studying adult mammalian urothelial biology *in vitro* until the advances made by Southgate *et al.* which allowed for the cultivation of NHU cells in a stroma-free environment (Jennifer Southgate et al., 1994).

The exchange of permissible signals between urothelium and stroma appears to occur in both adult and developing mammalian bladders, as demonstrated in studies with rat fetal bladders at a stage prior to tissue differentiation (Baskin *et al.,* 1996). Upon grafting onto a syngeneic adult host, bladders left intact or bladder mesenchyme that was recombined with urothelium were found to fully express smooth muscle differentiation markers. However, grafted bladder mesenchyme that was isolated and separated from accompanying urothelium displayed poor

growth and no signs of differentiation, potentially implicating signalling from the urothelium through the secretion of diffusible growth factors as a vital component of stromal differentiation (Baskin *et al.,* 1996). However, due to the aforementioned advances made in studying human urothelial cells *in vitro*, limited progress has been made in intervening years to identify the molecular pathways involved in stromal:urothelial signalling in the adult human bladder.

5.1.3 Sonic Hedgehog signalling pathway

An example of a pathway that could be involved in human stromal:urothelial signalling is the Sonic Hedgehog (SHH) pathway, which has previously been implicated in rodent bladder development, homeostasis and repair (Figure 5.1; Shin *et al.,* 2011; Shin *et al.,* 2014b). SHH ligand (also entitled SHH) is the most commonly expressed member of the Hedgehog family of proteins in mammalian tissues and was first identified as being an important morphogen in the development and tissue patterning of the human embryo (Echelard *et al.,* 1993). The 45kDa precursor SHH protein undergoes auto-proteolytic internal cleavage into an inactive carboxy-terminal domain and a 19kDa active amino-terminal domain entitled SHH-N (Porter *et al.,* 1996a). The signalling molecule then undergoes further addition of cholesterol and palmitoyl moieties (at the C and N terminals, respectively) by the acyltransferase Skinny Hedgehog (Chamoun *et al.,* 2001). These post-translational modifications assist in increasing the activity of SHH-N while facilitating paracrine signalling over relatively large distances, potentially via helping to promote association with the exoplasmic membrane (Kohtz *et al.,* 2001; Koleva *et al.,* 2015; Lewis *et al.,* 2001).

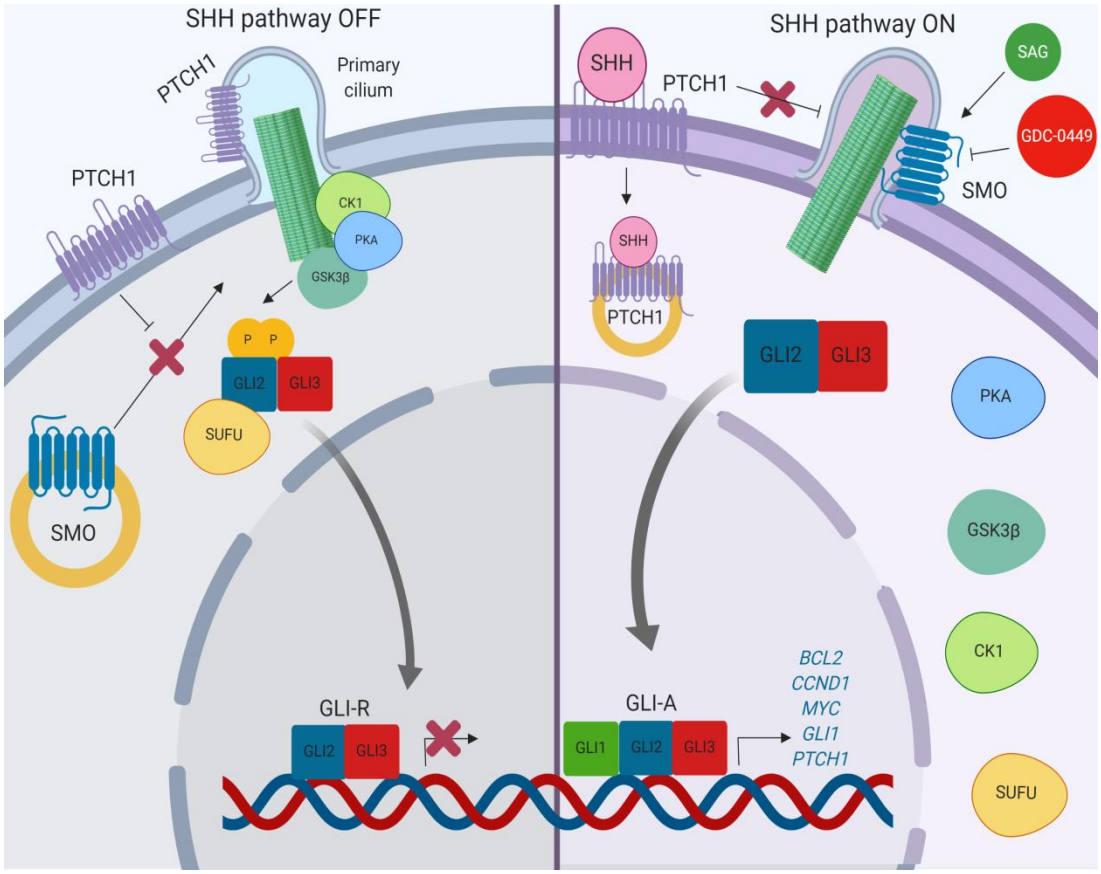

Figure 5.1: Canonical mammalian SHH pathway signalling

Canonical SHH signalling is initiated through the binding of SHH ligand to the extracellular region of PTCH1. In the absence of SHH, PTCH1 is localised primarily to the primary cilia of cells, where it can inhibit the translocation of signal regulator SMO from intracellular endosomes (Milenkovic *et al.,* 2009). Microtubule-bound kinases PKA, GSK3β and CK1 phosphorylate GLI2 and GLI3, inducing proteolysis and generation of truncated, GLI-R repressor forms of the transcription factors. GLI-R can bind to DNA in the nucleus but lacks an activation domain, thereby rendering it unable to induce GLI-mediated transcription. Binding with SHH inhibits PTCH1 activity and allows SMO to translocate to primary cilia, thereby leaving GLI2 and GLI3 in an unprocessed, active (GLI-A) state. GLI-A dissociates from inhibitory SUFU protein and translocates to the nucleus where it can induce transcription of various target genes, including *GLI1.* Activation of GLI activity additionally induces negative regulator *PTCH1*, resulting in a subsequent inhibition of signalling in normal cells through the form of a negative feedback loop. Pharmacological activation or inhibition of canonical SHH signalling can be performed through binding of the heptahelical bundle of cilia-localised SMO by SAG or GDC-0449, respectively. Diagram adapted from a review of SHH pathway signalling by Riobo, 2014.

SHH-N ligand is able to activate the canonical Hedgehog pathway in cells in both an autocrine or paracrine cell manner by binding to (and inhibiting) the 12-span transmembrane protein Patched-1 (PTCH1; Stone *et al.,* 1996), a protein which catalytically inhibits the constitutive activity of G-protein-coupled receptor-like protein Smoothened (SMO) in the absence of SHH (Taipale *et al.,* 2002). Repressed SMO activity inhibits SHH pathway signalling through sequential phosphorylation events of the glioma-associated oncogene (GLI) family of zinc finger transcription factors by Protein Kinase A (PKA), Casein Kinase 1 (CK1) and GSK3β (Price *et al.,* 2002); a kinase observed to become itself phosphorylated (and therefore inactivated) by components downstream of EGFR in NHU cells (Georgopoulos *et al.,* 2014). These inhibitory phosphorylation events result in the processing of GLI family members GLI2 and GLI3 into transcriptional repressors (sometimes referred to as GLI-R) which possess a truncated C-terminal activation domain alongside N-terminal repressor and DNA-binding domains (Sasaki *et al.,* 1999). Inhibition of PTCH1 allows for translocation and activation of SMO in the primary cilia of cells, microtubule-based organelles that protrude from the cell surface (Bailey *et al.,* 2009). Translocation of SMO therefore activates a downstream signalling cascade whereby the proteolytic processing of GLI2 and GLI3 is bypassed and the proteins dissociate from the inhibitory Suppressor of Fused (SUFU) protein complex (Svärd *et al.,* 2006). Activated GLI2 and GLI3 (GLI-A) are subsequently able to translocate to the nucleus and influence the transcription of various target genes, including *GLI1* and *PTCH1* (Fig. 5.1; Lee *et al.,* 1997). Upregulation of *PTCH1* therefore ensures eventual inhibition of GLI-mediated signalling in the form of a negative feedback loop. Additional evidence exists for SHH/PTCH1-independent (non-canonical) activation of GLI signalling, whereby signal transducers such as RAS, MEK and AKT activate GLI in the absence of SHH/PTCH1 binding (Riobo *et al.,* 2006; Stecca *et al.,* 2007) In this context, tumour suppressors such as p53 and Phosphatase and Tensin Homolog (PTEN; a negative regulator of PI3K/AKT signalling) negatively regulate non-canonical pathway activation in order to maintain tissue homeostasis (Gruber-Filbin *et al.,* 2013; Stecca *et al.,* 2009).

Depending on the ratio of GLI1-A to GLI-R in a given cell, GLI transcription factors can act as either transcriptional activators or repressors, resulting in a highly complex, dynamic and context-specific output signal. This, alongside the type of cell responding to SHH ligand, the length of time in which this signal is propagated, the concentration of morphogen present and the environment in which the cell is inhabiting will all help to shape a particular cellular response to SHH activation, thus accounting for the apparently pleiotropic effect that SHH (and its pathway products) can have on multiple cellular processes (reviewed by Aberger *et al.,* 2014).

5.1.4 Role of SHH signalling in bladder development and repair

The importance of SHH signalling in bladder biology has been well characterised in *in vivo* rodent models. Evidence that SHH signalling could play a role in stromal: urothelial interactions was initially demonstrated in the developing metanephric kidney of the mouse, as urothelial precursor cells were required to produce Shh in order to induce development in the surrounding mesenchyme. Ptch1-expressing mesenchymal cells subsequently expressed Bmp4 in order to induce differentiation of said mesenchymal cells into smooth muscle (J. Yu et al., 2002), hence elucidating the potential molecular basis behind the urothelial-mediated mesenchymal cell differentiation process identified in earlier studies (Section 5.1.2). When tracking smooth muscle differentiation in the developing mouse bladder, Shh was found to be expressed at an early stage, preceding expression of any smooth muscle differentiation-associated proteins. The importance of Shh morphogen in the differentiation process was confirmed with the use of Smo inhibitor cyclopamine, which inhibited smooth muscle differentiation; and treatment of cultured bladder mesenchyme cells with recombinant Shh, which induced differentiation (Shiroyanagi *et al.,* 2007). This pattern of expression was similar to that found during normal human urinary tract development, with precursor SHH protein expressed by the urothelium while expression of PTCH1, SMO and BMP4 were immunolocalised in the same cells of the residing mesenchyme (Jenkins *et al.,* 2007).

Beyond the role of the pathway in organogenesis, multiple publications by Shin *et al.* have demonstrated the importance of Shh signalling in the maintenance of postnatal bladder tissue homeostasis in mice. It was initially reported that mouse basal (Krt5+) urothelial cells produce and released Shh ligand upon tissue injury by bacterial or chemical means (Shin *et al.,* 2011). Conversely, Gli1 was found to be exclusively expressed in the stroma, with expression of the protein (in addition to Ptch1) increased after injury. Evidence of an active, SHH-mediated paracrine signalling loop in the repairing bladder was provided through the use of Gli1-mutant bladders which experienced a reduction in the level of urothelial proliferation post-injury compared to wild-type (Shin *et al.,* 2011). These findings were later complemented in a study of adult rat bladder where expression of Shh, Gli1 and Bmp4 were found to be induced after subtotal cystectomy (Peyton *et al.,* 2012). Examples of the Gli1-dependent genes induced by injured stromal cells in mice included *Wnt2*, *Wnt4*, *Fgf16* and *Bmp4*, while both basal urothelial and stromal cell types were found to upregulate expression of Wnt/β-catenin target gene *Axin2* (Shin *et al.,* 2011). Activation of *Axin2* expression (through treatment with GSK3β inhibitor LiCl) in Gli1-mutant bladders was sufficient to rescue the proliferative phenotype of recovering urothelial cells post-injury; implicating Wnt/β-catenin pathway activation as an ultimate consequence of paracrine SHH pathway activity in this context (Shin *et al.,* 2011).

5.1.5 Dysregulation of SHH signalling in cancer

As previously stated (Section 5.1.3), SMO can accumulate in the primary cilium and activate downstream GLI signalling constitutively if PTCH1 function is disabled. Mutations of the *PTCH1* gene thus provide the most commonly cited mechanism of ligand-independent SHH pathway dysregulation in cancer, as seen in cases of basal cell carcinoma (BCC) of the skin and medulloblastoma (Gailani *et al.,* 1996; Pietsch *et al.,* 1997). Both cancer types can develop from Gorlin syndrome, a condition which is primarily caused by hemizygous deletion of *PTCH1* at chromosome 9q22 (Shimkets *et al.,* 1996), a locus which is lost in ~50% of NMIBC cases (Aboulkassim *et al.,* 2003). As a result of this, both BCC and medulloblastoma have been shown to be amenable to therapy using inhibitors of constitutive SMO activity, such as

Vismodegib (GDC-0449). Through binding to SMO at its heptahelical bundle domain in a similar fashion to cyclopamine (Chen *et al.,* 2002a), GDC-0449 was found to significantly reduce the growth of BCC and medulloblastoma tumours (Amin *et al.,* 2010; Rudin *et al.,* 2009) and is currently approved by the FDA for use in treatment of metastatic BCC (Ingram, 2012). Despite this, the efficacy of GDC-0449 treatment in the context of NMIBC has not yet been tested.

Aberrant activation of SHH ligand activity (i.e. ligand-dependent tumours) has also been observed in various human malignancies, including pancreatic, breast and lung cancer (Bailey *et al.,* 2009; Mukherjee *et al.,* 2006; Yuan *et al.,* 2007). Furthermore, aberrant expression of GLI1 and GLI2 can be induced through non-canonical (SHH/PTCH1-independent) means, as evidenced in diseases such as renal cell carcinoma (J. Zhou et al., 2016). Cancers displaying a SHH/PTCH1-independent phenotype of SHH pathway activation remain unaffected by addition of SHH blocking ligands or canonical pathway antagonists, yet GLI signalling can be inhibited through blockade of crosstalk with other signalling cascades, such as RAS/MEK/ERK and PI3K/AKT (Kasiri *et al.,* 2017; Po *et al.,* 2017).

Investigation into the role of SHH signalling in mouse MIBC has previously focused on the potential status of Shh-expressing basal cells as a stem cell-like population. Lineage tracing of normal mouse Shh+/Krt5+ urothelial cells after several rounds of bladder injury revealed that all layers of the urothelium expressed the fluorescent reporter protein, granting credence to the author's hypothesis that the Shh+/Krt5+ basal urothelial cells can be identified as a form of progenitor stem cell population in mouse bladder (Shin *et al.,* 2011). After treatment of bladders with the pro-carcinogen N-butyl-N-4-hydroxybutyl nitrosamine (BBN), it was determined that the basal Shh+/Krt5+ population also inevitably contained the cell of origin for the subsequent MIBC that arose (Shin *et al.,* 2014a). However, expression of Shh was found to be absent in the eventual invasive tumours alongside a corresponding loss of *Gli1* and *Ptch1* in the surrounding stroma (Shin *et al.,* 2014a; Shin *et al.,* 2014b).
The observations compiled by Shin *et al.* suggest that unlike in various other cancer types (Thayer et al., 2003; Yuan et al., 2007), activated SHH signalling actually serves as a rate-limiting step in mouse urothelial carcinoma development.

Unbiased clustering of RNAseq analysis from TCGA cohort of human MIBC found that the well-differentiated luminal papillary bladder cancers could be clustered based on their expression of *SHH* and *BMP5* (Robertson *et al.,* 2017). However, reports of SHH pathway activity in human urothelial carcinoma are heavily conflicting: histological analysis of SHH pathway components in two studies determined that expression of SHH, PTCH1, GLI1 and GLI2 was overexpressed in high grade tumours and correlated with a reduced overall survival rate (He *et al.,* 2012; Islam *et al.,* 2016). By contrast, other studies concluded that GLI1 expression was lower in MIBC samples compared to NMIBC (Sverrisson *et al.,* 2014) and SHH protein expression did not correlate with tumour stage or survival rate (Nedjadi *et al.,* 2018). Such notable differences in interpretation could possibly be as a result of the notoriously low quality antibodies (in terms of specificity) historically available for components of the pathway (reviewed by Van Den Brink, 2007). On the basis of these observations, further research is clearly required to elucidate the expression of SHH pathway components in normal urothelium and MIBC and to understand the processes by which dysregulation of SHH signalling can potentially initialise MIBC progression, invasion and self-renewal.

5.2 Aims and hypothesis

SHH pathway-mediated paracrine interactions between the urothelium and underlying stroma are reportedly essential for rodent bladder development and adult tissue homeostasis, yet as discussed in Section 1.3, *in vitro* studies of adult NHU cells have found the cells to be capable of autonomous growth. Furthermore, NHU cells power autonomous growth through various signalling pathways downstream of autocrine activation of EGFR, some of which have previously been implicated in SHH/PTCH1-independent, non-canonical SHH pathway signalling.

Therefore, the overall aims of this chapter were to elucidate whether a SHH pathway signalling loop was active between human urothelium and stroma, determine whether this activation is affected in cases of MIBC through mutation or modulation in expression of key genes, and to understand whether undifferentiated NHU cells exhibit non-canonical SHH pathway activation through a pathway downstream of EGFR. It was hypothesised that, like in rodent bladder, adult human urothelial and stromal cells express the necessary components of the canonical SHH pathway to facilitate paracrine activation of GLI1 in stromal cells. This signalling axis would subsequently be affected in both undifferentiated NHU cells (which exhibit GLI activation through autocrine EGFR signalling) and a subset of MIBC tumours (due to dysregulated expression of canonical SHH genes).

Based on this hypothesis, the specific experimental objectives were to:

- Determine transcript and protein expression of SHH pathway components in urothelium *in situ* and compare to their expression *in vitro* in order to confirm that the cells express the required components needed for activation of the pathway (Section 5.4.1-2).

- Establish whether NuHS or normal bladder-derived human stromal (NbHS) cells possess the ability to activate canonical SHH signalling using specific agonists and antagonist. Visualise whether this activation results in changes to the expression and localisation of SHH pathway proteins (Section 5.4.3),

before quantifying the most globally upregulated genes in NuHS and NbHS cells after canonical pathway induction (Section 5.4.4).

- Ascertain what the effect of inhibiting EGFR or PI3K/AKT has on expression of active SHH pathway signalling (Section 5.4.5) in undifferentiated NHU cells.

- Determine whether gene expression of SHH pathway components is dysregulated in the different molecular subtypes of MIBC and identify novel subgroups of tumours with aberrant expression of pathway components compared to normal urothelium (Section 5.4.6).

5.3 Experimental approach

5.3.1 Characterisation of SHH pathway component expression in urothelium

Previously undertaken in-house RNAseq experiments were collated to quantify transcript expression of the primary gene components of the SHH pathway (*SHH, PTCH1, SMO, GLI1, GLI2, GLI3, HHIP*) in samples from undifferentiated NHU cells (n=6), NHU cells differentiated using the ABS/Ca^{2+} method (n=19) and urothelium *in situ* (n=10). Urothelium *in situ* samples were further separated on the basis of their organ of origin (n=6 ureter versus n=4 bladder samples) to determine whether there was a difference in expression of pathway components between tissue types.

Sections of normal adult ureter tissue (n=1 for SHH, n=2 for PTCH1) were labelled using immunohistochemistry to determine whether protein expression of SHH and PTCH1 aligned with the urothelial *in situ* transcript expression described in the previous analysis.

5.3.2 Activation of canonical SHH signalling in stromal cells

Determination of whether NuHS cells possessed an inducible SHH pathway response was accomplished by treating cells with agonists of the pathway and quantifying the response using induction of reporter gene/protein GLI1 expression. Two canonical SHH pathway agonists were used in this study: recombinant, *E. coli*-derived N-terminal mature SHH ligand (rSHH) and the synthetic chlorobenzothiophene-containing SAG. As *in vivo*, rSHH binds to membrane-localised PTCH1 to induce pathway activation while SAG is PTCH1-independent and binds directly to the heptahelical bundle of SMO (Chen *et al.,* 2002b). Similarly, synthetic antagonist GDC-0449 binds to the same heptahelical bundle (Fig. 5.1) and was used as a competitive inhibitor of SMO activity. SAG activity was titrated on confluent NuHS cells (n=1) following serum starvation due to previous reports that determined that optimal formation of primary cilium occurred in confluent, serum-free conditions (Spann *et al.,* 2015). Expression of GLI1 in SAG-treated NuHS cells was compared to that found in mouse embryonic fibroblast 3T3-J2 cells, a previously validated SHH-responsive cell line (Martinez-Chinchilla *et al.,* 2008). NuHS (n=3 independent cell lines) and NbHS (n=2 cell lines) were subsequently treated with SAG (in the presence and absence of GDC-0449) for periods of 24h and

48h to determine whether activation of canonical pathway signalling affected transcript and protein expression of other components of the SHH pathway.

To reveal the identity of downstream targets induced by GLI1 activation in stromal cells, cultures were treated with 100 nM SAG for 24h and 48h and the sample RNA sequenced. Two NuHS and one NbHS cell line were sequenced, with Y875 and Y1027 derived from ureter and Y879 derived from bladder. RT-qPCR analysis was used to confirm that each sample displayed a ≥ 2-fold induction of *PTCH1* and *GLI1* before they were sequenced. Differential expression analysis was performed to determine what the most upregulated/downregulated genes were after canonical pathway activation. Changes in expression to previously cited GLI target genes *CCND1, CCND2, MYCN* and *BCL2* (Kasper *et al.,* 2006; Yoon *et al.,* 2002) and selected genes associated with WNT, FGF, BMP and Hippo signalling were additionally examined as part of the analysis. Gene ontology analysis of the genes found to have a Log_2 fold change values ≥ 1 in each dataset was used to infer the biological functions related to GLI1 activation in stromal cells.

5.3.3 Non-canonical induction of *GLI1* expression in NHU cells

To determine whether undifferentiated NHU cells express *GLI1* through a non-canonical mechanism, cells were treated with a combination of PD153035, SAG and GDC-0449 for a period of 24h (n=3 independent cell lines). Relative expression of *PTCH1* and *GLI1* was compared between samples by RT-qPCR due to their status as reporter genes of SHH pathway activation. The inhibition of an alternative signal transducing pathway active in NHU cells, PI3K/AKT signalling, was also explored in relation to expression of *GLI1.* Modulation of PI3K/AKT signalling was achieved by treating NHU cells with a PI3K inhibitor LY294002 in isolation or in combination with PD153035 (n=1 NHU cell line), before observing GLI1 transcript and protein expression by RT-PCR and immunofluorescence approaches.

5.3.4 SHH pathway dysregulation in MIBC

To explore the possibility that the SHH pathway was dysregulated in cases of MIBC, RNAseq samples from TCGA MIBC cohort (n=404) were separated into previously defined molecular subtypes (Section 1.4.3) and expression of *SHH*, *PTCH1*, *GLI1* and *GLI2* compared to the expression of these genes in normal urothelium (using *in situ* expression data collated from previous in-house RNAseq experiments; n=6).

The frequency of mutations in said genes in TCGA cohort was additionally analysed to determine whether SHH pathway genes (e.g. *PTCH1*) found to be commonly mutated in other forms of human cancer were also found to be commonplace in MIBC. Information on the mutation status of TCGA MIBC samples was obtained from the cBioPortal for Cancer Genomics (https://www.cbioportal.org/). Following confirmation of urothelium-specific *GLI2* upregulation in a subset of basal/squamous tumours, the tumours were analysed to determine the most common mutations inherent to this group and what the most differentially expressed genes were in comparison to the remaining basal/squamous tumours. The identity of a potential transcription factor that induced the expression of highly upregulated genes in the *GLI2*-high group was determined through use of the GeneHancer database of gene enhancers and their respective target genes (Fishilevich *et al.,* 2017). Analysis of the changes in gene expression of previously identified markers of neuroendocrine-like MIBC tumours (Aine *et al.,* 2015) was additionally performed to observe whether this novel subgroup also exhibited an increase in expression of these targets. Finally, the overall survival of patients with *GLI2*-high basal/squamous tumours was compared to the remaining basal/squamous tumour patients to determine whether upregulation of *GLI2* was associated with a reduced survival rate.

5.4 Results

5.4.1 RNAseq analysis of SHH pathway genes in NHU cells

Urothelial cells expressed multiple components of the SHH pathway, including *SHH* transcript (Fig. 5.2A). However, NHU cells (in both undifferentiated and serum differentiated states) had significantly lower expression of *SHH* compared to urothelium *in situ* ($p \leq 0.001$). *PTCH1*, *SMO*, and *GLI3* were expressed by urothelium *in situ* and NHU cells, with no significant differences in expression found when comparing cell conditions. Urothelium *in situ* (in addition to differentiated NHU cells) was not found to express *GLI1* or GLI-mediated negative pathway regulator *HHIP*, although NHU cells cultured in an undifferentiated state were found to induce a 10-fold and 8-fold increase in expression of either gene, respectively. *GLI2* expression was absent in all urothelial samples.

After separating the *in situ* samples on the basis of whether the sample was acquired from ureter or bladder tissue, it was determined that *SHH* expression was significantly higher in bladder urothelial samples (Fig. 5.2B; $p \leq 0.001$), but no significant differences in expression of the other genes was observed. The above analysis therefore confirmed that urothelial cells expressed the necessary gene (*SHH*) required to participate in paracrine SHH signalling with another cell type, with a greater expression of the gene found in bladder urothelium compared to ureter. However, a lack of *GLI1*/*GLI2* expression in both *in* vitro and *in situ* differentiated urothelium suggested the absence of autocrine SHH pathway signalling in these physiological contexts. A visual summary of the components of the SHH pathway expressed in NHU cells in an undifferentiated and ABS/Ca^{2+} differentiated state is provided in Fig. 5.3 and Table 5.1.

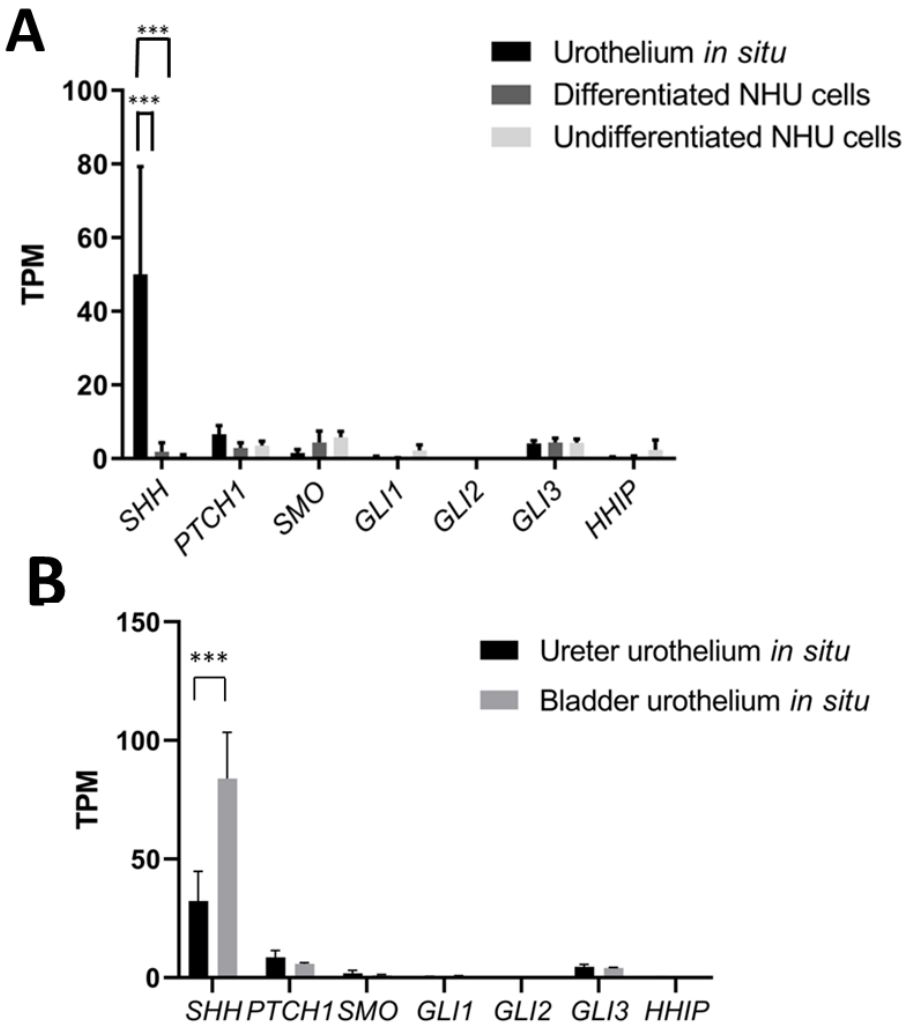

Figure 5.2: Urothelial cells express key components of the SHH signalling pathway

Bioinformatics analysis of multiple RNAseq experiments was performed to identify the expression pattern of SHH pathway components in urothelial cells under different conditions. Graph (**A**) denotes expression of *SHH*, *PTCH1*, *SMO*, *GLI1*, *GLI2*, *GLI3* and *HHIP* in RNAseq samples from undifferentiated NHU cells (n=9), (ABS/Ca^{2+}) differentiated NHU cells (n=13) and urothelium *in situ* (n=6). Graph (**B**) is a comparison of expression of SHH pathway genes in *in situ* urothelium when split by ureter (n=3) or bladder (n=3) derivation. Gene expression is measured in Transcripts per Million mapped reads (TPM), with error bars representing standard deviation of the mean. Significance between groups was determined by a two-way ANOVA with Tukey's (**A**) or Sidak's (**B**) multiple comparisons post-hoc tests. ***=p<0.001.

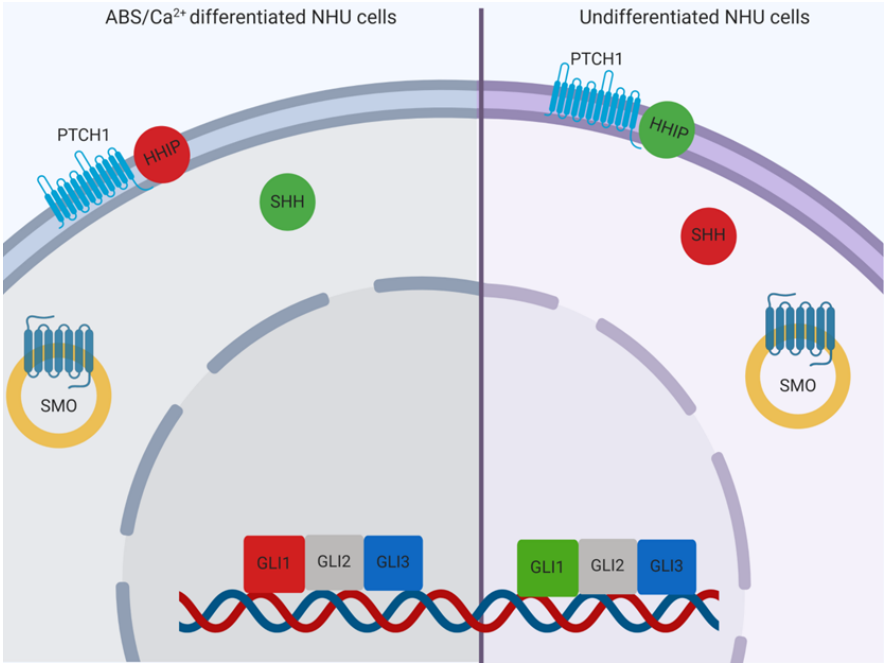

Figure 5.3: Schematic representation of expressed gene components of the SHH pathway in NHU cells

Genes that have a $\log_2$ fold change increase in expression in the specified cell state compared to the other are coloured green while genes that have a $\log_2$ fold change decrease in expression are coloured red. Genes that are expressed by NHU cells in both undifferentiated and ABS/Ca^{2+} differentiated states are coloured blue. *GLI2* is not expressed in any urothelial state so is coloured grey. Differences in fold change for each gene is detailed in Table 5.1.

Gene	Log_2 fold change
SHH	1.905
PTCH1	-0.322
SMO	-0.398
GLI1	-4.740
GLI2	N/A
GLI3	0.035
HHIP	-2.821

Table 5.1: Log_2 fold change differences in SHH pathway component transcript expression in ABS/Ca^{2+} differentiated NHU cells compared to undifferentiated NHU cells

Genes that experienced a $\log_2$ fold change increase ≥ 1 are highlighted in green, while genes with a $\log_2$ fold change decrease ≤ -1 are highlighted in red.

5.4.2 SHH and PTCH1 protein expression in native urothelium

Preliminary immunohistochemical analysis of FFPE human ureter using antibodies specific to N-terminal SHH (n=1 ureter) and PTCH1 (n=2 ureters) suggested that urothelium *in situ* expressed both proteins in addition to transcript. SHH was found to be expressed exclusively by urothelium, with an absence of expression visualised in the surrounding lamina propria (Fig. 5.4A). Expression of SHH appeared primarily cytoplasmic and was consistently expressed throughout all layers of the urothelium. However, additional nuclear SHH-N labelling was also observed in the intermediate and superficial layers of the urothelium. Intense PTCH1 expression was found localised to the apical membrane of superficial cells, with weaker cytoplasmic labelling found throughout the other urothelial cell layers (Fig. 5.4B). PTCH1 was also found to be expressed by cells residing in the lamina propria and smooth muscle which manifested itself in a distinctive, concentrated subcellular labelling pattern, thereby highlighting potential cells that receive a SHH signal.

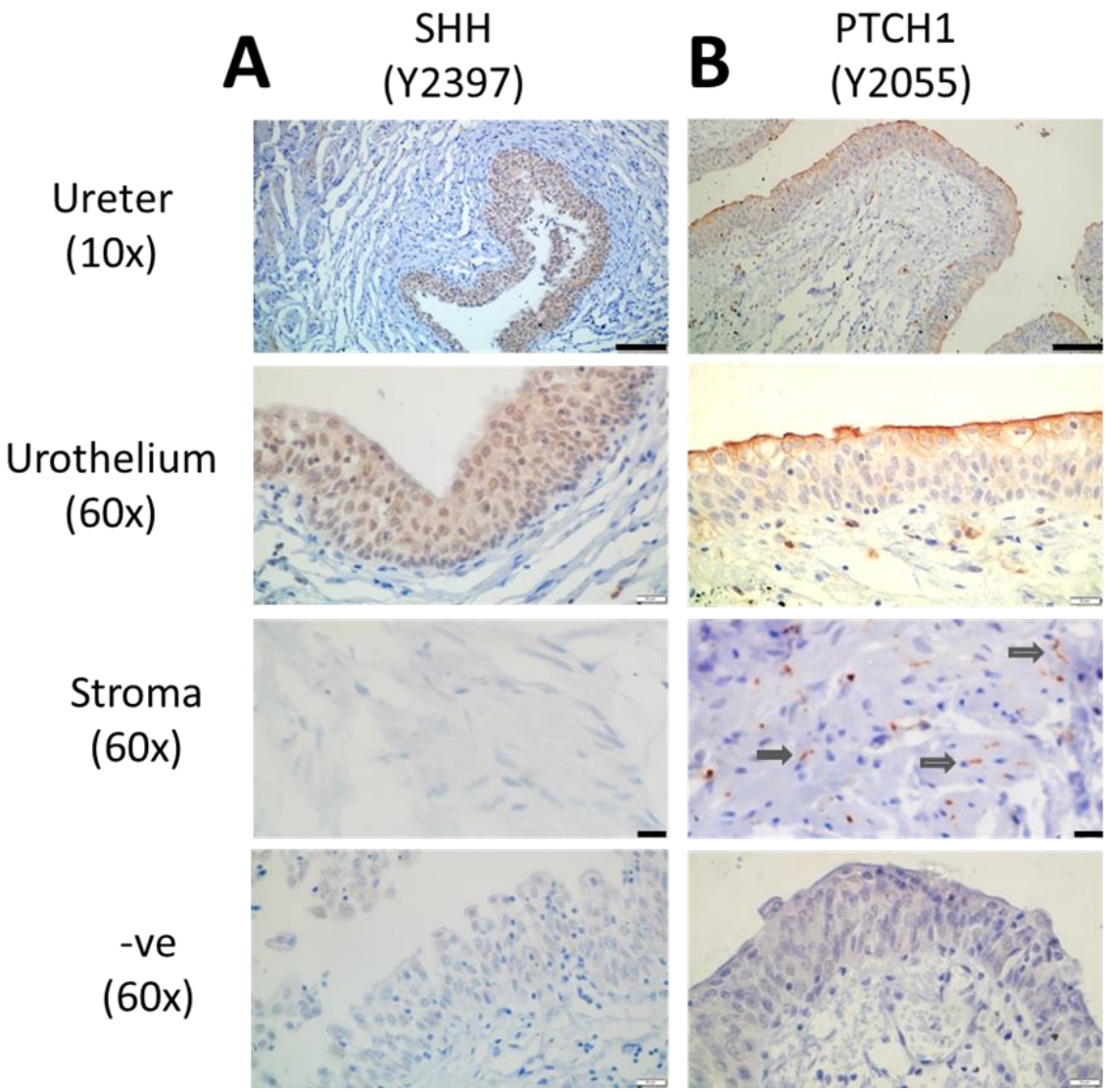

Figure 5.4: SHH expression in human ureter is restricted to the urothelium whereas both urothelial and stromal cells express SHH-binding protein PTCH1

Labelling of N-terminal SHH (**A**) and PTCH1 (**B**) in normal human ureters (Y2397 and Y2055, respectively). Grey arrows highlight examples of the localisation of PTCH1 expression in cells of the lamina propria. The phenotype of SHH expression was observed in one ureter, whilst PTCH1 expression was indicative of two independent samples of ureter (Appendix xiv). Sections that received no primary antibody were used as negative controls. Scale bar= 100 µm (top row images), 20 µm (all other images).

5.4.3 Activation of the canonical SHH pathway in stromal cells

5.4.3.1 Titration of SAG on stromal cells

To investigate SHH pathway activation *in vitro*, validation of reagents that could induce a canonical pathway response was required. Treatment of mouse 3T3-J2 fibroblasts with 1 µg/mL rSHH and 250 nM SAG both succeeded in inducing GLI1 protein expression, confirming that both reagents were capable of inducing a SHH pathway response in a suitable cell type (Fig. 5.5A). Immunoblotting of NuHS cell line Y929A determined that, unlike 3T3-J2 cells, NuHS cells expressed GLI1 protein in the absence of drug treatment, indicative of constitutive activity (Fig. 5.5B). Treatment of Y929A cells with a titration of SAG between 0-1 µM concluded that 100 nM SAG induced the greatest up-regulation of GLI1 protein when compared to control, with a 2.4-fold increase in expression (Fig. 5.5B-C).

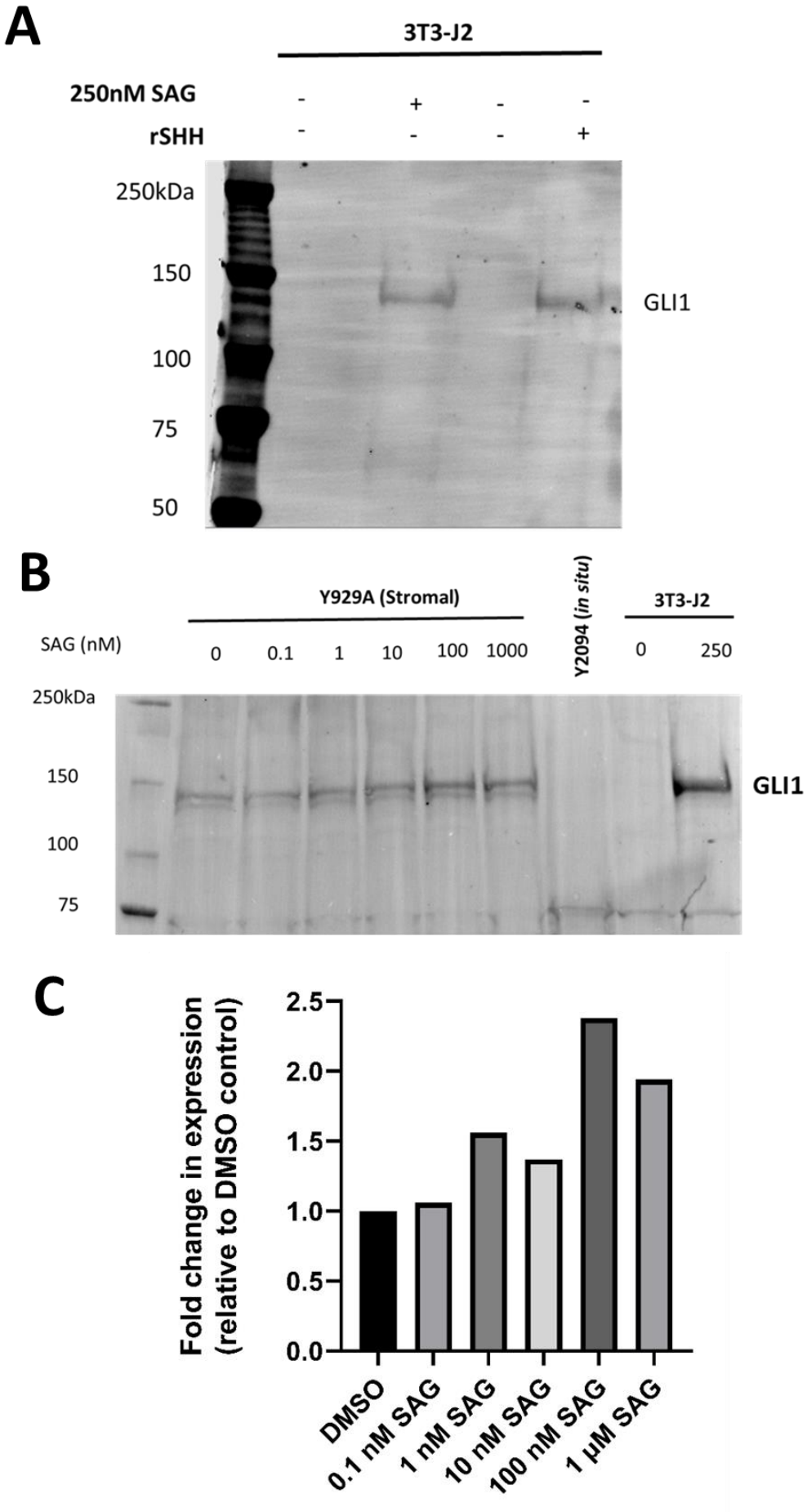
A
3T3-J2
250nM SAG
rSHH
- + - -
- - - +
250kDa
150
100
75
50
GLI1
B
Y929A (Stromal)
Y2094 (in situ)
3T3-J2
SAG (nM)
0 0.1 1 10 100 1000
0 250
250kDa
150
100
75
GLI1
C
Fold change in expression (relative to DMSO control)
2.5
2.0
1.5
1.0
0.5
0.0
DMSO
0.1 nM SAG
1 nM SAG
10 nM SAG
100 nM SAG
1 µM SAG

Figure 5.5: Validation of GLI1 induction in stromal cells using synthetic and recombinant SHH pathway agonists

A) Immunoblot image of GLI1 expression in mouse fibroblast 3T3-J2 cells treated with 250nM SAG, 1 µg/mL rSHH or DMSO vehicle control for a period of 24h. All conditions were treated with 0.1% DMSO to control for non-specific solvent effects. **B)** Immunoblot image of GLI1 expression in Y929A NuHS cells (n=1) treated with a titration of SAG (0 to 1000 nM) for 24h. Protein from 3T3-J2 cells treated with and without 250nM SAG was used as a positive control for GLI1 induction in cells. Protein from *in situ* urothelium (Y2094) was used as a negative control as this cell type had previously been demonstrated to lack *GLI1* transcript expression. **C)** Densitometry analysis of Y929A GLI1 expression in (**B**). The fold changes in expression of GLI1 in each condition were calculated against the densitometry value of GLI1 expression in the DMSO control lysate.

5.4.3.2 Effect of SAG treatment on SHH pathway gene expression in stromal cells

To characterise transcript expression of SHH pathway components in NuHS cells, non-quantitative RT-PCR analysis of said cells treated with 100 nM or 250 nM SAG for periods of 24h and 48h was performed. Phase contrast micrographs of NuHS cells grown *in vitro* revealed that these cells exhibited an elongated, fibroblast-like morphology when sparse but adopted a uniform, flattened morphology upon reaching confluence (Appendix xiv). Stromal cells were treated with SAG upon reaching visual confluence, with no notable changes in morphology observed after drug treatment when compared to control. Expression of *GLI1* and *PTCH1* transcripts were induced in stromal cells by SAG in a concentration and time-related manner (Fig. 5.6A). *GLI2* and *GLI3* were also expressed by NuHS cells, with expression found to be relatively consistent (*GLI2)* or displaying different phenotypes dependent on cell line or condition type (*GLI3*). Despite evidence that demonstrated that all of the primary downstream components of the pathway were expressed, NuHS cells were not found to express *SHH* transcript under any of the conditions assayed, consistent with earlier immunohistochemistry analysis.

When assaying the RNA samples by RT-qPCR in independent NuHS (n=3) and NbHS (n=2) cell lines, a significant increase in *PTCH1* and *GLI1* expression was observed after 24h 100 nM SAG treatment ($p \leq 0.01$) in cells from both derivations (Fig. 5.6B). NuHS cells treated with 100 nM SAG with a concurrent addition of GDC-0449 were found to significantly abrogate induction of *PTCH1* and *GLI1* transcript (Fig. 5.6C; $p \leq 0.01$); confirming that activation of the pathway in this cell type was SMO-dependent.

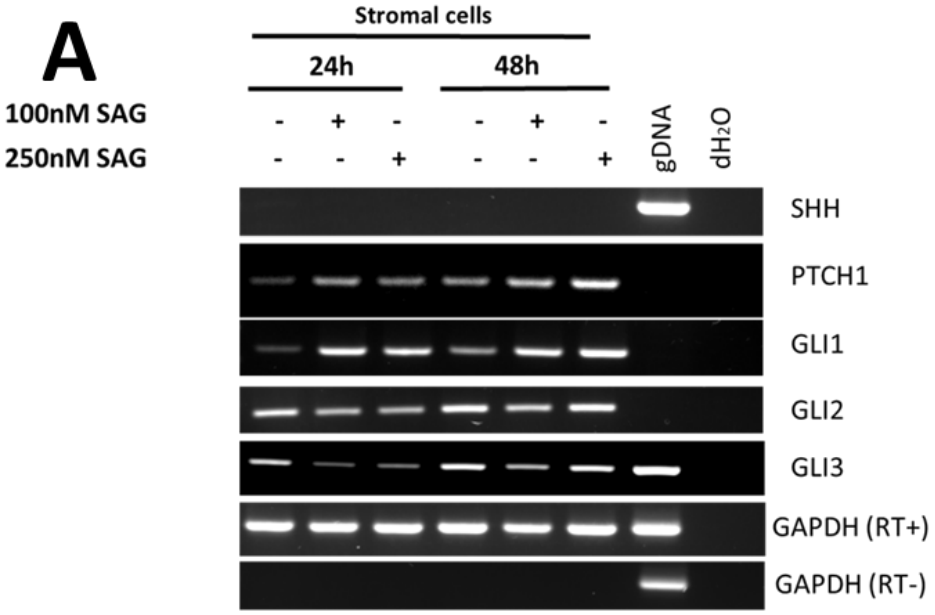
A
Stromal cells
24h
48h
100nM SAG
250nM SAG
- + - - + -
- - + - - +
gDNA
dH2O
SHH
PTCH1
GLI1
GLI2
GLI3
GAPDH (RT+)
GAPDH (RT-)

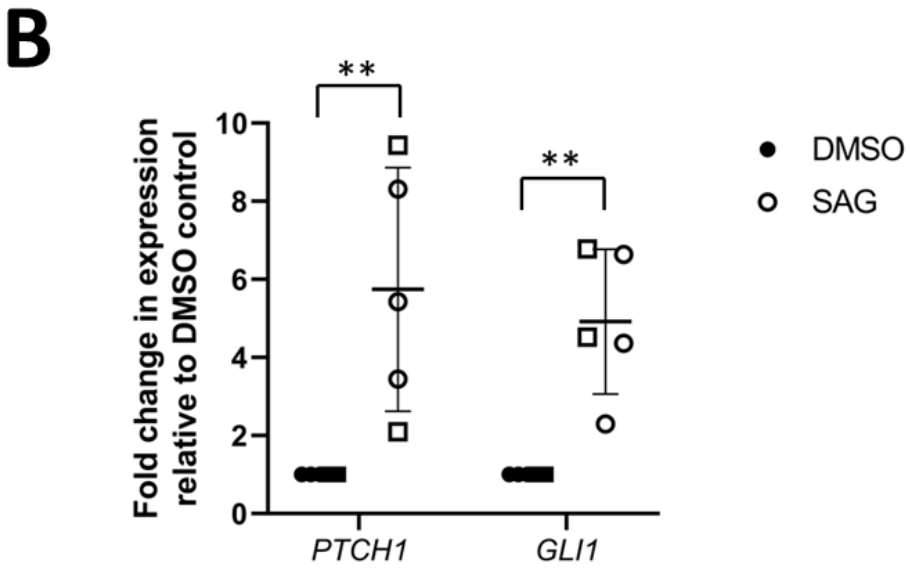
B
**
**
Fold change in expression relative to DMSO control
10
8
6
4
2
0
PTCH1
GLI1
DMSO
SAG

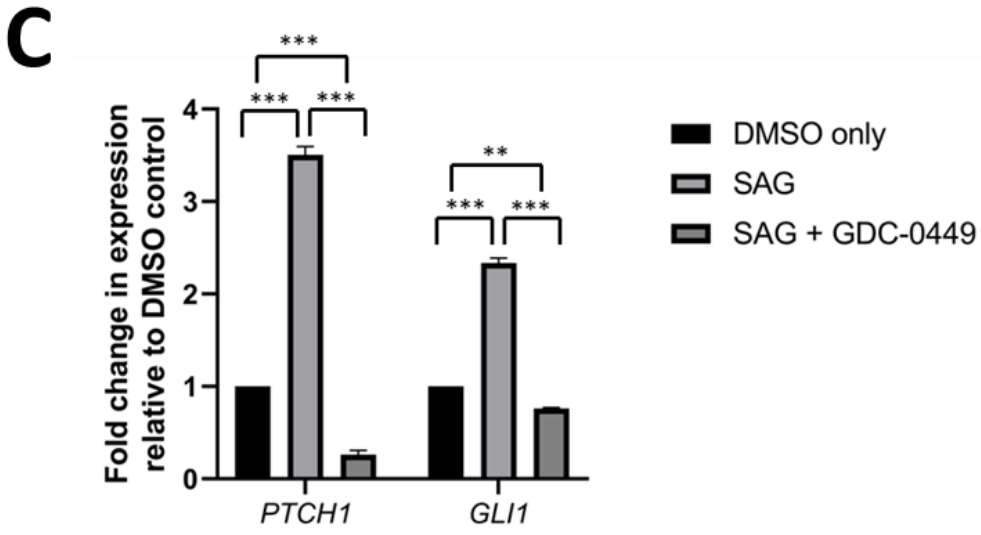
C
***
***
***
**
***
***
Fold change in expression relative to DMSO control
4
3
2
1
0
PTCH1
GLI1
DMSO only
SAG
SAG + GDC-0449

Figure 5.6: Treatment of NuHS cells with SAG induced increased expression of *PTCH1* and *GLI1* transcript

A) RT-PCR analysis of *SHH*, *PTCH1*, *GLI1*, *GLI2*, *GLI3* transcript expression in Y875 NuHS cells (n=1). Cells were treated with 100 or 250 nM SAG for periods of 24h (lanes 1-3), or 48h (lane 4-6) compared to DMSO only controls. All conditions were treated with 0.1% DMSO to control for non-specific solvent effects. Each cDNA synthesis used 1 µg starting template RNA, with cDNA undergoing PCR amplification up to 32 cycles *(SHH*, all other targets up to 30 cycles). The primers used for *PTCH1*, *GLI1* and *GLI2* expression were intron-spanning and therefore did not produce positive gDNA bands of the same size. Housekeeping gene *GAPDH* was used to confirm equal loading between samples (25 cycles). A no template (H_2O only) sample was used as a negative control for each primer set. **B**) qRT-PCR analysis of *PTCH1* and *GLI1* expression in five independent stromal cell lines (three derived from ureter, two derived from bladder) treated with 100 nM SAG for 24h. Circle icons represent data from NuHS samples while square icons represent data from NbHS samples. **C)** qRT-PCR analysis of *PTCH1* and *GLI1* expression in three independent NuHS cell lines treated with 100 nM SAG ± 10 µM GDC-0449 for 24h. Values shown in figures (**B-C**) represent the fold change in expression between DMSO control and treatment conditions, with all values normalised to *GAPDH* expression. Significance between groups was determined by a two-way ANOVA test performed with Tukey's multiple comparisons post-hoc test. **=p≤0.01; ***=p≤0.001.

5.4.3.3 Expression and localisation of SHH pathway proteins in stromal cells after canonical pathway activation/inhibition

By immunoblotting, Y875 stromal cells were also found to induce expression of GLI1 protein after treatment with 100 nM SAG, with the greatest induction of protein found at 24h rather than 48h (Fig. 5.7).

Immunofluorescence images of Y886 stromal cells revealed that PTCH1 localised intensely to cilia-like projections (Fig. 5.8A). Interestingly, this phenotype was also observed when cells were treated with SAG, suggesting that no internalisation of PTCH1 takes place when activating the canonical pathway at the level of SMO. Expression of PTCH1 was lost when treated concurrently with SAG and GDC-0449. GLI1 expression after SAG treatment was localised intensely to the nuclei of cells, but expression of the protein was also lost in GDC-0449 treated cells (Fig. 5.8B). Overall, the evidence presented in Section 5.4.3 revealed that NuHS cells did not express *SHH*, yet were amenable to exogenous activation of the canonical SHH pathway, potentially indicative of a SHH-receiving cell type in a paracrine signalling relationship.

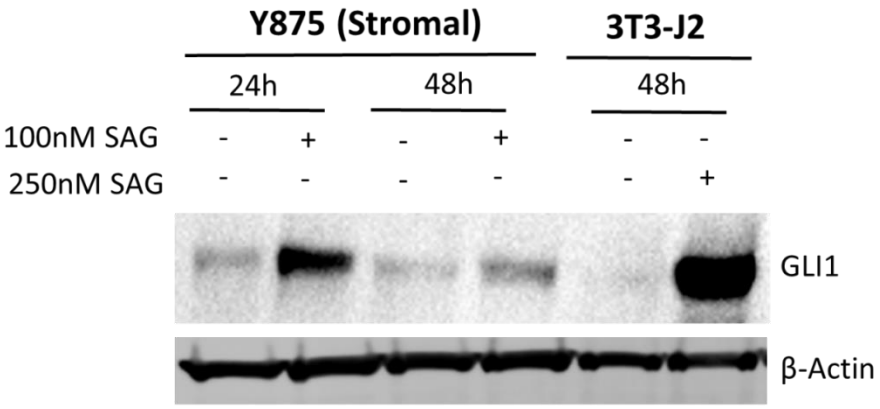

Figure 5.7: Canonical SHH pathway activation induces GLI1 protein in NuHS cells

After determining that SAG treatment induced a significant increase in *GLI1* transcript, immunoblot analysis of GLI1 expression in Y875 stromal cells (n=1) treated with 100nM SAG for periods of 24 and 48h was performed. Mouse 3T3-J2 fibroblast cells treated with vehicle control or 250nM SAG for 48h were used as negative and positive controls for GLI1 induction, respectively. All conditions were treated with 0.1% DMSO to control for non-specific solvent effects. Expression of β-Actin was used to confirm equal loading of samples.

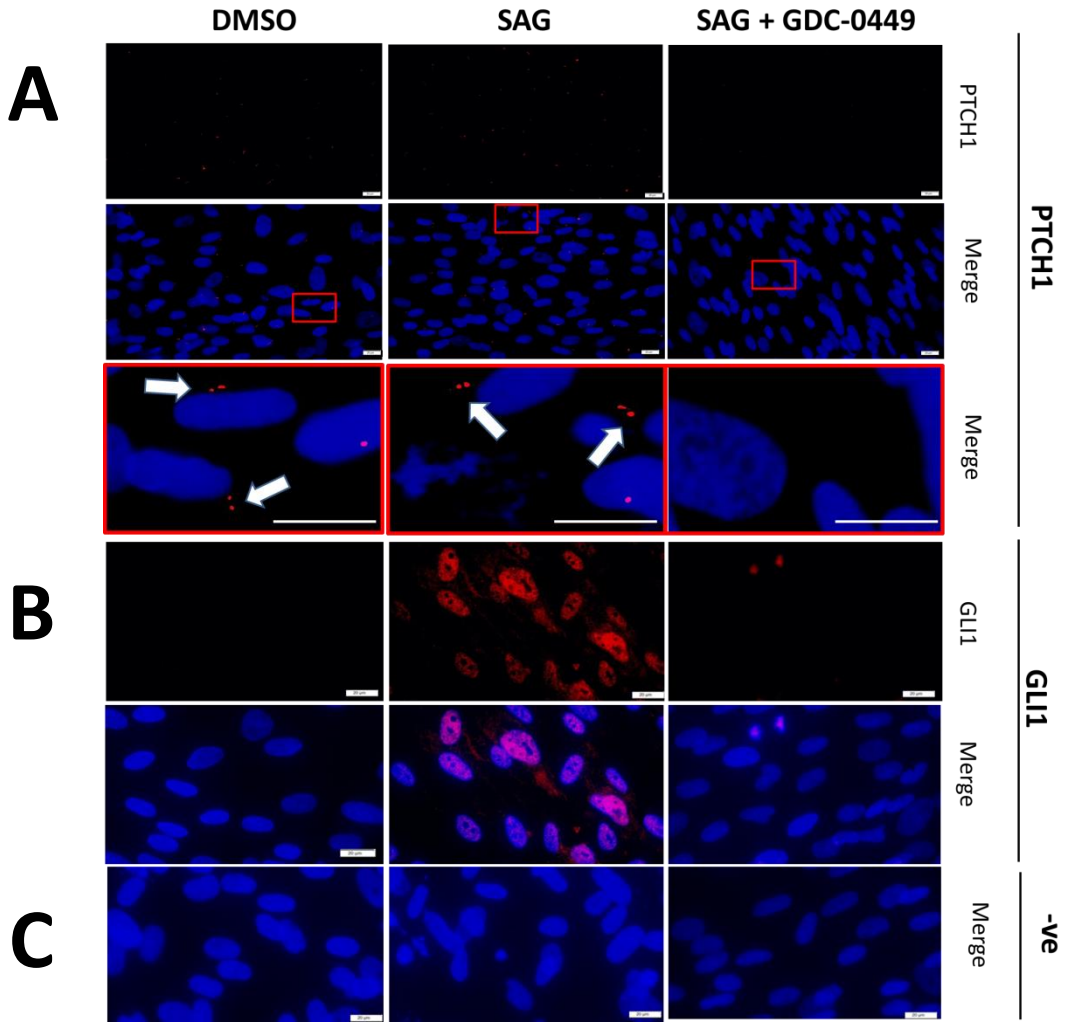

Figure 5.8: Canonical SHH pathway activation induces nuclear GLI1 while concurrent inhibition of the pathway abrogates GLI1 and PTCH1 expression in NuHS cells

Immunofluorescence imaging of PTCH1 (**A**) and GLI1 (**B**) expression in Y886 stromal cells treated with 100 nM SAG ± 10 µM GDC-0449 for 24h. All conditions were treated with 0.1% DMSO to control for non-specific solvent effects. Prior to labelling, cells grown on glass slides had undergone formalin fixation and were Triton X-100 permeabilised. Red boxes in (**A**) images highlight area of interest in PTCH1-labelled cells magnified to display detail. White arrows indicate localisation of PTCH1 in stromal cells to cilia-like formations in DMSO and SAG treated cultures. The pattern of PTCH1 expression is representative of one NuHS cell line, whilst nuclear induction of GLI1 after SAG treatment was confirmed in two independent stromal cell lines, images of which can be found in Appendix xiv. Cells receiving no primary antibody (**C**) were used as a negative control. Images were all taken at same exposure and are shown with or without overlaid Hoechst 33258 DNA staining. Scale bar= 20µm.

5.4.4 RNAseq of stromal cells treated with SAG

5.4.4.1 Differential expression analysis of SAG-treated stromal cells

To determine what genes were upregulated following activation of the canonical SHH pathway, RNAseq analysis of NuHS and NbHS cells treated with SAG was performed. Quality control of samples was first undertaken by confirming expression of reporter genes by RT-qPCR and by validating raw sequencing read quality using FastQC (both Appendix xi). Examination of genes of the SHH pathway in the sequenced samples determined that *GLI1*, but not *PTCH1*, was significantly upregulated by SAG treatment at both time points assayed (Fig. 5.9; $p \leq 0.01$). A significant difference was additionally found between expression of *GLI2* at 24h DMSO and 48h DMSO ($p \leq 0.01$), but not between DMSO and SAG-treated samples at either time-point. Expression of *SMO*, *GLI3* and *HHIP* remained consistent throughout conditions, while expression of *SHH* was negative in all samples, supporting previous data.

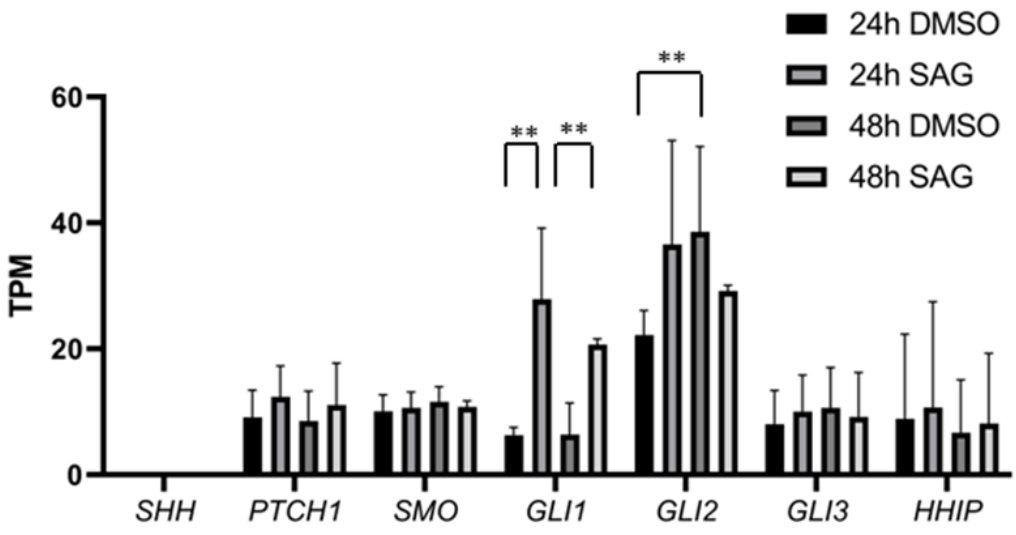

Figure 5.9: Expression of SHH pathway target genes in NuHS and NbHS cells after SAG treatment

RNAseq expression data of *SHH*, *PTCH1*, *SMO*, *GLI1*, *GLI2*, *GLI3* and *HHIP* in NuHS (n=2) and NbHS (n=1) cells treated with SAG versus vehicle controls. All conditions were treated with 0.1% DMSO to control for non-specific solvent effects. Gene expression is measured in TPM, with error bars representing standard deviation of the mean (n=3 replicates). Significance between groups was determined by a two-way ANOVA test performed with Tukey's post-hoc test.**=≤0.01.

Differential expression analysis was performed to compare three different sets of expression data from the SAG treatment experiment: 24h DMSO versus 24h SAG (24h), 48h DMSO versus 48h SAG (48h) and all DMSO versus all SAG values (24/48h). It was determined that both 24h and 48h analyses had 84 genes with $\log_2$ fold change values ≥1, while 24/48h had 39 genes that passed the same metric. Of these genes, 33 were classed as protein-coding in 24h, 16 in 48h and 10 for 24/48h (Tables 5.2-5.4). For each analysis, *GLI1* was confirmed to be the gene with either the highest (48h, 24/48h) or third highest (24h) $\log_2$ fold change value while also exhibiting the lowest false discovery rate-adjusted p value (q value) of any gene. Despite this, differential expression analysis determined that no gene was found to have a significant q value in any of the three comparisons. When inputting the 24h protein-coding gene list for Gene Ontology (GO) enrichment analysis, it was revealed SAG treatment was significantly associated with upregulation of genes involved in the assembly of basement membrane (Table 5.5). The same approach revealed no significant GO term association with the gene lists of 48h and 24/48h.

No.	Gene	Mean DMSO TPM	Mean SAG TPM	Log_2fold change	pval	qval
1	*ITGB4*	1.82	16.20	2.203	0.067	0.971
2	*LAMC2*	3.23	30.06	2.134	0.078	1
3	*GLI1*	6.28	27.86	1.890	1.98E-05	0.307
4	*ACO68631.2*	12.26	18.42	1.772	1	1
5	*FCRL3*	2.71	7.50	1.645	0.165	1
6	*EIF3CL*	2.80	7.60	1.576	0.106	1
7	*AC008393.2*	44.12	53.66	1.559	0.809	1
8	*TNFRSF6B*	1.70	4.31	1.516	1	1
9	*TRBJ2-4*	0.00	2.67	1.473	1	1
10	*TRBJ2-3*	5.78	5.10	1.448	1	1
11	*LAMA3*	10.27	17.11	1.370	0.285	1
12	*BIVM-ERCC5*	2.20	3.93	1.366	0.097	1
13	*SMIM11A*	21.28	25.25	1.356	0.651	1
14	*AREG*	13.62	43.53	1.349	0.476	1
15	*ATP8B1*	2.50	10.93	1.334	0.010	0.818
16	*G0S2*	28.48	46.65	1.316	1	1
17	*LAMB3*	6.95	24.87	1.307	0.073	0.987
18	*AL035078.4*	52.34	58.48	1.295	0.510	1
19	*PTHLH*	5.19	11.14	1.187	0.285	1
20	*EIF4A3*	8.08	13.20	1.155	0.173	1
21	*ANO9*	1.34	3.08	1.134	0.388	1
22	*MDFI*	1.40	5.30	1.133	0.046	0.915
23	*AC068547.1*	1.73	4.14	1.113	0.110	1
24	*PIGY-DT*	0.00	1.68	1.082	1	1
25	*PLEK2*	1.26	4.82	1.079	0.107	1
26	*PWP2*	1.88	3.92	1.075	0.662	1
27	*FAM83A*	1.13	3.90	1.062	0.0233	0.889
28	*COL17A1*	1.18	5.72	1.057	1	1
29	*BX470111.1*	0.25	2.19	1.041	1	1
30	*AC012254.2*	0.00	1.56	1.027	1	1
31	*SFN*	26.12	35.41	1.021	0.009	0.818
32	*TEX22*	0.93	3.44	1.019	0.003	0.818
33	*CARNS1*	0.45	2.30	1.013	0.001	0.818

Table 5.2: List of protein-coding genes from the 24h analyses with the highest log_2 fold change values. Genes are displayed in descending order, with the gene with the highest log_2 fold change (*ITGB4*) shown first.

No.	Gene	Mean DMSO TPM	Mean SAG TPM	Log_2fold change	pval	qval
1	*GLI1*	6.38	20.67	2.0396	0.006	0.378
2	*C19orf33*	1.05	6.71	1.850	1	1
3	*ZACN*	1.90	7.22	1.680	0.263	0.755
4	*PPP1R1B*	0.07	3.49	1.582	1	1
5	*AL132780.3*	1.27	6.43	1.540	0.042	0.487
6	*TRBJ2-5*	2.93	3.21	1.515	1	1
7	*SLPI*	3.04	5.04	1.424	1	1
8	*NRSN1*	0.76	5.68	1.409	0.493	0.886
9	*S100A2*	10.87	10.50	1.396	1	1
10	*GNG8*	1.27	3.99	1.372	1	1
11	*MMEL1*	0.02	2.08	1.247	1	1
12	*COMMD3-BMI1*	3.49	5.12	1.220	1	1
13	*PACRG*	2.41	6.79	1.220	1	1
14	*GNGT2*	0.36	2.55	1.130	0.000	0.378
15	*CEMP1*	0.03	1.72	1.071	1	1
16	*CFTR*	2.17	4.19	1.008	0.094	0.610

Table 5.3: List of protein-coding genes from the 48h analyses with the highest log_2 fold change values.

No.	Gene	Mean DMSO TPM	Mean SAG TPM	Log_2fold change	pval	qval
1	*GLI1*	6.33	24.27	1.967	2.31E-05	0.118
2	*ITGB4*	2.18	8.97	1.482	0.456	1
3	*LAMC2*	2.63	15.94	1.436	0.201	1
4	*C19orf33*	6.87	18.81	1.388	0.609	1
5	*S100A2*	128.85	242.92	1.203	0.820	1
6	*TRBJ2-3*	4.40	3.92	1.199	1	1
7	*AC068631.2*	14.01	16.51	1.166	1	1
8	*TRBJ2-2P*	1.38	2.00	1.131	1	1
9	*EIF3CL*	2.75	5.26	1.034	0.158	1
10	*TNFRSF6B*	1.30	2.68	1.008	0.234	1

Table 5.4: List of protein-coding genes from the 24/48h analyses with the highest log_2 fold change values.

GO biological process	pval	qval
hemidesmosome assembly (GO:0031581)	2.24E-10	3.56E-06
cell-substrate junction assembly (GO:0007044)	5.28E-08	4.21E-04

GO cellular component	pval	qval
laminin-5 complex (GO:0005610)	4.52E-05	4.55E-02
laminin complex (GO:0043256)	3.34E-06	6.73E-03
basement membrane (GO:0005604)	6.08E-05	4.09E-02

Table 5.5: The list of genes with a log_2 fold change increase ≥1 from the 24h analyses were input into the GO enrichment analysis PANTHER overrepresentation test (http://geneontology.org/).

5.4.4.2 Expression of other genes of interest in stromal cells

Despite having determined that no gene was significantly upregulated by SAG treatment following a global analysis of changes between the 24h or 48h conditions, the RNAseq transcriptome resource was subsequently used to analyse expression of selected genes of interest. Vehicle control-treated NuHS/NbHS cells were found to express GLI1 target genes *CCND1* and *MYCN*, but no change in expression was found upon treatment with SAG (Fig. 5.10A). Previously cited GLI1 target gene *BCL2* was not expressed by NuHS/NbHS cells in any condition. Pathways that have previously been demonstrated to be active in rodent bladder stromal cell signal transduction, such as WNT, FGF and BMP signalling, were additionally investigated. This analysis revealed that *WNT5A* and *WNT5B* are the most expressed genes of the WNT ligand family in control cells (Fig. 5.10B), while *FZD2* and *FZD7* are the most highly expressed genes encoding for the Frizzled trans-membrane WNT receptor proteins (Fig. 5.10C). Other genes of interest include high expression of *FGF7* (Fig. 5.10D) and BMP genes *BMP1* and *BMP4* (Fig. 5.10E). None of the above targets were affected by SAG treatment at either time-point.

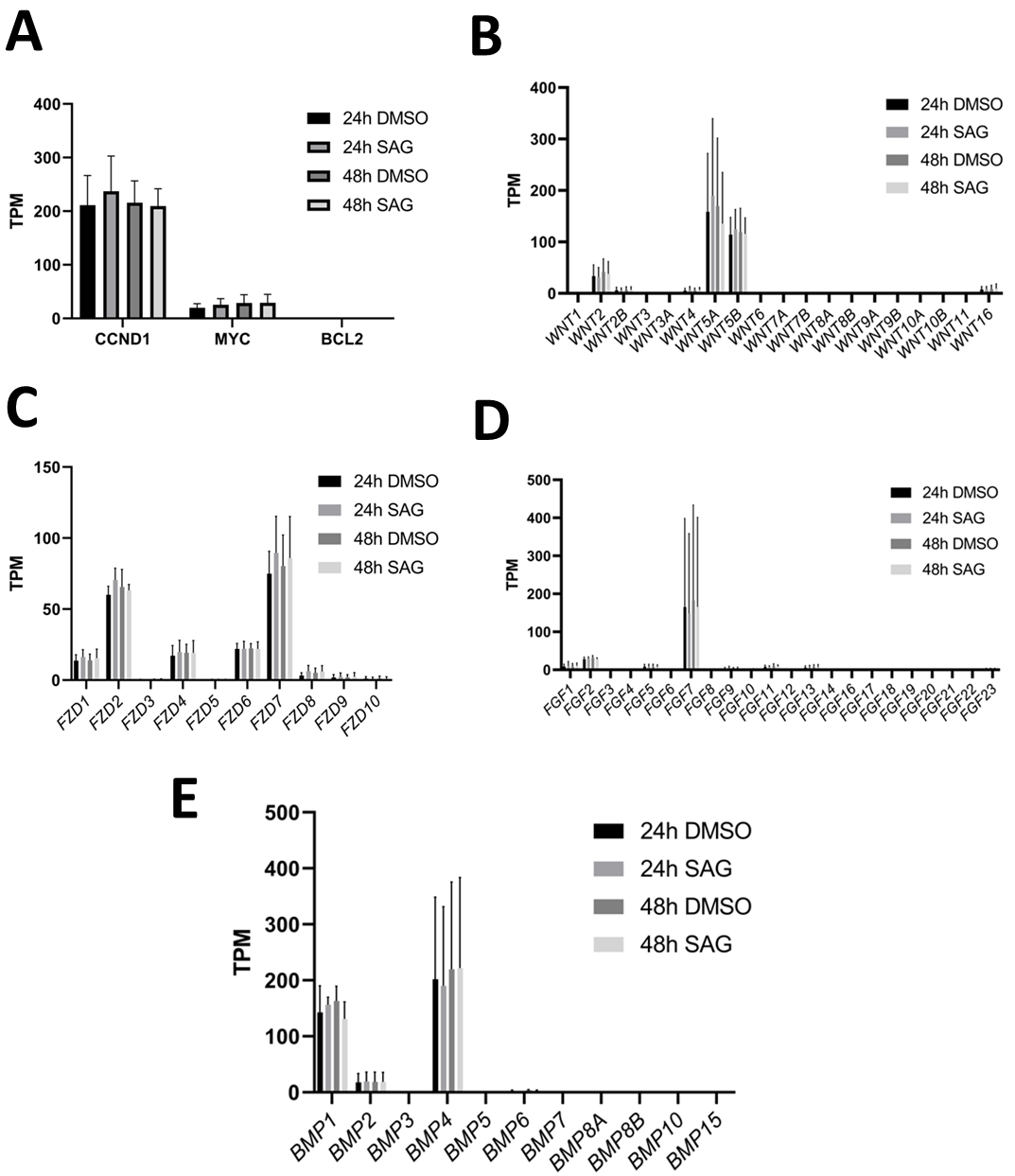

Figure 5.10: Activation of GLI1 had no effect on expression of WNT, FGF or BMP signalling genes in NuHS/NbHS cells

RNAseq analysis of expression of genes involved in different signalling pathways in NuHS/NbHS cells after treatment with SAG for 24h or 48h. Graph (**A**) displays previously cited targets of GLI activation (*CCND1*, *MYCN* and *BCL2*), graph (**B**) denotes gene expression of members of the WNT family of ligands, graph (**C**) denotes expression of Frizzled receptor genes, graph (**D**) denotes expression of FGF ligand genes and graph (**E**) displays expression of BMP ligand genes. No significant difference in expression of any gene analysed was found between conditions. Significance between groups was determined by a two-way ANOVA test performed with Tukey's multiple comparisons post-hoc test.

Due to its previously cited role in bladder connective tissue synthesis (Section 3.1.2), the expression of YAP/TAZ signalling components was also examined. Transcript expression of *YAP1* and *WWTR*1 (TAZ) was found to be expressed in stromal cells, along with high expression of YAP/TAZ target genes *AXL*, *ANKRD1*, *CTGF* and *CYR61* (Fig. 5.11). As with previous targets, treatment with SAG was not found to affect the expression of YAP/TAZ target genes at either time-point.

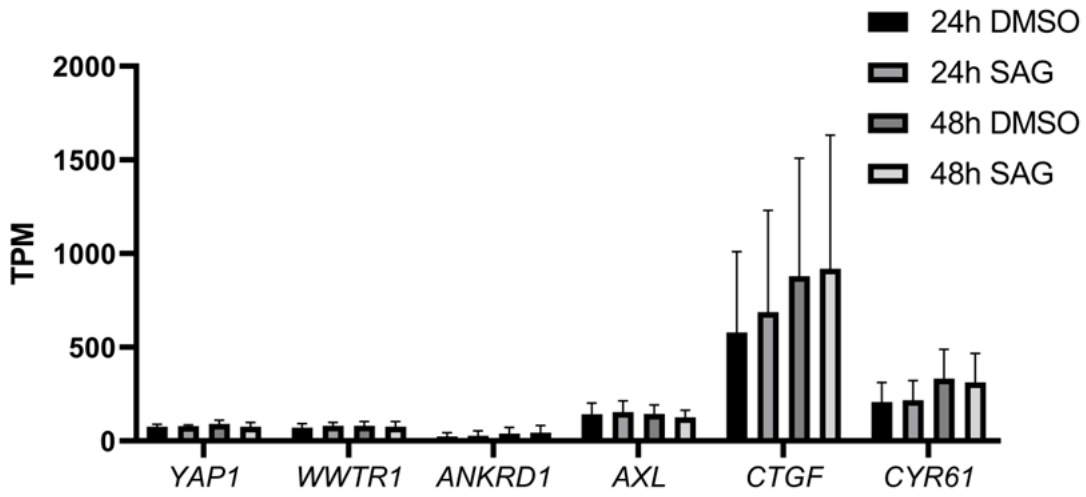

Figure 5.11: YAP/TAZ target genes *CTGF* and *CYR61* were highly expressed in NuHS/NbHS cells, but activation of canonical SHH signalling had no effect on expression

Expression of *YAP1*, *WWTR1*, *ANKRD1*, *AXL*, *CTGF* and *CYR61* expression from RNAseq data of NuHS/NbHS cells treated with 100 nM SAG for periods of 24h or 48h. Significance between groups was determined by a two-way ANOVA test performed with Tukey's multiple comparisons post-hoc test.

As basement membrane assembly was a cell function that was implicated as being significantly altered upon SAG treatment, genes related to this process were additionally investigated. *LAMA3*, *LAMB3* and *LAMC2* (encoding for laminin subunits α1, β3 and γ2, respectively) experienced an increase in mean expression in stromal cells treated with SAG for 24h compared to control (Fig. 5.12). However, this phenotype was not replicated in the 48h conditions and the difference in fold change at 24h was primarily attributable to the NbHS Y879 cell line, with the NuHS Y875 and Y1027 samples experiencing little difference in expression of the above genes. Overall, RNAseq analysis of stromal cells revealed that little to no consistent changes in the global transcriptome occurred following treatment with SAG in this context, other than the inducible reporter gene *GLI1*.

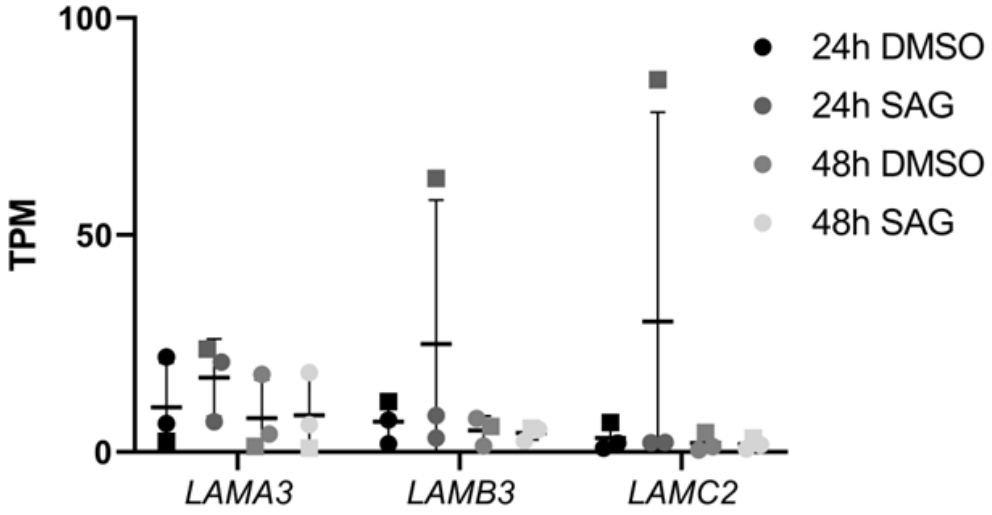

Figure 5.12: Induction of laminin expression following SAG treatment was observed in bladder-derived stromal cells only

RNAseq analysis of expression of genes involved in laminin production (*LAMA3, LAMB3, LAMC2*) in NuHS/NbHS cells after treatment with SAG for 24h or 48h. Icons of the same shape represent TPM values from stromal samples of the same derivation (circle icons for ureter-derived, square icon for bladder-derived). No significant difference in expression of any gene analysed was found between conditions. Significance between groups was determined by a two-way ANOVA test performed with Tukey's multiple comparisons post-hoc test.

5.4.5 Non-canonical SHH signalling crosstalk in NHU cells

5.4.5.1 Effect on SHH pathway gene expression in NHU cells following treatment with PD153035 alongside SAG and/or GDC-0449

RNAseq analysis of components of the SHH pathway in urothelial cells had previously revealed that expression of most genes was similar between urothelium *in situ* and NHU cells *in vitro*, with the primary exceptions observed to be a reduction in *SHH* and a gain of previously absent *GLI1* expression in undifferentiated cells (Section 5.4.1). This observation suggested that *GLI1* expression was potentially being induced in undifferentiated cells through a non-canonical, SHH/PTCH1/SMO-independent pathway.

To address this hypothesis, undifferentiated NHU cells were treated with PD153035 for 24h to determine whether blockade of downstream EGFR signalling would abrogate expression of *GLI1*, with the drug applied either in isolation or in tandem with canonical agonist/antagonist SAG and GDC-0449, respectively. While treatment of Y1756 cells with SAG or GDC-0449 appeared to have no effect on the expression of *GLI1,* treatment with PD153035 alone was sufficient to abrogate *GLI1* expression (Fig. 5.13A). In comparison, *GLI2* expression remained absent and *GLI3* was consistently expressed in all conditions. Non-quantitative RT-PCR analysis of cells treated with PD153035 in addition to SAG revealed that expression of *GLI1* appeared to have recovered slightly compared to cells treated with PD153035 alone. However, this was not reflected in the RT-qPCR analysis of three independent cell lines that showed a similar fold change loss of *GLI1* expression in any sample treated with PD153035 (Fig. 5.13B). RT-qPCR analysis confirmed that treatment of NHU cells with PD153035 significantly reduced the expression of *PTCH1* and *GLI1* ($p \leq 0.01$), while expression of both genes was unaltered by treatment of cells with GDC-0449 alone (Fig. 5.13B). This evidence therefore suggested that *GLI1* expression in undifferentiated NHU cells was controlled through a SHH/PTCH1/SMO-independent mechanism.

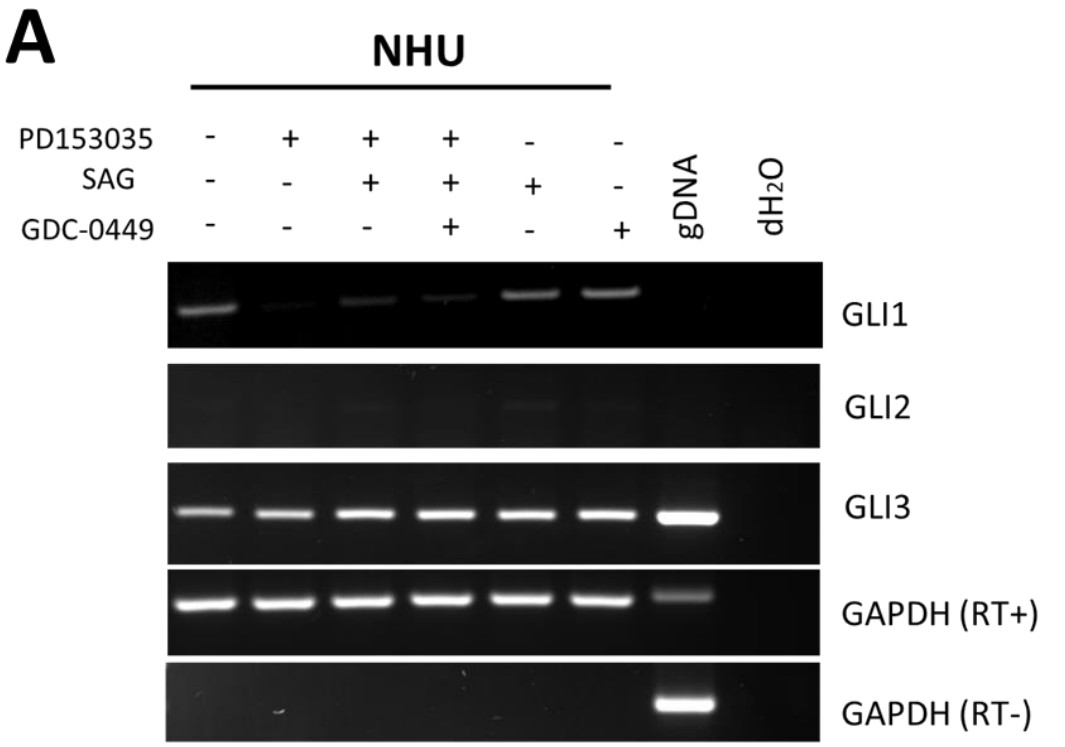
A
NHU
PD153035 - + + + - -
SAG - - + + + -
GDC-0449 - - - + - +
gDNA
dH2O
GLI1
GLI2
GLI3
GAPDH (RT+)
GAPDH (RT-)

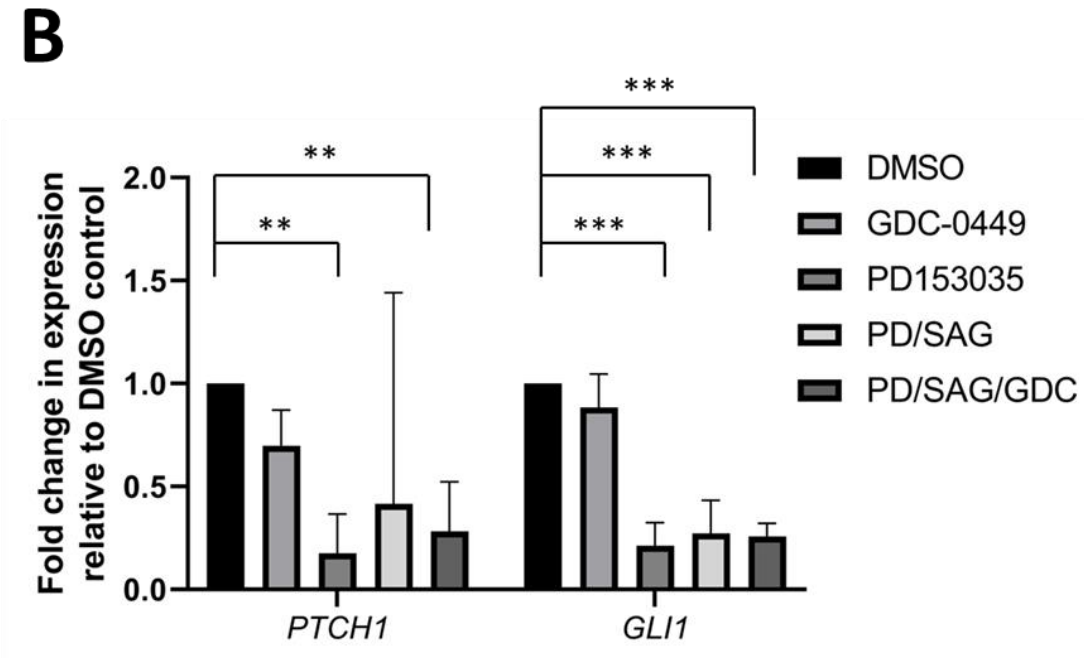
B
Fold change in expression relative to DMSO control
2.0
1.5
1.0
0.5
0.0
**
**
***
***
***
PTCH1
GLI1
DMSO
GDC-0449
PD153035
PD/SAG
PD/SAG/GDC

Figure 5.13: EGFR-mediated non-canonical activation of *GLI1* expression in undifferentiated NHU cells

A) RT-PCR analysis of undifferentiated Y1756 cells (n=1) treated with 1 µM PD153035, 100 nM SAG or 10 µM GDC-0449 (or a combination of the above) for a period of 24h compared to vehicle DMSO control. All conditions were treated with 0.1% DMSO to control for non-specific solvent effects. Each cDNA synthesis used 1 µg starting template RNA, with cDNA undergoing PCR amplification up to 32 cycles. The primers used for *GLI1* and *GLI2* expression were intron-spanning and therefore did not produce positive gDNA bands of the same size. Housekeeping gene *GAPDH* was used to confirm equal loading between samples (25 cycles). A no template (H_2O only) sample was used as a negative control for each primer set. **B)** RT-qPCR analysis of *PTCH1* and *GLI1* expression in three independent undifferentiated NHU cell lines treated with the same conditions as in (**A**)**.** Values shown represent the fold change in expression between DMSO control and treatment conditions. Significance between groups was determined by an ANOVA with Tukey's multiple comparisons post-hoc test. **= ≤ 0.01; ***= ≤ 0.001. A full list of significant differences between groups can be found in Appendix xiv.

5.4.5.2 Effect on GLI1 expression following inhibition of PI3K/AKT signalling in NHU cells

One candidate pathway that was modulating *GLI1* expression in undifferentiated cells following modulation of EGFR was postulated to be PI3K/AKT, a signalling cascade that had previously been demonstrated to participate in non-canonical SHH pathway activation (Section 5.1.3).

Treatment of Y1237 cells with a combination of PD153035 and PI3K/AKT inhibitor LY294002 revealed that *GLI1* expression was reduced by PD153035 treatment alone, as seen previously (Fig. 5.14). However, blockade of PI3K/AKT with LY294002 (in the presence or absence of PD153035) caused a complete abrogation of *GLI1* expression. Immunofluorescence analysis of NHU cells treated with said inhibitors confirmed this phenotype, as the nuclear GLI1 expression observed in control cells was inhibited by PD153035 or LY294002 (but not GDC-0449) treatment (Fig. 5.15). The preceding observations therefore suggested that PI3K/AKT signalling is a potential pathway involved in the induction of non-canonical SHH pathway signalling in undifferentiated NHU cells.

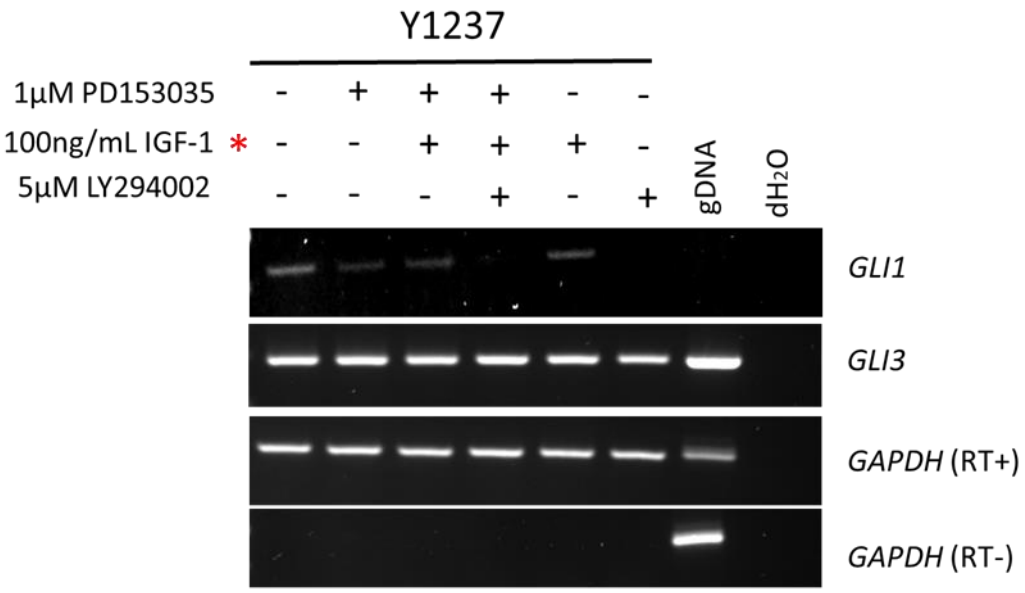

Figure 5.14: PI3K/AKT blockade abrogates *GLI1* expression in undifferentiated NHU cells

RT-PCR analysis of *GLI1* and *GLI3* expression in Y1237 (n=1) undifferentiated NHU cells treated with 1 µM PD153035 or 5 µM LY294002 (or a combination of the above) for a period of 24h compared to a vehicle control. Each cDNA synthesis used 1 µg starting template RNA, with cDNA undergoing PCR amplification up to 30 cycles. The primers used for *GLI1* expression were intron-spanning and therefore did not produce positive gDNA bands of the same size. Housekeeping gene *GAPDH* was used to confirm equal loading between samples (25 cycles). A no template (H_2O only) sample was used as a negative control for each primer set. Conditions marked with a red asterisk are not relevant to the figure.

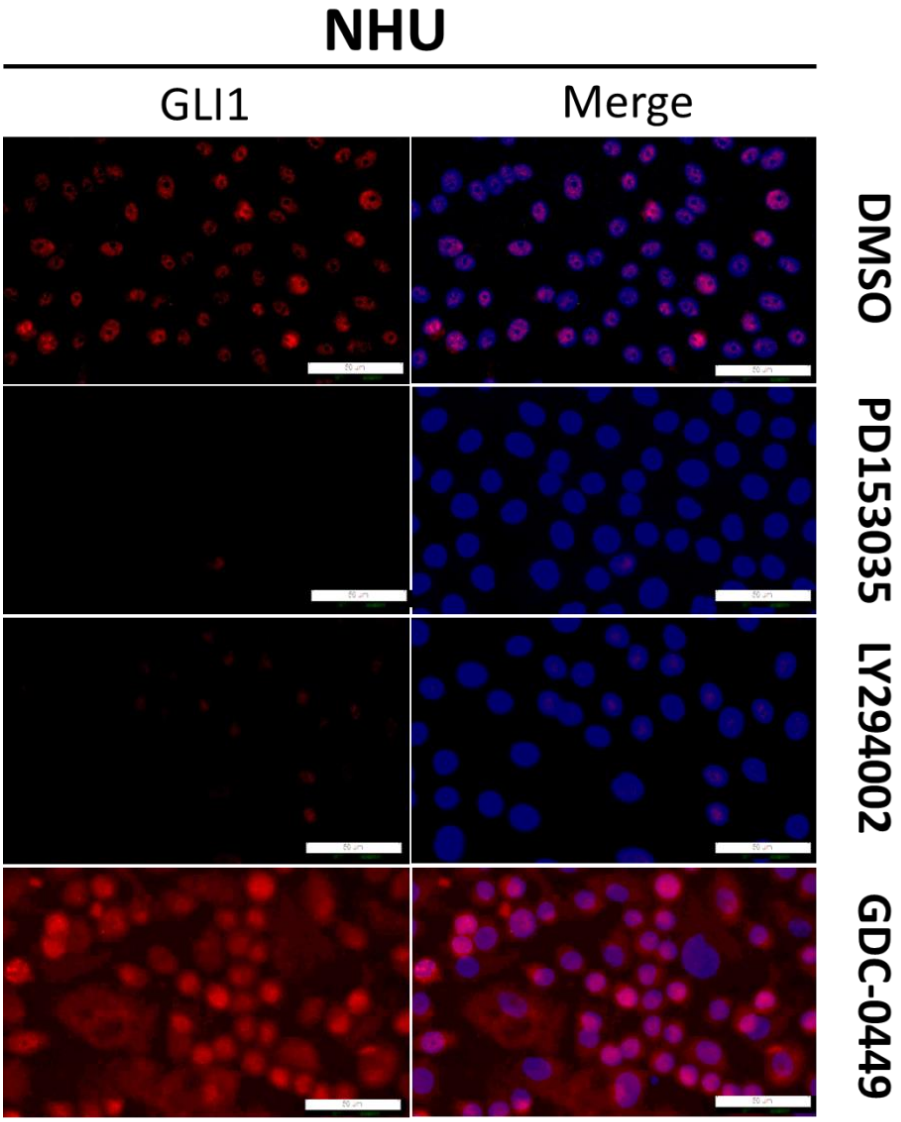

Figure 5.15: Non-canonical inhibition of nuclear GLI1 in undifferentiated NHU cells

Immunofluorescence imaging of GLI1 expression in Y1483 cells (n=1) treated with 1 µM PD153035, 5 µM LY294002 or 10µM GDC-0449 for 24h. Scale bar= 50 µm. Cells that received no primary antibody were used as negative controls, images of which can be found in Appendix xiv.

5.4.6 SHH signalling in MIBC

5.4.6.1 Transcriptomic analysis of SHH pathway genes in MIBC subtypes

Previous RNAseq analysis determined that normal urothelium *in situ* expressed *SHH* transcript but lacked expression of *GLI1* and *GLI2*, possibly indicative of a signal-inducing cell type in a paracrine SHH signalling loop (Section 5.4.1). To observe whether expression of these key pathway genes were dysregulated in MIBC, expression of said genes in isolated, stroma-free normal urothelium *in situ* was compared to TCGA MIBC samples.

No significant difference in *SHH* expression was observed between normal urothelium and luminal papillary tumours (Fig. 5.16), demonstrating that expression of the gene is retained in a majority of differentiated tumours rather than overexpressed, as suggested in previous studies (Section 5.1.5). In comparison, luminal non-specified, luminal unstable and basal/squamous tumours were all found to have significantly reduced expression of *SHH* in comparison to normal urothelium or luminal papillary tumours ($p \leq 0.01$).

Whilst expression of *PTCH1* was low across all samples, expression of the gene was significantly reduced in all MIBC subtypes (apart from the low sample-number neuroendocrine-like tumours) when compared to normal urothelium (Fig. 5.17).

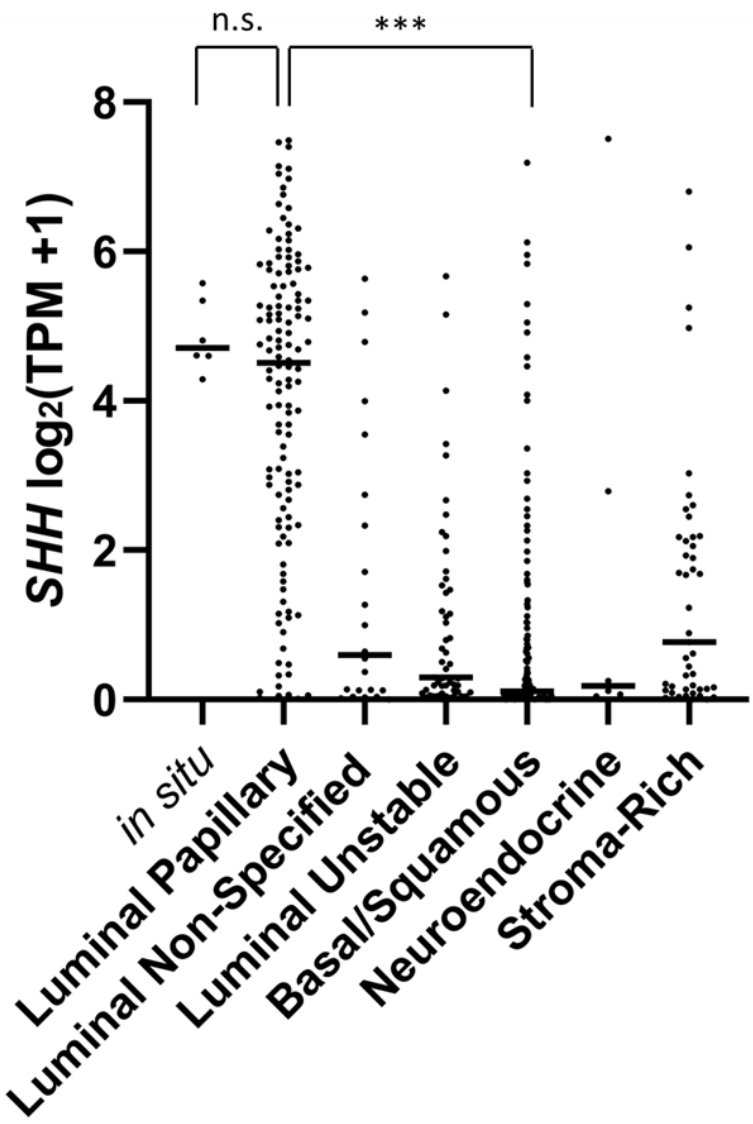

Figure 5.16: *SHH* expression is retained in a majority of luminal papillary tumours but lost in basal/squamous MIBC

RNAseq gene expression data from TCGA MIBC cohort (n=404) was separated into the consensus molecular subtypes based on previously published gene classification (Kamoun *et al.,* 2020) and compared to normal urothelium *in situ* samples processed in-house (n=6). Figure 5.16 depicts $\log_2$ (TPM+1) transformed gene expression of *SHH* in said groups, with the median value for each condition displayed. Significance between groups was determined by a Kruskal-Wallis ANOVA with Dunn's multiple comparisons post-hoc test. ***=p<0.001. Other significant changes between groups were omitted for clarity and are detailed in Appendix xiv.

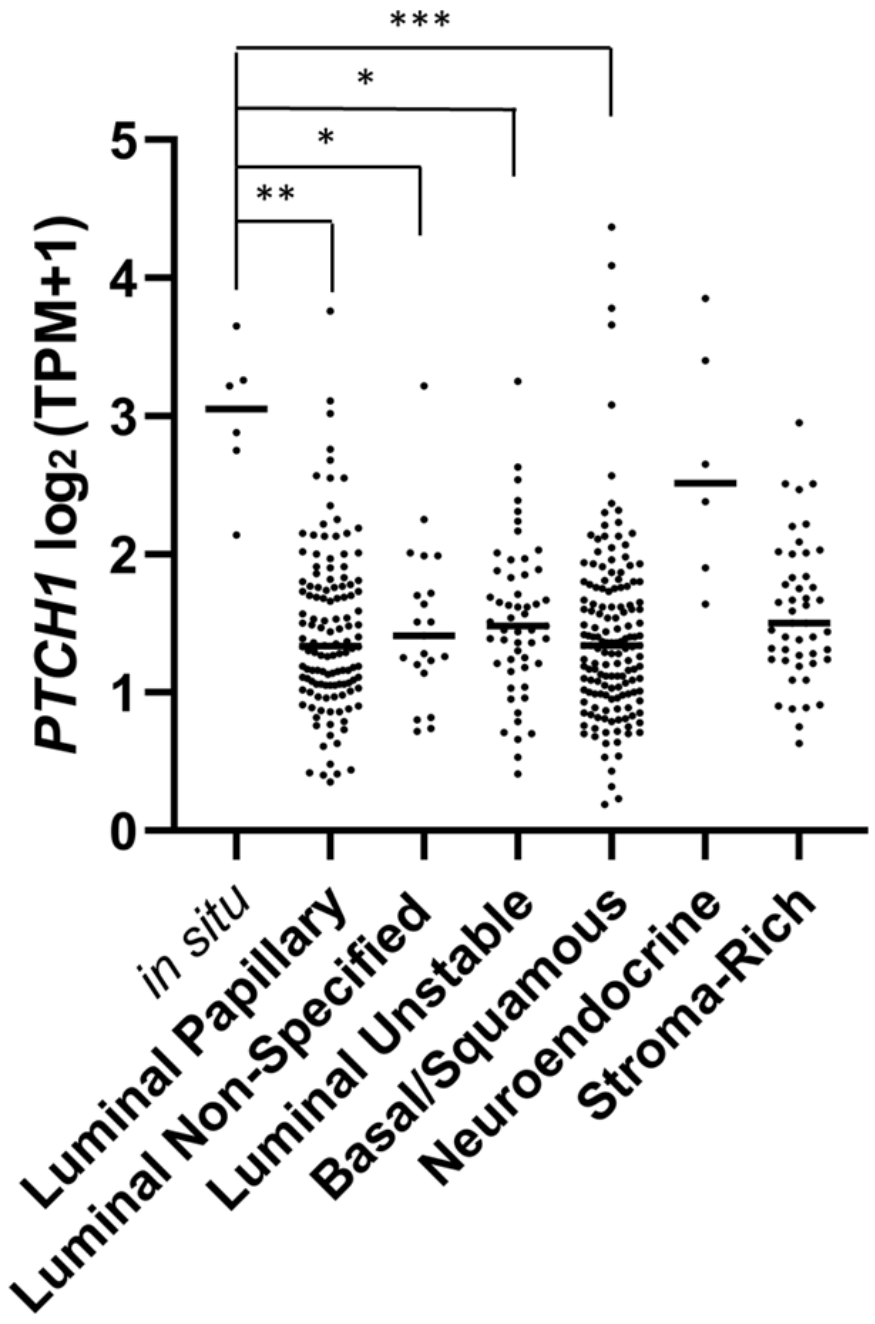

Figure 5.17: *PTCH1* expression is reduced in MIBC compared to normal urothelium

Log_2 transformed expression of *PTCH1* in normal urothelium *in situ* (n=6) compared to the different molecular subtypes of TCGA MIBC cohort (n=404). Significance between groups was determined by a Kruskal-Wallis ANOVA with Dunn's multiple comparisons post-hoc test. **=p<0.01; ***=p<0.001. Other significant changes between groups were omitted for clarity and are detailed in Appendix xiv.

Expression of *GLI1* was found to be significantly increased in luminal non-specified tumours ($p \leq 0.01$), yet overall expression of the gene remained low across all subtypes (Fig. 5.18). Furthermore, the highest median expression of the gene was observed in the heavily infiltrated stroma-rich subtype, indicating a potential stromal-derived contaminating signal that accounted for any increased *GLI1* expression found in TCGA dataset compared to isolated normal urothelium.

Median *GLI2* expression was similarly highest in the stroma-rich MIBC subtype when compared to all other subtypes and normal urothelium *in situ* (Fig. 5.19). However unlike *GLI1*, *GLI2* expression was significantly higher in basal/squamous MIBC compared to both normal urothelium and luminal papillary tumours ($p \leq 0.001$). Furthermore, a subset of basal/squamous tumours collectively exhibited approximately two-fold the expression of *GLI2* compared to the next highest tumour sample, while the stroma-rich tumour samples with the highest *GLI2* expression (n=2; highlighted by square icons in Fig. 5.19) were determined to be most closely correlated to the basal/squamous classification centroid, indicative of heavily-infiltrated basal/squamous tumours.

To determine whether the increased expression of *GLI2* observed in a subset of MIBC tumours was a result of activated autocrine SHH signalling, hierarchical clustering of the MIBC cohort based on *SHH* and *GLI2* expression was used to determine whether the MIBC tumours were found to co-express both genes. Clustering analysis revealed that the tumours separated into mutually exclusive *SHH*-high (primarily luminal papillary) and *GLI2*-high (primarily basal/squamous) groups, suggesting that activation of *GLI2* in a subset of basal/squamous tumours was not *SHH*-mediated (Fig. 5.20).

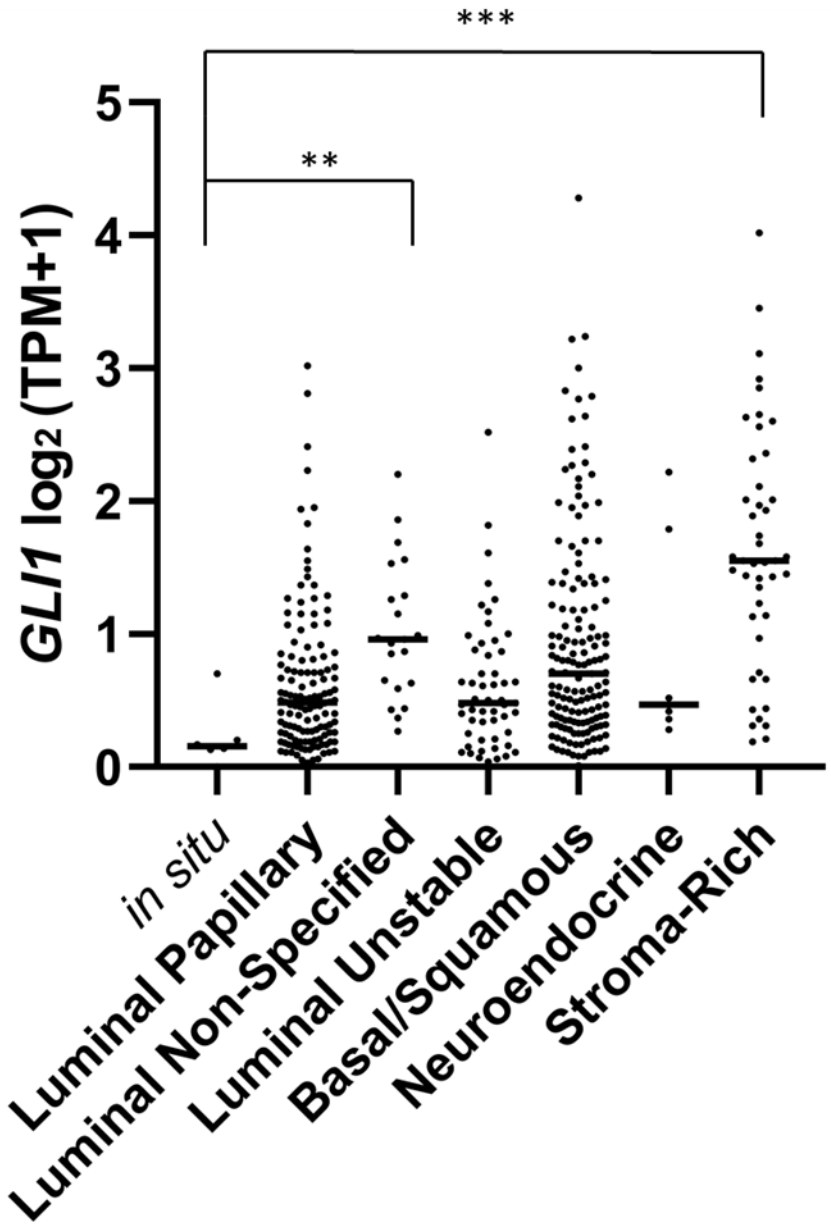

Figure 5.18: *GLI1* expression is highest in the heavily infiltrated stroma-rich MIBC subtype

Log_2 transformed expression of *GLI1* in normal urothelium *in situ* (n=6) compared to the different molecular subtypes of TCGA MIBC cohort (n=404). Significance between groups was determined by a Kruskal-Wallis ANOVA with Dunn's multiple comparisons post-hoc test. *=p<0.05; **=p<0.01; ***=p<0.001. Other significant changes between groups were omitted for clarity and are detailed in Appendix xiv.

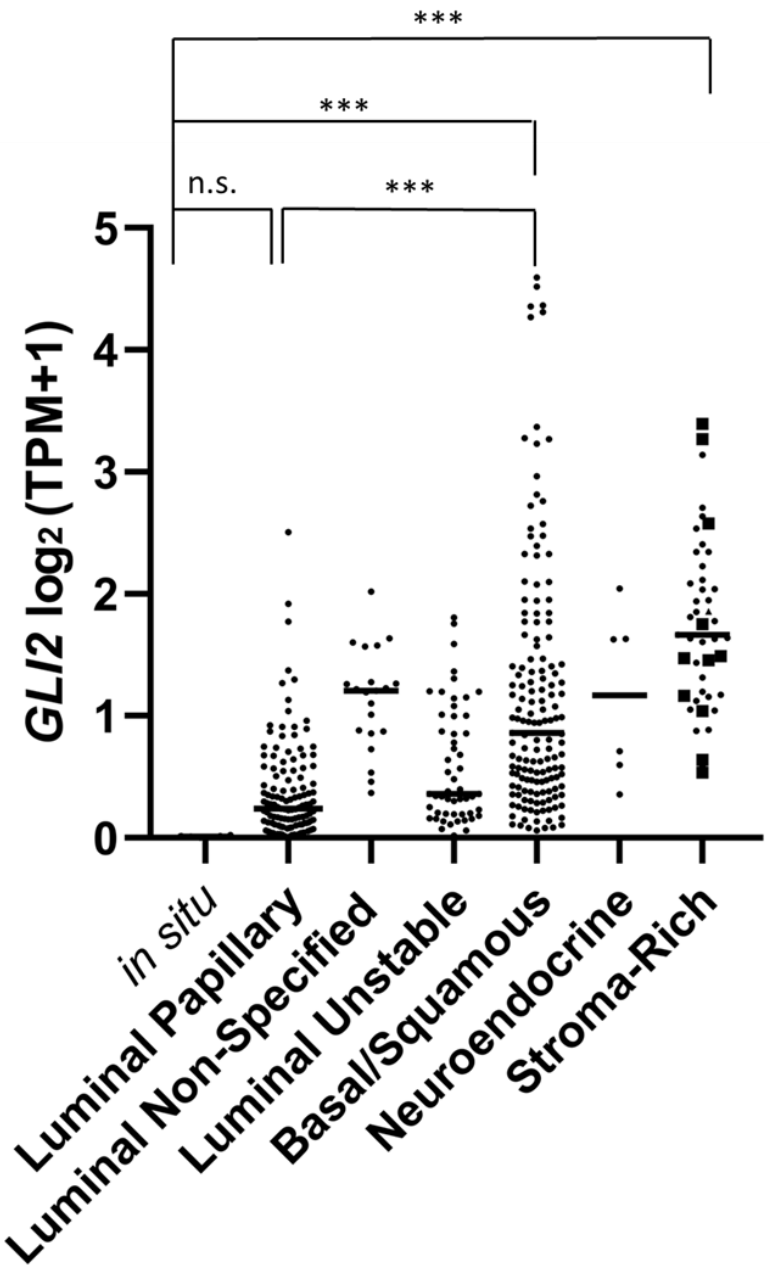

Figure 5.19: *GLI2* is overexpressed in a subset of basal/squamous MIBC

Log_2 transformed expression of *GLI2* in normal urothelium *in situ* (n=6) compared to the different molecular subtypes of TCGA MIBC cohort (n=404). The square icons in the stroma-rich subtype signify the tumours of that subtype that were found to be most closely correlated to the basal/squamous classification centroid. Significance between groups was determined by a Kruskal-Wallis ANOVA with Dunn's multiple comparisons post-hoc test. ***=p<0.001. Other significant changes between groups were omitted for clarity and are detailed in Appendix xiv.

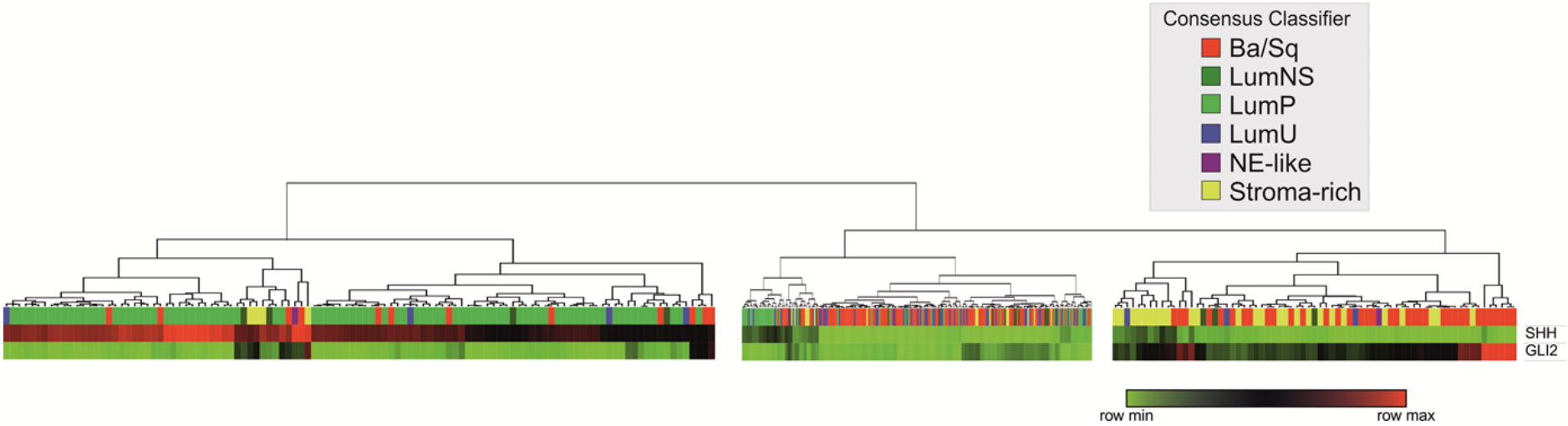

Figure 5.20: Loss of *SHH* and gain of *GLI2* expression is a hallmark of a subset of basal/squamous MIBC

Unsupervised hierarchical clustering performed on RNAseq Log_2 transformed expression of *SHH* and *GLI2* in TCGA MIBC cohort (n=404). Clustering of tumours using the two genes divided the samples into a primarily luminal *SHH*-high group, a *GLI2*-high group consisting mostly of basal/squamous and stroma-rich tumours and a mixed population of tumours that expressed neither gene. The cluster of tumours that had absent expression of both genes was condensed for clarity. Samples were clustered using the one minus Spearman rank correlation method with complete linkage. A colour-coded tumour subtype classifier is provided above each tumour sample. Clustering was performed using Morpheus software (https://software.broadinstitute.org/morpheus/).

5.4.6.2 Mutation analysis of SHH pathway effector genes in MIBC

Examination of the mutation status of *SHH*, *PTCH1*, *GLI1* and *GLI2* in TCGA MIBC cohort revealed a relatively low (non-synonymous) mutation rate for all four genes (Fig. 5.21). *GLI2* was found to be the most commonly mutated gene in the pathway, with 4.1% of all tumours carrying a non-synonymous *GLI2* somatic mutation. Co-occurring mutations between SHH pathway genes were rare in MIBC samples, with 2/412 tumours (sample # A54R and A9T8) displaying missense mutations in both *SHH* and *GLI2* genes while a single tumour (A6AW) displayed both *GLI1* and *GLI2* missense mutations. *PTCH1* was found to be mutated in 3.9% of samples but was found to have no overlap with tumours that carried *GLI2* mutations. A statistical test for co-occurrence of mutations in the cohort revealed a lack of a significantly associated relationship between any two genes, indicating that mutations in components of SHH signalling in MIBC, when present, was predominantly mutually exclusive (Table 5.6).

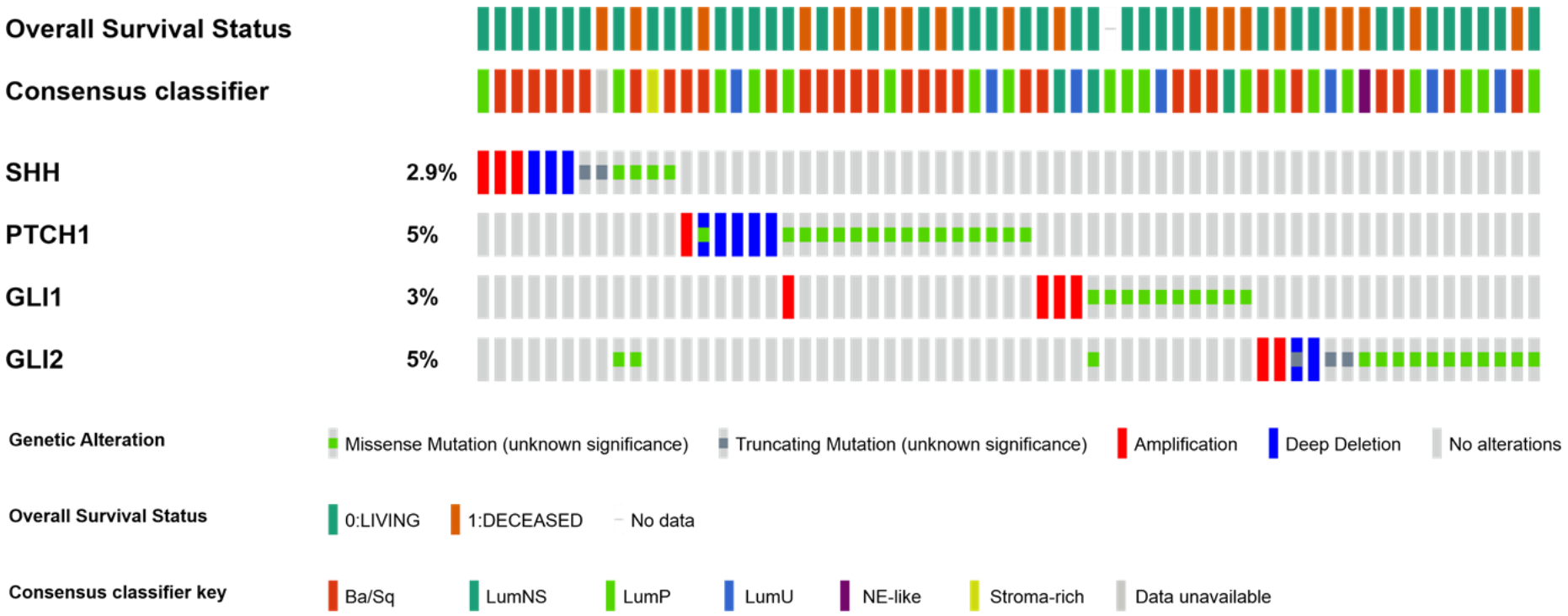

Figure 5.21: *PTCH1* and *GLI2* are mutated in a mutually exclusive manner in MIBC

Profile of genetic alterations and mutations in *SHH*, *PTCH1, GLI1* and *GLI2* genes in TCGA MIBC cohort. For clarity, only a proportion of the tumours in the cohort are displayed, with the remaining tumours expressing wild-type versions of all four genes. Mutation data and graphic were obtained from the cBioPortal for Cancer Genomics (https://www.cbioportal.org/)

Gene 1	Gene 2	Alteration in 1 only (C)	Alteration in 2 only (D)	Alteration in both (A)	Alteration in neither (B)	Log_2 odds ratio	pval
SHH	*PTCH1*	12	21	0	375	<-3	0.526
SHH	*GLI1*	12	14	0	382	<-3	0.654
SHH	*GLI2*	10	17	2	379	2.157	0.103
PTCH1	*GLI1*	20	13	1	374	0.525	0.529
PTCH1	*GLI2*	21	19	0	368	<-3	0.358
GLI1	*GLI2*	13	18	1	376	0.684	0.493

Table 5.6: Co-occurrence ratio of *SHH, PTCH1, GLI1* and *GLI2* alterations in MIBC.

The likelihood of two genes being altered in the same cancer sample (odds ratio) was calculated using the equation (A x B) / (C x D), where A= samples where both genes are altered; B= samples where gene 1 but not gene 2 is altered; C= samples where gene 2 but not gene 1 is altered and D= samples where neither gene is altered. The calculated Log_2 odds ratio was used as an indicator of whether the relationship between alterations in the two genes is mutually exclusive or co-occurring (a ratio of >2 indicates a tendency towards co-occurrence). A Fisher's Exact Test was used to calculate the significance between gene relationships, with no significant relationship determined between any combinations of SHH pathway gene mutations. Information on the mutation status of TCGA MIBC samples was obtained from the cBioPortal for Cancer Genomics (https://www.cbioportal.org/).

5.4.6.3 Generation of a *GLI2*-high basal/squamous MIBC subset

To verify that the high expression of *GLI2* observed in a subset of basal/squamous tumours was not as a result of expression from contaminating infiltrating cell types, basal/squamous tumours were split based on transcript expression of desmin (*DES*) or CD45 (*PTPRC*), genes expressed exclusively by stromal or immunocyte cell types, respectively. Four of the six tumours with the highest expression of *GLI2* in the subtype were classed as '*DES*-low' tumours, while five of the six *GLI2*-high tumours had low *PTPRC* expression, with no significant difference in *GLI2* expression observed between *DES*-low/*PTPRC*-low and *DES*-high/*PTPRC*-high groups (Fig. 5.22A-B). Additional evidence of *GLI2* overexpression in malignant urothelial cells was observed in a subset of bladder cancer cell lines grown (in the absence of stroma or immunocytes) *in vitro*, with bladder cancer lines overall observed to have significantly increased expression of *GLI2* in comparison to NHU cells, regardless of whether the NHU cells were exposed to serum (Fig. 5.22C; $p \leq 0.001$). Of the thirty cell lines analysed, five (1A6, 253JP, J82, TCCSup and UM-UC-15) were found to express a similar amount of *GLI2* to that found in the *GLI2*-high basal/squamous subset.

The preceding analysis therefore suggested that overexpression of *GLI2* could occur in the urothelial cells of basal/squamous MIBC, resulting in the creation of a '*GLI2*-high basal/squamous' subset group, consisting of the ten basal/squamous tumours with the highest *GLI2* expression alongside two *GLI2*-high stroma-rich tumours which were most closely correlated with the basal/squamous classification centroid (Samples # AA6Q, A3IB, A3OS, A42Q, A3WC, AA4N, A871, AATQ, A1AE, A3IQ, A5RI and A5ZZ; Fig. 5.23). Ten other stroma-rich tumours that most closely correlated with the basal/squamous centroid when compared to all other subtypes were combined with the remaining basal/squamous tumours to create the *GLI2*-low basal/squamous group (n=153 tumours).

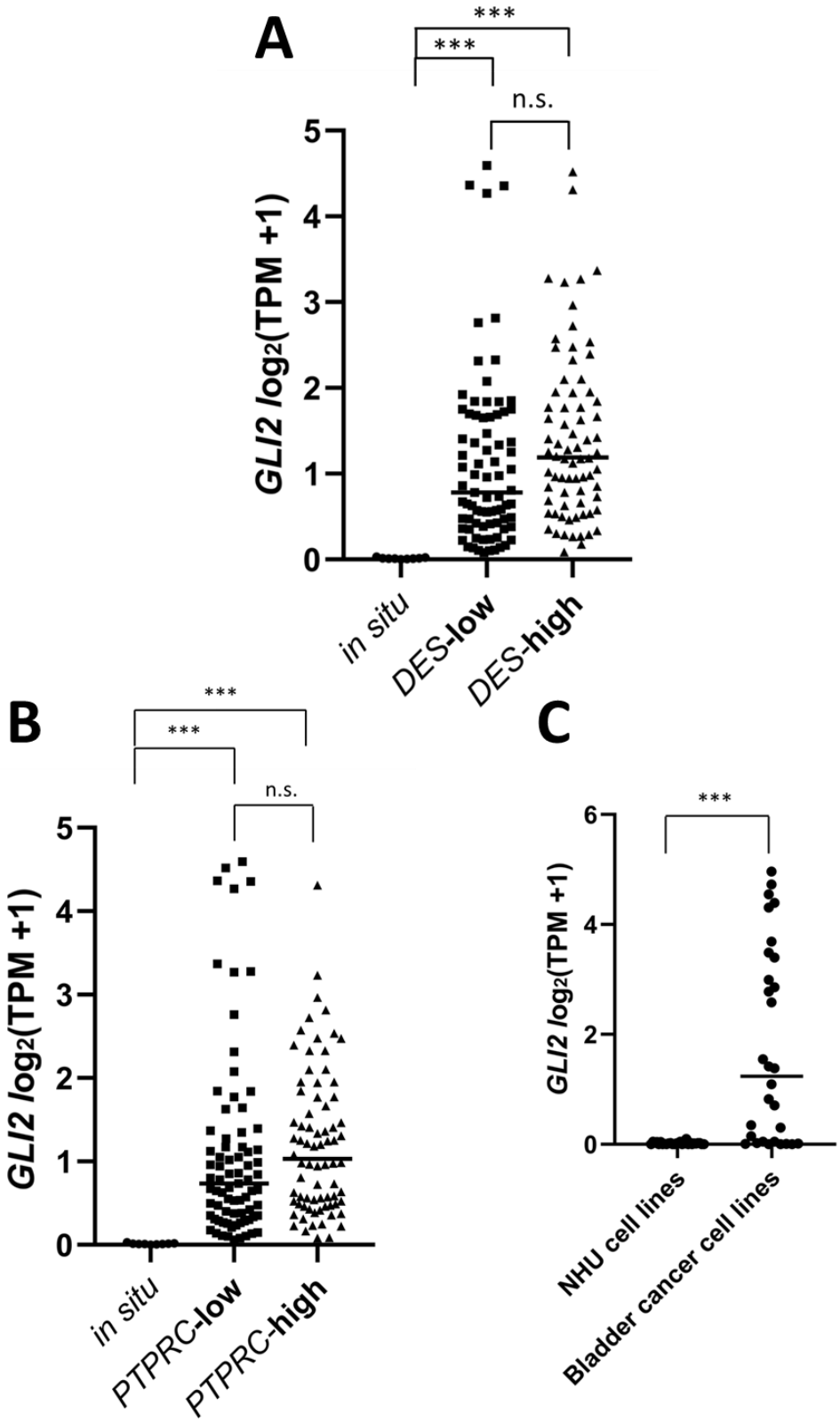
A
***
***
n.s.
GLI2 log2(TPM +1)
0
1
2
3
4
5
in situ
DES-low
DES-high
B
***
***
n.s.
GLI2 log2(TPM +1)
0
1
2
3
4
5
in situ
PTPRC-low
PTPRC-high
C
***
GLI2 log2(TPM +1)
0
2
4
6
NHU cell lines
Bladder cancer cell lines

Figure 5.22: *GLI2* overexpression in a subset of basal/squamous MIBC and bladder cancer cell lines, independent of stromal or immune infiltration

A-B) Basal/squamous MIBC samples (n=165) were separated based on their expression of stromal-specific gene *DES* (**A**) or immunocyte-specific gene *PTPRC* (**B**) and their expression of Log_2 transformed *GLI2* subsequently compared to normal urothelium *in situ*, with tumours with *DES* TPM values <40 (median *DES* TPM in subtype) or *PTPRC* TPM values <9.5 (median *PTPRC* TPM in subtype) designated as being '*DES*-low' or '*PTPRC*-low', respectively. **C**) Log_2 transformed expression of *GLI2* in NHU cells in an undifferentiated or ABS/Ca^{2+} differentiated state (n=28) compared to a cohort of bladder cancer cell lines (n=30). Significance between groups was determined by a Kruskal-Wallis ANOVA with Dunn's multiple comparisons post-hoc test (**A-B**) or a Mann-Whitney T test (**C**). ***=p<0.001.

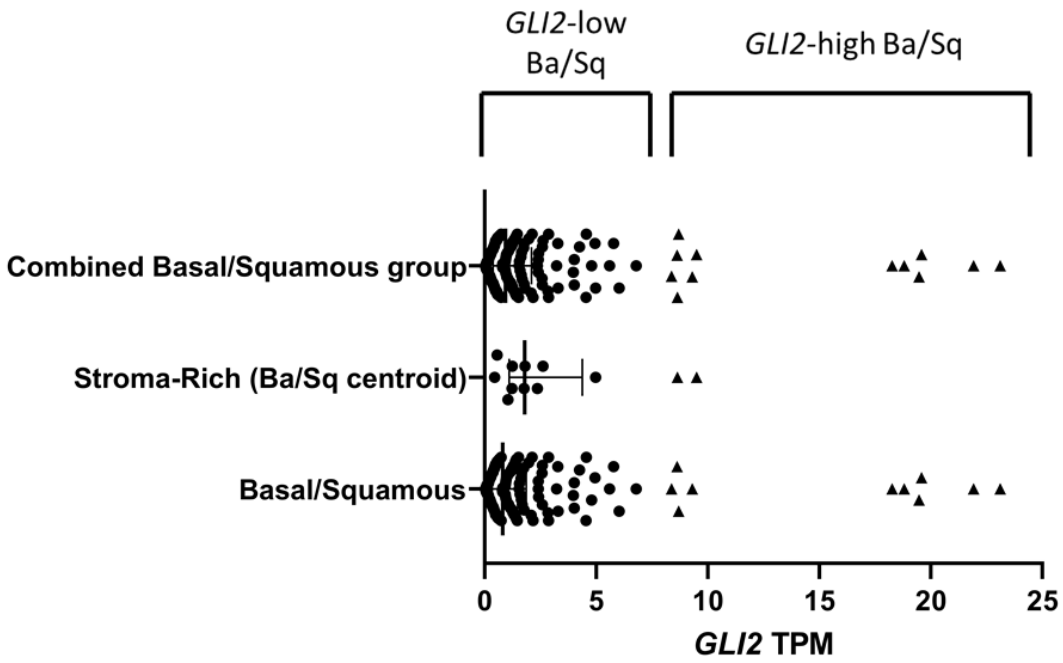

Figure 5.23: Stratification of basal/squamous MIBC into *GLI2*-high and *GLI2*-low subsets

Visualisation of unlogged *GLI2* expression in samples of basal/squamous (n=153) and stroma-rich MIBC (with closest correlation to the basal/squamous centroid; n=12), with the bars representing the median and interquartile range values. The two sample sets were combined and split based on *GLI2* expression into *GLI2*-high (n=12) and *GLI2*-low (n=153) basal/squamous tumour subsets, with the triangular icons representing *GLI2*-high samples and the circular icons representing *GLI2*-low samples. The 1.5 x interquartile range rule was applied to confirm that the *GLI2* TPM values of each tumour in the *GLI2*-high basal/squamous subset were outliers of the overall pattern of distribution.

5.4.6.4 Mutation status of *GLI2*-high basal/squamous MIBC

To predict what mutations were potentially contributing to the overexpression of *GLI2* observed in the *GLI2*-high basal/squamous subset, analysis of the mutated genes inherent to these tumours was performed. *GLI2* itself with not mutated in any of the tumours in the subset, while *PTCH1* was the only SHH pathway gene found to be mutated, with a single missense mutation at the Q1285H site found in the A3IB sample. In total, 18 genes were found to be mutated in at least 3 of the tumours in the subset (25%), with *TP53* found to be the most common alteration (7/12 tumours; Table 5.7). However, this gene was found to be mutated at the same frequency in both *GLI2*-high and *GLI2*-low basal/squamous groups. A binomial test was subsequently performed on each frequently mutated gene to determine whether any of the aforementioned genes were significantly overrepresented in the *GLI2*-high subset compared to the *GLI2*-low subset. Interestingly, key genes of the oxidative stress response KEAP1-NRF2 pathway were found to be mutated at a significantly higher frequency in the *GLI2*-high subtype when compared to both the GLI1-low subset ($p \leq 0.01$) and the entire MIBC cohort, with 18.5% of all *NFE2L2*-mutated tumours and 37.5% of all *KEAP1*-mutated tumours in TCGA cohort also found within the *GLI2*-high basal/squamous group.

Analysis of the mutational signature of the 12 individual tumours comprising the *GLI2*-high basal/squamous subset revealed that the only mutation common to the two tumours with the highest expression of *GLI2* (#AA6Q and #A42Q) was loss-of-function mutations of *CDKN2A* (Table 5.8). Activating mutations in *NFE2L2* and loss-of-function mutations in *KEAP1* were found to be mutually exclusive in the *GLI2*-high subset, meaning that 8/12 tumours in the subset carried mutations that would be predicted to induce aberrant NRF2 activity. This analysis therefore identified the KEAP1-NRF2 pathway as one potential source of non-canonical *GLI2* expression in basal/squamous MIBC.

Gene	Mutation frequency in *GLI2*-high subset (n=12)	Mutation frequency in *GLI2*-low subset (n=153)	Mutation frequency in TCGA (n=404)	Predicted mutation frequency in n=12 Ba/Sq sample	pval
TP53	58.3%	58.8%	47.9%	58.2%	0.2286
KMT2D	50%	30.1%	28.3%	31.5%	0.0933
NFE2L2	41.7%	7.8%	6.3%	10.2%	**0.0041**
PIK3CA	33.3%	22.9%	22%	23.6%	0.1782
KDM6A	33.3%	19%	25.9%	20%	0.1329
CSMD3	33.3%	13.1%	13.8%	14.6%	0.0632
OLFM3	33.3%	0.7%	2.4%	3%	**0.0003**
TTN	33.3%	46.4%	47.2%	45.4%	0.1661
ARID1A	25%	22.9%	24.5%	23.1%	0.2549
CDKN2A	25%	7.8%	6.5%	9%	0.0686
FAT1	25%	12.4%	12.3%	13%	0.1380
KEAP1	25%	0.7%	1.7%	2%	**0.0015**
MUC16	25%	25.5%	28.3%	25.4%	0.2579
MYT1	25%	2%	2.2%	3.6%	**0.0074**
NUP188	25%	3.9%	4.8%	5.4%	**0.0210**
SCN1A	25%	3.9%	7%	5%	**0.0173**
SF3B1	25%	4.6%	5.6%	7%	**0.0393**
XIRP2	25%	11.1%	12.1%	12%	0.1277

Table 5.7: Overrepresented mutations in *GLI2*-high basal/squamous MIBC tumours

Point mutation data for the tumours in the *GLI2*-high basal/squamous subset (n=12) and the *GLI2*-high J82 bladder cancer cell line were collated to determine the most common mutations inherent to these tumours. A predicted mutation frequency for each gene (in a random selection of n=12 basal/squamous tumours) was calculated based on the frequency of mutations of the genes across all basal/squamous samples. A binomial test was performed to determine whether the observed mutation frequency of any of the genes enriched in the subset was statistically significant, with significant p values

highlighted in bold. The percentage of somatic mutations present in TCGA cohort for each gene was obtained from cBioPortal (https://www.cbioportal.org/).

	AA6Q	A42Q	A3IB	A3OS	A3WC	AA4N	A871	AATQ	A1AE	A3IQ	A5RI	A5ZZ
TP53	X		X	X	X	X					X	X
KMT2D			X		X	X			X		X	X
NFE2L2	X		X					X	X		X	
PIK3CA	X				X	X		X				
KDM6A							X		X		X	
CSMD3						X		X	X	X		
OLFM3					X		X		X		X	
TTN	X				X				X	X		
ARID1A							X		X			X
CDKN2A	X	X		X								
FAT1	X				X					X		
KEAP1		X			X	X						
MUC16	X		X								X	
MYT1	X				X							X
NUP188	X				X							X
SCN1A			X			X				X		
SF3B1							X		X			X
XIRP2			X					X				X

Table 5.8: Matrix of overrepresented mutations in the *GLI2*-high basal/squamous subset

The 12 tumours of the *GLI2*-high basal/squamous subset were arranged in order of *GLI2* expression, with sample #AA6Q displaying the highest *GLI2* TPM value and #A5ZZ displaying the (relatively) lowest *GLI2* TPM of the subset.

Investigation of underrepresented mutations in the *GLI2*-high basal/squamous subset revealed six genes commonly mutated in basal/squamous tumours that exhibited no mutations in any of the *GLI2*-high tumours, including tumour suppressor *RB1* and *ERBB2* (Table 5.9). However, none of the six genes examined had a statistically significant difference in enrichment between groups.

Gene	Mutation frequency in *GLI2*-high subset (n=12)	Mutation frequency in *GLI2*-low subset (n=153)	Mutation frequency in TCGA (n=404)	Predicted mutation frequency in n=12 Ba/Sq sample	pval
FLG	0%	20.9%	16.5%	19.4%	0.0754
RB1	0%	19.6%	17.4%	18.1%	0.0911
EP300	0%	19%	15.3%	17.6%	0.0980
HMCN1	0%	18.3%	18.4%	17%	0.1075
AHNAK2	0%	17.6%	12.1%	16.3%	0.1179
ERBB2	0%	17%	12.1%	15.8%	0.1277

Table 5.9: Underrepresented mutations in *GLI2*-high basal/squamous MIBC tumours

The most common point mutations in the basal/squamous MIBC group were collated to determine if any genes were not mutated in the *GLI2*-high basal/squamous subset (n=12). Only mutations found in at least 15% of the total basal/squamous group and none of the *GLI2*-high basal/squamous tumours were included.

5.4.6.5 Phenotype of *GLI2*-high basal/squamous MIBC

Differential expression analysis of the *GLI2*-high versus *GLI2*-low basal/squamous subgroups revealed 389 genes that experienced an absolute $\log_2$ fold change in expression ≥ 2 and had a q value ≤0.001 when comparing the two groups (Fig. 5.24A). Alongside *GLI2*, some of the most upregulated genes in the *GLI2*-high subtype included genes involved in inhibiting WNT pathway signalling, such as *SOST* (sclerostin) and *WIF1* (WNT inhibitory factor 1); in addition to ATP-binding cassette transporters *ABCC1* and *ABCC6* (multidrug resistance protein 1 and 6, respectively). Genes that have previously been inferred to have NRF2 transcriptional binding sites in the GeneHancer database, such as *ADH1C* (alcohol dehydrogenase 1c) and *GSTM2*/*GSTM3* (glutathione S-transferase mu 2 and 3, respectively) were found to be some of the most upregulated genes in the *GLI2*-high basal/squamous subset. Furthermore, the two downregulated genes with the smallest q values in the comparison were determined to be KEAP1 paralog *KLHDC7B* and its associated lncRNA U62317.1, granting further credence to the possibility that the KEAP1-NRF2 pathway is dysregulated in the *GLI2*-high basal/squamous subset. Notable other examples of the most downregulated genes in the *GLI2*-high subset included genes involved in apoptosis (*CASP14*; caspase 14), immune cell recruitment (*ACKR2*; atypical chemokine receptor 2), suppression of metastasis (*KISS1*; kisspeptin) and several genes associated with a differentiated urothelial phenotype (*VGLL1, PPARG, UPK2*, *UPK3B*, *KRT20*). GSEA analysis of the differentially expressed genes supported these observations, as the analysis revealed a significant enrichment of genes associated with the reactive oxygen species (ROS) pathway and a suppression of various pathways involved in inflammatory responses in the *GLI2*-high subset (Fig. 5.24B). Overall, the preceding results potentially suggest that *GLI2*-high subset of basal/squamous tumours exhibit a less differentiated, more highly invasive and reduced chemo-sensitive phenotype than other basal/squamous tumours.

Expression of previously identified neuroendocrine-like tumour markers *SOX2*, *SOX21*, *ENO2*, *CHGA*, *CHGB*, *SYP*, *SGC2* and *SCG3* were analysed to confirm that the *GLI2*-high basal/squamous subset did not exhibit features of the neuroendocrine-like phenotype. Of these genes, only *CHGA* (chromogranin A) was found to be

altered between groups, with a $\log_2$ fold increase of 3.39 in the *GLI2*-high subtype. To confirm that the overexpression of *GLI2* in this context was independent of the canonical SHH pathway, changes in expression of *SHH*, *PTCH1, SMO*, *GLI1*, *GLI3* and *HHIP* were analysed. It was determined that none of the above genes experienced a significant change in expression when comparing *GLI2*-low and *GLI2*-high basal/squamous subsets.

To determine whether the observed phenotype resulted in a reduced overall survival of *GLI2*-high tumours compared to other basal/squamous tumours, a Kaplan-Meier survival analysis was performed. Strikingly, 75% of *GLI2*-high patients had died within 18 months of diagnosis compared to 37% of *GLI2*-low patients. This resulted in a reduced median survival time and a significantly reduced overall survival of *GLI2*-high basal/squamous tumours when compared to *GLI2*-low tumours (median time to death 385 days versus 795 days, respectively; $p \leq 0.05$; Fig. 5.25).

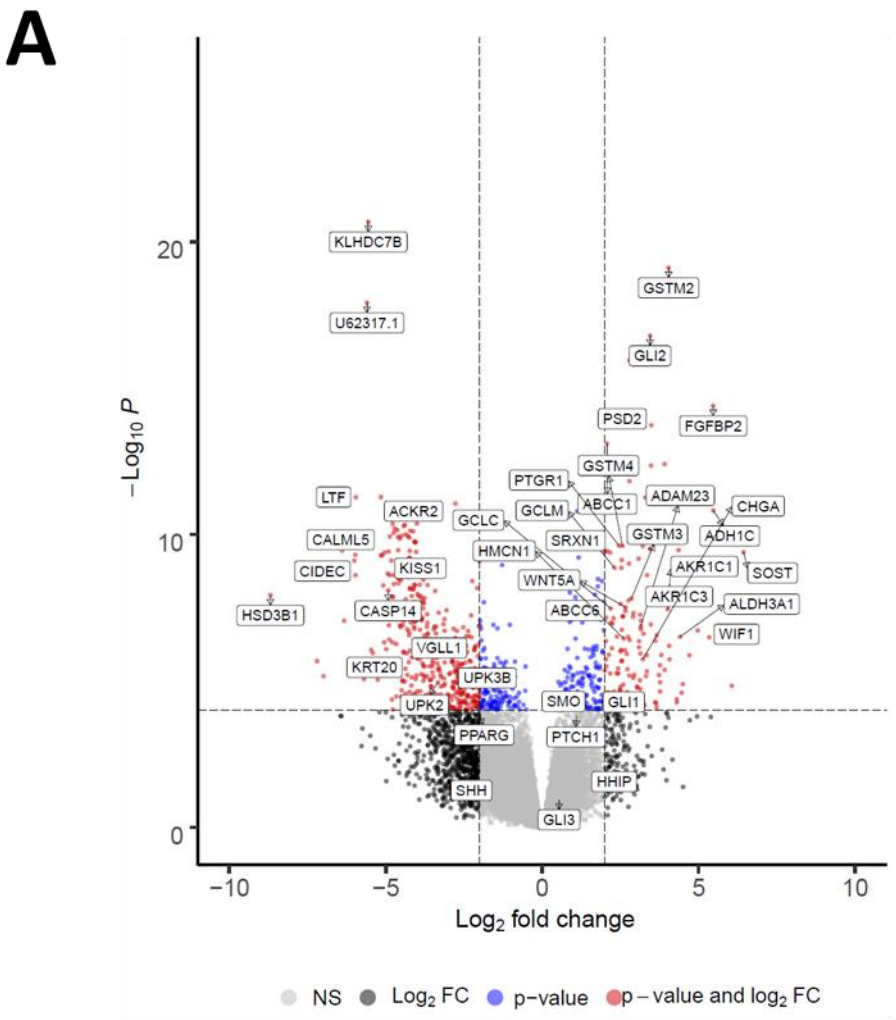
A
KLHDC7B
U62317.1
GSTM2
GLI2
PSD2
FGFBP2
GSTM4
PTGR1
ADAM23
LTF
ACKR2
GCLC
GCLM
ABCC1
CHGA
CALML5
SRXN1
GSTM3
ADH1C
HMCN1
CIDEC
KISS1
WNT5A
AKR1C1
SOST
HSD3B1
CASP14
ABCC6
AKR1C3
ALDH3A1
WIF1
VGLL1
KRT20
UPK3B
UPK2
SMO
GLI1
PPARG
PTCH1
HHIP
SHH
GLI3
20
10
0
−10
−5
0
5
10
−Log10 P
Log2 fold change
NS
Log2 FC
p−value
p − value and log2 FC
B
Hallmark pathways Normalized Enrichment Score from GSEA
HALLMARK_REACTIVE_OXYGEN_SPECIES_PATHWAY
HALLMARK_UV_RESPONSE_DN
HALLMARK_ESTROGEN_RESPONSE_EARLY
HALLMARK_ESTROGEN_RESPONSE_LATE
HALLMARK_COAGULATION
HALLMARK_PI3K_AKT_MTOR_SIGNALING
HALLMARK_IL2_STAT5_SIGNALING
HALLMARK_APOPTOSIS
HALLMARK_KRAS_SIGNALING_UP
HALLMARK_TNFA_SIGNALING_VIA_NFKB
HALLMARK_COMPLEMENT
HALLMARK_IL6_JAK_STAT3_SIGNALING
HALLMARK_INFLAMMATORY_RESPONSE
HALLMARK_INTERFERON_ALPHA_RESPONSE
HALLMARK_INTERFERON_GAMMA_RESPONSE
HALLMARK_ALLOGRAFT_REJECTION
Pathway
−3
−2
−1
0
1
2
Normalized Enrichment Score
padj ≤ 0.05
Suppressed
Enriched

Figure 5.24: *GLI2*–high Basal/Squamous tumours have significantly increased expression of NRF2 target genes

A) Volcano plot of the most differentially expressed genes in *GLI2*-high basal/squamous tumours (n=12) in comparison to *GLI2*-low basal/squamous tumours (n=153). Genes that pass the criteria of having a q value ≤0.001 and a $\log_2$ fold change in expression ≥ 2 or ≤-2 are represented as red dots. Notable genes that pass the criteria set above are highlighted on the plot. A complete list of genes with a q value ≤0.001 and a $\log_2$ fold change in expression ≥ 2 or ≤-2 can be found in Appendix xiv. **B)** GSEA analysis of signalling pathways that are differentially expressed between *GLI2*-high and *GLI2*-low basal/squamous subsets. Each pathway analysed is assigned a normalised enrichment score, with only pathways that have a significant q value ≤0.05 displayed.

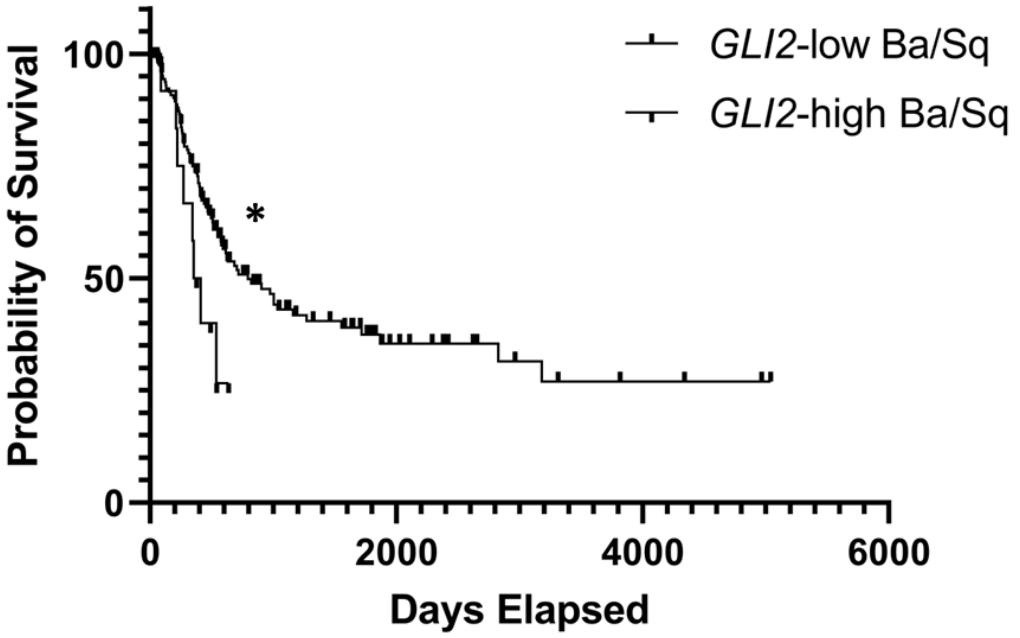

Figure 5.25: *GLI2*–high Basal/Squamous MIBC patients have reduced overall survival

Kaplan-Meier survival plot of the groups created by separating basal/squamous tumours into *GLI2*-high and *GLI2*-low subtypes. The Log-Rank (Mantel-Cox) test was used to determine significance between the overall survival of groups. Median survival time of *GLI2*-high basal/squamous subset (n=12) = 385 days, *GLI2*-low basal/squamous group (n=143) = 795 days. *=p<0.05.

5.5 Discussion

5.5.1 Canonical and non-canonical SHH pathway signalling in urothelium

SHH-mediated paracrine signalling between the urothelium and stroma has previously been implicated in human (Jenkins *et al.,* 2007) and mouse (Haraguchi *et al.,* 2007; Shiroyanagi *et al.,* 2007; Caubit *et al.,* 2008; Cheng *et al.,* 2008; Cao *et al.,* 2010; DeSouza *et al.,* 2013) fetal bladder development, in addition to the regulation of tissue homeostasis (and subsequent inhibition of hyperplasia) in adult murine bladders (Shin *et al.,* 2011; Shin *et al.,* 2014a; Shin *et al.,* 2014b). This study provides evidence that the same directional paracrine signalling relationship could also exist in adult human bladder through confirmation of expression (and targeted induction) of pathway components in urothelial and stromal cell types.

5.5.1.1 *In situ* expression of SHH and PTCH1 in urothelium

Urothelial-specific expression of SHH was validated through both transcriptomic analysis and a preliminary study of its protein localisation in native urothelium. Of the SHH pathway genes examined, *SHH* was the only gene that exhibited significant differential expression when comparing *in situ* urothelium of bladder and ureter derivation, or comparing expression in ureter-derived *in situ* urothelium to NHU cells. The urothelia of bladder and ureter are derived from separate embryological origins but have been confirmed to share striking similarities in morphology (Hicks, 1965) and gene expression profile (Böck *et al.,* 2014). A significantly higher expression of *SHH* in bladder urothelial cells may therefore indicate a tissue-specific differential response to signals received by the underlying stroma that could regulate *SHH* expression. Further examination of the potential differences in signalling phenotype of bladder and ureter-derived stromal cells are discussed in Section 5.5.3.2.

A significant reduction in *SHH* expression in ABS/Ca^{2+} differentiated cells when compared to native urothelium would also seem to suggest that inductive factors from stromal or other cell types that are absent from the *in vitro* culture environment are important to induce expression of the gene. The SHH ligand undergoes a series of post-translational modifications such as palmitoylation and cholesterol binding to generate its mature, active N-terminal state (Porter *et al.,*

1996b; Pepinsky *et al.,* 1998). Palmitic acid is not a constituent component of KSFMc; thus highlighting a probable scenario where NHU cells are unable to correctly synthesise SHH without exogenous administration of the fatty acid, meaning its effect on urothelial phenotype (if any) is not normally observed *in vitro*.

Aside from its expression in both native and *in vitro* cultured stromal cells, PTCH1 was also found to be intensely expressed at the apical membrane of superficial ureter urothelium, indicative of a receptor that readily receives secreted molecules from the lumen. This raises the question of why urothelial cells would express PTCH1 if autocrine downstream pathway signalling (as mediated by SHH/PTCH1 binding) is not found in this cell type. Due to its known status as a tumour suppressor gene in other cell types (Gailani *et al.,* 1996), the function of PTCH1 in urothelial cells may therefore be to provide a constitutive inhibitor of SMO (and subsequent downstream GLI) activity. How urothelial-secreted SHH morphogen would fail to bind to urothelial PTCH1 to activate autocrine pathway signalling (yet is able to bind to PTCH1 receptor in the surrounding stroma) may result from a lack of PTCH1-presenting primary cilium organelle structures, although studies to confirm the absence of primary cilium in urothelium have not been undertaken.

5.5.1.2 Non-canonical induction of GLI1 expression in undifferentiated NHU cells

Expression of downstream pathway effector GLI1 has been described in urothelial cells *in vitro* in studies of MIBC cell lines T24, 5637 and VM-CUB-1 (Fei *et al.,* 2012; Kitagawa *et al.,* 2019), whilst an initial study into SHH signalling in undifferentiated NHU cells concluded that expression of downstream components of the pathway were present due to an increase in luciferase activity using a GLI-dependent promoter (Thievessen *et al.,* 2005). Thievessen *et al.* speculated that expression of *GLI1* may be a result of crosstalk with active signal transduction pathways, which was confirmed in this study through the inhibition of EGFR and/or PI3K/AKT (but not SMO) signalling, thereby implicating a non-canonical mechanism of pathway activation. PI3K/AKT pathway signalling has been implicated in the activation of non-canonical GLI signalling in other epithelial cell types (Zhou *et al.,* 2016; Kasiri *et al.,* 2017), with AKT postulated to mediate the inhibition of PKA-regulated GLI-A degradation and thus allowing for the induction of *GLI1* (Riobo *et al.,* 2006). Future

work with GLI1-expressing undifferentiated NHU cells treated with a GLI-specific inhibitor such as GANT61 (Lauth *et al.,* 2007) may prove to elucidate the specific effect that GLI1 expression has on downstream EGFR and PI3K/AKT-mediated processes such as proliferation.

5.5.2 Paracrine canonical SHH pathway activation in urothelial stroma

Both bladder and ureter-derived stromal cells were demonstrated to not express SHH, yet possessed canonical, SMO-mediated SHH signalling responses following activation with natural (rSHH) and synthetic (SAG) agonists, as demonstrated by a significant increase in *GLI1* transcript and a striking increase in nuclear protein expression.

The specific rod-like expression pattern of PTCH1 in untreated, serum-starved NuHS cells observed in this study was speculated to indicate the localisation of PTCH1 to the primary cilium of these cells. In order to verify this, a dual-labelling immunofluorescence approach that visualises both PTCH1 and a marker of primary cilium, such as acetylated α-tubulin (Cambray-Deakin *et al.,* 1987), would need to be performed. A study in NIH-3T3 fibroblast cells revealed that while Shh/Ptch1 binding was required for Smo ciliary accumulation, the subsequent ejection of Ptch1 from the primary cilium is independent from the process of Smo activation (Kim *et al.,* 2015b), perhaps explaining why the localisation of PTCH1 was not observed to have changed following 24h SAG treatment. A subsequent loss of PTCH1 labelling observed in GDC-0449 treated cells is likely to signify a breakdown of the existing PTCH1 protein following inhibition of its transcript.

5.5.3 RNAseq analysis of SHH pathway-active stromal cells

5.5.3.1 Troubleshooting data

RNAseq analysis of SAG-treated NbHS and NuHS cells suggested that minimal consistent transcriptional changes occurred within the stromal cultures following agonist treatment, other than induction of *GLI1*. Some potential explanations for this observation are discussed below.

One conclusion that could be made from the data is that GLI1 activation in NuHS/NbHS cells is inducible but has little effect on downstream signalling

processes, although the possibility that a fully functional signal transduction pathway exists in these cells but has no physiological relevance seems unlikely. Alternatively, the induction of GLI1-specific targets may optimally take place at a later time-point than the times in which the RNAseq samples were harvested, despite the relatively rapid induction of GLI1 protein observed in the nuclei of SAG-treated NuHS cells. The most probable explanation however stems from the use of a NuHS/NbHS cell model that currently lacks clarity as to the identity of the specific cell types it contains.

As demonstrated in previous studies of cultured stromal cells, isolation of NuHS cells from ureter-derived stromal explants results in a highly heterogeneous cell population that express markers specific to various stromal cell types (Kimuli *et al.,* 2004; Baker *et al.*, 2008). Considering previous reports that demonstrated differential responses of mouse bladder mesenchymal cells to Shh signalling based on their stromal cell type (Cheng *et al.,* 2008; DeSouza *et al.,* 2013), it is therefore possible that a mixed population of adult human stromal cells would also possess a differential capability to respond to SHH pathway agonism. This would thus account for the large variation in *GLI1* induction observed between stromal cell lines from different donors that contained, for example, a low ratio of lamina propria-originating fibroblast cells in the total cell population.

5.5.3.2 Candidate genes of GLI1-mediated transcription in NbHS cells

GLI1-mediated transcriptional changes may also be tissue-specific, as demonstrated by notable fold change increases in expression of laminin genes *LAMA3*, *LAMB3* and *LAMC2* and laminin receptor *ITGB4* (Integrin β4) in NbHS cells (n=1) only. A relationship between GLI1 activation and integrin β4 expression has previously been implicated in a model of ovarian cancer, where inhibition of GLI1 resulted in a significant reduction in *ITGB4* expression in SK-OV-3 cells (Chen *et al.,* 2014). Integrin proteins have known roles in regulating epithelial cell polarity (W. Yu et al., 2005) and remodelling of the basement membrane following shear stress (Béguin *et al.,* 2020), while low expression of integrin β4 has previously been implicated in the propensity for high-grade MIBC cell lines to exhibit a highly migratory phenotype when implanted into mouse bladder (Harabayashi *et al.,* 1999). That

NbHS cells upregulate *ITGB4* and various laminin genes in this context would suggest potentially fascinating implications for the role of canonical SHH signalling in the regulation of urothelial organisation, assembly of basement membrane and protection against a migratory, invasive phenotype in bladder, but this observation would need to be further validated *in vitro*.

To conclude, one or more of the aforementioned variables may account for the overall lack of a consistent gene upregulation response observed in the pathway-activated stromal transcriptome, but due to the potential importance of this signalling axis in human bladder, it would be worth further study.

5.5.3.3 Human urothelial stromal cell data resource

Beyond its original intended use, this RNAseq cohort is seemingly the first curation of a human bladder/ureter-derived stromal cell transcriptome dataset, and may therefore prove to be a valuable resource for use in future studies that examine bladder/ureter stromal cell phenotype. For example, analysis of expression of genes encompassing the FGF family of ligands in NuHS/NbHS cells revealed that *FGF7* was the predominantly expressed FGF gene, exhibiting high expression in both control and treated samples. Fgf7 has previously been shown to be vital for the complete stratification of mouse urothelium (Tash *et al.,* 2001), making it an ideal candidate ligand to study in regards to its effect on FGFR3 signalling, a receptor whose natural ligand in urothelium has yet to be identified.

5.5.4 SHH pathway dysregulation in MIBC

5.5.4.1 Abrogation of SHH expression in MIBC

The pattern of gene expression of canonical SHH pathway components in MIBC supports the hypothesis that aberrant expression (*i.e.* an inhibition of *SHH* expression in all but luminal papillary MIBC) is indicative of a progression to a more aggressive and invasive disease state. A recent study by Kim *et al.* implicated hypermethylation of the CpG shore upstream of the *Shh* promoter as a potential causative factor behind the loss of *Shh* expression in high-grade murine MIBC. Inhibition of DNA methyltransferase activity using 5'-azacitidine was observed to halt the development of murine MIBC, a phenotype postulated to occur as a result

of reactivated Shh expression and a corresponding increase in stromal Gli activity (Kim *et al.,* 2019b). Studies that have analysed the efficacy of treatments that target DNA methyltransferase activity in MIBC are currently limited (Dhawan *et al.,* 2013; Wang *et al.,* 2015), but may prove to be beneficial in tumours with aberrant *SHH* expression based on the current evidence.

5.5.4.2 GLI2-high phenotype in basal/squamous MIBC

The overexpression of previously absent *GLI2* in a subset of basal/squamous tumours was unexpected, but provides a potentially interesting insight into the molecular basis behind a highly aggressive, poor survival phenotype. Examination of *GLI2* expression in a cohort of MIBC cell lines previously determined that high basal expression of *GLI2* in a cell line such as UM-UC-3 correlated with invasiveness (Mechlin *et al.,* 2010). Mechlin *et al.* observed that this *GLI2*-high phenotype was neither correlated with high expression of canonical SHH pathway genes, or was amenable to treatment by inhibitors of autocrine SHH activity, yet were unable to identify a potential source of the *GLI2* expression that they observed.

Analysis of the *GLI2*-high basal/squamous subgroup revealed enriched mutations in both *NFE2L2* and *KEAP1* genes, alongside significantly increased expression of multiple NRF2-KEAP1 pathway target genes such as *GSTM2*, *GSTM3*, *GCLC* and *ABCC1*. In normal, unstressed cells, the transcription factor NRF2 is bound to the adapter protein KEAP1 which mediates its ubiquitination and continual degradation (Kobayashi *et al.,* 2004). In response to endogenous or exogenous stresses such as reactive oxygen species or electrophiles, NRF2 is able to circumvent KEAP1 inhibition and induce a battery of target genes involved in cellular detoxification (Itoh *et al.,* 1997), thus implicating KEAP1-NRF2 signalling as a pivotal pathway in the oxidative stress response. Inactivating mutations to *KEAP1* or activating mutations to *NFE2L2* therefore induce aberrant NRF2 activity and result in cancers with a chemo-resistant phenotype (Shibata *et al.,* 2008). Previous studies using mouse embryonic fibroblast cells have identified *Gli2* as a Nrf2 transcriptional target (Malhotra *et al.,* 2010; Martin-Hurtado *et al.,* 2019), yet this is the first study to potentially identify such a signalling relationship in human cells. It is currently unclear as to the specific effect that the aberrant *GLI2* expression observed in the

NRF2 pathway-active, *GLI2*-high subgroup is having on cell phenotype. However, a recent study that inhibited GLI2 in the GLI2-high MIBC cell lines UM-UC-3 and 253J-BV demonstrated that these cells exhibited reduced viability and increased apoptosis, thereby providing evidence that expression of the protein in MIBC contributes to an anti-apoptotic phenotype (Raven *et al.,* 2019).

5.5.4.3 GLI2 expression in NHU cells

Expression of *GLI2* was undetectable in all NHU cell lines assayed, regardless of differentiation state. Currently unpublished work from the laboratory has identified a NRF2-mediated oxidative stress response in NHU cells treated with plant-derived antioxidant sulforaphane, with sulforaphane-treated cells exhibiting a higher viability to control when cultured in the presence of toxic unsaturated aldehyde acrolein. It would therefore be interesting to observe whether activation of NRF2 signalling induces expression of previously absent *GLI2* in normal urothelium, and if so, determine what effect that this activation has on NHU cell phenotype. A summary diagram of the potential mechanisms of non-canonical GLI1 and GLI2 activation in urothelial cells is provided in Figure 5.26.

5.5.5 Chapter conclusions

To summarise, the findings in this chapter confirm that urothelial and stromal-derived cells express the necessary components of the SHH pathway in order to participate in a directional paracrine signalling axis, with urothelium *in situ* expressing SHH and the underlying stromal cells expressing PTCH1 and GLI1, with transcript expression of both genes exhibiting a significant induction upon treatment of said cells with SHH pathway agonists. Analysis of proliferating, undifferentiated NHU cells revealed an induction of GLI1 expression through a non-canonical mechanism, with PI3K/AKT signalling postulated to play a key role. Examination of MIBC tumours identified that a loss of *SHH* and a gain of previously absent *GLI2* expression is indicative of a highly aggressive basal/squamous MIBC subtype that exhibits dysregulation of KEAP1-NRF2 signalling, a chemo-resistant phenotype and a poor survival rate.

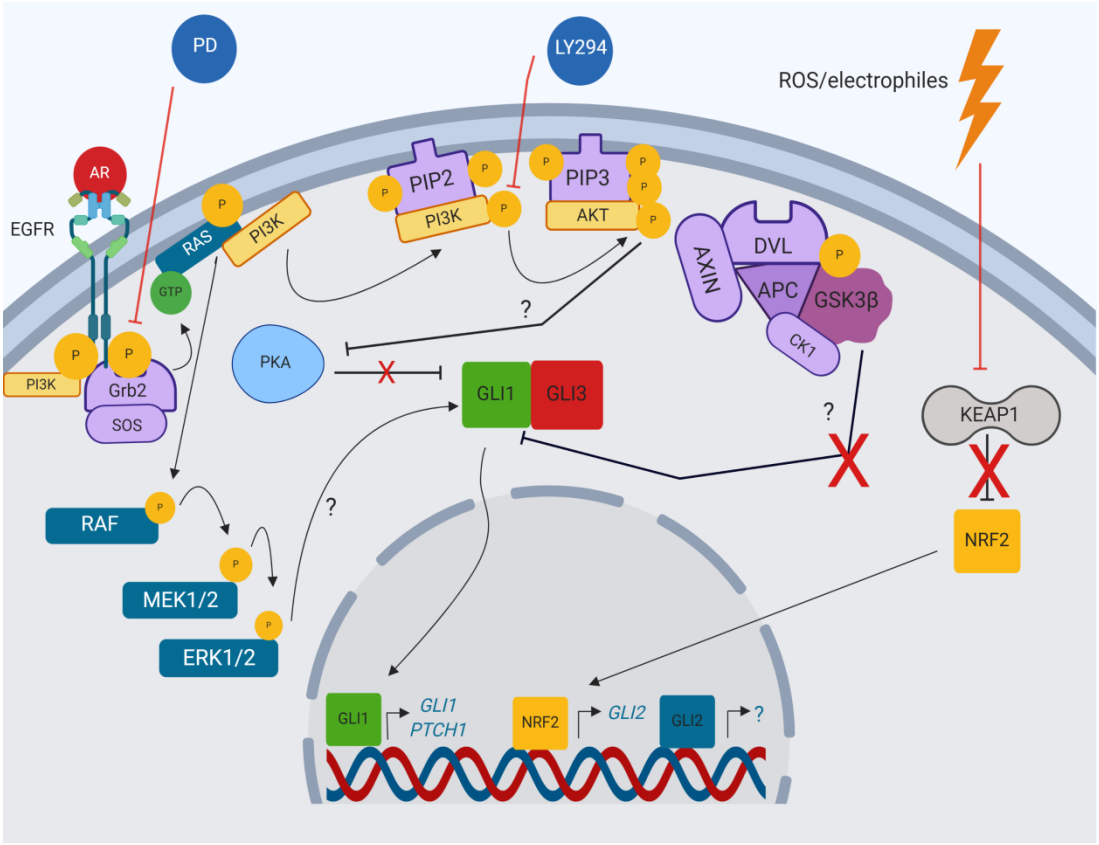

Figure 5.26: Potential mechanisms of non-canonical GLI1 and GLI2 induction in urothelium

Nuclear GLI1 was observed to be expressed in undifferentiated NHU cells, with this expression abrogated following blockade of EGFR and/or PI3K/AKT signalling. *GLI2* was not found to be expressed by NHU cells in the observed contexts of this study, but a subset of basal/squamous MIBC tumours exhibited high expression of the gene following aberrant activation of NRF2 signalling. Outstanding questions include whether AKT-mediated expression of GLI1 is dependent on PKA inhibition and confirming if RAS/RAF/MEK/ERK signalling additionally plays a role in expression of the protein. Based on previous reports that demonstrated that active GSK3β contributes to GLI degradation (Price *et al.,* 2002), it would be predicted that dephosphorylation of GSK3β following PD153035 treatment (Georgopoulos *et al.,* 2014) would additionally influence expression of GLI1 in NHU cells, although this hypothesis was not tested. Confirmation of *GLI2* expression in NHU cells with activated NRF2 signalling and elucidation of its specific downstream target genes would help to reveal its potential role in mediating the urothelial oxidative stress response.

5.6 Summary of results

- Urothelial cells expressed the necessary components of the SHH pathway (SHH, PTCH1) to both produce and receive a SHH signal, but had absent expression of downstream components of the pathway (*GLI1*, *GLI2*), suggesting that this cell type does not participate in autocrine SHH signalling.

- Ureter and bladder-derived stromal cells did not express SHH but were both found to induce *PTCH1* and GLI1 expression upon treatment with SHH pathway agonists, implicating this cell type as a receiver of SHH ligand as part of a paracrine signalling loop. However, treatment of stromal cells with SAG resulted in no significant alterations to global gene expression other than *GLI1.*

- Despite being absent in urothelium *in situ*, expression of *GLI1* was upregulated in undifferentiated NHU cells. Treatment of NHU cells with agonists and antagonists of canonical SHH signalling had no effect on the expression of *GLI1*, suggesting that this occurrence was a result of non-canonical, SMO-independent GLI activation. Expression of this gene was instead found to be modulated through inhibition of both EGFR and PI3K/AKT signalling axes.

- Cases of MIBC were found to exhibit reduced expression of *SHH* and *PTCH1* in comparison to normal urothelium, but mutations in the genes was relatively rare. A subset of the highly aggressive basal/squamous tumours were found to exhibit *SHH*-independent overexpression of *GLI2*, which resulted a downregulation of genes associated with differentiation, an upregulation of genes involved in anti-chemosensitivity and a reduced overall survival rate. This subgroup may arise through mutations in key genes of the KEAP1-NRF2 pathway.

6: Discussion

6.1 Thesis overview

This thesis has provided the first evidence that VGLL1, a previously unstudied transcriptional co-activator in urothelium, is an important protein in the regulation of urothelial tissue homeostasis. This function does not appear to arise through a traditional Hippo pathway role of inhibition of proliferation/migration-associated YAP/TAZ signalling, as initially hypothesised following a review of previous studies that examined the role of VGLL1 in other human tissues (Section 3.1.3). Instead, this study has demonstrated that expression of VGLL1 serves to inhibit cellular proliferation in both undifferentiated NHU and T24 cells, whilst helping to maintain a mitotically-quiescent phenotype once NHU cells have entered a late differentiation state. When differentiated urothelial tissues are wounded, evidence in this study suggests that VGLL1 plays an important role in regulating both the initial wound healing response and controlling the proportion of cells that re-enter the cell cycle to repopulate the damaged tissue. Analysis of a publically-available MIBC cohort resource determined that overexpression of the gene in a subset of tumours was potentially as a consequence of inactivating mutations to the chromatin remodelling gene *ARID1A* and related processes. MIBC tumours that exhibited *VGLL1* overexpression expressed genes involved in anti-apoptotic processes and exhibited a poor survival rate, indicative of a loss of normal VGLL1 function.

Additionally, this study has also confirmed the capability of adult human urothelium and stroma to communicate via a paracrine SHH signalling axis, as hypothesised based on previous studies that demonstrated the same axis in adult murine and developing human bladders (Section 5.1.4). A loss of *SHH* expression observed in a majority of MIBC tumours not subtyped as luminal papillary was suggestive of an abrogation of this signalling in high-grade MIBC. In an undifferentiated state, NHU cells were demonstrated to induce expression of *GLI1* through a SHH/PTCH1/SMO-independent, PI3K-AKT-mediated non-canonical mechanism. This activation of *GLI1* appears to be independent of *GLI2,* a gene not found to be expressed in NHU cells in any contexts studied here. However, *GLI2* was discovered to be aberrantly

expressed in a subset of basal/squamous MIBC, potentially as a novel target gene of KEAP1-NRF2 signalling dysregulation.

Collectively, the evidence provided in this thesis has successfully achieved the initial aim of this study, which was to understand how Hippo and SHH signalling, two previously little-studied pathways in adult human normal urothelium, affected urothelial tissue physiology through regulation of individual cell phenotype.

6.2 Use of experimental urothelial models

The unique, specialised function of the urothelium is an ideal cell type to investigate the mechanisms of tissue homeostasis due to its innate plasticity to rapidly switch between a mitotically-quiescent and a wound-healing migratory phenotype *in vivo* (Levi *et al.,* 1969; Lavelle *et al.,* 2002). This phenotype is recapitulated *in vitro*, as demonstrated by the functional differentiation and ability to self-repair exhibited by ABS/Ca^{2+} differentiated NHU cells (Cross *et al.,* 2005; Fleming *et al.,* 2012), a cell state that confers a morphology and protein expression profile comparable to that found in urothelium *in situ* (Cross *et al.,* 2005; Smith *et al.,* 2015). Use of non-transformed NHU cells in a differentiated (by two independent methods), regenerating or actively proliferating undifferentiated state thus granted an extensive *in vitro* resource in which to investigate context-specific alterations to phenotype. This, allied with *in silico* analysis of normal and malignant urothelial phenotype through the use of both published (Fishwick *et al.,* 2017; The Cancer Genome Atlas Research Network, 2014) and as-of-yet unpublished RNAseq datasets, therefore allowed for a more holistic inference of the role of signalling pathways in urothelial tissue homeostasis than can be achieved when studying immortalised or established cancer-derived cell lines (that have by definition evaded tissue regulatory mechanisms), or tissue types with a constitutive turnover rate.

As previously stated, the comparative cell types of the human bladder and ureter exhibit extensive similarities in morphology and transcriptomic profiles (Hicks, 1965; Böck *et al.,* 2014). However, as the bladder and ureter arise from two separate embryological derivations, this inevitably results in subtle differences

between the tissues of the two organs, as demonstrated by the results collated in Chapter 5. Due to the logistical difficulties involved in acquiring normal human bladder tissue, all NHU cell lines used in this thesis (aside from select bladder NHU cell lines that were processed for RNAseq analysis) were derived from ureter. It would therefore be of great interest, if possible, to directly compare the phenotypes of bladder and ureter-derived NHU cells in regards to the observations made on VGLL1 function in this study, in a manner similar to the comparisons performed between NuHS and NbHS cells in Chapter 5. This approach would also potentially grant a further insight into the predicted mechanisms behind the dysregulation of VGLL1-high MIBC, a disease that overwhelmingly arises in bladder urothelium (Siegel *et al.,* 2019).

A key assay used in this study that facilitated inferences about the phenotype of proteins in certain physiological contexts (particular following urothelial scratch wounding) was immunofluorescence labelling. While this technique was imperative in establishing the predicted function and potential relationship to other proteins that VGLL1 possesses in differentiated NHU cells, these conclusions were often based on the subjective interpretation of single, representative, high magnification immunofluorescence images from each cell line/condition. Quantification of the aforementioned immunofluorescence labelling using established image analysis methodology (referenced below) would therefore strengthen the conclusions made in this study. Examples of this would include the quantification of VGLL1, p63 and p-SMAD3 nuclear positivity (using a macro similar to that performed on Ki67/MCM2 labelled images in Figures 3.38 and 3.43), a quantification of the mean nuclear-to-cytoplasmic ratio of YAP and PPARγ expression (as demonstrated by Grune *et al.,* 2018), or a comparison of the number of dissolved layers of ZO-3 at the wound edge of scratched urothelial cultures (using an analysis similar to that described by Terryn *et al.,* 2013).

6.3 Hippo pathway regulation of YAP/TAZ signalling

6.3.1 Relationship of VGLL1 to YAP/TAZ

Analysis of YAP activity and induction of downstream gene targets in NHU and MIBC cell lines with modified VGLL1 expression revealed little to suggest that VGLL1 functions in an antagonistic capacity to YAP/TAZ, inconsistent with reports of VGLL1 function in other human cell types (Pobbati *et al.,* 2012). Four reasons supporting this conclusion on VGLL1 function are detailed below.

1. *Preferential binding of VGLL1 and YAP/TAZ to different TEAD proteins in urothelium*

Transcriptomic analysis of TEAD transcription factors in normal urothelium revealed that *TEAD1* and *TEAD3* were the predominantly expressed TEAD family members in this cell type, while principal component analysis of Hippo pathway components in MIBC revealed striking associations of *VGLL1* (*TEAD3*) and *YAP1* and YAP downstream target genes (*TEAD1*) to different TEAD genes. Human TEAD1 protein has previously been demonstrated to bind to Vg and substitute for Sd function when expressed in *Drosophila* (Deshpande *et al.,* 1997), while the core VxxHF TEAD binding motif is retained in all four VGLL proteins (Pobbati *et al.,* 2012). The evolutionary divergence from a single Vg and Sd protein in *Drosophila* to four VGLL and TEAD proteins in mammals does however raise the question as to the level of functional redundancy that may or may not exist between the various VGLL and TEAD proteins. Does mammalian VGLL1 possess a similar binding affinity to each of the four TEAD proteins? A recent study undertaken using a synthetic peptide derived from mouse Vgll1 suggests this to be true (Bokhovchuk *et al.,* 2019), but a comprehensive interrogation of whether preferential binding of human VGLL1 to a specific TEAD is dependent on tissue specificity or a cell signalling-specific context has yet to be performed.

2. *Lack of effect on YAP/TAZ-mediated activity in urothelial cells with manipulated VGLL1 expression*

Overexpression of VGLL1 had no effect on the amount of inactive, phosphorylated YAP in NHU cells, which appeared consistent between undifferentiated and

differentiated cell states. Knockdown of VGLL1 was observed to have no effect on the nuclear:cytoplasmic ratio of total YAP in wounded differentiated cells. Subsequent validation of the aforementioned observations in MIBC cell lines 5637, T24 and ScaBer revealed that these cells additionally did not exhibit changes to YAP activation, localisation or expression of commonly cited YAP/TAZ target genes.

3. *VGLL4-specific inhibitory function of YAP/TAZ signalling?*

Various studies have implicated mammalian VGLL4 as having a direct role in inhibiting YAP/TAZ signalling through competitive binding to TEAD1 (Zhang *et al.,* 2017), TEAD2 (Koontz *et al.,* 2013) or TEAD4 (Jiao *et al.,* 2014). However, unique to the structure of VGLL4 compared to other members of the VGLL family is a second VxxHF TEAD binding domain (Chen *et al.,* 2004). This second binding domain was demonstrated to be vital for VGLL4-mediated inhibition of downstream YAP/TAZ target genes (Zhang *et al.,* 2017), thus perhaps offering an additional explanation as to why the forced expression of VGLL1 in urothelial cells fails to confer a similar effect.

4. *Lack of evidence for role of VGLL1 in YAP/TAZ competitive inhibition in other cell models*

Currently the only evidence for the existence of VGLL1 and YAP mutual antagonism was obtained from a transformed human cell model by Pobbati *et al.* Through site-directed mutagenesis of H44 and F45 in the VxxHF region of VGLL1, Pobbati *et al.* demonstrated a significant reduction in the amount of co-immunoprecipitated VGLL1 to TEAD4 in HEK293 cells, confirming the ability of the transcription factor and transcriptional co-activator to bind to one another. However, the study claims that a 55% reduction in YAP/TEAD4 co-immunoprecipitation is observed when VGLL1 is overexpressed in the HEK293 cell line, which appears to be an exaggerated figure based on the accompanying immunoblot image displayed. Furthermore, this observation is not validated in the prostate cancer cell lines PC-3 and LnCAP, with the increase in anchorage-independent cell proliferation observed in said lines following VGLL1 overexpression offering little conclusive evidence to support the

main stated conclusion of the study that VGLL1 directly antagonises YAP/TEAD binding (Pobbati *et al.,* 2012).

Through the evidence provided in this thesis, it can be thus be concluded that there is an overall lack of compelling evidence for the assumed role of VGLL1 in Hippo pathway signalling, as defined as a restriction of tissue growth through the inhibition of YAP/TAZ signalling.

6.3.2 Phenotype of YAP/TAZ in urothelium

While seemingly unrelated to VGLL1 activity in urothelium, experimental evidence in this study suggested a shift in the proportion of nuclear and cytoplasmic YAP in NHU cells that was sensitive to both inhibition of autocrine EGFR signalling and cell-cell contact. Expression of YAP/TAZ target genes *AXL* and *CYR61* were additionally found to be significantly downregulated in differentiated NHU cells when compared to their matched sub-confluent, undifferentiated state. Investigation into the role that YAP/TAZ plays in the urothelial tissue homeostatic phenotype may therefore warrant its own separate study. Genomic analysis of a pan-cancer cohort revealed that cases of MIBC collectively exhibited one of the highest copy number amplification frequencies of *YAP1*/*WWTR1* in human cancer (Wang *et al.,* 2018). Use of the benzoporphyrin derivative verteporfin has previously been shown to block the interaction between YAP/TAZ and TEAD and thus inhibit YAP/TAZ-mediated signalling (Liu-Chittenden *et al.,* 2012), with this drug later demonstrated to successfully inhibit the proliferation of MIBC cell lines 5637 and UM-UC-3 (Dong *et al.,* 2018). Treatment of proliferating and/or regenerating NHU cells with verteporfin or YAP siRNA could therefore help to elucidate the role that activation of YAP/TAZ signalling (independent of VGLL1) plays in regulating tissue homeostasis in normal urothelium, and provide a greater understanding as to whether aberrant YAP/TAZ signalling is a mediator of MIBC cell growth.

6.4 Concluding remarks and future work

6.4.1 Hippo pathway signalling and VGLL1

In this study the predicted transcriptional co-activator *VGLL1* was identified as being associated to differentiation in NHU cells and as such, was designated as a candidate regulator of Hippo signalling in urothelium. VGLL1 expression was found to be induced in NHU cells following differentiation, contact inhibition, formation of E-cadherin-mediated cell-cell adherens junctions and/or blockade of the EGFR/RAS/RAF/MEK/ERK signalling axis. Genetic manipulation of VGLL1 revealed a likely role for the protein in the maintenance of urothelial tissue homeostasis, as knockdown of the gene resulted in reduced barrier tightness, inhibition of differentiation-associated proteins and increased re-entry into the cell cycle in differentiated NHU cells following scratch wounding. Conversely, overexpression of VGLL1 in undifferentiated NHU cells and T24 cells resulted in cell cycle arrest and an inhibition of proliferation in a YAP/TAZ signalling-independent mechanism. In MIBC, the *VGLL1* gene was not mutated and expression was retained in a majority of cases, although specific subgroups of tumours that exhibited a complete loss or overexpression of the gene were observed. Examination of the *VGLL1*-high subtype of MIBC revealed an enrichment of *ARID1A* mutations and a patient group that exhibited a significantly increased mortality rate, indicative of a physiological redundancy of VGLL1 function and a dysregulation of its expression in these tumours.

The cumulative observations made of VGLL1 in urothelial cells in this study have led to the following hypothesis as to its function in urothelium, as depicted in Figure 6.1. The evidence collated collectively points to a potential binding relationship between VGLL1 and the transcription factor TEAD3. Co-immunoprecipitation and/or proximity ligation assay studies would confirm binding between the two proteins, whilst Chromatin Immunopreciptation sequencing of TEAD3-bound DNA sequences in control versus VGLL1 knockdown differentiated NHU cells would provide a comprehensive list of genes upregulated through this interaction. In differentiated urothelium, a reduction or inhibition of VGLL1/TEAD3-mediated transcriptional targets such as PAR6 and PLEKHG6 results in the production of a

faulty tissue barrier, thus accounting for the weaker barrier tightness observed in VGLL1 knockdown cells. PAR6 and PLEKHG6-associated RHOA signalling has additionally been implicated in the TGFβR-mediated dissolution of tight junctions that occurs following wounding, meaning that reduced expression of these proteins results in dysregulated TGFβR signalling and an impaired wound response. Loss of genes transcribed through VGLL1 transcriptional co-activity subsequently cause an increase in p-AKT activity and a loss of control regarding re-entry into the cell cycle. To verify the preliminary link established in this study between VGLL1 and a negative regulation of PI3K/AKT signalling, further NHU cell lines would be transduced with VGLL1 overexpression constructs to confirm this phenomenon. In differentiated urothelium, ARID1A functions to allow access of the VGLL1/TEAD3 transcriptional complex to specific regions of the DNA, possibly through direct binding to the complex. To test this phenotype *in vitro*, Rapid Immunoprecipitation Mass spectrometry of Endogenous proteins would be performed to confirm the presence or absence of bound ARID1A to VGLL1/TEAD3 in NHU cells, followed by observing cell phenotype in cells with manipulated (through either site-directed mutagenesis or shRNA knockdown) ARID1A. Analysis of the viability of HT1376 and HT1197 cells following treatment with inhibitors against PI3K/AKT, HDAC, FGFR3 and ATR would thus identify potentially viable treatment options against the *VGLL1*-high, *ARID1A*-mutated MIBC phenotype.

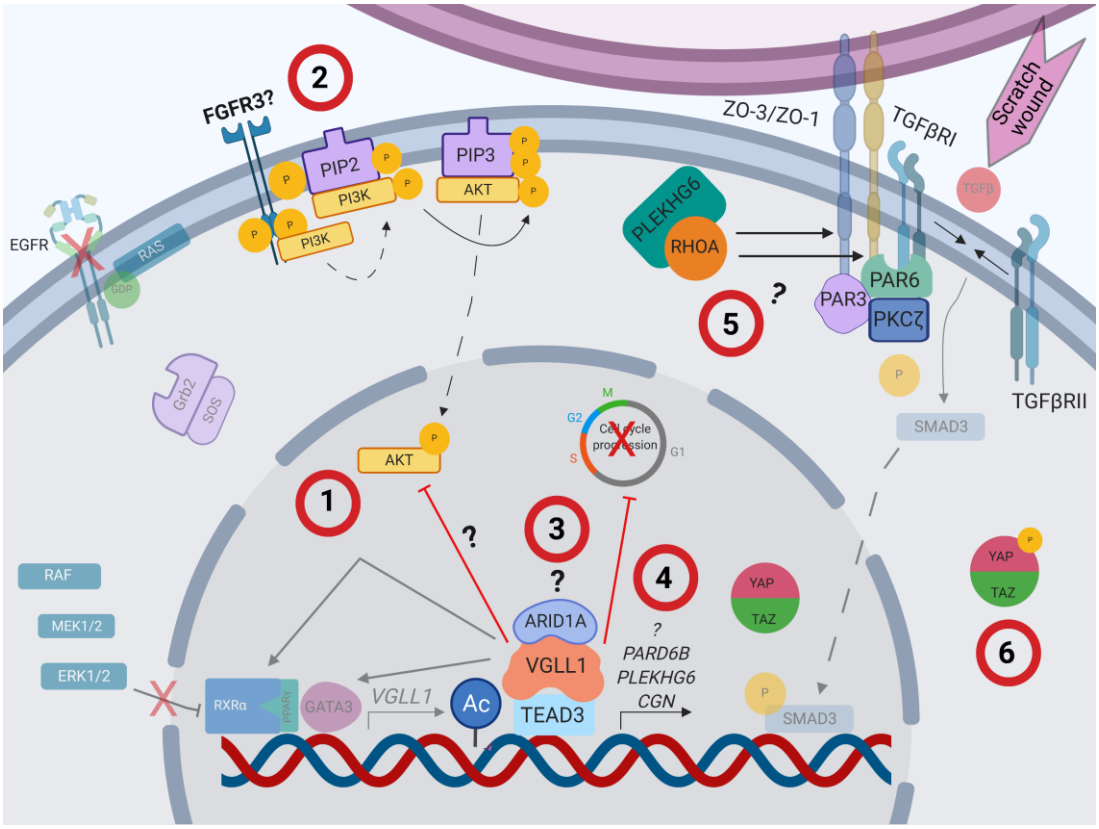

Figure 6.1: Proposed mechanisms of VGLL1 function in urothelium

A revision of the diagram presented in Figure 3.44, with opaque icons designating genes and/or proteins that were further investigated through *in vitro* or *in silico* analysis in Chapter 4. In a similar manner to undifferentiated NHU cells, forced expression of VGLL1 in T24 cells resulted in G0/G1 cell cycle arrest and an inhibition of phosphorylated AKT (**1**), a signalling pathway that is potentially activated in EGFR-blockaded NHU cells through FGFR3 signalling (**2**). In differentiated urothelium, VGLL1 is predicted to bind to constitutively expressed TEAD3, with the VGLL1/TEAD3 transcriptional complex possibly requiring wild-type function of the ARID1A-containing SWI/SNF complex in order to access target gene promoter regions (**3**). Expression of VGLL1/TEAD3 target genes, potential examples of which being *PARD6B, PLEKHG6* and *CGN* (**4**), help to maintain a quiescent phenotype and tight barrier in unwounded cells, but are also required to indirectly regulate AKT inhibition and mediate phosphorylation of SMAD3 upon TGFβR heterodimerisation (**5**), as predicted through their previously analysed functions in other cell types. Activation of SMAD3 in wounded urothelium subsequently results in a dissolution of tight junctions, effective wound repair and subsequent return to quiescence. Manipulation of VGLL1 was consistently observed to have no effect on YAP activity (**6**), thereby questioning the previously assumed role of VGLL1 as a regulator of Hippo signalling.

6.4.2 SHH pathway signalling

Urothelium *in situ* and differentiated NHU cells were found to express *SHH* but not downstream pathway activators *GLI1* or *GLI2*, suggesting that the human urothelium does not participate in canonical, autocrine SHH signalling but instead potentially participates in a paracrine signalling relationship with a surrounding cell type. Cultured NuHS/NbHS cells were confirmed to engage in canonical SHH pathway activation following treatment with both natural and synthetic agonists of the pathway, yet determination of the *GLI1*-specific target genes expressed by stromal cells following treatment was inconclusive. A group of tumours from the highly aggressive basal/squamous subtype (in addition to basal/squamous MIBC cell lines) exhibited an inhibition of *SHH* expression but increased expression of previously undetectable *GLI2*, with this subgroup marked by aberrant activation of genes associated with NRF2 signalling and a significantly decreased survival rate compared to other basal/squamous tumours.

To interrogate the reasoning behind a lack of a reproducible GLI1-mediated response in stromal cells, a more comprehensive characterisation of NuHS/NbHS cell population identity would be performed. Separation of NuHS/NbHS cells into different populations (i.e. lamina propria and smooth muscle-derived cells) by immunoisolation using specific cell surface antigens would elucidate whether the different stromal subtypes exhibited differential responses to SAG treatment. Once a highly SAG-responsive cell population was identified, single-cell RNAseq of samples would be performed to identify whether specific stromal subtypes exhibit a consistent GLI1-mediated gene expression profile. Exogenous administration (or manipulation of) identified candidate proteins from the RNAseq analysis on NHU cells would subsequently be performed to determine whether said molecules affect *in vitro* urothelial cell phenotype in processes such as differentiation and wound repair. To examine the role of the potential NRF2-mediated *GLI2* induction in normal urothelium, the ability of sulforaphane-treated NHU cells to survive oxidative stress following siRNA knockdown of *GLI2* would be explored.

7: Appendix

Appendix i: List of suppliers

Company name	Company website
Abcam	https://www.abcam.com/
Agilent Technologies	https://www.agilent.com/
American Type Culture Collection	https://www.atcc.org/
Atlas Antibodies	https://www.atlasantibodies.com/
BD Bioscience	https://www.bdbiosciences.com/
BioIVT	https://bioivt.com/
Bioline	https://www.bioline.com/
Bio-Rad	https://www.bio-rad.com/
Cambridge Bioscience	https://www.bioscience.co.uk/
Cayman Chemical	https://www.caymanchem.com/
Cellpath	https://www.cellpath.com/
Cell Guidance Systems	https://www.cellgs.com/
Cell Signalling Technology	https://www.cellsignal.co.uk/
Developmental Studies Hybridoma Bank	https://dshb.biology.uiowa.edu/
Eurofins Genomics	https://www.eurofinsgenomics.eu/
Formedium	https://www.formedium.com/
Fisher Scientific	https://www.fishersci.co.uk/
Greiner	https://www.gbo.com/
Hendley Essex	http://www.hendley-essex.com/
Leica Biosystems	https://www.leicabiosystems.com/
Li-Cor	https://www.licor.com/
Melford Laboratories	https://www.melford.co.uk/
Merck Milipore	https://www.merckmillipore.com/
nanoAnalytics	https://www.nanoanalytics.com/
New England Biolabs	https://www.neb.uk.com/
Novus Biologicals	https://www.novusbio.com/
Olympus	https://www.olympus-lifescience.com/
PanReac Applichem	https://www.itwreagents.com/
Promega	https://www.promega.co.uk/
Proteintech	https://www.ptglab.com/
Qiagen	https://www.qiagen.com/
R&D Systems	https://www.rndsystems.com/
Rockland	https://rockland-inc.com/
Santa Cruz Biotechnology	https://www.scbt.com/
Sarstedt	https://www.sarstedt.com/
Selleck Chemicals	https://www.selleckchem.com/
Sigma-Aldrich	https://www.sigmaaldrich.com/
Takara Bio	https://www.takarabio.com/

Thermo Fisher	https://www.thermofisher.com/
Tocris	https://www.tocris.com/
Vector Laboratories	https://vectorlabs.com/
VWR	https://uk.vwr.com/

Table 7.1: List of suppliers used in study

Appendix ii: List of stock solution recipes

General solutions

PBS

- 10x PBS tablets (Thermo Fisher; pH 7.3)/L dH_2O. Solution was autoclaved prior to storage at ambient temperature.

TBS

- 1.21 g (10 mM) Tris-HCl (pH 7.6) and 8.18 g (140 mM) NaCl in 1 L dH_2O, with final solution equilibrated to pH 7.4. 0.1% Tween-20 was added to 1 L TBS to make TBST (pH 7.4). Both solutions were stored at ambient temperature.

Tissue culture solutions

EDTA

- 0.1% (w/v) EDTA in PBS. Solution was autoclaved before storage at ambient temperature.

Transport medium

- 500 mL Hank's Balanced Salt Solution (Thermo Fisher; contains Ca^{2+}/Mg^{2+}) containing 10 mM HEPES (pH 7.6) and 20 kallikrein inactivating units (KIU)/mL Aprotinin (Sigma-Aldrich). Solution stored at 4 ^{o}C.

10% (v/v) formalin

- 100 mL 10% Richard-Allan Scientific™ Neutral Buffered Formalin (Thermo Fisher) in 900 mL PBSc (PBS + 0.5 mM $MgCl_2$ + 0.9 mM $CaCl_2$). Solution stored at ambient temperature.

Stripper medium

- Transport medium and 0.1% (w/v) EDTA. Solution stored at 4 ^{o}C.

Collagenase IV

- Collagenase (Sigma-Aldrich) diluted to a working concentration of 100 U/mL in transport medium. Solution filter sterilised into 5 mL aliquots and frozen at -20 ^{o}C.

TV

- 10% trypsin (Sigma-Aldrich; isolated from porcine pancreas) and 2% (w/v) EDTA in Hank's Balanced Salt Solution. Solution was kept in 5 mL aliquots and stored at -20 ^{o}C.

Trypsin inhibitor

- 100 mg tryspin inhibitor (Sigma-Aldrich; derived from soybean) in 5 mL PBS. Solution was filter sterilised into 100 µL aliquots and stored at -20 ^{o}C.

Enterokinase buffer

- 2.5 mL 1 M Tris-HCl (pH 8.0), 3.3 mL 3 M NaCl, 100 µL 1 M $CaCl_2$ and 0.1% Tween-20 made up to 50 mL in sterile dH_2O. Buffer stored at 4 ^{o}C.

Molecular biology solutions

10x TBE buffer

- 108 g Tris, 55 g boric acid and 20 mL 1 M EDTA made up in 1 L dH_2O and stored at ambient temperature. Further 1:10 dilution in dH_2O makes working 1x solution.

Lysogeny broth (LB) medium

- 10 g bacto-tryptone, 10 g NaCl and 5 g yeast extract made up in 1 L dH_2O (pH 7.0). Medium aliquotted into glass bottles and autoclaved immediately following generation and stored at ambient temperature.

LB agar

- 1 L LB medium supplemented with 15 g agar. Solution aliquotted into glass bottles, autoclaved and stored at ambient temperature. Before use, the solid LB agar was melted in the microwave and poured into plastic Petri

dishes (under aseptic conditions) before allowing solution to solidify. Agar-containing Petri dishes were stored at 4 ^{o}C for up to a month.

Histology solutions

Citric Acid Buffer pH 6.0

- 2.4 g citric acid (10 mM) in 1050 mL dH_2O, pH adjusted to 6.0 using NaOH. Solution kept at ambient temperature.

Immunoblotting solutions

SDS sample buffer

- 10 mL glycerol (20% v/v), 6.25 mL 125 mM Tris-HCl (pH 6.8), 1 g SDS (2% w/v), 0.446 g $Na_4P_2O_7$, 0.42 g NaF and 18.4 mg Na_3PO_4 made up to 50 mL in dH_2O. Solution was mixed vigorously before aliquotting into 1.5 mL microfuge tubes and stored at -20 ^{o}C.

Transfer buffer

- 1.45 g (12mM) Tris, 7.2 g (96mM) glycine and 200 mL methanol made up to 1 L in dH_2O. Solution made at time of use and stored on ice.

Ponceau Red

- 5 g Ponceau S and 10 mL glacial acetic acid made up to 100 mL in dH_2O.

Appendix iii: List of patient samples

Y number	Derivation	Cell Type Used	Age (years)	Sex	Operation	Date
Y499	Bladder	Urothelial	3	Unknown	Ureteric reimplantation	27/01/2004
Y499	Ureter	Urothelial	3	Unknown	Ureteric reimplantation	27/01/2004
Y719	Bladder	Urothelial	Unknown	Unknown	Unknown	25/01/2006
Y719	Ureter	Urothelial	Unknown	Unknown	Unknown	25/01/2006
Y732	Bladder	NbHS	38	M	Nephrectomy	23/02/2006
Y781	Bladder	NbHS	65	M	Radical prostaectomy	Unknown
Y815	Bladder	Urothelial	Unknown	Unknown	Ureteric reimplantation	06/09/2006
Y815	Ureter	Urothelial	Unknown	Unknown	Ureteric reimplantation	06/09/2006
Y836	Bladder	Urothelial	10	M	Ureteric reimplantation	01/11/2006
Y836	Ureter	Urothelial	10	M	Ureteric reimplantation	01/11/2006
Y875	Renal pelvis	NuHS	9	Unknown	Pyeloplasty	23/05/2007
Y879	Bladder	NbHS	Paediatric	Unknown	Unknown	05/06/2007
Y886	Bladder	NbHS	68	M	Transurethral resection of the prostate	03/07/2007
Y896	Ureter	NHU	74	F	Nephrectomy	14/08/2007
Y919	Ureter	NuHS	67	M	Nephrectomy	08/01/2008
Y929	Bladder	NbHS	Paediatric	Unknown	Ureteric reimplantation	15/04/2008
Y929	Ureter	Urothelial	Paediatric	Unknown	Ureteric reimplantation	15/04/2008
Y929	Ureter	NuHS	Paediatric	Unknown	Ureteric reimplantation	15/04/2008
Y967	*Ureter*	*NHU*	*Unknown*	*Unknown*	*Pyeloplasty*	*05/03/2009*
Y1026	*Ureter*	*NHU*	*38*	*M*	*Unknown*	*10/10/2009*
Y1027	Ureter	NuHS	54	F	Unknown	10/10/2009
Y1077	*Ureter*	*NHU*	*76*	*M*	*Nephrectomy*	*29/10/2010*
Y1108	*Ureter*	*NHU*	*57*	*M*	*Nephrectomy*	*15/03/2011*
Y1171	*Ureter*	*Urothelium in situ*	*67*	*M*	*Unknown*	*10/10/2011*
Y1174	*Ureter*	*Urothelium in situ*	*49*	*F*	*Nephrectomy*	*25/10/2011*
Y1178	*Ureter*	*Urothelium in situ*	*57*	*F*	*Nephrectomy*	*02/11/2011*
Y1192	*Ureter*	*NHU*	*27*	*M*	*Nephrectomy*	*20/02/2012*
Y1214	*Ureter*	*NHU*	*76*	*F*	*Nephrectomy*	*23/05/2012*
Y1226	Ureter	NHU	78	M	Nephrectomy	26/07/2012
Y1237	Ureter	NHU	73	M	Nephrectomy	22/10/2012
Y1336	Ureter	NHU	63	F	Nephrectomy	24/07/2013

Y1356	Ureter		63	M	Renal transplant	02/09/2013
Y1588	Ureter		57	F	Renal transplant	06/11/2014
Y1601	Ureter		22	Unknown	Renal transplant	19/11/2014
Y1651	Ureter		Unknown	Unknown	Unknown	21/01/2015
Y1652	Ureter	NHU	0	M	Renal transplant	23/01/2015
Y1696	Ureter	NHU	63	M	Nephrectomy	25/03/2015
Y1756	Ureter	NHU	42	M	Nephrectomy	03/07/2015
Y1811	Ureter	NHU	66	F	Renal transplant	14/10/2015
Y1837	Ureter	NHU	54	F	Renal transplant	13/11/2015
Y1858	Ureter	NHU	72	F	Nephrectomy	04/01/2016
Y1866	Ureter	NHU	23	F	Renal transplant	29/01/2016
Y1870	Ureter	IHC	0	F	Nephrectomy	03/02/2016
Y1897	Ureter	NHU	66	Unknown	Lap nephrectomy	10/03/2016
Y1898	Ureter	NHU	65	Unknown	Renal transplant	16/03/2016
Y1914	Ureter	NHU	61	F	Nephrectomy	20/04/2016
Y1946	Ureter	NHU	37	M	Nephrectomy	09/06/2016
Y1947	Ureter	NHU	90	F	Nephrectomy	15/06/2016
Y2055	Ureter	NHU	42	F	Renal transplant	07/12/2016
Y2145	Ureter	NHU	58	M	Nephrectomy	16/05/2017
Y2167	Ureter	NHU	58	M	Renal transplant	05/07/2017
Y2303	Ureter	NHU	50	F	Transplant	07/03/2018
Y2318	Ureter	NHU	Unknown	M	Pyeloplasty	24/03/2018
Y2324	Ureter	NHU	76	F	Nephrectomy	28/03/2018
Y2340	*Bladder*	*Urothelium in situ*	*66*	*F*	*Cystoscopy*	*17/04/2018*
Y2351	Ureter	NHU	Unknown	M	Transplant	27/04/2018
Y2361	*Bladder*	*Urothelium in situ*	*Unknown*	*F*	*Cystoscopy*	*11/05/2018*
Y2366	*Bladder*	*Urothelium in situ*	*73*	*F*	*Cystoscopy*	*15/05/2018*
Y2391	*Ureter*	*Urothelium in situ*	*49*	*F*	*Renal transplant*	*21/06/2018*
Y2392	*Ureter*	*Urothelium in situ*	*43*	*F*	*Renal transplant*	*21/06/2018*
Y2396	*Ureter*	*Urothelium in situ*	*Unknown*	*M*	*Renal transplant*	*05/07/2018*
Y2397	Ureter	IHC	78	F	Nephrectomy	10/07/2018
Y2425	Ureter	NHU	58	M	Renal transplant	05/09/2018
Y2442	Ureter	IHC & NHU	44	F	Renal	24/10/2018

					transplant	
Y2444	Ureter	IHC	42	M	Renal transplant	24/10/2018
Y2467	Ureter	NHU	17	F	Renal transplant	30/11/2018
Y2640	Ureter	Urothelium *in situ*	54	M	Renal transplant	25/10/2019
Y2696	Ureter	NHU	44	F	Renal transplant	25/02/2019

Table 7.2: List of normal bladder/urinary tract samples used in study

Rows in italics indicate NHU samples that were previously processed by RNAseq and used as a transcriptomic resource in this study. Boxes labelled 'unknown' refers to information that was not recorded at the time of processing.

Appendix iv: List of PCR, RT-PCR and RT-qPCR primer sequences

Primer(s)	Application	Fwd sequence	Rev sequence
ANKRD1	RT-qPCR	GCCAAAGACAGAGAAGGAGATAC	GAGATCCGCGCCATACATAAT
CTGF	RT-qPCR	GGAAATGCTGCGAGGAGTGG	GAACAGGCGCTCCACTCTGTG
CXCL8	RT-PCR	ATGACTTCCAAGCTGGCCGTGGCT	TCTCAGCCCTCTTCAAAAACTTCTC
CYR61	RT-qPCR	CACACCAAGGGGCTGGAATG	CCCGTTTTGGTAGATTCTGG
EGFR	RT-PCR	CCAGGAGGTGGCTGGTTATG	TGCAGGTTTTCCAAAGGAATTC
ELF3	RT-qPCR	TCAACGAGGGCCTCATGAA	TCGGAGCGCAGGAACTTG
FABP4	RT-qPCR	GCGTCATGAAAGGCGTCACT	GTCAACGTCCCTTGGCTTATG
FGFR3	RT-PCR	ACTGTCTGGGTCAAGGATGG	TGTGTCCACACCTGTGTCCT
GAPDH	RT-PCR	ACCCAGAAGACTGTGGATGG	TTCTAGACGGCAGGTCAGGT
GAPDH	RT-qPCR	CAAGGTCATCCATGACAACTTTG	GGGCCATCCACAGTCTTCTG
GATA3	RT-qPCR		
GLI1	RT-PCR	CTTGTGGTCCCCATGACTCT	GATTCAGGCTCACGCTTCTC
GLI1	RT-qPCR	AACATGTCAAGACAGTGCATGGT	CCCACGGTGCCGTTTG
GLI2	RT-PCR	CATGGAGCACTACCTCCGTTC	CGAGGGTCATCTGGTGGTAAT
GLI3	RT-PCR	ACTTCCGCCTTATCTAGTAGCC	CCACGGGTTGCTGAGATCAT
IL6	RT-PCR	ACTCACCTCTTCAGAACGAATTG	CCATCTTTGGAAGGTTCAGGTTG
MKI67	RT-PCR	TTGAAAAGAAGGCGTGTGTC	TCTTCAGGACAGGTGGAGTG
PTCH1	RT-PCR	TCAGCAATGTCACAGCCTTC	GTCGTGTGTGTCGGTGTAGG
PTCH1	RT-qPCR	CCGCGCAGAGACGCTTT	CAGCGGGCCCTATTGCTA
SHH	RT-PCR	CCAAGGCACATATCCACTGCT	GTCTCGATCACGTAGAAGACCT
SP6 (Cloning; Rev)	PCR	N/A	CGATTTAGGTGACACTATAG
T7 (Cloning; Fwd)	PCR	TAATACGACTCACTATAGGG	N/A
U6 (Cloning; Fwd)	PCR	GGGCAGGAAGAGGGCCTAT	N/A
VGLL1	RT-qPCR	GGCAACCCTGGCCAGATAG	CGGGAGGCAGGTTGAAGA

Table 7.3: List of primer sets used in study

Appendix v: RT-qPCR primer set dissociation curves

RT-qPCR primers specific to *ELF3*, *FAPB4*, *GAPDH* and *GATA3* had been validated for their ability to give a single peak when assessing the dissociation curve (indicative of the primers producing a single amplified product) and a linear response over a dilution range of control cDNA prior to their use in this study. Primers specific to *ANKRD1, CTGF, CYR61, GLI1, PTCH1* and *VGLL1* were similarly validated and the resulting dissociation curves shown in Figure 7.1.

A

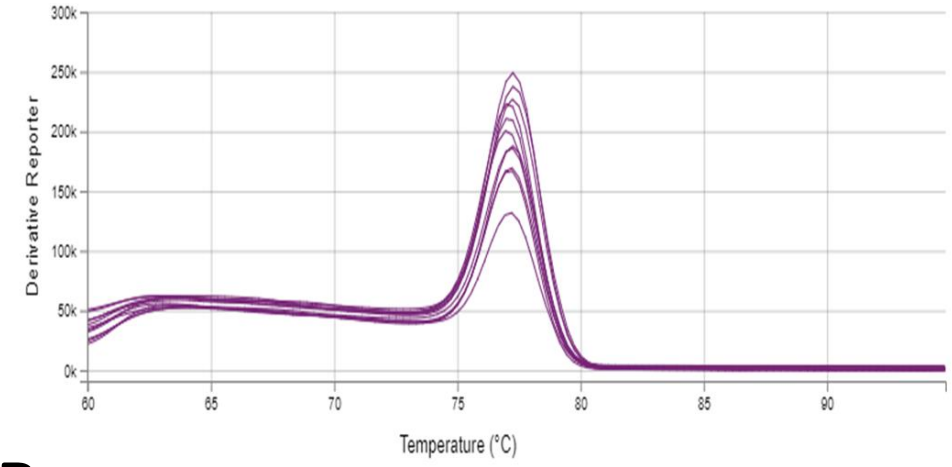

B

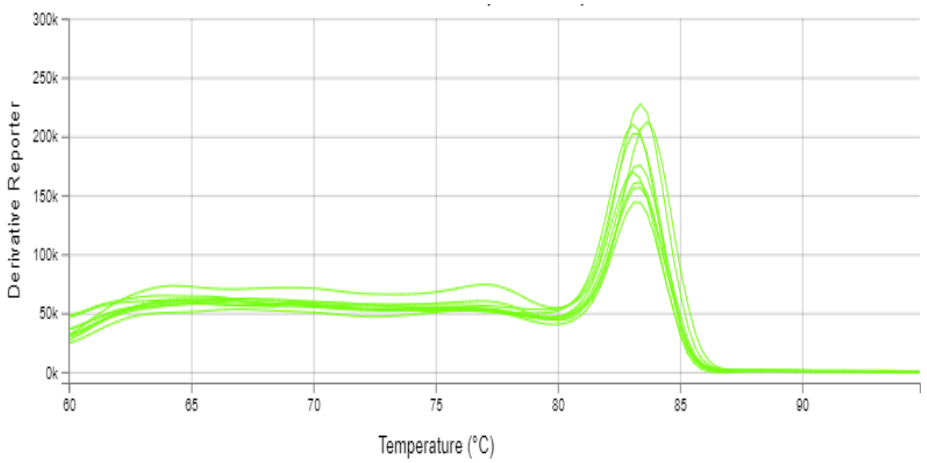

C

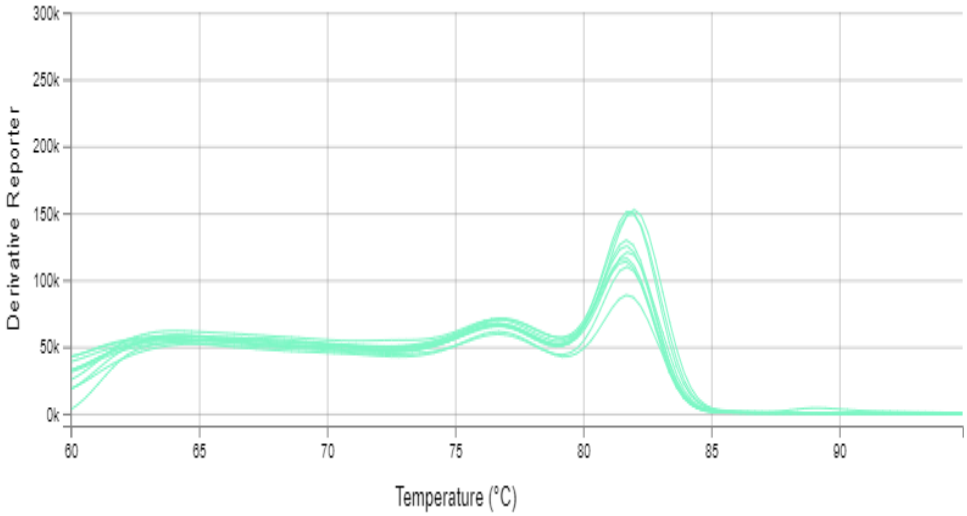
300k
250k
200k
150k
100k
50k
0k
Derivative Reporter
60
65
70
75
80
85
90
Temperature (°C)

D

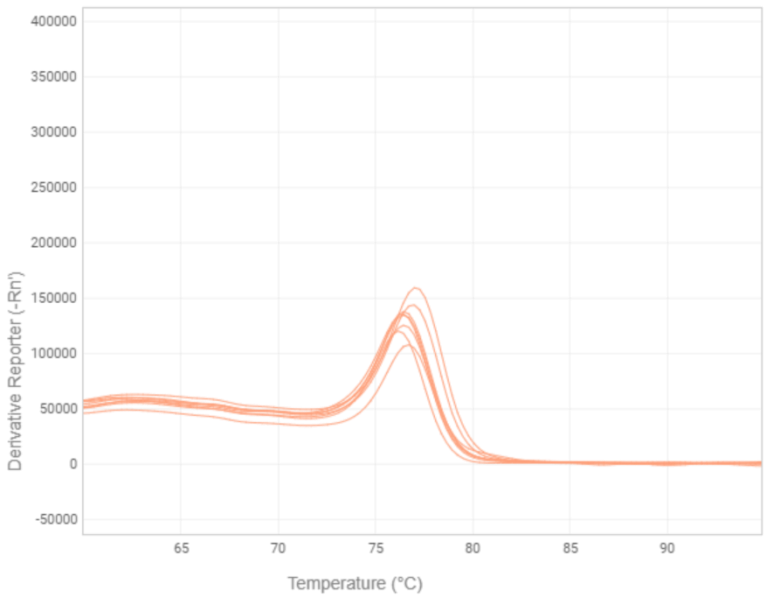
400000
350000
300000
250000
200000
150000
100000
50000
0
-50000
Derivative Reporter (-Rn')
65
70
75
80
85
90
Temperature (°C)

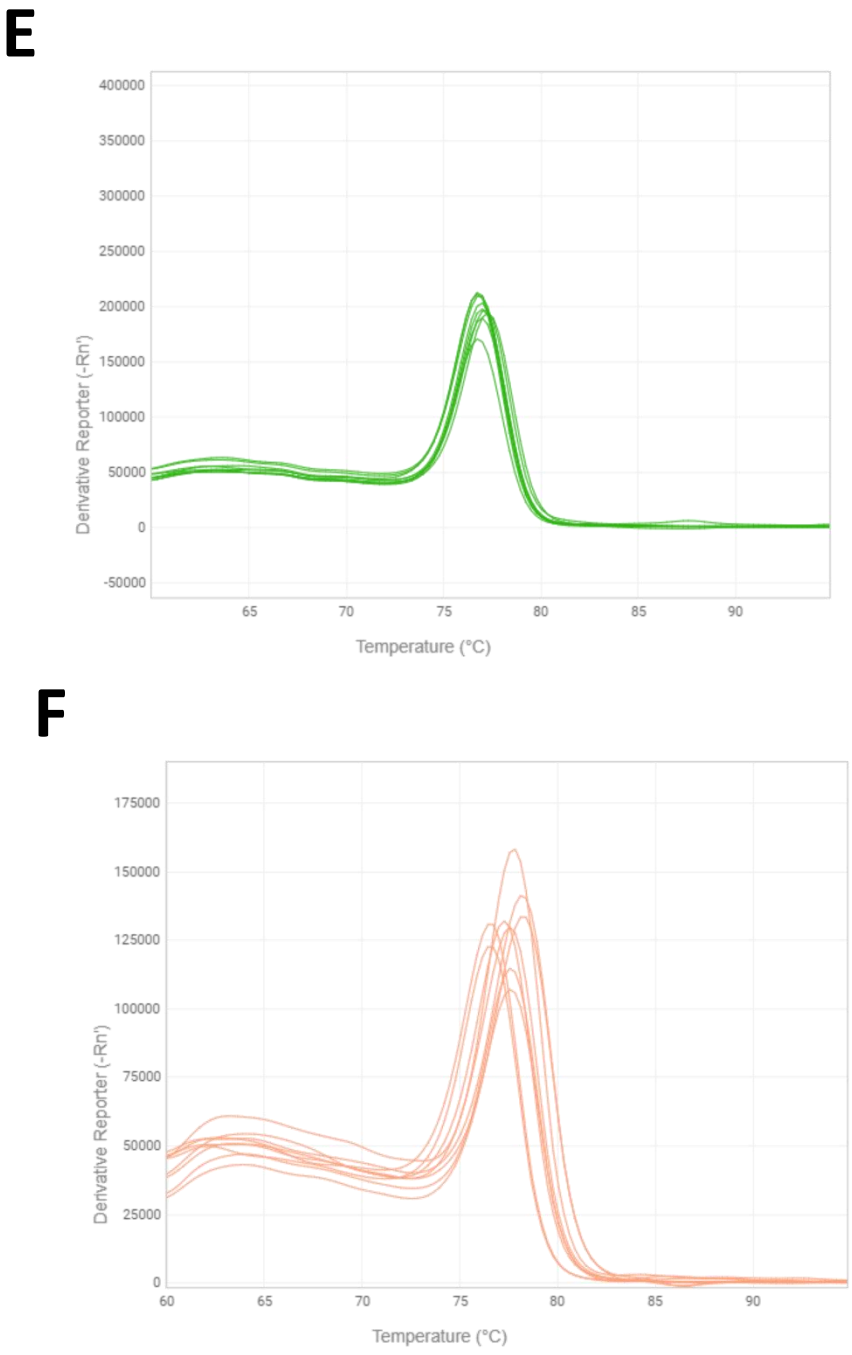

Figure 7.1: RT-qPCR primer set dissociation curves

Primers specific to *ANKRD1* (**A**), *CTGF* (**B**), *CYR61* (**C**), *GLI1* (**D**), *PTCH1* (**E**) and *VGLL1* (**F**) were validated before use.

Appendix vi: Validation of commercially available VGLL1, YAP and TEAD antibodies

Commercial rabbit polyclonal antibodies against VGLL1 were tested by comparing their efficacy in various immunolabelling assays. VGLL1 antibodies procured from Proteintech (10124-2-AP) and Atlas Antibodies (HPA042403) had both previously been used in publications pertaining to VGLL1 (Castilla et al., 2014; Soncin et al., 2018), with HPA042403 also in use as part of the Human Protein Atlas.

Due to the observation in Section 3.4.1.3 that *VGLL1* transcript was associated to differentiation, validation of both VGLL1 antibodies was first performed on NHU cells grown in the presence or absence of TZ/PD by immunoblotting. This approach demonstrated that both of the tested VGLL1 antibodies produced a band at the correct molecular weight of 29 kDa that correlated with the expression pattern found at the transcript level (Fig. 7.2A-B). However, the 10124-2-AP antibody produced intense bands above the 25 kDa mark and light bands in the 37 kDa and ~60 kDa areas which did not appear to be affected by cell treatment, while HPA042403 was found to produce light bands in both lanes at the 75kDa size. These extraneous bands were not found on the blots when imaged after application of the rabbit secondary antibody alone (Fig. 7.2C-D), suggesting that both affinity-purified mono-specific antibodies were also found to produce additional non-specific bands.

Visualisation of VGLL1 expression in formalin-fixed TZ/PD differentiated NHU cells by immunofluorescence determined that both antibodies produced primarily nuclear labelling, as expected through its previously cited role as a transcriptional co-activator (Fig. 7.2E-F). Additional weak cytoplasmic expression in differentiated cells was observed when labelled with 10124-2-AP, while DMSO treated NHU cells were also found to exhibit weak nuclear labelling of VGLL1 when labelled with HPA042403.

Use of both antibodies on FFPE sections of ureter resulted in similar expression patterns in the urothelium, which consisted of a combination of strong labelling in the nuclei of cells with additional weaker cytoplasmic labelling (Fig. 7.2G-H). Labelling of the Y1870 ureter with 10124-2-AP additionally labelled some cells of

the lamina propria, whereas no such labelling was observed with application of HPA042403. Despite the aforementioned limitations of each reagent, through validation of both antibodies in each immunoassay it was concluded that HPA042403 was the superior antibody for immunoblotting and immunohistochemistry purposes and 10124-2-AP was preferable for use by immunofluorescence. Each antibody was therefore used for their highlighted assays for the remainder of the study.

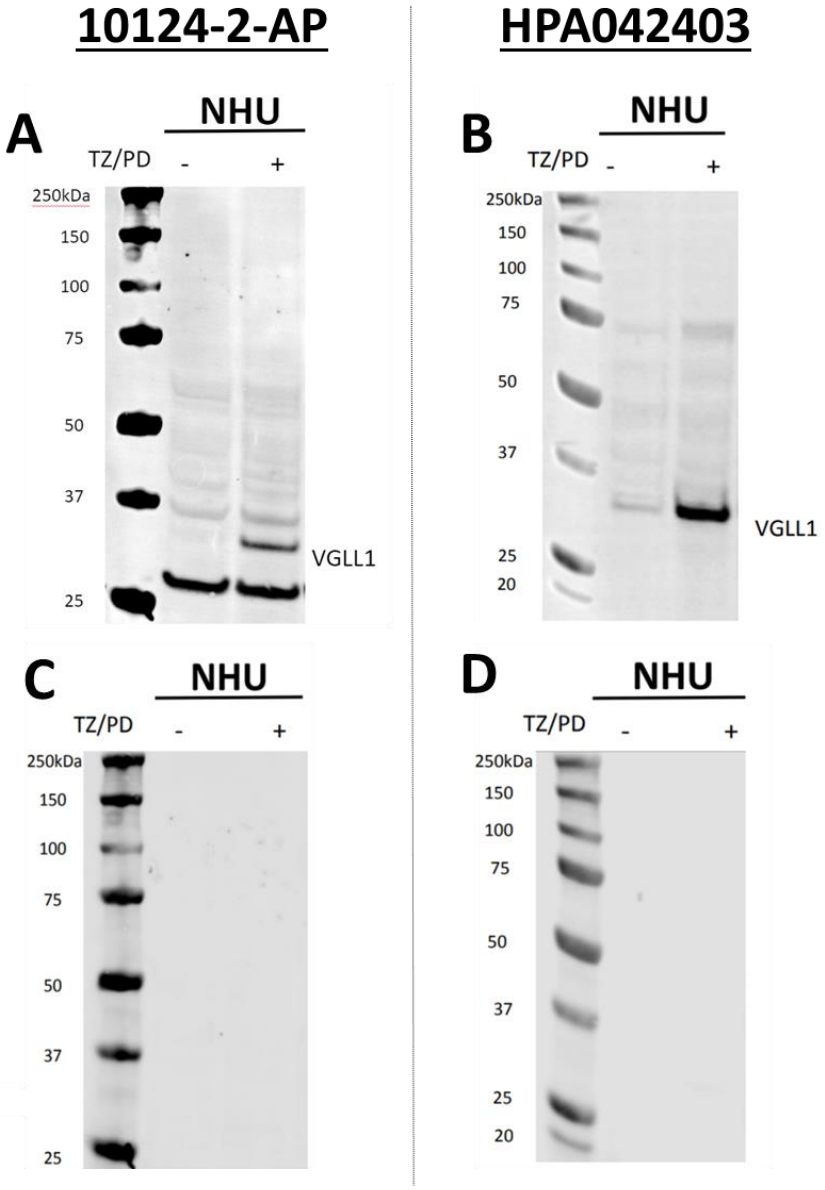

Figure 7.2: Evaluation of VGLL1 protein expression in NHU cells and native urothelium using two different antibodies

The efficacy of two rabbit polyclonal VGLL1 antibodies, 10124-2-AP (Proteintech) and HPA042403 (Atlas Antibodies), was examined in a variety of immuno-based assays. Panels (**A**-**B**) visualise VGLL1 expression in Y1858 cells treated with or without TZ/PD for a period of 72h, with 10124-2-AP (**A**) and HPA042403 (**B**) both demonstrating induction of a band at the correct molecular weight of VGLL1 in cytodifferentiated samples. Despite this, both antibodies produced additional, unknown bands in both lanes of lysate. Panels (**C-D**) display images of blots (**A**-**B**) when bound to rabbit secondary antibodies alone, confirming that the non-specific bands observed in (**A**-**B**) are as a result of the primary antibodies used.

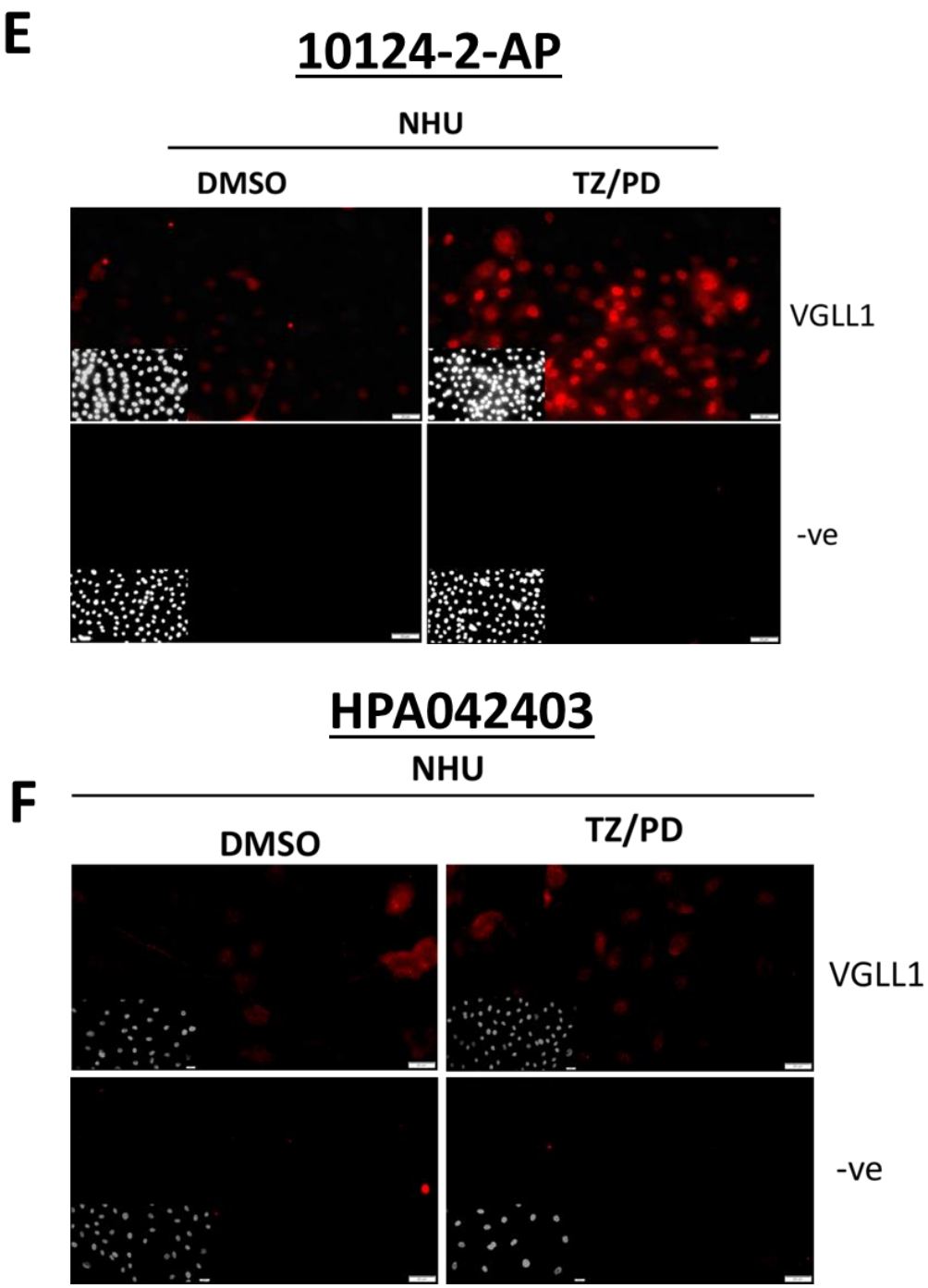

Figure 7.2: Evaluation of VGLL1 protein expression in NHU cells and native urothelium using two different antibodies

Panels (**E-F**) represent immunofluorescence micrograph images of Y1858 (**E**) and Y1651 (**F**) cells treated using the same conditions as (**A**-**D**), with 10124-2-AP used to visualise VGLL1 in (**E**) and HPA042403 used in (**F**). For each condition, cells were labelled with no primary antibody as a negative control. Images were all taken at same exposure, with the accompanying overlaid Hoechst 33258 DNA stain shown in the bottom left corner of images to confirm the presence of cells in each image. Scale bar= 20µm.

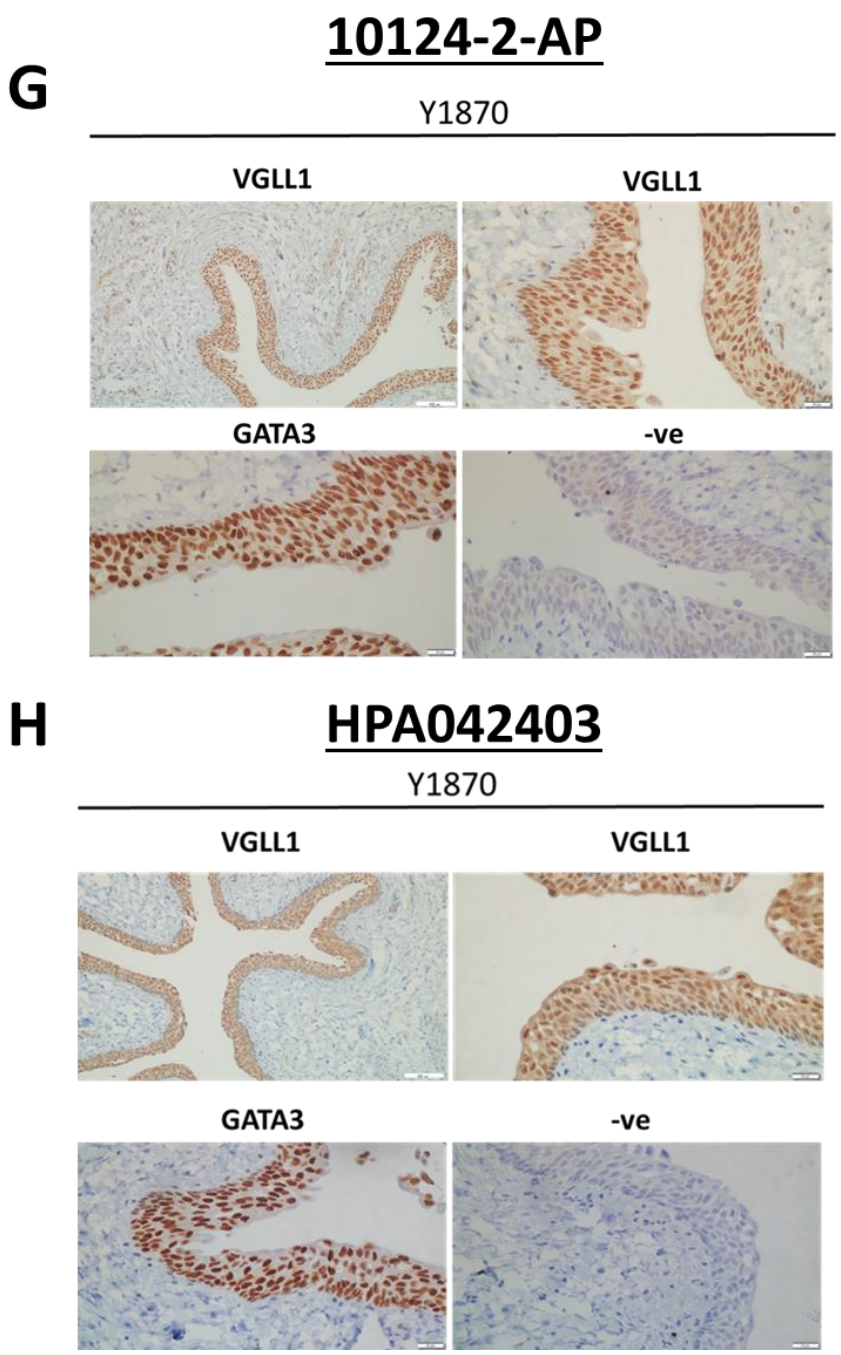

Figure 7.2: Evaluation of VGLL1 protein expression in NHU cells and native urothelium using two different antibodies

Panels (**G**-**H**) demonstrate the localisation of VGLL1 expression in FFPE sections of Y1870 ureter, using antibodies 10124-2-AP (**G**) and HPA042403 (**H**). Note the absence of lamina propria labelling in the images of VGLL1 labelling (top row) in panel (**H**) compared to the corresponding images in (**G**). Sections that were labelled with rabbit monoclonal GATA3 (bottom left) or no primary antibody (bottom right) were used as positive and negative controls, respectively. Scale bar= 100 µm (top left images) or 20 µm (all other images).

Expression of total and phosphorylated (S127) forms of YAP expression was analysed by immunoblotting in epidermoid carcinoma A431 cells lysed in a sub-confluent state or left to grow to visual confluence due to this cell line previously demonstrating a density-dependent induction of p-YAP activity (Li *et al.,* 2016b). Each cell condition was found to be specifically labelled as a doublet band by the total YAP (63.7) antibody, with one band of the doublet found at the 65 kDa region that YAP protein resides in (Fig. 7.3A). The 63.7 antibody additionally labels bands in the 49 kDa region, potentially relating to re-association of YAP with the lower MW protein TAZ that is expressed by the cell type. Labelling of the same lysates with an antibody specific to phosphorylated (S127) YAP expression (#4911) revealed strong bands at the same molecular weight as total YAP, while bands also appeared in the 49 kDa region but were very weak (Fig. 7.3B), perhaps indicating limited binding of p-YAP to p-TAZ in this context. Expression of p-YAP increased in A431 cells lysed at visual confluence compared to cells at sub-confluence, an observation in line with findings reported by Li *et al.*

Immunofluorescence labelling of A431 cells with the 63.7 antibody revealed a primarily nuclear expression pattern in A431 cells, with additional weak cytoplasmic labelling (Fig. 7.3C). Despite previous reports that concluded that expression of inactive YAP was solely localised to the cytoplasm of cells (Section 3.1.1), labelling with the #4911 antibody determined a primarily nuclear expression of p-YAP in A431 cells, although expression appeared to be more heterogeneous amongst the culture in comparison to total YAP/TAZ expression. This observation, alongside the fact that the #4911 antibody had not been validated for use in immunofluorescence by Cell Signalling, meant that the antibody was used for immunoblotting purposes only in subsequent experiments.

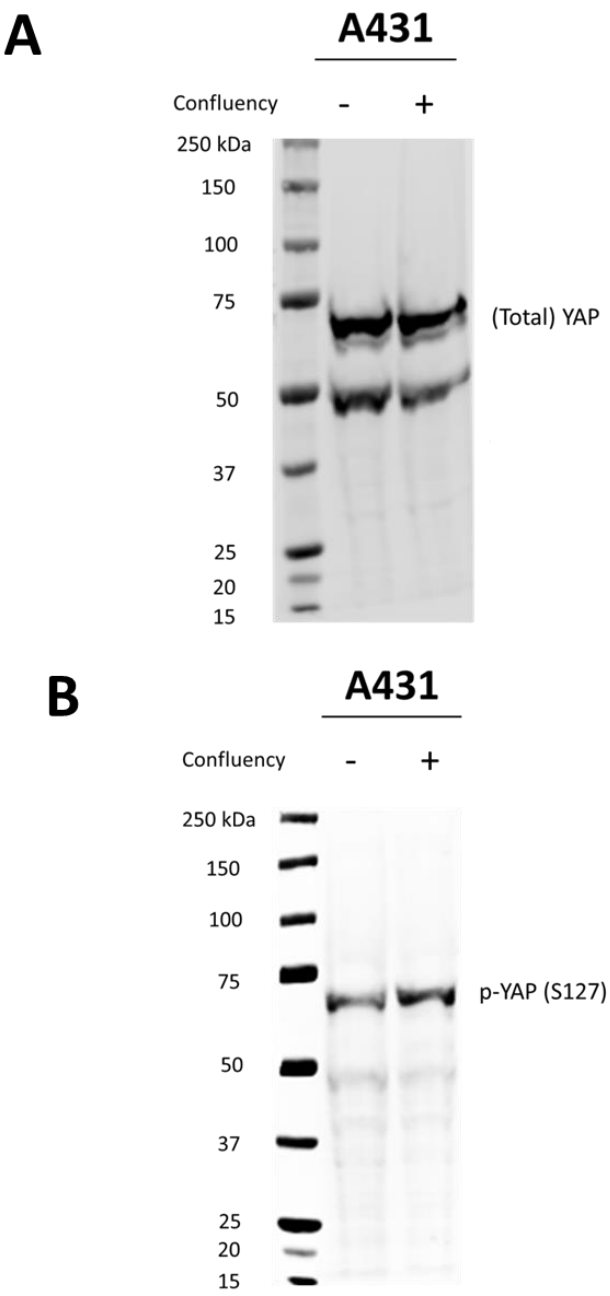

Figure 7.3: Expression of total and phosphorylated (S127) YAP in A431 cells

Antibodies targeting the total and phosphorylated forms of YAP where titrated on endometroid carcinoma cell line A431 to confirm specific labelling of each antibody. Image (**A**) depicts expression of Total YAP (and additional bands in the 49 kDa region which potentially denote Total TAZ expression) in an immunoblot analysis of A431 cells lysed in both a subconfluent and confluent state. Expression of Total YAP was found to be consistent between conditions. Image (**B**) demonstrates expression of p-YAP in the same conditions as (**A**), with an increase of p-YAP visualised in cells left to grow to visual confluence.

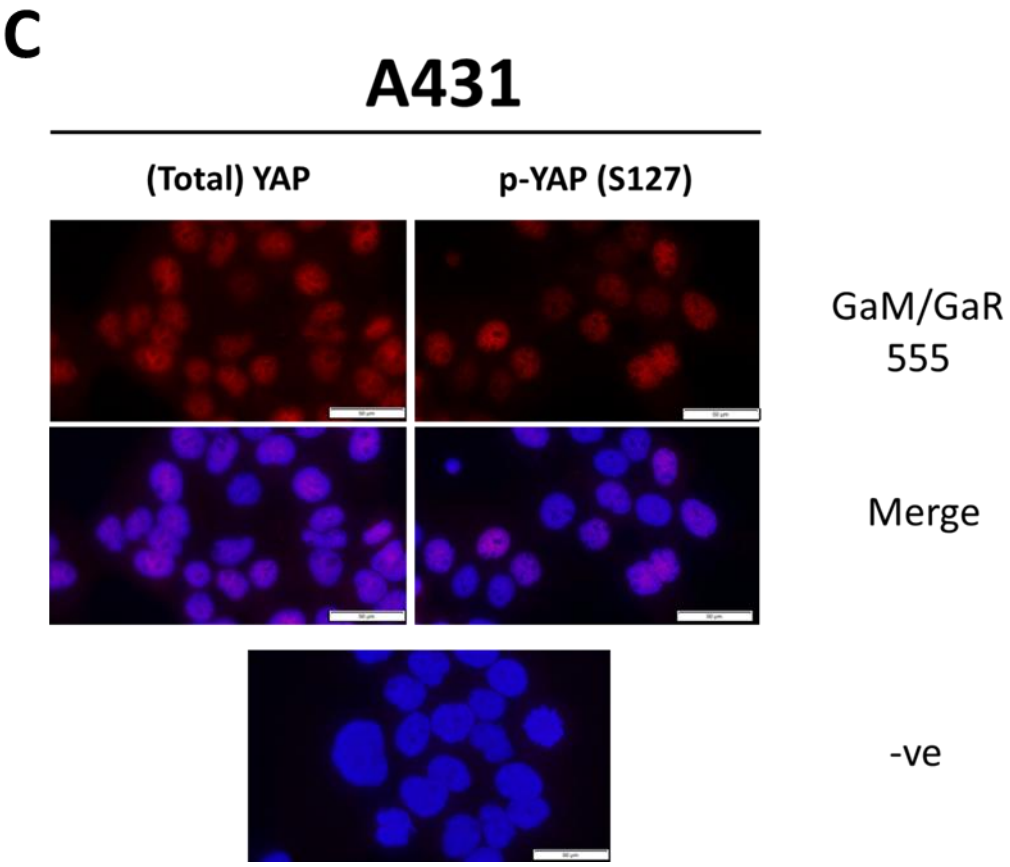

Figure 7.3: Expression of total and phosphorylated (S127) YAP in A431 cells

C) Immunofluorescence analysis of total and phosphorylated YAP expression in A431 cells**.** Both antibodies were found to primarily label nuclei of cells, with weak cytoplasmic labelling also observed. Cells receiving no primary antibody were used as a negative control. Images were all taken at same exposure and are shown with or without overlaid Hoechst 33258 DNA staining. Scale bar= 50µm.

Transcription factors *TEAD1* and *TEAD3* had previously been demonstrated to be expressed at the transcript level by NHU cells (Section 3.4.1.2). Immunofluorescence analysis of Y1756 NHU cells treated with or without TZ/PD for 72h was therefore used to confirm the validity of a rabbit "pan-TEAD" mAb that recognised all four TEAD proteins. The analysis revealed a predominantly nuclear localisation of TEAD proteins in both conditions, although some weak cytoplasmic expression was additionally visualised in TZ/PD differentiated cells (Fig. 7.4). Due to the nature of the antibody and assay used, identification of what specific TEAD proteins were being expressed by either cell type was not possible as part of this validation.

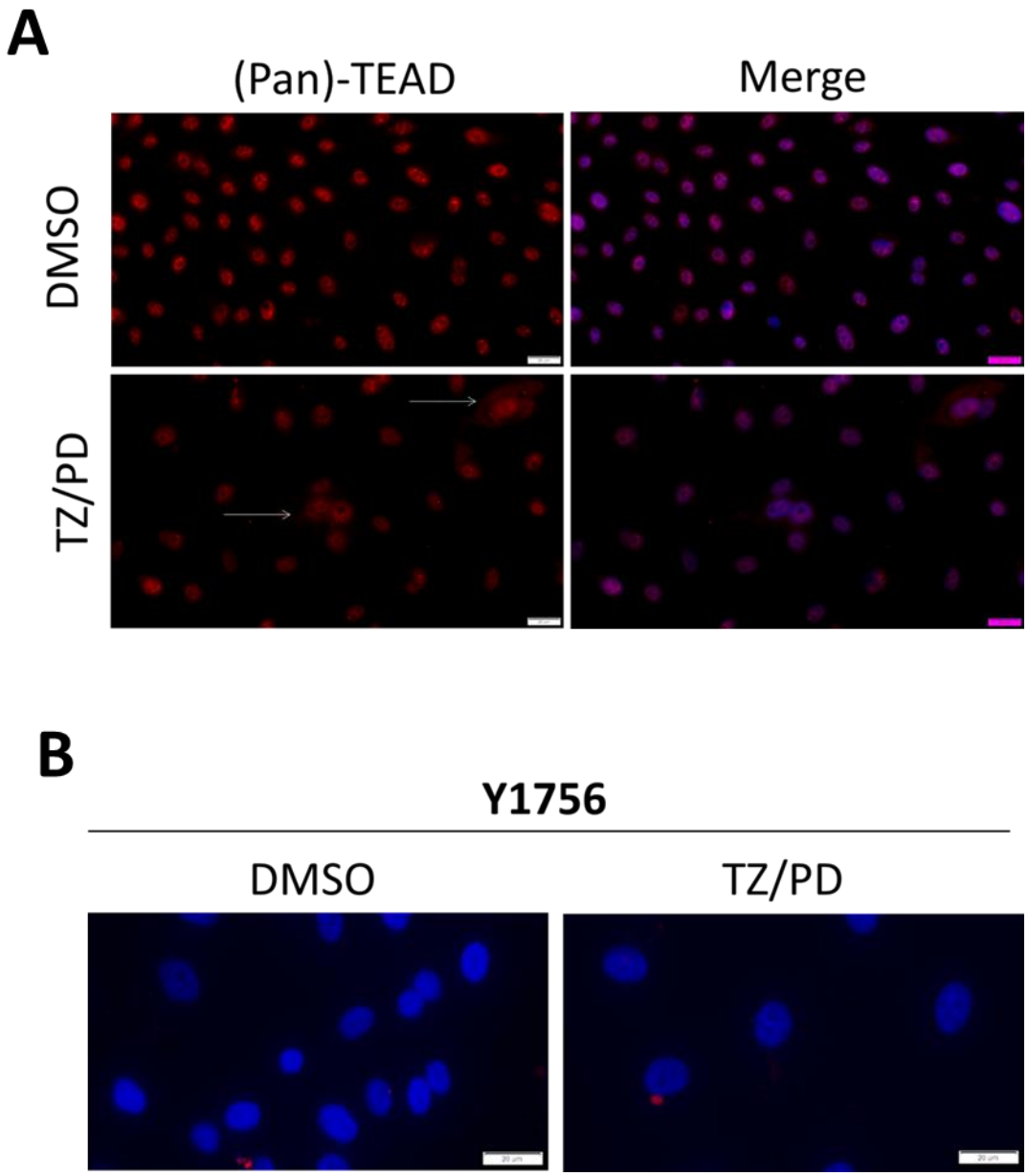

Figure 7.4: Nuclear-localised expression of TEAD in undifferentiated and differentiated NHU cells

Immunofluorescence analysis of TEAD expression using the pan-TEAD antibody in Y1756 cells treated with vehicle control or TZ/PD for 72h (**A**)**.** TEAD expression is expressed in both conditions in a predominantly nuclear localisation, although expression appears weaker in TZ/PD differentiated cells. The white arrows also indicate the appearance of weak cytoplasmic labelling of a subset of cells that were treated with TZ/PD. Cells receiving no primary antibody (**B**) for each condition were used as negative controls. Images were all taken at same exposure and are shown with or without overlaid Hoechst 33258 DNA staining. Scale bar= 20µm.

Appendix vii: EGFR-mediated induction of FGFR3 expression in urothelium

To determine if modulation of signal transduction pathways downstream of EGFR was able to initiate the induction of FGFR3 (in a similar manner to VGLL1) in *FGFR3*-absent NHU cells, expression was examined at both the transcript and protein level in undifferentiated Y1237 cells treated with PD153035, LY294002 or a combination of both drugs. RT-PCR analysis of the above samples revealed that *FGFR3* expression was upregulated in samples treated with PD153035 compared to control, where no expression was visualised at the cycle amplification number used (Fig. 7.5A). Little difference in *FGFR3* expression was observed when cells were treated concurrently with PD153035 alongside LY294002, while LY294002 alone was unable to induce *FGFR3*. Immunoblot analysis of the donor-matched protein lysates confirmed this observation, with FGFR3 induced only when Y1237 cells were treated with PD153035 (Fig. 7.5B). Immunoblotting with the FGFR3-specific mouse mAb (B-9) revealed a strong induction of doublet bands in the 85-100 kDa area, consistent with the molecular weight of the FGFR3b isoform in a glycosylated and non-glycosylated state observed in previous studies (Tomlinson *et al.,* 2005a).

Expression of FGFR3 protein was additionally assayed in immunoblot analysis of Y1226 cells treated with PD153035, with expression compared to that in various bladder cancer cell lines. As before, FGFR3 expression was strongly induced in cells treated with PD153035 compared to control (Fig. 7.5C). A comparison of FGFR3 expression in five bladder cancer cell lines to EGFR-blockaded NHU cells determined that none of the cell lines assayed expressed FGFR3 in the manner found in PD153035-treated NHU cells. However, the B-9 antibody was found to display expression of a single band at a larger molecular weight in RT4 cells, a cell line that was previously cited to express the *FGFR3-TACC3* fusion gene commonly found in NMIBC and luminal papillary MIBC (Section 1.4.4).

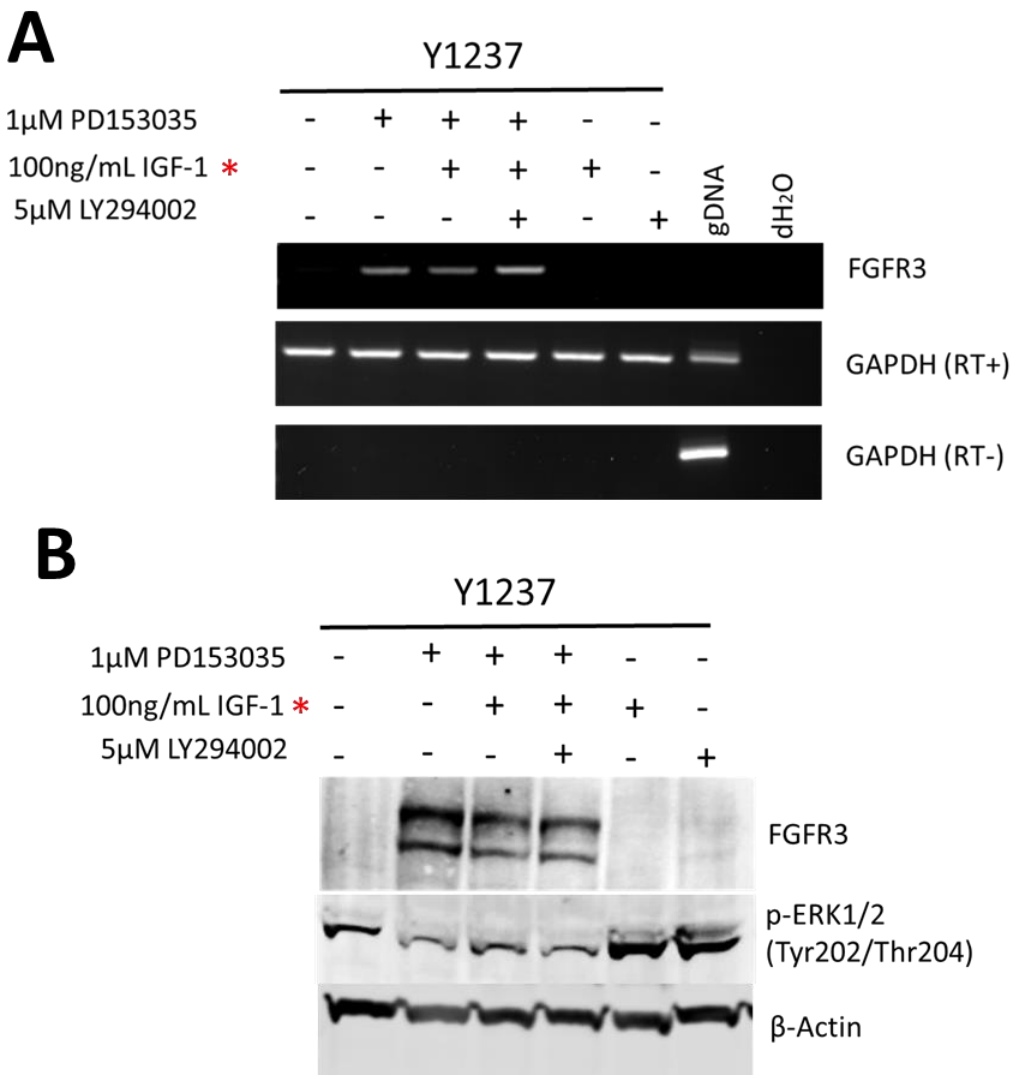

Figure 7.5: Induction of FGFR3 transcript and protein expression in undifferentiated NHU cells in response to EGFR blockade

A) RT-PCR analysis of *FGFR3* and housekeeping gene *GAPDH* transcript expression in Y1237 undifferentiated NHU cells. Cells were treated with 1 µM PD153035 or 5 µM LY294002 (or a combination of the above) for a period of 24h compared to a vehicle control. Each cDNA synthesis used 1 µg starting template RNA, with cDNA undergoing PCR amplification up to 30 cycles. The primers used for *FGFR3* expression were intron-spanning and therefore did not produce positive gDNA bands of the same size. **B)** Immunoblot image of FGFR3 and p-ERK expression in Y1237 undifferentiated NHU cells treated with the same conditions as above for 48h. FGFR3 expression was blotted using a mouse monoclonal antibody from Santa Cruz (B-9) which gave a doublet band at approximately 85 and 100 kDa. Expression of β-Actin was used to confirm equal loading of samples. Conditions marked with a red asterisk are not relevant to the figure.

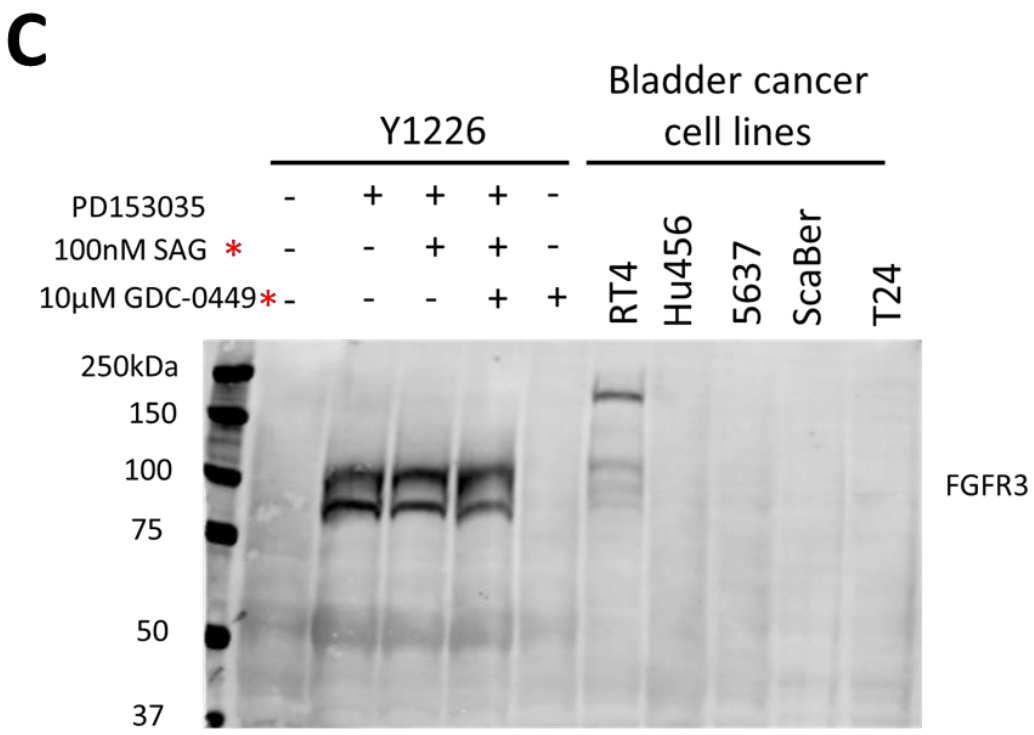

Figure 7.5: Induction of FGFR3 transcript and protein expression in undifferentiated NHU cells in response to EGFR blockade

C) Immunoblot image of FGFR3 expression in Y1226 undifferentiated NHU cells treated with 1 µM PD153035 for a period of 24h compared to five MIBC cell lines. Y1226 cells gave a similar labelling pattern of FGFR3 as that visualised in (**B**) while RT4 was the only cancer cell line to express FGFR3, with a single band found in the 175 kDa region, indicative of expression of an altered version of the protein. Conditions marked with a red asterisk are not relevant to the figure.

Appendix viii: Titration of UO126 and PD98059 on NHU cultures

MEK inhibitors U0126 and PD98059 were titrated prior to their use in Section 3.4.7.3. Treatment of proliferating, undifferentiated NHU cells with different concentrations of U0126 determined that 5 μM of drug was required to inhibit p44 phosphorylated ERK1/2 expression at a similar rate to PD153035 (Fig. 7.6A). Similarly, administration of 5 μM PD98059 was also found to be sufficient to block phosphorylated ERK1/2 activation at both 30 minutes (Fig. 7.6B) and 2h (Fig. 7.6C) post-treatment, confirming the ability of both reagents to effectively inhibit canonical EGFR/MEK/ERK signalling through inhibition of MEK1/2 (U0126) or MEK1 (PD98059). Jack Birch Unit member Mr Zhen Liu additionally titrated the ERK1/2 inhibitor FR180204 (FR180) for use in this study, with the optimum concentration of the drug found to be 1 μM.

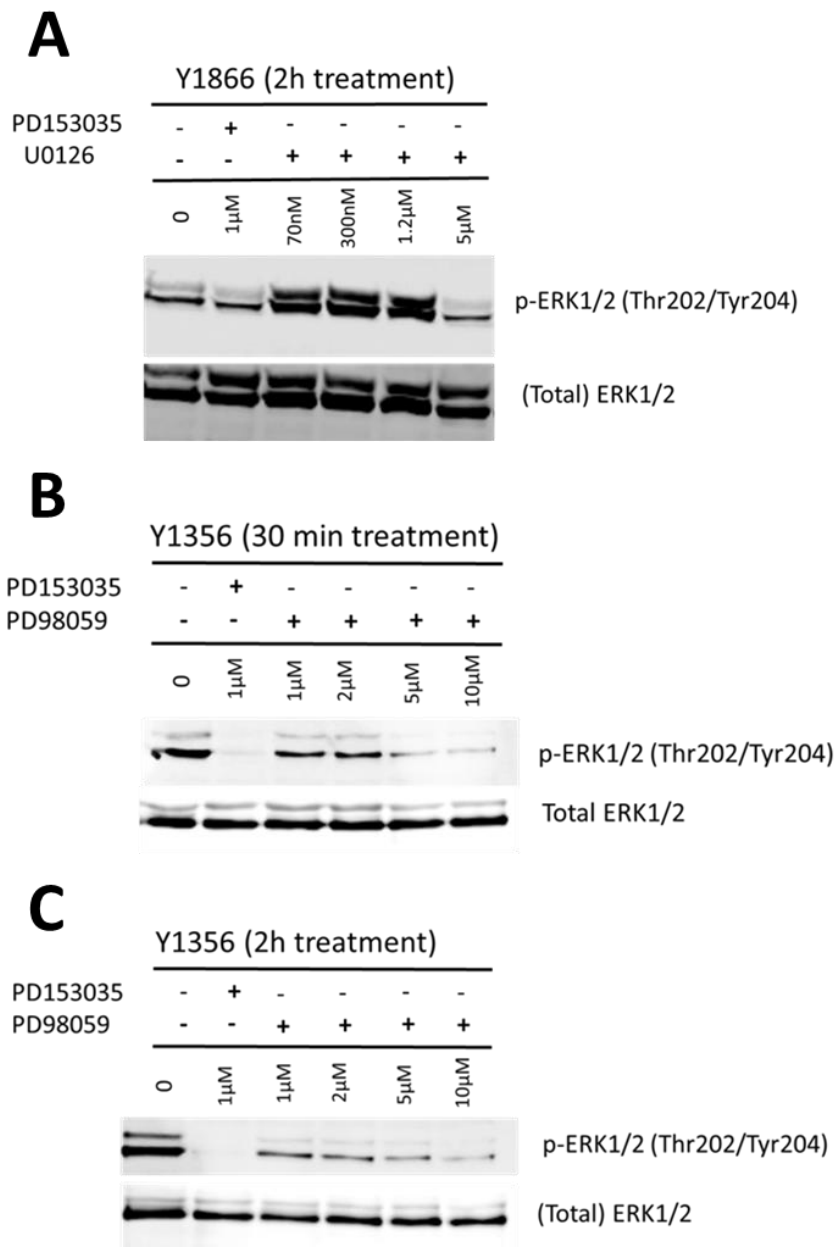

Figure 7.6: Effective concentrations of U0126 and PD98059 activity on NHU cells

UO126 and PD98059 were titrated on sub-confluent, actively proliferating NHU cells to determine the optimum concentration to use to inhibit MEK1/2 or MEK1, respectively. Inhibition of p-ERK expression by immunoblotting analysis was used as a proxy for effective inhibition. Y1866 cells were treated with U0126 for a period of 2h to analyse its downstream effect (**A**), while Y1356 cells were treated with PD98 for periods of 30 minutes (**B**) and 2h (**C**). Treatment of cells with PD153035 was used in each case as a positive control for inhibition of p-ERK. Both drugs were found to effectively reduce activation of ERK in all time points assayed at a concentration of 5 µM. Expression of Total ERK1/2 was used as a loading control in each experiment.

Appendix ix: Generation of a VGLL1-overexpressing retroviral vector

Specific details on methodology can be found in Section 2.7.2.2. Primers specific to the full length VGLL1 coding sequence (Ensembl Transcript ID- ENST00000370634.8) were designed to incorporate the forward and reverse strands alongside the inclusion of restriction enzyme sites and a Kozak sequence (Table 7.4).

Direction	Sequence
Forward primer	AAAAAAGTTAACACCATGGAAGAAATGAAGAAGAAGACTGCC
Reverse primer	AAAAAAGGATCCCTAAAAGATGCTGCAGGTATCGATGTGG

Table 7.4: **Primer sequences for amplification of full length VGLL1 coding sequence**
Poly-A tails were added at the 5' end of both primers in order to aid ligation into the pGEM-T Easy vector. Sequences in red and green designate the HpaI and BamHI restriction sites, respectively. Sequence in orange designates the Kozak sequence in the forward strand. Sequences in blue match the VGLL1 cDNA sequence (forward and reverse).

RNA from NHU cells (Y1858) that had been TZ/PD treated for a period of 144h was used to synthesise 2 µg of cDNA containing the VGLL1 coding sequence by RT-PCR (Fig. 7.7).

The amplified VGLL1 sequence was purified, concentrated and ligated with linearised pGEM-T Easy vector before being introduced into XL1-blue *E. coli* via bacterial transformation. The identity of successfully transformed bacteria was confirmed using gel electrophoresis of colony PCR products (Fig. 7.8).

Plasmids were extracted from positive bacterial cultures and sequenced for validation that they contained the VGLL1 sequence in the correct orientation. Restriction digests were used to cut out and isolate the VGLL1 sequence from the subcloning vector pGEM-T Easy (Fig. 7.9), allowing for ligation of said sequences into the retroviral mammalian expression vector pLXSN.

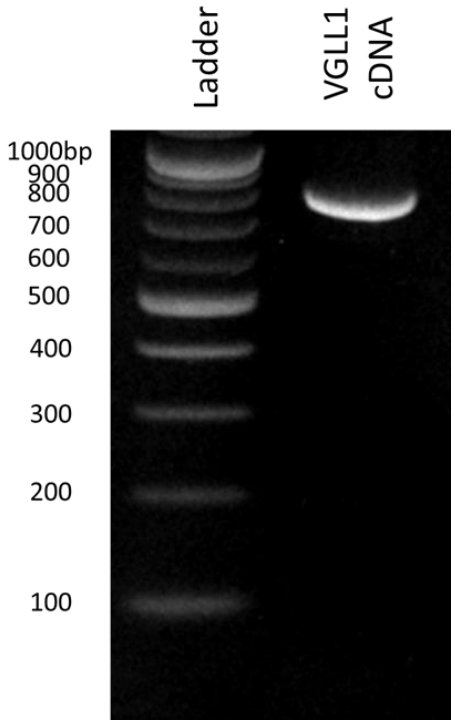

Figure 7.7: Amplified VGLL1 sequence from NHU cells

Verification by gel electrophoresis that a product of the correct molecular size (777bp) had been produced by PCR before undergoing purification of the product.

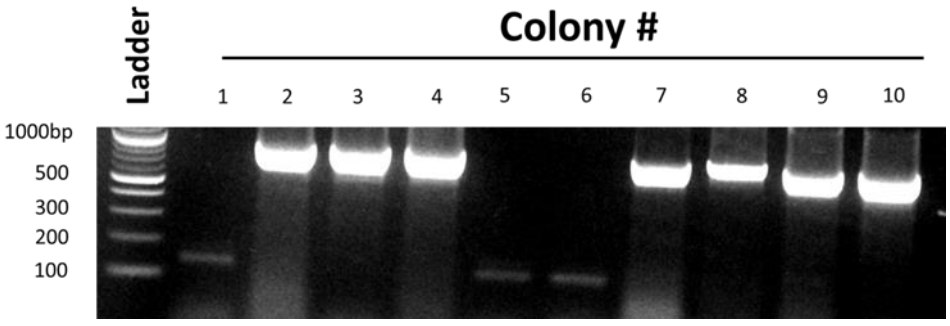

Figure 7.8: Colony PCR of transformed XL1-Blue colonies

Verification of XL1-Blue bacteria successfully expressing pGEM-T Easy vector containing the ligated VGLL1 coding sequence.

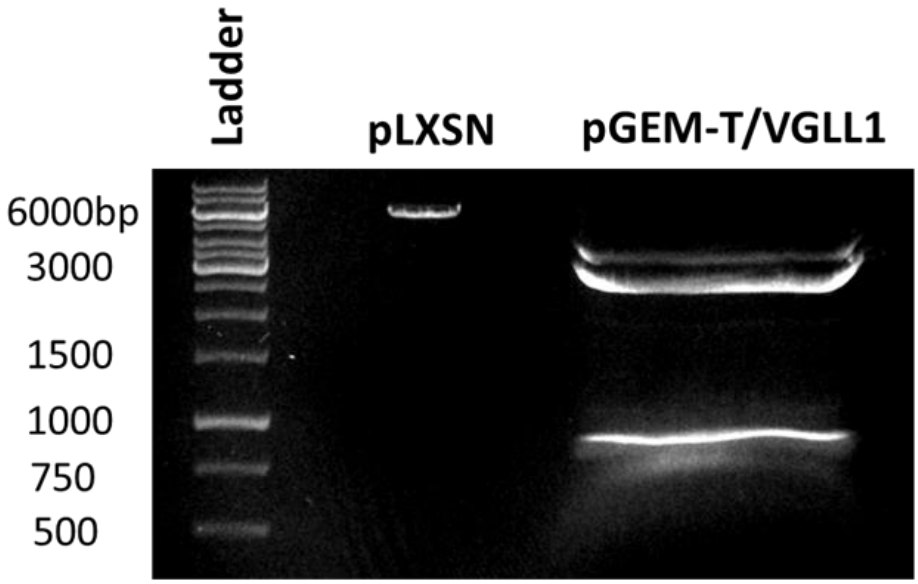

Figure 7.9: Restriction digests of pLXSN and pGEM-T Easy plasmids

Verification of digestion of the VGLL1 coding sequence from the pGEM-T Easy plasmid backbone. Linearised pLXSN plasmid and the VGLL1 sequence were extracted from the gel, purified and ligated together.

Appendix x: Generation of VGLL1 shRNA retroviral vectors

Specific details on methodology can be found in Section 2.7.2.3. Bioinformatic analysis of the full length coding sequence of VGLL1 was used to select three sequences that were predicted to possess siRNA activity against the *VGLL1* gene. Three 69bp hairpin sequences were created that contained the siRNA sequences alongside restriction digest sites, a terminator sequence and a hairpin loop sequence (Table 7.5).

shRNA #	Oligonucleotide sequence
VGLL1 shRNA #1 sense	5'-GATCCGACAAAGCCACAACCAGAAGTTTCAAGAGAACTTCTGGTTGTGGCTTTGTCTTTTTTACGCGTG-3'
VGLL1 shRNA #1 antisense	5'-AATTCACGCGTAAAAAAGACAAAGCCACAACCAGAAGTTCTCTTGAAACTTCTGGTTGTGGCTTTGTCG--3'
VGLL1 shRNA #2 sense	5'-GATCCGCAAACAGAAGCCTATAAAGATTCAAGAGATCTTTATAGGCTTCTGTTTGCTTTTTTACGCGTG--3'
VGLL1 shRNA #2 antisense	5'-AATTCACGCGTAAAAAAGCAAACAGAAGCCTATAAAGATCTCTTGAATCTTTATAGGCTTCTGTTTGCG--3'
VGLL1 shRNA #3 sense	5'-GATCCGCCAGTACCAGCCTTCCAAATTTCAAGAGAATTTGGAAGGCTGGTACTGGCTTTTTTACGCGTG--3'
VGLL1 shRNA #3 antisense	5'-AATTCACGCGTAAAAAAGCCAGTACCAGCCTTCCAAATTCTCTTGAAATTTGGAAGGCTGGTACTGGCG--3'

Table 7.5: Oligonucleotide sequences used to produce shRNAs specific to VGLL1

The BamHI (GATCC) and EcoRI (AATTC) sites are in red, the MluI site is in blue and the hairpin loop sequence is in green.

The shRNA oligonucleotide strands were annealed together and ligated into the pSIREN-RetroQ retroviral vector. Following bacterial transformation and colony PCR, restriction digest analysis using the MluI enzyme was used to confirm that the shRNA inserts were correctly inserted into the vectors (Fig. 7.10).

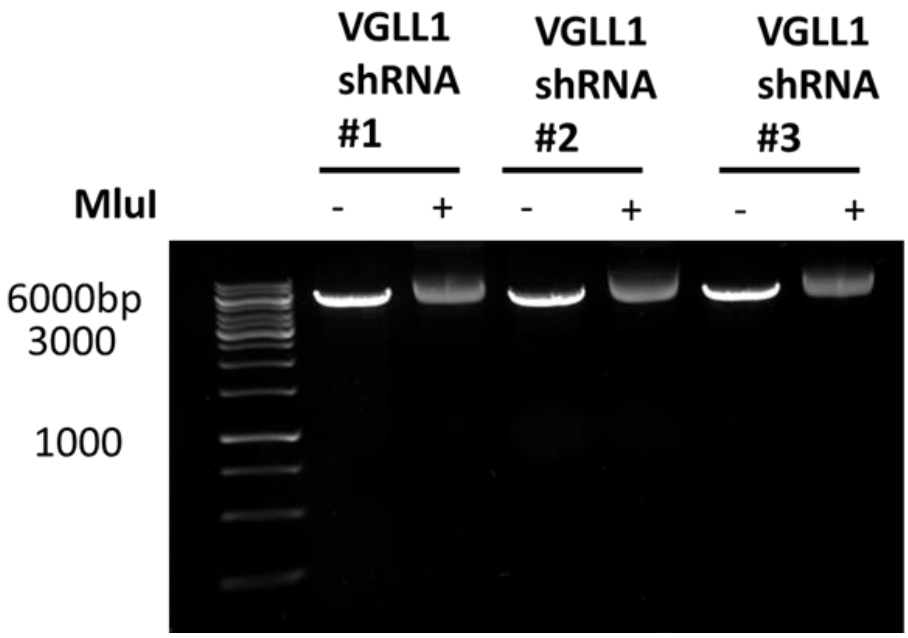

Figure 7.10: Restriction digests of pSIREN plasmids

Verification of a single enzymatic cut in the pSIREN plasmid using the MluI site downstream of the shRNA terminator sequence.

Appendix xi: Quality control of NuHS/NbHS cell RNAseq samples

To determine what genes were being upregulated by the canonical SHH pathway in stromal cells treated with inducing reagents, RNAseq analysis was performed. RT-qPCR analysis of the three cell lines treated with SAG demonstrated a ≥ 2-fold induction of *PTCH1* and *GLI1* for each cell line and at each time point, and were thus considered suitable candidate samples to sequence (Fig. 7.11A). Three NbHS cell lines were additionally treated with rSHH, with two lines (Y879 and Y886) found to induce *GLI1* expression to a similar degree as observed with SAG treatment. However, Y732 cells treated with rSHH were found to not induce *GLI1* expression and were therefore not sequenced (Fig. 7.11B). The quality of the raw sequencing reads from the SAG treatment experiment was confirmed using FastQC (Fig. 7.12); meaning that no trimming of reads was required. The total number of mapped reads was greater than 22 million for each sample, resulting in a minimum of 3.4 billion sequenced bases for each sample (Table 7.6).

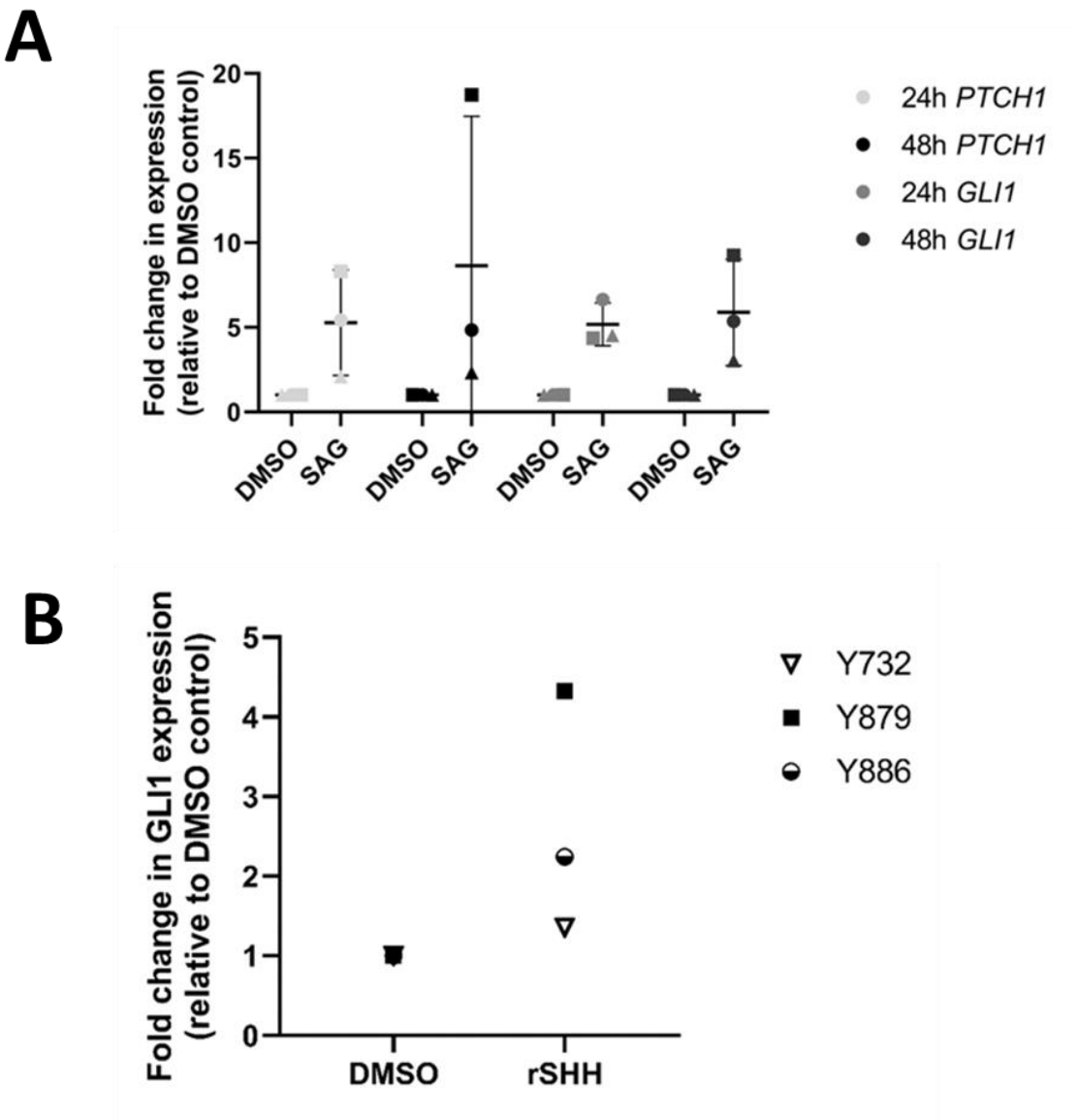

Figure 7.11: Validation of canonical SHH pathway signalling in ureteric and bladder stromal RNAseq samples

Stromal cell lines Y875, Y879 and Y1027 were treated with 100 nM SAG for 24h and 48h, while Y732, Y879 and Y886 cells were treated in the presence and absence of 1 µg/mL rSHH for 24h. Graph (**A**) details qRT-PCR analysis of *PTCH1* and *GLI1* expression in the three independent stromal cell lines treated with SAG, while graph (**B**) displays *GLI1* expression in the three NbHS cell lines treated with rSHH. Values shown represent the fold change in expression between DMSO control and treatment conditions after normalisation against *GAPDH* expression. Icons of the same shape represent fold change values from donor-matched stromal samples. NbHS cells treated with rSHH were not subsequently analysed by RNAseq due to a lack of *GLI1* induction in Y732 cells.

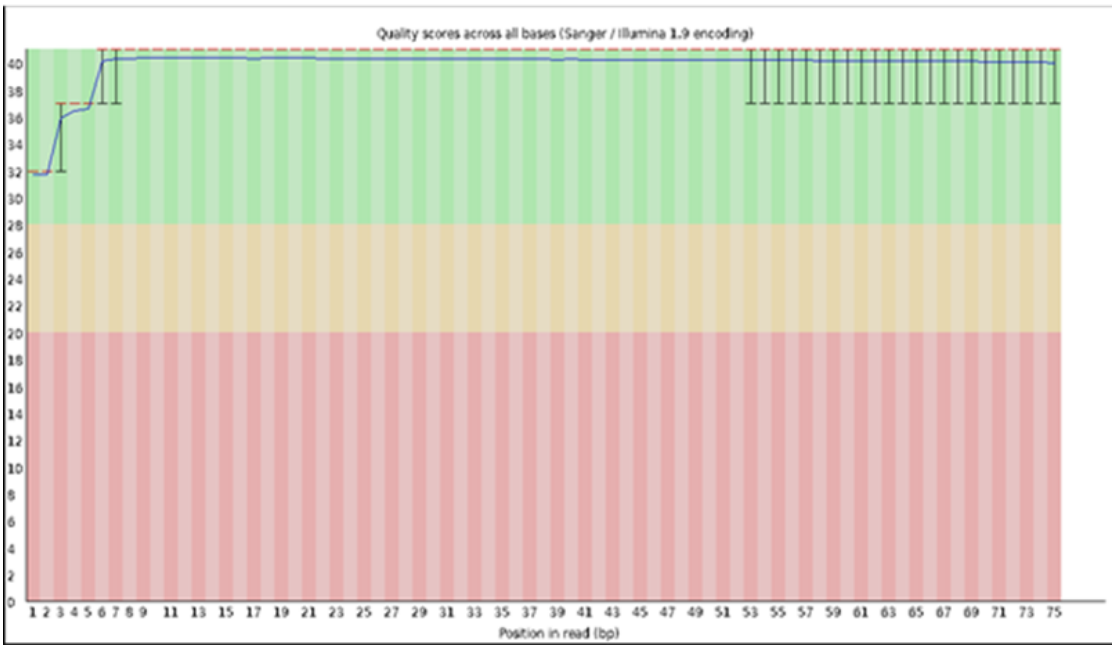

Figure 7.12: FastQC sequencing read analysis of stromal cell RNA

The base quality of raw 75 bp paired-end sequencing reads of Y875, Y879 and Y1027 cells treated with and without SAG was confirmed using FastQC. This figure demonstrates the average base quality scores of Y879 DMSO reads without trimming.

Sample	Total mapped reads and sequences (bases)
Y875 24h DMSO	27.3 million
	4.1 billion
Y875 24h SAG	26 million
	3.9 billion
Y875 48h DMSO	26.7 million
	4.0 billion
Y875 48h SAG	24.7 million
	3.7 billion
Y879 24h DMSO	24 million
	3.6 billion
Y879 24h SAG	26 million
	3.9 billion
Y879 48h DMSO	28 million
	4.2 billion
Y879 48h SAG	24.7 million
	3.7 billion
Y1027 24h DMSO	22.7 million
	3.4 billion
Y1027 24h SAG	28.7 million
	4.3 billion
Y1027 48h DMSO	30.7 million
	4.6 billion
Y1027 48h SAG	25.3 million
	3.8 billion

Table 7.6: Total numbers of mapped reads (top number) and read bases (bottom number) for each RNAseq sample

Sequencing reads from the SAG treatment experiment were considered to be of a high quality (as determined through FastQC analysis) and thus were not trimmed prior to downstream processes.

Appendix xii: Chapter 3 auxiliary results

Gene	Comparison	Significant?	Summary	pval
PPARG	Urothelium *in situ* vs. Differentiated NHU cells	No	ns	0.9331
PPARG	Urothelium *in situ* vs. Undifferentiated NHU cells	Yes	***	<0.0001
PPARG	Differentiated NHU cells vs. Undifferentiated NHU cells	Yes	***	<0.0001
GATA3	Urothelium *in situ* vs. Differentiated NHU cells	No	ns	0.156
GATA3	Urothelium *in situ* vs. Undifferentiated NHU cells	Yes	***	<0.0001
GATA3	Differentiated NHU cells vs. Undifferentiated NHU cells	Yes	***	<0.0001
FOXA1	Urothelium *in situ* vs. Differentiated NHU cells	No	ns	0.304
FOXA1	Urothelium *in situ* vs. Undifferentiated NHU cells	Yes	**	0.0014
FOXA1	Differentiated NHU cells vs. Undifferentiated NHU cells	Yes	***	<0.0001
ELF3	Urothelium *in situ* vs. Differentiated NHU cells	Yes	*	0.0152
ELF3	Urothelium *in situ* vs. Undifferentiated NHU cells	Yes	***	<0.0001
ELF3	Differentiated NHU cells vs. Undifferentiated NHU cells	Yes	***	<0.0001
TP63	Urothelium *in situ* vs. Differentiated NHU cells	No	ns	0.1359
TP63	Urothelium *in situ* vs. Undifferentiated NHU cells	Yes	**	0.0031
TP63	Differentiated NHU cells vs. Undifferentiated NHU cells	Yes	***	<0.0001
UPK2	Urothelium *in situ* vs. Differentiated NHU cells	Yes	***	<0.0001
UPK2	Urothelium *in situ* vs. Undifferentiated NHU cells	Yes	***	<0.0001
UPK2	Differentiated NHU cells vs. Undifferentiated NHU cells	Yes	***	<0.0001

Table 7.7: Tukey's multiple comparisons test of conditions in Figure 3.3.

Gene	Comparison	Significant?	Summary	pval
YAP1	Urothelium *in situ* vs. Differentiated NHU cells	No	ns	>0.9999
YAP1	Urothelium *in situ* vs. Undifferentiated NHU cells	No	ns	0.1406
YAP1	Differentiated NHU cells vs. Undifferentiated NHU cells	No	ns	0.1439
WWTR1	Urothelium *in situ* vs. Differentiated NHU cells	No	ns	0.6764
WWTR1	Urothelium *in situ* vs. Undifferentiated NHU cells	No	ns	0.072
WWTR1	Differentiated NHU cells vs. Undifferentiated NHU cells	No	ns	0.3482
ANKRD1	Urothelium *in situ* vs. Differentiated NHU cells	No	ns	0.9961
ANKRD1	Urothelium *in situ* vs. Undifferentiated NHU cells	No	ns	>0.9999
ANKRD1	Differentiated NHU cells vs. Undifferentiated NHU cells	No	ns	0.9969
AXL	Urothelium *in situ* vs. Differentiated NHU cells	No	ns	0.9835
AXL	Urothelium *in situ* vs. Undifferentiated NHU cells	Yes	***	<0.0001
AXL	Differentiated NHU cells vs. Undifferentiated NHU cells	Yes	***	<0.0001
CTGF	Urothelium *in situ* vs. Differentiated NHU cells	Yes	***	<0.0001
CTGF	Urothelium *in situ* vs. Undifferentiated NHU cells	Yes	***	<0.0001
CTGF	Differentiated NHU cells vs. Undifferentiated NHU cells	No	ns	0.3967
CYR61	Urothelium *in situ* vs. Differentiated NHU cells	Yes	***	<0.0001
CYR61	Urothelium *in situ* vs. Undifferentiated NHU cells	Yes	***	<0.0001
CYR61	Differentiated NHU cells vs. Undifferentiated NHU cells	Yes	***	<0.0001
TEAD1	Urothelium *in situ* vs. Differentiated NHU cells	Yes	*	0.0342
TEAD1	Urothelium *in situ* vs. Undifferentiated NHU cells	Yes	*	0.0335
TEAD1	Differentiated NHU cells vs. Undifferentiated NHU cells	No	ns	>0.9999
TEAD2	Urothelium *in situ* vs. Differentiated NHU cells	No	ns	0.7664
TEAD2	Urothelium *in situ* vs. Undifferentiated NHU cells	No	ns	0.7656
TEAD2	Differentiated NHU cells vs.	No	ns	>0.9999

	Undifferentiated NHU cells			
TEAD3	Urothelium *in situ* vs. Differentiated NHU cells	No	ns	0.9142
TEAD3	Urothelium *in situ* vs. Undifferentiated NHU cells	No	ns	0.0562
TEAD3	Differentiated NHU cells vs. Undifferentiated NHU cells	No	ns	0.1339
TEAD4	Urothelium *in situ* vs. Differentiated NHU cells	No	ns	0.9957
TEAD4	Urothelium *in situ* vs. Undifferentiated NHU cells	No	ns	0.8752
TEAD4	Differentiated NHU cells vs. Undifferentiated NHU cells	No	ns	0.8308

Table 7.8: Tukey's multiple comparisons test of conditions in Figure 3.4.

A

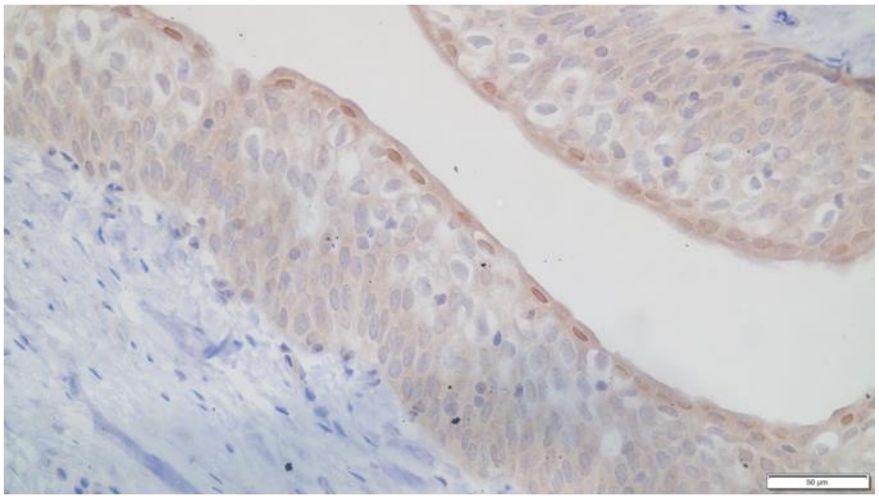

B

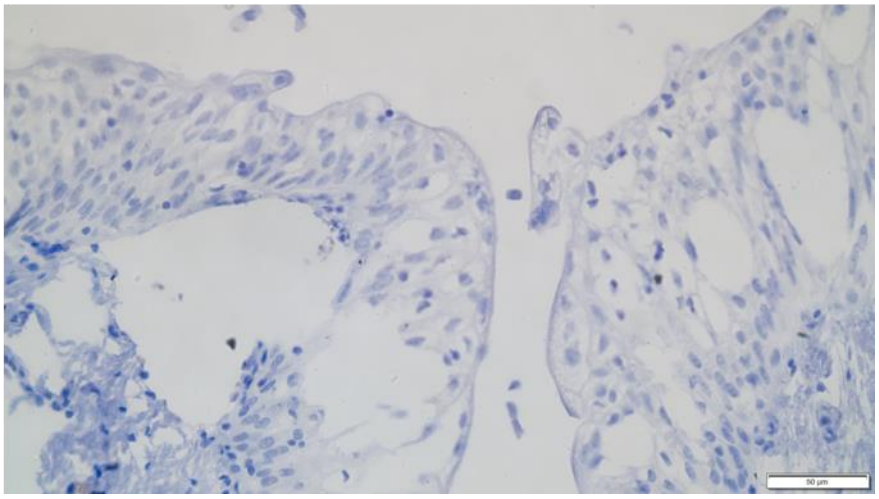

Figure 7.13: VGLL1 expression in native urothelium

Biological replicate from Figure 3.8 of VGLL1 expression and localisation in Y2444 ureter (**A**)**.** Sections that were labelled with no primary antibody (**B**) were used as negative controls. Scale bar= 50 µm.

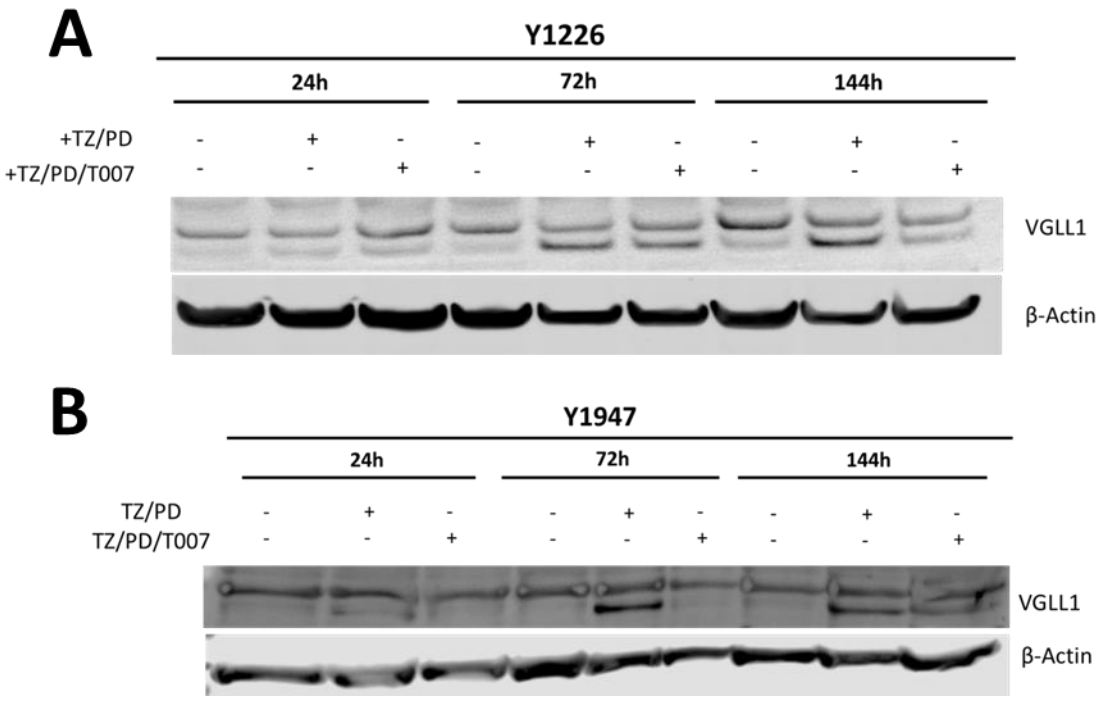

Figure 7.14: VGLL1 in TZ/PD differentiated NHU cells following PPARγ inhibition

Biological replicates from Figure 3.15 of VGLL1 expression Y1226 (**A**) and Y1947 (**B**) NHU cells treated with a combination of TZ, PD and T0070907 over a time-course of 144h**.** Densitometry analysis of the above immunoblots in addition to the immunoblot displayed in Figure 3.15 was used to calculate the mean expression of VGLL1 for each condition (Fig. 3.15B).

Gene	Comparison	Significant?	Summary	pval
GATA3	Ctrl siRNA DMSO vs. Ctrl siRNA TZ/PD	Yes	***	<0.0001
GATA3	Ctrl siRNA DMSO vs. GATA3 siRNA #1 TZ/PD	No	ns	0.4489
GATA3	Ctrl siRNA DMSO vs. GATA3 siRNA #2 TZ/PD	Yes	***	0.0007
GATA3	Ctrl siRNA TZ/PD vs. GATA3 siRNA #1 TZ/PD	Yes	***	<0.0001
GATA3	Ctrl siRNA TZ/PD vs. GATA3 siRNA #2 TZ/PD	Yes	***	<0.0001
GATA3	GATA3 siRNA #1 TZ/PD vs. GATA3 siRNA #2 TZ/PD	Yes	*	0.0142
VGLL1	Ctrl siRNA DMSO vs. Ctrl siRNA TZ/PD	Yes	***	<0.0001
VGLL1	Ctrl siRNA DMSO vs. GATA3 siRNA #1 TZ/PD	Yes	***	<0.0001
VGLL1	Ctrl siRNA DMSO vs. GATA3 siRNA #2 TZ/PD	Yes	***	<0.0001
VGLL1	Ctrl siRNA TZ/PD vs. GATA3 siRNA #1 TZ/PD	Yes	**	0.0012
VGLL1	Ctrl siRNA TZ/PD vs. GATA3 siRNA #2 TZ/PD	Yes	***	0.0003
VGLL1	GATA3 siRNA #1 TZ/PD vs. GATA3 siRNA #2 TZ/PD	No	ns	0.8948

Table 7.9: Tukey's multiple comparisons test of conditions in Figure 3.17.

Gene	Comparison	Significant?	Summary	pval
VGLL1	Subconfluent DMSO vs. Confluent DMSO	No	ns	0.7863
VGLL1	Subconfluent DMSO vs. Confluent TZ	No	ns	0.9789
VGLL1	Subconfluent DMSO vs. Confluent PD	No	*	0.0424
VGLL1	Subconfluent DMSO vs. Confluent T007	No	ns	0.8656
VGLL1	Subconfluent DMSO vs. Confluent TZ/T007	No	ns	0.9453
VGLL1	Subconfluent DMSO vs. Confluent PD/T007	Yes	**	0.0013
VGLL1	Subconfluent DMSO vs. Confluent TZ/PD	Yes	**	0.0045
VGLL1	Confluent DMSO vs. Confluent TZ	No	ns	0.9984
VGLL1	Confluent DMSO vs. Confluent PD	No	ns	0.5595
VGLL1	Confluent DMSO vs. Confluent T007	No	ns	>0.9999
VGLL1	Confluent DMSO vs. Confluent TZ/T007	No	ns	0.9999
VGLL1	Confluent DMSO vs. Confluent PD/T007	Yes	*	0.0252
VGLL1	Confluent DMSO vs. Confluent TZ/PD	No	ns	0.0821
VGLL1	Confluent TZ vs. Confluent PD	No	ns	0.257
VGLL1	Confluent TZ vs. Confluent T007	No	ns	0.9998
VGLL1	Confluent TZ vs. Confluent TZ/T007	No	ns	>0.9999
VGLL1	Confluent TZ vs. Confluent PD/T007	Yes	**	0.0079
VGLL1	Confluent TZ vs. Confluent TZ/PD	Yes	*	0.0268
VGLL1	Confluent PD vs. Confluent T007	No	ns	0.4619
VGLL1	Confluent PD vs. Confluent TZ/T007	No	ns	0.3371
VGLL1	Confluent PD vs. Confluent PD/T007	No	ns	0.5661
VGLL1	Confluent PD vs. Confluent TZ/PD	No	ns	0.895
VGLL1	Confluent T007 vs. Confluent TZ/T007	No	ns	>0.9999
VGLL1	Confluent T007 vs. Confluent PD/T007	Yes	*	0.0182
VGLL1	Confluent T007 vs. Confluent TZ/PD	No	ns	0.0603
VGLL1	Confluent TZ/T007 vs. Confluent PD/T007	Yes	*	0.0114
VGLL1	Confluent TZ/T007 vs. Confluent TZ/PD	Yes	*	0.0383
VGLL1	Confluent PD/T007 vs. Confluent TZ/PD	No	ns	0.9978

Table 7.10: Tukey's multiple comparisons test of conditions in Figure 3.22.

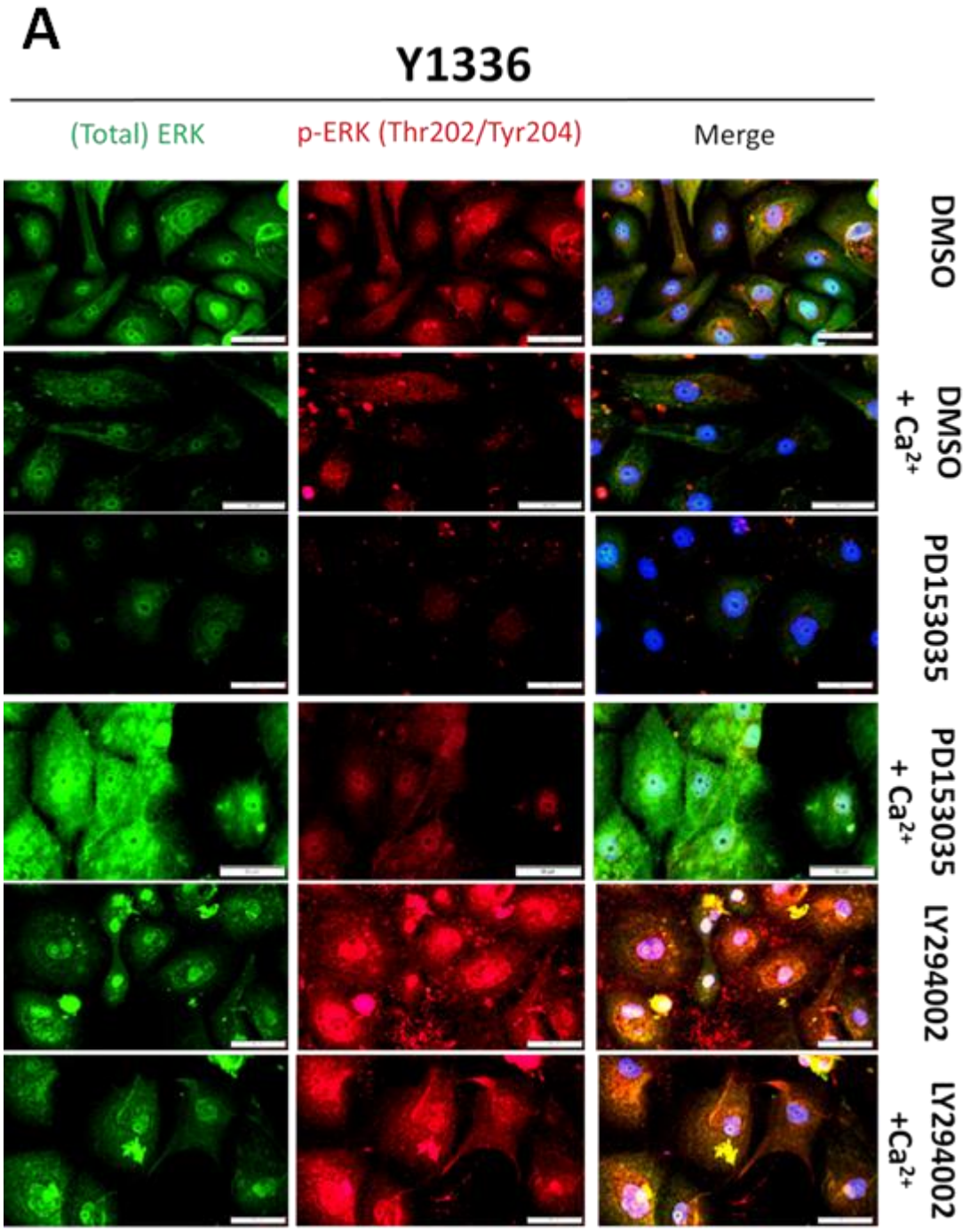

Figure 7.15: ERK1/2 expression in NHU cells grown in high Ca^{2+} alongside treatment with PD153035 or LY294002

Labelling of total and phosphorylated (Thr202/Tyr204) ERK1/2 expression in Y1336 cells treated as described in Figure 3.23**.** p-ERK expression was reduced compared to control when treated with high Ca^{2+} or PD153035, but increased following LY294002 treatment. Scale bar= 50 µm.

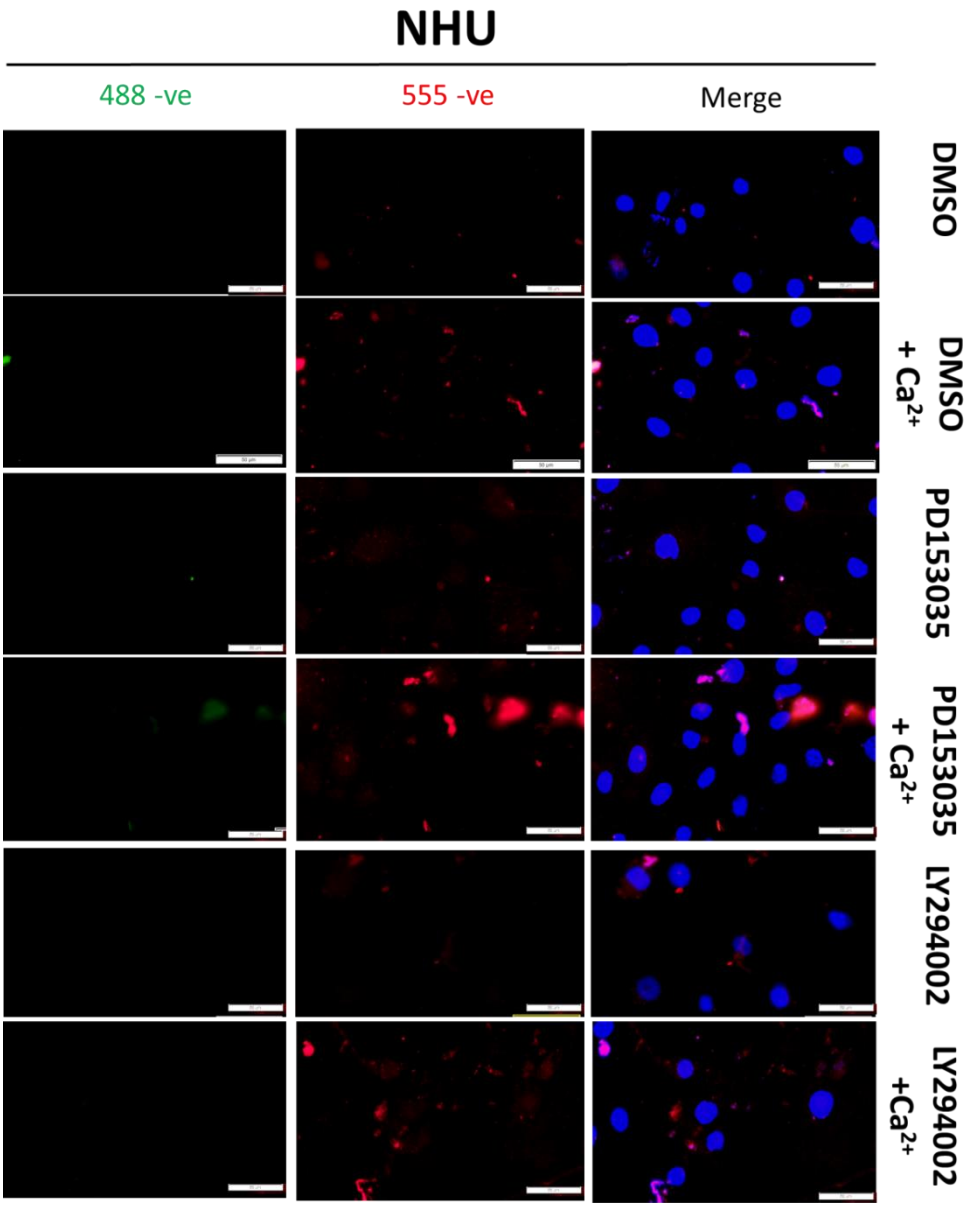

Figure 7.16: Negative controls for Figure 3.23

Cells receiving no primary antibody were used as a negative control. Images were all taken at same exposure and are shown with or without overlaid Hoechst 33258 DNA staining. Scale bar= 50µm.

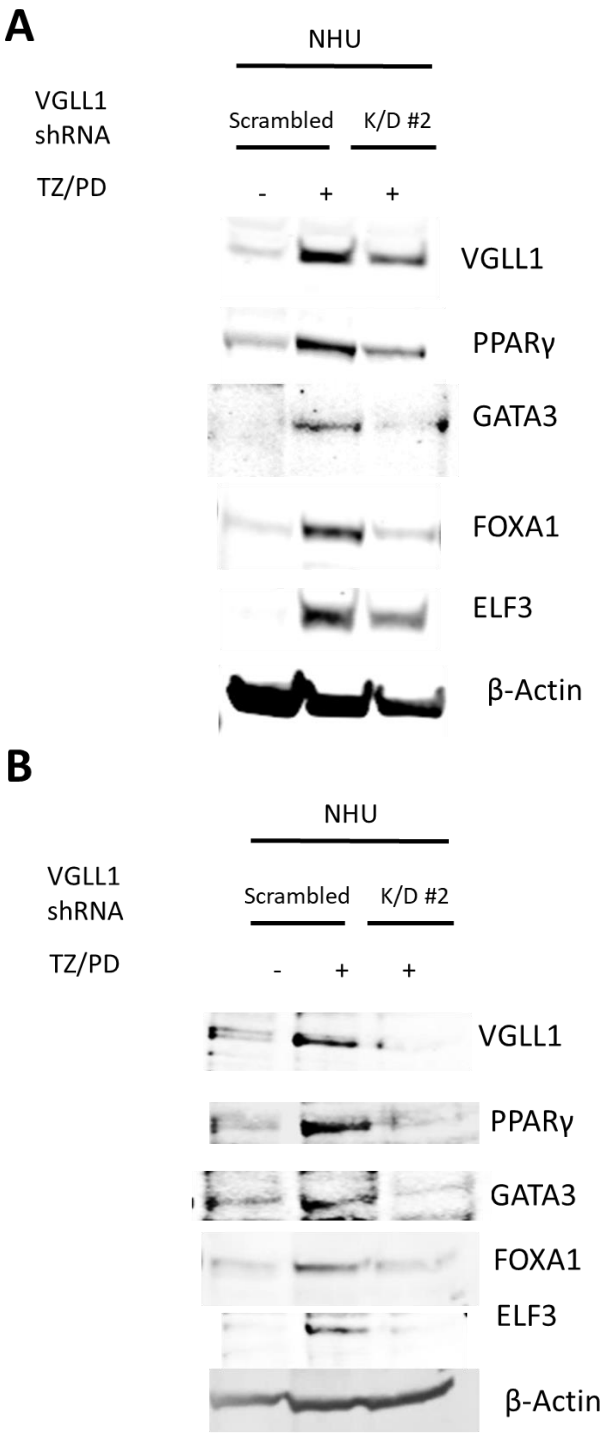

Figure 7.17: VGLL1 knockdown in TZ/PD differentiated NHU cells

Biological replicates from Figure 3.30 depicting expression of VGLL1, PPARγ, GATA3, FOXA1 and ELF3 in Y1811 (**A**) and Y2318 (**B**) cells following VGLL1 knockdown and 72h TZ/PD differentiation. Analysis of the above immunoblot images was used to produce the densitometry quantification found in Figure 3.30. Expression of β-Actin was used to confirm equal loading of samples.

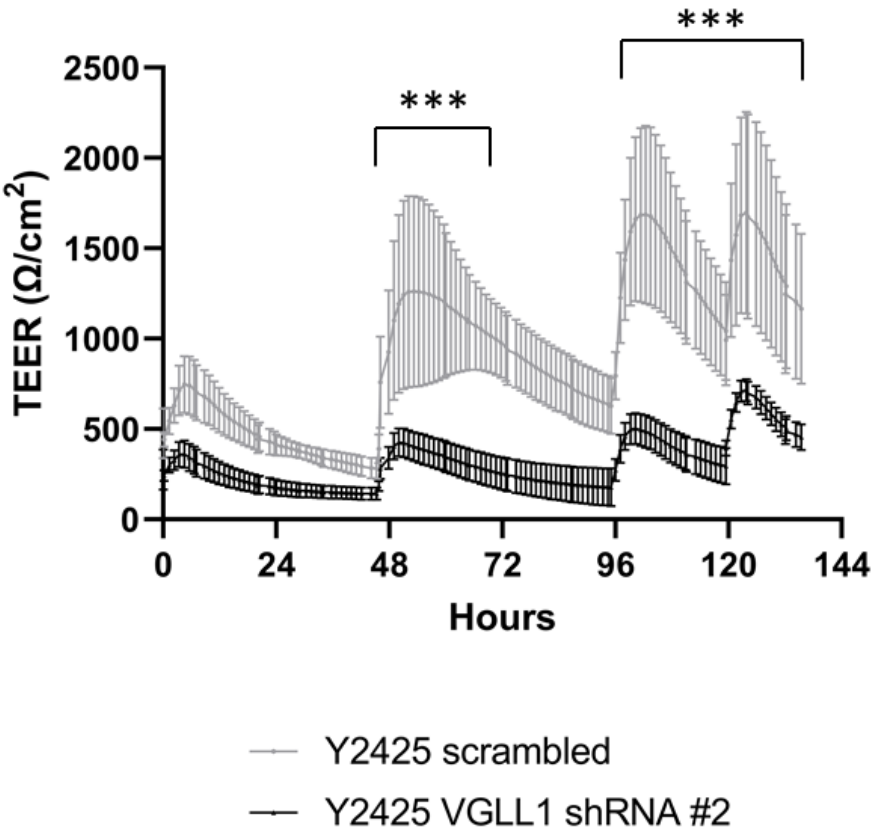

Figure 7.18: Analysis of TEER in VGLL1 knockdown ABS/Ca^{2+} differentiated NHU cells

Biological replicate from Figure 3.31 of barrier impedance in Y2425 cells following VGLL1 knockdown and ABS/Ca^{2+} differentiation. As seen in Figure 3.31, VGLL1 knockdown results in a consistently (and significantly) weaker barrier when compared to control in an unwounded state. Significance in barrier tightness between conditions was determined using a two-way repeated measure ANOVA with Sidak's multiple comparsions post-hoc test.

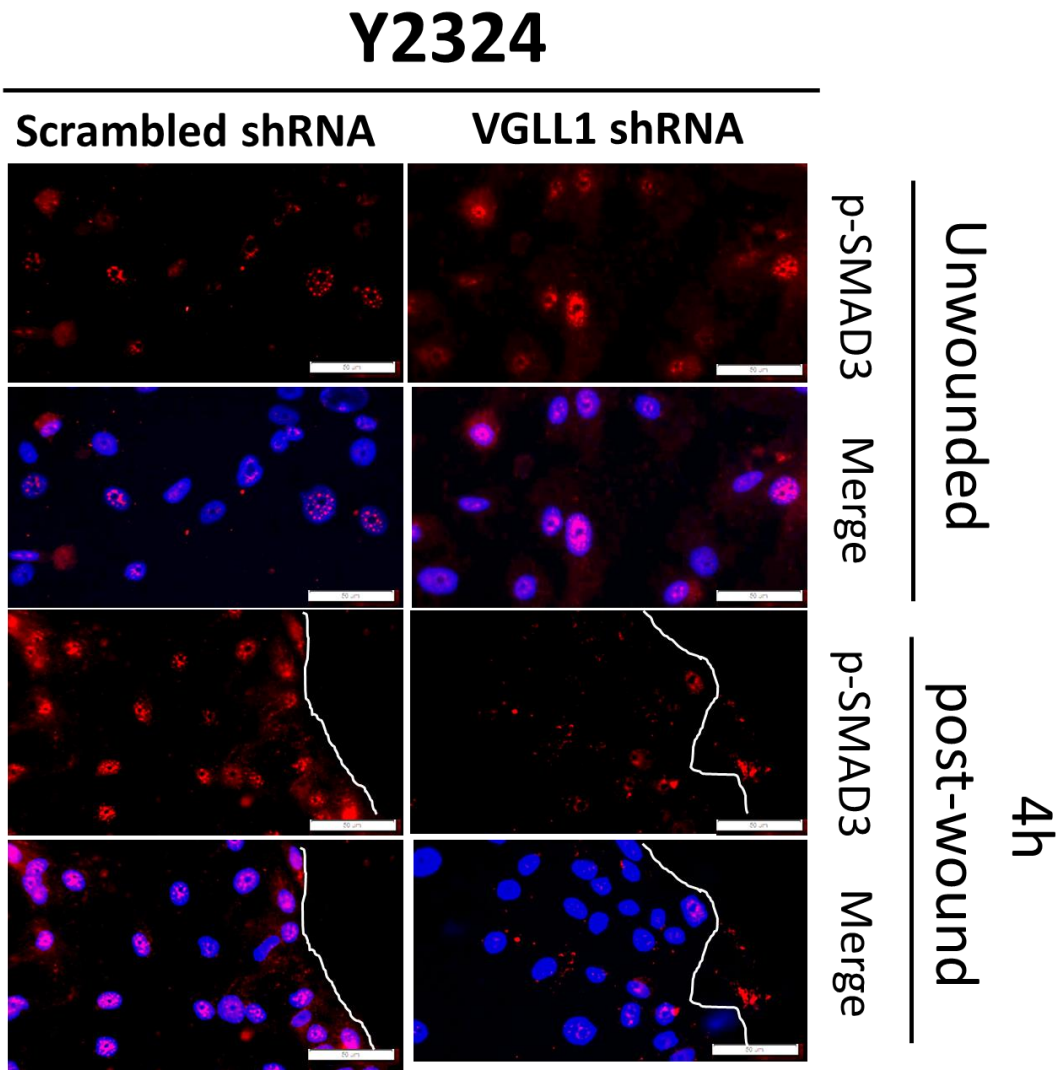

Figure 7.19: p-SMAD3 expression in VGLL1 knockdown differentiated NHU cells

Biological replicate from Figure 3.35 of wounded Y2324 cells following VGLL1 knockdown and ABS/Ca^{2+} differentiation. As seen in Figure 3.35, p-SMAD3 expression is inhibited at the wound edge of VGLL1 knockdown cells 4h post-wound. White lines indicate the position of the wound edge. Scale bar = 50 µm.

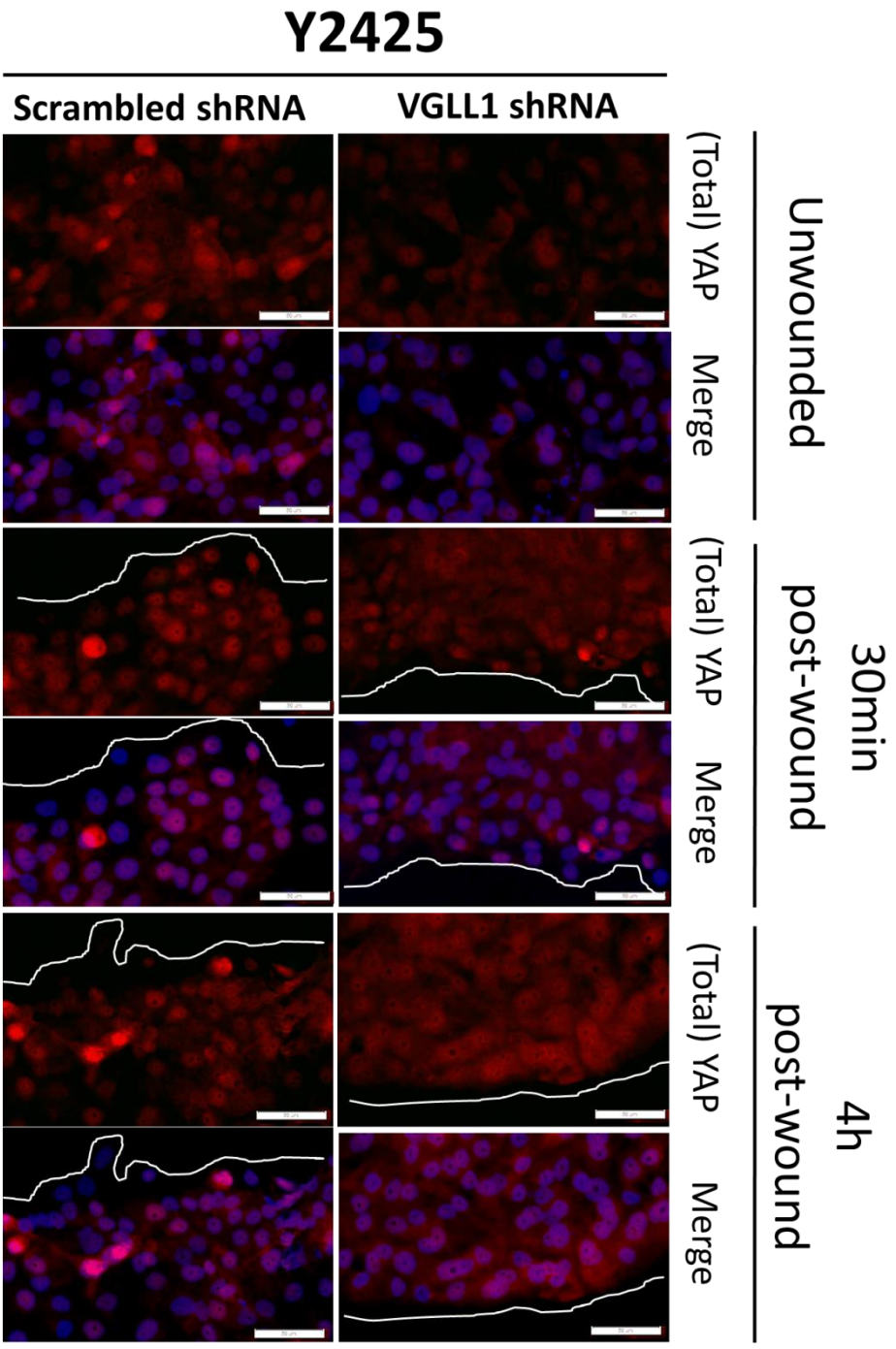

Figure 7.20: Total YAP expression in VGLL1 knockdown differentiated NHU cells

Biological replicate from Figure 3.36 of wounded Y2425 cells following VGLL1 knockdown and ABS/Ca^{2+} differentiation. As seen in Figure 3.36, YAP localisation does not appear to change based on VGLL1 inhibition or upon wounding of cultures. White lines indicate the position of the wound edge. Scale bar = 50 µm.

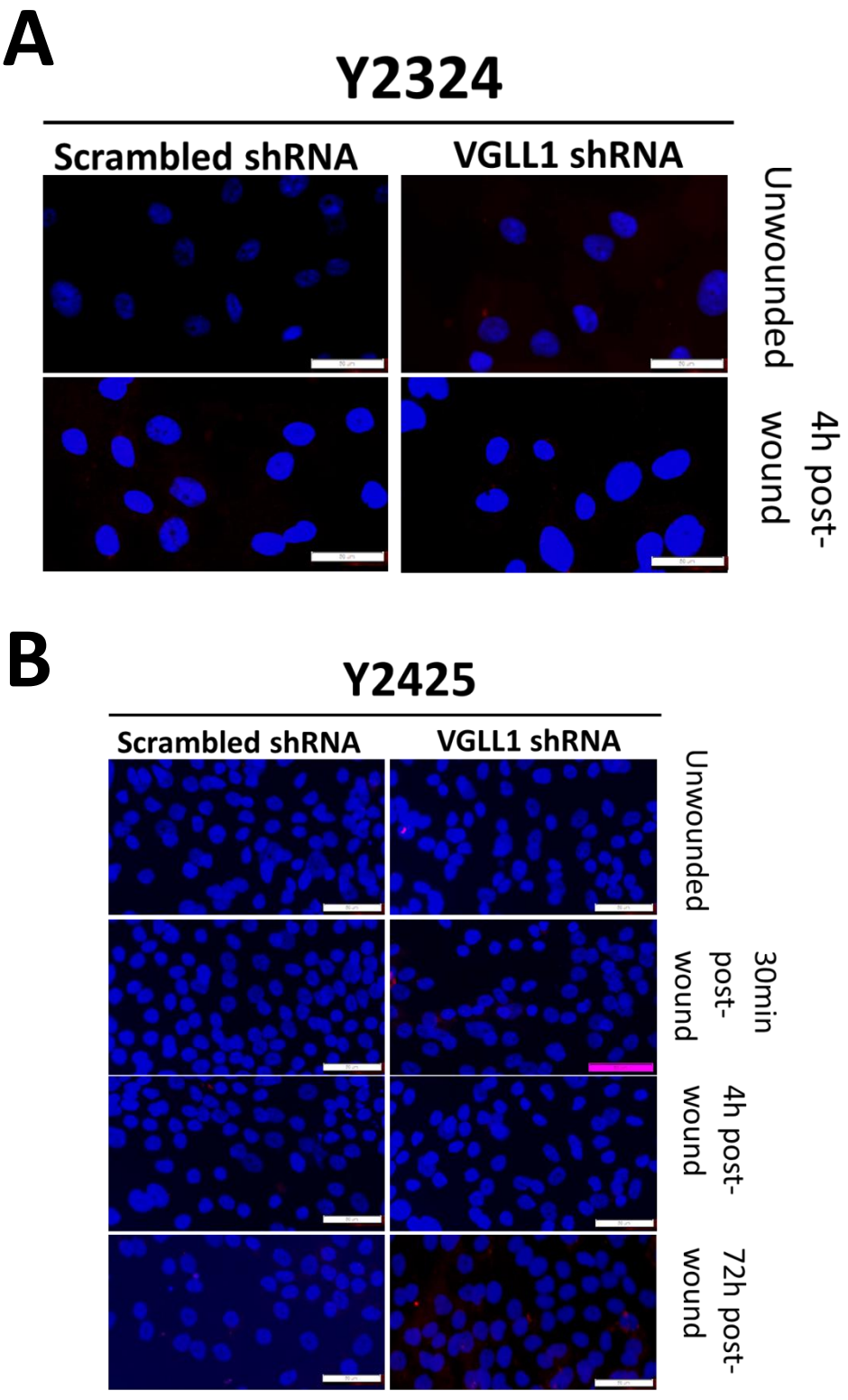

Figure 7.21: Negative controls for Figures 3.33- 3.36

Y2324 (**A**) and Y2425 (**B)** cells receiving no primary antibody at all time points were used as negative controls. Images were all taken at same exposure and are shown with overlaid Hoechst 33258 DNA staining. Scale bar= 50µm.

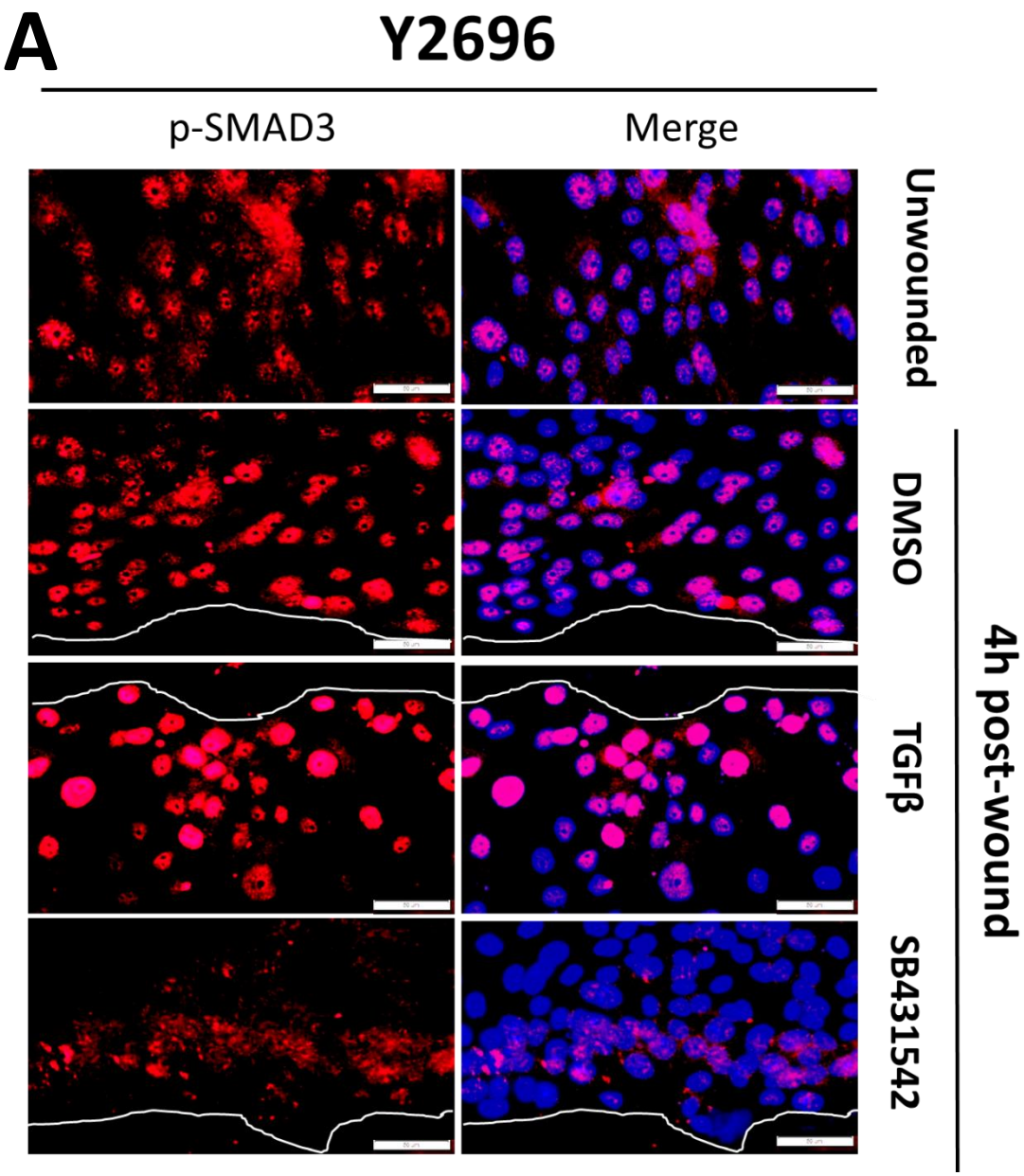

Figure 7.22: p-SMAD3 expression in TGFβ agonist and antagonist-treated differentiated NHU cells

Biological replicate from Figure 3.39 of Y2696 cells following ABS/Ca^{2+} differentiation and pretreatment with TGFβ or SB431542 and prior to wounding. Panel (**A**) depicts p-SMAD3 expression in cells in either an unwounded state or 4h post-wound. As seen in Figure 3.39, p-SMAD3 is intensely expressed at the wound edge of TGFβ treated cells but is inhibited at the wound edge of SB431542 treated cells. White lines indicate the position of the wound edge. Scale bar = 50 µm.

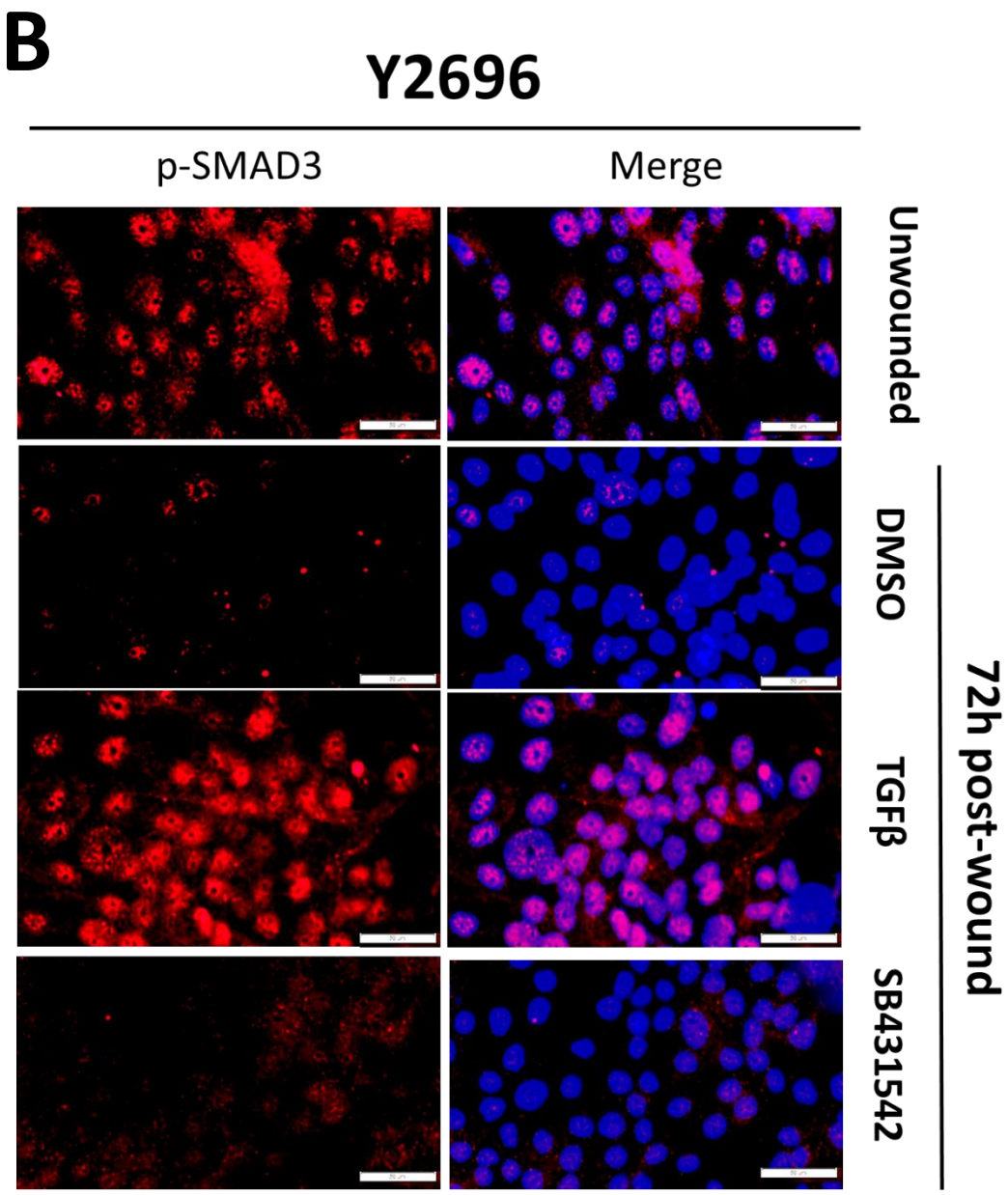

Figure 7.22: p-SMAD3 expression in TGFβ agonist and antagonist-treated differentiated NHU cells

Biological replicate from Figure 3.39 of Y2696 cells following ABS/Ca^{2+} differentiation and pretreatment with TGFβ or SB431542 and prior to wounding. Panel (**B**) depicts p-SMAD3 expression in cells in either an unwounded state or 72h post-wound. As seen in Figure 3.39, p-SMAD3 is lost in control cells following wound recovery but is retained in TGFβ treated cells. Scale bar = 50 µm.

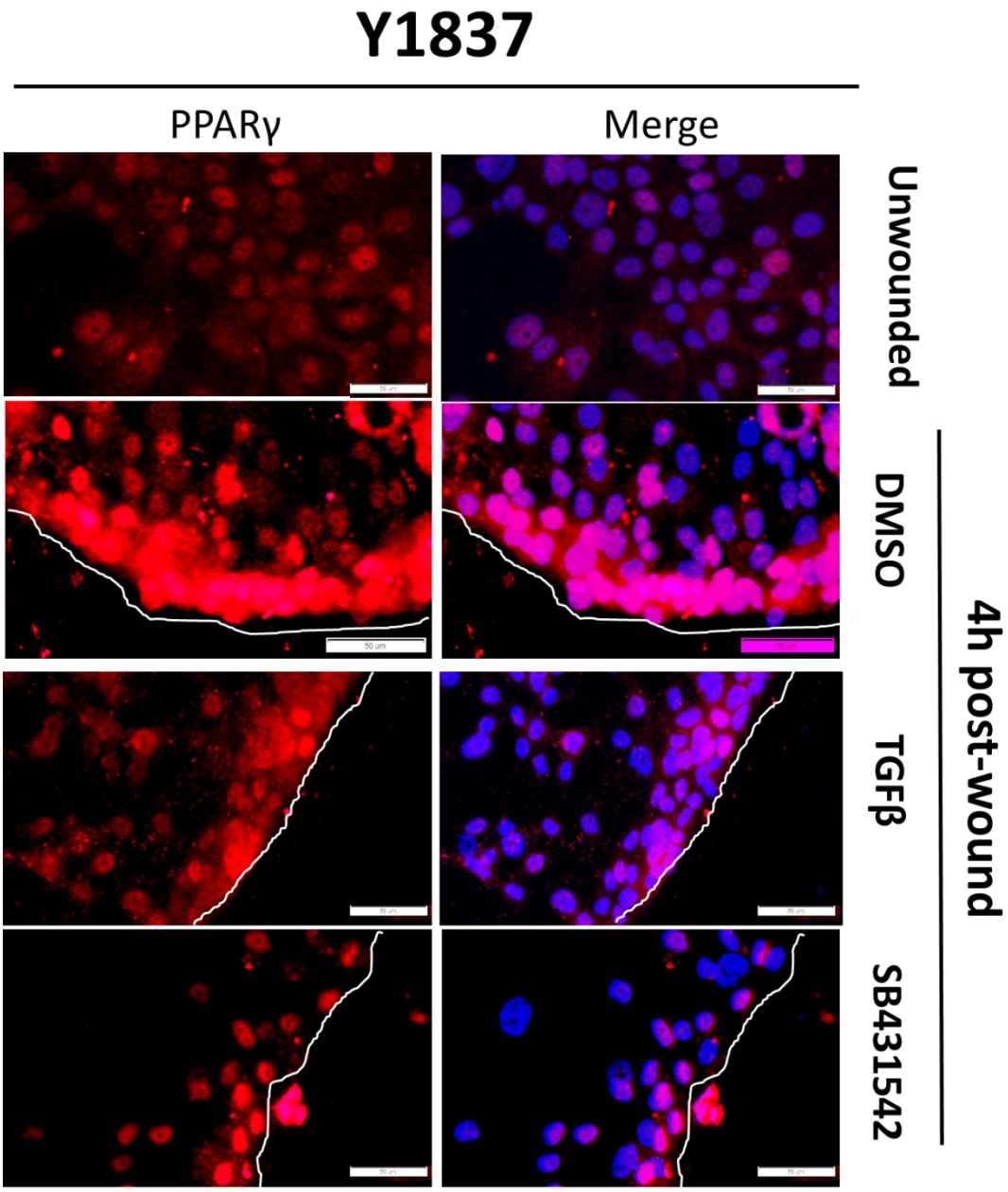

Figure 7.23: PPARγ expression in TGFβ agonist and antagonist-treated differentiated NHU cells

Biological replicate from Figure 3.41 of Y1837 cells following ABS/Ca^{2+} differentiation and pretreatment with TGFβ or SB431542 and prior to wounding. As seen in Figure 3.41, PPARγ exhibits a cytoplasmic localisation at the wound edge of control and TGFβ treated cells but is nuclear in SB431542 treated cells. White lines indicate the position of the wound edge. Scale bar = 50 µm.

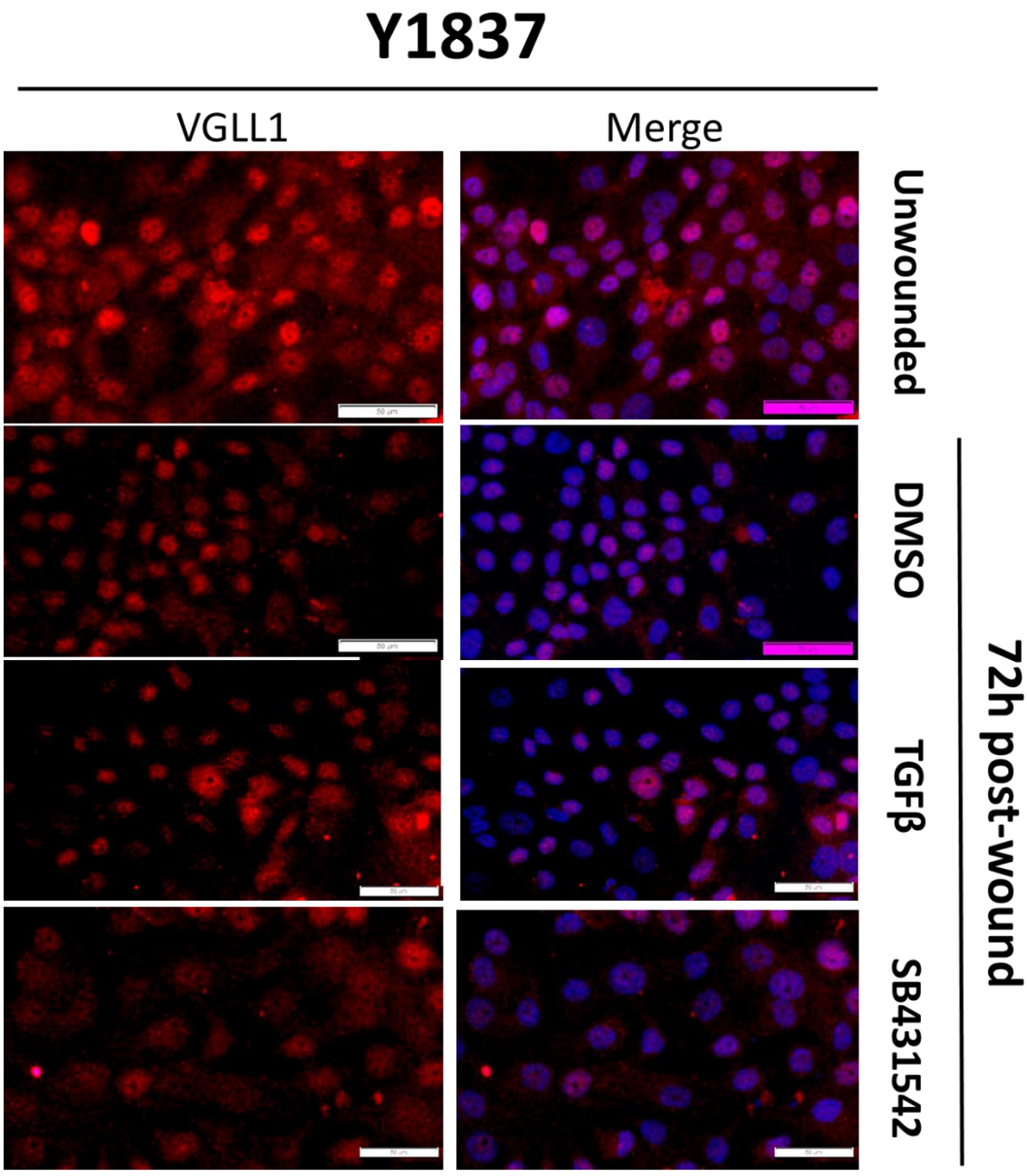

Figure 7.24: VGLL1 expression in TGFβ agonist and antagonist-treated differentiated NHU cells

Biological replicate from Figure 3.42 of Y1837 cells following ABS/Ca^{2+} differentiation and pretreatment with TGFβ or SB431542 and prior to wounding. As seen in Figure 3.42, treatment with TGFβ or SB431542 before wounding of differentiated NHU cultures did not appear to affect VGLL1 expression. Scale bar = 50 µm.

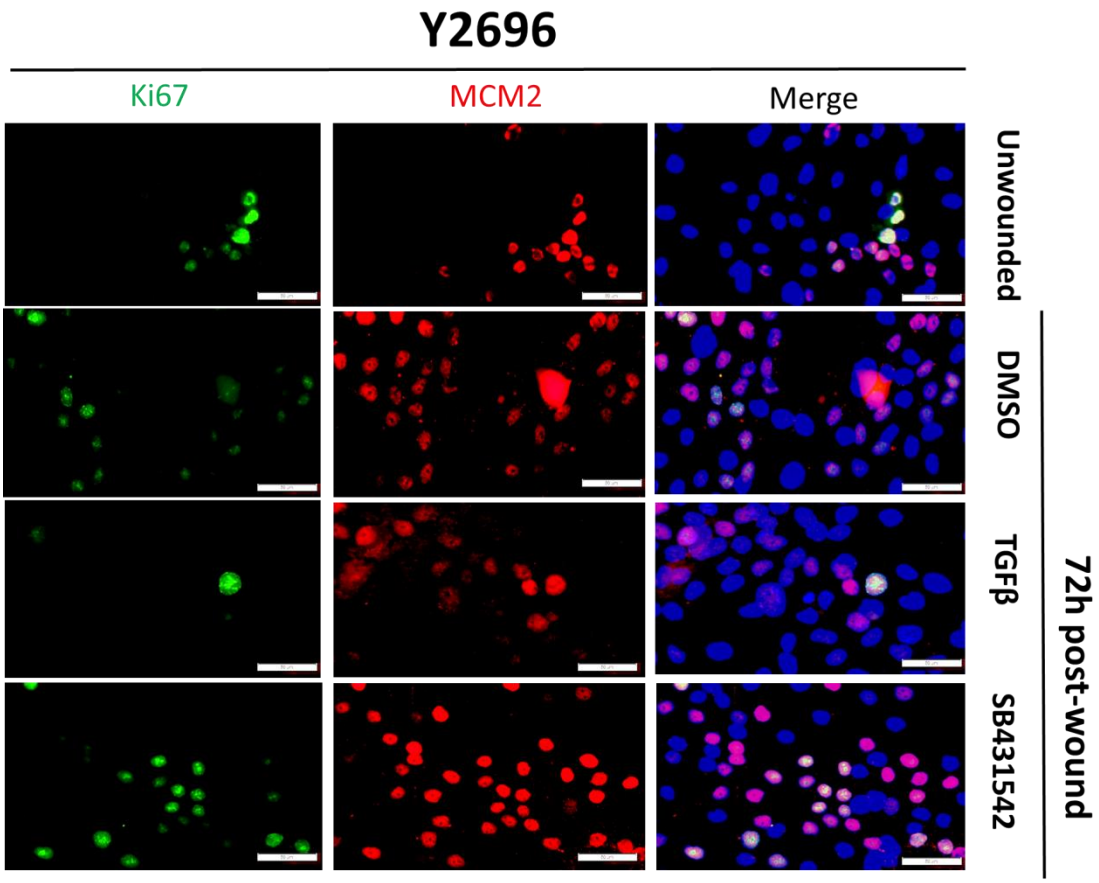

Figure 7.25: Ki67/MCM2 expression in TGFβ agonist and antagonist-treated differentiated NHU cells

Biological replicate from Figure 3.43 of Y2696 cells following ABS/Ca^{2+} differentiation and pretreatment with TGFβ or SB431542 and prior to wounding. As seen in Figure 3.43, treatment with TGFβ inhibited the increase in Ki67 and MCM2 expression observed in control cells following wounding, while SB431542 treatment induced further cell cycle activation. Scale bar = 50 µm.

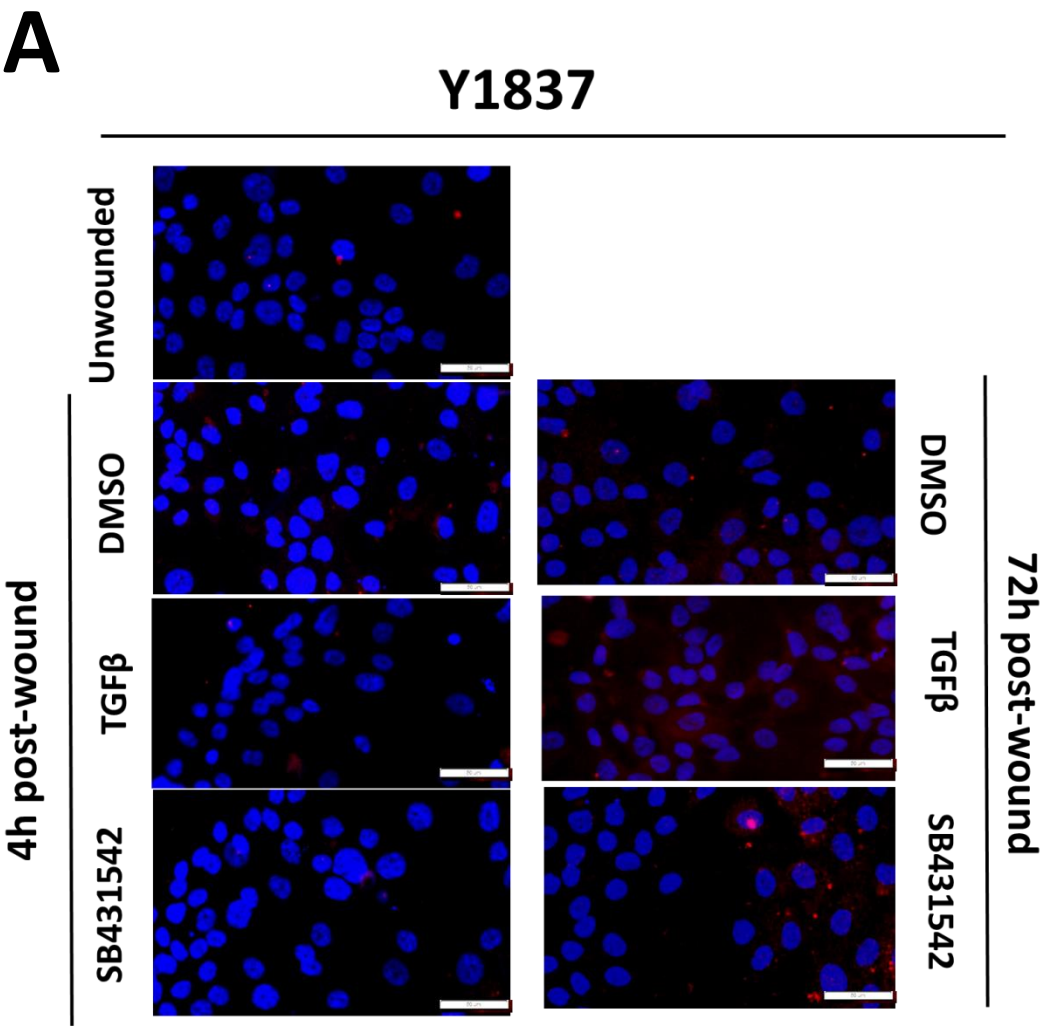

Figure 7.26: Negative controls for Figures 3.39- 3.43

Y1837 (**A**) cells receiving no primary antibody at all time points were used as negative controls. Images were all taken at same exposure and are shown with overlaid Hoechst 33258 DNA staining. Scale bar= 50µm.

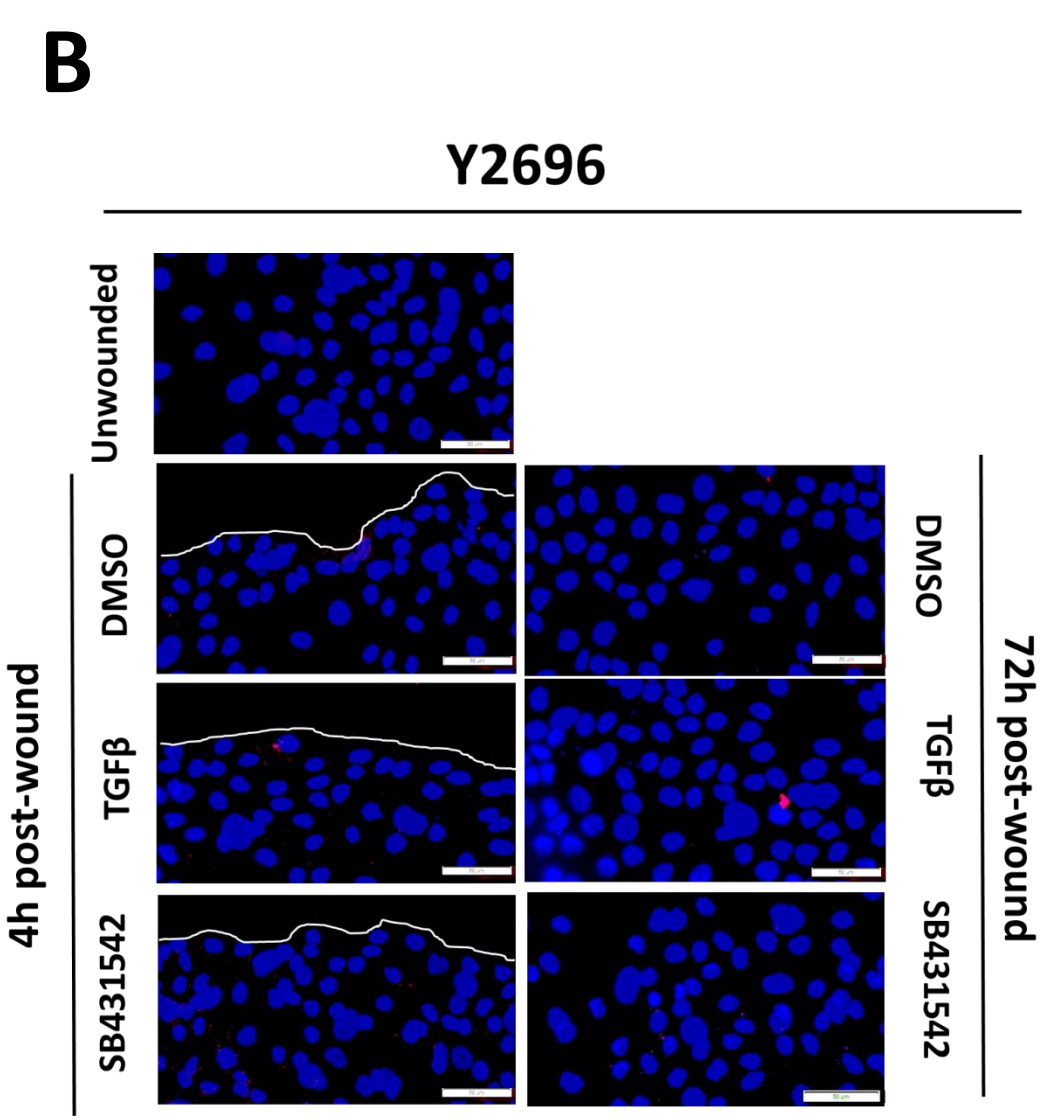

Figure 7.26: Negative controls for figures 3.39- 3.43

Y2696 (**B**) cells receiving no primary antibody at all time points were used as negative controls. Images were all taken at same exposure and are shown with overlaid Hoechst 33258 DNA staining. Scale bar= 50µm.

Appendix xiii: Chapter 4 auxiliary results

Gene	5637	HT1197	HT1376	RT112	RT4	SCaBER	T24	UM-UC-9
TERT	Mut.	Mut.	Mut.	Mut.	Mut.	Mut.	Mut.	Mut.
FGFR3	WT	S249C	WT	FGFR3-TACC3 fusion	FGFR3-TACC3 fusion	WT	WT	WT
PIK3CA	WT	E545K	WT	WT	WT	WT	WT	WT
AKT	WT	Unk.	Unk.	WT	Unk.	Unk.	WT	WT
PTEN	LOH	WT	WT	WT	LOH	WT	N48I/G44G	p.D24Y
H-RAS	WT	WT	WT	WT	WT	WT	G12V	WT
K-RAS	WT	WT	WT	WT	WT	WT	WT	Unk.
N-RAS	WT	Q61R	WT	WT	WT	WT	WT	Unk.
CDKN2A	WT	WT	WT	HD	HD	LOH	LOH	LOH
RB1	c.975T>A	Unk.	c.2104C>T	Unk.	Unk.	Unk.	Unk.	Unk.
TP53	c.839G>C	c.1094A->G	c.749C>T	c.743G>A&c.548C->G	WT	c.329G>T	c.378C>G	Mut.

Table 7.11: Mutational status of commonly mutated MIBC genes in bladder cancer cell lines

Cells highlighted in red indicate a previously identified alteration to a gene in a specific cell line. HD= homozygous deletion, LOH= loss of heterozygosity. Table adapted from a previous study performed on a cohort of bladder cancer cell lines by Earl *et al.*

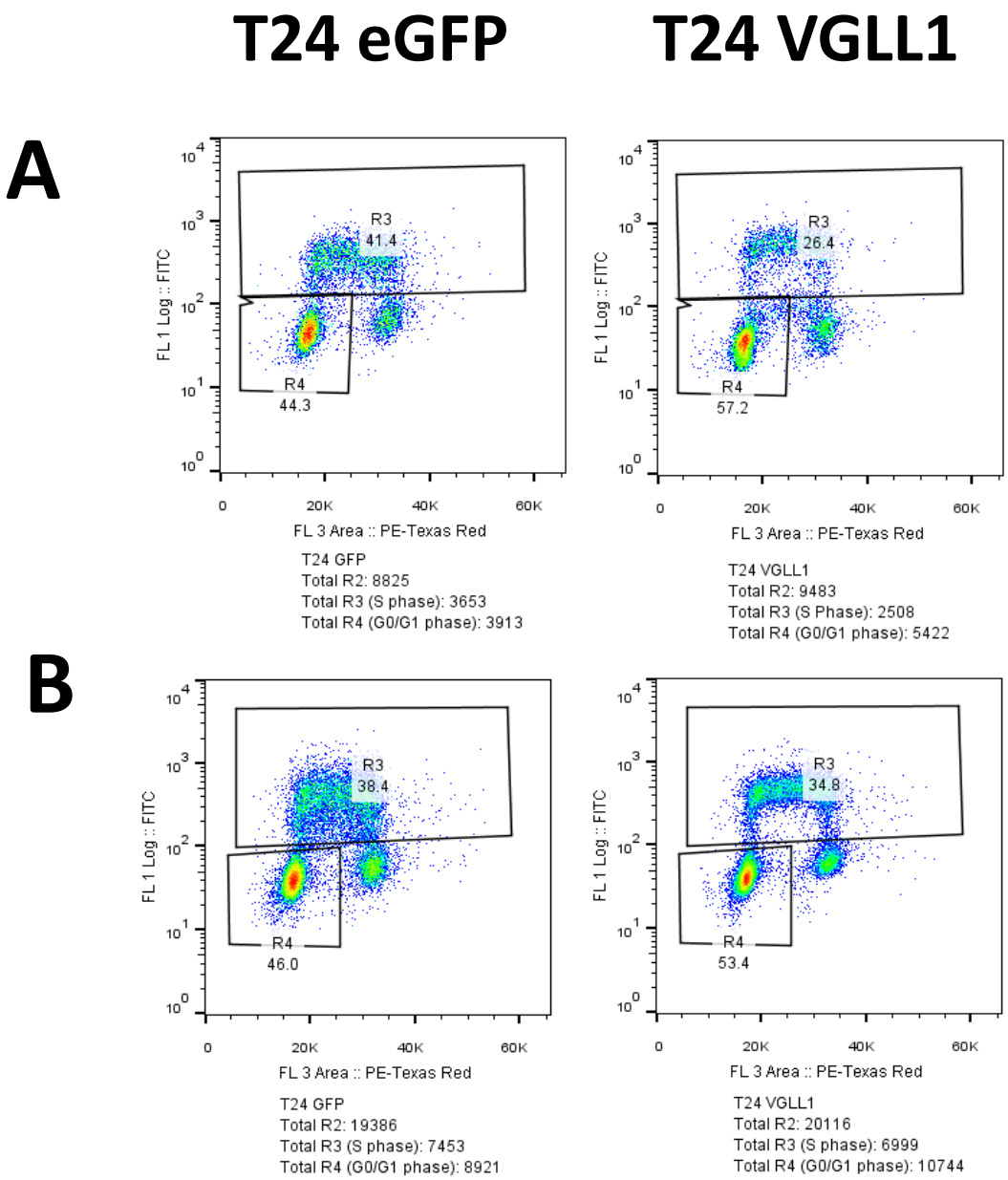

Figure 7.27: Cell cycle analysis of T24 eGFP and VGLL1 overexpressing cells

Technical replicates from Figure 4.12 of flow cytometry analysis of T24 cells pulsed with BrdU and labelled with a BrdU-specific antibody. (**A**) and (**B**) represent propidium iodide versus BrdU scatter plots of transfected T24 cells fixed independently, with both occasions demonstrating a G0/G1 arrest in T24 VGLL1 cells compared to control, as seen in figure 4.12.

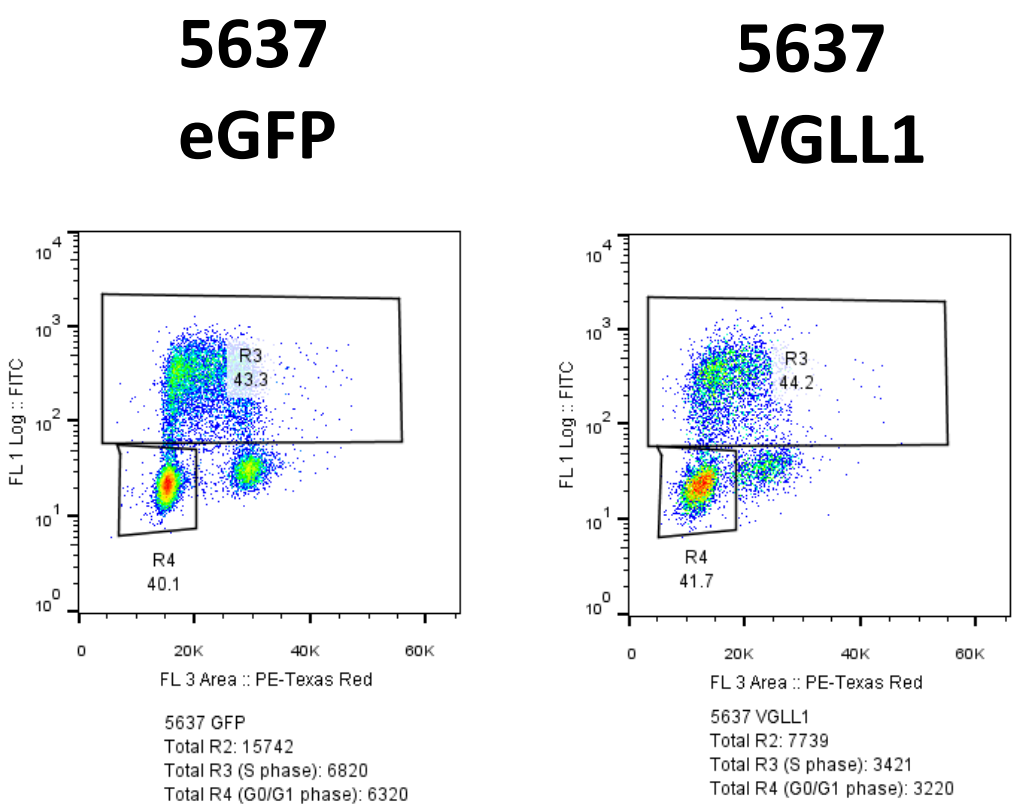

Figure 7.28: Cell cycle analysis of 5637 eGFP and VGLL1 overexpressing cells

Technical replicate from Figure 4.13 of flow cytometry analysis of 5637 cells pulsed with BrdU and labelled with a BrdU-specific antibody. As seen in figure 4.13, overexpression of VGLL1 in 5637 cells has little effect on the proportion of cells in the G0/G1 and S phases of the cell cycle.

Gene	Comparison	Significant?	Summary	pval
VGLL1	Urothelium *in situ* vs. Luminal Papillary	No	ns	>0.9999
VGLL1	Urothelium *in situ* vs. Luminal Non-Specified	No	ns	0.1021
VGLL1	Urothelium *in situ* vs. Luminal Unstable	Yes	*	0.0426
VGLL1	Urothelium *in situ* vs. Basal/Squamous	No	ns	>0.9999
VGLL1	Urothelium *in situ* vs. Neuroendocrine	No	ns	>0.9999
VGLL1	Urothelium *in situ* vs. Stroma-Rich	No	ns	>0.9999
VGLL1	Luminal Papillary vs. Luminal Non-Specified	No	ns	0.1077
VGLL1	Luminal Papillary vs. Luminal Unstable	Yes	***	0.0006
VGLL1	Luminal Papillary vs. Basal/Squamous	Yes	***	<0.0001
VGLL1	Luminal Papillary vs. Neuroendocrine	Yes	**	0.0023
VGLL1	Luminal Papillary vs. Stroma-Rich	No	ns	>0.9999
VGLL1	Luminal Non-Specified vs. Luminal Unstable	No	ns	>0.9999
VGLL1	Luminal Non-Specified vs. Basal/Squamous	Yes	***	<0.0001
VGLL1	Luminal Non-Specified vs. Neuroendocrine	Yes	***	<0.0001
VGLL1	Luminal Non-Specified vs. Stroma-Rich	No	ns	0.1799
VGLL1	Luminal Unstable vs. Basal/Squamous	Yes	***	<0.0001
VGLL1	Luminal Unstable vs. Neuroendocrine	Yes	***	<0.0001
VGLL1	Luminal Unstable vs. Stroma-Rich	Yes	**	0.0079
VGLL1	Basal/Squamous vs. Neuroendocrine	No	ns	>0.9999
VGLL1	Basal/Squamous vs. Stroma-Rich	Yes	***	0.0001
VGLL1	Neuroendocrine vs. Stroma-Rich	Yes	**	0.0058

Table 7.12: Dunn's multiple comparisons test of conditions in Figure 4.14.

Tumour ID	Mutation type	Protein alteration	Copy #	Predicted effect
A9KW	X1367_splice	Splice	Shallow del.	Likely loss-of-function
A2LD	Y500Lfs*123	FS Ins	Shallow del.	Likely loss-of-function
A3SR	Q605E	Missense	Gain	Unknown
A3JV	Q1363*	Nonsense	Shallow del.	Likely loss-of-function
A9KI	S740_Q743delins*	Nonsense	WT	Likely loss-of-function
A3PH	E2035*	Nonsense	WT	Likely loss-of-function
A40G	Unknown	Unknown	Unknown	Unknown
A3IT	Unknown	Unknown	Unknown	Unknown

Table 7.13: Information on *ARID1A* mutations in *VGLL1*-high MIBC subtype

Information was downloaded from cBioPortal. 5/8 tumours with *ARID1A* mutations were predicted to have loss of function of ARID1A, with the predicted phenotype caused by the mutations in the remaining 3 tumours not available on cBioPortal. FS Ins= frameshift insertion.

Gene	AA Mutation	CDS Mutation	Zygosity	Validated	Type	Position
ARID1A	p.S2264L	c.6791C>T	Heterozygous	Unverified	Missense	1:26780689.. 26780689
ARID1A	p.S2256*	c.6767C>A	Heterozygous	Unverified	Nonsense	1:26780665.. 26780665

Table 7.14: Information on *ARID1A* mutations in HT1197 cells

Information was downloaded from the COSMIC database (https://cancer.sanger.ac.uk/cosmic). The list of mutations inherent to T24 cells revealed that no mutations in the *ARID1A* gene have been discovered in that cell line.

Gene	AA Mutation	CDS Mutation	Zygosity	Validated	Type	Position
ARID1A	p.S186fs*209	c.557_570 del14	Heterozygous	Verified	Frameshift deletion	1:26696960.. 26696973
ARID1A	p.T1302S	c.3905C>G	Heterozygous	Unverified	Missense	1:26773618.. 26773618

Table 7.15: Information on *ARID1A* mutations in HT1376 cells

Information was downloaded from the COSMIC database.

Gene	Log_2 fold change	pval	qval
FTHL17	-21.69129073	1.58E-23	4.71E-19
LIN28A	5.575709122	1.71E-22	2.56E-18
NR6A1	2.17491435	1.30E-16	1.30E-12
CLEC1A	3.078366756	8.70E-16	6.50E-12
HTR7	-5.006224837	2.47E-15	1.48E-11
GCM1	4.525459814	6.75E-15	2.88E-11
DSG3	-7.724638095	1.58E-14	5.90E-11
HMGA2	-6.653485821	1.81E-14	6.00E-11
MMP10	-5.728936107	2.21E-13	6.00E-10
KRT4	-6.829501743	2.10E-13	6.00E-10
PMEL	2.484728939	3.41E-13	8.49E-10
BNC1	-7.839103133	4.56E-13	1.05E-09
KRT6B	-7.906156579	6.29E-13	1.34E-09
CD55	2.231098495	1.30E-12	2.59E-09
IRX3	-4.099034614	2.11E-12	3.95E-09
MMP12	-4.801547591	2.46E-12	4.32E-09
CLCA2	-5.406682884	6.17E-12	9.70E-09
SERPINB4	-6.76221952	6.05E-12	9.70E-09
LINC00519	-3.945129041	1.00E-11	1.50E-08
KRT13	-5.446432666	1.31E-11	1.80E-08
DAPL1	-5.983756554	1.44E-11	1.80E-08
TENM2	-6.390382891	1.38E-11	1.80E-08
KRT6C	-7.631061725	1.35E-11	1.80E-08
KLK10	-6.185783258	1.56E-11	1.86E-08
S100A2	-4.430455423	1.80E-11	1.99E-08
KRT5	-5.641261736	1.76E-11	1.99E-08
SERPINB3	-6.272218417	1.90E-11	2.03E-08
LINC01960	3.730352562	2.73E-11	2.81E-08
BRWD1-AS1	2.889343023	3.62E-11	3.61E-08
KRT6A	-6.286607315	4.03E-11	3.89E-08
VSNL1	-4.641258846	6.91E-11	6.45E-08
KRT75	-8.225238623	8.36E-11	7.57E-08
GJA5	2.978216748	9.21E-11	8.10E-08
AC011374.1	-4.866299647	1.12E-10	9.54E-08
CYP1A1	-7.311626923	1.16E-10	9.61E-08
SRGAP3	-2.495949863	1.43E-10	1.15E-07
LINC01752	-4.064161117	1.58E-10	1.25E-07
FOXE1	-5.353626756	1.64E-10	1.26E-07
KRT17	-3.557700016	1.82E-10	1.36E-07
MIR222HG	-2.490666644	1.91E-10	1.39E-07
C1orf105	5.149508172	2.64E-10	1.79E-07
ATP7B	2.672310082	2.59E-10	1.79E-07
PI3	-5.770410685	2.81E-10	1.86E-07

CDH3	-3.273657984	3.03E-10	1.97E-07
MYOSLID	-4.411910467	3.81E-10	2.37E-07
MMP13	-4.635516684	3.78E-10	2.37E-07
WDR66	-3.433476093	4.01E-10	2.40E-07
SERPINB13	-6.001910175	3.99E-10	2.40E-07
AC103746.1	2.209384493	4.68E-10	2.64E-07
CA12	-3.128413505	4.68E-10	2.64E-07
FGFBP1	-5.341334682	4.61E-10	2.64E-07
PPP2R2C	-4.601084692	4.81E-10	2.66E-07
AIM2	-3.933089062	5.21E-10	2.83E-07
WNT10A	-3.712551401	6.54E-10	3.49E-07
KLK11	-5.642509116	7.10E-10	3.72E-07
KRT1	-6.076054801	8.00E-10	4.12E-07
KRT16	-4.775957096	9.51E-10	4.82E-07
PKP1	-3.764757525	1.59E-09	7.80E-07
NCF4-AS1	5.054246856	1.75E-09	8.42E-07
C12orf54	-4.009991739	1.96E-09	9.28E-07
CRTAC1	-5.089708224	2.10E-09	9.80E-07
SLC38A5	-3.327043157	2.17E-09	9.82E-07
CLCA4	-5.185819704	2.14E-09	9.82E-07
LGALS7B	-5.534561733	2.30E-09	1.03E-06
AC018553.1	-3.407003029	3.52E-09	1.52E-06
EPO	3.5552921	4.05E-09	1.73E-06
BAALC	-3.767534123	4.23E-09	1.78E-06
ERVW-1	3.747899777	4.41E-09	1.83E-06
CYP27C1	-3.370878003	4.65E-09	1.91E-06
KRT74	-5.415434136	6.97E-09	2.78E-06
TAC4	2.664669727	7.30E-09	2.87E-06
ALDH3A1	-4.369161067	8.10E-09	3.14E-06
ATP6V1C2	2.006335017	8.25E-09	3.16E-06
GNLY	-3.561956062	8.34E-09	3.16E-06
LINC00900	-3.42352445	8.79E-09	3.20E-06
SLC47A2	-4.18437741	8.68E-09	3.20E-06
KRT31	-5.823715935	8.70E-09	3.20E-06
DUSP13	3.638181043	1.32E-08	4.70E-06
SHOX	4.235141495	1.44E-08	5.02E-06
EN1	-5.114578156	1.43E-08	5.02E-06
KLRC1	-3.244654777	1.52E-08	5.23E-06
SFTPB	-4.815174074	1.59E-08	5.41E-06
SPOCD1	-3.215192645	1.62E-08	5.45E-06
GRAMD2	3.25049971	1.72E-08	5.71E-06
AKR1C1	-3.707499051	2.31E-08	7.57E-06
KRT17P3	-4.060028145	2.45E-08	7.96E-06
PTPRZ1	-5.413696849	2.49E-08	7.99E-06

CDKN1C	2.369823682	2.63E-08	8.36E-06
CSF3R	2.689029093	3.09E-08	9.54E-06
SDR16C5	-4.756253808	3.13E-08	9.56E-06
TMEM45A	-3.27685897	3.30E-08	9.97E-06
AC041040.1	-3.342613077	3.45E-08	1.02E-05
LINC01314	-4.47997102	3.44E-08	1.02E-05
CPA4	-4.072905344	3.50E-08	1.03E-05
KRT15	-3.654913424	3.64E-08	1.05E-05
S100A7	-5.599701824	3.63E-08	1.05E-05
BCL11B	-2.375461711	3.73E-08	1.06E-05
LINC01503	-2.020969935	3.91E-08	1.09E-05
LINC00707	-4.858530131	4.26E-08	1.18E-05
IDO1	-3.975204407	4.61E-08	1.26E-05
CLEC2B	-2.62251103	5.49E-08	1.45E-05
ZFPM2-AS1	-3.070048277	5.33E-08	1.45E-05
GSC	-3.856182952	5.42E-08	1.45E-05
ALDH1L1-AS2	-3.998178733	5.42E-08	1.45E-05
S100A3	-2.84082339	5.68E-08	1.49E-05
AC099796.1	-5.40706202	6.28E-08	1.63E-05
SCGB1A1	-7.24921193	6.72E-08	1.70E-05
HEPHL1	-4.159280971	6.86E-08	1.72E-05
SLC22A11	5.067930662	7.06E-08	1.73E-05
MED12L	2.060002868	7.13E-08	1.73E-05
CALML3	-4.769825217	7.05E-08	1.73E-05
KLK13	-5.334404816	7.11E-08	1.73E-05
HIC2	2.305329786	7.35E-08	1.77E-05
POU3F1	-3.568577604	7.50E-08	1.78E-05
PTHLH	-3.859522433	7.47E-08	1.78E-05
KRT17P6	-4.081871842	7.78E-08	1.81E-05
IL36G	-4.563702847	7.76E-08	1.81E-05
KRTDAP	-5.313360858	7.81E-08	1.81E-05
AC080013.4	2.575150954	8.42E-08	1.94E-05
CD44	-2.297397445	9.23E-08	2.06E-05
COLCA1	-3.461605968	9.15E-08	2.06E-05
MMP1	-3.711827106	9.10E-08	2.06E-05
NMRAL2P	-4.599336682	9.14E-08	2.06E-05
PLA2G4A	-2.070981851	9.65E-08	2.14E-05
ADH7	-5.99178322	1.02E-07	2.24E-05
AC018647.1	2.212886671	1.06E-07	2.29E-05
AC002401.4	-3.632861258	1.06E-07	2.29E-05
LINC00460	-5.041793477	1.09E-07	2.33E-05
PICSAR	-4.903903911	1.12E-07	2.40E-05
TMPRSS11D	-5.626454291	1.13E-07	2.40E-05
ZNF812P	-3.286259243	1.16E-07	2.45E-05

ADCY10	2.660973686	1.26E-07	2.61E-05
LINC00704	-4.179539581	1.34E-07	2.76E-05
NPBWR1	-3.798221989	1.39E-07	2.85E-05
KRT16P6	-4.905872467	1.44E-07	2.94E-05
SPRR1B	-4.601312586	1.52E-07	3.06E-05
IFI16	-2.135829946	1.53E-07	3.08E-05
M1AP	-3.565151187	1.65E-07	3.27E-05
LINP1	-4.404182261	1.65E-07	3.27E-05
UGT1A8	-5.425135369	1.90E-07	3.71E-05
PGLYRP3	-4.79651469	1.94E-07	3.76E-05
KRT77	-4.799645677	2.01E-07	3.87E-05
CP	-4.009238513	2.03E-07	3.90E-05
FOLR1	4.146258211	2.17E-07	4.10E-05
AC012501.2	-5.117726066	2.15E-07	4.10E-05
FAM26F	-2.541177675	2.20E-07	4.13E-05
LY6G6C	3.538214275	2.36E-07	4.36E-05
TNFRSF18	-2.512554438	2.36E-07	4.36E-05
KLK5	-6.754695498	2.33E-07	4.36E-05
SEZ6L	-4.654205319	2.52E-07	4.59E-05
MUC2	-4.722024027	2.51E-07	4.59E-05
L1CAM	-4.023889052	2.58E-07	4.68E-05
CA9	-3.419588657	2.84E-07	5.08E-05
SLURP1	-3.93751084	2.83E-07	5.08E-05
PNMA5	-5.799924186	2.86E-07	5.09E-05
CCNA1	-4.524737898	2.97E-07	5.23E-05
FABP4	-4.200874145	3.09E-07	5.37E-05
CTAGE3P	3.105878376	3.32E-07	5.68E-05
ADSSL1	-2.155273374	3.34E-07	5.68E-05
BBOX1	-3.222458447	3.32E-07	5.68E-05
LINC02154	-4.913882573	3.30E-07	5.68E-05
LINC01587	-4.927318822	3.43E-07	5.79E-05
ACHE	2.739802714	3.60E-07	6.05E-05
ECHDC3	-3.157976356	3.72E-07	6.15E-05
NKAIN2	-3.818076595	3.71E-07	6.15E-05
CASP1	-2.098048972	4.12E-07	6.66E-05
TMEM246	-2.500800394	4.11E-07	6.66E-05
IGFBP6	-2.660060843	4.15E-07	6.66E-05
CSMD1	-4.333907791	4.19E-07	6.70E-05
IL31RA	-4.081686937	4.32E-07	6.83E-05
KIR2DL4	-3.383611505	4.49E-07	7.06E-05
KRT14	-4.78755817	4.71E-07	7.29E-05
CARD17	-4.38899694	4.80E-07	7.40E-05
AL354766.2	-5.466534774	4.96E-07	7.60E-05
SHISA2	-3.369196869	5.04E-07	7.68E-05

SERPINA1	-3.094356448	5.14E-07	7.76E-05
KRT79	-4.092978523	5.13E-07	7.76E-05
AL365356.3	-4.074546304	5.50E-07	8.22E-05
AC024940.1	-2.772850725	5.74E-07	8.53E-05
ADGRE1	-3.1358715	5.79E-07	8.57E-05
LGR5	-3.851270392	6.24E-07	9.14E-05
CHRM5	2.275437127	6.50E-07	9.47E-05
SUN3	2.901943649	6.60E-07	9.58E-05
S100A7A	-6.392424693	6.69E-07	9.67E-05
ERVMER34-1	2.203708858	6.96E-07	1.00E-04
LCMT1-AS2	2.387500049	7.12E-07	0.000102
LINC00540	-4.177998039	7.28E-07	0.000104
CALB2	-3.477352387	7.53E-07	0.000107
LINC02446	-3.960769561	7.78E-07	0.00011
BRINP1	-3.939335136	8.02E-07	0.000112
NELL2	-2.984685834	8.61E-07	0.00012
SBSN	-4.317450565	8.70E-07	0.00012
BMS1P8	-5.701133966	9.58E-07	0.000131
PROC	-2.392241384	9.83E-07	0.000133
NTS	-4.174938708	9.75E-07	0.000133
LINC01686	2.064680282	1.01E-06	0.000136
KRT42P	-2.700485055	1.03E-06	0.000138
DEC1	-4.331219522	1.12E-06	0.000149
KRT78	-3.124657093	1.14E-06	0.000152
AC068987.4	2.674090608	1.17E-06	0.000154
GKN1	-5.864174347	1.18E-06	0.000155
PPP4R4	-3.903869829	1.28E-06	0.000166
MROH2A	-3.748667563	1.28E-06	0.000166
RNY3P8	-3.083470778	1.37E-06	0.000176
AC108751.5	2.085160587	1.44E-06	0.000181
RYR1	-2.742677817	1.43E-06	0.000181
KLK12	-6.011363636	1.44E-06	0.000181
SOX2	-3.639979686	1.50E-06	0.000188
SOSTDC1	-4.194435	1.60E-06	0.000198
AP000424.1	-3.788824386	1.61E-06	0.000198
B3GAT1	-3.379793518	1.69E-06	0.000207
MT1X	-2.472672118	1.74E-06	0.000212
PLA2G4E	-3.865825658	1.77E-06	0.000214
GBP5	-3.232310228	1.78E-06	0.000215
TGFBI	-2.603609923	1.81E-06	0.000216
KRT17P1	-3.09246939	1.83E-06	0.000219
AL354919.2	-3.094876921	1.89E-06	0.000224
AP001505.1	-5.203510915	1.95E-06	0.00023
SHH	-4.086354701	2.05E-06	0.000241

LINC01871	-2.879112493	2.07E-06	0.000241
AC022182.2	-3.730176396	2.07E-06	0.000241
MEFV	-2.640085589	2.16E-06	0.000251
NEFM	-4.405980203	2.21E-06	0.000254
UGT2B28	-4.737730649	2.26E-06	0.000258
AL122017.1	3.220121926	2.34E-06	0.000266
COL22A1	-3.20966787	2.38E-06	0.00027
MAGEA4	-5.727745263	2.41E-06	0.000271
GZMB	-2.831560344	2.46E-06	0.000276
CALB1	-4.15852608	2.51E-06	0.000279
GJB2	-2.77292457	2.58E-06	0.000285
BCL11A	-2.393098114	2.87E-06	0.000311
LINC01121	-2.752371955	2.87E-06	0.000311
NHLH2	-3.721545253	2.88E-06	0.000311
GDPD4	2.535468009	2.92E-06	0.000314
CHP2	-3.739072654	2.96E-06	0.000318
VIM-AS1	-2.327696881	3.07E-06	0.000327
PRF1	-2.573041653	3.12E-06	0.00033
SYT14	-3.370745458	3.36E-06	0.000352
FLG	-3.492303461	3.41E-06	0.000357
SPNS2	2.165466078	3.44E-06	0.000358
AC078788.1	-3.613836793	3.48E-06	0.000362
CADM1	-2.448115532	3.54E-06	0.000363
ATOH8	-2.829044687	3.53E-06	0.000363
SLCO1B3	-6.05324827	3.74E-06	0.000382
AC113383.1	-2.900501067	3.76E-06	0.000382
MTND1P23	-3.584521391	3.86E-06	0.000391
RTBDN	2.971724018	3.87E-06	0.000391
TRBC2	-2.30934756	4.01E-06	0.000403
LAMA3	-3.029452223	4.04E-06	0.000404
RASSF10	-2.540690882	4.10E-06	0.000405
KRT81	-3.794270714	4.07E-06	0.000405
AL135818.2	-2.669888733	4.32E-06	0.000423
ERVFRD-1	2.994795051	4.35E-06	0.000425
DACH2	-3.576471673	4.42E-06	0.000429
AC008011.2	-4.066071794	4.41E-06	0.000429
SULT4A1	-4.35967906	4.49E-06	0.000433
AC005035.1	-3.712216269	4.50E-06	0.000433
HSPA7	-2.089868963	4.54E-06	0.000435
AC011997.1	-2.328132674	4.68E-06	0.000446
COL17A1	-3.166917926	4.73E-06	0.000448
AL133330.1	-2.695318114	4.86E-06	0.00046
ALB	-4.603637111	4.99E-06	0.000469
BEGAIN	-2.266942007	5.09E-06	0.000477

AKR1B10	-3.759414956	5.27E-06	0.000492
AL356215.1	-2.73659178	5.42E-06	0.000502
TMEM72-AS1	2.015120942	5.50E-06	0.000508
NRG1	-3.115516149	5.56E-06	0.00051
SPOCK3	-3.594736965	5.57E-06	0.00051
AFAP1-AS1	-3.737675601	6.17E-06	0.00056
ST8SIA2	-3.418928704	6.23E-06	0.000565
AC011453.1	3.058315573	6.33E-06	0.000572
LINC02323	-2.586427415	6.62E-06	0.000596
KRT16P2	-3.756751728	6.91E-06	0.000618
ADGRD2	-3.899522523	6.94E-06	0.000619
RBP1	-2.343519706	7.11E-06	0.000628
FRMPD4	-4.089699477	7.35E-06	0.000646
G0S2	-2.431726051	7.46E-06	0.000654
LAMB3	-2.176652414	7.49E-06	0.000655
BMPER	-2.31737868	7.55E-06	0.000656
LINC00643	3.449975434	7.85E-06	0.000678
AC130686.1	-2.159521765	8.12E-06	0.000699
SMOC1	-3.0896068	8.26E-06	0.000709
C11orf53	-2.829367747	8.62E-06	0.000736
MTCYBP18	-3.135402166	8.68E-06	0.000737
XDH	-2.163041879	8.84E-06	0.000749
PINLYP	-2.038587587	9.12E-06	0.000764
AK4	-2.178262408	9.10E-06	0.000764
FAM83A-AS1	-2.833141772	9.08E-06	0.000764
VGLL1	2.427341053	9.22E-06	0.00077
ZP1	-2.61580685	9.29E-06	0.000773
RAD51AP2	-3.512851566	9.44E-06	0.000782
DKK4	-3.403875137	9.63E-06	0.000793
AMTN	-4.678779508	9.66E-06	0.000793
SERPINA5	-2.80510705	9.70E-06	0.000794
ATP13A4	2.853522812	9.84E-06	0.000799
DPYD	-2.058037367	9.80E-06	0.000799
AACSP1	-4.223458456	9.83E-06	0.000799
GFI1	-2.093938181	9.99E-06	0.00081
GRP	-3.985914427	1.02E-05	0.00082
IL12RB2	-2.720026552	1.05E-05	0.000842
SLPI	-2.929776292	1.06E-05	0.000842
CLEC4G	-3.087704022	1.05E-05	0.000842
FGG	-5.771079569	1.06E-05	0.000842
MIR205HG	-2.141534633	1.08E-05	0.000858
STAR	-2.354407611	1.09E-05	0.00086
KBTBD12	-3.605749318	1.09E-05	0.00086
AADAC	-3.723907169	1.12E-05	0.000882

AC069366.1	2.68138141	1.13E-05	0.000883
CACNA1B	-3.725992841	1.13E-05	0.000884
FGF19	-6.100637039	1.18E-05	0.000918
SPRR2E	-5.307338853	1.18E-05	0.000919
ASS1	2.170787768	1.20E-05	0.000928
TMEM31	2.161268506	1.21E-05	0.000931
LSP1	-2.198845741	1.31E-05	0.000997
TRBJ2-3	-3.51844333	1.31E-05	0.000997
AC078883.4	-2.644135071	1.33E-05	0.00101
ARID3A	2.004034568	1.37E-05	0.001036
LGR6	-2.692040217	1.39E-05	0.001046
AL160408.1	-3.445237962	1.47E-05	0.001093
LINC01249	-6.199710775	1.49E-05	0.00111
SPINK4	-3.915561217	1.53E-05	0.001133
ADGRG5	-2.290866541	1.56E-05	0.001154
RHCG	-3.235306101	1.58E-05	0.001159
COX6B2	-2.203097728	1.60E-05	0.001175
S100A8	-3.504543415	1.62E-05	0.001186
MUCL1	-3.507556505	1.69E-05	0.001224
HAS2	-2.36731517	1.73E-05	0.001253
PLCH2	-2.216283161	1.78E-05	0.001279
KLRC2	-3.357536855	1.80E-05	0.001289
MCF2	-2.481791994	1.81E-05	0.001295
AL118508.1	-3.002401028	1.89E-05	0.001329
KRT17P2	-3.064496006	1.90E-05	0.001337
HP	-3.81741461	1.96E-05	0.001371
KRT84	-5.260117588	1.96E-05	0.001371
IFNG	-3.213234679	1.98E-05	0.00138
SOST	-4.796476699	1.98E-05	0.00138
CCR3	2.144887908	2.04E-05	0.001409
CAGE1	-2.740288126	2.04E-05	0.001409
WNT3A	-3.040121098	2.04E-05	0.001409
NKX2-1	-5.548537478	2.05E-05	0.001412
RGS9BP	2.161096297	2.16E-05	0.001475
LGALS9C	-3.091427922	2.19E-05	0.001492
PAX7	-5.876108883	2.19E-05	0.001492
CGB3	3.414581035	2.22E-05	0.001502
MOGAT2	-3.574893348	2.22E-05	0.001502
AL035446.1	-3.267201488	2.25E-05	0.00152
MT1G	-2.373078807	2.32E-05	0.001559
VAX1	-5.142383939	2.39E-05	0.001603
MYLK4	-2.370553387	2.42E-05	0.001616
DPY19L2P1	-2.824846592	2.41E-05	0.001616
S100A12	-2.976297018	2.43E-05	0.001617

TPTEP1	-2.868495013	2.50E-05	0.001654
FOXG1	-5.851647518	2.52E-05	0.001664
TMPRSS11A	-3.338869379	2.53E-05	0.001666
CLDN6	3.39486995	2.54E-05	0.001667
SST	-5.9593918	2.57E-05	0.00168
GDNF	-2.395388803	2.61E-05	0.001701
EFHD1	2.290675754	2.63E-05	0.00171
CASP1P2	-3.27073107	2.67E-05	0.001729
SLC30A10	-3.547641401	2.68E-05	0.001729
ROS1	-3.89145916	2.68E-05	0.001729
B4GALNT2	-4.143023017	2.68E-05	0.001729
KEL	-2.428544829	2.72E-05	0.001748
WARS	-2.003260858	2.74E-05	0.001756
ARSJ	-2.183696268	2.78E-05	0.001757
ADGRB1	-2.25297352	2.79E-05	0.001757
CDH2	-2.61626594	2.79E-05	0.001757
TMPRSS11E	-3.095261742	2.82E-05	0.001769
KLK6	-4.375023412	2.84E-05	0.001777
AC108136.1	-2.693638205	2.88E-05	0.001803
IGFL3	-5.195190716	2.90E-05	0.001806
SPRR2F	-4.772274344	2.91E-05	0.001808
BARX1	-3.262121908	3.03E-05	0.001863
KRT32	-4.14105293	3.02E-05	0.001863
DNAI1	2.62151024	3.05E-05	0.001873
AC097478.1	-3.343422612	3.13E-05	0.001915
CDH12	-4.875518101	3.14E-05	0.001919
DUOX2	-2.646471759	3.17E-05	0.001932
SPINK5	-2.434765821	3.20E-05	0.001936
CLEC12A-AS1	-3.993949979	3.20E-05	0.001936
MT1H	-2.702155741	3.23E-05	0.001951
OCA2	-4.170782675	3.29E-05	0.001977
TKTL1	-4.318271001	3.53E-05	0.002108
SLC35F3	-3.231436534	3.57E-05	0.002128
ADD2	-2.831637763	3.61E-05	0.002143
LINC02195	-2.692525731	3.65E-05	0.002154
SIGLEC12	-2.592140858	3.67E-05	0.002166
RN7SL684P	-3.084411846	3.68E-05	0.002168
WIF1	-4.590117189	3.71E-05	0.002179
FLG-AS1	-2.236460218	3.73E-05	0.002183
CD209	-2.338856831	3.75E-05	0.002185
AL671277.1	-2.386190378	3.75E-05	0.002185
LINC01550	-2.345107428	3.83E-05	0.002221
TUSC5	-5.243279461	3.83E-05	0.002221
SFTPD	-2.254820543	3.84E-05	0.002223

FAM131B	-2.060506839	3.89E-05	0.002243
LINC00520	-3.434303917	3.94E-05	0.002269
CASP5	-2.731656235	3.98E-05	0.002285
WNT5A	-2.115988321	4.02E-05	0.002296
ALOXE3	2.306080183	4.08E-05	0.002322
AC023906.2	-4.175428023	4.08E-05	0.002322
MMP9	-2.582671135	4.10E-05	0.002331
LGALS7	-4.832441389	4.38E-05	0.00247
LINC01268	-2.281167908	4.40E-05	0.002478
AC131097.3	-2.542190505	4.44E-05	0.002494
LEMD1	-3.101577461	4.46E-05	0.002501
AL357833.1	2.8808956	4.47E-05	0.002503
LDHAL6A	-3.549487376	4.48E-05	0.002503
AC091182.2	-2.805996974	4.51E-05	0.002512
NKG7	-2.258020851	4.55E-05	0.002528
AMOT	2.228553688	4.59E-05	0.002543
CTLA4	-2.05810334	4.61E-05	0.002549
FXYD2	-2.333390466	4.62E-05	0.002549
BLACAT1	-2.592450532	4.63E-05	0.00255
LRRC38	-4.209845379	4.66E-05	0.002559
TRDC	-2.303893023	4.75E-05	0.002602
CYP4X1	-2.204944299	4.78E-05	0.002612
UTS2	-2.840021232	4.81E-05	0.00262
IL1A	-2.619513427	4.85E-05	0.002634
ACVR1C	-2.133499553	4.98E-05	0.002693
TM4SF19	-2.895994657	4.98E-05	0.002693
HLA-U	-2.145427329	5.15E-05	0.002779
APCDD1L-AS1	-2.941195892	5.17E-05	0.002779
LGSN	-4.440051147	5.16E-05	0.002779
MT2A	-2.280543713	5.25E-05	0.002811
SCIN	2.141074006	5.41E-05	0.002863
HR	-2.011124713	5.40E-05	0.002863
NDUFA4L2	-2.289554643	5.39E-05	0.002863
MARCO	-2.913708148	5.41E-05	0.002863
AL096829.2	-2.666948613	5.53E-05	0.002913
DCAF4L2	-8.492541663	5.56E-05	0.002917
AC090409.1	-2.239804378	5.58E-05	0.002923
FAM181B	-2.283654619	5.59E-05	0.002923
ISM2	2.353028795	5.63E-05	0.002928
LILRP2	-3.113867177	5.62E-05	0.002928
LBP	-2.917029877	5.82E-05	0.003017
EDN2	-2.545039683	5.85E-05	0.003018
GREB1L	2.655310767	5.97E-05	0.003068
CCL20	-2.761489105	5.97E-05	0.003068

LYPD1	-2.073640835	6.08E-05	0.003111
LINC00479	2.110585104	6.13E-05	0.003132
S100B	-2.009676078	6.15E-05	0.003136
SELL	-2.507884352	6.16E-05	0.003136
LAMC2	-2.398771908	6.37E-05	0.003232
GZMA	-2.301238976	6.50E-05	0.003291
FGA	-5.95181005	6.72E-05	0.003394
LRP2	2.649493299	6.77E-05	0.003408
STEAP1B	-2.811579644	6.77E-05	0.003408
AC004687.1	-2.138520765	6.85E-05	0.003435
NTSR1	-3.275369338	6.86E-05	0.003435
AK5	-2.280890138	6.89E-05	0.003442
CXCL11	-2.876488231	6.96E-05	0.003469
NPW	-2.290096443	7.07E-05	0.003504
CD70	-2.507222808	7.11E-05	0.003519
MT2P1	-2.490416168	7.16E-05	0.00353
TDRD9	-2.882206985	7.17E-05	0.003531
LINC00944	-2.763067215	7.28E-05	0.00358
USP30-AS1	-2.090049005	7.46E-05	0.003647
DMBT1	-3.256035127	7.47E-05	0.003647
AC100801.1	-5.074731115	7.50E-05	0.003656
UCHL1	-2.617883871	7.51E-05	0.003656
CCL4	-2.090568106	7.70E-05	0.003726
MSTN	-2.608274745	7.74E-05	0.003736
EREG	-3.141934464	7.77E-05	0.003745
AC112251.1	-4.827046051	7.86E-05	0.003777
LINC00327	-2.52203689	7.90E-05	0.003789
CALR4P	2.085896931	7.95E-05	0.003802
FASLG	-2.35952689	7.94E-05	0.003802
FIGNL2	2.511678841	8.00E-05	0.00382
GABRG2	-5.524845148	8.03E-05	0.00382
GFI1B	-3.484130957	8.06E-05	0.003823
NPPC	-2.982353859	8.09E-05	0.003825
CNR1	-2.672332004	8.34E-05	0.003927
IGKV1-12	-3.559685548	8.36E-05	0.003931
OSBPL6	-2.248799725	8.40E-05	0.003941
LINC01564	-2.457041623	8.50E-05	0.003977
AL034346.1	-2.476012724	8.50E-05	0.003977
SPAG6	-2.876547823	8.64E-05	0.004024
PRTG	2.023740454	8.68E-05	0.004033
CD44-AS1	-2.008560434	8.76E-05	0.004068
MIA	-2.933358664	8.96E-05	0.004121
AC226118.1	-3.324619362	9.09E-05	0.004165
C16orf54	-2.202908441	9.10E-05	0.004166

LYPD2	-3.622130376	9.16E-05	0.004183
SPINK6	-4.227773418	9.16E-05	0.004183
PCDHA1	-3.259314162	9.42E-05	0.004285
WNT5A-AS1	-2.113452335	9.45E-05	0.004293
AC010735.2	-2.118534077	9.47E-05	0.004295
AL033381.2	-4.373260936	9.50E-05	0.004303
CROCC2	-2.917803834	9.57E-05	0.00432
CHRNA9	-3.680609968	9.56E-05	0.00432
ARC	-2.231234199	9.74E-05	0.004394
FAT2	-2.47550085	9.83E-05	0.004419
MTCO1P40	-2.446596776	0.0001	0.00449
RASSF9	-2.416473049	0.000102	0.004539
AC036176.3	-3.16939908	0.000102	0.004539
DPP10-AS1	-5.931053882	0.000103	0.00457
AL033519.3	2.631073924	0.000103	0.004573
CCL23	-2.452243614	0.000105	0.00462
LAG3	-2.110224594	0.000109	0.004778
AC026782.2	-3.240779178	0.000109	0.004778
AC002384.1	-2.777926382	0.000109	0.004788
IL20RB	-2.565726449	0.00011	0.004794
FDCSP	-3.840551838	0.00011	0.004794
CTSE	-3.287671773	0.000111	0.004843
RARRES1	2.526014731	0.000117	0.005051
CXCL2	-2.343978087	0.000119	0.005115
AC005722.2	-3.709461606	0.000121	0.005185
NEFH	-2.191305665	0.000122	0.005234
CCL13	-2.375278828	0.000123	0.005247
AP005117.1	-3.872890084	0.000124	0.00526
CDH8	-2.18781003	0.000124	0.00526
ASPG	-2.437292387	0.000124	0.00526
RAET1L	-2.731597101	0.000124	0.00526
NLRP3P1	-2.295143606	0.000128	0.005382
AC005532.1	2.158341359	0.000128	0.005383
ALDOB	-2.941779659	0.00013	0.005434
PLA2G4D	-2.279414184	0.000132	0.00551
AL683807.1	-2.375847683	0.000135	0.005606
GSTM1	-3.78522604	0.000137	0.005641
TGM3	-2.877530452	0.000139	0.005703
KLK14	-2.581278178	0.00014	0.005718
NGFR	-2.403102406	0.00014	0.005727
AL161630.1	-4.744423159	0.000141	0.005736
AC011473.4	-5.52506497	0.000142	0.005785
KIT	-2.188992785	0.000143	0.005791
RPSAP52	-2.812100918	0.000143	0.005791

AC099066.2	-2.382618352	0.000145	0.005846
GPR15	-2.841406133	0.000146	0.00585
UGT2A1	-4.11955576	0.000146	0.00585
AC011632.1	-3.655829248	0.000147	0.005903
PGLYRP4	-2.911869437	0.000149	0.005947
AP000439.3	-4.127922117	0.000149	0.005947
TTC4P1	4.200277063	0.00015	0.005987
LINC00456	2.677610792	0.000151	0.005987
SERPINB7	-3.399459231	0.00015	0.005987
AC023794.3	-2.510559002	0.000153	0.006049
CYP11A1	2.76944053	0.000154	0.006057
SULF2	-2.014164903	0.000154	0.006057
DNAI2	-2.596800432	0.000154	0.006057
LGALS17A	-3.24452801	0.000153	0.006057
DSCAM	-3.832774362	0.000157	0.00618
CD69	-2.070715999	0.00016	0.006245
SERPINB11	-4.064933119	0.000162	0.006286
GRIN2A	-2.80169566	0.000163	0.006316
AC010307.4	-3.047872246	0.000164	0.006367
TMSB15A	-2.2757969	0.000165	0.006378
PNCK	-2.613090501	0.000165	0.00639
ART3	-2.376236879	0.000166	0.006395
ADH4	-2.761438399	0.000166	0.006395
AC021218.1	-2.912986827	0.000167	0.006404
BPIFB4	-3.863353261	0.000168	0.006431
GPR25	-2.649041732	0.000169	0.006454
ADIPOQ	-5.902584602	0.000172	0.006495
CYP26B1	2.063969736	0.000175	0.006566
LINC02159	-2.783315633	0.000174	0.006566
HSD3B1	4.107666237	0.000177	0.006625
LINC00923	-3.229811329	0.000178	0.006652
BMPR1B	-2.588897934	0.000183	0.006799
AC013264.1	-2.939230381	0.000184	0.006807
EYA1	-2.212068585	0.000185	0.00682
AC010275.1	-3.951680283	0.000185	0.00682
LCE3E	-5.531217635	0.000185	0.00682
C8orf74	-2.969085792	0.000187	0.006852
LINC00973	-5.160908505	0.000191	0.006981
AC006058.1	-2.52277978	0.000193	0.007055
LINC01807	-4.160438551	0.000196	0.007152
CHODL	-2.39550201	0.000198	0.007192
KCNQ5	-2.899086267	0.000198	0.007192
MICD	-3.423705844	0.0002	0.007263
RBMS3-AS3	-3.15723637	0.000201	0.007266

C2orf72	2.670235117	0.000202	0.007289
PLEKHG4B	2.636775161	0.000205	0.007349
AC113346.1	-3.0106194	0.000204	0.007349
CYP1A2	-4.701803217	0.000207	0.007404
TM4SF4	3.72584061	0.000208	0.007424
SLCO5A1	-2.225919991	0.00021	0.007453
PLA2G2A	-2.79637978	0.000211	0.007498
AC007991.2	-4.082310733	0.000214	0.007575
LHX9	-2.772562952	0.000215	0.007614
CSF2	-2.499033494	0.000216	0.00763
TSGA10IP	-2.655692998	0.000219	0.007709
HTR3A	-3.600246635	0.000221	0.007739
TREML2	2.12314735	0.000221	0.007746
AL499606.1	-2.800562684	0.000221	0.007747
OTOF	-2.124604335	0.000228	0.007953
UBD	-2.621199469	0.000228	0.007953
SAA1	-2.961223929	0.000236	0.008203
IGLC7	-3.163716424	0.000239	0.008288
ANKUB1	-2.834693747	0.000241	0.00831
CLCA3P	-2.539420124	0.000247	0.008496
CHGB	-2.464475082	0.000247	0.008505
CDSN	-4.258521882	0.000252	0.00865
AC112206.3	-3.241972976	0.000253	0.008666
ALDH1A1	-2.274880452	0.000257	0.008742
AC092384.2	-2.463485392	0.000257	0.008752
LINC01901	-4.121086079	0.000262	0.008874
IGHV2-70	-3.218511814	0.000263	0.008902
PAX5	-2.425533713	0.000265	0.008975
PRKAG3	-3.225095535	0.000267	0.009001
APOA1	-2.633835727	0.000272	0.00913
SOAT2	-2.404775553	0.000275	0.009202
AC010735.1	-2.711923517	0.000279	0.00928
PTX3	-2.316679002	0.000284	0.009416
SLCO6A1	-3.017635274	0.000289	0.009531
PIWIL3	4.143800326	0.000297	0.009776
LINC01139	-3.571626937	0.000297	0.009776
ARHGEF4	-2.029145158	0.000303	0.009894
AC023157.1	-2.508828523	0.000302	0.009894
KRT3	-2.632006967	0.000302	0.009894
AL160408.4	-3.331728811	0.000302	0.009894
WFDC12	-4.423277806	0.000304	0.009896
FABP5P7	-2.118041447	0.000306	0.009969
IL13RA2	-2.281999003	0.000307	0.009976
AC078993.1	-2.585081902	0.000308	0.009984

ZNF385B	-2.727871412	0.000309	0.009984
C6orf15	-4.448935157	0.000309	0.009984
CD1A	-2.204181093	0.000312	0.010031
SMIM2	2.15031704	0.000313	0.01004
DUSP27	-3.481219971	0.000314	0.010074
RPTN	-4.351627163	0.000317	0.010141
IQCA1	-2.103696661	0.000318	0.010154
PRRT4	-2.062532316	0.000321	0.010205
TRGC2	-2.064472685	0.000324	0.010289
STMN2	-2.768206868	0.000324	0.010305
ZFHX4-AS1	-2.974464603	0.000327	0.010342
TMEM82	2.687808838	0.000329	0.010386
JPH3	-2.485384147	0.000339	0.010666
TNIP3	-2.214671859	0.000341	0.010699
SCN2A	-2.452538231	0.000342	0.010723
CD38	-2.024347484	0.000344	0.010775
NAA11	-4.937315577	0.000346	0.010806
TBX18	-2.255829348	0.000347	0.010813
LCE1C	-4.291021459	0.000347	0.010813
TAGLN3	-2.718031616	0.000351	0.010908
SERPINA3	-3.041961748	0.000357	0.011053
HRASLS2	2.723920991	0.000357	0.011062
SLCO1A2	-2.863250472	0.000358	0.01107
AL023754.1	-4.17119933	0.000364	0.011185
FAM9C	4.164361946	0.000365	0.01119
AC106865.1	-2.279145256	0.000367	0.011205
AC018552.3	-2.919190862	0.000369	0.011241
AL033384.1	-2.992511811	0.000368	0.011241
SSTR5-AS1	-4.116227336	0.00037	0.011241
DDX53	-5.304465043	0.000369	0.011241
CES1	-2.660528766	0.000373	0.011285
PROKR2	4.975652203	0.000375	0.011332
BTG4	-3.439804063	0.000383	0.011439
NNAT	-2.530886608	0.000385	0.011447
NTRK2	-2.29005608	0.00039	0.01151
AC016717.2	-2.930230469	0.000393	0.011577
PEG10	2.497191753	0.000396	0.011606
AC007384.1	-2.130348639	0.000396	0.011606
SFTA1P	-2.648212852	0.000404	0.011838
AC128709.1	-2.88692417	0.000417	0.012135
ALDH1L1	-2.152528383	0.000419	0.012148
AC106799.3	-4.621008677	0.000419	0.012153
CSF3	-2.942516727	0.000425	0.012276
DLX2	-2.511700594	0.000427	0.012296

MYL7	-3.951400592	0.000429	0.012328
UGT1A1	-2.839740463	0.000432	0.012391
PROX1-AS1	-3.238741339	0.000434	0.012417
LEFTY1	-2.342774508	0.000435	0.012448
AC004870.2	-5.090194783	0.000436	0.012451
SLC6A14	-2.760519622	0.000437	0.012476
PCDHA10	-2.295216525	0.000438	0.012482
SPRR2A	-3.446489781	0.000438	0.012486
SIGLEC14	2.414498535	0.00044	0.012524
AC078880.3	-3.069369753	0.00044	0.012525
ORM1	-3.902661073	0.000442	0.012563
DLX3	2.23304294	0.000445	0.012629
AADACP1	-2.989117149	0.000448	0.012664
PTPRN	-2.288977936	0.000448	0.012672
C11orf87	-3.661616498	0.000451	0.012741
SH2D5	-2.374800516	0.000452	0.012753
AL390755.1	-4.175162427	0.000454	0.012766
GJB6	-2.053419075	0.00046	0.012891
AC040174.2	-3.257158225	0.000467	0.012993
SMLR1	2.790485732	0.000471	0.013069
AC073115.1	3.150676691	0.000473	0.013095
CEACAM4	-2.007535662	0.000472	0.013095
MIR221	-2.404799119	0.000473	0.013095
RNF17	-2.4298492	0.000483	0.013231
PPARGC1A	-2.547206323	0.000483	0.013231
AC007991.4	-3.763515208	0.000486	0.013278
PRODH	-2.02123723	0.000488	0.013317
DPP10	-4.069329733	0.000489	0.013341
PAX3	-4.078254266	0.000492	0.013373
AC016397.2	-2.414852465	0.000495	0.013441
LINC00942	-2.178037456	0.000497	0.01345
VTA1P1	-3.399990172	0.000506	0.013657
SORCS2	-2.07738025	0.000508	0.013682
AC087783.2	-3.029227162	0.000508	0.013687
KRT82	-3.523355605	0.000511	0.013738
LINC01714	2.279108976	0.000512	0.013761
GNG4	-2.416559004	0.00052	0.013845
KHDC1L	-3.615941801	0.00052	0.013845
OR2I1P	-2.506981021	0.000525	0.013928
C14orf39	-2.847764971	0.000525	0.013928
ARHGDIG	-2.955263949	0.000533	0.014078
FMO3	-2.006835214	0.000538	0.014148
ZNF683	-2.207189203	0.000546	0.014295
LINC01615	-2.205693314	0.000551	0.014427

TMPRSS4	-2.093949503	0.000558	0.014524
LINC01088	-2.161233582	0.000574	0.014905
AP003174.1	-4.754438798	0.000575	0.014909
C5orf66-AS1	-2.150958499	0.000576	0.014914
CNTNAP5	-3.670108683	0.000578	0.014935
MTND4P24	-2.662105367	0.000579	0.014948
HSPB3	-3.163992678	0.000582	0.015001
TMEM179	-2.950972145	0.000584	0.015036
MTCO3P12	-2.004723602	0.000586	0.015048
HLA-V	-2.065795798	0.000593	0.015181
TLL1	-2.172648734	0.000596	0.015237
LINC01583	-3.555156022	0.000616	0.015607
CCL24	-2.350944623	0.000619	0.015633
TNFRSF19	-2.107151752	0.00062	0.015653
TPRXL	-2.281232639	0.000623	0.015687
CXCL10	-2.327885285	0.000625	0.015717
SLC6A10P	-4.643165337	0.000626	0.015717
SCN5A	-2.075366013	0.000628	0.015742
TTC24	-2.272032146	0.000629	0.01576
KIF1A	-2.945025369	0.000631	0.015787
DTHD1	-2.145785077	0.000636	0.015903
PTPN20CP	-2.829174383	0.000646	0.016069
AC068647.2	-3.586063925	0.000647	0.016089
LINC02345	-2.013276199	0.00065	0.016105
GJA3	-2.254784457	0.000649	0.016105
LINC00930	-2.919831666	0.000655	0.016197
NGB	-3.239320309	0.00066	0.0163
PCYT1B	-2.197392293	0.000673	0.016492
LINC00943	-2.745309865	0.000679	0.016608
EGOT	-2.411562153	0.00068	0.016614
BPIFA1	-4.480019881	0.000688	0.016758
CFHR1	-3.420363582	0.000691	0.016826
LINC01115	-3.565036449	0.000692	0.016826
SYT12	-2.077149111	0.000698	0.016917
SPANXB1	-6.324343505	0.000698	0.016917
ALOX12B	-2.209491452	0.000702	0.016974
FTLP15	3.464269373	0.00071	0.017115
AC005064.1	-3.628388653	0.000712	0.017142
AL357507.1	-4.49703446	0.000714	0.017173
IGFN1	-2.602933208	0.000718	0.017208
CAPN6	2.928906569	0.000721	0.017229
MSLN	-2.771378798	0.000728	0.017359
AP000696.1	-2.708275708	0.00073	0.017406
UGT1A9	-2.896353918	0.000731	0.017408

SERPINA9	-3.962578776	0.000737	0.017509
TBC1D3D	-4.861244717	0.000754	0.017839
KCNJ18	-4.177834455	0.000785	0.018339
IGHV2-5	-2.771669251	0.000788	0.018362
PAK5	-3.219461608	0.000789	0.018378
SLC19A3	2.098494251	0.000794	0.018445
AC122710.3	-2.150159181	0.000799	0.018491
SPINK7	-2.890234712	0.000801	0.018497
LURAP1L-AS1	-3.222787205	0.0008	0.018497
CT83	-5.755865453	0.000804	0.018549
TF	-2.177163563	0.000823	0.018916
TRBV30	-2.272530471	0.000828	0.018987
AC022274.1	-2.545460904	0.000829	0.018988
MPPED1	-3.630186263	0.000833	0.019028
SLC13A5	-2.046312188	0.000837	0.019065
FGF20	-4.042670438	0.000838	0.019065
CTCFL	-4.205133855	0.000839	0.019065
HKDC1	-2.363067764	0.000861	0.019475
GZMH	-2.027690147	0.000864	0.019514
GBP6	-2.443929703	0.000882	0.019811
CA8	-2.235051537	0.000886	0.019868
BX324167.1	-2.909637899	0.000889	0.019903
AC093627.6	-2.853609829	0.000894	0.019969
AC019171.1	-2.00314279	0.000897	0.020017
OR9A4	-3.815901455	0.000902	0.020073
AC005009.1	-2.485985253	0.000907	0.020151
DNER	-2.700440762	0.000911	0.020216
MT1M	-2.101774376	0.000914	0.020232
LINC01215	-2.147973316	0.000921	0.020325
IL22RA2	-2.390230732	0.000921	0.020325
DUOXA2	-2.39468372	0.000921	0.020325
RPS4XP23	-2.369597255	0.000925	0.020338
LINC01854	-5.043544796	0.000931	0.020452
SCN11A	-2.033078927	0.000956	0.020855
AC020922.1	-2.862616098	0.00096	0.020901
LINC01546	-2.184114032	0.000973	0.021145
IL33	-2.052444648	0.000981	0.021218
SGCG	-2.568777855	0.000979	0.021218
PYDC1	-3.502470347	0.000997	0.02148
AP000904.1	-3.701718137	0.00101	0.02165
C15orf53	-2.680153743	0.001012	0.02169
MED15P9	-4.547171036	0.00102	0.021817
FAM83A	-2.073891931	0.001028	0.021953
U8	-2.129827763	0.001029	0.021953

LINC00221	-6.104305706	0.001035	0.022004
FCGR3B	-2.077639354	0.001045	0.022162
AC010754.1	-2.364486876	0.001054	0.022284
AC002454.1	-2.400210725	0.001074	0.022575
AL157931.1	-4.011689286	0.001097	0.022899
AC104078.1	-2.880726345	0.001101	0.022947
SAGE1	-4.832578738	0.001115	0.023116
LRP1B	-2.517881658	0.00112	0.023174
KNG1	-4.145317246	0.001128	0.023269
LINC01998	-3.234959836	0.001132	0.02333
EEF1DP5	-3.886933066	0.001134	0.023371
FGF5	-2.628291395	0.001141	0.02345
TCN1	-2.769403933	0.001141	0.02345
GAL3ST1	2.058629083	0.001142	0.023454
AC243829.4	-2.288474679	0.001153	0.023598
LGALS9B	-2.799105077	0.00116	0.023725
CXCL1	-2.087383272	0.001191	0.024172
AP005264.1	-2.307841266	0.001191	0.024172
SPRR2C	-5.694033218	0.00119	0.024172
SLC27A6	2.626284615	0.001194	0.024208
PNLIPRP3	-4.723733517	0.001196	0.024224
AP005131.2	-2.220388287	0.00121	0.024384
AC078880.5	-2.81369498	0.001213	0.024384
SAA2-SAA4	-3.21467226	0.001215	0.024384
CES1P1	-3.343941333	0.00121	0.024384
AC010894.5	-2.361984437	0.00122	0.024465
MESP1	2.065763465	0.001227	0.024516
GAP43	-2.315361694	0.001228	0.024516
MIR3681HG	-2.521616619	0.001245	0.024753
SH3GL2	-2.863609857	0.001247	0.024768
C1orf68	-4.557211476	0.001248	0.024768
AC126768.2	-3.016196415	0.001252	0.024796
PHACTR3	-2.005128507	0.001255	0.024804
LINC02086	-2.077544089	0.001261	0.024873
AC017048.3	-2.22287428	0.001263	0.024903
LINC02242	-3.638575721	0.001264	0.024903
AL591468.1	-3.27541953	0.001277	0.025082
PTCHD3	-3.704990025	0.001279	0.025103
MTCO2P16	-3.026755706	0.001292	0.025205
MIR27B	-3.07009666	0.001297	0.025267
AC000032.1	-4.454225176	0.001297	0.025267
CRNN	-4.566652309	0.001301	0.025288
LINC02152	-5.146498055	0.001306	0.025298
AC022872.1	2.154584857	0.001308	0.025316

AC012501.1	-3.234709724	0.001313	0.025378
MRGPRX3	-3.860190882	0.001315	0.025389
AC083805.1	-2.478101707	0.001329	0.025593
C8orf89	-2.475150707	0.00135	0.025872
AC004241.4	-2.05733952	0.001366	0.026108
CLDN10	-2.437749977	0.00138	0.026325
CXCR2P1	-2.278832818	0.001388	0.02642
TRPM8	-2.05690014	0.001389	0.026433
ATP12A	-2.722551922	0.00139	0.026433
AP001999.1	-3.377098213	0.001403	0.026627
TRGV10	-2.099963354	0.001408	0.026678
AL021877.2	-3.185478727	0.001431	0.027006
AL035252.2	-3.242637995	0.001431	0.027006
AP003486.1	-2.036031874	0.001433	0.027026
ERVH48-1	3.074584993	0.001442	0.027124
LINC01338	-2.19407131	0.001446	0.027187
RPRM	-2.049382292	0.001491	0.027729
IGLV3-27	-2.671929349	0.001503	0.027888
AL645939.5	-3.01897623	0.001504	0.027897
AC092769.1	2.633686769	0.001515	0.027981
IRX6	-2.982863267	0.001514	0.027981
BEND4	-2.186600726	0.001522	0.028038
DLX1	-2.190179097	0.00152	0.028038
AC010998.3	-2.979089029	0.001519	0.028038
KRT72	-2.815173815	0.001533	0.0282
IGKV1OR2-6	-3.141036558	0.001538	0.028244
FAM19A4	-3.517239962	0.001549	0.028377
KLRC4	-2.502795572	0.001552	0.02841
PROK2	-2.197958782	0.001567	0.028554
WFDC5	-2.56995252	0.001569	0.028554
AC055854.1	-2.748400555	0.001565	0.028554
AC114786.3	-3.30674798	0.001562	0.028554
AL139246.4	-2.15979804	0.001585	0.028783
SLC2A2	-3.849144184	0.001595	0.028877
GUCA1A	-2.212504427	0.001601	0.028932
CFAP77	-2.352578634	0.001604	0.028932
FAM133A	-3.264086508	0.001602	0.028932
SLITRK4	-2.150879745	0.001609	0.028966
CCDC185	-2.244157146	0.001626	0.029237
PIWIL1	-2.720090889	0.001628	0.029257
AL772337.1	-3.11229497	0.00163	0.029264
HMP19	-2.66265529	0.001642	0.029409
LINC00626	-3.627922349	0.001649	0.029503
NAP1L6	-2.852970069	0.001659	0.029614

C20orf166-AS1	-2.348056567	0.001674	0.029773
AC010280.2	-2.412794475	0.001678	0.029778
TFPI2	-2.103567256	0.001686	0.029863
PTPRT	-2.340193378	0.001703	0.030089
DNAH11	-2.296247633	0.001713	0.030167
NYAP2	-2.562052013	0.001711	0.030167
C7orf65	-2.853930504	0.001715	0.030173
LCE3D	-4.975246654	0.001723	0.030225
AL136088.1	-2.904753996	0.001733	0.030388
AF106564.1	-3.359400127	0.00174	0.030477
KRT34	-2.673873177	0.001755	0.030592
LINC02029	-2.462951148	0.001766	0.030708
BCHE	-2.043495909	0.001774	0.030824
PRAME	-3.264233492	0.001776	0.030847
UGT2B17	-2.663056319	0.00178	0.030903
AF274855.1	-3.743314763	0.001798	0.031112
CGA	2.761665289	0.001802	0.03115
AC026495.1	-3.267938261	0.001807	0.031209
PPY	2.578306048	0.001812	0.031269
ELFN2	-2.301846293	0.001826	0.031432
AC022075.2	-2.277066219	0.001829	0.031453
TM4SF19-TCTEX1D2	-2.057788564	0.001832	0.031463
MS4A8	-3.623454128	0.001834	0.031463
TUBA3E	-3.872424005	0.001832	0.031463
XIST	-3.590899771	0.001837	0.031493
CXCL13	-2.125770406	0.00185	0.031673
AC105460.1	-4.633704537	0.001854	0.031688
AL355601.1	-3.607074322	0.001863	0.031794
C11orf44	-3.232783217	0.001874	0.031914
ELANE	-2.371844915	0.001877	0.031947
AL391704.1	-4.35343115	0.001902	0.032232
AC012498.2	-3.608795	0.001906	0.032263
BOK-AS1	-3.528100575	0.001916	0.032358
AKR1C2	-2.037094798	0.001944	0.032759
CALML5	-3.04998459	0.001981	0.033212
VSTM2L	2.018537637	0.002003	0.033467
DEFB1	-2.151400118	0.002013	0.033586
MT1A	-2.192072549	0.002016	0.033617
C20orf141	-3.68061537	0.002022	0.033696
SPRR4	-3.279271782	0.002025	0.033697
AL355596.1	-2.33196447	0.002032	0.033766
CPB1	-3.199263939	0.00203	0.033766
CD36	-2.0449001	0.002067	0.034248
GPR142	-2.677664964	0.002069	0.034248

AL139095.3	-3.24302511	0.002069	0.034248
SLC22A31	-2.274606048	0.002074	0.034278
AC234772.3	-2.132363547	0.002076	0.03429
C1orf186	-2.1607558	0.00208	0.03434
AC110618.1	-2.089401194	0.002091	0.034494
SGK2	2.052175716	0.002098	0.034555
IGLV1-51	-2.064534816	0.0021	0.03457
LINC00504	-2.612009996	0.00211	0.034628
MIR23B	-3.3179136	0.002111	0.034628
AFP	-3.434022606	0.00211	0.034628
CALHM3	-2.281459843	0.00212	0.03473
AC009955.2	-2.322060601	0.002139	0.034964
CTAGE12P	-2.566392107	0.002142	0.034984
AL022342.1	-2.288214303	0.002151	0.035045
KLK7	-3.581456291	0.00221	0.035757
PRSS33	-3.0109695	0.00222	0.035851
CHL1	-2.164389566	0.002224	0.035871
AP000943.2	-3.076703738	0.002223	0.035871
PIGR	-2.550495839	0.002234	0.035987
MUC21	-2.855304318	0.002241	0.036002
FGB	-4.078684959	0.002244	0.03602
AC120036.2	-2.007587943	0.002254	0.036067
FAM163B	-2.256908711	0.002261	0.036067
AC025016.1	-4.901165626	0.002265	0.036072
CLRN3	-2.348531893	0.002285	0.036306
AC079630.2	-3.110543564	0.002288	0.036306
IGKV1D-33	-3.673576048	0.002296	0.036411
LINC02450	-2.213810905	0.002303	0.036457
ZFP57	-2.76325187	0.00231	0.036561
TGFB2-AS1	-2.082252694	0.002322	0.03669
SDR9C7	-2.28576258	0.002334	0.036796
VCX3A	-2.9238814	0.002334	0.036796
MT1P3	-3.167606008	0.002353	0.03698
ACTBL2	-2.83079711	0.002363	0.037087
TMPRSS11F	-3.774737603	0.002376	0.03722
AGMO	-2.344736763	0.002382	0.037274
LINC01698	-2.809265813	0.002411	0.037561
AC025884.1	-2.726311824	0.002415	0.037589
BCAR4	2.852891994	0.00243	0.037717
IGLV1-40	-2.27405514	0.00245	0.037948
PI16	-2.346533126	0.00246	0.038067
FLJ42969	2.240854592	0.002465	0.038103
CYP4Z1	-2.001050141	0.002479	0.038217
DBET	-2.875626509	0.002501	0.038418

FOXN1	-2.105651499	0.002506	0.038422
RTL1	-4.366691696	0.002511	0.038456
CCAT1	-3.171071714	0.002518	0.038517
NFE4	-2.781668169	0.002531	0.038648
IFNK	-4.810385681	0.002543	0.038798
AC087672.3	-2.031383764	0.002546	0.038836
AC091173.1	-2.948306777	0.00255	0.038862
AL121949.1	-3.98013946	0.002558	0.038914
AC092811.1	-2.417286837	0.002566	0.038957
AC007907.1	-3.490686389	0.002565	0.038957
KLK8	-3.586291633	0.002571	0.038994
FCRL5	-2.05554166	0.002583	0.039121
IGHV4-4	-2.65673949	0.002584	0.039121
KCNA1	-3.454988932	0.002633	0.039563
MIR548XHG	-4.012679706	0.002634	0.039563
AC024337.1	2.776634605	0.002638	0.03958
KC6	-2.643713248	0.002647	0.039623
MUC16	-2.647970979	0.002654	0.039691
PENK	-2.670613156	0.002653	0.039691
AL136018.1	-3.78779298	0.002693	0.040106
AC015656.1	-2.794219883	0.0027	0.040194
RPE65	-3.37055988	0.002711	0.04029
RPS16P9	2.785560189	0.002726	0.040357
CHRNA4	-3.274137138	0.002735	0.040479
IGKV3D-15	-2.522969235	0.002762	0.040809
LOR	-3.024709153	0.002782	0.040967
AC012174.1	-2.417505106	0.002804	0.041174
AC122685.1	-4.30721626	0.002815	0.041244
AC016769.3	-2.626151786	0.002829	0.041409
TTLL11-IT1	-2.131544199	0.002841	0.041563
AIPL1	-2.906691293	0.002857	0.041665
SERPINA10	-2.854826012	0.002876	0.041831
AC093833.1	-2.780668837	0.00288	0.041861
LUCAT1	-2.042351162	0.0029	0.042006
GABRG3	-2.774947062	0.00291	0.042046
AC037486.1	-2.696172146	0.002921	0.042141
GOLGA6L7P	-3.315384229	0.002932	0.042261
LPA	-2.374788335	0.002941	0.042302
SPRR2B	-4.641805409	0.002938	0.042302
LINC01792	-2.641584576	0.002943	0.042321
AC021723.1	-2.189413131	0.002978	0.04267
SSX1	-4.79886094	0.002976	0.04267
PNLDC1	-2.12162452	0.002984	0.042714
VIL1	-2.484749543	0.002996	0.042837

AC025881.1	-3.648383573	0.003008	0.042927
IGHV3-43	-2.387355112	0.003027	0.043126
TCAM1P	-2.383177747	0.003051	0.043374
AC079209.1	-2.000776411	0.003076	0.043638
AC015908.2	2.167351464	0.003098	0.043874
NUTM2E	-2.526015455	0.003118	0.044068
LINC02432	-2.543005434	0.003118	0.044068
SYNPR	-3.876299494	0.003133	0.044242
PRAC1	-3.969744007	0.003137	0.044281
IGHV3-48	-2.310441374	0.003143	0.044343
IGKV1-9	-2.271687064	0.003162	0.044444
AC105384.2	-2.168437187	0.003166	0.044478
AC114776.1	-2.95905246	0.003172	0.0445
NBEAP1	-2.113650698	0.003207	0.044864
AC090578.1	-2.78816597	0.003229	0.045015
THEG	-2.804316794	0.003249	0.045168
PSG9	2.837300554	0.003287	0.045407
AC093063.1	-3.508187517	0.003331	0.045868
AC010343.3	-3.321640182	0.003339	0.045925
IGLV5-37	-3.267137169	0.003347	0.045996
SERPINA11	-3.767240282	0.00335	0.046022
ABCC13	-2.193243579	0.003364	0.046193
CIDEA	-2.03618672	0.003367	0.046213
AC023310.4	-2.571734362	0.003436	0.046862
LRRC3B	-2.973391151	0.003458	0.047021
MMP7	-2.040002507	0.003536	0.047874
AL445531.1	-2.753373887	0.003568	0.048148
SLC7A11-AS1	-2.392557606	0.003577	0.048234
ZG16	2.459406132	0.003684	0.049164
AL445437.1	-2.228800546	0.003686	0.049164
AL390334.1	-2.848271613	0.003691	0.049196
ELAVL3	-2.341692571	0.003708	0.049313
ALG1L3P	-2.318885338	0.003734	0.049546
AC128709.2	-2.793682188	0.003772	0.049876
PSAT1P1	2.049320551	0.003783	0.049996

Table 7.16: List of significantly altered genes between *VGLL1*-high and *VGLL1*-low MIBC groups, arranged in order of lowest q value.

Appendix xiv: Chapter 5 auxiliary results

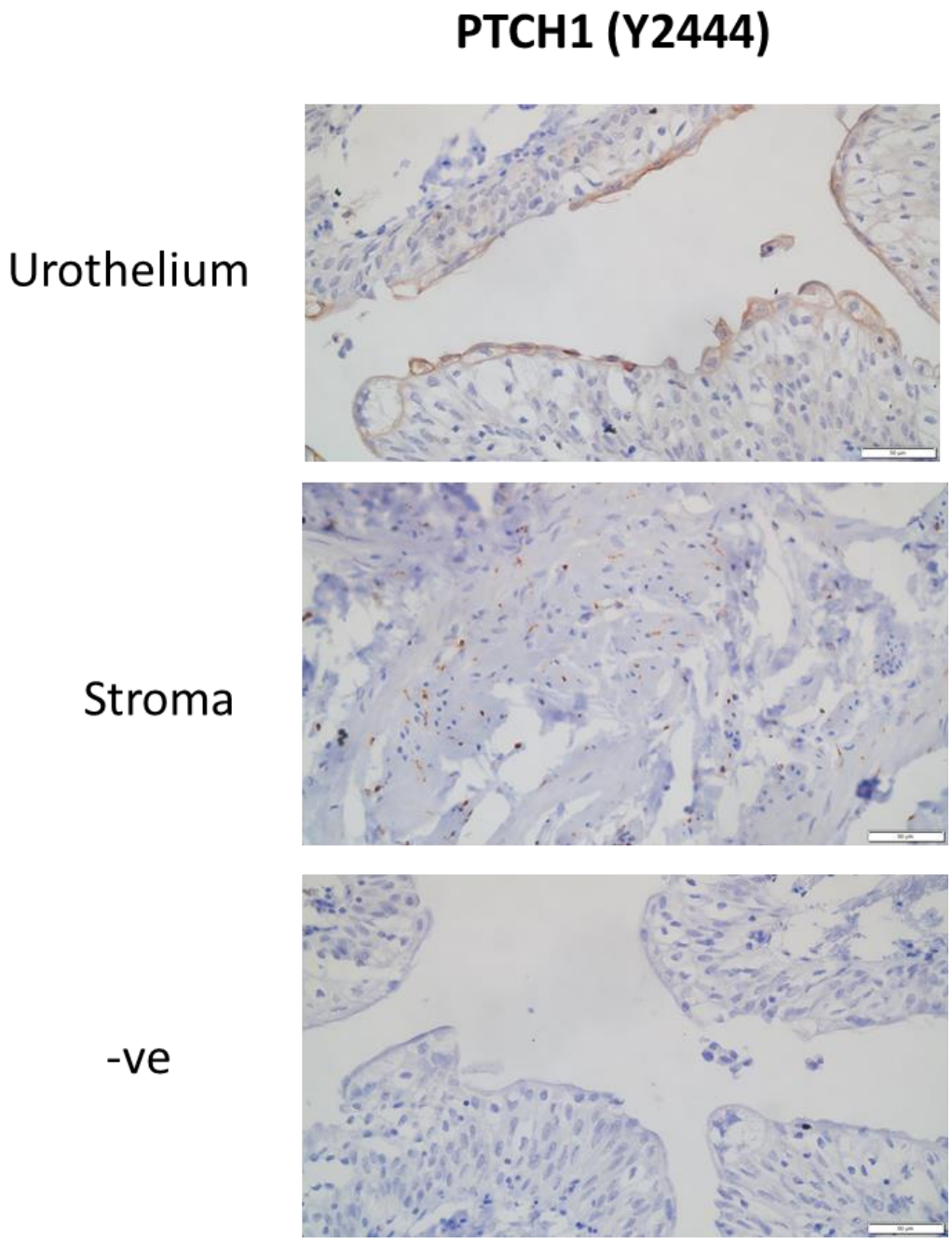

Figure 7.29: PTCH1 expression in native urothelium

Biological replicate from Figure 5.4 of PTCH1 expression and localisation in Y2444 ureter (**A**)**.** Sections that were labelled with no primary antibody were used as negative controls. Scale bar= 50 µm.

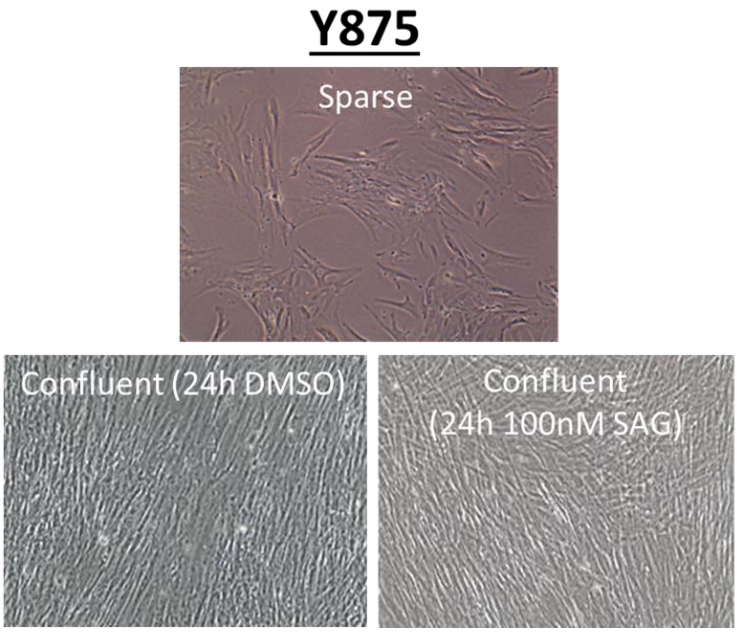

Figure 7.30: NuHS cell morphology before and following SAG treatment

Phase micrograph images of Y875 NuHS cells in sparse (top image) and confluent (bottom images) cultures. Once confluent, cells were serum starved for 24h before subsequent treatment with either vehicle DMSO (bottom left image) or 100 nM SAG (bottom right image) for a period of 24h before the image was captured.

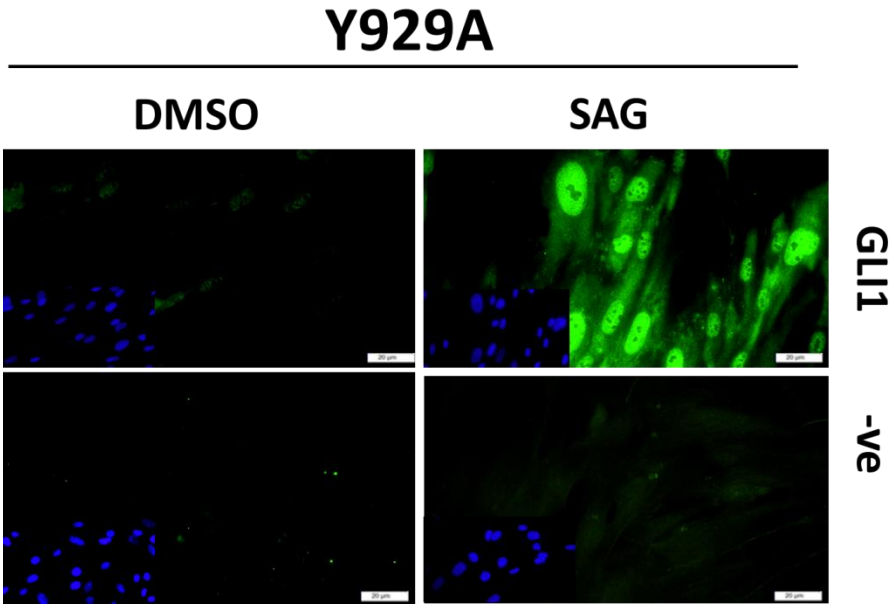

Figure 7.31: GLI1 induction by SAG in NuHS cells

Biological replicate from Figure 5.8 of GLI1 expression in Y929A NuHS cells following 24h 100 nM SAG treatment**.** Cells that were labelled with no primary antibody were used as negative controls. An accompanying Hoechst 33528 DNA staining image is provided in the left hand corner of each immunofluorescence image. Scale bar= 20 µm.

Gene	Comparison	Significant?	Summary	pval
PTCH1	DMSO vs. PD153035	Yes	**	0.0043
PTCH1	DMSO vs. PD/SAG	No	ns	0.6366
PTCH1	DMSO vs. PD/SAG/GDC	Yes	**	0.0095
PTCH1	DMSO vs. GDC-0449	No	ns	0.6083
PTCH1	PD153035 vs. PD/SAG	No	ns	0.9756
PTCH1	PD153035 vs. PD/SAG/GDC	No	ns	>0.9999
PTCH1	PD153035 vs. GDC-0449	No	ns	0.0853
PTCH1	PD/SAG vs. PD/SAG/GDC	No	ns	0.9974
PTCH1	PD/SAG/GDC vs. GDC-0449	No	ns	0.2196
GLI1	DMSO vs. PD153035	Yes	***	0.0001
GLI1	DMSO vs. PD/SAG	Yes	***	0.0002
GLI1	DMSO vs. PD/SAG/GDC	Yes	***	0.0002
GLI1	DMSO vs. GDC-0449	No	ns	>0.9999
GLI1	PD153035 vs. PD/SAG	No	ns	>0.9999
GLI1	PD153035 vs. PD/SAG/GDC	No	ns	>0.9999
GLI1	PD153035 vs. GDC-0449	Yes	***	0.0009
GLI1	PD/SAG vs. PD/SAG/GDC	No	ns	>0.9999
GLI1	PD/SAG vs. GDC-0449	Yes	**	0.0019
GLI1	PD/SAG/GDC vs. GDC-0449	Yes	**	0.0016

Table 7.17: Tukey's multiple comparisons test of conditions in Figure 5.13.

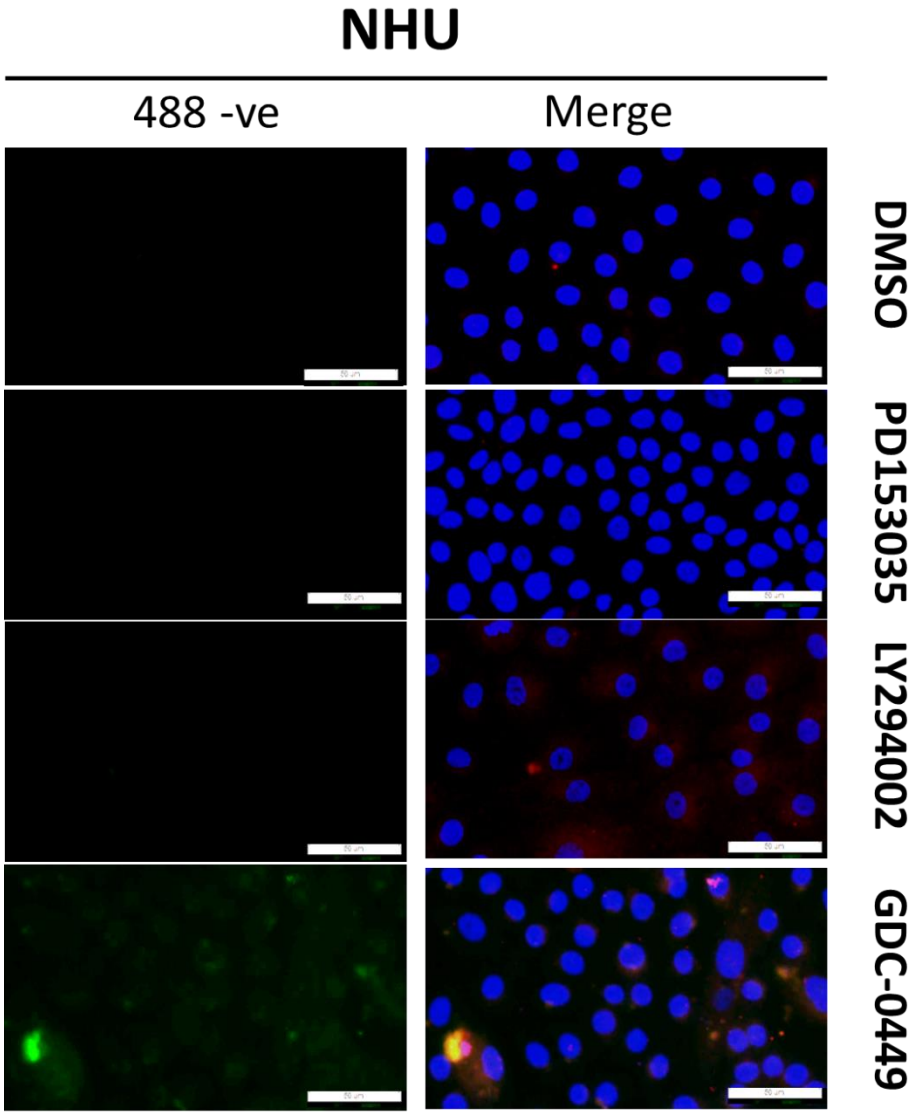

Figure 7.32: Negative controls for Figure 5.15

Y1483 cells receiving no primary antibody at all time points were used as negative controls. Images were all taken at same exposure and are shown with overlaid Hoechst 33258 DNA staining. Scale bar= 50µm.

Gene	Comparison	Significant?	Summary	pval
SHH	*in situ* vs. Luminal Papillary	No	ns	>0.9999
SHH	*in situ* vs. Luminal Non-Specified	No	ns	0.0974
SHH	*in situ* vs. Luminal Unstable	Yes	*	0.0176
SHH	*in situ* vs. Basal/Squamous	Yes	***	0.0006
SHH	*in situ* vs. Neuroendocrine	No	ns	0.5169
SHH	*in situ* vs. Stroma-Rich	No	ns	0.0831
SHH	Luminal Papillary vs. Luminal Non-Specified	Yes	***	0.0002
SHH	Luminal Papillary vs. Luminal Unstable	Yes	****	<0.0001
SHH	Luminal Papillary vs. Basal/Squamous	Yes	****	<0.0001
SHH	Luminal Papillary vs. Neuroendocrine	No	ns	0.2903
SHH	Luminal Papillary vs. Stroma-Rich	Yes	****	<0.0001
SHH	Luminal Non-Specified vs. Luminal Unstable	No	ns	>0.9999
SHH	Luminal Non-Specified vs. Basal/Squamous	No	ns	>0.9999
SHH	Luminal Non-Specified vs. Neuroendocrine	No	ns	>0.9999
SHH	Luminal Non-Specified vs. Stroma-Rich	No	ns	>0.9999
SHH	Luminal Unstable vs. Basal/Squamous	No	ns	>0.9999
SHH	Luminal Unstable vs. Neuroendocrine	No	ns	>0.9999
SHH	Luminal Unstable vs. Stroma-Rich	No	ns	>0.9999
SHH	Basal/Squamous vs. Neuroendocrine	No	ns	>0.9999
SHH	Basal/Squamous vs. Stroma-Rich	No	ns	0.0875
SHH	Neuroendocrine vs. Stroma-Rich	No	ns	>0.9999

Table 7.18: Dunn's multiple comparisons test of conditions in Figure 5.16.

Gene	Comparison	Significant?	Summary	pval
PTCH1	*in situ* vs. Luminal Papillary	Yes	**	0.0018
PTCH1	*in situ* vs. Luminal Non-Specified	Yes	*	0.0172
PTCH1	*in situ* vs. Luminal Unstable	Yes	*	0.0151
PTCH1	*in situ* vs. Basal/Squamous	Yes	***	0.0006
PTCH1	*in situ* vs. Neuroendocrine	No	ns	>0.9999
PTCH1	*in situ* vs. Stroma-Rich	Yes	*	0.0339
PTCH1	Luminal Papillary vs. Luminal Non-Specified	No	ns	>0.9999
PTCH1	Luminal Papillary vs. Luminal Unstable	No	ns	>0.9999
PTCH1	Luminal Papillary vs. Basal/Squamous	No	ns	>0.9999
PTCH1	Luminal Papillary vs. Neuroendocrine	Yes	*	0.0189
PTCH1	Luminal Papillary vs. Stroma-Rich	No	ns	>0.9999
PTCH1	Luminal Non-Specified vs. Luminal Unstable	No	ns	>0.9999
PTCH1	Luminal Non-Specified vs. Basal/Squamous	No	ns	>0.9999
PTCH1	Luminal Non-Specified vs. Neuroendocrine	No	ns	0.1094
PTCH1	Luminal Non-Specified vs. Stroma-Rich	No	ns	>0.9999
PTCH1	Luminal Unstable vs. Basal/Squamous	No	ns	>0.9999
PTCH1	Luminal Unstable vs. Neuroendocrine	No	ns	0.1114
PTCH1	Luminal Unstable vs. Stroma-Rich	No	ns	>0.9999
PTCH1	Basal/Squamous vs. Neuroendocrine	Yes	**	0.0079
PTCH1	Basal/Squamous vs. Stroma-Rich	No	ns	0.5654
PTCH1	Neuroendocrine vs. Stroma-Rich	No	ns	0.2176

Table 7.19: Dunn's multiple comparisons test of conditions in Figure 5.17.

Gene	Comparison	Significant?	Summary	pval
GLI1	*in situ* vs. Luminal Papillary	No	ns	0.8105
GLI1	*in situ* vs. Luminal Non-Specified	Yes	**	0.0087
GLI1	*in situ* vs. Luminal Unstable	No	ns	0.9572
GLI1	*in situ* vs. Basal/Squamous	No	ns	0.0525
GLI1	*in situ* vs. Neuroendocrine	No	ns	0.7044
GLI1	*in situ* vs. Stroma-Rich	Yes	****	<0.0001
GLI1	Luminal Papillary vs. Luminal Non-Specified	Yes	*	0.0219
GLI1	Luminal Papillary vs. Luminal Unstable	No	ns	>0.9999
GLI1	Luminal Papillary vs. Basal/Squamous	Yes	*	0.0197
GLI1	Luminal Papillary vs. Neuroendocrine	No	ns	>0.9999
GLI1	Luminal Papillary vs. Stroma-Rich	Yes	****	<0.0001
GLI1	Luminal Non-Specified vs. Luminal Unstable	No	ns	0.0567
GLI1	Luminal Non-Specified vs. Basal/Squamous	No	ns	>0.9999
GLI1	Luminal Non-Specified vs. Neuroendocrine	No	ns	>0.9999
GLI1	Luminal Non-Specified vs. Stroma-Rich	No	ns	>0.9999
GLI1	Luminal Unstable vs. Basal/Squamous	No	ns	0.267
GLI1	Luminal Unstable vs. Neuroendocrine	No	ns	>0.9999
GLI1	Luminal Unstable vs. Stroma-Rich	Yes	****	<0.0001
GLI1	Basal/Squamous vs. Neuroendocrine	No	ns	>0.9999
GLI1	Basal/Squamous vs. Stroma-Rich	Yes	****	<0.0001
GLI1	Neuroendocrine vs. Stroma-Rich	No	ns	>0.9999

Table 7.20: Dunn's multiple comparisons test of conditions in Figure 5.18.

Gene	Comparison	Significant?	Summary	pval
GLI2	*in situ* vs. Luminal Papillary	No	ns	0.3866
GLI2	*in situ* vs. Luminal Non-Specified	Yes	****	<0.0001
GLI2	*in situ* vs. Luminal Unstable	Yes	*	0.0204
GLI2	*in situ* vs. Basal/Squamous	Yes	****	<0.0001
GLI2	*in situ* vs. Neuroendocrine	Yes	**	0.0022
GLI2	*in situ* vs. Stroma-Rich	Yes	****	<0.0001
GLI2	Luminal Papillary vs. Luminal Non-Specified	Yes	****	<0.0001
GLI2	Luminal Papillary vs. Luminal Unstable	No	ns	0.1547
GLI2	Luminal Papillary vs. Basal/Squamous	Yes	****	<0.0001
GLI2	Luminal Papillary vs. Neuroendocrine	No	ns	0.0543
GLI2	Luminal Papillary vs. Stroma-Rich	Yes	****	<0.0001
GLI2	Luminal Non-Specified vs. Luminal Unstable	Yes	*	0.0115
GLI2	Luminal Non-Specified vs. Basal/Squamous	No	ns	>0.9999
GLI2	Luminal Non-Specified vs. Neuroendocrine	No	ns	>0.9999
GLI2	Luminal Non-Specified vs. Stroma-Rich	No	ns	>0.9999
GLI2	Luminal Unstable vs. Basal/Squamous	Yes	**	0.0035
GLI2	Luminal Unstable vs. Neuroendocrine	No	ns	>0.9999
GLI2	Luminal Unstable vs. Stroma-Rich	Yes	****	<0.0001
GLI2	Basal/Squamous vs. Neuroendocrine	No	ns	>0.9999
GLI2	Basal/Squamous vs. Stroma-Rich	Yes	***	0.0002
GLI2	Neuroendocrine vs. Stroma-Rich	No	ns	>0.9999

Table 7.21: Dunn's multiple comparisons test of conditions in Figure 5.19.

Gene	log_2 fold change	pval	qval
KLHDC7B	-5.556864704	2.11E-21	5.79E-17
GSTM2	4.042492238	7.80E-20	1.07E-15
U62317.1	-5.5999835	1.23E-18	1.12E-14
GLI2	3.448127657	1.63E-17	1.12E-13
AP000688.1	2.786853663	1.14E-16	6.26E-13
FGFBP2	5.463622964	4.07E-15	1.86E-11
PSD2	3.486184918	1.85E-14	7.27E-11
ABCC1	2.072706781	7.94E-14	2.72E-10
TREML3P	3.912880726	3.96E-13	1.21E-09
F2RL2	3.480595587	4.45E-13	1.22E-09
CABYR	2.78654588	1.52E-12	3.79E-09
LTF	-5.955470485	5.38E-12	1.07E-08
IGLV6-57	-5.151473665	5.27E-12	1.07E-08
SOX11	3.295994639	5.46E-12	1.07E-08
AL355303.1	4.021524635	6.94E-12	1.24E-08
U8	4.334193506	7.22E-12	1.24E-08
ANXA3	-2.769645751	8.83E-12	1.43E-08
ADH1C	5.469687727	1.52E-11	2.31E-08
IGLV3-21	-4.781074286	4.33E-11	5.40E-08
MZB1	-4.002502823	4.23E-11	5.40E-08
IGLC2	-4.387943721	4.67E-11	5.58E-08
ACKR2	-4.422559767	5.19E-11	5.93E-08
CXCL5	-4.712743982	6.28E-11	6.89E-08
IGLV2-23	-4.632817248	7.09E-11	7.49E-08
IGLC3	-4.217846703	7.50E-11	7.62E-08
FCRLA	-4.121992113	7.82E-11	7.66E-08
IGHV4-31	-4.749990056	8.79E-11	8.32E-08
IGKV1-5	-4.361328065	9.89E-11	9.05E-08
IGLV1-36	-4.867918687	1.18E-10	9.74E-08
SAA2	-4.606693751	1.21E-10	9.74E-08
IGKV1-16	-4.491579718	1.12E-10	9.74E-08
FCRL5	-4.289303387	1.14E-10	9.74E-08
IGKV3-11	-4.243587806	1.27E-10	9.97E-08
IGHV3-21	-4.545267431	1.38E-10	1.00E-07
IGLV1-44	-4.084995431	1.72E-10	1.21E-07
IGKC	-4.068257789	1.86E-10	1.25E-07
FCGR3B	-4.037251516	1.82E-10	1.25E-07
PTGR1	2.455970946	2.41E-10	1.52E-07
GSTM4	2.567564661	2.46E-10	1.52E-07
SLC47A1	3.21398786	2.49E-10	1.52E-07
NECAB2	3.449092113	3.25E-10	1.94E-07
MT-TH	-6.393174329	3.54E-10	1.96E-07
IGKV1-9	-4.602012883	3.43E-10	1.96E-07

IGHV4-34	-4.232039564	3.62E-10	1.96E-07
AC004889.1	2.069718635	3.63E-10	1.96E-07
STXBP5L	4.360664941	3.40E-10	1.96E-07
IGLV3-10	-4.909376391	3.83E-10	2.01E-07
IGHG1	-4.028745432	3.91E-10	2.01E-07
SLC35G1	2.003232314	3.95E-10	2.01E-07
IGLV4-69	-5.041918009	4.13E-10	2.01E-07
SRXN1	2.171467981	4.18E-10	2.01E-07
SOST	6.437246464	4.04E-10	2.01E-07
CALML5	-5.970795598	4.95E-10	2.34E-07
IGLV10-54	-5.104517793	5.10E-10	2.37E-07
IGLV3-27	-5.158433766	5.18E-10	2.37E-07
IGLV1-40	-4.255499539	6.34E-10	2.76E-07
IGHV3-30	-4.231736045	6.32E-10	2.76E-07
LINC02010	3.080405746	6.75E-10	2.89E-07
AL121758.1	2.542330631	7.45E-10	3.14E-07
FDCSP	-6.002171448	7.85E-10	3.18E-07
IGHV3-73	-4.815599993	7.80E-10	3.18E-07
IGHV4-39	-4.420081974	7.87E-10	3.18E-07
IGHV1-46	-4.359243517	8.06E-10	3.20E-07
SVIP	-2.005780552	8.20E-10	3.22E-07
IGHG2	-4.126642567	8.63E-10	3.34E-07
IGHGP	-3.967366264	9.45E-10	3.60E-07
MDGA1	2.776465447	9.84E-10	3.70E-07
GLDC	-4.268608911	1.01E-09	3.76E-07
IGKV3-15	-4.192738873	1.10E-09	3.97E-07
IGHV3-48	-4.519585287	1.23E-09	4.39E-07
GCLM	2.30944184	1.37E-09	4.81E-07
HECW1	2.530760705	1.38E-09	4.81E-07
AC108865.1	4.445714392	2.08E-09	7.12E-07
AFAP1-AS1	-4.933630537	2.15E-09	7.27E-07
IGLV10-67	-4.307159081	2.25E-09	7.51E-07
CIDEC	-5.966849362	2.46E-09	7.80E-07
KISS1	-4.875145929	2.47E-09	7.80E-07
IGHV3-66	-4.744111922	2.44E-09	7.80E-07
JCHAIN	-3.571384715	2.46E-09	7.80E-07
NAT16	3.352228189	2.45E-09	7.80E-07
AC245369.3	-4.460620794	2.61E-09	8.15E-07
IGHV5-51	-4.190415774	2.67E-09	8.25E-07
IGHV3-53	-4.285604523	2.83E-09	8.64E-07
Z98257.1	-4.611997509	3.12E-09	9.40E-07
IGHV3-13	-4.559220279	3.23E-09	9.63E-07
IGHV3-74	-3.798569278	3.51E-09	1.03E-06
IGKV1-8	-4.511649081	3.59E-09	1.04E-06

BATF	-2.233504043	3.89E-09	1.10E-06
MS4A1	-4.594789441	4.66E-09	1.31E-06
IGHV1-69	-4.740351055	4.92E-09	1.36E-06
IGHV3-33	-4.088673951	5.17E-09	1.42E-06
IGHG4	-3.915188757	5.24E-09	1.42E-06
IGHA1	-3.662656219	5.33E-09	1.44E-06
PSORS1C2	-5.07718539	5.50E-09	1.45E-06
IGLV2-11	-4.057478571	5.47E-09	1.45E-06
TNFRSF17	-4.229034664	6.62E-09	1.71E-06
ADAM8	-2.079057105	6.78E-09	1.74E-06
IGKV1-27	-4.122472455	7.04E-09	1.77E-06
AKR1C7P	3.519539221	7.01E-09	1.77E-06
IGHV1-24	-4.223449976	7.44E-09	1.86E-06
IGLV3-19	-4.125197608	7.53E-09	1.86E-06
CASP14	-4.920166264	8.14E-09	1.99E-06
MARCO	-3.415982922	8.53E-09	2.07E-06
IGHV3-15	-3.983471793	1.07E-08	2.56E-06
HSD3B1	-8.686495164	1.18E-08	2.77E-06
IGKV1D-8	-4.16993594	1.27E-08	2.93E-06
IGLV2-14	-3.951523807	1.27E-08	2.93E-06
CCL19	-3.872539929	1.29E-08	2.95E-06
IGHV2-70	-4.777530223	1.32E-08	2.99E-06
IGLC7	-4.784907278	1.39E-08	3.10E-06
IGHG3	-3.760030035	1.49E-08	3.30E-06
GSTM3	2.852639311	1.55E-08	3.41E-06
CYP11A1	-4.364993228	1.63E-08	3.55E-06
IGHM	-3.848529616	1.68E-08	3.63E-06
IGLON5	2.760245865	1.77E-08	3.79E-06
IGKV1-17	-4.080905114	1.98E-08	4.21E-06
IGKV4-1	-3.800526858	2.05E-08	4.29E-06
PLA2G2D	-4.401004745	2.25E-08	4.54E-06
IGLV3-25	-3.959741974	2.25E-08	4.54E-06
IGKV3-20	-3.781655209	2.26E-08	4.54E-06
AKR1C3	3.685421864	2.22E-08	4.54E-06
TCL1A	-4.767287124	2.28E-08	4.54E-06
IGLV3-9	-4.542915403	2.33E-08	4.60E-06
PURG	2.504599315	2.35E-08	4.60E-06
IGHD	-4.537242165	2.75E-08	5.28E-06
IGLV3-1	-4.091498122	2.73E-08	5.28E-06
WNT5A	2.666281297	3.11E-08	5.92E-06
IGLV2-8	-3.804384929	3.30E-08	6.21E-06
GCLC	2.191739574	3.36E-08	6.27E-06
IGLV7-43	-4.31551621	3.44E-08	6.37E-06
IGHV2-26	-4.575212452	3.51E-08	6.47E-06

AKR1C1	4.015195925	3.59E-08	6.57E-06
RDH16	-3.057532904	3.85E-08	6.99E-06
SLC6A15	-4.482555654	3.92E-08	7.08E-06
DCC	2.657676922	4.09E-08	7.34E-06
CLDN9	-4.464375129	4.72E-08	8.35E-06
OLR1	-3.307594025	4.70E-08	8.35E-06
ADGRB1	2.918830918	4.84E-08	8.51E-06
CXCL11	-3.676896029	5.28E-08	9.24E-06
IGLV8-61	-3.916609122	5.34E-08	9.28E-06
MRAP2	3.135527411	5.50E-08	9.44E-06
SLC1A3	-2.269572772	5.80E-08	9.89E-06
PNMA5	-5.808211324	6.20E-08	1.04E-05
CALB1	-5.445055205	6.26E-08	1.04E-05
AC145207.8	2.589246254	6.19E-08	1.04E-05
OSGIN1	2.572477271	6.32E-08	1.04E-05
SPP1	2.905648472	6.47E-08	1.06E-05
AC099329.2	-4.261058083	6.65E-08	1.08E-05
IGHV1-18	-3.828580817	6.86E-08	1.10E-05
ABCC6	2.045702066	6.94E-08	1.11E-05
IGHV4-61	-3.974252899	7.23E-08	1.14E-05
AC243965.2	2.285957141	7.25E-08	1.14E-05
CCL18	-3.122827201	7.82E-08	1.23E-05
IGKV1OR2-11	-3.853121871	8.29E-08	1.27E-05
IGLV5-45	-3.853033151	8.27E-08	1.27E-05
LINC02476	-6.331594411	8.80E-08	1.32E-05
IGHV2-5	-4.431663787	8.76E-08	1.32E-05
NUDT10	3.158042403	8.79E-08	1.32E-05
IGHV1-2	-4.032902281	9.21E-08	1.37E-05
IGKV3D-20	-4.089709997	9.31E-08	1.38E-05
IGKV2D-29	-4.193834518	1.02E-07	1.48E-05
TRIM16L	2.200077972	1.03E-07	1.49E-05
ZNF350-AS1	-3.667678541	1.04E-07	1.50E-05
CDH4	2.24592075	1.11E-07	1.59E-05
CHI3L2	-3.154296253	1.16E-07	1.66E-05
TSPAN7	3.474874076	1.18E-07	1.68E-05
IGKV5-2	-4.900695335	1.26E-07	1.73E-05
IGHV3-20	-4.545289391	1.25E-07	1.73E-05
CR2	-4.451356831	1.25E-07	1.73E-05
IGKV1D-16	-4.090914477	1.36E-07	1.86E-05
ADAM23	3.15238359	1.36E-07	1.86E-05
UNC13D	-2.025552847	1.38E-07	1.87E-05
IGHA2	-3.44484748	1.40E-07	1.89E-05
CD79A	-3.393291359	1.41E-07	1.89E-05
IGKV2-24	-3.683189365	1.42E-07	1.91E-05

ALPP	-4.528818271	1.46E-07	1.94E-05
U62317.2	-2.519633091	1.46E-07	1.94E-05
SERPINA1	-2.831313136	1.66E-07	2.17E-05
IGHV4-28	-4.082377622	1.68E-07	2.19E-05
MEG9	3.1557138	1.71E-07	2.21E-05
MIA	-4.307857977	1.73E-07	2.22E-05
LINC01217	-3.463209984	1.78E-07	2.28E-05
IGKV1-6	-3.904685601	1.79E-07	2.28E-05
SLC17A7	2.5466855	1.81E-07	2.30E-05
LINC01510	4.971065592	1.90E-07	2.40E-05
AC104024.2	-3.119675821	1.94E-07	2.43E-05
CYSRT1	-2.722138201	1.95E-07	2.43E-05
AL158206.1	-2.366120914	1.98E-07	2.46E-05
IGKV3D-15	-4.255807882	2.12E-07	2.63E-05
IGHV3-23	-3.65185603	2.36E-07	2.90E-05
FAM30A	-3.388262596	2.44E-07	2.98E-05
JAKMIP3	3.239657502	2.44E-07	2.98E-05
DHRS2	-3.670406363	2.71E-07	3.29E-05
FOXJ1	-4.249645248	2.77E-07	3.34E-05
COLCA1	3.659015226	2.82E-07	3.39E-05
FCRL2	-3.769788284	2.83E-07	3.40E-05
U62317.5	-2.342949961	2.95E-07	3.52E-05
HLA-DQB1	-2.42754085	3.00E-07	3.56E-05
PDZD4	2.390140527	3.06E-07	3.62E-05
ALDH3A1	4.406257915	3.11E-07	3.66E-05
SNCB	2.746166015	3.15E-07	3.69E-05
FMO1	-2.257838419	3.22E-07	3.76E-05
WIF1	5.339570193	3.25E-07	3.78E-05
ZBP1	-2.781142182	3.36E-07	3.89E-05
HMCN1	2.605673032	3.56E-07	4.10E-05
IGKV1-39	-4.88667974	3.88E-07	4.44E-05
AKR1C6P	2.79456123	4.00E-07	4.55E-05
IGHV4-55	-3.865513931	4.12E-07	4.65E-05
IGHJ3	-3.978510246	4.17E-07	4.69E-05
MAFA-AS1	3.616933709	4.27E-07	4.79E-05
PELI2	2.037901701	4.38E-07	4.89E-05
AXDND1	3.098808147	4.41E-07	4.90E-05
IGHV3-43	-3.748578599	4.68E-07	5.18E-05
AC245369.1	-5.047694076	4.80E-07	5.29E-05
S100A7	-4.789957997	4.83E-07	5.30E-05
AC002401.4	-3.224334541	5.33E-07	5.83E-05
EPYC	-3.857963738	5.40E-07	5.88E-05
IGHV3-64	-4.663354455	5.49E-07	5.90E-05
NETO1	-3.900694596	5.45E-07	5.90E-05

AL589765.4	-2.031764913	5.47E-07	5.90E-05
KRT7	-3.117695751	5.74E-07	6.15E-05
XDH	-2.456116724	6.08E-07	6.50E-05
UCA1	-3.709735465	6.15E-07	6.54E-05
MC4R	4.060506937	6.32E-07	6.70E-05
AC008760.2	-2.919388044	6.35E-07	6.70E-05
HLA-DQA1	-2.441186406	6.50E-07	6.81E-05
OASL	-2.143376214	6.70E-07	6.99E-05
IGKV3D-11	-3.854491869	6.73E-07	7.00E-05
TDRKH-AS1	-2.135567015	6.90E-07	7.15E-05
ADRA2C	3.09714452	7.13E-07	7.32E-05
IGHV6-1	-3.819575394	7.40E-07	7.58E-05
ACKR3	2.228141088	7.67E-07	7.80E-05
RORC	-3.002175362	7.75E-07	7.85E-05
IGKV1D-43	-4.980553933	8.22E-07	8.21E-05
IGLL5	-3.310875072	8.23E-07	8.21E-05
JSRP1	-2.771611329	8.27E-07	8.23E-05
HLA-DRB1	-2.160113346	8.51E-07	8.38E-05
PRSS2	-5.463202261	8.65E-07	8.45E-05
MEG3	2.522739914	8.68E-07	8.45E-05
LILRA5	-2.175798862	8.89E-07	8.62E-05
MAP2	2.644599616	8.96E-07	8.66E-05
SHC3	-2.495696843	9.01E-07	8.68E-05
LEP	-4.232114608	9.26E-07	8.86E-05
CHI3L1	-2.557061024	9.58E-07	9.09E-05
RNASE7	-3.342775421	9.64E-07	9.13E-05
SAMD5	2.510022122	9.75E-07	9.20E-05
TFF1	-4.431231031	1.01E-06	9.45E-05
IGHV3-49	-3.647023259	1.03E-06	9.65E-05
RNF223	-2.396561802	1.04E-06	9.66E-05
IGKV2D-40	-4.420189754	1.10E-06	0.000101
IGLV9-49	-4.03216802	1.11E-06	0.000102
IGKV2-28	-5.413517447	1.13E-06	0.000104
IGHV1OR15-2	-4.32137214	1.14E-06	0.000104
IGLV2-18	-3.656096422	1.16E-06	0.000105
AC005481.1	3.140699355	1.16E-06	0.000105
FAM43B	2.705416616	1.21E-06	0.00011
SAA1	-3.556609461	1.24E-06	0.000112
GCK	2.130385994	1.28E-06	0.000115
FAM189A1	3.808996804	1.30E-06	0.000117
HHIPL2	3.343226919	1.33E-06	0.000118
SP9	4.707113362	1.33E-06	0.000118
IFIT2	-2.059645199	1.41E-06	0.000125
C4BPB	-4.001179458	1.56E-06	0.000137

IGLV1-50	-4.164943431	1.57E-06	0.000138
TNFRSF13B	-3.365084153	1.62E-06	0.000142
IGLV4-60	-3.999755816	1.67E-06	0.000145
AC097478.1	-3.920026207	1.79E-06	0.000154
CHGA	3.219022991	1.81E-06	0.000154
CCDC189	2.040241829	1.83E-06	0.000155
AC108865.2	4.07207284	1.83E-06	0.000155
AL512488.1	-2.864639392	1.96E-06	0.000165
BLK	-3.49231898	2.00E-06	0.000168
XK	-2.321419741	2.01E-06	0.000169
NOTUM	2.557089401	2.04E-06	0.000171
NAA11	-7.19357506	2.11E-06	0.000175
OLFM1	2.530691885	2.11E-06	0.000175
IL2RG	-2.284692837	2.19E-06	0.000182
KRT71	-2.860784412	2.22E-06	0.000183
AC004233.3	-2.888803083	2.26E-06	0.000185
ART4	-4.26111962	2.30E-06	0.000188
MACROD2	-2.70670238	2.31E-06	0.000188
SPIB	-3.117959117	2.34E-06	0.000189
ACER2	-2.461444367	2.40E-06	0.000194
IFNG-AS1	-4.536727253	2.44E-06	0.000196
IGHV4-59	-3.500234613	2.45E-06	0.000196
IFNL1	-3.828043162	2.49E-06	0.000198
TRPV6	-3.352466475	2.52E-06	0.000201
LINC02364	-2.569387711	2.60E-06	0.000206
AL353150.1	-2.559225587	2.71E-06	0.000213
FCRL3	-2.653941528	2.91E-06	0.000228
NMRAL2P	3.764391752	2.91E-06	0.000228
CXCL9	-2.809712227	2.98E-06	0.000233
PLA2G2F	-3.790653271	3.02E-06	0.000235
IGKV2-30	-3.509969824	3.15E-06	0.000244
TH	-3.607600334	3.19E-06	0.000245
AL354798.1	2.052380851	3.21E-06	0.000246
SAA2-SAA4	-3.770883799	3.24E-06	0.000247
VGLL1	-3.295312002	3.46E-06	0.000261
CHRNA1	-2.692618896	3.45E-06	0.000261
RSAD2	-2.15195298	3.64E-06	0.000269
TMEM155	2.426861618	3.74E-06	0.000276
IGLV3-16	-4.370871874	3.84E-06	0.000282
DPYSL4	2.724756024	3.99E-06	0.000291
IL27	-2.29419433	4.00E-06	0.000292
LINC00520	-3.33690998	4.11E-06	0.000299
LINC01699	3.917989925	4.21E-06	0.000304
NAT8B	-2.715175274	4.22E-06	0.000304

LINC02006	-2.771046541	4.25E-06	0.000305
TBC1D27	-3.276295749	4.30E-06	0.000308
AC107294.2	2.005776291	4.53E-06	0.000324
NTRK2	3.346105561	4.69E-06	0.000335
AC133644.2	-2.791104145	4.87E-06	0.000347
C4orf26	-3.50961947	5.10E-06	0.000361
TMPRSS3	-2.744700775	5.35E-06	0.000376
ART3	-2.934830961	5.38E-06	0.000377
HLA-DRB5	-2.144356022	5.45E-06	0.000379
NPR3	2.381435421	5.45E-06	0.000379
AC107294.1	2.175279368	5.56E-06	0.000385
CFAP46	2.435183197	5.59E-06	0.000386
GPAT2	-2.972212805	5.85E-06	0.000401
C20orf144	-3.863455642	5.88E-06	0.000402
IGHV3-11	-3.246511133	6.07E-06	0.000413
STEAP4	-2.391226269	6.11E-06	0.000415
AC093865.1	2.939426835	6.17E-06	0.000418
KRT20	-4.313072903	6.23E-06	0.000421
CYP2A6	3.736515844	6.30E-06	0.000423
TRHDE-AS1	-4.012900415	6.47E-06	0.000431
DMBT1	-3.787239899	6.45E-06	0.000431
DYNLL1P4	2.788290055	6.54E-06	0.000435
SYT12	-2.688442626	6.64E-06	0.00044
KRT18P8	-2.243560277	6.76E-06	0.000446
AC105118.1	3.323294677	6.82E-06	0.000447
ADIPOQ	-6.988353189	6.88E-06	0.00045
CTSE	-3.671316797	6.97E-06	0.000454
FOLR1	-3.476689768	7.21E-06	0.000466
KRT7-AS	-3.230311027	7.41E-06	0.000478
TRHDE	-3.755523413	7.51E-06	0.000483
IGHV1OR15-9	-4.1715302	7.56E-06	0.000484
CATSPER1	-2.530524808	7.57E-06	0.000484
SLC7A11	2.914189747	7.93E-06	0.000504
COL11A1	-2.714937965	8.04E-06	0.00051
AL512625.3	-3.134474695	8.08E-06	0.000511
IL24	-2.441989635	8.49E-06	0.000531
CRCT1	-4.042030662	8.60E-06	0.000537
LINC01423	-5.691929294	8.71E-06	0.000542
MCHR1	-2.264697885	9.02E-06	0.00056
IGLV5-37	-5.255888548	9.08E-06	0.000562
AC103563.3	-4.461730996	9.24E-06	0.000569
IGHV3-7	-3.549841812	9.24E-06	0.000569
IGLV1-41	-3.590897066	9.40E-06	0.000575
CYP4F11	3.126450534	9.54E-06	0.000582

NCF1B	-2.403315486	9.66E-06	0.000587
AC023301.1	-3.79656028	9.87E-06	0.000598
IGLV2-28	-4.467610722	1.03E-05	0.000621
AL162414.1	-4.389585577	1.06E-05	0.000634
SMIM6	-2.840453254	1.07E-05	0.000638
LINC00462	-2.722934429	1.08E-05	0.000642
LINC00944	3.7688567	1.11E-05	0.000659
UPK2	-3.329143445	1.12E-05	0.000661
HMGB2P1	-2.818504083	1.15E-05	0.000674
TMEM53	-2.725976123	1.20E-05	0.000699
ADTRP	-2.230311494	1.20E-05	0.0007
IGHV3-72	-3.115045697	1.24E-05	0.000718
C11orf87	4.495360229	1.28E-05	0.00074
RARRES3	-2.199135859	1.30E-05	0.000749
AC012414.5	2.594067044	1.34E-05	0.000769
LILRB4	-2.079000594	1.36E-05	0.000777
EXOC3L4	-2.538895026	1.40E-05	0.000795
IGKV1D-13	-4.176212316	1.43E-05	0.000809
NR0B1	6.062678099	1.46E-05	0.000822
ZSCAN4	-3.141519179	1.47E-05	0.000827
AC090826.2	-3.561683743	1.51E-05	0.000845
PRSS27	-2.128996309	1.52E-05	0.000848
PLIN1	-3.241143938	1.53E-05	0.000849
RARRES2	-2.106966613	1.53E-05	0.000849
AL391427.1	3.038048781	1.55E-05	0.000857
TRBV10-3	-3.531245199	1.56E-05	0.000858
SALL1	2.498939369	1.59E-05	0.000871
NRIR	-2.154233013	1.60E-05	0.000872
NCF1	-2.053745213	1.60E-05	0.000872
LINC00518	-2.875492657	1.60E-05	0.000872
UBD	-2.83076893	1.65E-05	0.000896
MIR3945HG	-2.627557766	1.65E-05	0.000896
CCL17	-2.226654069	1.67E-05	0.000902
NMNAT2	-2.192891291	1.70E-05	0.000915
AL355796.1	3.038633732	1.73E-05	0.000926
UPK3B	-2.837833778	1.82E-05	0.00097
RXFP1	-2.640101022	1.87E-05	0.00099
PLPPR3	3.131927707	1.87E-05	0.00099

Table 7.22: List of significantly altered genes between *GLI2*-high and *GLI2*-low basal/squamous MIBC groups, arranged in order of lowest q value.

Appendix xv: Unix shell/R scripts

FastQC script (Unix)

```
#!/bin/sh

## qsub –N submission_name ./RNAseq_fastqc.sh /path/fastq

# Grid Engine options

#$ -cwd

#$ -l h_rt=1:00:00

#$ -l h_vmem=2G

#$ -V

#$ -R y

#$ -pe smp 4

#$ -j y

#$ -o /dev/null

Export MALLOC_ARENA_MAX=4

# Load modules

Module load fastqc/0.11.5

# Generate outname variable

Outname=`echo $1 | rev | cut –d'/' –f1 | rev | cut –d. –f1`

Outdir=`pwd`

# run fastqc

fastqc –o $outdir –t 3 $1

rm ${outname}_fastqc.zip
```

Trimmomatic script (Unix)

```
#!/bin/sh

## qsub –N submission_name ./RNAseq_trimming.sh /path/read1.fastq.gz/path/read2.fastq.gz

# Grid engine options

#$ -cwd

#$ -l h_rt=8:00:00

#$ -l h_vmem=2G

#$ -R y

#$ -pe smp 9

#$ -j y

#$ -V

## -o /dev/null

Export MALLOC-ARENA_MAX=4

vmArgs=" -Xmx1G –XX:ParallelGCThreads=9"

# Load modules

module load fastqc/0.11.5

# Generate outname variable

outname=`echo $1 | rev | cut –d'/' –f1 | rev | cut –d. –f1 | sed 's/_read1//g' | sed 's/_read2//g''

# Run trimmomatic

# generate output files for the paired data, and also the reads which were binned, resulting in their pairs being binned (UP, orphan reads)
```

#Use a given file of adapters etc taken from from the FASTQC output and use palindromic trimming to get contamination on the other read in the pair

 # enabling 2 mismatches, match must get a score of 30

 # use a sliding window approach to check quality, average in 4bp windows if the quality drops below 20, trims the read

 # remove read if length drops below 49 (arbitrary threshold, mapping should still work down to ~25bp)

java $vmArgs –jar $TRIMMOMATIC-JAR PE –phred33 $1 $2 ${outname}_read1-PE.fastq.gz ${outname}_read1=UP.fastq.gz ${outname}_read2-PE.fastq.gz ${outname}_read2.UP.fastq.gz \ ILLUMINACLIP:/scratch/RNAseq_adapters_list.fa:2:30:10 \ SLIDINGWINDOW: 4 :20 MINLEN : 49

#for i in ${outname}_read1-PE.fastq.gz ${outname}_read1-UP.fastq.gz ${outname}_read2-PE.fastq.gz ${outname}_read2.UP.fastq.gz; do echo”`zcat $i | wc -1` /4” | bc; done

 # perform new fastqc of PE read 1 to confirm improvement

Fastqc –t 6 -0 ./ ${outname}_read1.PE.fastq.gz

rm ${outname}_read1-PE_fastqc.zip

Pseudo read assignment script (Unix)

```
#!/bin/sh

##qsub –N submission_name ./RNAseq_05_pre-kallisto_read_manipulation_GE.sh /path/sample

# Grid Engine options

#$ -cwd

#$ -l h_rt=3:00:00

#$ -l h_vmem=2G

#$ -R y

#$ -j y

#$ -V

# -o /dev/null

# define outnames – those from the original read1 file which are now unpaired, need pseudo mates (which will be read2 reads) and vice versa

read1UPmatch=`echo $1 | rev | cut –d’/’ –f1 | rev`”_pseudo_read2.fastq”

read2UPmatch=`echo $1 | rev | cut –d’/’ –f1 | rev`”_pseudo_read1.fastq”

# iterate through headers in read1UP and generate pseudoread2

zcat $1”_read1-UP.fastq.gz” | grep “^@K00” | sed ‘s/ 1\:N/ 2\:N/g’  | awk ‘{print $1 “ “ $2 “\nNNNNNNNNNNNNNNNNNNNNNNNNNNNNNNNNNNNNNNNNNNNNNNNNNNNNNNNNNNNNNNNNNNNNNNNNNNNNN\n+\n!!!!!!!!!!!!!!!!!!!!!!!!!!!!!!!!!!!!!!!!!!!!!!!!!!!!!!!!!!!!!!!!!!!!!!!!!!!

gzip $read1UPmatch

# iterate through headers in read2UP and generate pseudoread1

zcat $1”_read2-UP.fastq.gz” | grep “^@K00” | sed ‘s/ 1\:N/ 2\:N/g’  | awk ‘{print $1 “ “ $2 “\nNNNNNNNNNNNNNNNNNNNNNNNNNNNNNNNNNNNNNNNNNNNNNNNNNNNNNN
```

```
NNNNNNNNNNNNNNNNNNNN\n+\n!!!!!!!!!!!!!!!!!!!!!!!!!!!!!!!!!!!!!!!!!!!!!!!!!!!!!!!!!!!!!!!!!!!!!!!!!!!

gzip $read2UPmatch

# create composite read1 then read2 files

samplename=`echo $1  | rev  | cut –d’/’ –f1  | rev`

cat $1”_read1-PE.fastq.gz” $1”_read1-UP.fastq.gz” $read2UPmatch”.gz” > $samplename”-merged_read1.fastq.gz”

cat $1”_read2-PE.fastq.gz” $1read1-UPmatch”.gz” $1”_read2-UP.fastq.gz” > $samplename”-merged_read2.fastq.gz”

# remove the pseudo files

rm $read1UPmatch”.gz” $read2UPmatch”.gz”
```

Kalisto script (Unix)

```
#!/bin/sh

## qsub –N submission_name ./RNAseq_kallisto_mapping.sh /path/read_pseudo/path/index_file

# Grid Engine options

#$ -cwd

#$ -l h_rt=08:00:00

#$ -l h_vmem=2G

#$ -R y

#$ -j y

#$ -V

#$ -pe smp 9

# -o/dev/null

# Load modules

module load kallisto/0.44.0

# Generate outname variable

basename=`echo $1 | sed 's/-merged//g' | rev | cut –d'/' –f1 | rev`

# Run kallisto quantification

# 100 bootstraps given for technical repeats when analysing by sleuth

# also the – fusion flag for detecting fusion genes

kallisto quant --index $2 –fusion –output-dir=${basename} –threads 8 –bootstrap-samples=100 $1_read1.fastq.gz $1_read2.fastq.gz
```

tximport script (R)

```
>library("tximport")

>library("biomaRt")


>mart <- useEnsembl(biomart="ensembl", dataset="hsapiens_gene_ensembl")

>t2g <- biomaRt::getBM(attributes = c("ensembl_transcript_id", "transcript_version", "ensembl_gene_id", "external_gene_name"), mart = mart)

>t2g2 <- dplyr::select(t2g, ensembl_transcript_id, external_gene_name)


>setwd("path")

>files <- list.files(".","tsv$")

>names(files) <- gsub("_abundance.tsv", "", files)


>txi <- tximport(files, type = "kallisto", tx2gene = t2g2, ignoreTxVersion = TRUE)

>write.csv(as.data.frame(txi$abundance),file="merged_TPMs.csv")
```

sleuth script (R)

#load library

```
>library("tidyverse")

>library("sleuth")

>library("biomaRt")
```

 # create gene level database

```
>mart <- biomaRt::useMart(biomart = "ENSEMBL_MART_ENSEMBL", dataset = "hsapiens_gene_ensembl", host = 'ensembl.org')

>t2g <- biomaRt::getBM(attributes = c("ensembl_transcript_id", "transcript_version", "ensembl_gene_id", "external_gene_name"), mart = mart)

>t2g <- dplyr::select(t2g, target_id = ensembl_transcript_id, ens_gene = ensembl_gene_id, ext_gene = external_gene_name)
```

 # set working directory (directory where the individual file folders are) and load sample file

```
>setwd(PATH)

>s2c <- read.table("sample_info.txt", header=TRUE, stringsAsFactors=FALSE)
```

 # one variable (group vs group - "express")

```
>so <- sleuth_prep(s2c, ~express, extra_bootstrap_summary=TRUE, num_cores=1, target_mapping=t2g, transformation_function = function(x) log2(x+1.5), gene_mode=TRUE, aggregation_column = 'ext_gene')

>so <- sleuth_fit(so, ~express, 'full')

>so <- sleuth_wt(so, 'express')
```

>sleuth_table <- sleuth_results(so, 'express', test_type='wt', show_all = FALSE)

>write.table(distinct(as.data.frame(sleuth_table)[,c("target_id","qval","b")]),file="1wayWT_results.tsv",sep="\t",row.names=FALSE,col.names=FALSE)

>rm(so)

 # two variables (group vs group but control for donor - "biorep")

>so <- sleuth_prep(s2c, ~express + biorep, extra_bootstrap_summary=TRUE, num_cores=1, target_mapping=t2g, transformation_function = function(x) log2(x+1.5), gene_mode=TRUE, aggregation_column = 'ext_gene')

>so <- sleuth_fit(so, ~express + biorep, 'full')

>so <- sleuth_fit(so, ~biorep, 'reduced')

>so <- sleuth_lrt(so, 'reduced', 'full')

>sleuth_table <- sleuth_results(so, 'reduced:full', test_type='lrt', show_all = FALSE)

>write.table(distinct(as.data.frame(sleuth_table)[,c("target_id","qval")]),file="2wayLRT_results.tsv",sep="\t",row.names=FALSE,col.names=FALSE)

>rm(so)

>rm(s2c)

DESeq2 script (R)

```
>if (!requireNamespace("BiocManager", quietly = TRUE))
  install.packages("BiocManager")
>BiocManager::install("DESeq2")
>BiocManager::install("BiocParallel")
>library(plyr)
```

#Read in TCGA counts "cts" data

```
>cts <- as.matrix(read.csv("counts_data.txt" ,sep="\t",row.names="gene_id"))
>head(cts)
```

#Read in new groupings

```
>groups = read.table("DESeq_groups_file.txt", header = FALSE)
>colnames(groups) = c("id", "variable")
```

 # head(groups) to check correct format

```
>groups$id <- as.factor(groups$id)
>groups$variable <- as.factor(groups$variable)
>coldata <- groups[,c("id","variable")]
>rownames(coldata) = coldata$id
>head(cts,2)
>head(coldata)
```

#Check if all row/col names in cts and coldata match - should return "TRUE"

```
>all(rownames(coldata) %in% colnames(cts))
```

#Check if all row/col names in cts and coldata are sorted in the same way – may return "TRUE/FALSE"

```
>all(rownames(coldata) == colnames(cts))
```

#If needed (ie FALSE above): Sort cts based on rownames in coldata

```
>cts <- cts[, rownames(coldata)]
```

 # If needed: Re-check if all row/col names in cts and coldata are sorted in the same way - must return "TRUE"

```
>all(rownames(coldata) == colnames(cts))
```

#Build a DESeqDataSet

```
>library("DESeq2")

>dds <- DESeqDataSetFromMatrix(countData = cts,

                    colData = coldata,

                    design = ~ variable)

>dds
```

#Pre-filtering - remove rows with fewer than 404 counts (ie 1 per sample)

```
>keep <- rowSums(counts(dds)) >= 404

>dds <- dds[keep,]

>dds
```

#Choose reference or "control" group - default is group 1 which from the dendrogram_cut might be a hi/lo group

```
>dds <- dds[, dds$variable %in% c("0","1")]

>dds$variable <- droplevels(dds$variable)

>dds
```

 # Differential expression analysis

```
>dds <- DESeq(dds)

>res <- results(dds)

>res
```

#Write results table for Excel

```
>write.table(res, "results_file_name.txt", sep="\t")
```

EnhancedVolcano script (R)

#complete DEG analyses by DESeq2 then run this code on res function

```
>if (!requireNamespace('BiocManager', quietly = TRUE))
  install.packages('BiocManager')

>BiocManager::install('EnhancedVolcano')

>library(EnhancedVolcano)

>EnhancedVolcano(res,
        lab = rownames(res),
        x = 'log2FoldChange',
        y = 'pvalue',
        xlim = c(-10, 10),
        title = 'name_of_analysis',
        FCcutoff = 2,
        pCutoff = 0.0038,
        pointSize = 1.0,
        labSize = 4.0,
```

```
col=c('grey', 'black', 'blue', 'red3'),

legendPosition = 'bottom',

legendLabSize = 16,

legendIconSize = 5.0,

boxedLabels = TRUE,

drawConnectors = TRUE,

widthConnectors = 0.2,

colConnectors = 'black',

gridlines.major = FALSE,

gridlines.minor = FALSE,

selectLab = c('gene1','gene2', 'gene3'))
```

fgsea script (R)

#complete DEG analyses by DESeq2 then run this code on res function

```
>res <- results(dds, tidy = TRUE)

>readr::write_csv(res, path="deseq2_results_file.csv")

>library(tidyverse)

>res <- read_csv("deseq2_results_file.csv")

>res
```

 # remove other data from res function, leaving only row and stat columns

```
>res2 <- res %>%

 >dplyr::select(row, stat) %>%

 na.omit() %>%

 distinct() %>%

 group_by(row) %>%

 summarize(stat=mean(stat))

>res2
```

#install and load fgsea

```
>if (!requireNamespace("BiocManager", quietly = TRUE))

 install.packages("BiocManager")


>BiocManager::install("fgsea")

>library(fgsea)
```

#create tibble of named vector of test statistics

```
>ranks <- deframe(res2)
```

```
>head(ranks, 20)

# load pathways downloaded from MsigDB website

>pathways.hallmark <- gmtPathways("c2.cp.biocarta.v7.2.symbols.gmt")

#Show first few pathways with first few genes only

>pathways.hallmark %>%

 head() %>%

 lapply(head)

# run fgsea algorithm with 1000 permutations and tidy results

>fgseaRes <- fgsea(pathways=pathways.hallmark, stats=ranks, nperm=1000)

>fgseaResTidy <- fgseaRes %>%

 as_tibble() %>%

 arrange(desc(NES))

# install DT table package

>install.packages('DT')

#Display results in DT table

>fgseaResTidy %>%

 dplyr::select(-leadingEdge, -ES, -nMoreExtreme) %>%

 arrange(padj) %>%

 DT::datatable()

# Plot normalised enrichment scores

>ggplot(fgseaResTidy, aes(reorder(pathway, NES), NES)) +

 geom_col(aes(fill=padj<0.05)) +

 coord_flip() +
```

```
  labs(x="Pathway", y="Normalized Enrichment Score",
       title="Hallmark pathways NES from GSEA") +
  theme_classic()
```

#display tibble showing gene q values and what hallmark gene set they enrich

```
>pathways.hallmark %>%
  enframe("pathway", "row") %>%
  unnest() %>%
  inner_join(res, by="row") %>%
  arrange(padj)
```

#plot GSEA table plot

```
>topUp <- fgseaResTidy %>%
  filter(ES > 0) %>%
  top_n(10, wt=-padj)
>topDown <- fgseaResTidy %>%
  filter(ES < 0) %>%
  top_n(10, wt=-padj)
>topPathways <- bind_rows(topUp, topDown) %>%
  arrange(-ES)
>plotGseaTable(pathways.hallmark[topPathways$pathway],
               ranks,
               fgseaResTidy,
               gseaParam = 0.5)
```

prcomp/ggbiplot script (R)

```
>library("devtools")

# Load programs

>install_github("vqv/ggbiplot")

>library(ggbiplot)

# Run PCA on dataset (change number of columns to number of genes being analysed)

>genes.pca <- prcomp(file_name[, c(2:10)], center = TRUE, scale = FALSE)

#Show % of principle components in data

>summary(genes.pca)

# Create group of sample subtypes

>Subtype <- as.factor(file_name$Subtype[1:21])

# Add classifications and ellipses to PCA

>g <- ggbiplot(genes.pca, obs.scale = 1, var.scale = 1, groups = Subtype, ellipse = TRUE, label.repel = TRUE)

# Assign specific colours to Subtypes

>cols <- c("group1" = "green", "group2" = "darkgreen", "group3" = "violet", "group4" = "red", "group5" = "yellow3", "group6" = "blue")

>g <- g + scale_color_manual(values = cols)

>g <- g + theme(legend.direction = 'horizontal', legend.position = 'top')

# Display PCA and remove grey background

>print(g + theme_classic())
```

List of used acronyms

Acronym	Full name
ABS	Adult Bovine Serum
ACTA2	α-Smooth muscle actin
ANOVA	One-way Analysis of Variance
ARID1A	AT-rich interactive domain-containing protein 1A
AUM	Asymmetric Unit Membrane
Ba/Sq	Basal/Squamous
BCG	Bacillus Calmette-Guérin
BCS	Bovine calf serum
BrdU	Bromodeoxyuridine
cDNA	complementary DNA
CGN	Cingulin
CIS	Carcinoma *in situ*
CK	Cytokeratin
Ct	Cycle threshold
DAB	3,3'Diaminobenzidine
DBD	DNA-Binding Domain
DEPC	Diethylpyrocarbonate
DES	Desmin
DMEM	Dulbecco's Modified Eagle's Medium
DTT	Dithiothreitol
ECM	Extracellular Matrix
EDTA	Ethylenediaminetetra-acetic acid
EGF	Epidermal Growth Factor
EGFR	EGF Receptor
ELF3	ETS-related transcription factor 3
ER	Endoplasmic Reticulum
ERK1/2	Extracellular signal-regulated kinase
FAIREseq	Formaldehyde-Assisted Isolation of Regulatory Elements coupled with next-generation sequencing
FBS	Fetal Bovine Serum
FFPE	Formalin-Fixed, Paraffin-Embedded
FGF	Fibroblast Growth Factor
FGFR	FGF Receptor
FOXA1	Forkhead Box A1
FR180	FR180204
GaM	Goat anti-Mouse
GaR	Goat anti-Rabbit
GLI	Glioma-associated oncogene
GSEA	Gene Set Enrichment Analysis
GSK3β	Glycogen Synthase Kinase 3 Beta

HIER	Heat-Induced Epitope Retrieval
hpo	Hippo
IGF-1	Insulin Growth Factor-1
IHC	Immunohistochemistry
IRF-1	Interferon Regulatory Factor-1
KSFMc	Keratinocyte Serum-Free Medium (complete)
LDS	Lithium Dodecyl Sulfate
lncRNA	long non-coding RNA
LTR	Long terminal repeat
LumNS	Luminal Non-Specific
LumP	Luminal Papillary
LumU	Luminal Unstable
LY	LY294002
MEK1/2	Mitogen-activated protein kinase kinase
MIBC	Muscle-Invasive Bladder Cancer
MW	Microwave method (IHC)
NbHS	Normal (bladder-derived) Human Stromal
NE	Neuroendocrine-like
NHU	Normal Human Urothelial
NMIBC	Non-Muscle-Invasive Bladder Cancer
NuHS	Normal (ureter-derived) Human Stromal
PAGE	Polyacrylamide Gel Electrophoresis
PBS	Phosphate-Buffered Saline
PC	Pressure cooker method (IHC)
PD	PD153035
PD98	PD98059
PI3K	Phosphoinositide 3-Kinase
POU5F1	OCT4
PPARγ	Peroxisome proliferator-activated receptor gamma
PPRE	PPAR Response Elements
PTCH1	Patched 1
PTPRC	CD45
PVDF	Polyvinylidene Difluoride
RB	Retinoblastoma protein
RHOA	Ras homolog family member A
RNAseq	RNA sequencing
ROS	Reactive Oxygen Species
RT+/-	Reverse Transcriptase
RTK	Receptor Tyrosine Kinase
RT-PCR	Reverse Transcription Polymerase Chain Reaction
RT-qPCR	Quantitative Reverse Transcription Polymerase Chain Reaction

RXRα	Retinoid X Receptor Alpha
sav	Salvador
sd	Scalloped
SDS	Sodium Docecyl Sulfate
SHH	Sonic Hedgehog
shRNA	short hairpin RNA
siRNA	small interfering RNA
SMO	Smoothened
SR	Stroma-Rich
T007	T0070907
TBS	Tris-Buffered Saline
TEER	Transepithelial Electrical Resistance
TGFβ	Transforming Growth Factor Beta
Tm	Primer melting temperature
TPM	Transcripts Per Million
TV	Tryspin-Versene
TZ	Troglitazone
VG	Vestigial
VGLL	Vg-like
WT	Wild-type
wts	Warts
WWTR1	Taz; transcriptional co-activator with PDZ binding motif
YAP	Yes-associated protein
yki	Yorkie
ZO	Zonular Occludens

References

Aberger, F., & Ruiz i Altaba, A. (2014). Context-dependent signal integration by the GLI code: The oncogenic load, pathways, modifiers and implications for cancer therapy. In *Seminars in Cell and Developmental Biology* (Vol. 33, Issue 100, pp. 93–104). Elsevier Ltd. https://doi.org/10.1016/j.semcdb.2014.05.003

Aberle, H., Bauer, A., Stappert, J., Kispert, A., & Kemler, R. (1997). β-catenin is a target for the ubiquitin-proteasome pathway. *EMBO Journal*, *16*(13), 3797–3804. https://doi.org/10.1093/emboj/16.13.3797

Aboulkassim, T. O., LaRue, H., Lemieux, P., Rousseau, F., & Fradet, Y. (2003). Alteration of the PATCHED locus in superficial bladder cancer. *Oncogene*, *22*(19), 2967–2971. https://doi.org/10.1038/sj.onc.1206513

Aine, M., Eriksson, P., Liedberg, F., Sjödahl, G., & Höglund, M. (2015). Biological determinants of bladder cancer gene expression subtypes. *Scientific Reports*, *5*(1), 10957. https://doi.org/10.1038/srep10957

Alver, B. H., Kim, K. H., Lu, P., Wang, X., Manchester, H. E., Wang, W., Haswell, J. R., Park, P. J., & Roberts, C. W. M. (2017). The SWI/SNF chromatin remodelling complex is required for maintenance of lineage specific enhancers. *Nature Communications*, *8*. https://doi.org/10.1038/ncomms14648

Amin, S. H., Tibes, R., Kim, J. E., & Hybarger, C. P. (2010). Hedgehog antagonist GDC-0449 is effective in the treatment of advanced basal cell carcinoma. *Laryngoscope*, *120*(12), 2456–2459. https://doi.org/10.1002/lary.21145

Bailey, J. M., Mohr, A. M., & Hollingsworth, M. A. (2009). Sonic hedgehog paracrine signaling regulates metastasis and lymphangiogenesis in pancreatic cancer. *Oncogene*, *28*(40), 3513–3525. https://doi.org/10.1038/onc.2009.220

Baker, S. C., & Southgate, J. (2008). Towards control of smooth muscle cell differentiation in synthetic 3D scaffolds. *Biomaterials*, *29*(23), 3357–3366. https://doi.org/10.1016/j.biomaterials.2008.04.033

Balbás-Martínez, C., Rodríguez-Pinilla, M., Casanova, A., Domínguez, O., Pisano, D. G., Gómez, G., Lloreta, J., Lorente, J. A., Malats, N., & Real, F. X. (2013). ARID1A Alterations Are Associated with FGFR3-Wild Type, Poor-Prognosis, Urothelial Bladder Tumors. *PLoS ONE*, *8*(5). https://doi.org/10.1371/journal.pone.0062483

Balsara, Z. R., & Li, X. (2017). Sleeping beauty: Awakening urothelium from its slumber. In *American Journal of Physiology - Renal Physiology* (Vol. 312, Issue 4, pp. F732–F743). American Physiological Society. https://doi.org/10.1152/ajprenal.00337.2016

Baskin, L. S., Hayward, S. W., Young, P., & Cunha, G. R. (1996). Role of mesenchymal-epithelial interactions in normal bladder development. *Journal of Urology*, *156*(5), 1820–1827. https://doi.org/10.1016/S0022-5347(01)65545-9

Béguin, E. P., Janssen, E. F. J., Hoogenboezem, M., Meijer, A. B., Hoogendijk, A. J., & van den Biggelaar, M. (2020). Flow-induced Reorganization of Laminin-integrin Networks Within the Endothelial Basement Membrane Uncovered by Proteomics. *Molecular & Cellular Proteomics : MCP*, *19*(7), 1179–1192. https://doi.org/10.1074/mcp.RA120.001964

Behrens, J., Von Kries, J. P., Kühl, M., Bruhn, L., Wedlich, D., Grosschedl, R., & Birchmeier, W. (1996). Functional interaction of β-catenin with the transcription factor LEF- 1. *Nature*, *382*(6592), 638–642. https://doi.org/10.1038/382638a0

Bell, S. M., Zhang, L., Mendell, A., Xu, Y., Haitchi, H. M., Lessard, J. L., & Whitsett, J. A. (2011). Kruppel-like factor 5 is required for formation and differentiation of the bladder urothelium. *Developmental Biology*, *358*(1), 79–90. https://doi.org/10.1016/j.ydbio.2011.07.020

Bernard-Pierrot, I., Brams, A., Dunois-Lardé, C., Caillault, A., Diez de Medina, S. G., Cappellen, D., Graff, G., Thiery, J. P., Chopin, D., Ricol, D., & Radvanyi, F. (2006). Oncogenic properties of the mutated forms of fibroblast growth factor receptor 3b. *Carcinogenesis*, *27*(4), 740–747. https://doi.org/10.1093/carcin/bgi290

Bhat-Nakshatri, P., Goswami, C. P., Badve, S., Magnani, L., Lupien, M., & Nakshatri, H. (2016). Molecular insights of pathways resulting from two common PIK3CA mutations in breast cancer. *Cancer Research*, *76*(13), 3989–4001. https://doi.org/10.1158/0008-5472.CAN-15-3174

Biton, A., Bernard-Pierrot, I., Lou, Y., Krucker, C., Chapeaublanc, E., Rubio-Pérez, C., López-Bigas, N., Kamoun, A., Neuzillet, Y., Gestraud, P., Grieco, L., Rebouissou, S., DeReyniès, A., Benhamou, S., Lebret, T., Southgate, J., Barillot, E., Allory, Y., Zinovyev, A., & Radvanyi, F. (2014). Independent Component Analysis Uncovers the Landscape of the Bladder Tumor Transcriptome and Reveals Insights into Luminal and Basal Subtypes. *Cell Reports*, *9*(4), 1235–1245. https://doi.org/10.1016/j.celrep.2014.10.035

Blaveri, E., Simko, J. P., Korkola, J. E., Brewer, J. L., Baehner, F., Mehta, K., DeVries, S., Koppie, T., Pejavar, S., Carroll, P., & Waldman, F. M. (2005). Bladder cancer outcome and subtype classification by gene expression. *Clinical Cancer Research*, *11*(11), 4044–4055. https://doi.org/10.1158/1078-0432.CCR-04-2409

Böck, M., Hinley, J., Schmitt, C., Wahlicht, T., Kramer, S., & Southgate, J. (2014). Identification of ELF3 as an early transcriptional regulator of human urothelium. *Developmental Biology*, *386*(2), 321–330. https://doi.org/10.1016/j.ydbio.2013.12.028

Bokhovchuk, F., Mesrouze, Y., Izaac, A., Meyerhofer, M., Zimmermann, C., Fontana, P., Schmelzle, T., Erdmann, D., Furet, P., Kallen, J., & Chène, P. (2019). Molecular and structural characterization of a TEAD mutation at the origin of Sveinsson's chorioretinal atrophy. *FEBS Journal*, *286*(12), 2381–2398. https://doi.org/10.1111/febs.14817

Bolger, A. M., Lohse, M., & Usadel, B. (2014). Trimmomatic: A flexible trimmer for Illumina sequence data. *Bioinformatics*, *30*(15), 2114–2120. https://doi.org/10.1093/bioinformatics/btu170

Bradley, S. D., Talukder, A. H., Lai, I., Davis, R., Alvarez, H., Tiriac, H., Zhang, M., Chiu, Y., Melendez, B., Jackson, K. R., Katailiha, A., Sonnemann, H. M., Li, F., Kang, Y., Qiao, N., Pan, B. F., Lorenzi, P. L., Hurd, M., Mittendorf, E. A., … Lizée, G. (2020). Vestigial-like 1 is a shared targetable cancer-placenta antigen expressed by pancreatic and basal-like breast cancers. *Nature Communications*, *11*(1). https://doi.org/10.1038/s41467-020-19141-w

Bray, N. L., Pimentel, H., Melsted, P., & Pachter, L. (2016). Near-optimal probabilistic RNA-

seq quantification. *Nature Biotechnology*, *34*(5), 525–527. https://doi.org/10.1038/nbt.3519

Burgering, B. M. T., & Coffer, P. J. (1995). Protein kinase B (c-Akt) in phosphatidylinositol-3-OH kinase signal transduction. In *Nature* (Vol. 376, Issue 6541, pp. 599–602). Nature Publishing Group. https://doi.org/10.1038/376599a0

Burgermeister, E., Chuderland, D., Hanoch, T., Meyer, M., Liscovitch, M., & Seger, R. (2007). Interaction with MEK Causes Nuclear Export and Downregulation of Peroxisome Proliferator-Activated Receptor. *Molecular and Cellular Biology*, *27*(3), 803–817. https://doi.org/10.1128/mcb.00601-06

Cambray-Deakin, M. A., & Burgoyne, R. D. (1987). Acetylated and detyrosinated alpha-tubulins are co-localized in stable microtubules in rat meningeal fibroblasts. *Cell Motility and the Cytoskeleton*, *8*(3), 284–291. https://doi.org/10.1002/cm.970080309

Camp, H. S., & Tafuri, S. R. (1997). Regulation of peroxisome proliferator-activated receptor γ activity by mitogen-activated protein kinase. *Journal of Biological Chemistry*, *272*(16), 10811–10816. https://doi.org/10.1074/jbc.272.16.10811

Cancer Research UK. (2019). *Bladder cancer statistics*. Www.Cancerresearchuk.Org/Cancer-Info/Cancerstats/. http://www.cancerresearchuk.org/health-professional/cancer-statistics

Cao, M., Tasian, G., Wang, M. H., Liu, B., Cunha, G., & Baskin, L. (2010). Urothelium-derived Sonic hedgehog promotes mesenchymal proliferation and induces bladder smooth muscle differentiation. *Differentiation*, *79*(4–5), 244–250. https://doi.org/10.1016/j.diff.2010.02.002

Castilla, M. A., Lopez-Garcia, M. A., Atienza, M. R., Rosa-Rosa, J. M., Diaz-Martin, J., Pecero, M. L., Vieites, B., Romero-Perez, L., Benitez, J., Calcabrini, A., & Palacios, J. (2014). VGLL1 expression is associated with a triple-negative basal-like phenotype in breast cancer. *Endocrine Related Cancer*, *21*(4), 587–599. https://doi.org/10.1530/ERC-13-0485

Caubit, X., Lye, C. M., Martin, E., Coré, N., Long, D. A., Vola, C., Jenkins, D., Garratt, A. N., Skaer, H., Woolf, A. S., & Fasano, L. (2008). Teashirt 3 is necessary for ureteral smooth muscle differentiation downstream of SHH and BMP4. *Development*, *135*(19), 3301–3310. https://doi.org/10.1242/dev.022442

Chamie, K., Litwin, M. S., Bassett, J. C., Daskivich, T. J., Lai, J., Hanley, J. M., Konety, B. R., & Saigal, C. S. (2013). Recurrence of high-risk bladder cancer: A population-based analysis. *Cancer*, *119*(17), 3219–3227. https://doi.org/10.1002/cncr.28147

Chamoun, Z., Mann, R. K., Nellen, D., von Kessler, D. P., Bellotto, M., Beachy, P. A., & Basler, K. (2001). Skinny hedgehog, an acyltransferase required for palmitoylation and activity of the hedgehog signal. *Science (New York, N.Y.)*, *293*(5537), 2080–2084. https://doi.org/10.1126/science.1064437

Chen, H. H., Mullett, S. J., & Stewart, A. F. R. (2004). Vgl-4, a novel member of the vestigial-like family of transcription cofactors, regulates α1-adrenergic activation of gene expression in cardiac myocytes. *Journal of Biological Chemistry*, *279*(29), 30800–30806. https://doi.org/10.1074/jbc.M400154200

Chen, J. K., Taipale, J., Cooper, M. K., & Beachy, P. A. (2002). Inhibition of Hedgehog

signaling by direct binding of cyclopamine to Smoothened. *Genes and Development*, *16*(21), 2743–2748. https://doi.org/10.1101/gad.1025302

Chen, J. K., Taipale, J., Young, K. E., Maiti, T., & Beachy, P. A. (2002). Small molecule modulation of Smoothened activity. *Proceedings of the National Academy of Sciences of the United States of America*, *99*(22), 14071–14076. https://doi.org/10.1073/pnas.182542899

Chen, Q., Xu, R., Zeng, C., Lu, Q., Huang, D., Shi, C., Zhang, W., Deng, L., Yan, R., Rao, H., Gao, G., & Luo, S. (2014). Down-regulation of Gli transcription factor leads to the inhibition of migration and invasion of ovarian cancer cells via integrin β4-mediated FAK signaling. *PLoS ONE*, *9*(2). https://doi.org/10.1371/journal.pone.0088386

Cheng, W., Yeung, C. K., Ng, Y. K., Zhang, J. R., Hui, C. C., & Kim, P. C. W. (2008). Sonic Hedgehog Mediator Gli2 Regulates Bladder Mesenchymal Patterning. *Journal of Urology*, *180*(4), 1543–1550. https://doi.org/10.1016/j.juro.2008.06.003

Chlapowski, F. J., & Haynes, L. (1979). The Growth And Differentiation Of Transitional Epithelium In Vitro. *Journal Of Cell Biology*, *83*(December). https://www.ncbi.nlm.nih.gov/pmc/articles/PMC2110519/pdf/jc833605.pdf

Choi, W., Czerniak, B., Ochoa, A., Su, X., Siefker-Radtke, A., Dinney, C., & McConkey, D. J. (2014). Intrinsic basal and luminal subtypes of muscle-invasive bladder cancer. *Nature Reviews Urology*, *11*(7), 400–410. https://doi.org/10.1038/nrurol.2014.129

Choi, W., Porten, S., Kim, S., Willis, D., Plimack, E. R., Hoffman-Censits, J., Roth, B., Cheng, T., Tran, M., Lee, I.-L., Melquist, J., Bondaruk, J., Majewski, T., Zhang, S., Pretzsch, S., Baggerly, K., Siefker-Radtke, A., Czerniak, B., Dinney, C. P. N., & McConkey, D. J. (2014a). Identification of Distinct Basal and Luminal Subtypes of Muscle-Invasive Bladder Cancer with Different Sensitivities to Frontline Chemotherapy. *Cancer Cell*, *25*(2), 152–165. https://doi.org/10.1016/j.ccr.2014.01.009

Choi, W., Porten, S., Kim, S., Willis, D., Plimack, E. R., Hoffman-Censits, J., Roth, B., Cheng, T., Tran, M., Lee, I. L., Melquist, J., Bondaruk, J., Majewski, T., Zhang, S., Pretzsch, S., Baggerly, K., Siefker-Radtke, A., Czerniak, B., Dinney, C. P. N., & McConkey, D. J. (2014b). Identification of Distinct Basal and Luminal Subtypes of Muscle-Invasive Bladder Cancer with Different Sensitivities to Frontline Chemotherapy. *Cancer Cell*, *25*(2), 152–165. https://doi.org/10.1016/j.ccr.2014.01.009

Choi, W., Shah, J. B., Tran, M., Svatek, R., Marquis, L., Lee, I. L., Yu, D., Adam, L., Wen, S., Shen, Y., Dinney, C., McConkey, D. J., & Siefker-Radtke, A. (2012). p63 expression defines a lethal subset of muscle-invasive bladder cancers. *PLoS ONE*, *7*(1). https://doi.org/10.1371/journal.pone.0030206

Chopra, B., Hinley, J., Oleksiewicz, M. B., & Southgate, J. (2008). Trans-Species Comparison of PPAR and RXR Expression by Rat and Human Urothelial Tissues. *Toxicologic Pathology*, *36*(3), 485–495. https://doi.org/10.1177/0192623308315672

Cirillo, L. A., Lin, F. R., Cuesta, I., Friedman, D., Jarnik, M., & Zaret, K. S. (2002). Opening of compacted chromatin by early developmental transcription factors HNF3 (FoxA) and GATA-4. *Molecular Cell*, *9*(2), 279–289. https://doi.org/10.1016/S1097-2765(02)00459-8

Cook, K. D., & Miller, J. (2010). TCR-Dependent Translational Control of GATA-3 Enhances

Th2 Differentiation. *The Journal of Immunology*, *185*(6), 3209–3216. https://doi.org/10.4049/jimmunol.0902544

Cross, W. R., Eardley, I., Leese, H. J., & Southgate, J. (2005). A biomimetic tissue from cultured normal human urothelial cells: analysis of physiological function. *American Journal of Physiology. Renal Physiology*, *289*(2), F459–F468. https://doi.org/10.1152/ajprenal.00040.2005

Dadhania, V., Zhang, M., Zhang, L., Bondaruk, J., Siefker-radtke, A., Guo, C., Dinney, C., David, E., Zhang, S., Lee, S., Lee, J. G., Weinstein, J. N., Baggerly, K., Mcconkey, D., & Czerniak, B. (2016). Meta-Analysis of the Luminal and Basal Subtypes of Bladder Cancer and the Identification of Signature Immunohistochemical Markers for Clinical Use. *EBIOM*, *12*, 105–117. https://doi.org/10.1016/j.ebiom.2016.08.036

Dahm, P., & Gschwend, J. E. (2003). Malignant Non-Urothelial Neoplasms of the Urinary Bladder: A Review. In *European Urology* (Vol. 44, Issue 6, pp. 672–681). Elsevier. https://doi.org/10.1016/S0302-2838(03)00416-0

Damrauer, J. S., Hoadley, K. A., Chism, D. D., Fan, C., Tiganelli, C. J., Wobker, S. E., Yeh, J. J., Milowsky, M. I., Iyer, G., Parker, J. S., & Kim, W. Y. (2014). Intrinsic subtypes of high-grade bladder cancer reflect the hallmarks of breast cancer biology. *Proceedings of the National Academy of Sciences of the United States of America*, *111*(8), 3110–3115. https://doi.org/10.1073/pnas.1318376111

De, P., & Dey, N. (2019). Mutation-driven signals of ARID1A and PI3K pathways in ovarian carcinomas: Alteration is an opportunity. In *International Journal of Molecular Sciences* (Vol. 20, Issue 22, p. 5732). MDPI AG. https://doi.org/10.3390/ijms20225732

DeGraff, D. J., Cates, J. M., Mauney, J. R., Clark, P. E., Matusik, R. J., & Adam, R. M. (2013). When urothelial differentiation pathways go wrong: Implications for bladder cancer development and progression. In *Urologic Oncology: Seminars and Original Investigations* (Vol. 31, Issue 6, pp. 802–811). https://doi.org/10.1016/j.urolonc.2011.07.017

DeGraff, D. J., Clark, P. E., Cates, J. M., Yamashita, H., Robinson, V. L., Yu, X., Smolkin, M. E., Chang, S. S., Cookson, M. S., Herrick, M. K., Shariat, S. F., Steinberg, G. D., Frierson, H. F., Wu, X. R., Theodorescu, D., & Matusik, R. J. (2012). Loss of the urothelial differentiation marker FOXA1 is associated with high grade, late stage bladder cancer and increased tumor proliferation. *PLoS ONE*, *7*(5), 36669. https://doi.org/10.1371/journal.pone.0036669

Deshpande, N., Chopra, A., Rangarajan, A., Shashidhara, L. S., Rodrigues, V., & Krishna, S. (1997). The human transcription enhancer factor-1, TEF-1, can substitute for Drosophila scalloped during wingblade development. *Journal of Biological Chemistry*, *272*(16), 10664–10668. https://doi.org/10.1074/jbc.272.16.10664

DeSouza, K. R., Saha, M., Carpenter, A. R., Scott, M., & McHugh, K. M. (2013). Analysis of the Sonic Hedgehog Signaling Pathway in Normal and Abnormal Bladder Development. *PLoS ONE*, *8*(1), e53675. https://doi.org/10.1371/journal.pone.0053675

Dhawan, D., Ramos-Vara, J. A., Hahn, N. M., Waddell, J., Olbricht, G. R., Zheng, R., Stewart, J. C., & Knapp, D. W. (2013). DNMT1: An emerging target in the treatment of invasive urinary bladder cancer. *Urologic Oncology: Seminars and Original Investigations*, *31*(8), 1761–1769. https://doi.org/10.1016/j.urolonc.2012.03.015

Dixon, J. S., & Gosling, J. A. (1983). Histology and fine structure of the muscularis mucosae of the human urinary bladder. *Journal of Anatomy*, *136*(Pt 2), 265–271. http://www.ncbi.nlm.nih.gov/pubmed/6682849

Dominick, M. A., White, M. R., Sanderson, T. P., Van Vleet, T., Cohen, S. M., Arnold, L. E., Cano, M., Tannehill-Gregg, S., Moehlenkamp, J. D., Waites, C. R., & Schilling, B. E. (2006). Urothelial Carcinogenesis in the Urinary Bladder of Male Rats Treated with Muraglitazar, a PPARα/γ Agonist: Evidence for Urolithiasis as the Inciting Event in the Mode of Action. *Toxicologic Pathology*, *34*(7), 903–920. https://doi.org/10.1080/01926230601072327

Dong, L., Lin, F., Wu, W., Liu, Y., & Huang, W. (2018). Verteporfin inhibits YAP-induced bladder cancer cell growth and invasion via hippo signaling pathway. *International Journal of Medical Sciences*, *15*(6), 645–652. https://doi.org/10.7150/ijms.23460

Dyrskjøt, L., Thykjaer, T., Kruhøffer, M., Jensen, J. L., Marcussen, N., Hamilton-Dutoit, S., Wolf, H., & Ørntoft, T. F. (2003). Identifying distinct classes of bladder carcinoma using microarrays. *Nature Genetics*, *33*(1), 90–96. https://doi.org/10.1038/ng1061

Earl, J., Rico, D., Carrillo-de-Santa-Pau, E., Rodríguez-Santiago, B., Méndez-Pertuz, M., Auer, H., Gómez, G., Grossman, H. B., Pisano, D. G., Schulz, W. A., Pérez-Jurado, L. A., Carrato, A., Theodorescu, D., Chanock, S., Valencia, A., & Real, F. X. (2015). The UBC-40 Urothelial Bladder Cancer cell line index: a genomic resource for functional studies. *BMC Genomics*, *16*(1), 403. https://doi.org/10.1186/s12864-015-1450-3

Ebnet, K., Aurrand-Lions, M., Kuhn, A., Kiefer, F., Butz, S., Zander, K., Meyer zu Brickwedde, M. K., Suzuki, A., Imhof, B. A., & Vestweber, D. (2003). The junctional adhesion molecule (JAM) family members JAM-2 and JAM-3 associate with the cell polarity protein PAR-3: A possible role for JAMs in endothelial cell polarity. *Journal of Cell Science*, *116*(19), 3879–3891. https://doi.org/10.1242/jcs.00704

Echelard, Y., Epstein, D. J., St-Jacques, B., Shen, L., Mohler, J., McMahon, J. A., & McMahon, A. P. (1993). Sonic hedgehog, a member of a family of putative signaling molecules, is implicated in the regulation of CNS polarity. *Cell*, *75*(7), 1417–1430. https://doi.org/10.1016/0092-8674(93)90627-3

Elbadawi, A. (1996). Functional anatomy of the organs of micturition. *Urologic Clinics of North America*, *23*(2), 177–210. https://doi.org/10.1016/S0094-0143(05)70304-9

Elliott, A. Y., Stein, N., & Fraley, E. E. (1975). Technique for cultivation of transitional epithelium from mammalian urinary bladder. *In Vitro: Journal of the Tissue Culture Association*, *11*(5), 251–254. https://doi.org/10.1007/BF02615635

Fanning, A. S., Jameson, B. J., Jesaitis, L. A., & Anderson, J. M. (1998). The tight junction protein ZO-1 establishes a link between the transmembrane protein occludin and the actin cytoskeleton. *Journal of Biological Chemistry*, *273*(45), 29745–29753. https://doi.org/10.1074/jbc.273.45.29745

Fei, D. L., Sanchez-Mejias, A., Wang, Z., Flaveny, C., Long, J., Singh, S., Rodriguez-Blanco, J., Tokhunts, R., Giambelli, C., Briegel, K. J., Schulz, W. A., Gandolfi, A. J., Karagas, M., Zimmers, T. A., Jorda, M., Bejarano, P., Capobianco, A. J., & Robbins, D. J. (2012). Hedgehog signaling regulates bladder cancer growth and tumorigenicity. *Cancer Research*, *72*(17), 4449–4458. https://doi.org/10.1158/0008-5472.CAN-11-4123

Fishilevich, S., Nudel, R., Rappaport, N., Hadar, R., Plaschkes, I., Iny Stein, T., Rosen, N., Kohn, A., Twik, M., Safran, M., Lancet, D., & Cohen, D. (2017). GeneHancer: genome-wide integration of enhancers and target genes in GeneCards. *Database : The Journal of Biological Databases and Curation*, *2017*, 1–17. https://doi.org/10.1093/database/bax028

Fishwick, C., Higgins, J., Percival-Alwyn, L., Hustler, A., Pearson, J., Bastkowski, S., Moxon, S., Swarbreck, D., Greenman, C. D., & Southgate, J. (2017). Heterarchy of transcription factors driving basal and luminal cell phenotypes in human urothelium. *Cell Death and Differentiation*, *24*(5), 809–818. https://doi.org/10.1038/cdd.2017.10

Fleming, J. M., Shabir, S., Varley, C. L., Kirkwood, L. A., White, A., Holder, J., Trejdosiewicz, L. K., & Southgate, J. (2012). Differentiation-Associated Reprogramming of the Transforming Growth Factor β Receptor Pathway Establishes the Circuitry for Epithelial Autocrine/Paracrine Repair. *PLoS ONE*, *7*(12), e51404. https://doi.org/10.1371/journal.pone.0051404

Fromter, E., & Diamond, J. (1972). Route of Passive Ion Permeation in Epithelia. *Nature New Biology*, *235*(53), 9–13. https://doi.org/10.1038/10.1038/newbio235009a0

Frost, S. J., Simpson, D. J., & Farrell, W. E. (2001). Decreased proliferation and cell cycle arrest in neoplastic rat pituitary cells is associated with transforming growth factor-β1-induced expression of p15/INK4B. *Molecular and Cellular Endocrinology*, *176*(1–2), 29–37. https://doi.org/10.1016/S0303-7207(01)00477-4

Fujii, M., Toyoda, T., Nakanishi, H., Yatabe, Y., Sato, A., Matsudaira, Y., Ito, H., Murakami, H., Kondo, Y., Kondo, E., Hida, T., Tsujimura, T., Osada, H., & Sekido, Y. (2012). TGF-β synergizes with defects in the Hippo pathway to stimulate human malignant mesothelioma growth. *Journal of Experimental Medicine*, *209*(3), 479–494. https://doi.org/10.1084/jem.20111653

Fukumoto, T., Park, P. H., Wu, S., Fatkhutdinov, N., Karakashev, S., Nacarelli, T., Kossenkov, A. V., Speicher, D. W., Jean, S., Zhang, L., Wang, T. L., Shih, I. M., Conejo-Garcia, J. R., Bitler, B. G., & Zhang, R. (2018). Repurposing Pan-HDAC Inhibitors for ARID1A-Mutated Ovarian Cancer. *Cell Reports*, *22*(13), 3393–3400. https://doi.org/10.1016/j.celrep.2018.03.019

Furuse, M., Fujita, K., Hiiragi, T., Fujimoto, K., & Tsukita, S. (1998). Claudin-1 and-2: Novel Integral Membrane Proteins Localizing at Tight Junctions with No Sequence Similarity to Occludin. In *The Journal of Cell Biology* (Vol. 141, Issue 7). http://www.jcb.org

Furuse, M., Hirase, T., Itoh, M., Nagafuchi, A., Yonemura, S., Tsukita, S., & Tsukita, S. (1993). Occludin: A novel integral membrane protein localizing at tight junctions. *Journal of Cell Biology*, *123*(6 II), 1777–1788. https://doi.org/10.1083/jcb.123.6.1777

Gailani, M. R., Stahle-Backdahl, M., Leffell, D. J., Glynn, M., Zaphiropoulos, P. G., Pressman, C., Unden, A. B., Dean, M., Brash, D. E., Bale, A. E., & Toftgard, R. (1996). The role of the human homologue of Drosophila patched in sporadic basal cell carcinomas. *Nature Genetics*, *14*(1), 78–81. https://doi.org/10.1038/ng0996-78

Georgopoulos, N. T., Kirkwood, L. A., & Southgate, J. (2014). A novel bidirectional positive-feedback loop between Wnt-β-catenin and EGFR-ERK plays a role in context-specific modulation of epithelial tissue regeneration. *Journal of Cell Science*, *127*(Pt 13), 2967–2982. https://doi.org/10.1242/jcs.150888

Georgopoulos, N. T., Kirkwood, L. A., Walker, D. C., & Southgate, J. (2010). Differential regulation of growth-promoting signalling pathways by E-cadherin. *PLoS ONE*, *5*(10), e13621. https://doi.org/10.1371/journal.pone.0013621

Ghosh, A. K., Bhattacharyya, S., Lakos, G., Chen, S. J., Mori, Y., & Varga, J. (2004). Disruption of Transforming Growth Factor β Signaling and Profibrotic Responses in Normal Skin Fibroblasts by Peroxisome Proliferator-Activated Receptor γ. *Arthritis and Rheumatism*, *50*(4), 1305–1318. https://doi.org/10.1002/art.20104

Ghosh, A. K., Wei, J., Wu, M., & Varga, J. (2008). Constitutive Smad signaling and Smad-dependent collagen gene expression in mouse embryonic fibroblasts lacking peroxisome proliferator-activated receptor-γ. *Biochemical and Biophysical Research Communications*, *374*(2), 231–236. https://doi.org/10.1016/j.bbrc.2008.07.014

Gondkar, K., Patel, K., Krishnappa, S., Patil, A., Nair, B., Sundaram, G. M., Zea, T. T., & Kumar, P. (2019). E74 like ETS transcription factor 3 (ELF3) is a negative regulator of epithelial- mesenchymal transition in bladder carcinoma. *Cancer Biomarkers*, *25*(2), 223–232. https://doi.org/10.3233/CBM-190013

Gruber Filbin, M., Dabral, S. K., Pazyra-Murphy, M. F., Ramkissoon, S., Kung, A. L., Pak, E., Chung, J., Theisen, M. A., Sun, Y., Franchetti, Y., Sun, Y., Shulman, D. S., Redjal, N., Tabak, B., Beroukhim, R., Wang, Q., Zhao, J., Dorsch, M., Buonamici, S., … Segal, R. A. (2013). Coordinate activation of Shh and PI3K signaling in PTEN-deficient glioblastoma: New therapeutic opportunities. *Nature Medicine*, *19*(11), 1518–1523. https://doi.org/10.1038/nm.3328

Grune, T., Kehm, R., Höhn, A., & Jung, T. (2018). "Cyt/Nuc," a Customizable and Documenting ImageJ Macro for Evaluation of Protein Distributions Between Cytosol and Nucleus. *Biotechnology Journal*, *13*(5). https://doi.org/10.1002/biot.201700652

Guillemot, L., & Citi, S. (2006). Cingulin regulates claudin-2 expression and cell proliferation through the small GTPase RhoA. *Molecular Biology of the Cell*, *17*(8), 3569–3577. https://doi.org/10.1091/mbc.E06-02-0122

Guo, Y., Chen, D., Su, X., Chen, J., & Li, Y. (2019). The lncRNA ELF3-AS1 promotes bladder cancer progression by interaction with Krüppel-like factor 8. *Biochemical and Biophysical Research Communications*, *508*(3), 762–768. https://doi.org/10.1016/j.bbrc.2018.11.183

Gupta, S., Albertson, D. J., Parnell, T. J., Butterfield, A., Weston, A., Pappas, L. M., Dalley, B., O'Shea, J. M., Lowrance, W. T., Cairns, B. R., Schiffman, J. D., & Sharma, S. (2019). Histone deacetylase inhibition has targeted clinical benefit in ARID1A-mutated advanced urothelial carcinoma. *Molecular Cancer Therapeutics*, *18*(1), 185–195. https://doi.org/10.1158/1535-7163.MCT-17-0957

Halstead, A. M., Kapadia, C. D., Bolzenius, J., Chu, C. E., Schriefer, A., Wartman, L. D., Bowman, G. R., & Arora, V. K. (2017). Bladder-cancer-associated mutations in RXRA activate peroxisome proliferator-activated receptors to drive urothelial proliferation. *ELife*, *6*. https://doi.org/10.7554/eLife.30862

Hannon, G. J., & Beach, D. (1994). Pl5INK4B is a potentia| effector of TGF-β-induced cell cycle arrest. *Nature*, *371*(6494), 257–261. https://doi.org/10.1038/371257a0

Harabayashi, T., Kanai, Y., Yamada, T., Sakamoto, M., Ochiai, A., Kakizoe, T., Koyanagi, T., &

Hirohashi, S. (1999). Reduction of integrin β4 and enhanced migration on laminin in association with intraepithelial spreading of urinary bladder carcinomas. *Journal of Urology*, *161*(4), 1364–1371. https://doi.org/10.1016/S0022-5347(01)61685-9

Haraguchi, R., Motoyama, J., Sasaki, H., Satoh, Y., Miyagawa, S., Nakagata, N., Moon, A., & Yamada, G. (2007). Molecular analysis of coordinated bladder and urogenital organ formation by Hedgehog signaling. *Development*, *134*(3), 525–533. https://doi.org/10.1242/dev.02736

Harnden, P., & Southgate, J. (1997). Cytokeratin 14 as a marker of squamous differentiation in transitional cell carcinomas. *Journal of Clinical Pathology*, *50*(12), 1032–1033. https://doi.org/10.1136/jcp.50.12.1032

Hasegawa, H., Fujita, H., Katoh, H., Aoki, J., Nakamura, K., Ichikawa, A., & Negishi, M. (1999). Opposite regulation of transepithelial electrical resistance and paracellular permeability by Rho in Madin-Darby canine kidney cells. *Journal of Biological Chemistry*, *274*(30), 20982–20988. https://doi.org/10.1074/jbc.274.30.20982

He, H. C., Chen, J. H., Chen, X. Bin, Qin, G. Q., Cai, C., Liang, Y. X., Han, Z. D., Dai, Q. S., Chen, Y. R., Zeng, G. H., Zhu, J. G., Jiang, F. N., & Zhong, W. De. (2012). Expression of hedgehog pathway components is associated with bladder cancer progression and clinical outcome. *Pathology and Oncology Research*, *18*(2), 349–355. https://doi.org/10.1007/s12253-011-9451-2

Hickling, D. R., Sun, T.-T., & Wu, X.-R. (2015). Anatomy and Physiology of the Urinary Tract: Relation to Host Defense and Microbial Infection. *Microbiology Spectrum*, *3*(4). https://doi.org/10.1128/microbiolspec.uti-0016-2012

Hicks, R. M. (1965). The fine structure of the transitional epithelium of rat ureter. *The Journal of Cell Biology*, *26*(1), 25–48. https://doi.org/10.1083/jcb.26.1.25

Hicks, R. Marian. (1975). The Mammalian Urinary Bladder: An Accomodating Organ. *Biological Reviews*, *50*(2), 215–246. https://doi.org/10.1111/j.1469-185X.1975.tb01057.x

Hirata, Y., Hayashi, H., Ito, S., Kikawa, Y., Ishibashi, M., Sudo, M., Miyazaki, H., Fukushima, M., Narumiya, S., & Hayaishi, O. (1988). Occurrence of 9-deoxy-Δ9,Δ12-13,14-dihydroprostaglandin D2 in human urine. *Journal of Biological Chemistry*, *263*(32), 16619–16625.

Hodges, G. M., Hicks, R. M., & Spacey, G. D. (1977). Epithelial-stromal interactions in normal and chemical carcinogen-treated adult bladder. *Cancer Research*, *37*(10), 3720–3730. http://www.ncbi.nlm.nih.gov/pubmed/332338

Howlett, A. R., Hodges, G. M., & Rowlatt, C. (1986). Epithelial-stromal interactions in the adult bladder: urothelial growth, differentiation, and maturation on culture facsimiles of bladder stroma. *Developmental Biology*, *118*(2), 403–415. http://www.ncbi.nlm.nih.gov/pubmed/3792617

Hsu, Y. L., Hung, J. Y., Chou, S. H., Huang, M. S., Tsai, M. J., Lin, Y. S., Chiang, S. Y., Ho, Y. W., Wu, C. Y., & Kuo, P. L. (2015). Angiomotin decreases lung cancer progression by sequestering oncogenic YAP/TAZ and decreasing Cyr61 expression. *Oncogene*, *34*(31), 4056–4068. https://doi.org/10.1038/onc.2014.333

Hu, P., Meyers, S., Liang, F. X., Deng, F. M., Kachar, B., Zeidel, M. L., & Sun, T. T. (2002). Role

of membrane proteins in permeability barrier function: Uroplakin ablation elevates urothelial permeability. *American Journal of Physiology - Renal Physiology*, *283*(6 52-6). https://doi.org/10.1152/ajprenal.00043.2002

Hurlstone, A. F. L., Olave, I. A., Barker, N., Van Noort, M., & Clevers, H. (2002). Cloning and characterization of hELD/0SA1, a novel BRG1 interacting protein. *Biochemical Journal*, *364*(1), 255–264. https://doi.org/10.1042/bj3640255

Hustler, A., Eardley, I., Hinley, J., Pearson, J., Wezel, F., Radvanyi, F., Baker, S. C., & Southgate, J. (2018). Differential transcription factor expression by human epithelial cells of buccal and urothelial derivation. *Experimental Cell Research*, *369*(2), 284–294. https://doi.org/10.1016/j.yexcr.2018.05.031

Im, J. Y., Kim, D. M., Park, H., Kang, M. J., Kim, D. Y., Chang, K. Y., Kim, B. K., & Won, M. (2021). VGLL1 phosphorylation and activation promotes gastric cancer malignancy via TGF-β/ERK/RSK2 signaling. *Biochimica et Biophysica Acta - Molecular Cell Research*, *1868*(1). https://doi.org/10.1016/j.bbamcr.2020.118892

Ingram, I. (2012). Vismodegib granted FDA approval for treatment of basal cell carcinoma. *Oncology*, *26*(2), 1–2.

Islam, S. S., Mokhtari, R. B., Noman, A. S., Uddin, M., Rahman, M. Z., Azadi, M. A., Zlotta, A., van der Kwast, T., Yeger, H., & Farhat, W. A. (2016). Sonic hedgehog (Shh) signaling promotes tumorigenicity and stemness via activation of epithelial-to-mesenchymal transition (EMT) in bladder cancer. *Molecular Carcinogenesis*, *55*(5), 537–551. https://doi.org/10.1002/mc.22300

Issemann, I., & Green, S. (1990). Activation of a member of the steroid hormone receptor superfamily by peroxisome proliferators. *Nature*, *347*(6294), 645–650. https://doi.org/10.1038/347645a0

Itoh, K., Chiba, T., Takahashi, S., Ishii, T., Igarashi, K., Katoh, Y., Oyake, T., Hayashi, N., Satoh, K., Hatayama, I., Yamamoto, M., & Nabeshima, Y. ichi. (1997). An Nrf2/small Maf heterodimer mediates the induction of phase II detoxifying enzyme genes through antioxidant response elements. *Biochemical and Biophysical Research Communications*, *236*(2), 313–322. https://doi.org/10.1006/bbrc.1997.6943

Jacob, A., Budhiraja, S., & Reichel, R. R. (1999). The HNF-3α transcription factor is a primary target for retinoic acid action. *Experimental Cell Research*, *250*(1), 1–9. https://doi.org/10.1006/excr.1999.4512

Jenkins, D., Winyard, P. J. D., & Woolf, A. S. (2007). Immunohistochemical analysis of Sonic hedgehog signalling in normal human urinary tract development. *Journal of Anatomy*, *211*(5), 620–629. https://doi.org/10.1111/j.1469-7580.2007.00808.x

Jerman, U. D., Veranič, P., Cirman, T., & Kreft, M. E. (2020). Human Amniotic Membrane Enriched with Urinary Bladder Fibroblasts Promote the Re-Epithelization of Urothelial Injury. *Cell Transplantation*, *29*. https://doi.org/10.1177/0963689720946668

Jiang, G., Wang, X., Sheng, D., Zhou, L., Liu, Y., Xu, C., Liu, S., & Zhang, J. (2019). Cooperativity of co-factor NR2F2 with pioneer factors GATA3, FOXA1 in promoting ERα function. *Theranostics*, *9*(22), 6501–6516. https://doi.org/10.7150/thno.34874

Jiang, W., Yao, F., He, J., Lv, B., Fang, W., Zhu, W., He, G., Chen, J., & He, J. (2015). Downregulation of VGLL4 in the progression of esophageal squamous cell carcinoma.

Tumor Biology, *36*(2), 1289–1297. https://doi.org/10.1007/s13277-014-2701-7

Jiang, X., Castelao, J. E., Yuan, J.-M., Stern, M. C., Conti, D. V, Cortessis, V. K., Pike, M. C., & Gago-Dominguez, M. (2012). Cigarette Smoking and Subtypes of Bladder Cancer. *Int J Cancer*, *130*(4), 896–901. https://doi.org/10.1002/ijc.26068

Jiao, S., Li, C., Hao, Q., Miao, H., Zhang, L., Li, L., & Zhou, Z. (2017). VGLL4 targets a TCF4–TEAD4 complex to coregulate Wnt and Hippo signalling in colorectal cancer. *Nature Communications*, *8*, 14058. https://doi.org/10.1038/ncomms14058

Jiao, S., Wang, H., Shi, Z., Dong, A., Zhang, W., Song, X., He, F., Wang, Y., Zhang, Z., Wang, W., Wang, X., Guo, T., Li, P., Zhao, Y., Ji, H., Zhang, L., & Zhou, Z. (2014). A Peptide Mimicking VGLL4 Function Acts as a YAP Antagonist Therapy against Gastric Cancer. *Cancer Cell*, *25*(2), 166–180. https://doi.org/10.1016/j.ccr.2014.01.010

Joberty, G., Petersen, C., Gao, L., & Macara, I. G. (2000). The cell-polarity protein Par6 links Par3 and atypical protein kinase C to Cdc42. *Nature Cell Biology*, *2*(8), 531–539. https://doi.org/10.1038/35019573

Jost, S. P., Gosling, J. A., & Dixon, J. S. (1989). The morphology of normal human bladder urothelium. *Journal of Anatomy*, *167*, 103–115. http://www.ncbi.nlm.nih.gov/pubmed/2630525%0Ahttp://www.pubmedcentral.nih.gov/articlerender.fcgi?artid=PMC1256824

Kamoun, A., de Reyniès, A., Allory, Y., Sjödahl, G., Robertson, A. G., Seiler, R., Hoadley, K. A., Groeneveld, C. S., Al-Ahmadie, H., Choi, W., Castro, M. A. A., Fontugne, J., Eriksson, P., Mo, Q., Kardos, J., Zlotta, A., Hartmann, A., Dinney, C. P., Bellmunt, J., … Weinstein, J. (2020). A Consensus Molecular Classification of Muscle-invasive Bladder Cancer. *European Urology*, *77*(4), 420–433. https://doi.org/10.1016/j.eururo.2019.09.006

Kamoun, A., Reyniès, A. de, Allory, Y., Sjödahl, G., Robertson, A. G., Seiler, R., Hoadley, K. A., Al-Ahmadie, H., Choi, W., Groeneveld, C. S., Castro, M. A. A., Fontugne, J., Eriksson, P., Mo, Q., Kardos, J., Zlotta, A., Hartmann, A., Dinney, C. P., Bellmunt, J., … Group, T. B. C. M. T. (2019). A consensus molecular classification of muscle-invasive bladder cancer. *BioRxiv*, 488460. https://doi.org/10.1101/488460

Kasiri, S., Shao, C., Chen, B., Wilson, A. N., Yenerall, P., Timmons, B. C., Girard, L., Tian, H., Behrens, C., Wistuba, I. I., Gazdar, A. F., & Kim, J. (2017). GLI1 blockade potentiates the antitumor activity of PI3K antagonists in lung squamous cell carcinoma. *Cancer Research*, *77*(16), 4448–4459. https://doi.org/10.1158/0008-5472.CAN-16-3315

Kasper, M., Schnidar, H., Neill, G. W., Hanneder, M., Klingler, S., Blaas, L., Schmid, C., Hauser-Kronberger, C., Regl, G., Philpott, M. P., & Aberger, F. (2006). Selective Modulation of Hedgehog/GLI Target Gene Expression by Epidermal Growth Factor Signaling in Human Keratinocytes. *Molecular and Cellular Biology*, *26*(16), 6283–6298. https://doi.org/10.1128/mcb.02317-05

Kauffmann-Zeh, A., Rodriguez-Viciana, P., Ulrich, E., Gilbert, C., Coffer, P., Downward, J., & Evan, G. (1997). Suppression of c-Myc-induced apoptosis by Ras signalling through PI(3)K and PKB. *Nature*, *385*(6616), 544–548. https://doi.org/10.1038/385544a0

Kim, B.-K., Jae-Ho, C., Joo-Young, I., Ban, H. S., Seon-Kyu, K., Mi-Jung, K., Lee, J., Seon-Young, K., Kyung-Chan, P., Paik, S., & Won, M. (2019). PI3K/AKT/β-catenin signaling regulates vestigial-like 1 which predicts poor prognosis and enhances malignant

phenotype in gastric cancer. *Cancers*, *11*(12), 1923. https://doi.org/10.3390/cancers11121923

Kim, J., Hsia, E. Y. C., Brigui, A., Plessis, A., Beachy, P. A., & Zheng, X. (2015). The role of ciliary trafficking in Hedgehog receptor signaling. *Science Signaling*, *8*(379), ra55–ra55. https://doi.org/10.1126/scisignal.aaa5622

Kim, S., Kim, Y., Kong, J., Kim, E., Choi, J. H., Yuk, H. D., Lee, H., Kim, H. R., Lee, K. H., Kang, M., Roe, J. S., Moon, K. C., Kim, S., Ku, J. H., & Shin, K. (2019). Epigenetic regulation of mammalian hedgehog signaling to the stroma determines the molecular subtype of bladder cancer. *ELife*, *8*. https://doi.org/10.7554/eLife.43024

Kim, T. H., Yoo, J. Y., Wang, Z., Lydon, J. P., Khatri, S., Hawkins, S. M., Leach, R. E., Fazleabas, A. T., Young, S. L., Lessey, B. A., Ku, B. J., & Jeong, J. W. (2015). ARID1A Is Essential for Endometrial Function during Early Pregnancy. *PLoS Genetics*, *11*(9). https://doi.org/10.1371/journal.pgen.1005537

Kimuli, M., Eardley, I., & Southgate, J. (2004a). In vitro assessment of decellularized porcine dermis as a matrix for urinary tract reconstruction. *BJU International*, *94*(6), 859–866. https://doi.org/10.1111/j.1464-410X.2004.05047.x

Kimuli, M., Eardley, I., & Southgate, J. (2004b). In vitro assessment of decellularized porcine dermis as a matrix for urinary tract reconstruction. *BJU International*, *94*(6), 859–866. https://doi.org/10.1111/j.1464-410X.2004.05047.x

Kitagawa, K., Shigemura, K., Sung, S. Y., Chen, K. C., Huang, C. C., Chiang, Y. Te, Liu, M. C., Huang, T. W., Yamamichi, F., Shirakawa, T., & Fujisawa, M. (2019). Possible correlation of sonic hedgehog signaling with epithelial–mesenchymal transition in muscle-invasive bladder cancer progression. *Journal of Cancer Research and Clinical Oncology*, *145*(9), 2261–2271. https://doi.org/10.1007/s00432-019-02987-z

Kliewer, S. A., Umesono, K., Noonan, D. J., Heyman, R. A., & Evans, R. M. (1992). Convergence of 9-cis retinoic acid and peroxisome proliferator signalling pathways through heterodimer formation of their receptors. *Nature*, *358*(6389), 771–774. https://doi.org/10.1038/358771a0

Kobayashi, A., Kang, M.-I., Okawa, H., Ohtsuji, M., Zenke, Y., Chiba, T., Igarashi, K., & Yamamoto, M. (2004). Oxidative Stress Sensor Keap1 Functions as an Adaptor for Cul3-Based E3 Ligase To Regulate Proteasomal Degradation of Nrf2. *Molecular and Cellular Biology*, *24*(16), 7130–7139. https://doi.org/10.1128/mcb.24.16.7130-7139.2004

Kogevinas, M., 'T Mannetje, A., Cordier, S., Ranft, U., González, C. A., Vineis, P., Chang-Claude, J., Lynge, E., Wahrendorf, J., Tzonou, A., Jöckel, K. H., Serra, C., Porru, S., Hours, M., Greiser, E., & Boffetta, P. (2003). Occupation and bladder cancer among men in Western Europe. *Cancer Causes and Control*, *14*(10), 907–914. https://doi.org/10.1023/B:CACO.0000007962.19066.9c

Kohtz, J. D., Lee, H. Y., Gaiano, N., Segal, J., Ng, E., Larson, T., Baker, D. P., Garber, E. A., Williams, K. P., & Fishell, G. (2001). N-terminal fatty-acylation of sonic hedgehog enhances the induction of rodent ventral forebrain neurons. *Development (Cambridge, England)*, *128*(12), 2351–2363. http://www.ncbi.nlm.nih.gov/pubmed/11493554

Koleva, M. V., Rothery, S., Spitaler, M., Neil, M. A. A., & Magee, A. I. (2015). Sonic hedgehog multimerization: A self-organizing event driven by post-translational modifications? *Molecular Membrane Biology*, *32*(3), 65–74. https://doi.org/10.3109/09687688.2015.1066895

Kong, X. T., Deng, F. M., Hu, P., Liang, F. X., Zhou, G., Auerbach, A. B., Genieser, N., Nelson, P. K., Robbins, E. S., Shapiro, E., Kachar, B., & Sun, T. T. (2004). Roles of uroplakins in plaque formation, umbrella cell enlargement, and urinary tract diseases. *Journal of Cell Biology*, *167*(6), 1195–1204. https://doi.org/10.1083/jcb.200406025

Koontz, L. M., Liu-Chittenden, Y., Yin, F., Zheng, Y., Yu, J., Huang, B., Chen, Q., Wu, S., & Pan, D. (2013). The Hippo Effector Yorkie Controls Normal Tissue Growth by Antagonizing Scalloped-Mediated Default Repression. *Developmental Cell*, *25*(4), 388–401. https://doi.org/10.1016/j.devcel.2013.04.021

Kouros-Mehr, H., Slorach, E. M., Sternlicht, M. D., & Werb, Z. (2006). GATA-3 Maintains the Differentiation of the Luminal Cell Fate in the Mammary Gland. *Cell*, *127*(5), 1041–1055. https://doi.org/10.1016/j.cell.2006.09.048

Kreft, M. E., Sterle, M., & Jezernik, K. (2006). Distribution of junction- and differentiation-related proteins in urothelial cells at the leading edge of primary explant outgrowths. *Histochemistry and Cell Biology*, *125*(5), 475–485. https://doi.org/10.1007/s00418-005-0104-y

Kreft, M. E., Sterle, M., Veranič, P., & Jezernik, K. (2005). Urothelial injuries and the early wound healing response: Tight junctions and urothelial cytodifferentiation. *Histochemistry and Cell Biology*, *123*(4–5), 529–539. https://doi.org/10.1007/s00418-005-0770-9

Kwon, H., Imbalzano, A. N., Khavari, P. A., Kingston, R. E., & Green, M. R. (1994). Nucleosome disruption and enhancement of activator binding by a human SW1/SNF complex. *Nature*, *370*(6489), 477–481. https://doi.org/10.1038/370477a0

Latz, S., Umbach, T., Goltz, D., Kristiansen, G., Müller, S. C., & Ellinger, J. (2016). Cytoplasmatic and nuclear YAP1 and pYAP1 staining in urothelial bladder cancer. *Urologia Internationalis*, *96*(1), 39–45. https://doi.org/10.1159/000438868

Lauth, M., Bergström, Å., Shimokawa, T., & Toftgård, R. (2007). Inhibition of GLI-mediated transcription and tumor cell growth by small-molecule antagonists. *Proceedings of the National Academy of Sciences of the United States of America*, *104*(20), 8455–8460. https://doi.org/10.1073/pnas.0609699104

Lavelle, J., Meyers, S., Ramage, R., Bastacky, S., Doty, D., Apodaca, G., & Zeidel, M. L. (2002). Bladder permeability barrier: recovery from selective injury of surface epithelial cells. *Am J Physiol Renal Physiol*, *283*(2), F242-53. https://doi.org/10.1152/ajprenal.00307.2001

Lawrence, M. S., Stojanov, P., Polak, P., Kryukov, G. V., Cibulskis, K., Sivachenko, A., Carter, S. L., Stewart, C., Mermel, C. H., Roberts, S. A., Kiezun, A., Hammerman, P. S., McKenna, A., Drier, Y., Zou, L., Ramos, A. H., Pugh, T. J., Stransky, N., Helman, E., … Getz, G. (2013). Mutational heterogeneity in cancer and the search for new cancer-associated genes. *Nature*, *499*(7457), 214–218. https://doi.org/10.1038/nature12213

Lecanda, J., Ganapathy, V., D'Aquino-Ardalan, C., Evans, B., Cadacio, C., Ayala, A., & Gold, L.

I. (2009). TGFβ prevents proteasomal degradation of the cyclin-dependent kinase inhibitor p27kip1 for cell cycle arrest. *Cell Cycle*, *8*(5), 742–756. https://doi.org/10.4161/cc.8.5.7871

Lee, J., Platt, K. A., Censullo, P., & Ruiz I Altaba, A. (1997). Gli1 is a target of Sonic hedgehog that induces ventral neural tube development. *Development*, *124*(13), 2537–2552. https://dev.biologists.org/content/124/13/2537

Levi, P. E., Cowen, D. M., & Cooper, E. H. (1969). Induction of cell proliferation in the mouse bladder by 4-ethylsulphonyl-naphthalene-1-sulphonamide. *Cell Proliferation*, *2*(3), 249–262. https://doi.org/10.1111/j.1365-2184.1969.tb00234.x

Lewis, P. M., Dunn, M. P., McMahon, J. A., Logan, M., Martin, J. F., St-Jacques, B., & McMahon, A. P. (2001). Cholesterol modification of sonic hedgehog is required for long-range signaling activity and effective modulation of signaling by Ptc1. *Cell*, *105*(5), 599–612. https://doi.org/10.1016/S0092-8674(01)00369-5

Li, J., Lu, S., Lombardo, K., Monahan, R., & Amin, A. (2016). ARID1A alteration in aggressive urothelial carcinoma and variants of urothelial carcinoma. *Human Pathology*, *55*, 17–23. https://doi.org/10.1016/j.humpath.2016.04.006

Li, L., Yuan, H., Weaver, C. D., Mao, J., Farr, G. H., Sussman, D. J., Jonkers, J., Kimelman, D., & Wu, D. (1999). Axin and Frat1 interact with Dvl and GSK, bridging Dvl to GSK in Wnt-mediated regulation of LEF-1. *EMBO Journal*, *18*(15), 4233–4240. https://doi.org/10.1093/emboj/18.15.4233

Li, W., Yang, L., He, Q., Hu, C., Zhu, L., Ma, X., Ma, X., Bao, S., Li, L., Chen, Y., Deng, X., Zhang, X., Cen, J., Zhang, L., Wang, Z., Xie, W. F., Li, H., Li, Y., & Hui, L. (2019). A Homeostatic Arid1a-Dependent Permissive Chromatin State Licenses Hepatocyte Responsiveness to Liver-Injury-Associated YAP Signaling. *Cell Stem Cell*, *25*(1), 54-68.e5. https://doi.org/10.1016/j.stem.2019.06.008

Li, Yi, Ishiguro, H., Kawahara, T., Kashiwagi, E., Izumi, K., & Miyamoto, H. (2014). Loss of GATA3 in bladder cancer promotes cell migration and invasion. *Cancer Biology and Therapy*, *15*(4), 428–435. https://doi.org/10.4161/cbt.27631

Li, Yunguang, Kong, F., Wang, J., Hu, E., Wang, R., Liu, J., Xiao, Q., Zhang, W., He, D., & Xiao, X. (2016). S100A7 induction is repressed by YAP via the Hippo pathway in A431 cells. *Oncotarget*, *7*(25), 38133–38142. https://doi.org/10.18632/oncotarget.9477

Liang, H., Cheung, L. W. T., Li, J., Ju, Z., Yu, S., Stemke-Hale, K., Dogruluk, T., Lu, Y., Liu, X., Gu, C., Guo, W., Scherer, S. E., Carter, H., Westin, S. N., Dyer, M. D., Verhaak, R. G. W., Zhang, F., Karchin, R., Liu, C. G., … Mills, G. B. (2012). Whole-exome sequencing combined with functional genomics reveals novel candidate driver cancer genes in endometrial cancer. *Genome Research*, *22*(11), 2120–2129. https://doi.org/10.1101/gr.137596.112

Liu-Chittenden, Y., Huang, B., Shim, J. S., Chen, Q., Lee, S. J., Anders, R. A., Liu, J. O., & Pan, D. (2012). Genetic and pharmacological disruption of the TEAD-YAP complex suppresses the oncogenic activity of YAP. *Genes and Development*, *26*(12), 1300–1305. https://doi.org/10.1101/gad.192856.112

Liu, J. Y., Li, Y. H., Lin, H. X., Liao, Y. J., Mai, S. J., Liu, Z. W., Zhang, Z. L., Jiang, L. J., Zhang, J. X., Kung, H. F., Zeng, Y. X., Zhou, F. J., & Xie, D. (2013). Overexpression of YAP 1

contributes to progressive features and poor prognosis of human urothelial carcinoma of the bladder. *BMC Cancer*, *13*, 349. https://doi.org/10.1186/1471-2407-13-349

Liu, Y. D., Yu, S. L., Wang, R., Liu, J. N., Jin, Y. S., Li, Y. F., & An, R. H. (2019). Rosiglitazone Suppresses Calcium Oxalate Crystal Binding and Oxalate-Induced Oxidative Stress in Renal Epithelial Cells by Promoting PPAR- γ Activation and Subsequent Regulation of TGF- β 1 and HGF Expression. *Oxidative Medicine and Cellular Longevity*, *2019*. https://doi.org/10.1155/2019/4826525

Lobban, E. D., Smith, B. A., Hall, G. D., Harnden, P., Roberts, P., Selby, P. J., Trejdosiewicz, L. K., & Southgate, J. (1998). Uroplakin gene expression by normal and neoplastic human urothelium. *The American Journal of Pathology*, *153*(6), 1957–1967. https://doi.org/10.1016/S0002-9440(10)65709-4

MacLaine, N. J., Wood, M. D., Holder, J. C., Rees, R. W., & Southgate, J. (2008). Sensitivity of normal, paramalignant, and malignant human urothelial cells to inhibitors of the epidermal growth factor receptor signaling pathway. *Molecular Cancer Research*, *6*(1), 53–63. https://doi.org/10.1158/1541-7786.MCR-07-0134

Malhotra, D., Portales-Casamar, E., Singh, A., Srivastava, S., Arenillas, D., Happel, C., Shyr, C., Wakabayashi, N., Kensler, T. W., Wasserman, W. W., & Biswal, S. (2010). Global mapping of binding sites for Nrf2 identifies novel targets in cell survival response through chip-seq profiling and network analysis. *Nucleic Acids Research*, *38*(17), 5718–5734. https://doi.org/10.1093/nar/gkq212

Marques, E., Englund, J. I., Tervonen, T. A., Virkunen, E., Laakso, M., Myllynen, M., Mäkelä, A., Ahvenainen, M., Lepikhova, T., Monni, O., Hautaniemi, S., & Klefström, J. (2016). Par6G suppresses cell proliferation and is targeted by loss-of-function mutations in multiple cancers. *Oncogene*, *35*(11), 1386–1398. https://doi.org/10.1038/onc.2015.196

Marshall, V. F., & Whitmore, W. F. (1949). A technique for the extension of radical surgery in the treatment of vesical cancer. *Cancer*, *2*(3), 424–428. https://doi.org/10.1002/1097-0142(194905)2:3<424::AID-CNCR2820020306>3.0.CO;2-Y

Martin-Hurtado, A., Martin-Morales, R., Robledinos-Antón, N., Blanco, R., Palacios-Blanco, I., Lastres-Becker, I., Cuadrado, A., & Garcia-Gonzalo, F. R. (2019). NRF2-dependent gene expression promotes ciliogenesis and Hedgehog signaling. *Scientific Reports*, *9*(1). https://doi.org/10.1038/s41598-019-50356-0

Martinez-Chinchilla, P., & Riobo, N. A. (2008). Chapter 11 Purification and Bioassay of Hedgehog Ligands for the Study of Cell Death and Survival. In *Methods in Enzymology* (Vol. 446, pp. 189–204). https://doi.org/10.1016/S0076-6879(08)01611-X

Marzouka, N. A. D., Eriksson, P., Rovira, C., Liedberg, F., Sjödahl, G., & Höglund, M. (2018). A validation and extended description of the Lund taxonomy for urothelial carcinoma using the TCGA cohort. *Scientific Reports*, *8*(1), 1–12. https://doi.org/10.1038/s41598-018-22126-x

Mathur, R., Alver, B. H., San Roman, A. K., Wilson, B. G., Wang, X., Agoston, A. T., Park, P. J., Shivdasani, R. A., & Roberts, C. W. M. (2017). ARID1A loss impairs enhancer-mediated gene regulation and drives colon cancer in mice. *Nature Genetics*, *49*(2), 296–302.

https://doi.org/10.1038/ng.3744

McCrea, P. D., & Gumbiner, B. M. (1991). Purification of a 92-kDa cytoplasmic protein tightly associated with the cell-cell adhesion molecule E-cadherin (uvomorulin): Characterization and extractability of the protein complex from the cell cytostructure. *Journal of Biological Chemistry*, *266*(7), 4514–4520.

Mechlin, C. W., Tanner, M. J., Chen, M., Buttyan, R., Levin, R. M., & Mian, B. M. (2010). Gli2 Expression and Human Bladder Transitional Carcinoma Cell Invasiveness. *Journal of Urology*, *184*(1), 344–351. https://doi.org/10.1016/j.juro.2010.03.007

Messier, B., & Leblond, C. P. (1960). Cell proliferation and migration as revealed by radioautography after injection of thymidine-H3 into male rats and mice. *American Journal of Anatomy*, *106*(3), 247–285. https://doi.org/10.1002/aja.1001060305

Milenkovic, L., Scott, M. P., & Rohatgi, R. (2009). Lateral transport of Smoothened from the plasma membrane to the membrane of the cilium. *Journal of Cell Biology*, *187*(3), 365–374. https://doi.org/10.1083/jcb.200907126

Miyamoto, H., Izumi, K., Yao, J. L., Li, Y., Yang, Q., McMahon, L. A., Gonzalez-Roibon, N., Hicks, D. G., Tacha, D., & Netto, G. J. (2012). GATA binding protein 3 is down-regulated in bladder cancer yet strong expression is an independent predictor of poor prognosis in invasive tumor. *Human Pathology*, *43*(11), 2033–2040. https://doi.org/10.1016/j.humpath.2012.02.011

Mizuno, T., Murakami, H., Fujii, M., Ishiguro, F., Tanaka, I., Kondo, Y., Akatsuka, S., Toyokuni, S., Yokoi, K., Osada, H., & Sekido, Y. (2012). YAP induces malignant mesothelioma cell proliferation by upregulating transcription of cell cycle-promoting genes. *Oncogene*, *31*(49), 5117–5122. https://doi.org/10.1038/onc.2012.5

Moll, R., Achtstatter, T., Becht, E., Balcarova-Stander, J., Ittensohn, M., & Franke, W. W. (1988). Cytokeratins in normal and malignant transitional epithelium. Maintenance of expression of urothelial differentiation features in transitional cell carcinomas and bladder carcinoma cell culture lines. *American Journal of Pathology*, *132*(1), 123–144.

Moll, R., Lowe, A., Laufer, J., & Franke, W. W. (1992). Cytokeratin 20 in human carcinomas: A new histodiagnostic marker detected by monoclonal antibodies. *American Journal of Pathology*, *140*(2), 427–447.

Montesano, R., & Orci, L. (1988). Transforming growth factor beta stimulates collagen-matrix contraction by fibroblasts: implications for wound healing. *Proceedings of the National Academy of Sciences of the United States of America*, *85*(13), 4894–4897. https://doi.org/10.1073/pnas.85.13.4894

Morales, A., Eidinger, D., & Bruce, A. W. (1976). Intracavitary Bacillus Calmette Guerin in the treatment of superficial bladder tumors. *Journal of Urology*, *116*(2), 180–182. https://doi.org/10.1016/s0022-5347(17)58737-6

Mukherjee, S., Frolova, N., Sadlonova, A., Novak, Z., Steg, A., Page, G. P., Welch, D. R., Lobo-Ruppert, S. M., Michael Ruppert, J., Johnson, M. R., & Frost, A. R. (2006). Hedgehog signaling and response to cyclopamine differ in epithelial and stromal cells in benign breast and breast cancer. *Cancer Biology and Therapy*, *5*(6), 674–683. https://doi.org/10.4161/cbt.5.6.2906

Murakami, H., Mizuno, T., Taniguchi, T., Fujii, M., Ishiguro, F., Fukui, T., Akatsuka, S., Horio,

Y., Hida, T., Kondo, Y., Toyokuni, S., Osada, H., & Sekido, Y. (2011). LATS2 is a tumor suppressor gene of malignant mesothelioma. *Cancer Research*, *71*(3), 873–883. https://doi.org/10.1158/0008-5472.CAN-10-2164

Nakashiro, K. I., Hayashi, Y., Kita, A., Tamatani, T., Chlenski, A., Usuda, N., Hattori, K., Reddy, J. K., & Oyasu, R. (2001). Role of peroxisome proliferator-activated receptor γ and its ligands in non-neoplastic and neoplastic human urothelial cells. *American Journal of Pathology*, *159*(2), 591–597. https://doi.org/10.1016/S0002-9440(10)61730-0

National Institutes of Diabetes and Digestive and Kidney Diseases. (2014). *The Urinary Tract & How It Works*. https://www.niddk.nih.gov/health-information/urologic-diseases/urinary-tract-how-it-works

Nedjadi, T., Salem, N., Khayyat, D., Al-Sayyad, A., Al-Ammari, A., & Al-Maghrabi, J. (2018). Sonic Hedgehog Expression is Associated with Lymph Node Invasion in Urothelial Bladder Cancer. *Pathology & Oncology Research*, 1–7. https://doi.org/10.1007/s12253-018-0477-6

Negrete, H. O., Lavelle, J. P., Berg, J., Lewis, S. A., & Zeidel, M. L. (1996). Permeability properties of the intact mammalian bladder epithelium. *American Journal of Physiology - Renal Fluid and Electrolyte Physiology*, *271*(4 40-4). https://doi.org/10.1152/ajprenal.1996.271.4.f886

Nelson, C. M., & Chen, C. S. (2002). Cell-cell signaling by direct contact increases cell proliferation via a PI3K-dependent signal. *FEBS Letters*, *514*(2–3), 238–242. https://doi.org/10.1016/S0014-5793(02)02370-0

Nguyen, A. H. T., Tremblay, M., Haigh, K., Hervékoumakpayi, I., Paquet, M., Pandolfi, P. P., Mes-Masson, A. M., Saad, F., Haigh, J. J., & Bouchard, M. (2013). Gata3 antagonizes cancer progression in pten-deficient prostates. *Human Molecular Genetics*, *22*(12), 2400–2410. https://doi.org/10.1093/hmg/ddt088

Okada, T., Enkhjargal, B., Travis, Z. D., Ocak, U., Tang, J., Suzuki, H., & Zhang, J. H. (2019). FGF-2 Attenuates Neuronal Apoptosis via FGFR3/PI3k/Akt Signaling Pathway After Subarachnoid Hemorrhage. *Molecular Neurobiology*, *56*(12), 8203–8219. https://doi.org/10.1007/s12035-019-01668-9

Oottamasathien, S., Wang, Y. Q., Williams, K., Franco, O. E., Wills, M. L., Thomas, J. C., Saba, K., Sharif-Afshar, A. R., Makari, J. H., Bhowmick, N. A., DeMarco, R. T., Hipkens, S., Magnuson, M., Brock, J. W., Hayward, S. W., Pope IV, J. C., & Matusik, R. J. (2007). Directed differentiation of embryonic stem cells into bladder tissue. *Developmental Biology*, *304*(2), 556–566. https://doi.org/10.1016/j.ydbio.2007.01.010

Ozdamar, B., Bose, R., Barrios-Rodiles, M., Wang, H. R., Zhang, Y., & Wrana, J. L. (2005). Regulation of the polarity protein Par6 by TGFβ receptors controls epithelial cell plasticity. *Science*, *307*(5715), 1603–1609. https://doi.org/10.1126/science.1105718

Pang, K. H., & Noon, A. P. (2019). Selection of patients and benefit of immediate radical cystectomy for non-muscle invasive bladder cancer. *Translational Andrology and Urology*, *8*(1), 101–107. https://doi.org/10.21037/tau.2018.09.06

Pepinsky, R. B., Zeng, C., Went, D., Rayhorn, P., Baker, D. P., Williams, K. P., Bixler, S. A., Ambrose, C. M., Garber, E. A., Miatkowski, K., Taylor, F. R., Wang, E. A., & Galdes, A. (1998). Identification of a palmitic acid-modified form of human Sonic hedgehog.

Journal of Biological Chemistry, *273*(22), 14037–14045. https://doi.org/10.1074/jbc.273.22.14037

Perou, C. M., Sørlie, T., Eisen, M. B., van de Rijn, M., Jeffrey, S. S., Rees, C. A., Pollack, J. R., Ross, D. T., Johnsen, H., Akslen, L. A., Fluge, O., Pergamenschikov, A., Williams, C., Zhu, S. X., Lønning, P. E., Børresen-Dale, a L., Brown, P. O., & Botstein, D. (2000). Molecular portraits of human breast tumours. *Nature*, *406*(6797), 747–752. https://doi.org/10.1038/35021093

Peyton, C. C., Burmeister, D., Petersen, B., Andersson, K. E., & Christ, G. (2012). Characterization of the Early Proliferative Response of the Rodent Bladder to Subtotal Cystectomy: A Unique Model of Mammalian Organ Regeneration. *PLoS ONE*, *7*(10). https://doi.org/10.1371/journal.pone.0047414

Pierucci-Alves, F., Yi, S., & Schultz, B. D. (2012). Transforming growth factor beta 1 induces tight junction disruptions and loss of transepithelial resistance across porcine vas deferens epithelial cells. *Biology of Reproduction*, *86*(2). https://doi.org/10.1095/biolreprod.111.092262

Pietsch, T., Waha, A., Koch, A., Kraus, J., Albrecht, S., Tonn, J., Sörensen, N., Berthold, F., Henk, B., Schmandt, N., Wolf, H. K., Von Deimling, A., Wainwright, B., Chenevix-Trench, G., Wiestler, O. D., & Wicking, C. (1997). Medulloblastomas of the desmoplastic variant carry mutations of the human homologue of Drosophila patched. *Cancer Research*, *57*(11), 2085–2088. https://pubmed.ncbi.nlm.nih.gov/9187099/

Pietzak, E. J., Bagrodia, A., Cha, E. K., Drill, E. N., Iyer, G., Isharwal, S., Ostrovnaya, I., Baez, P., Li, Q., Berger, M. F., Zehir, A., Schultz, N., Rosenberg, J. E., Bajorin, D. F., Dalbagni, G., Al-Ahmadie, H., Solit, D. B., & Bochner, B. H. (2017). Next-generation Sequencing of Nonmuscle Invasive Bladder Cancer Reveals Potential Biomarkers and Rational Therapeutic Targets. *European Urology*, *72*(6), 952–959. https://doi.org/10.1016/j.eururo.2017.05.032

Pignon, J. C., Grisanzio, C., Geng, Y., Song, J., Shivdasani, R. A., & Signoretti, S. (2013). p63-expressing cells are the stem cells of developing prostate, bladder, and colorectal epithelia. *Proceedings of the National Academy of Sciences of the United States of America*, *110*(20), 8105–8110. https://doi.org/10.1073/pnas.1221216110

Pimentel, H., Bray, N. L., Puente, S., Melsted, P., & Pachter, L. (2017). Differential analysis of RNA-seq incorporating quantification uncertainty. *Nature Methods*, *14*(7), 687–690. https://doi.org/10.1038/nmeth.4324

Plouffe, S. W., Meng, Z., Lin, K. C., Lin, B., Hong, A. W., Chun, J. V., & Guan, K. L. (2016). Characterization of Hippo Pathway Components by Gene Inactivation. *Molecular Cell*, *64*(5), 993–1008. https://doi.org/10.1016/j.molcel.2016.10.034

Po, A., Silvano, M., Miele, E., Capalbo, C., Eramo, A., Salvati, V., Todaro, M., Besharat, Z. M., Catanzaro, G., Cucchi, D., Coni, S., Di Marcotullio, L., Canettieri, G., Vacca, A., Stassi, G., De Smaele, E., Tartaglia, M., Screpanti, I., De Maria, R., & Ferretti, E. (2017). Noncanonical GLI1 signaling promotes stemness features and in vivo growth in lung adenocarcinoma. *Oncogene*, *36*(32), 4641–4652. https://doi.org/10.1038/onc.2017.91

Pobbati, A. V, Chan, S. W., Lee, I., Song, H., & Hong, W. (2012). Structural and functional

similarity between the Vgll1-TEAD and the YAP-TEAD complexes. *Structure*, *20*(7), 1135–1140. https://doi.org/10.1016/j.str.2012.04.004

Porter, J. A., Ekker, S. C., Park, W. J., Von Kessler, D. P., Young, K. E., Chen, C. H., Ma, Y., Woods, A. S., Cotter, R. J., Koonin, E. V, & Beachy, P. A. (1996). Hedgehog patterning activity: Role of a lipophilic modification mediated by the carboxy-terminal autoprocessing domain. *Cell*, *86*(1), 21–34. https://doi.org/10.1016/S0092-8674(00)80074-4

Porter, J. A., Young, K. E., & Beachy, P. A. (1996). Cholesterol modification of hedgehog signaling proteins in animal development. *Science*, *274*(5285), 255–259. https://doi.org/10.1126/science.274.5285.255

Postlethwaite, A. E., Keski-Oja, J., Moses, H. L., & Kang, A. H. (1987). Stimulation of the chemotactic migration of human fibroblasts by transforming growth factor β. *Journal of Experimental Medicine*, *165*(1), 251–256. https://doi.org/10.1084/jem.165.1.251

Prelich, G. (2012). Gene overexpression: Uses, mechanisms, and interpretation. In *Genetics* (Vol. 190, Issue 3, pp. 841–854). Genetics. https://doi.org/10.1534/genetics.111.136911

Price, M. A., & Kalderon, D. (2002). Proteolysis of the Hedgehog signaling effector Cubitus interruptus requires phosphorylation by Glycogen Synthase Kinase 3 and Casein Kinase 1. *Cell*, *108*(6), 823–835. https://doi.org/10.1016/S0092-8674(02)00664-5

Raven, P. A., Lysakowski, S., Tan, Z., D'Costa, N. M., Moskalev, I., Frees, S., Struss, W., Matsui, Y., Narita, S., Buttyan, R., Chavez-Munoz, C., & So, A. I. (2019). Inhibition of GLI2 with antisense-oligonucleotides: A potential therapy for the treatment of bladder cancer. *Journal of Cellular Physiology*, *234*(11), 20634–20647. https://doi.org/10.1002/jcp.28669

Rebouissou, S., Bernard-Pierrot, I., de Reynies, A., Lepage, M.-L., Krucker, C., Chapeaublanc, E., Herault, A., Kamoun, A., Caillault, A., Letouze, E., Elarouci, N., Neuzillet, Y., Denoux, Y., Molinie, V., Vordos, D., Laplanche, A., Maille, P., Soyeux, P., Ofualuka, K., … Radvanyi, F. (2014). EGFR as a potential therapeutic target for a subset of muscle-invasive bladder cancers presenting a basal-like phenotype. *Science Translational Medicine*, *6*(244), 244ra91-244ra91. https://doi.org/10.1126/scitranslmed.3008970

Reddy, O. L., Cates, J. M., Gellert, L. L., Crist, H. S., Yang, Z., Yamashita, H., Taylor, J. A., Smith, J. A., Chang, S. S., Cookson, M. S., You, C., Barocas, D. A., Grabowska, M. M., Ye, F., Wu, X. R., Yi, Y., Matusik, R. J., Kaestner, K. H., Clark, P. E., & Degraff, D. J. (2015). Loss of FOXA1 drives sexually dimorphic changes in urothelial differentiation and is an independent predictor of poor prognosis in bladder cancer. *American Journal of Pathology*, *185*(5), 1385–1395. https://doi.org/10.1016/j.ajpath.2015.01.014

Reka, A. K., Kurapati, H., Narala, V. R., Bommer, G., Chen, J., Standiford, T. J., & Keshamouni, V. G. (2010). Peroxisome proliferator-activated receptor-g activation inhibits tumor metastasis by antagonizing smad3-mediated epithelial-mesenchymal transition. *Molecular Cancer Therapeutics*, *9*(12), 3221–3232. https://doi.org/10.1158/1535-7163.MCT-10-0570

Reynisdóttir, I., Polyak, K., Iavarone, A., & Massagué, J. (1995). Kip/Cip and Ink4 Cdk inhibitors cooperate to induce cell cycle arrest in response to TGF-β. *Genes and Development*, *9*(15), 1831–1845. https://doi.org/10.1101/gad.9.15.1831

Rheinwald, J. G., & Green, H. (1975). Serial cultivation of strains of human epidermal keratinocytes: the formation of keratinizing colonies from single cells. *Cell*, *6*(3), 331–343. http://www.ncbi.nlm.nih.gov/pubmed/1052771

Riley, G. F., Potosky, A. L., Lubitz, J. D., & Kessler, L. G. (1995). Medicare payments from diagnosis to death for elderly cancer patients by stage at diagnosis. *Medical Care*, *33*(8), 828–841. https://doi.org/10.1097/00005650-199508000-00007

Riobo, N. A., Lu, K., Ai, X., Haines, G. M., & Emerson, C. P. (2006). Phosphoinositide 3-kinase and Akt are essential for Sonic Hedgehog signaling. *Proceedings of the National Academy of Sciences*, *103*(12), 4505–4510. https://doi.org/10.1073/pnas.0504337103

Robertson, A. G., Kim, J., Al-Ahmadie, H., Bellmunt, J., Guo, G., Cherniack, A. D., Hinoue, T., Laird, P. W., Hoadley, K. A., Akbani, R., Castro, M. A. A., Gibb, E. A., Kanchi, R. S., Gordenin, D. A., Shukla, S. A., Sanchez-Vega, F., Hansel, D. E., Czerniak, B. A., Reuter, V. E., … Zwarthoff, E. C. (2017). Comprehensive Molecular Characterization of Muscle-Invasive Bladder Cancer. *Cell*, *171*(3), 540-556.e25. https://doi.org/10.1016/j.cell.2017.09.007

Roche, S., Koegl, M., & Courtneidge, S. A. (1994). The phosphatidylinositol 3-kinase α is required for DNA synthesis induced by some, but not all, growth factors. *Proceedings of the National Academy of Sciences of the United States of America*, *91*(19), 9185–9189. https://doi.org/10.1073/pnas.91.19.9185

Rochel, N., Krucker, C., Coutos-Thévenot, L., Osz, J., Zhang, R., Guyon, E., Zita, W., Vanthong, S., Hernandez, O. A., Bourguet, M., Badawy, K. Al, Dufour, F., Peluso-Iltis, C., Heckler-Beji, S., Dejaegere, A., Kamoun, A., de Reyniès, A., Neuzillet, Y., Rebouissou, S., … Bernard-Pierrot, I. (2019). Recurrent activating mutations of PPARγ associated with luminal bladder tumors. *Nature Communications*, *10*(1), 253. https://doi.org/10.1038/s41467-018-08157-y

Rodriguez-Viciana, P., Warne, P. H., Khwaja, A., Marte, B. M., Pappin, D., Das, P., Waterfield, M. D., Ridley, A., & Downward, J. (1997). Role of phosphoinositide 3-OH kinase in cell transformation and control of the actin cytoskeleton by Ras. *Cell*, *89*(3), 457–467. https://doi.org/10.1016/S0092-8674(00)80226-3

Romano, R. A., Ortt, K., Birkaya, B., Smalley, K., & Sinha, S. (2009). An active role of the ΔN isoform of p63 in regulating basal keratin genes K5 and K14 and directing epidermal cell fate. *PLoS ONE*, *4*(5). https://doi.org/10.1371/journal.pone.0005623

Rosen, E. D., Sarraf, P., Troy, A. E., Bradwin, G., Moore, K., Milstone, D. S., Spiegelman, B. M., & Mortensen, R. M. (1999). PPARγ is required for the differentiation of adipose tissue in vivo and in vitro. *Molecular Cell*, *4*(4), 611–617. https://doi.org/10.1016/S1097-2765(00)80211-7

Rosenberg, J. E., Hoffman-Censits, J., Powles, T., Van Der Heijden, M. S., Balar, A. V., Necchi, A., Dawson, N., O'Donnell, P. H., Balmanoukian, A., Loriot, Y., Srinivas, S., Retz, M. M., Grivas, P., Joseph, R. W., Galsky, M. D., Fleming, M. T., Petrylak, D. P., Perez-Gracia, J. L., Burris, H. A., … Dreicer, R. (2016). Atezolizumab in patients with locally advanced and metastatic urothelial carcinoma who have progressed following treatment with platinum-based chemotherapy: A single-arm, multicentre, phase 2 trial. *The Lancet*, *387*(10031), 1909–1920. https://doi.org/10.1016/S0140-6736(16)00561-4

Rudin, C. M., Hann, C. L., Laterra, J., Yauch, R. L., Callahan, C. A., Fu, L., Holcomb, T., Stinson,

J., Gould, S. E., Coleman, B., LoRusso, P. M., Von Hoff, D. D., De Sauvage, F. J., & Low, J. A. (2009). Treatment of medulloblastoma with hedgehog pathway inhibitor GDC-0449. *New England Journal of Medicine*, *361*(12), 1173–1178. https://doi.org/10.1056/NEJMoa0902903

Salazar, L., Kashiwada, T., Krejci, P., Muchowski, P., Donoghue, D., Wilcox, W. R., & Thompson, L. M. (2009). A novel interaction between fibroblast growth factor receptor 3 and the p85 subunit of phosphoinositide 3-kinase: Activation-dependent regulation of ERK by p85 in multiple myeloma cells. *Human Molecular Genetics*, *18*(11), 1951–1961. https://doi.org/10.1093/hmg/ddp116

Samartzis, E. P., Gutsche, K., Dedes, K. J., Fink, D., Stucki, M., & Imesch, P. (2014). Loss of ARID1A expression sensitizes cancer cells to PI3K- and AKT-inhibition. *Oncotarget*, *5*(14), 5295–5303. https://doi.org/10.18632/oncotarget.2092

Sasaki, H., Nishizaki, Y., Hui, C. C., Nakafuku, M., & Kondoh, H. (1999). Regulation of Gli2 and Gli3 activities by an amino-terminal repression domain: Implication of Gli2 and Gli3 as primary mediators of Shh signaling. *Development*, *126*(17), 3915–3924. https://pubmed.ncbi.nlm.nih.gov/10433919/?from_single_result=Regulation+of+Gli2+and+Gli3+activities+by+an+amino-terminal+repression+domain%3A+implication+of+Gli2+and+Gli3+as+primary+mediators+of+Shh+signaling&expanded_search_query=Regulation+of+Gli2+and+G

Saxén, L., & Sariola, H. (1987). Early organogenesis of the kidney. *Pediatric Nephrology*, *1*(3), 385–392. https://doi.org/10.1007/BF00849241

Schaafsma, H. E., Ramaekers, F. C. S., Van Muijen, G. N. P., Lane, E. B., Leigh, I. M., Robben, H., Huijsmans, A., Ooms, E. C. M., & Ruiter, D. J. (1990). Distribution of cytokeratin polypeptides in human transitional cell carcinomas, with special emphasis on changing expression patterns during tumor progression. *American Journal of Pathology*, *136*(2), 329–343.

Schaafsma, H. E., Ramaekers, F. C. S., van Muijen, G. N. P., Ooms, E. C. M., & Ruiter, D. J. (1989). Distribution of cytokeratin polypeptides in epithelia of the adult human urinary tract. *Histochemistry*, *91*(2), 151–159. https://doi.org/10.1007/BF00492389

Schlegel, N., Meir, M., Spindler, V., Germer, C. T., & Waschke, J. (2011). Differential role of Rho GTPases in intestinal epithelial barrier regulation in vitro. *Journal of Cellular Physiology*, *226*(5), 1196–1203. https://doi.org/10.1002/jcp.22446

Schrier, B. P., Hollander, M. P., Van Rhijn, B. W. G., Kiemeney, L. A. L. M., & Witjes, J. A. (2004). Prognosis of Muscle-Invasive Bladder Cancer: Difference between Primary and Progressive Tumours and Implications for Therapy. *European Urology*, *45*(3), 292–296. https://doi.org/10.1016/j.eururo.2003.10.006

Scriven, S. D., Booth, C., Thomas, D. F. M., Trejdosiewicz, L. K., Southgate, J., Shapiro, E., Atala, A., Close, C. E., & Dewan, P. A. (1997). Reconstitution of human urothelium from monolayer cultures. *Journal of Urology*, *158*(3 SUPPL.), 1147–1152. https://doi.org/10.1016/S0022-5347(01)64407-0

Sha, W., Thompson, K., South, J., Baron, M., & Leask, A. (2012). Loss of PPARγ expression by fibroblasts enhances dermal wound closure. *Fibrogenesis and Tissue Repair*, *5*(1). https://doi.org/10.1186/1755-1536-5-5

Shapiro, L., Fannon, A. M., Kwong, P. D., Thompson, A., Lehmann, M. S., Gerhard, G., Als-Nielsen, J., Als-Nielsen, J., Colman, D. R., & Hendrickson, W. A. (1995). Structural basis of cell-cell adhesion by cadherins. *Nature*, *374*(6520), 327–337. https://doi.org/10.1038/374327a0

Shibata, T., Kokubu, A., Gotoh, M., Ojima, H., Ohta, T., Yamamoto, M., & Hirohashi, S. (2008). Genetic Alteration of Keap1 Confers Constitutive Nrf2 Activation and Resistance to Chemotherapy in Gallbladder Cancer. *Gastroenterology*, *135*(4), 1358-1368.e4. https://doi.org/10.1053/j.gastro.2008.06.082

Shimkets, R., Gailani, M. R., Siu, V. M., Yang-Feng, T., Pressman, C. L., Levanat, S., Goldstein, A., Dean, M., & Bale, A. E. (1996). Molecular analysis of chromosome 9q deletions in two Gorlin syndrome patients. *American Journal of Human Genetics*, *59*(2), 417–422.

Shin, K., Lee, J., Guo, N., Kim, J., Lim, A., Qu, L., Mysorekar, I. U., & Beachy, P. A. (2011). Hedgehog/Wnt feedback supports regenerative proliferation of epithelial stem cells in bladder. *Nature*, *472*(7341), 110–116. https://doi.org/10.1038/nature09851

Shin, K., Lim, A., Odegaard, J. I., Honeycutt, J. D., Kawano, S., Hsieh, M. H., & Beachy, P. A. (2014). Cellular origin of bladder neoplasia and tissue dynamics of its progression to invasive carcinoma. *Nature Cell Biology*, *16*(5), 469–478. https://doi.org/10.1038/ncb2956

Shin, K., Lim, A., Zhao, C., Sahoo, D., Pan, Y., Spiekerkoetter, E., Liao, J. C., & Beachy, P. A. (2014). Hedgehog Signaling Restrains Bladder Cancer Progression by Eliciting Stromal Production of Urothelial Differentiation Factors. *Cancer Cell*, *26*(4), 521–533. https://doi.org/10.1016/j.ccell.2014.09.001

Shiroyanagi, Y., Liu, B., Cao, M., Agras, K., Li, J., Hsieh, M. H., Willingham, E. J., & Baskin, L. S. (2007). Urothelial sonic hedgehog signaling plays an important role in bladder smooth muscle formation. *Differentiation*, *75*(10), 968–977. https://doi.org/10.1111/j.1432-0436.2007.00187.x

Siegel, R. L., Miller, K. D., & Jemal, A. (2019). Cancer statistics, 2019. *CA: A Cancer Journal for Clinicians*, *69*(1), 7–34. https://doi.org/10.3322/caac.21551

Sjödahl, G., Lauss, M., Lövgren, K., Chebil, G., Gudjonsson, S., Veerla, S., Patschan, O., Aine, M., Fernö, M., Ringnér, M., Månsson, W., Liedberg, F., Lindgren, D., & Höglund, M. (2012). A molecular taxonomy for urothelial carcinoma. *Clinical Cancer Research*, *18*(12), 3377–3386. https://doi.org/10.1158/1078-0432.CCR-12-0077-T

Smith, N. J., Hinley, J., Varley, C. L., Eardley, I., Trejdosiewicz, L. K., & Southgate, J. (2015). The human urothelial tight junction: claudin 3 and the ZO-1α + switch HHS Public Access. *Bladder (San Franc)*, *2*(1). https://doi.org/10.14440/bladder.2015.33

Soncin, F., Khater, M., To, C., Pizzo, D., Farah, O., Wakeland, A., Rajan, K. A. N., Nelson, K. K., Chang, C. W., Moretto-Zita, M., Natale, D. R., Laurent, L. C., & Parast, M. M. (2018). Comparative analysis of mouse and human placentae across gestation reveals species-specific regulators of placental development. *Development (Cambridge)*, *145*(2). https://doi.org/10.1242/dev.156273

Soneson, C., Love, M. I., & Robinson, M. D. (2016). Differential analyses for RNA-seq: transcript-level estimates improve gene-level inferences. *F1000Research*, *4*, 1521. https://doi.org/10.12688/f1000research.7563.2

Southgate, J. (1999). Cytokeratin expression patterns in normal and malignant urothelium: A review of the biological and diagnostic implications. In *Histology and Histopathology* (Vol. 14, Issue 2, pp. 657–664). Histology and Histopathology. https://doi.org/10.14670/HH-14.657

Southgate, Jennifer, Hutton, K. A., Thomas, D. F. M., & Trejdosiewicz, L. K. (1994). Normal human urothelial cells in vitro: proliferation and induction of stratification. *Laboratory Investigation; a Journal of Technical Methods and Pathology*, *71*(4), 583–594. http://www.ncbi.nlm.nih.gov/pubmed/7967513

Southgate, Jennifer, Masters, J., & Trejdosiewicz, L. (2002). Culture of human urothelium. *Culture of Epithelial Cells*, *8*(1997), 2397. https://doi.org/10.1002/0471221201.ch12

Southgate, Jennifer, Varley, C. L., Garthwaite, M. A. E., Hinley, J., Marsh, F., Stahlschmidt, J., Trejdosiewicz, L. K., & Eardley, I. (2007). Differentiation potential of urothelium from patients with benign bladder dysfunction. *BJU International*, *99*(6), 1506–1516. https://doi.org/10.1111/j.1464-410X.2007.06795.x

Spann, A. L., Yuan, K., Goliwas, K. F., Steg, A. D., Kausfük, D. D., Won, Y. J., & Frost, A. R. (2015). The presence of primary cilia in cancer cells does not predict responsiveness to modulation of smoothened activity. *International Journal of Oncology*, *47*(1), 269–279. https://doi.org/10.3892/ijo.2015.3006

Stahlschmidt, J., Varley, C. L., Toogood, G., Selby, P. J., & Southgate, J. (2005). Urothelial differentiation in chronically urine-deprived bladders of patients with end-stage renal disease. *Kidney International*, *68*(3), 1032–1040. https://doi.org/10.1111/j.1523-1755.2005.00495.x

Stecca, B., Mas, C., Clement, V., Zbinden, M., Correa, R., Piguet, V., Beermann, F., & Ruiz I Altaba, A. (2007). Melanomas require HEDGEHOG-GLI signaling regulated by interactions between GLI1 and the RAS-MEK/AKT pathways. *Proceedings of the National Academy of Sciences of the United States of America*, *104*(14), 5895–5900. https://doi.org/10.1073/pnas.0700776104

Stecca, B., & Ruiz Altaba, A. (2009). A GLI1-p53 inhibitory loop controls neural stem cell and tumour cell numbers. *The EMBO Journal*, *28*, 663–676. https://doi.org/10.1038/emboj.2009.16

Stone, D. M., Hynes, M., Armanini, M., Swanson, T. A., Gu, Q., Johnson, R. L., Scott, M. P., Pennica, D., Goddard, A., Phillips, H., Noll, M., Hooper, J. E., De Sauvage, F., & Rosenthal, A. (1996). The tumour-suppressor gene patched encodes a candidate receptor for Sonic hedgehog. *Nature*, *384*(6605), 129–134. https://doi.org/10.1038/384129a0

Svärd, J., Henricson, K. H., Persson-Lek, M., Rozell, B., Lauth, M., Bergström, Å., Ericson, J., Toftgård, R., & Teglund, S. (2006). Genetic elimination of suppressor of fused reveals an essential repressor function in the mammalian hedgehog signaling pathway. *Developmental Cell*, *10*(2), 187–197. https://doi.org/10.1016/j.devcel.2005.12.013

Sverrisson, E. F., Zens, M. S., Liang Fei, D., Andrews, A., Schned, A., Robbins, D., Kelsey, K. T., Li, H., DiRenzo, J., Karagas, M. R., & Seigne, J. D. (2014). Clinicopathological correlates of Gli1 expression in a population-based cohort of patients with newly diagnosed bladder cancer. In *Urologic Oncology: Seminars and Original Investigations* (Vol. 32, Issue 5, pp. 539–545). Elsevier Inc.

https://doi.org/10.1016/j.urolonc.2014.03.006

Taipale, J., Cooper, M. K., Maiti, T., & Beachy, P. A. (2002). Patched acts catalytically to suppress the activity of Smoothened. *Nature*, *418*(6900), 892–896. https://doi.org/10.1038/nature00989

Takahashi, K., & Suzuki, K. (1996). Density-dependent inhibition of growth involves prevention of EGF receptor activation by E-cadherin-mediated cell-cell adhesion. *Experimental Cell Research*, *226*(1), 214–222. https://doi.org/10.1006/excr.1996.0221

Tash, J. A., David, S. G., Vaughan, E. D., & Herzlinger, D. A. (2001). Fibroblast growth factor-7 regulates stratification of the bladder urothelium. *Journal of Urology*, *166*(6), 2536–2541. https://doi.org/10.1016/S0022-5347(05)65630-3

Terryn, C., Sellami, M., Fichel, C., Diebold, M. D., Gangloff, S., Le Naour, R., Polette, M., & Zahm, J. M. (2013). Rapid method of quantification of tight-junction organization using image analysis. *Cytometry Part A*, *83 A*(2), 235–241. https://doi.org/10.1002/cyto.a.22239

Thayer, S. P., Di Magliano, M. P., Heiser, P. W., Nielsen, C. M., Roberts, D. J., Lauwers, G. Y., Qi, Y. P., Gysin, S., Fernández-del Castillo, C., Yajnik, V., Antoniu, B., McMahon, M., Warshaw, A. L., & Hebrok, M. (2003). Hedgehog is an early and late mediator of pancreatic cancer tumorigenesis. *Nature*, *425*(6960), 851–856. https://doi.org/10.1038/nature02009

The Cancer Genome Atlas Research Network. (2014). Comprehensive molecular characterization of urothelial bladder carcinoma. *Nature*, *507*(7492), 315–322. https://doi.org/10.1038/nature12965

Thievessen, I., Wolter, M., Prior, A., Seifert, H. H., & Schulz, W. A. (2005). Hedgehog signaling in normal urothelial cells and in urothelial carcinoma cell lines. *Journal of Cellular Physiology*, *203*(2), 372–377. https://doi.org/10.1002/jcp.20248

Tomlinson, D. C., Baldo, O., Hamden, P., & Knowles, M. A. (2007). FGFR3 protein expression and its relationship to mutation status and prognostic variables in bladder cancer. *Journal of Pathology*, *213*(1), 91–98. https://doi.org/10.1002/path.2207

Tomlinson, Darren C, L'hôte, C. G., Kennedy, W., Pitt, E., & Knowles, M. A. (2005a). *Alternative Splicing of Fibroblast Growth Factor Receptor 3 Produces a Secreted Isoform That Inhibits Fibroblast Growth Factor-Induced Proliferation and Is Repressed in Urothelial Carcinoma Cell Lines*. https://doi.org/10.1158/0008-5472.CAN-05-1718

Tomlinson, Darren C, L'hôte, C. G., Kennedy, W., Pitt, E., & Knowles, M. A. (2005b). *Alternative Splicing of Fibroblast Growth Factor Receptor 3 Produces a Secreted Isoform That Inhibits Fibroblast Growth Factor-Induced Proliferation and Is Repressed in Urothelial Carcinoma Cell Lines*. https://doi.org/10.1158/0008-5472.CAN-05-1718

Van Den Brink, G. R. (2007). Hedgehog signaling in development and homeostasis of the gastrointestinal tract. In *Physiological Reviews* (Vol. 87, Issue 4, pp. 1343–1375). American Physiological Society. https://doi.org/10.1152/physrev.00054.2006

Varley, C., Hill, G., Pellegrin, S., Shaw, N. J., Selby, P. J., Trejdosiewicz, L. K., & Southgate, J. (2005). Autocrine regulation of human urothelial cell proliferation and migration during regenerative responses in vitro. *Experimental Cell Research*, *306*(1), 216–229. https://doi.org/10.1016/j.yexcr.2005.02.004

Varley, C L, Bacon, E. J., Holder, J. C., & Southgate, J. (2009). FOXA1 and IRF-1 intermediary transcriptional regulators of PPARgamma-induced urothelial cytodifferentiation. *Cell Death and Differentiation*, *16*(1), 103–114. https://doi.org/10.1038/cdd.2008.116

Varley, Claire L., Stahlschmidt, J., Lee, W.-C., Holder, J., Diggle, C., Selby, P. J., Trejdosiewicz, L. K., & Southgate, J. (2004). Role of PPARgamma and EGFR signalling in the urothelial terminal differentiation programme. *Journal of Cell Science*, *117*(10), 2029–2036. https://doi.org/10.1242/jcs.01042

Varley, Claire L. (2004). Role of PPAR and EGFR signalling in the urothelial terminal differentiation programme. *Journal of Cell Science*, *117*(10), 2029–2036. https://doi.org/10.1242/jcs.01042

Varley, Claire L, Garthwaite, M. A. E., Cross, W., Hinley, J., Trejdosiewicz, L. K., & Southgate, J. (2006). PPARγ-regulated tight junction development during human urothelial cytodifferentiation. *Journal of Cellular Physiology*, *208*(2), 407–417. https://doi.org/10.1002/jcp.20676

Varley, Claire Lucy, Stahlschmidt, J., Smith, B., Stower, M., & Southgate, J. (2004). Activation of Peroxisome Proliferator-Activated Receptor-γ Reverses Squamous Metaplasia and Induces Transitional Differentiation in Normal Human Urothelial Cells. *American Journal of Pathology*, *164*(5), 1789–1798. https://doi.org/10.1016/S0002-9440(10)63737-6

Walker, B. E. (1960). Renewal of cell populations in the female mouse. *American Journal of Anatomy*, *107*(2), 95–105. https://doi.org/10.1002/aja.1001070202

Wang, C. C., Tsai, Y. C., & Jeng, Y. M. (2019). Biological significance of GATA3, cytokeratin 20, cytokeratin 5/6 and p53 expression in muscle-invasive bladder cancer. *PLoS ONE*, *14*(8). https://doi.org/10.1371/journal.pone.0221785

Wang, X., Zhang, L., Ding, N., Yang, X., Zhang, J., He, J., Li, Z., & Sun, L. Q. (2015). Identification and characterization of DNAzymes targeting DNA methyltransferase i for suppressing bladder cancer proliferation. *Biochemical and Biophysical Research Communications*, *461*(2), 329–333. https://doi.org/10.1016/j.bbrc.2015.04.033

Wang, Y., Xu, X., Maglic, D., Dill, M. T., Mojumdar, K., Ng, P. K. S., Jeong, K. J., Tsang, Y. H., Moreno, D., Bhavana, V. H., Peng, X., Ge, Z., Chen, H., Li, J., Chen, Z., Zhang, H., Han, L., Du, D., Creighton, C. J., … Liang, H. (2018). Comprehensive Molecular Characterization of the Hippo Signaling Pathway in Cancer. *Cell Reports*, *25*(5), 1304-1317.e5. https://doi.org/10.1016/j.celrep.2018.10.001

Warrick, J. I., Walter, V., Yamashita, H., Chung, E., Shuman, L., Amponsa, V. O., Zheng, Z., Chan, W., Whitcomb, T. L., Yue, F., Iyyanki, T., Kawasawa, Y. I., Kaag, M., Guo, W., Raman, J. D., Park, J.-S., & DeGraff, D. J. (2016). FOXA1, GATA3 and PPARɣ Cooperate to Drive Luminal Subtype in Bladder Cancer: A Molecular Analysis of Established Human Cell Lines. *Scientific Reports*, *6*(1), 38531. https://doi.org/10.1038/srep38531

Watanabe, R., Ui, A., Kanno, S. I., Ogiwara, H., Nagase, T., Kohno, T., & Yasui, A. (2014). SWI/SNF factors required for cellular resistance to DNA damage include ARID1A and ARID1B and show interdependent protein stability. *Cancer Research*, *74*(9), 2465–2475. https://doi.org/10.1158/0008-5472.CAN-13-3608

Weber, J. D., Raben, D. M., Phillips, P. J., & Baldassare, J. J. (1997). Sustained activation of

extracellular-signal-regulated kinase 1 (ERK1) is required for the continued expression of cyclin D1 in G 1 phase. In *Biochem. J* (Vol. 326).

Wezel, F., Pearson, J., Kirkwood, L. A., & Southgate, J. (2013). Differential expression of oct4 variants and pseudogenes in normal urothelium and urothelial cancer. *American Journal of Pathology*, *183*(4), 1128–1136. https://doi.org/10.1016/j.ajpath.2013.06.025

Williams, S. V., Hurst, C. D., & Knowles, M. A. (2013). Oncogenic FGFR3 gene fusions in bladder cancer. *Human Molecular Genetics*, *22*(4), 795–803. https://doi.org/10.1093/hmg/dds486

Williamson, C. T., Miller, R., Pemberton, H. N., Jones, S. E., Campbell, J., Konde, A., Badham, N., Rafiq, R., Brough, R., Gulati, A., Ryan, C. J., Francis, J., Vermulen, P. B., Reynolds, A. R., Reaper, P. M., Pollard, J. R., Ashworth, A., & Lord, C. J. (2016). ATR inhibitors as a synthetic lethal therapy for tumours deficient in ARID1A. *Nature Communications*, *7*(1), 1–13. https://doi.org/10.1038/ncomms13837

Wilsker, D., Patsialou, A., Zumbrun, S. D., Kim, S., Chen, Y., Dallas, P. B., & Moran, E. (2004). The DNA-binding properties of the ARID-containing subunits of yeast and mammalian SWI/SNF complexes. *Nucleic Acids Research*, *32*(4), 1345–1353. https://doi.org/10.1093/nar/gkh277

Wu, D., Asiedu, M., & Wei, Q. (2009). Myosin-interacting guanine exchange factor (MyoGEF) regulates the invasion activity of MDA-MB-231 breast cancer cells through activation of RhoA and RhoC. *Oncogene*, *28*(22), 2219–2230. https://doi.org/10.1038/onc.2009.96

Wu, X. R., Manabe, M., Yu, J., & Sun, T. T. (1990). Large scale purification and immunolocalization of bovine uroplakins I, II, and III. Molecular markers of urothelial differentiation. *The Journal of Biological Chemistry*, *265*(31), 19170–19179. http://www.ncbi.nlm.nih.gov/pubmed/2229070

Yagoda, A. (1979). Phase II trials with cis-dichlorodiammineplatinum(II) in the treatment of urothelial cancer. In *Cancer Treatment Reports* (Vol. 63, Issues 9–10, pp. 1565–1572). https://pubmed.ncbi.nlm.nih.gov/387226/

Yang, Y., Wang, X., Yang, J., Duan, J., Wu, Z., Yang, F., Zhang, X., & Xiao, S. (2019). Loss of ARID1A promotes proliferation, migration and invasion via the Akt signaling pathway in NPC. *Cancer Management and Research*, *Volume 11*, 4931–4946. https://doi.org/10.2147/cmar.s207329

Yin, Y., & Ornitz, D. M. (2020). FGF9 and FGF10 activate distinct signaling pathways to direct lung epithelial specification and branching. *Science Signaling*, *13*(621), eaay4353. https://doi.org/10.1126/scisignal.aay4353

Yoon, J. W., Kita, Y., Frank, D. J., Majewski, R. R., Konicek, B. A., Nobrega, M. A., Jacob, H., Walterhouse, D., & Iannaccone, P. (2002). Gene Expression Profiling Leads to Identification of GLI1-binding Elements in Target Genes and a Role for Multiple Downstream Pathways in GLI1-induced Cell Transformation. *Journal of Biological Chemistry*, *277*(7), 5548–5555. https://doi.org/10.1074/jbc.M105708200

Yu, J., Carroll, T. J., & McMahon, A. P. (2002). Sonic hedgehog regulates proliferation and differentiation of mesenchymal cells in the mouse metanephric kidney. In

Development (Vol. 129, Issue 22, pp. 5301–5312). https://pubmed.ncbi.nlm.nih.gov/12399320/

Yu, W., Datta, A., Leroy, P., O'Brien, L. E., Mak, G., Jou, T. S., Matlin, K. S., Mostov, K. E., & Zegers, M. M. P. (2005). β1-integrin orients epithelial polarity via Rac1 and laminin. *Molecular Biology of the Cell*, *16*(2), 433–445. https://doi.org/10.1091/mbc.E04-05-0435

Yu, Z., Mannik, J., Soto, A., Lin, K. K., & Andersen, B. (2009). The epidermal differentiation-associated Grainyhead gene Get1/Grhl3 also regulates urothelial differentiation. *EMBO Journal*, *28*(13), 1890–1903. https://doi.org/10.1038/emboj.2009.142

Yuan, Z., Goetz, J. A., Singh, S., Ogden, S. K., Petty, W. J., Black, C. C., Memoli, V. A., Dmitrovsky, E., & Robbins, D. J. (2007). Frequent requirement of hedgehog signaling in non-small cell lung carcinoma. *Oncogene*, *26*(7), 1046–1055. https://doi.org/10.1038/sj.onc.1209860

Zanconato, F., Forcato, M., Battilana, G., Azzolin, L., Quaranta, E., Bodega, B., Rosato, A., Bicciato, S., Cordenonsi, M., & Piccolo, S. (2015). Genome-wide association between YAP/TAZ/TEAD and AP-1 at enhancers drives oncogenic growth. *Nature Cell Biology*, *17*(9), 1218–1227. https://doi.org/10.1038/ncb3216

Zhang, K., Zhang, H., Xiang, H., Liu, J., Liu, Y., Zhang, X., Wang, J., & Tang, Y. (2013). TGF-β1 induces the dissolution of tight junctions in human renal proximal tubular cells: Role of the RhoA/ROCK signaling pathway. *International Journal of Molecular Medicine*, *32*(2), 464–468. https://doi.org/10.3892/ijmm.2013.1396

Zhang, W., Gao, Y., Li, P., Shi, Z., Guo, T., Li, F., Han, X., Feng, Y., Zheng, C., Wang, Z., Li, F., Chen, H., Zhou, Z., Zhang, L., & Ji, H. (2014). VGLL4 functions as a new tumor suppressor in lung cancer by negatively regulating the YAP-TEAD transcriptional complex. *Cell Research*, *24*(3), 331–343. https://doi.org/10.1038/cr.2014.10

Zhang, Y., Shen, H., Withers, H. G., Yang, N., Denson, K. E., Mussell, A. L., Truskinovsky, A., Fan, Q., Gelman, I. H., Frangou, C., & Zhang, J. (2017). VGLL4 Selectively Represses YAP-Dependent Gene Induction and Tumorigenic Phenotypes in Breast Cancer. *Scientific Reports*, *7*(1), 6190. https://doi.org/10.1038/s41598-017-06227-7

Zhou, J., Zhu, G., Huang, J., Li, L., Du, Y., Gao, Y., Wu, D., Wang, X., Hsieh, J. T., He, D., & Wu, K. (2016). Non-canonical GLI1/2 activation by PI3K/AKT signaling in renal cell carcinoma: A novel potential therapeutic target. *Cancer Letters*, *370*(2), 313–323. https://doi.org/10.1016/j.canlet.2015.11.006

Zhou, Q., Dai, J., Chen, T., Dada, L. A., Zhang, X., Zhang, W., DeCamp, M. M., Winn, R. A., Sznajder, J. I., & Zhou, G. (2017). Downregulation of PKCζ/Pard3/Pard6b is responsible for lung adenocarcinoma cell EMT and invasion. *Cellular Signalling*, *38*, 49–59. https://doi.org/10.1016/j.cellsig.2017.06.016

Zhu, H. Y., Li, C., Zheng, Z., Zhou, Q., Guan, H., Su, L. L., Han, J. T., Zhu, X. X., Wang, S. Y., Li, J., & Hu, D. H. (2015). Peroxisome proliferator-activated receptor-γ (PPAR-γ) agonist inhibits collagen synthesis in human hypertrophic scar fibroblasts by targeting Smad3 via miR-145. *Biochemical and Biophysical Research Communications*, *459*(1), 49–53. https://doi.org/10.1016/j.bbrc.2015.02.061